Long-Term Ground Response For Borehole Heat Exchangers In Clay

by

Despina M. Zymnis

B.A. and M.Eng. in Civil Engineering (2007)
Trinity College, Cambridge University

S.M. in Geotechnical Engineering and Geomechanics (2009)
Massachusetts Institute ofTechnology

Submitted to the Department of Civil and Environmental Engineering in Partial Fulfillment of the Requirements for the Degree of

Doctor of Philosophy in Civil and Environmental Engineering

at the Massachusetts Institute of Technology
September 2016

Signature of Author: Signature redacted
Department of Civil and Environmental Engineering
June 6, 2016

Certified by: Signature redacted
Andrew J. Whittle
Edmund K. Turner Professor of Civil and Environmental Engineering
Thesis Supervisor

Accepted by: Signature redacted
Heidi Nepf
Donald and Martha Harleman Professor of Civil and Environmental Engineering
Chair, Graduate Program Committee

Long-Term Ground Response For Borehole Heat Exchangers In Clay

by
Despina M. Zymnis

Submitted to the Department of Civil and Environmental Engineering on June 6, 2016
in Partial Fulfillment of the Requirements for the Degree of
Doctor of Philosophy in Civil and Environmental Engineering

ABSTRACT

The use of ground source heat pumps to transfer heat to and from the ground via borehole heat exchangers is among the most energy efficient techniques for space heating and cooling. Designs for seasonal heat exchange systems are becoming increasingly popular in urban environments to reduce energy costs and contribute in decreasing carbon emissions. Broader applications require more careful evaluation of hydro-mechanical behavior of soil to understand the long-term ground response to seasonal cycles of heating and cooling and the impacts on adjacent structures.

The goal of this thesis is to develop reliable methods for studying the coupled thermo-hydro-mechanical (THM) response of clay to long-term seasonal heating and cooling induced by vertical heat exchanger arrays in clay. The research investigates and implements a new class of constitutive models based on the work by Zhang and Cheng (2013). The proposed Tsinghua Thermosoil (TTS) model is capable of simulating the cyclic thermo-mechanical response more realistically than other available constitutive models and can describe the accumulation of volumetric strain due to cyclic heating and cooling. Irreversible deformations in the TTS model are simulated through the conversion of bound to free water, a process that has been studied via laboratory measurements of specific gravity variations with temperature for three clays of differing mineralogy. The thesis describes the calibration of the TTS model in detail, using recently published cyclic thermal tests on Geneva clay (Di Donna and Laloui, 2015).

The TTS model is integrated within a finite difference framework to solve coupled THM problems in 1-D and axisymmetric spaces. The FD simulator is applied to a prototype project that uses an array of borehole heat exchangers for seasonal heating and cooling. The ground conditions represent typical stress history profiles found in Geneva, Switzerland. An extensive parametric study is undertaken to study the long-term THM response of clay for a broad range of heat exchanger design parameters. The results show that significant settlements can be induced due to their long-term operation (i.e., over periods from 10–50 years), especially within normally consolidated clay. The parametric study gives useful guidelines for heat exchanger design and identifies a design space of optimum solutions that meet pre-specified foundation settlement criteria. The study provides a systematic framework for analyzing the long-term THM response of clay to seasonal heating and cooling. These analyses highlight the need to incorporate geotechnical characterization in the design of large borehole heat exchanger arrays to ensure their reliable long-term performance and to minimize adverse effects on adjacent structures.

Thesis Supervisor: Andrew J. Whittle
Title: Edmund K. Turner Professor of Civil and Environmental Engineering

Acknowledgements

I would like to thank Professor Whittle, not only for his tremendous help and support as my academic advisor, but also as my mentor and role-model. Professor Whittle, you have been by my side at some of the best moments of my life and this means the world to me. I would like to thank Professor Germaine (our beloved Dr. G.) for accepting me in his lab even though I hadn't taken his class (something I will regret forever) and for being the amazing person he is. Tufts is very lucky to have you! I would like to thank Professor Einstein for playing such a key role in helping me define the scope of my thesis and for being so supportive from the beginning of this program. I would also like to thank Professor Norford for sharing his expertise in energy in buildings and for so patiently participating in all of our theoretical soil behavior discussions!

Thank you to the Low Carbon Energy University Alliance (LCEUA) for funding my research; it has been an amazing experience working with all our colleagues at Tsinghua University, Cambridge University and EPFL and traveling to all these beautiful countries for our meetings. Special thanks to Zhichao Zhang and Prof. Cheng for their help in analyzing the TTS model, to Dr. Di Donna and Professor Laloui for their help with the Geneva clay lab data and Dr. Olivella for his help with Code_Bright. Thank you to the SMART program for providing me access to the Davinci Cluster. Huge thank you to the Onassis Foundation, the Martin Foundation, Robert A. Brown and Exponent for the fellowships.

I want to thank my friends and colleagues at MIT: Nina thank you for being such a great friend and for supporting me always; Yixing thank you for helping me with my work on numerous occasions and especially thank you for providing the basis for the FD simulators; Antonis I feel very lucky to have been your office-mate and friend for so many years; Zhandos thank you for your invaluable help with all of my computer problems and for taking all of these amazing group photos; Eva, Ivo, Leon, Jana, Amer, Vasso, Mauro, Jialiang, thank you for being such great friends and for making MIT a wonderful place! I would also like to thank Kris Kipp, Jeanette Marchocki, and Kiley Clapper for their tremendous support and also the MIT Libraries for contributing in making MIT one of the best universities in the world.

Thank you to my amazing Boston friends: the Guttels, Miriam, the Moraitakis family and the Greeks at MIT for making Boston feel like my second home! Huge thank you to my friends back home, for having been an integral part of my life for so many years. Pavlo thank you for being by my side.

Thank you to my Zymnis and Nanopoulos families for always believing in me, encouraging me and helping me become the person I am today. Last but not least, thank you to my beloved husband Constantine. This Ph.D. would have never been completed without your love and support. You bring so much joy in my life and this is just the beginning! To Con & Des, for A Sky Full of Stars…

"This may be the last time in your life you can fully immerse yourself in thinking about one thing for an appreciable time. It will be exhilarating both to be fully absorbed and to believe you know more about a subject than anyone else in the world... What I really want to say is do what you enjoy, build a life with your spouse, and don't worry. Things will work out - they always have."

Barrett Hazeltine, "Letters to My 25-year-old Self"

Table of Contents

List of Tables

List of Figures

List of Notations

Lower Case

a	TTS model input constant that controls rate effects
b	Compressibility
c	Specific heat capacity
c_{VH}	Coefficient of consolidation
c_{VT}	Thermal diffusivity of the soil medium
e	Void ratio
$\underset{\sim}{f}$	Body forces vector
f^{w}	Source/sink of water
f^{Q}	Source/sink of heat
h	TTS model input constant that controls hysteretic strains
$\underset{\sim}{j}$	Flux
k	Hydraulic conductivity of soil medium
m_v	Compressibility of soil
m_1	TTS model input constant that controls elastic strain evolution
m_2	TTS model input constant that controls elastic strain evolution and location of reload curve
m_3	TTS model input constant that controls the contribution of volumetric and deviatoric strains on granular temperature production
m_4	TTS model input constant that controls the rate of granular temperature production
m_5	TTS model input constant that controls the amount of thermal volumetric strains produced due to heating and cooling
p	Mean total stress
p'	Mean effective stress
p_w	Excess pore water pressure
q	Shear stress

$\dot{\underset{\sim}{q}}_{cond}$	Heat flux due to conduction
$\dot{\underset{\sim}{q}}_{conv}$	Heat flux due to convection
$\underset{\sim}{q}_w$	Flux of pore water relative to soil skeleton
r	Radial distance
s	Entropy
t	Time
t_{BW}	Thickness of the bound water layer
$\underset{\sim}{u}$	Displacement vector
w	Water content
z	Depth

Upper Case

A_U	Cross-section area of the U-tube in BHE
B_0	TTS model input constant that controls location of VCL
B_1	TTS model input constant that controls slope of VCL
C_α	Secondary consolidation coefficient
C_c	Compressibility index
C_k	Change of hydraulic conductivity with void ratio
E	Specific internal energy
E'	Young's Modulus at effective stress
E'_{oed}	1-D stiffness of the soil skeleton
G_s	Specific gravity of soil
H	Depth of soil layer
H_e	Hydraulic head elevation
H_p	Hydraulic head
$\underset{\sim}{I}$	Unit vector
$\dot{I}_g$	Granular entropy conversion rate
I_p	Plasticity index
K_0	In-situ coefficient of earth pressure at rest
K_e	Secant elastic bulk modulus of the solid skeleton

L_D	Debye length
L_h	Total required length of BHEs
L_{hi}	Length of single BHE
L_T	TTS model input constant that controls the shift of the VCL due to increase in temperature
M	Mass
N_{BHE}	Number of BHEs
Q	Heat flux
Q_{max}	Maximum heat flux
$\dot{R}$	Energy dissipation rate
R	Half-distance between BHE in an array
R_b	Effective borehole thermal resistance
R_{HE}	Radius of heat exchanger
T	Temperature
T_g	Granular Temperature
V	Volume
V_n	Surface traction

Greek

α_{bf}	Input constant for TTS model that controls the conversion of bound to free water during heating
α_r	Input constant for the FD simulator that controls radial spacing
α_{st}	Physico-chemical coefficient of structural volume change caused by a change in temperature
β	Thermal expansion coefficient
γ_w	Unit weight of water
$\underset{\sim}{\varepsilon}$	Strain vector
ε_s	Deviatoric strain
ε_v	Volumetric strain
ε_{ij}^D	Irreversible strain
κ	Intrinsic permeability
λ	Thermal conductivity
μ	Dynamic viscosity of water

ν'	Poisson's ratio at effective stress
ξ	TTS model input constant that controls the coefficient of earth pressure at rest K_0
ρ	Mass density
ρ_d	Dry density of soil medium
$\underset{\sim}{\sigma}$	Total stress vector
$\underset{\sim}{\sigma}'$	Effective stress vector
σ'_p	Preconsolidation pressure
φ	Porosity
ω_e	Elastic potential energy density function

Superscripts

e	Elastic
h	Hysteretic
k	Value at time k

Subscripts

0	Reference initial state
20	At temperature 20°C
ave	Average
bw	Bound water
fw	Free water
lin	Linear
max	Maximum
min	Minimum
NC	Normally consolidated
NH	Input constant for FD simulator that controls number of grid points in vertical direction (=NH+1)
NR	Input constant for FD simulator that controls number of grid points in radial direction (=NR+1)
OC	Overconsolidated
r	Radial
s	Soil skeleton or solid particles

w	Water
z	Vertical

Abbreviations

BHE	Borehole Heat Exchanger
CSL	Critical State Line
COP	Coefficient of Performance
FD	Finite Difference
FE	Finite Element
GSHP	Ground Source Heat Pump
NC	Normally consolidated
OC	Overconsolidated
OCR	Overconsolidation Ratio
SSA	Specific Surface Area
SQD	Specimen Quality Designation
TE	Thermo-Elastic
TEP	Thermo-Elastoplastic
TOL	Tolerance
TTS	Tsinghua ThermoSoil Model
VCL	Virgin Consolidation Line

Chapter 1

Introduction

The use of geothermal heat pumps or ground source heat pumps (GSHP; Banks, 2012) to transfer heat to and from the ground is among the most energy efficient techniques for space heating and cooling. In the absence of external factors, ground temperatures within 100 – 200 m of the surface and below the zone of seasonal influence (approximately top 6m) are relatively constant with depth[1]. Figure 1.1 presents simulations of ground temperature at different depths for a site in Boston, where it can be seen that from depth equal to 6m, the ground temperature remains constant and equal to the mean annual air temperature (in Boston, 10.8°C). The stable ground temperature means that in the summer months the ground will be cooler than the surface air temperature, so heat can be rejected to the ground. Conversely, in winter the ground will be warmer than surface air temperature, and can be used as a heat source. These systems are often termed ground energy systems, ground source heat pump (GSHP) systems or shallow geothermal energy systems.

According to Kelley (2006) the first closed loop GSHP system was installed in 1945 by Robert C. Webber (Indianapolis). In 1948, a large groundwater-based open-loop heating and cooling scheme was installed for an office block in Portland, Oregon (ASME, 1980; Arnold, 2000). Interest in GSHP systems only became attractive following the oil crisis in the 1970's (Kelley, 2006) and with the introduction of low-cost polyethene pipes for the heat exchanger. The first borehole-based, vertical closed-loop systems were reported from Germany and Switzerland in 1980 (Sanner, 2001, 2006) and from Norway in 1985 (Midttømme et al., 2008). In Switzerland, in 2000, one-third of all newly built single-family homes utilized a heat pump, and of these, 40% were ground-sourced (Rybach and Sanner, 2000). In the past twenty years the installation of GSHP systems has increased significantly in the United States: 28000 GSHPs were installed

[1] In the UK, ground temperature increases by only 1–2°C for every 100 m depth as a result of geothermal gradients.

annually in 1994, rising to 50000 units per year by 2008 (Bouma, 2002; Lund et al., 2008). A total of up to 750000 units are believed to be currently in operation, with strong growth in the governmental and public sectors (Bouma, 2002; Lund et al., 2008).

GSHP systems are divided into two main categories: open-loop and closed-loop. Open-loop systems (Preene, 2008) pump groundwater from subsurface aquifers. The groundwater is then passed through a heat transfer system, before being disposed of (at a different temperature from before) either to waste or by re-injection back into the ground (Figure 1.2). In contrast, closed-loop systems circulate fluid (usually water with antifreeze such as ethylene glycol), through a closed loop of pipes buried in the ground (Figure 1.3). The circulating fluid passes through a heat transfer system at the surface, and is then re-circulated back through the buried ground loop, to exchange heat with the surrounding soil or rock.

Following the convention of Geoexchange BC (2007a) a ground energy system can be subdivided into three key elements (Figures 1.2 and 1.3):

a) the source side (the below-ground elements, such as boreholes, horizontal ground loops and energy foundations)
b) the load side (the building, its controls, users and the thermal load that results)
c) the heat transfer system (the heat pumps and associated control systems).

Typically the source side involves a system of absorber pipes arranged in ground loops installed in horizontal trenches or in the form of HDPE U-shaped tubes (Figure 1.4) inserted in boreholes that are filled with backfill or grout. 'Energy foundations' constitute a separate category of ground heat exchangers, where the absorber pipes are incorporated into foundation elements such as piles and tunnel linings (Figure 1.5). Because of the large number of boreholes typically required for closed-loop systems, and the need to arrange them in a grid pattern to maintain a minimum horizontal separation between them, significant site areas may be needed to accommodate the borehole array. The source side has a huge impact on the capital cost, operating costs and the efficiency of GSHP systems. Sound geotechnical design is therefore essential to the efficiency and economic effectiveness of ground energy systems.

The heat transfer system is the link between the source and the load side and takes the form of one or more heat pumps. A heat pump is a mechanical device that uses a

refrigerant vapor compression cycle to transfer heat efficiently from one reservoir to another. Although electricity is still needed in order to run the heat pump, for each 1 kW of electricity used to run the heat pump some 3-4 kW of heat are typically produced, thus providing 300-400% efficiency. Heat pumps are characterized by the coefficient of performance, COP:

$$COP=\frac{\text{Heat provided by heat pump}}{\text{Energy required to run heat pump}} \quad (1.1)$$

The efficiency of a heat pump strongly depends on the difference between the temperature of the carrier fluid entering the heat pump and that exiting the heat pump, since the higher the difference the more electricity is required to run the heat pump. Therefore temperature of the water entering the building should never be above 35°C - 45°C while the extraction temperature around the heat exchanger should not fall below 0-5°C (Brandl, 2006). GSHP systems are characterized by high COPs (typically COP = 3-5) compared to air source heat pumps that have COP = 2-3 and electric heaters that have COP = 1.

The GSHP technology has been proven to work successfully in a variety of projects across the world. It is most efficient in climates where there are large seasonal temperature variations and where both heating and cooling of buildings are required. Ideally, the net heat input to the ground should be equal to the net heat extracted over an annual cycle. Over a given period of time, any difference between the heat input and the heat extracted will result in a change in the average temperature of the ground, which could cause the system to degrade over a period of several years, until it reaches a point it cannot provide the design heating and cooling loads. It is rare that buildings have an annual balance between the total energy required for heating and the total energy required for cooling. Hybrid installations, coupled with control systems to ensure equal amounts of heating and cooling are exchanged with the ground annually, represent an ideal solution to the thermal imbalance problem. In hybrid systems, the GSHP system provides a portion of the thermal load, supplemented by other systems at times of peak demand, resulting in the installation of lower-capacity ground elements. This approach can significantly reduce capital costs while still achieving lower energy costs and meet target reductions in CO_2 emissions while maintaining a constant average ground temperature.

The energy consumed in buildings amounts to 40% of the carbon dioxide emissions in the USA (DOE, 2012), mainly because traditional heating and cooling systems use a large amount of fossil fuels and generate significant amounts of greenhouse emissions. Significant environmental and economic benefits will thus result from the reductions of energy used in buildings. In Europe, the Energy Performance of Buildings Directive (CEC, 2002) and resulting national guidance (ODPM, 2006) establish requirements for the planning of new and refurbished buildings to ensure that appropriate energy conservation measures are adopted, and that alternative sources of energy are considered. Ground energy systems represent one subset of low or zero carbon (LZC) technologies, since by interacting with the thermal resource of the ground beneath or around a building can allow significant reductions in fossil-based energy use.

Drivers promoting the use of ground energy systems (Table 1.1) suggest that the rate at which GSHP systems are installed will increase, with the technology becoming more and more attractive in financial terms as energy prices rise. Extending the current GSHP system scale from the individual building to the district and city scale will be very beneficial for the environment. For example, the GSHP technology applied at large-scale (e.g., via energy tunnels) could be one way to reduce the very high temperatures (30°C - 32°C) reported in London Underground stations in the summer. In fact, Adam and Markiewicz (2009) report that several infrastructure projects in Austria are already coupled with GSHP systems (e.g., the Lainzer tunnel that has been operating successfully since 2004). Zhang et al. (2014) conclude that an optimized GSHP district heating system, where surplus heating capacity is shared among neighboring buildings could meet the heating demand of all buildings in the City of Westminster. It is evident that as GSHP systems increase in size and become part of the urban planning process it is essential to have an in-depth understanding of all the long-term environmental impacts in the ground.

Coupled thermo-hydro-mechanical (THM) processes take place as a result of a GSHP system operating in saturated clay. Laboratory measurements show that temperature changes can significantly alter the properties of clays and cause thermally induced movements (Baldi et al., 1991; Campanella and Mitchell, 1968; Hueckel and Baldi, 1990; Abuel-Naga et al., 2006; Cekerevak and Laloui, 2004). Cyclic heating and

cooling can generate long-term accumulation of thermal strains in clays (Campanella and Mitchell, 1968; Hueckel et al., 1998; Di Donna and Laloui, 2015). Cyclic thermal loads imposed on clays due to the continuous operation of GSHP installations can therefore result in significant long-term settlements, which could adversely affect the overlying structures or adjacent foundations. Existing thermo-elastic constitutive models (Smith and Booker, 1989; Booker and Savvidou, 1985) cannot describe the irreversible thermal strains and hence, more advanced thermo-elastoplastic constitutive models must be used (Hueckel and Borsetto, 1990; Hueckel and Baldi, 1990; Laloui and Francois, 2009; Zhang and Cheng, 2013). When a saturated soil is heated (in the range of interest), all of the constituent components (soil particles and water) expand. Temperature changes also affect the strength of bonds between the adsorbed water and clay particles, leading to changes in the balance of physico-chemical forces[2] between the clay particles and inducing strains within the soil skeleton. It is evident that coupled THM analyses are necessary for fundamental investigations and detailed assessments of GSHP systems, especially of large complex systems. Preene and Powrie (2009) suggest that these studies will form the basis of future tools and programs needed for the routine design of GSHP systems.

The main sources of uncertainty in GSHP systems are related to the selection of ground properties and estimation of building thermal loads. A GSHP system might be unable to deliver the peak heating or cooling load for which it was designed, due to poor selection of ground thermal parameters and design of the ground heat exchanger. Typically, the cost of obtaining site-specific thermal parameters such as initial temperature, thermal conductivity and specific heat capacity of the ground may be substantial, and for small-scale systems thermal properties are often selected from generic correlations reported in the literature rather than from site-specific field or laboratory measurements. However, for large-scale projects the benefits of obtaining relevant in situ thermal parameters (using thermal response tests) are being increasingly recognized (Marcotte & Pasquier, 2008a). Long-term failures can result if there is a significant

[2] Physico-chemical forces correspond to the net effects of van der Waals attraction and electrostatic repulsion between charged clay particles. Lu and Likos (2006) describe the net inter-particle force (that controls deformations and shear strength properties) as the sum of the conventional (Terzaghi effective stress) and the physico-chemical stresses.

thermal imbalance over an annual cycle, resulting in a gradual increase or decrease in the ground temperature or a gradual reduction in system efficiency. For most of these failure modes, increased involvement of geotechnical and hydrogeological design and modeling skills is a primary way to reduce these risks. Preene and Powrie (2009) suggest that any large-scale adoption of ground energy systems requires detailed consideration of overall heat balance and interaction effects, and some form of regulatory intervention such as specific licensing requirements for ground energy systems. As ground energy systems become more popular, it thus will become increasingly necessary, especially in congested urban areas to consider interactions between adjacent ground energy systems.

Current GSHP design methods appear to be written primarily for building services engineers where the mechanical and electrical elements (pipework, heat pumps, building thermal loads) are dealt with in much more detail than the geotechnical elements (e.g., the ASHRAE recommendations, Kavanaugh and Rafferty, 1997). Computer simulations very often do not consider the mechanical properties of the soil and if they do, they assume thermo-elastic properties. As GSHP installations increase in size, detailed consideration of the likely long-term performance and sustainability of these systems through the development and application of sophisticated, coupled THM models is of major importance. The use of appropriate constitutive models able to accurately describe the thermo-mechanical response of the ground is essential for realistic prediction of the long-term ground response.

The focus of this thesis is the in-depth study of the THM response of clay to long-term seasonal heating and cooling induced by the continuous operation of a GSHP installation. The research focuses on borehole heat exchangers where the thermo-hydro-mechanical response of the surrounding clay is simulated using an advanced constitutive model, referred to as the Tsinghua ThermoSoil (TTS) model (Zhang and Cheng, 2013). The model is calibrated using data from recent laboratory experiments performed by colleagues at EPFL (Di Donna and Laloui, 2015) for a low plasticity Geneva clay. We develop a simple numerical simulator to investigate the performance of a single borehole heat exchanger (part of a larger array of BHEs). Numerical analyses are then performed to understand how the seasonal heating and cooling loads (and BHE spacing) affect ground deformations for long-term operation for a hypothetical GSHP system (operating

within the footprint of a building) at a site in Geneva, Switzerland. This model is the first study of its kind to integrate the role of geotechnical factors in the long-term performance of a GSHP system intended for urban application.

1.1 Thesis Outline

Chapter 2 presents a thorough literature review on different aspects of this study, related to heat transport in saturated soil and coupled thermo-hydro-mechanical response of clay. The chapter summarizes the simplified field equations for THM analyses in saturated clay with conductive heat transfer (i.e., zero convection case) and reviews key experimental results of the thermo-mechanical behavior of clay and the current understanding of thermo-hydro-mechanical constitutive behavior of clay. The chapter concludes with the preliminary investigation of the long-term effects of seasonal heating and cooling of clay from a borehole heat exchanger array.

Chapter 3 describes the formulation and key concepts of the 'transient-elastic' Tsinghua ThermoSoil (TTS) model developed by Zhang and Cheng (2013). The results from a program of laboratory experiments undertaken in order to measure the conversion of bound water to free water when heating a clay are also included in this chapter. Detailed calibration techniques have been proposed as part of this Ph.D. and are illustrated using recently measured cyclic thermal tests on Geneva Clay (Di Donna and Laloui, 2015).

Two numerical simulators, in the 1-D and axisymmetric space, were developed in order to study the fully coupled thermo-hydro-mechanical response of clays using the TTS model. Chapter 4 presents their formulation and validation against a reference multi-phase finite element program, Code_Bright (for thermo-elastic clay properties). Moreover, comparisons of THM clay response when assuming thermo-elastic and thermo-elastoplastic properties highlight the need to use reliable thermo-elastoplastic models when simulating heat exchangers in clay.

The axisymmetric simulator was then employed to simulate long-term response of clay around a single BHE using a model profile with Geneva clay. Chapter 5 includes an

in-depth parametric study carried out to study different spacing of BHEs and heating and cooling loads. The predicted ground response is then used to assess suitable design limits for BHE arrays at this site.

Chapter 6 provides a summary of the work, with conclusions and recommendations for future research.

Driver	Detail	Notes
Energy conservation	Modern building design focuses on reducing the energy demand of buildings by a variety of active and passive measures (Boyle, 2005; Thorne, 2006). Ground energy systems offer the chance to reduce significantly the energy consumed to heat and cool a building.	Ground energy systems do require external power in order to operate (unlike, for example, wind turbines and some forms of renewable energy). However, they are very energy efficient. Systems using heat pumps typically can provide 3–5 units of heat energy for every unit of electrical energy consumed (this is expressed as a coefficient of performance (COP) of 3–5).
Environment	Ground energy systems are classified as low or zero carbon (LZC) systems, and can offer significant reduction in carbon emissions compared with traditional systems.	At present buildings are responsible for around half of the UK's carbon emissions (DTI, 2006).
Economics	Ground energy systems can offer significantly lower annual operating costs than traditional heating and cooling systems.	The economic advantage stems mainly from the reduced energy consumption.
Regulation	In the UK and the rest of Europe, regulations applicable to significant new and refurbished buildings require that designers consider ways in which at least 10% of the building energy demand can be met from LZC sources.	The requirement to consider potential use of LZC systems for buildings is detailed in UK regional and national policy
Change in building needs	There is an increasing expectation by many users of commercial buildings that some form of cooling will be provided to control building temperatures. Ground energy systems can be an effective way of providing comfort cooling.	The combination of change in office working practices (with increased density of heat-generating office equipment) and predicted increases in summer temperatures, means that, without cooling, thermal discomfort in buildings will be a significant problem in the future.
Space and practicality	Traditional cooling systems typically require some plant space at roof level, for cooling towers or other plant that rejects building heat to air. Ground energy systems used for cooling can be entirely located in basement plant rooms, freeing up additional space that can be sold or let.	Space on the upper floors of a building may often be the most expensive or desirable. The value released by avoiding the need for roof-level plant rooms can potentially be a significant factor in the financial assessment of cooling systems based on the ground energy concept.

Table 1.1: Drivers for the use of GSHP systems (Preene & Powrie, 2009)

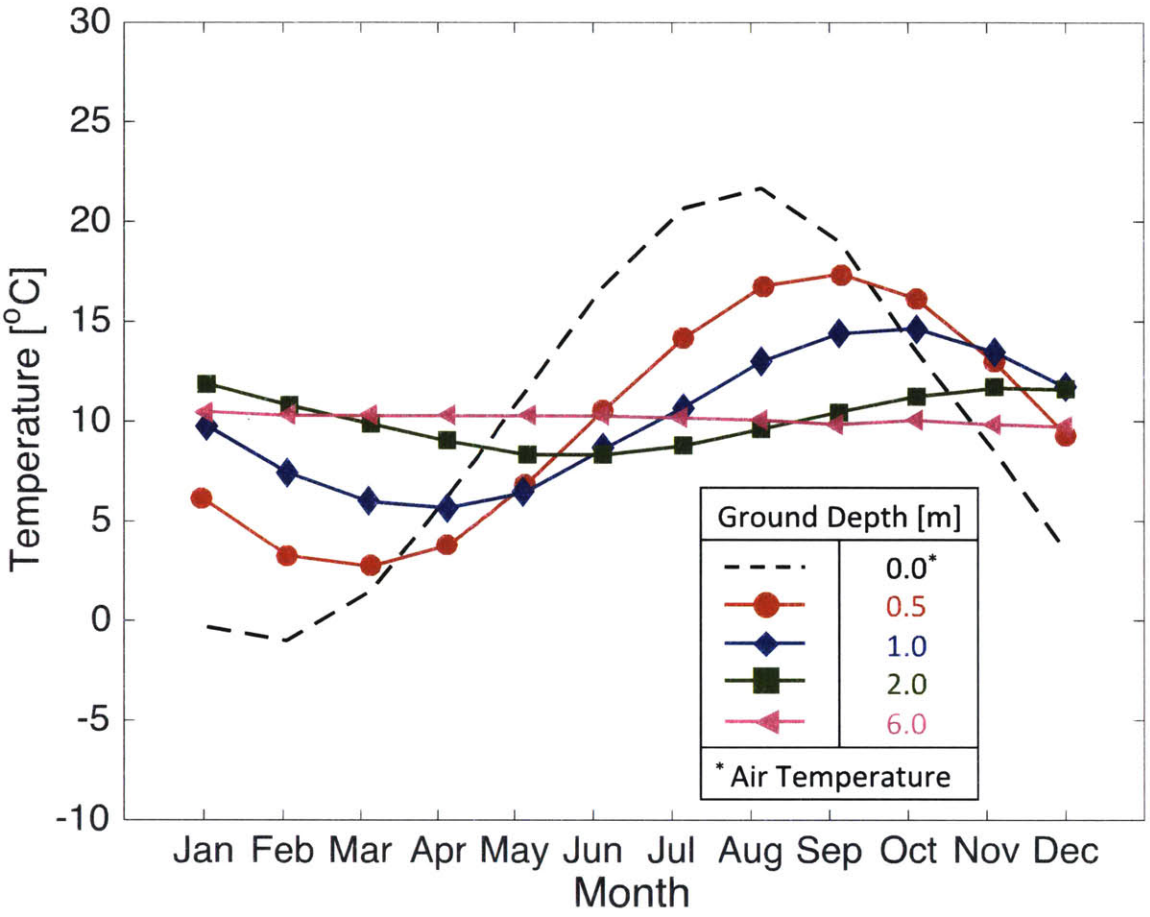

Figure 1.1: Simulated surface annual air temperature and ground temperature in Boston (after www.concord.org)

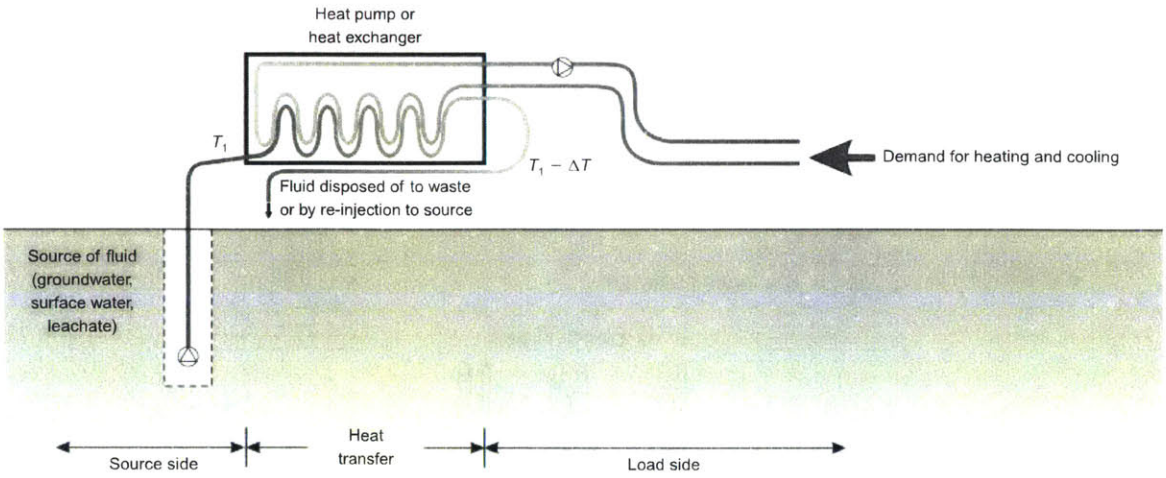

Figure 1.2: Open-loop ground energy system (Preene & Powrie, 2009)

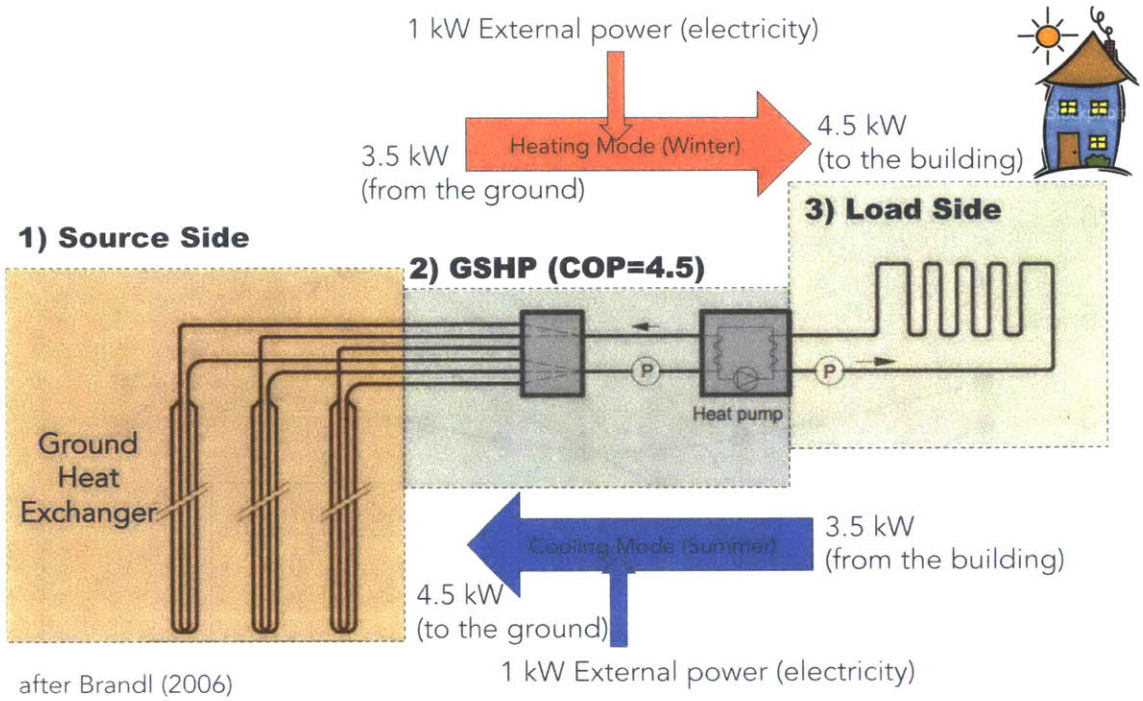

Figure 1.3: Closed-loop ground energy system (after Brandl, 2006)

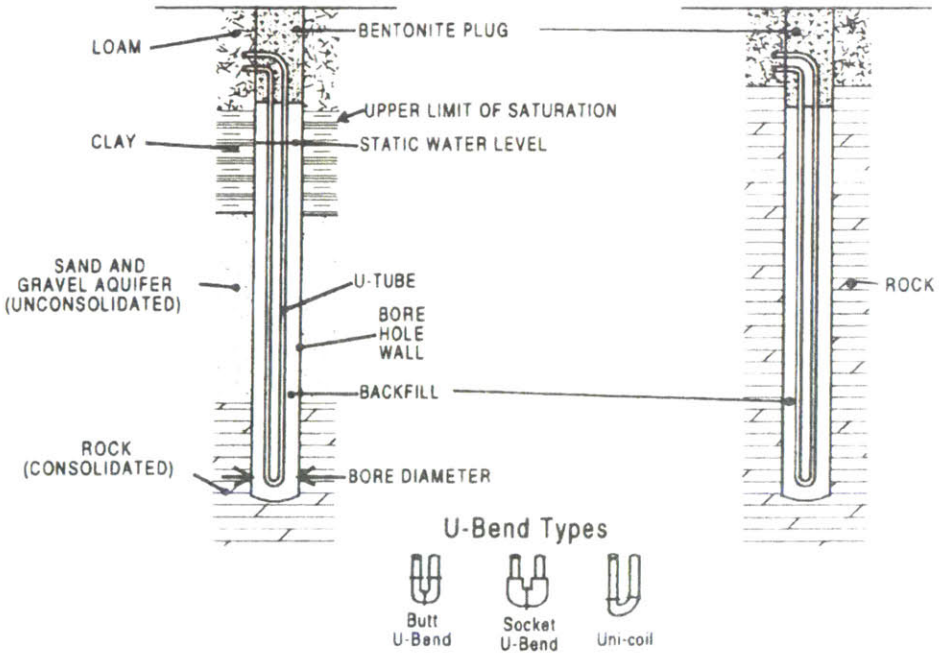

Figure 1.4: Typical BHE with U-tube installations (Kavanaugh and Rafferty, 1997)

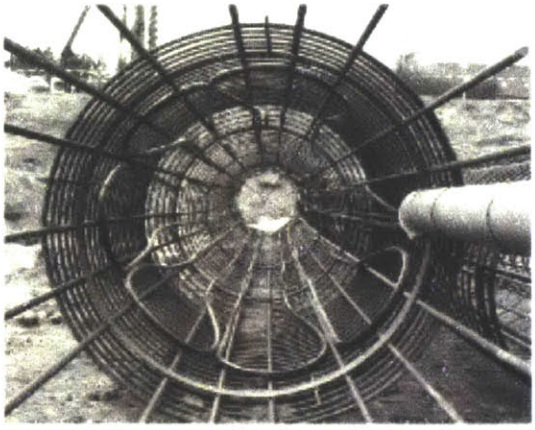

a) Energy Pile (Brandl, 2006)

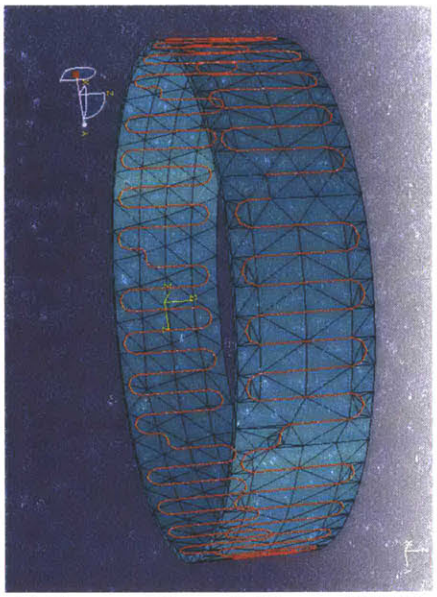

b) Energy Tunnel (Soga, 2011)

Figure 1.5: Examples of energy foundations

Chapter 2
Background Information

2.1 Introduction

This chapter reviews the literature pertinent to different aspects of this study, beginning in Section 2.2 with an introduction to the transport of heat in multi-phase soil (conduction and convection). Section 2.3 introduces the concept of thermo-hydro-mechanical (THM) coupling and presents the formulation for the case of saturated soils, based on general field equations. Although the thermal problem (temperature regime) can be solved independent of hydraulic and mechanical soil properties, it has a much more pronouncing coupling effect on the hydraulic and mechanical response of clay (e.g., affecting pore pressure generation and inducing strains and deformations within the soil skeleton). Section 2.4 presents the thermal properties of soils, while Section 2.5 introduces the dependence of the properties of water on temperature (i.e., the thermo-hydraulic coupling). Important experimental results to study the thermo-mechanical response of clay are summarized in Section 2.6, while Section 2.7 reviews current understanding of thermo-hydro-mechanical constitutive behavior of clay. The chapter concludes with the preliminary investigation of available thermo-poroelastic and thermo-poroelastoplastic models, as well as a summary of the study undertaken by Zymnis and Whittle (2014) to analyze the long-term effects of seasonal heating and cooling of clay from a borehole heat exchanger array, using the HB90 constitutive model (Hueckel and Borsetto, 1990) for clay.

2.2 Transport of Heat in Multi-Phase Soil

Heat transport in porous media takes place via many mechanisms with the three most important being: 1) conduction, 2) convection and 3) latent heat of vaporization due to phase change of water. Radiation can be neglected since its contribution is minimal in soils (less than 1% of the overall heat transfer in sands; Rees et al., 2000). The process of heat conduction involves heat transfer from one region of a medium to the next via

molecular motion, without visible motion of the medium. According to Fourier's law, the heat flux density $\dot{q}_{cond}$ due to conduction can be expressed by:

$$\dot{q}_{cond} = -\lambda \nabla T \tag{2.1}$$

where λ is the thermal conductivity of the medium and ∇T is the gradient of temperature.

During heat convection, heat is transferred via circulation flows. It is assumed that the solid phase is static and hence, convection effects are due to liquid and vapor transport. The heat flux generated by liquid convection, $\dot{q}_{w,conv}$ is given by:

$$\dot{q}_{w,conv} = c_w \rho_w \dot{u}_w \left(T - T_0\right) \tag{2.2}$$

where c_w is the specific heat capacity of water [J/kg °C], ρ_w is the mass density of water, $\dot{u}_w$ is the vector for velocity of water, and T_0 a reference temperature [°C].

Latent heat of vaporization takes place due to phase change of the water and should be considered when accounting for transport of vapor in the soil medium. This is beyond the scope of the current study, which focuses on fully saturated soils where temperatures are controlled in order to avoid vaporization.

As discussed in Chapter 1, GSHP systems are most cost effective for seasonal operation where there is an annual energy balance between heating and cooling. For seasonal heat exchange, low-permeability ground is favorable since water convection is minimal (i.e., there is minimal loss of heat through convection and hydraulic gradients; Brandl, 2006). In this case, the average temperature of the ground remains constant and the efficiency of the system should not deteriorate over the long-term. In contrast, if the GSHP is used solely for heating, the temperature of low-permeability ground will decrease, due to heat extraction from the ground leading to long-term deterioration in performance. This situation favors permeable soils and large hydraulic gradients since water convection can replenish the heat extracted from the ground during winter.

2.3 Coupled Thermo-Hydro-Mechanical (THM) Response of Clay

Several geotechnical problems involving heat transport, such as energy storage in the ground and the storage and disposal of high-level radioactive waste, can only be

solved by connecting thermal effects with the theory of hydro-mechanical (consolidation) coupling. Temperature is identified as a new state variable and the original hydro-mechanical consolidation problem is extended to account for non-isothermal processes, assuming thermal equilibrium between the solid and liquid phases. The field equations governing the non-isothermal consolidation of a saturated soil are based on fundamental principles presented by Gens (2010):

1) Mass balance of solid

$$\frac{\partial}{\partial t}\left[\rho_s(1-\phi)\right]+\nabla \underset{\sim}{j}_s = 0 \qquad (2.3a)$$

where φ is the porosity of the soil medium, ρ_s is the mass density of solid particles, $\underset{\sim}{j}_s$ is the flux of solid and is equal to the flux relative to a fixed reference system:

$$\underset{\sim}{j}_s = (1-\phi)\rho_s \underset{\sim}{\dot{u}} \qquad (2.3b)$$

where $\underset{\sim}{\dot{u}}$ is the time derivative of displacement (i.e., velocity). By combining eqns. 2.3a and 2.3b:

$$(1-\phi)\frac{\partial \rho_s}{\partial t}-\rho_s\frac{\partial \phi}{\partial t}+(1-\phi)\rho_s \nabla \cdot \underset{\sim}{\dot{u}} = 0$$

$$\therefore \frac{\partial \phi}{\partial t} = \frac{1}{\rho_s}\left[(1-\phi)\frac{\partial \rho_s}{\partial t}\right]+(1-\phi)\nabla \cdot \underset{\sim}{\dot{u}} \qquad (2.3c)$$

2) Mass balance of water

$$\frac{\partial}{\partial t}\left[\rho_w \phi\right]+\nabla \cdot \underset{\sim}{j}_w = f^w \qquad (2.4a)$$

where ρ_w is the mass density of water, f^w is a source/sink term and $\underset{\sim}{j}_w$ is the flux of water:

$$\underset{\sim}{j}_w = \phi \rho_w \underset{\sim}{\dot{u}} - \rho_w \cdot \underset{\sim}{q}_w \qquad (2.4b)$$

In this equation, the first term is equal to the flux relative to a fixed reference system and the second term corresponds to flux relative to the solid particles. By combining equations 2.4a, 2.4b and 2.3c:

$$\phi\frac{\partial \rho_w}{\partial t}+\frac{\rho_w}{\rho_s}(1-\phi)\frac{\partial \rho_s}{\partial t}+\rho_w \nabla \cdot \underset{\sim}{\dot{u}} = \nabla \cdot \left(\rho_w \cdot \underset{\sim}{q}_w\right)+f^w \qquad (2.4c)$$

3) Mass density of water and solid particles:

$$\rho_w = \rho_{w0} \exp\left[b_w (p_w - p_{w0}) + \beta_w (T - T_0)\right] \tag{2.5a}$$

$$\therefore \frac{\partial \rho_w}{\partial t} = \rho_w \left(\beta_w \frac{\partial T}{\partial t} + b_w \frac{\partial p_w}{\partial t} \right) \tag{2.5b}$$

$$\rho_s = \rho_{s0} \exp\left[b_s (p - p_0) + 3\beta_s (T - T_0)\right] \tag{2.6a}$$

$$\therefore \frac{\partial \rho_s}{\partial t} = \rho_s \left(3\beta_s \frac{\partial T}{\partial t} + b_s \frac{\partial p_s}{\partial t} \right) \tag{2.6b}$$

where $p = \sigma_{kk} / 3$ is the mean total stress, β_w is the volumetric thermal expansion coefficient of water, β_s is the linear thermal expansion coefficient of the solid particles, b_w and b_s are the compressibilities of water and solid particles, respectively, p_w is pore pressure, T is temperature and subscript 0 corresponds to a reference state. By incorporating eqns. 2.5b and 2.6b into eqn. 2.4c and dividing with ρ_w:

$$\phi\left[\beta_w \frac{\partial T}{\partial t} + b_w \frac{\partial p_w}{\partial t}\right] + (1-\phi)\left[3\beta_s \frac{\partial T}{\partial t} + b_s \frac{\partial p_s}{\partial t}\right] + \underset{\sim}{\nabla} \cdot \dot{\underset{\sim}{u}} = \frac{\underset{\sim}{\nabla} \cdot \left(\rho_w \cdot \underset{\sim}{q}_w\right)}{\rho_w} + \frac{f^w}{\rho_w} \tag{2.7a}$$

The current formulation assumes that the solid particles and water are incompressible (i.e., $b_w \approx b_s \approx 0$) such that there is no volume change in the soil particles due to mean total stress or in the pore water due to pressure. Using this approximation:

$$\left[\phi\beta_w + (1-\phi)3\beta_s\right]\frac{\partial T}{\partial t} + \underset{\sim}{\nabla} \cdot \dot{\underset{\sim}{u}} = \frac{\underset{\sim}{\nabla} \cdot \left(\rho_w \cdot \underset{\sim}{q}_w\right)}{\rho_w} + \frac{f^w}{\rho_w} \tag{2.7b}$$

4) Strain-deformation relations (infinitesimal strain assumption) for a continuous solid are:

$$\varepsilon_{ij} = \frac{1}{2}\left(\frac{\partial u_i}{\partial x_j} + \frac{\partial u_j}{\partial x_i} \right) \tag{2.8a}$$

where $\underset{\sim}{\varepsilon}$ is the strain vector and $\underset{\sim}{u}$ is the displacement vector. It follows that:

$$\varepsilon_v = \varepsilon_{kk} = \underset{\sim}{\nabla} \cdot \underset{\sim}{u} \tag{2.8b}$$

where ε_v is volumetric strain and $\underset{\sim}{\nabla} \cdot \underset{\sim}{u}$ is the gradient of the displacement vector.

By combining equations 2.7b and 2.8b, assuming that the spatial variability of the density of water is negligible (i.e., $\underset{\sim}{\nabla}\cdot\left(\rho_w \cdot \underset{\sim}{q}_w\right)=\rho_w \underset{\sim}{\nabla}\cdot \underset{\sim}{q}_w$) and assuming that the fluid sink/source term is zero (i.e., $f^w = 0$):

$$\left[\phi\beta_w+(1-\phi)3\beta_s\right]\frac{\partial T}{\partial t}+\varepsilon_v=\underset{\sim}{\nabla}\cdot \underset{\sim}{q}_w \tag{2.9}$$

where $\beta = 3\beta_s(1-\phi)+\beta_w\phi$ is the volumetric thermal expansion of the soil medium.

5) The flux of water $\underset{\sim}{q}_w$ [L/T] is well described by Darcy's Law:

$$\underset{\sim}{q}_w=-k\underset{\sim}{\nabla}\left(H_e+\frac{p_w}{\gamma_w}\right) \tag{2.10}$$

where k is a scalar corresponding to the hydraulic conductivity of the soil medium [L/T] (homogeneity is assumed), H_e is the hydraulic head elevation and γ_w the unit weight of water. Combining equations 2.9 and 2.10b results in the following expression[3]:

$$\frac{k}{\gamma_w}\nabla^2 p_w=-\frac{\partial \varepsilon_v}{\partial t}-\beta\frac{\partial T}{\partial t} \tag{2.11}$$

6) Internal energy balance for the medium

$$\frac{\partial}{\partial t}\left[E_s\rho_s(1-\phi)+E_w\rho_w\phi\right]+\underset{\sim}{\nabla}\cdot\left(\underset{\sim}{\dot{q}}_{cond}+\underset{\sim}{\dot{q}}_{s,conv}+\underset{\sim}{\dot{q}}_{w,conv}\right)=f^Q \tag{2.12}$$

where E is specific internal energy and subscripts s and w correspond to solid particles and water, respectively: $\underset{\sim}{\dot{q}}_{cond}$ is the heat flux density due to conduction in the soil medium, $\underset{\sim}{\dot{q}}_{s,conv}$ is the heat flux density due to convection of the solid particles, $\underset{\sim}{\dot{q}}_{w,conv}$ is the heat flux density due to convection of water and f^Q is a heat source/sink term. The specific internal energy of the solid particles and water in a saturated soil can be expressed by:

$$E_s = c_s T \tag{2.13a}$$

$$E_w = c_w T \tag{2.13b}$$

where c_s and c_w are the specific heat capacities of the solid particles and water, respectively. By incorporating equations 2.13a and 2.13b into equation 2.12 and

---

[3] $\nabla^2 H_e = 0$

assuming that heat in saturated clay is mainly transported due to conduction (i.e., $\dot{\underset{\sim}{q}}_{s,conv} \approx \dot{\underset{\sim}{q}}_{w,conv} \approx 0$):

$$\left[c_s\rho_s(1-\phi)+c_w\rho_w\phi\right]\frac{\partial T}{\partial t}+\nabla\cdot\left(\dot{\underset{\sim}{q}}_{cond}\right)=f^Q \tag{2.14}$$

By combining equation 2.14 with Fourier's law for heat conduction (cf., equation 2.1) the following equation is obtained for the heat conduction in clays:

$$c_{VT}\nabla^2 T=\frac{\partial T}{\partial t}-\frac{f^Q}{\phi\rho_w c_w+(1-\phi)\rho_s c_s} \tag{2.15a}$$

where c_{VT} [L^2T^{-1}] is the thermal diffusivity of the soil medium:

$$c_{VT}=\frac{\lambda}{\phi\rho_w c_w+(1-\phi)\rho_s c_s} \tag{2.15b}$$

7) Momentum balance for the soil medium (compression positive)

$$\underset{\sim}{\nabla}\cdot\underset{\sim}{\sigma}+\underset{\sim}{f}=0 \tag{2.16}$$

where $\underset{\sim}{\sigma}$ are total stresses and $\underset{\sim}{f}$ are body forces.

8) For saturated soils, it is generally assumed that all deformation (and shear strength properties) are controlled by changes in effective stresses. Assuming that the solid particles and water are incompressible (i.e., $b_w \approx b_s \approx 0$) the standard definition of (Terzaghi, 1921) effective stress is:

$$\underset{\sim}{\sigma}'=\underset{\sim}{\sigma}-p_w\underset{\sim}{I} \tag{2.17}$$

where $\underset{\sim}{\sigma}'$ is the effective stress vector, $\underset{\sim}{\sigma}$ is total stress and p_w is pore pressure and $\underset{\sim}{I}$ is the unit vector.

9) There are many possible constitutive laws connecting strain and temperature variations to changes in effective stresses. The simplest is to consider thermo-elastic soil properties:

$$\underset{\sim}{\sigma}'=\left[\frac{E'\nu'}{(1+\nu')(1-2\nu')}\varepsilon_v+\left(\frac{E'}{1-2\nu'}\right)\beta_s T\right]\underset{\sim}{I}+\frac{E'}{(1+\nu')}\underset{\sim}{\varepsilon} \tag{2.18}$$

where E' is the Young's Modulus and ν' is the Poisson's ratio at effective stress.

Figure 2.1 summarizes the main thermo-hydro-mechanical processes that take place in saturated clay. From Equation 2.15 it is evident that the thermal problem can be solved largely independent from the hydraulic and mechanical problems (coupling between mechanical and thermal properties is associated with clays in heat conduction,

while the hydraulic and thermal regimes are ruled mainly through heat convection, which is ignored in the current analyses).

It is interesting to note the similarity between thermal diffusivity c_{VT} and the coefficient of consolidation c_{VH} [L^2T^{-1}] controlling coupled fluid flow and deformation in saturated soils:

$$c_{VH} = \frac{kE'_{oed}}{\gamma_w} \tag{2.19}$$

where k [LT^{-1}] is the isotropic coefficient of hydraulic conductivity and E'_{oed} is the 1-D stiffness of the soil skeleton[4]. The resulting change in temperature has profound effects in both the hydraulic and the mechanical components. In saturated soils, heating induces thermal expansion of the pore water and the soil skeleton resulting in the buildup of thermal pore pressures (eqn. 2.11), reduction of the in situ effective stress (eqn. 2.17), and subsequent volume changes due to the dissipation of pore pressure and heat transfer. Thermal effects also have a direct impact on the mechanical problem through the constitutive relations (eqn. 2.18) resulting in the generation of volumetric strains and deformations of the soil skeleton. Although the thermal problem is largely decoupled, the thermo-hydro-mechanical coupling enables us to understand the complex processes that take place, such as the dissipation of thermally-induced pore pressures with time and the changes in the mechanical properties of the soil with temperature.

Campanella and Mitchell (1968) link thermal volumetric strains to the thermal dilation coefficients of the soil constituents, the corresponding porosities and the compressibility of water. The Authors suggest that during a drained heating experiment under constant stress conditions, volumetric strains are produced due to a change in temperature:

$$\dot{\varepsilon}_v = \frac{\Delta V_{DR} - \left(\beta_w V_w \Delta T + \beta_s V_s \Delta T\right)}{V} \tag{2.20}$$

where ΔV_{DR} is the volume of pore water drained from the sample, and V_w, V_s and V are the volumes of pore water, solid skeleton and soil specimen, respectively. The Authors

[4] $E'_{oed} = \frac{E'(1-\nu')}{(1+\nu')(1-2\nu')}$ where E' is the Young's modulus and ν' is the Poisson's ratio at effective stress

then propose the following formula to calculate the development of excess pore pressures p_w due to undrained (i.e., fast) heating:

$$p_w = \frac{\varphi \Delta T\left(\beta_s - \beta_w\right) + \alpha_{st}\Delta T}{m_v} \tag{2.21}$$

where α_{st} is a physico-chemical coefficient of structural volume change caused by a change in temperature and is negative if an increase in temperature causes a decrease in volume of the soil structure, and m_v, is the compressibility of soil. The sign of p_w is negative since an increase in excess pore pressure causes a decrease in volume. As equation 2.21 suggests, the magnitude of excess pore pressures developed due to a change in temperature depends on: i) the temperature change, ΔT; ii) the porosity of the soil, φ; iii) the difference between thermal expansion coefficients of the water and solid skeleton, $(\beta_s - \beta_w)$; iv) the volumetric strain due to physico-chemical effects, $\alpha_{st}\Delta T$; and v) the compressibility of soil, m_v.

Table 2.1 shows that the linear thermal expansion of water at room temperature ($\beta_{w,lin}$ = 69x10^{-6}/K) is four times larger than the typical value for clay minerals ($\beta_{s,lin}$ = 17x10^{-6}/K). Campanella and Mitchell (1968) were the first to provide the groundbreaking insight that compactive thermal strains in clays are linked to physicochemical changes in adsorbed water. Baldi et al. (1988) analyzed this further by connecting the effects of adsorbed water to double-layer theory as discussed in detail in Chapter 3.

Hueckel and Pellegrini (1992) considered the potential thermal collapse of the soil during undrained heating, since the development of large excess pore pressures results in an equal reduction of effective stress if the total stress remains constant. Subsequent dissipation of excess pore pressures and also continuing heat transfer produces additional volumetric strains and hence, ground movements.

Delage et al (2000) performed isotropic thermal consolidation tests on saturated specimens of natural lightly overconsolidated (OCR = 2.0) Boom clay (plasticity index, I_p = 50%, water content, w = 24 – 30% and porosity, φ = 40%) at different temperatures. Tests were carried out in an isotropic compression cell designed to support high pressures and high temperatures (up to 60 MPa and 100°C, respectively). Table 2.2 summarizes reference thermal and hydraulic properties of Boom clay. Standard triaxial samples (radius r = 19 mm and height h = 76 mm) were heated for approximately 1.5hrs, by

applying a constant temperature boundary condition all around the sample, while drainage was only allowed from the bottom. Figure 2.2 shows the volume of pore water outflow due to consolidation as a function of time at four temperature steps (50°C –60°C, 60°C – 70°C, 70°C – 80°C, and 80°C – 95°C). During the first 2.2 hrs the authors report a small water absorption (i.e., $\Delta V < 0$) due to the thermal expansion of the solid and water phases. However, as the test progresses, larger water expulsion (i.e., $\Delta V > 0$) is recorded due to excess pore pressure dissipation. In fact, the shape of the curves is similar to standard consolidation tests at different temperatures. The Authors assert that thermal equilibrium was reached very rapidly (after ~10 min) and the temperature of the sample was uniform for the remainder of the test. On the other hand, pore-pressure dissipation continued for more than 20 hrs with negligible water flux drained during the first 10 minutes. Delage et al (2000) therefore conclude that the thermal and hydraulic consolidation processes can reasonably be treated as uncoupled.

2.4 Thermal Properties of Soil

The main thermal properties of soil are specific heat capacity, c and thermal conductivity, λ. Heat capacity of the soil medium, c, represents the amount of energy stored in the soil per unit mass and per unit change in temperature. It is generally expressed as a linear function of the specific heat capacities of the different constituents according to their volume fractions. Assuming a fully saturated soil, the specific heat capacity of the soil c is given by:

$$c = c_s(1-\phi) + c_w\phi \qquad (2.22)$$

where φ is the porosity of the soil, c_s is the specific heat capacity of solids (see Table 2.1 for typical values) and c_w is the specific heat capacity of water (c_w = 4186 J/kg K at room temperature).

The heat capacity of a soil having more than two constituents can be calculated by simply adding more terms into equation 2.22. The specific heat capacity of soils is measured in the laboratory by mixing water and soil of different temperatures. If the total thermal energy of both components remains constant, and the specific heat capacity of one component is known (e.g., c_w of water), then the specific heat capacity of the soil, c_s,

can be determined (Brandl, 2006).

As soil is a multiphase medium, the thermal conductivity, λ, can only be expressed approximately and depends on the micro-structural arrangement of the material (Rees et al., 2000). The arithmetic mean (equation 2.23) is known to over-estimate the thermal conductivity of soil, while the harmonic mean (equation 2.24) underestimates it (Woodside and Messmer, 1961):

$$\lambda = \sum_{i=1}^{N} \phi_i \lambda_i \tag{2.23}$$

$$\lambda = \frac{1}{\sum_{i=1}^{N} \frac{\phi_i}{\lambda_i}} \tag{2.24}$$

where N is the number of constituents and φ_i and λ_i the porosity and thermal conductivity of each constituent, respectively. Woodside and Messmer (1961) suggest a "geometric mean" equation to represent the thermal conductivity of soil:

$$\lambda = \prod_{i=1}^{N} \lambda_i^{\phi_i} \tag{2.25a}$$

where $\sum_{i=1}^{N} \phi_i = 1.0$ and Π is the product of individual terms. Assuming a fully saturated soil, the thermal conductivity of soil, λ, is:

$$\lambda = \lambda_s^{(1-\phi)} \lambda_w^{\phi} \tag{2.25b}$$

where λ_s is the thermal conductivity of the solid mineral (see Table 2.1 for typical values) and λ_w is the thermal conductivity of liquid water (λ_w = 0.6 W/m K). This equation gives intermediate values between the arithmetic mean and harmonic mean equations as shown in Figure 2.3. The thermal conductivity of saturated soil is typically in the range, λ = 1 – 3 W/(mK), i.e., a much narrower range than the equivalent for hydraulic conductivity (Gens, 2010). Rees et al. (2000) presents a number of theoretical equations to calculate the soil thermal conductivity (after De Vries, 1966; Van Rooyen and Winterkorn, 1957). Empirical equations (e.g., Makowski and Mochlinski, 1956; Thomas et al., 1994) lack generality since they are suitable for particular soils under specific conditions.

Detailed soil investigation is essential for an accurate GSHP design and so thermal conductivity, λ, should be determined from field tests (e.g., the thermal response

test that can be performed directly with vertical heat exchangers) or laboratory tests (e.g., the steady state or transient method). In the steady state method, the power needed to create a constant temperature difference across the soil sample is measured, while in the transient method, a constant power is supplied and the resulting change of temperature within the sample is recorded (Clarke et al, 2007). Typical test procedures involve the hot-wire method (ASTM C1113), where an electrical wire is placed in the soil sample. A steady current is supplied to the electric wire and the radial temperature difference across the specimen is measured by a thermocouple and recorded over a short heating and cooling interval. An alternative method is the "guarded-comparative-longitudinal" heat flow technique (ASTM E1225), in which a specimen is clamped between two disks of material of known conductivity. The thermal conductivity of the soil is calculated by equating the heat transfer per unit area of soil specimen to the heat transfer per unit area of the disks.

2.5 Thermo – Hydraulic Response of Clay

Figures 2.4a and 2.4b show that the liquid water mass density depends on temperature and decreases slightly as temperature increases. According to ASTM recommendations, the density of 'free water', (i.e., the water that fully fills the macroscopic pores and flows according to Darcy's Law) is given by:

$$\rho_w = 1000.34038 - 7.77\times10^{-3}T - 4.95\times10^{-3}T^2$$
$$\text{where } [T] = {}^{o}C, \ [\rho_w] = \frac{kg}{m^3} \qquad (2.26)$$

As a result the thermal expansion coefficient of water increases as temperature increases and is given by:

$$\beta_w = -\frac{1}{\rho_w}\frac{\partial \rho_w}{\partial T} \qquad (2.27)$$

Delage et al. (2000), Morin and Silva (1984), Lima (2009) and Cho et al. (1999) conclude that the intrinsic permeability of clay solely depends on porosity and is independent of temperature. Delage et al (2000) performed permeability tests on

saturated Boom clay at various temperatures and the results can be seen in Figure 2.5. It is observed that hydraulic conductivity increases during heating and decreases during cooling. The authors then calculated the corresponding intrinsic permeability, κ [L^2]:

$$\kappa = \frac{k\mu(T)}{\gamma_w(T)} \tag{2.28}$$

where k [L/T] is the hydraulic conductivity, $\mu(T)$ is the dynamic viscosity of water and $\gamma_w(T)$ the unit weight of water.

In the range of temperatures considered, the unit weight of water was assumed constant and the following relation reported by Hillel (1980) for dynamic viscosity of free water was used:

$$\mu(T) = -0.00046575\ln(T) + 0.00239138, \quad [\mu(T)] = Pa \cdot s \tag{2.29}$$

The resulting intrinsic permeability is shown in Figure 2.6 leading to the conclusion that there is a linear relationship between the porosity and the logarithm of the intrinsic permeability of Boom clay. Therefore the change in hydraulic conductivity with temperature is solely due to the change of dynamic viscosity with temperature.

However, there are experimental studies on partially saturated clay (e.g., Romero et al. (2001) on Boom clay, Khemissa (1998) on kaolinite, and Volckaert et al. (1996) on montmorillonite) that show the intrinsic permeability is (slightly) affected by temperature due to phenomena such as porosity redistribution and thermo-chemical interactions that change the clay fabric.

2.6 Thermo-Mechanical Response of Clay

The thermo-mechanical response of clays has been studied over the years for different applications such as nuclear waste disposal (e.g., Gens, 2003; Gens & Olivella, 2001b, 2005; Gens et al., 2009a&b), energy foundations (e.g., Cekerevac & Laloui, 2004; Di Donna & Laloui, 2015) and ground heat storage. Sands react elastically to thermal load; they expand when heated and contract when cooled (Agar et al., 1986). In contrast, clays have a more complex response, which depends on their stress history and stress state. In this thesis we focus on saturated clays but additional work on partially saturated

soils can be found in Francois and Laloui (2008) and Olivella et al. (1994).

2.6.1 Thermal Volumetric Response

Extensive laboratory tests have been undertaken to study the response of soils to heating and cooling, for temperatures ranging from 0°C to 90°C. Temperatures below 0°C are generally avoided due to potential phase change (freeze-thaw) impacts in the soil that will affect the load bearing behavior. The thermal properties of freezing soils vary considerably, as thermal conductivity increases and specific heat capacity decreases, especially in a soil with high water content (Brandl, 2006).

Baldi et al. (1991) performed drained heating and cooling tests on isotropically consolidated Boom clay samples at different initial overconsolidation ratio, OCR[5] under constant total stress (Figure 2.7). For normally consolidated clay (OCR = 1.0), significant, irreversible contractive strains were recorded (~1.9%). Results for overconsolidated clay, with OCR = 6.0, show smaller expansive strains on heating (~ -0.5%) which are largely reversible upon cooling. The sample with intermediate overconsolidation ratio (OCR = 2) shows small, irreversible contractive strains (~0.5%). Similar data have been obtained for different types of clay (e.g., Campanella and Mitchell, 1968; Hueckel and Baldi, 1990; Abuel-Naga et al., 2006). Figure 2.8 presents volumetric deformations recorded by Cekerevak and Laloui (2004) for heating of Kaolin samples from ambient temperature (22°C) to 90°C at OCR's = 1.0 – 12.0. The data at low OCR ($\leq$ 2.0) show monotonically increasing compression with temperature, while results at OCR = 6.0, 12.0 show initial expansion to T = 50°C followed by contraction (T = 50°C - 90°C).

2.6.2 Thermal Cyclic Response

Cyclic thermal tests are very important when studying seasonal ground heat exchangers since they replicate the continuous heating and cooling that takes place in the

[5] In conventional 1-D consolidation tests, OCR = σ_p'/σ' where σ' is the effective stress and σ_p' is the preconsolidation pressure (maximum value of σ')

ground. Campanella and Mitchell (1968) performed cyclic thermal tests on remolded illite specimens that were first isotropically consolidated under 196kPa at 18°C. The samples underwent three complete heating/cooling cycles from 4°C to 60°C and the volume of water expelled or absorbed was recorded. Figure 2.9 presents the resulting volumetric strain versus temperature, where it is observed that cyclic heating and cooling of normally consolidated illite results in volumetric strain accumulation, with most of the plastic strains produced during the first heating-cooling cycle (~1%), and subsequent cycles of equal temperature change producing smaller irreversible contractive strains (~0.1%).

Hueckel et al. (1998) report a drained cyclic heating test on a normally consolidated carbonate clay, with a carbonate content of 18%. The test was done under a constant isotropic stress $\sigma' = 7MPa$, with an initial void ratio $e_0 = 0.54$. Figure 2.10 shows that the first heating/cooling cycle (20°C - 70°C - 20°C) induced irreversible contractive strains $\varepsilon_v = 0.7\%$ and that the second heating stage resulted in some hysteresis, followed by accumulation of significant contractive strain, due to the application of higher temperature (at 105°C, $\varepsilon_v = 1.2\%$).

Di Donna and Laloui (2015) performed drained cyclic thermal tests on natural Geneva Clay samples. The tests were done under constant vertical effective stress (following 1-D consolidation) with temperatures ranging from 5°C to 60°C. Figure 3.22 presents the results of all six cyclic thermal tests undertaken on four samples (S1, S3, S4 and S4b). Four of the tests were conducted on normally consolidated samples and two on highly overconsolidated samples (OCR = 16). Cyclic heating and cooling of the highly OC clays resulted in small dilative strains, while the NC clay resulted in accumulation of large irreversible contractive strains. The Authors attribute the differences observed between the four NC samples to the local differences in plasticity index (see Table 3.7), with higher thermo-plastic deformations achieved for higher plasticity index.

2.6.3 Effects of Temperature on Mechanical Properties

a) 1-D Consolidation Response

Campanella and Mitchell (1968) undertook triaxial consolidation tests on three remolded illite specimens, each at a different temperature for the entire duration of the test. The samples were initially consolidated to 196 kPa at temperatures of 25°C, 38°C and 51°C and maintained under this stress for four days in order to reach full equilibration prior to consolidation. Figure 2.11 shows that the higher the temperature, the lower the void ratio resulting from initial loading. All consolidation curves are parallel and so the compressibility index $\left(C_c = -de/d\log_{10}\sigma'_v\right)$ of remolded illite at a given stress is unaffected by temperature. Therefore the main effect of temperature is to increase density (reduce void ratio) at a given effective consolidation stress. It can be deduced that the location of the virgin consolidation line (VCL) depends on temperature, and hence, the apparent preconsolidation pressure, σ'_p, also decreases with temperature. Figure 2.12 shows the preconsolidation pressure as a function of temperature for different types of natural clay reported in the literature.

The effect of combined thermal and mechanical loading has been the subject of numerous studies (e.g., Sultan et al., 2002; Cui et al., 2009; Towhata et al., 1993; Burghignoli et al., 1995). Figure 2.13 shows laboratory measurements reported by Abuel-Naga et al. (2006), where a specimen of high plasticity, normally consolidated Bangkok clay is subjected to a heating-cooling cycle (25°-90°-25°C) before being reloaded mechanically. The cycle of heating and cooling generates an apparent overconsolidation of the specimen as subsequent loading (B-C) involves a stiff response with yield at C. This 'thermal hardening' effect is similar to drained creep (secondary compression) as observed by Leroueil and Marques (1996). Figure 2.14 shows the ductility in 1-D compression behavior measured in Constant Rate of Strain (CRS) tests at different strain rates $\left(\dot{\varepsilon} = 1.7\times10^{-7} - 1.7\times10^{-5}\, s^{-1}\right)$ and temperatures (T = 5°- 50°C). These results suggest that viscous properties of clay are thermally activated and may ultimately be linked.

b) Shear Response

Cekerevak and Laloui (2004) performed drained triaxial compression shear tests on Kaolin samples at two different temperatures (22°C and 90°C) in order to study the effects of stress history and temperature on shear behavior. All tests were pre-consolidated to maximum pressure σ'_p = 600kPa. The results indicate that specimens tested at high temperature show higher shear strength (Figure 2.15a). However, at critical state ($\partial q / \partial \varepsilon_s \approx \partial \varepsilon_v / \partial \varepsilon_s \approx 0$, where ε_S is the deviatoric strain), the shear stresses obtained at 90°C tend to the same critical state as samples tested at ambient temperature (Figure 2.15b). Figure 2.16 presents the Critical State Lines (CSLs) obtained at the two temperatures, by only considering tests where critical state was achieved. The slope of the CSL (C_c = 0.18) does not depend on temperature (although the scatter in data should be taken into consideration).

Figure 2.17 summarizes the effects of temperature on the friction angle measured at critical state for different types of clay. Most studies show that the friction angle remains constant (e.g., Cekerevac and Laloui (2004) on Kaolinite, Hueckel and Baldi (1990) on Pontida clay, Burghignoli et al. (2000) on Todi clay and Graham et al. (1982) on Illite). Hicher and Despax (1976) and Robinet et al (1997) report significant decreases in ctitical state friction angle with temperature for the case of Kaolinite, while Hueckel and Pellegrini (1989) report a slight increase in friction angle with temperature, for the case of Boom clay.

The laboratory measurements show that there are a lot of contradictory data regarding the effect of temperature on the shear response of clay (e.g., the critical state friction angle for kaolinite has been reported to both increase and decrease with temperature). However, the recorded effect of temperature on the consolidation response is consistent: temperature changes the location of the VCL and decreases the apparent preconsolidation pressure, σ'_p.

2.7 Constitutive Modeling of Thermo-Mechanical Response of Clay

2.7.1 Poro-Elastic Model

A series of analytical solutions have been obtained for thermo-mechanical problems assuming poro-elastic properties of the soil (Smith and Booker, 1989; Booker and Savvidou, 1985). Booker and Savvidou (1985) propose analytic solutions for the fundamental problem of a constant point heat source, Q, buried deep in a saturated clay, assuming that the soil can be modeled as a porous thermo-elastic continuum (see equations 2.30-2.33). An approximate solution to the problem of a cylindrical heat source was then found by integrating the solution for the point source over a cylindrical volume. The determination of temperature is completely uncoupled from that of the other variables and so the temperature evolution, T, at a point located a distance r from the heat source is:

$$T = \frac{Q}{4\pi\lambda r} f\left(\frac{c_{vT} t}{r^2}\right) \tag{2.30}$$

where t is time, λ is thermal conductivity of the soil medium and c_{VT} is the thermal diffusivity of the soil medium. Pore water pressures p_w are given by:

$$p_w = \left[\frac{\beta - \left(\frac{1+\nu'}{1-\nu'}\right)\beta_s}{\left(1-\frac{c_{vH}}{c_{vT}}\right)}\right]\frac{Q}{4\pi\lambda r}\left[f\left(\frac{c_{vT} t}{r^2}\right) - f\left(\frac{c_{vH} t}{r^2}\right)\right] \tag{2.31}$$

where β is the volumetric thermal expansion of the soil medium, β_s is the linear thermal expansion of the soil skeleton, c_{VH} is the coefficient of consolidation (cf., equation 2.19), E' is Young's Modulus and ν' is Poisson's ratio. Components of soil displacement, $\underset{\sim}{u}$, and total stress, $\underset{\sim}{\sigma}$, are obtained:

$$\underset{\sim}{u} = \beta \underset{\sim}{r} \frac{Q}{4\pi\lambda r} g^* \tag{2.32}$$

$$\sigma_{ij} = \left[2\frac{E'}{2(1+\nu')}\beta\right]\frac{Q}{4\pi\lambda r}\left[(f^* - g^*)\delta_{ij} + \frac{r_i r_j}{r^2}(3f^* - g^*)\right] \tag{2.33}$$

where functions f, f^* and g^* are given in Table 2.3.

In principle, these analytical solutions provide a useful basis for evaluating the accuracy of more complex numerical analysis, as discussed in Section 2.8. Figures 2.7 - 2.10 show that thermal loading of NC and lightly OC clays produce irrecoverable strains (i.e., observed in cycles of heating and cooling). These irreversible effects cannot be described by thermo-elastic models and therefore more advanced constitutive models are necessary for their accurate description.

2.7.2 Hueckel and Borsetto (HB, 1990)

Hueckel and Borsetto (1990) and Hueckel and Baldi (1990) proposed a thermo-elastoplastic framework, by extending the Modified Cam Clay (MCC; Roscoe and Burland, 1968) model to account for irrecoverable strains due to thermal effects.

In the Hueckel and Borsetto (1990) HB90 model the original elasto-plastic consistency equation was modified to consider temperature as a state variable. The elasticity law was generalized to thermal conditions by introducing a reversible thermal isotropic strain and by allowing for thermal changes of bulk modulus. The Authors proposed a yield surface, f that is a function not only of stress and plastic volumetric strain ε_v^{tp}, but also of temperature difference ΔT (Figure 2.18):

$$f = f\left(p', q, \varepsilon_v^{tp}, \Delta T\right) \tag{2.34}$$

where $p'=\frac{1}{3}\left(\sigma'_1+2\sigma'_3\right)$; $q=\left(\sigma'_1-\sigma'_3\right)$ are the mean effective stress and shear stress in triaxial space and, $\Delta T=T-T_0$, is reference to an initial temperature, T_0. Applying this formulation to the yield function of the MCC model, Hueckel and Baldi (1990) obtain the size of the yield function:

Yield function: $f = q^2 - M^2 p'\left(p'_c - p'\right)$ (2.35)

with pre-consolidation pressure:

$$p'_c = p'_{c0}\exp\left(\frac{1}{\lambda-\kappa_T}\left\{e_1-\left(1-\alpha_4\Delta T\right)\left[e_g-\left(1+e_0\right)\varepsilon_v^{tp}\right]\right\}\right)+\ldots$$
$$\ldots+2\left(\alpha_5\Delta T+\alpha_6\Delta T\left|\Delta T\right|\right) \tag{2.36}$$

$$\kappa_T = \left[\frac{\kappa_i}{1+e_0} + \left(\alpha_1 + \alpha_3 \Delta T\right)\Delta T\right]\left(1+e_0\right) \tag{2.37}$$

where ε_v^{tp} is thermo-plastic volumetric strain, p'$_{c0}$ is a reference stress (e.g., 100kPa), λ and κ_i are the isothermal virgin consolidation and unload-reload compression indices, α_5 and α_6 are input constants corresponding to a reduction of the semi-axis of the yield surface due to temperature alone, α_1 and α_3 are input constants corresponding to the thermal dependency of elastic moduli, e_0 is the initial void ratio at the geostatic state ($p'_c = p'_g$, $T = T_g$) and e_1 is the void ratio at a hypothetical state corresponding to $p'_c = p'_{c0}$, $T = T_0$, (see Figure 2.19). The value of e_g corresponds to the void ratio at maximum preconsolidation stress p'_{cg}, at which ε_v^{tp} is set equal to zero. The input constant α_4 has been introduced to simulate "thermal ductilization" of the response to uniaxial compression with the increasing temperature; however, the Authors suggest that ductilization can also be simulated without introduction of α_4 (i.e., $\alpha_4 = 0$). Assuming $\alpha_4 = 0$ and that $e_1 = e_g$, the expression for the preconsolidation pressure p_c simplifies to:

$$p'_c = p'_{c0}\exp\left(\frac{1+e_0}{\lambda-\kappa_T}\varepsilon_v^{tp}\right) + 2\left(\alpha_5\Delta T + \alpha_6\Delta T\left|\Delta T\right|\right) \tag{2.38}$$

The following equations show the incremental strain vs effective stress and temperature relations for the HB90 model:

$$\begin{Bmatrix} \dot{\varepsilon}_v \\ \dot{\varepsilon}_s \end{Bmatrix} = \begin{bmatrix} \frac{1}{K_{th}} + \frac{1}{H}\frac{\partial f}{\partial p'}\frac{\partial f}{\partial p'} & \frac{1}{H}\frac{\partial f}{\partial q}\frac{\partial f}{\partial p'} \\ \frac{1}{H}\frac{\partial f}{\partial p'}\frac{\partial f}{\partial q} & \frac{1}{3G} + \frac{1}{H}\frac{\partial f}{\partial q}\frac{\partial f}{\partial q} \end{bmatrix} \begin{Bmatrix} \dot{p}' \\ \dot{q} \end{Bmatrix} + \begin{bmatrix} A_T + \frac{1}{H}\frac{\partial f}{\partial T}\frac{\partial f}{\partial p'} \\ \frac{1}{H}\frac{\partial f}{\partial T}\frac{\partial f}{\partial q} \end{bmatrix} \dot{T} \tag{2.39}$$

where K_{th} is the compressibility of the soil in swelling:

$$K_{th} = \frac{1+e_0}{\kappa_i + \left(1+e_0\right)\left(\alpha_1 + \alpha_3\Delta T\right)\Delta T}p' \tag{2.40}$$

$$H = -\frac{\partial f}{\partial \varepsilon_v^{tp}}\frac{\partial f}{\partial p'} \tag{2.41}$$

and G is the elastic shear modulus. $A_T\dot{T}$ calculates the thermo-elastic volumetric strain rate and A_T is given by:

$$A_T = \alpha_0 + 2\alpha_2 \Delta T + \left(\alpha_1 + 2\alpha_3 \Delta T\right) \ln \frac{p'}{p_g} \tag{2.42}$$

where α_0 and α_2 are input constants corresponding to the production of elastic volumetric strains due to heating and cooling and α_1 and α_3 affect the thermal dependence of the elastic moduli and were defined earlier (equation 2.37).

The input parameters for the HB90 model include the original input constants for the MCC model (κ_i, λ, M, ν, e_0) plus six more thermal constants: α_1, α_3 (related to K_{th}), α_0, α_2 (related to A_T) and α_4, α_5, α_6 (relating to the preconsolidation pressure, σ'_p). It should be pointed out that when heating a normally consolidated clay the preconsolidation pressure remains constant since the increase of σ'_p due to the thermoplastic volumetric strains is equal and opposite to the decrease due to the change in temperature. Although the HB90 model successfully describes some of the key aspects of thermo-mechanical soil behavior, it is not able to simulate the accumulation of strain due to cycles of heating and cooling, as discussed in Section 2.8.2.

2.7.3 Extensions of the HB90 Thermo-Elastoplastic Models

Following Hueckel and Borsetto (1990), several models have been proposed, which extend the MCC model to account for thermal effects. Robinet et al. (1996) developed a model for non-expansive clays with two yield surfaces (one mechanical and the other thermal) and introduced "irreversible" thermal strains caused by microscopic phenomena. Similarly, Cui et al. (2000) suggested a second yield mechanism that enables the generation of thermal irrecoverable strains even at high OCR. Abuel-Naga et al. (2007) and Graham et al. (2001) have also developed thermo-elastoplastic constitutive models based on the MCC model.

The ACMEG-T formulation (Laloui and Francois, 2009) introduces two yield surfaces to separately describe isotropic and deviatoric irreversible processes. The bounding surface theory (Dafalias and Herrmann, 1980) is employed, in order to describe more accurately the progressive evolution of the isotropic yield limit during loading and unloading. The ACMEG-T formulation also conforms to assumptions of Critical State theory (Schofield and Wroth, 1968) and allow for thermal dependence of critical state. Most recently Di Donna (2014) refined ACMEG-T to account for accumulation of

volumetric strains during cyclic heating and cooling, by extending the bounding surface theory. Figure 2.19 presents ACMEG-T model predictions against four heating and cooling cycles (5°C – 60°C) on natural Geneva clay. It is observed that the model assumes a purely elastic response for the highly OC clay, while the lab measurements show accumulation of very small dilative strain. The model accurately predicts the first heating stage of the normally consolidated clay (points 1 – 5) but fails to describe the shape of subsequent heating stages (e.g., points 7 – 10). The ACMEG-T model accurately describes the total amount of accumulated volumetric thermal strain (~0.6%).

2.7.4 Tsinghua Thermosoil Model (Zhang and Cheng, 2013)

The Tsinghua Thermosoil (TTS) model was developed by Zhang and Cheng (2013) to describe the coupled thermo-hydro-mechanical response of fully saturated clays and sands. The model formulation is based on the framework of Granular Solid Hydrodynamics (Jiang and Liu, 2007) that link temperature and strain rate effects. The model describes features of soil behavior including virgin consolidation, hysteresis and accumulation of strains in cyclic loading. The reversible energy processes of the model are expressed as elastic deformations occurring at the soil particle contacts, that result in a stored elastic potential energy in the system. The irreversible processes include the energy dissipation mechanisms occurring both at the macroscopic and microscopic levels (rolling and friction of soil particles). These phenomena are expressed by a double entropy theory, where 'total' entropy describes the macroscopic phenomena while 'granular' entropy describes the microscopic phenomena. The TTS model assumes that water in the soil mixture can be divided into: i) free water, which fully fills the macroscopic pores and flows according to Darcy's Law, and ii) bound water, which is fully adsorbed by the soil particles and fills the microscopic pore space. In order to describe the irreversible thermal behavior of clays, the model assumes that during heating, part of the bound water is converted to free water, which results in irreversible rearrangement of the soil particles.

In contrast to prior formulations the TTS model is based on a more fundamental thermodynamic framework. The TTS model successfully describes all of the main

characteristics of thermal response of soils and can capture the accumulation of thermal volumetric strains due to cyclic heating and cooling (cf. Figures 2.9, 2.10 and 3.22). This component of the model is very important for studying the long-term response of clays to seasonal heating and cooling induced by shallow geothermal installations. Full details of the TTS model formulation and calibration are given in Chapter 3, while Chapter 5 uses the TTS model for simulations of long-term performance for BHE design.

2.8 Preliminary Investigations

2.8.1 Validation of THM Numerical Simulations Using Poro-Elastic Analytical Solutions

Thermo-hydro-mechanical (THM) numerical simulations assuming thermo-elastic soil properties were performed using the finite element program 'Code_Bright' (Olivella et al., 1996a and 1996b) and the results compared to analytical solutions presented by Booker and Savvidou (1985). This enabled us to check and debug the published analytical solutions and also to appreciate the approximations made in both analyses.

The first problem that was modeled is a deep, point heat source of magnitude Q, located at the origin of the axisymmetric space. Figure 2.20 shows the mesh and boundary conditions assumed in the FE model (using Code_Bright). Table 2.4 shows the input parameters used in the numerical and analytical models, which correspond to a saturated clay (the selected parameters do not correspond to a specific clay but were selected for validation of the analytical solutions). Figure 2.21 shows excellent agreement between the analytic solutions and the numerical model for predictions of temperature, excess pore pressure, displacement and stress evolution at a distance R from the heat source.

The second reference problem considers a radial heat source of strength Q = 40W and radius R = 1m, located at the centerline of an axisymmetric space. The input parameters that were assumed for the saturated clay are shown in Table 2.4 and Figure 2.22 presents the mesh and boundary conditions selected in the numerical model. The results were compared to the approximate analytic solutions developed by Booker and Savvidou (1985) for the cylindrical heat source. Figures 2.23a and 2.23b show the temperature and excess pore pressure evolution at points located at r/R = 1, 2 and 5 from

the center of the cylinder; while Figures 2.23c, d and e show comparisons to radial, hoop and vertical stresses, respectively. The predictions from the numerical model and analytical solutions are very similar and the small differences can be attributed primarily to the dependence of water viscosity on temperature (included in Code_Bright) while the analytical solutions assume a constant water viscosity.

It should be pointed out that since the heat transfer problem is uncoupled, predictions of temperature could have been obtained by considering just the thermal problem, using for example the analytical solutions proposed by Brandl (2006). However, a fully coupled THM analysis enables the prediction of excess pore pressures, stresses and corresponding strains and displacements, which are controlled by the hydro-mechanical response.

2.8.2 Validation of THM Numerical Simulations Using the HB90 Model

A simplified version of the HB90 model has already been integrated in Code_Bright, assuming that the swelling behavior is independent of temperature[6] such that $\alpha_1 = \alpha_3 = 0$ and $A_T = \alpha_0 + 2\alpha_2 \Delta T$. As part of the current research, the HB90 model was also implemented in Modlab, in order to study its performance in depth and to evaluate the simplifications assumed in the Code_Bright implementation. The flow chart that was used for our implementation is shown in Figure 2.24.

Both implementations of HB90 were calibrated for the case of highly plastic Bangkok Clay based on lab tests on intact samples obtained from 3-4m depth (Abuel-Naga et al., 2006). The input parameters assumed in each model are shown in Tables 2.5 and 2.6. Bangkok Clay consists of 54-71% smectite and illite, 28-36% kaolinite and mica.

Figure 2.25 shows hydrostatic compression tests at different temperatures (25°C, 70°C and 90°C) and demonstrates the simplification assumed in the Code_Bright implementation, where the swelling compressibility K_{th} is independent of temperature. Figure 2.26 shows drained deformations of Bangkok Clay due to heating and cooling

---

[6] $d\varepsilon_v^e = \frac{\kappa}{1+e}\frac{dp'}{p'} + \left(\alpha_0 + 2\alpha_2 \Delta T\right) dT$

tests between 25°C and 90°C at different initial OCRs. Clearly the volumetric strains induced for the NC clay are compressive (highly irrecoverable) and significantly larger than those that occur for highly OC clays (which are dilative and largely recoverable). The results in Figures 2.26a and 2.26b show some subtle differences in the results for normally consolidated clay (OCR =1). Predictions using the two implementations of the HB90 model differ most markedly for overconsolidated clay. The Code_Bright implementation assumes the same small dilative strains for OCR > 2.0, while the Modlab implementation accurately predicts small contractive strain at OCR = 2.0, minimal thermal strains at OCR = 4.0 and small dilative strains at OCR = 8.0.

Figure 2.27 shows HB90 model predictions of drained deformations of Bangkok Clay due to 20 heating and cooling cycles (25°C - 90°C) for normally consolidated and highly overconsolidated (OCR = 8) clay. The HB90 model predicts very small accumulation of volumetric strain (~0.1%) compared to the irreversible contractive strain measured after the first heating/cooling cycle of the normally consolidated clay (~6%). Previous experiments (cf. Figures 2.9 and 2.10) have shown that accumulation due to cyclic heating and cooling is more pronounced and therefore the underestimation of strain accumulation due to cyclic heating and cooling is one of the main limitations of the HB90 model.

2.8.3 Preliminary Study for a BHE Array Using the HB90 Model

Zymnis and Whittle (2014) present a preliminary study of the coupled thermo-hydro-mechanical response of the ground due to the continuous operation of a vertical heat exchange system that was designed for a large office building in Chicago. The building (12 storeys high, with one basement level and a floor area of 43000 m^2, shown in Figure 2.28a) was based on recommendations for typical DOE Commercial Benchmark Buildings (DOE, 2008). The heating and cooling loads of the building were calculated using the DOE EnergyPlus simulation program (DOE, 2008), assuming that the building is located in climate zone 5A (Chicago) and the results are shown in Figure 2.28b. Figure 2.28c shows the heating and cooling loads exchanged with the ground assuming a ground source heat pump with a coefficient of performance, COP = 4.5. In order to assume equal amounts of heating and cooling exchanged with the ground, the

ground heating and cooling loads were fitted as a first approximation by a sinusoidal function of amplitude 2000kW and of equal durations for the heating and cooling periods, with the peaks occurring at the months of January and July, according to the EnergyPlus simulations.

A hybrid system would be required to balance the heating and cooling needs of the office building, while the GSHP system provides the baseload. The borehole heat exchanger (BHE) array was designed using the method proposed by Kavanaugh and Rafferty (1997) and presented in Appendix A. Using weighted average thermal properties (thermal conductivity, λ = 2.75W/mK and thermal diffusivity, c_{VT} = 0.097m^2/day) the total required length of heat exchanger was calculated, L_h = 89.4km. Assuming an available area of 43000 m^2 the proposed design considers an array of 1118, 80m deep borehole heat exchangers spaced in a regular array at 6.2m centers (Figure 2.29a).

Numerical simulation of a single BHE was undertaken, using the finite element Code_Bright program, in order to study the full thermo-hydro-mechanical response of the soil due to continuous cycles of heating and cooling. Figure 2.29c shows the typical soil profile encountered in downtown Chicago (Finno & Roboski, 2005), which includes 9m of fill and sand, above 10m of clay overlaying limestone. Figure 2.29c also shows the geometry, mesh and boundary conditions assumed in the numerical model. The depth of the model is 80m, equal to the actual depth of each BHE, while the width is 3.1m, equal to half the distance between two adjacent BHEs, as shown in Figure 2.29a. The vertical heat exchanger was modeled as a nearly sinusoidal heat source (Figure 2.29b). Closed heat and water flow is assumed in the left vertical boundary due to symmetry of the problem and in the right boundary due to the existence of the adjacent wells that produce similar heat exchange with the ground. Closed heat flux is assumed at the top, which represents the interface between the ground and the building. The initial ground temperature was selected, T_0 = 10°C.

The vertical heat exchanger was studied using two sets of soil properties: 1) thermo-elastic properties in all units ("TE Model") and 2) thermo-elastoplastic properties for the clay layers only ("TEP Model"), using the HB90 model (Code_Bright approximation). The mechanical properties of the Chicago glacial clays are available from Finno and Cho (2011). Thermal properties for the TE model, Table 2.6, were based

on parameters quoted by Kavanaugh and Rafferty (1997). The volumetric thermal expansion coefficient for all soils $\beta = 3x10^{-5}$ $°C^{-1}$. As there were no available measurements of the thermo-elastoplastic behavior for the Chicago clays, the HB90 model was calibrated using thermo-mechanical laboratory tests reported by Abuel-Naga et al. (2006) on specimens on Bangkok clay, as reported in Table 2.7. It should be noted that in spite of differences in the index/mineralogical and in situ water contents of the Chicago and Bangkok clays, the two clays are characterized by the same MCC compressibility and critical state shear strength parameters. Given this approximation, the current analyses should be viewed as preliminary (pending more studies on thermo-mechanical properties of the local clays).

The numerical analyses were carried out for a total design life of 600 months (50 years) to observe the long-term response of the ground. Figure 2.30 shows the temperature developed near the top of the clay layer (10m depth) at three different radial distances from the heat source, in response to the sinusoidal heat exchange with the BHE. As expected, the same temperature distribution is observed in both the TEP and TE models, confirming that temperatures are largely independent of the mechanical properties of the soils. From Figure 2.30a it is observed that the temperature at r = 0.5m ranges from 4°C to 17°C, while seasonal fluctuations in temperature decrease with distance from the heat source. Figure 2.30b shows a small decrease (1°C) in the average temperature within the soil over the 50-year design life of the system.

Figure 2.31a shows that there is a progressive accumulation of ground surface displacements predicted by the TEP Model, while the TE model shows very small net heave at the surface. The current TEP analyses predict that thermal cycling of the ground will cause a net settlement of 20mm after 50 years of operation (Figure 2.32b). This could be an important long-term response that needs to be more carefully evaluated in design.

Figures 2.32 and 2.33 consider the volumetric strains and excess pores pressures within the soft (NC) and stiff (OC) clay units (cf. Figure 2.29b). The results for the TE model (thermo-elastic properties) show negligible accumulation of volumetric strains with seasonal thermal cycling in Figure 2.32. Larger cyclic volumetric strains occur in the OC clay due to thermoplastic properties considered in the TEP analysis using the

HB90 soil model ($\varepsilon_{vol} \approx \pm 0.1\%$). However, the net accumulation of strain over the design life is small. Much larger volumetric strains occur in the NC clay unit, with a progressive annual accumulation of strains (up to 0.35% after 50 years) that account for much of the computed surface settlement reported in Figure 2.31b. Figure 2.33 shows that significant excess pore pressures (up to ±20kPa for the OC unit using the TEP model) develop in the clay due to seasonal heating and cooling. In general, the thermo-elastic analysis predicts larger cyclic excess pore pressures than the TEP analysis using the HB90 model. However, there is no apparent accumulation of excess pore pressures within the clay over the design life of the system.

The results show that seasonal heating and cooling of the ground can induce a small (but not insignificant) long-term settlement of the building over an assumed 50year design life of the system. Further studies of this type are essential for understanding and predicting the performance of GSHP systems. There is clearly a need for more extensive information on site-specific thermo-mechanical properties of clays for these analyses.

2.9 Summary and Conclusions

Extensive laboratory experiments have shown that temperature has a significant effect on the response of clays and accumulation of irreversible strains takes place as a result of cyclic heating and cooling of a normally consolidated clay. Although the thermal problem is largely independent of mechanical behavior and groundwater processes (convective heat transfer is very small), a coupled thermo-hydro-mechanical analysis is necessary for understanding the generation and dissipation of excess pore pressures and resulting strains and ground displacements. Thermo-poroelastic solutions are not capable of describing the irreversible thermal strains induced due to heating and cooling of normally consolidated clay and so more advanced thermo-elastoplastic models are necessary. This chapter has highlighted the capabilities and limitations of the established thermo-elastoplastic HB90 model for simulating the elemental thermo-mechanical response of clays. The HB90 model was also used in a preliminary set of analyses (using Code_Bright) to simulate long-term performance of a BHE array with balanced seasonal heating and cooling. Refinements in modeling using the TTS soil model are expected to

achieve more realistic predictions of thermo-mechanical clay behavior and are investigated in subsequent chapters.

Substance	λ (W/mK)	c (J/kg K)	ρ (kg/m^3)	β_{lin}^* (10^{-6}/K)
Quartz	8.79	2010	2660	1
Clay minerals	2.93	2010	2650	17**
Water	0.57	4186	1000	69
Ice	2.18	1884	920	-
Air	0.025	1.256	1.25	-

Values have been converted to SI units from De Vries (1952)
* Linear thermal expansion coefficients are shown for comparison
** McKinstry (1965)

Table 2.1:Thermal properties of some soil materials (after Rees et al., 2000)

Thermal Problem		
Heat transfer length	r [mm]	19
Thermal diffusivity	c_{vT} [m^2/s]	5.96×10^{-7}
Thermal conductivity	λ [W/ mK]	1.7
Volumetric heat capacity	C [J/ K m^3]	2.85×10^6
Hydraulic problem		
Drainage length	h [mm]	76
Coeff. of consolidation	c_{vH} [m^2/s]	7.5
Hydraulic conductivity	k [m/s]	$2.5 - 6.2 \times 10^{-12}$

Table 2.2: Reference properties of thermal consolidation tests (after Delage et al. 2000)

Function	Analytical Solution
$f\left(\frac{c_{vT}t}{r^2}\right)$	$erfc\left(\frac{r}{2\sqrt{c_{vT}t}}\right)$
$g\left(\frac{c_{vT}t}{r^2}\right)$	$\frac{c_{vT}t}{r^2}+\left(\frac{1}{2}-\frac{c_{vT}t}{r^2}\right)erfc\left(\frac{r}{2\sqrt{c_{vT}t}}\right)-\sqrt{\frac{c_{vT}t}{\pi r^2}}e^{-r^2/4c_{vT}t}$
f^*	$\left[\frac{\beta-\left(\frac{1+\nu'}{1-\nu'}\right)\beta_s}{\left(1-\frac{c_{vH}}{c_{vT}}\right)\beta}+\frac{\left(\frac{1+\nu'}{1-\nu'}\right)\beta_s}{\beta}\right]f\left(\frac{c_{vT}t}{r^2}\right)-\left[\frac{\beta-\left(\frac{1+\nu'}{1-\nu'}\right)\beta_s}{\left(1-\frac{c_{vH}}{c_{vT}}\right)\beta}\right]f\left(\frac{c_{vH}t}{r^2}\right)$
g^*	$\left[\frac{\beta-\left(\frac{1+\nu'}{1-\nu'}\right)\beta_s}{\left(1-\frac{c_{vH}}{c_{vT}}\right)\beta}+\frac{\left(\frac{1+\nu'}{1-\nu'}\right)\beta_s}{\beta}\right]g\left(\frac{c_{vT}t}{r^2}\right)-\left[\frac{\beta-\left(\frac{1+\nu'}{1-\nu'}\right)\beta_s}{\left(1-\frac{c_{vH}}{c_{vT}}\right)\beta}\right]g\left(\frac{c_{vH}t}{r^2}\right)$

Table 2.3: Functions for analytical solutions in thermo-poroelasticity
(after Booker and Savvidou, 1985)

Measured Input Parameters	Value
Thermal conductivity, λ [W/mK]	2.5
Soil Density, ρ_s [kg/m^3]	1700
Specific heat capacity, c_s [J/kgK]	800
Young's Modulus E [MPa]	100
Poisson's ratio, ν [-]	0.4
Linear Thermal Expansion, $\beta_{s,lin}$ [1/C^o]	1×10^{-5}
Porosity, φ [-]	0.3
Intrinsic permeability, κ [m^2]	6.92×10^{-18}
Inferred Input Parameters	**Value**
c_{vT} [m^2/day]	0.0978
$c_{vH} = 2c_{vT}$ [m^2/day]	0.1955

Table 2.4: Soil parameters assumed in Code_Bright model and analytical solutions by Booker and Savvidou (1985)

HB90 Parameter	Modlab	Code_Bright
κ [-]	0.05	0.05
λ [-]	0.40	0.20
M [-]	1.2	1.2
φ' [°]	30°	30°
ν' [-]	0.30	0.30
e_0 [-]	1.0	1.0
α_0 [1/°C]	1.7×10^{-4}	2.3×10^{-4}
α_2 [1/°C^2]	5.0×10^{-6}	-1.5×10^{-6}
α_1 [1/°C]	-1.5×10^{-5}	-
α_3 [1/°C^2]	2.0×10^{-6}	
α_5 [MPa/°C]	-1.8×10^{-4}	-5.3×10^{-4}
α_6 [MPa/°C^2]	1.3×10^{-6}	3.8×10^{-6}

Table 2.5: Input constants for the HB90 model assumed for the Bangkok clay calibration in Modlab and Code_Bright implementations

Layer	Unit Weight (kN/m^3)	e_0	E' (MPa)	ν'	k (m/day)	λ (W/mK)	c_{vT} (m^2/ day)	C_p (J/kg K)
Fill	18.9	0.3	21	0.3	8.64E-01	2.94	0.09	946
Sand	19.7	0.3	85	0.3	8.64E-02	2.94	0.09	921
Soft Clay	18.9	0.3	121	0.3	8.64E-05	1.38	0.05	810
Stiff Clay	18.9	0.3	446	0.3	8.64E-05	1.38	0.05	810
Limestone	19.7	0.3	600	0.3	8.64E-05	3.11	0.11	921
		Design values (weighted average):				2.79	0.10	

Table 2.6: Thermo-elastic properties for the TE model (Zymnis and Whittle, 2014)

κ	0.03	α_0 α_2 α_5 α_6	1.8e-4/°C -1.5e-6/°C^2 -5.3e-4 MPa/°C 3.8e-6 MPa/°C^2
λ (C_c)	0.20 (0.46)	α_1, α_3, α_4	0
M (φ')	1.29 (32°)	OCR Soft Clay Stiff Clay	 1.0 2.0
ν'	0.30		
e_0	0.28		

Thermal Components of Hueckel & Borsetto (1990) model as implemented in CODE_BRIGHT:	
Preconsolidation stress	$p_c(T) = p_{c0} + 2(\alpha_5 \Delta T + \alpha_6 \Delta T \lvert \Delta T \rvert)$
Elastic volumetric strain	$d\varepsilon_v^e = \frac{\kappa}{1+e}\frac{dp'}{p'} + (\alpha_0 + 2\alpha_2 \Delta T)dT$
where p_{co}: initial preconsolidation mean stress ΔT: change of temperature from initial value T_0=10°C e: void ratio	

Table 2.7: Assumed thermo-mechanical properties of clay layers for Hueckel-Borsetto (HB90) soil model used in TEP analyses (Zymnis and Whittle, 2014)

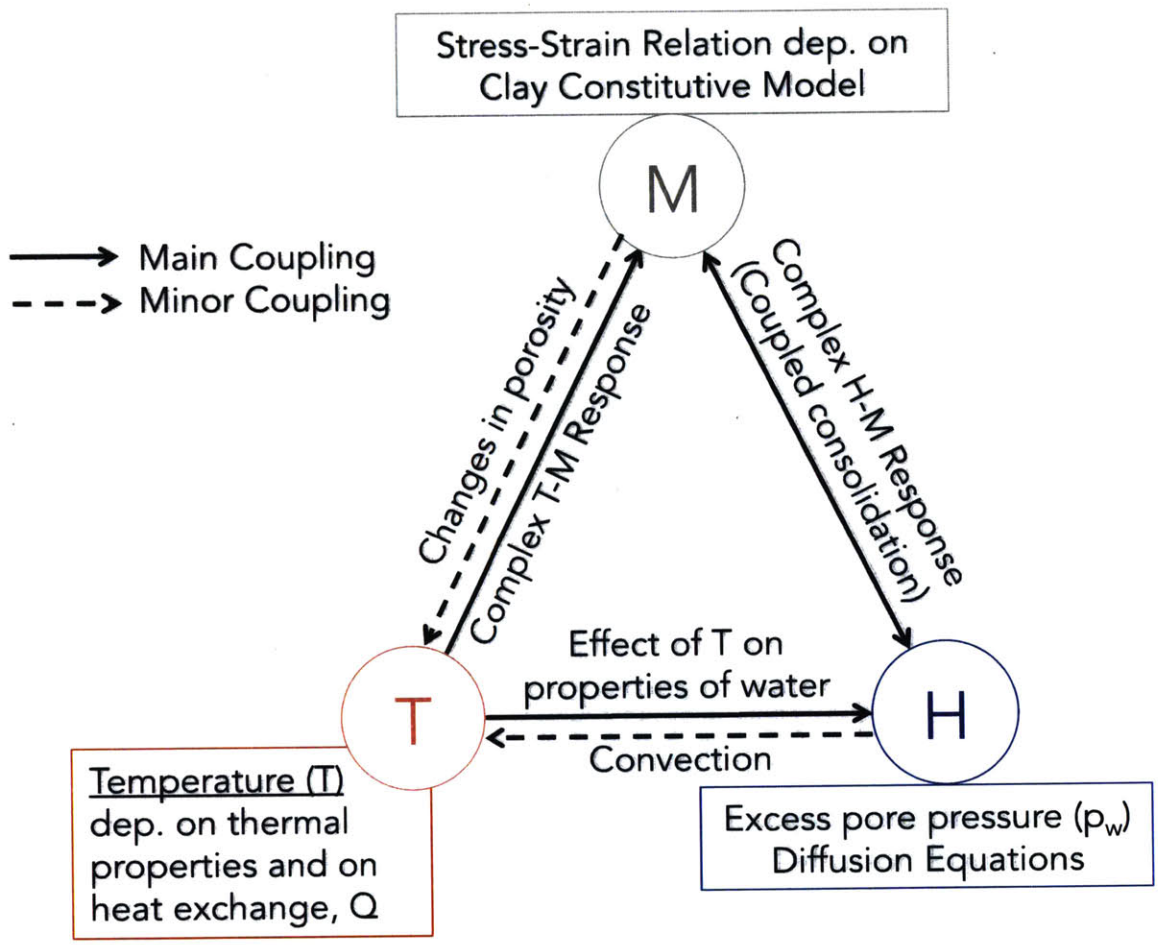

Figure 2.1: Conceptual diagram of thermo-hydro-mechanical coupling for heat conduction in saturated clay

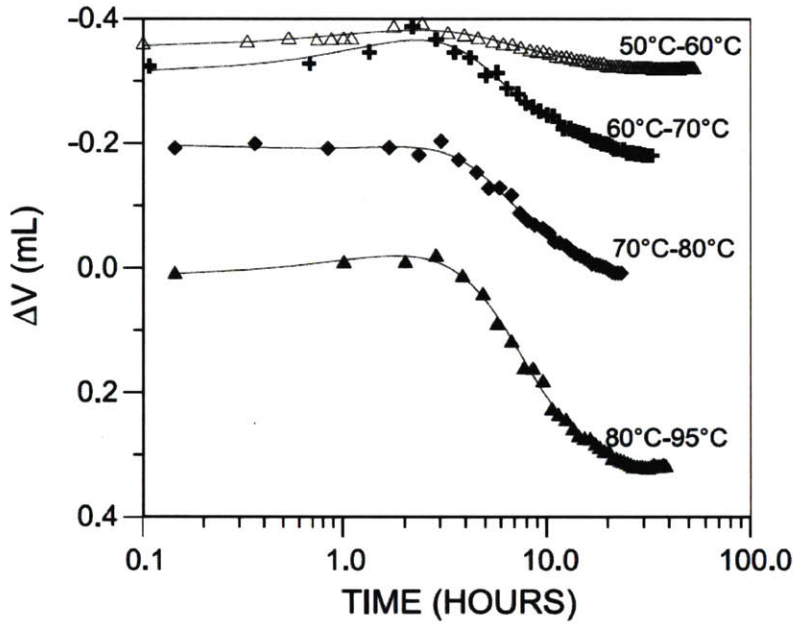

Figure 2.2: Outflow volume of pore water due to thermal consolidation measured for saturated natural Boom clay (OCR = 2.0) at different temperatures (Delage et al., 2000)

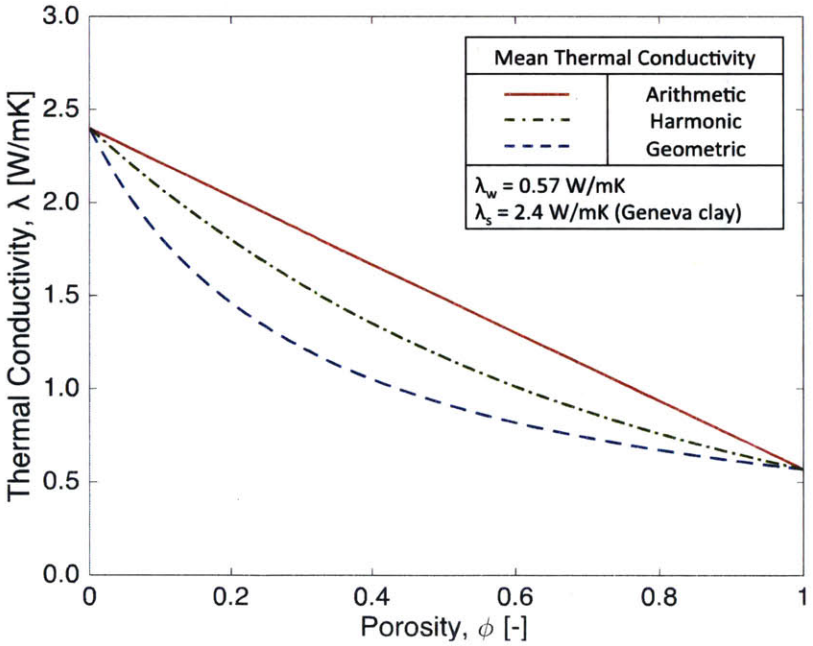

Figure 2.3: Thermal conductivity versus porosity as calculated by three different methods

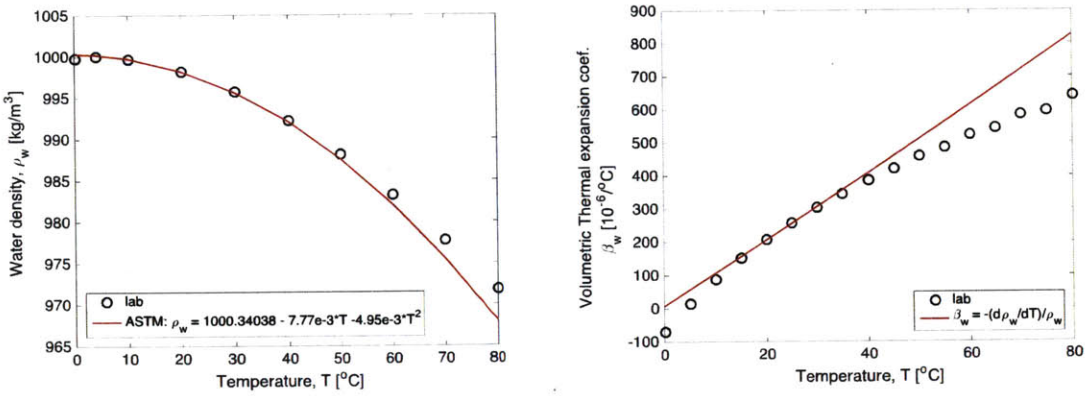

Figure 2.4: a) Variation of liquid water density with temperature; b) variation of the thermal expansion coefficient of water with temperature

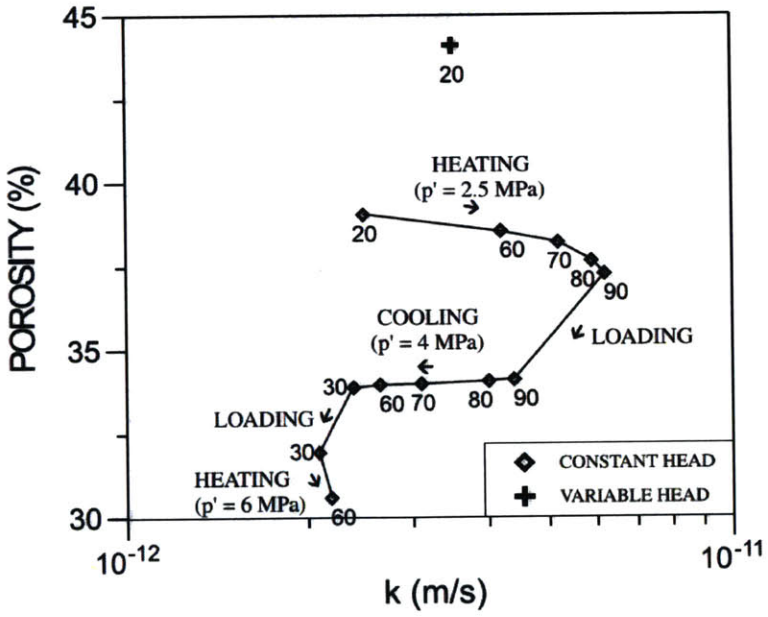

Figure 2.5: Hydraulic conductivity tests on saturated Boom clay at various stresses and temperatures (values shown are in °C) (Delage et al., 2000)

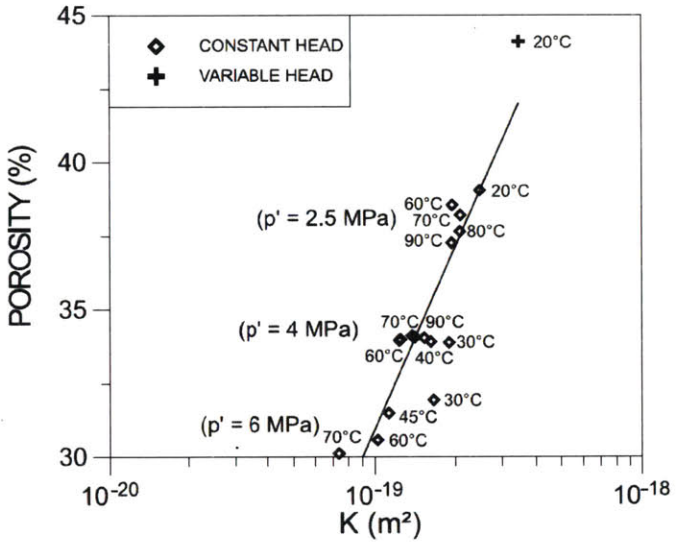

Figure 2.6: Variation of intrinsic permeability with porosity at various temperatures for saturated Boom clay (Delage et al., 2000)

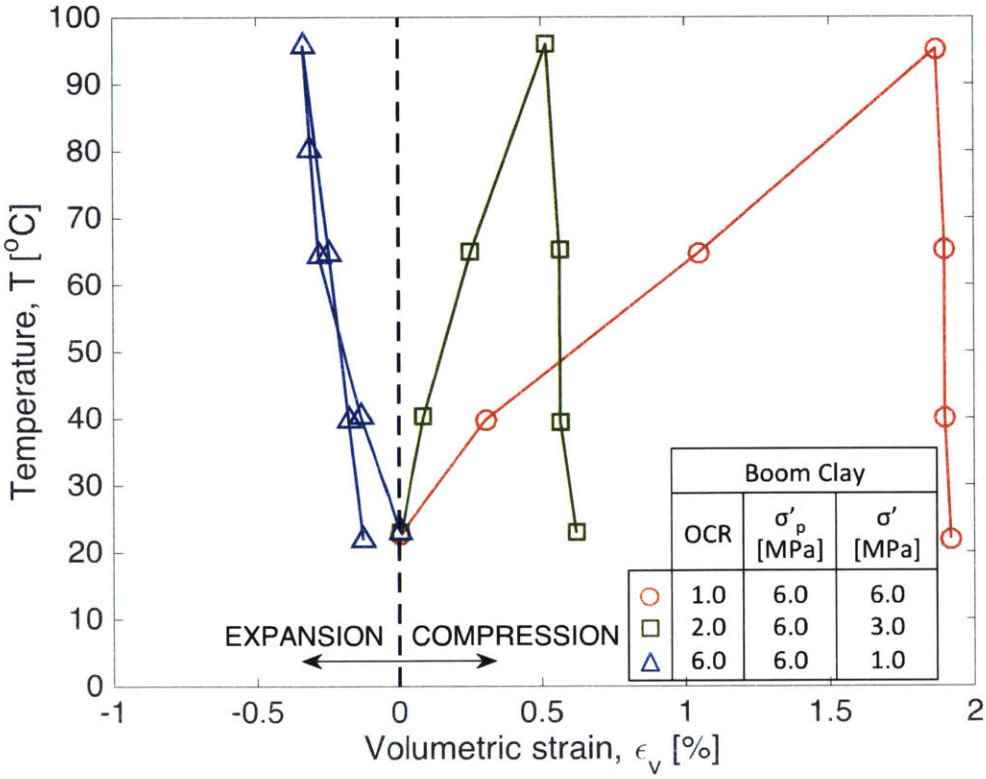

Figure 2.7: Volumetric strain during heating and cooling under constant isotropic effective stress conditions for isotropically consolidated natural Boom clay (after Baldi et al., 1991)

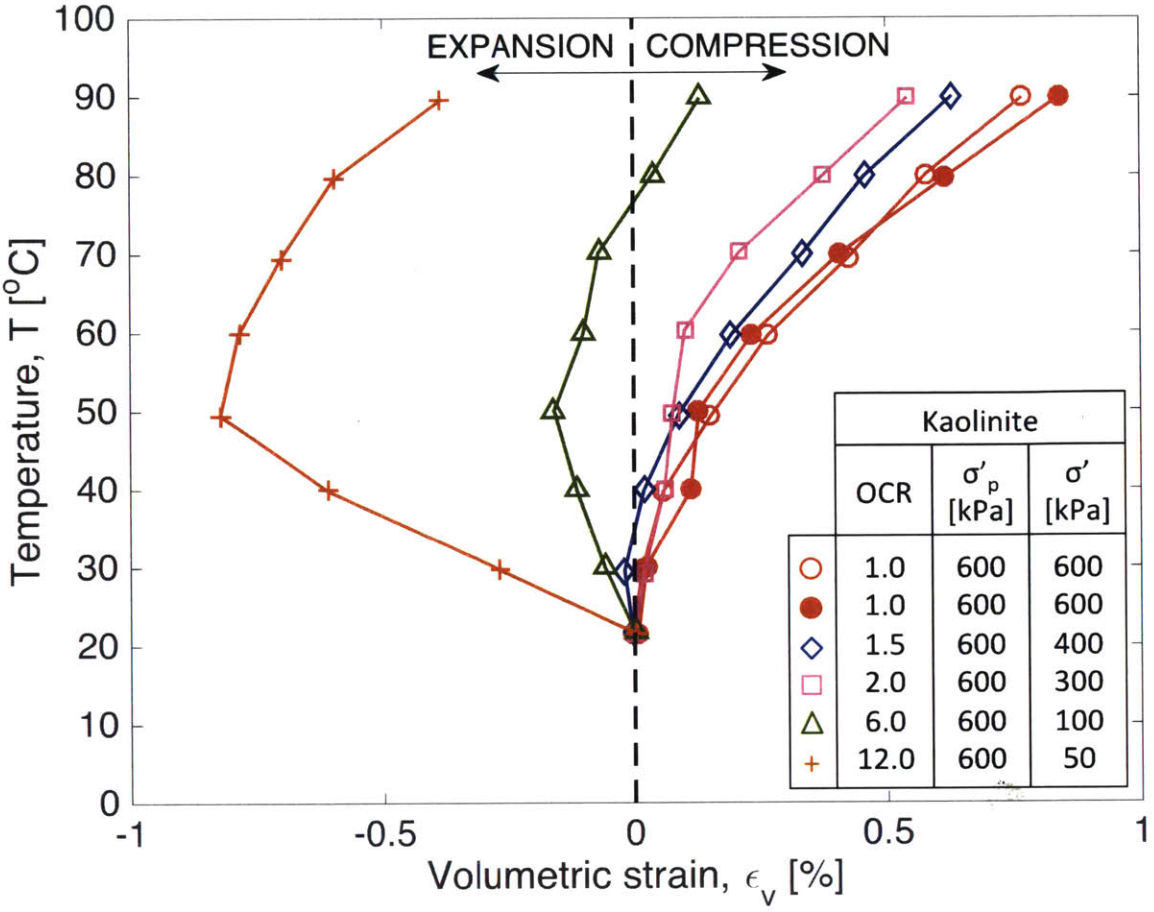

Figure 2.8: Thermal volumetric strain of isotropically consolidated Kaolinite during drained heating from 22 to 90°C (after Cekerevac and Laloui, 2004)

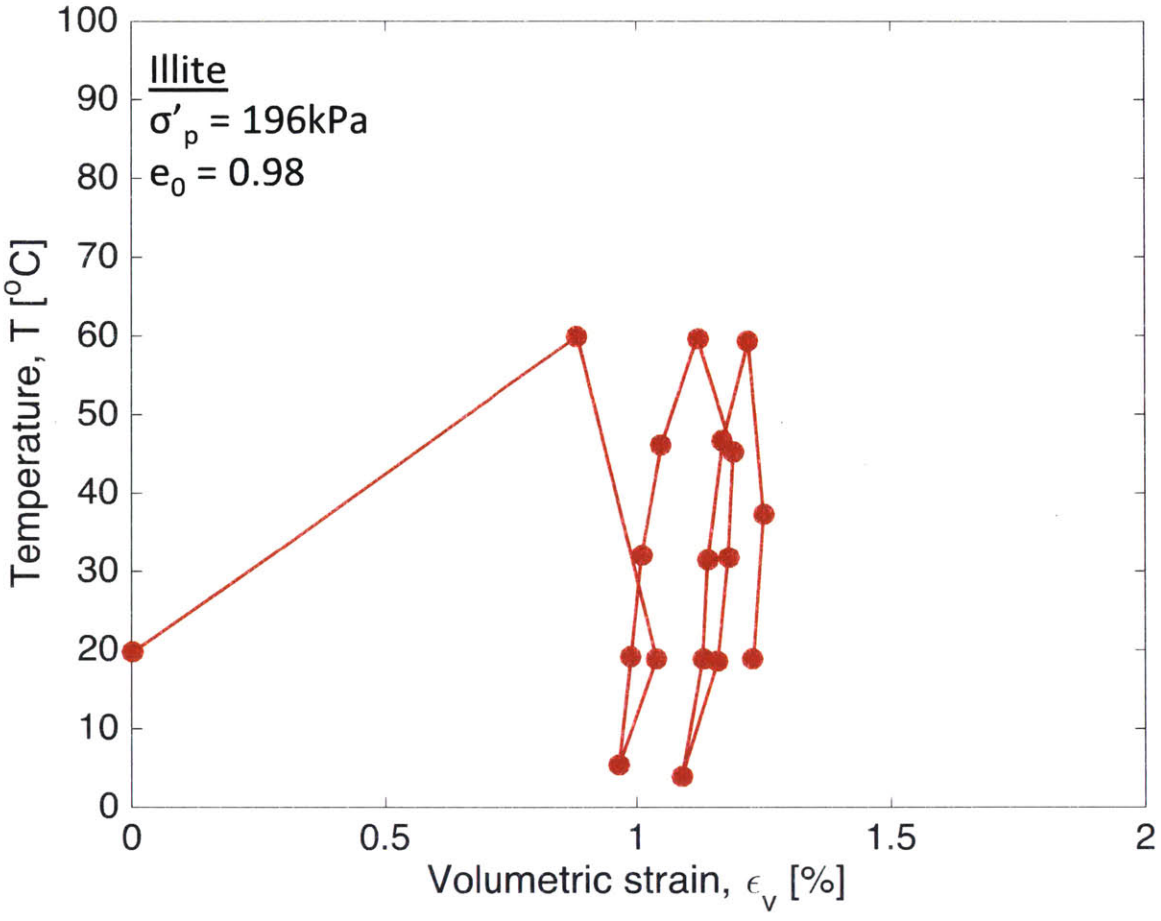

Figure 2.9: Thermal cyclic test on an isotropically consolidated NC illite (after Campanella & Mitchell, 1968)

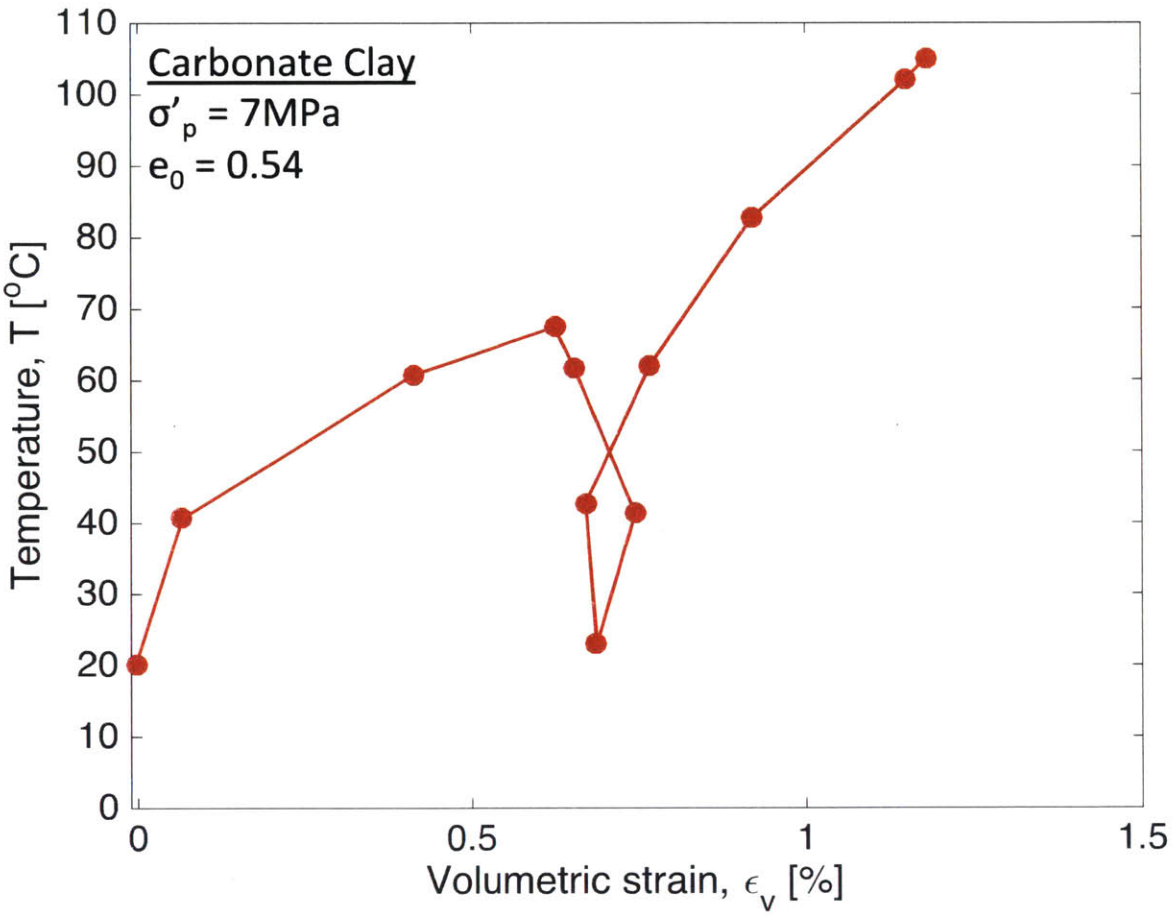

Figure 2.10: Thermal cyclic test on an isotropically consolidated natural NC carbonate clay (after Hueckel et al., 1998)

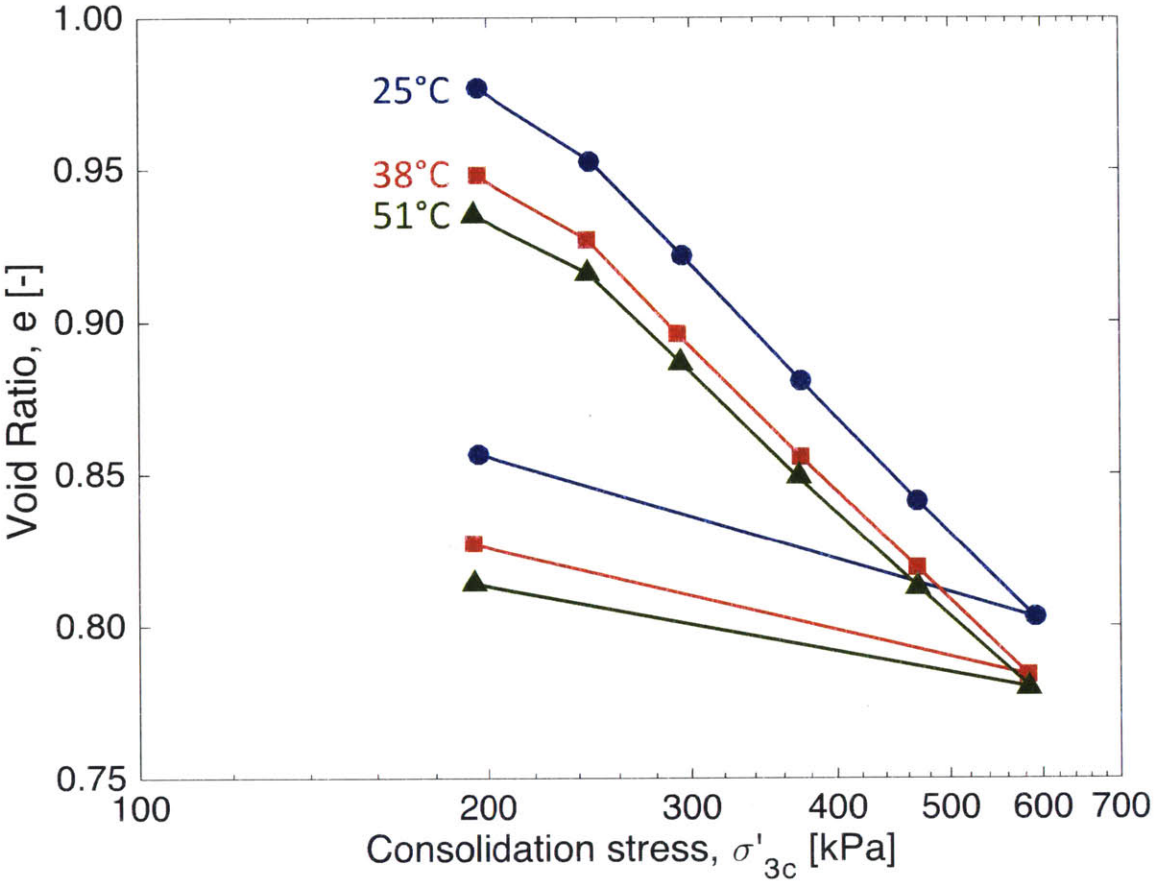

Figure 2.11: Effect of temperature on isotropic consolidation behavior of saturated illite (after Campanella and Mitchell, 1968)

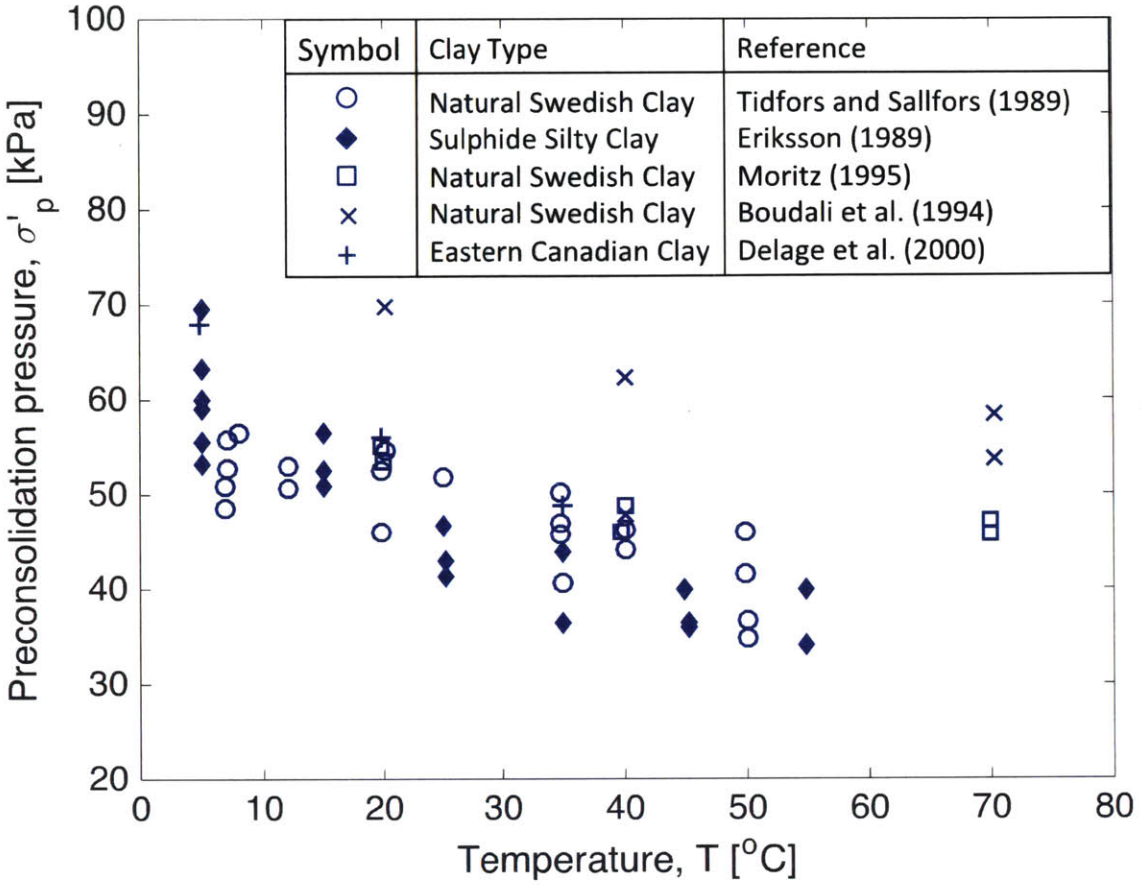

Figure 2.12: Variation of preconsolidation pressure with temperature for natural clays (after Cekerevac and Laloui, 2004)

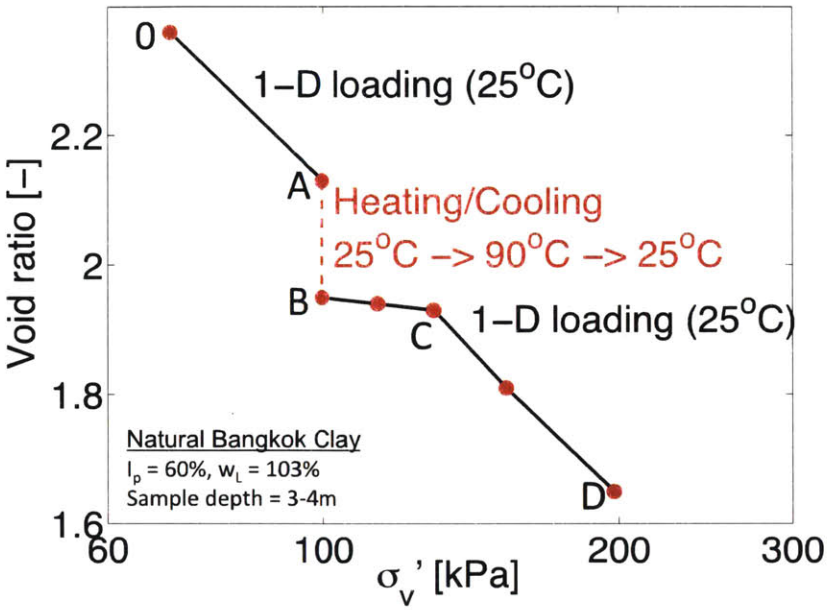

Figure 2.13: Combined mechanical loading and heating-cooling cycle on Bangkok clay (after Abuel-Naga et al., 2006)

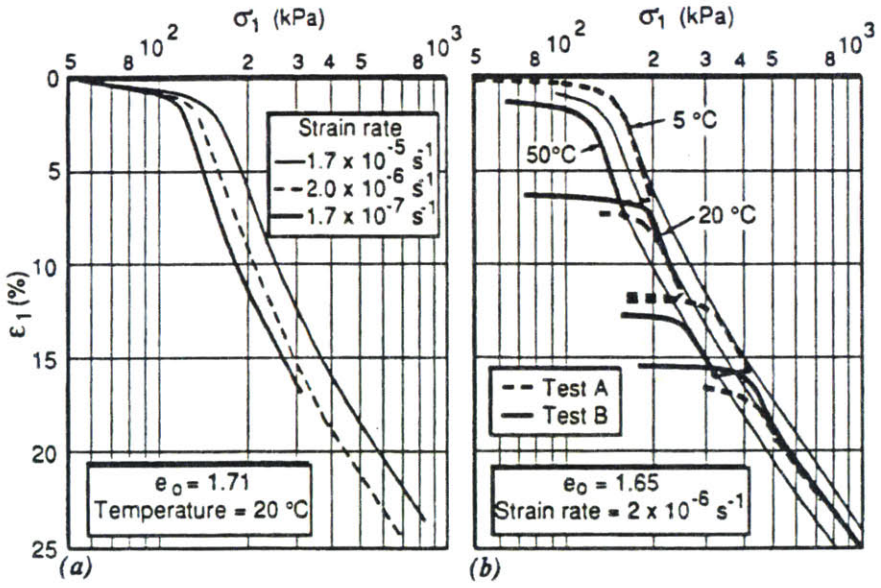

Figure 2.14: Effects on one-dimensional compression of St-Polycarpe clay (I_p =24%, w = 56%) of a) strain rate and b) temperature (Leroueil and Marques, 1996)

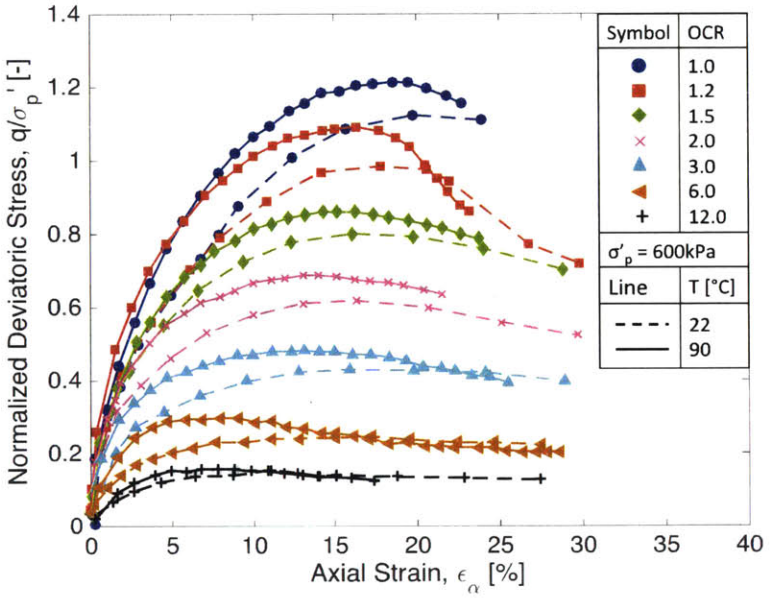

a) q/σ_p' vs ε_α

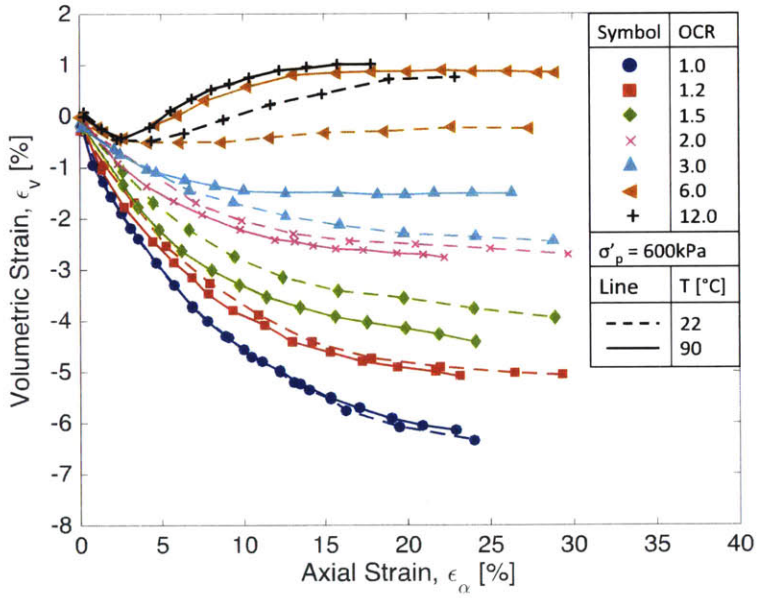

b) ε_v vs ε_α

Figure 2.15: Drained triaxial tests on Kaolinite at ambient (22°C – dashed lines) and high (90°C – solid lines) temperatures for different OCRs (after Cekerevac and Laloui, 2004)

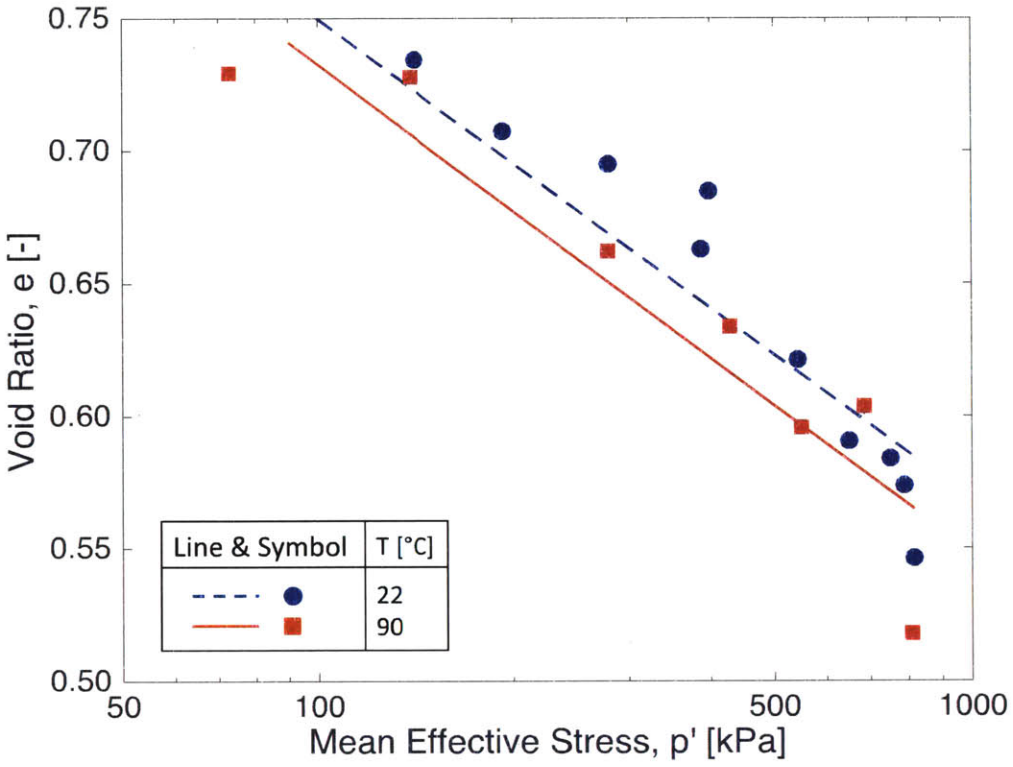

Figure 2.16: Influence of temperature on critical state line (CSL) in the volumetric plane (after Cekerevac and Laloui, 2004)

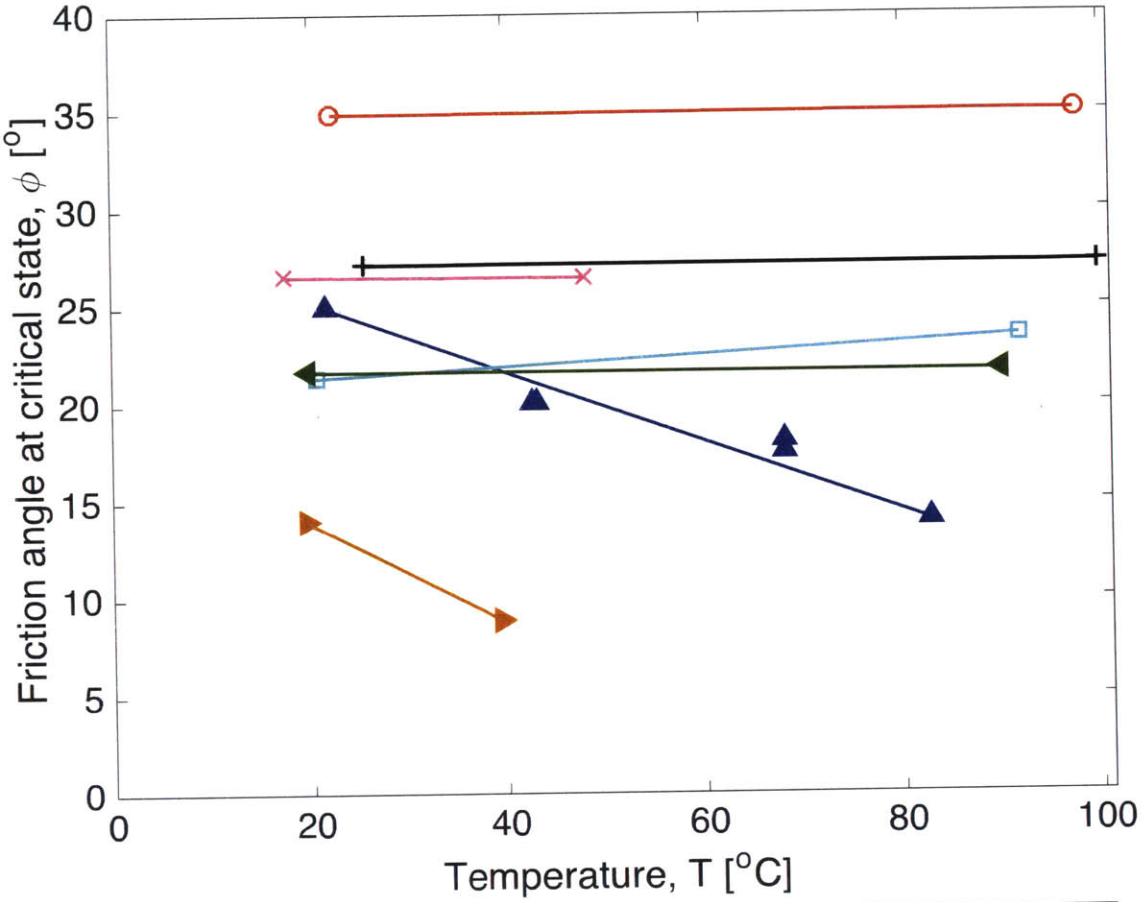

Symbol	Clay Type	Reference
▲	Kaolinite	Hicher and Despax (1976)
▶	Kaolinite	Robinet et al. (1997)
◀	Kaolinite	Cekerevac and Laloui (2004)
○	Pontida Clay	Hueckel and Baldi (1990)
□	Boom Clay	Hueckel and Pellegrini (1989)
×	Todi Clay	Burghignoli et al. (2000)
+	Illite	Graham et al. (2001)

Figure 2.17: Friction angle of different clays at critical state versus temperature (after Vulliet, Schrefler and Laloui, 2009)

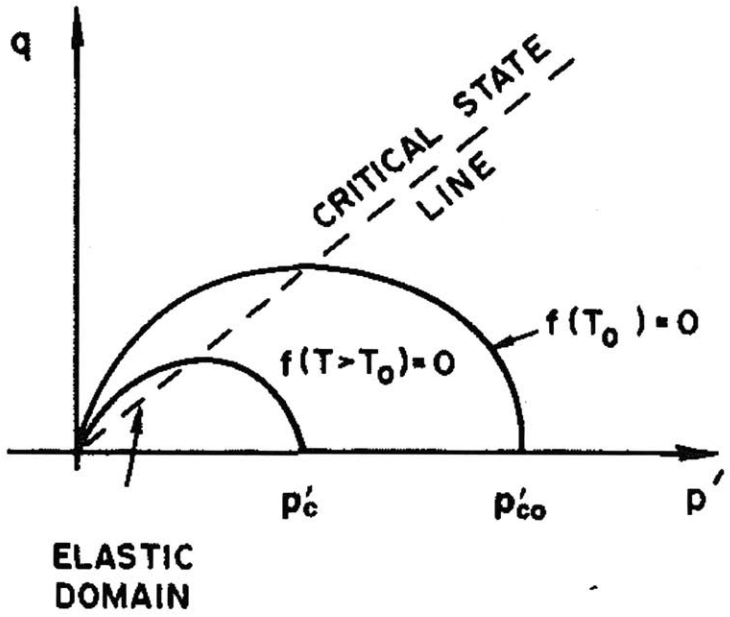

Figure 2.18: Thermal dependence of yield surface assumed in HB90 model (Hueckel and Borsetto, 1990)

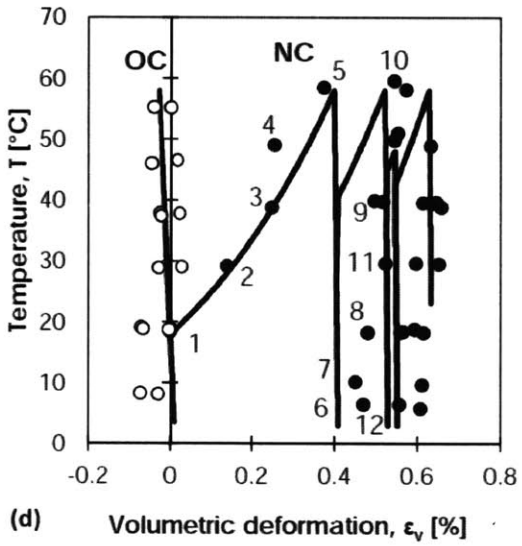

Figure 2.19: Comparison between lab measurements and ACMEG-T predictions of Geneva clay response to cyclic thermal tests (Di Donna, 2014)

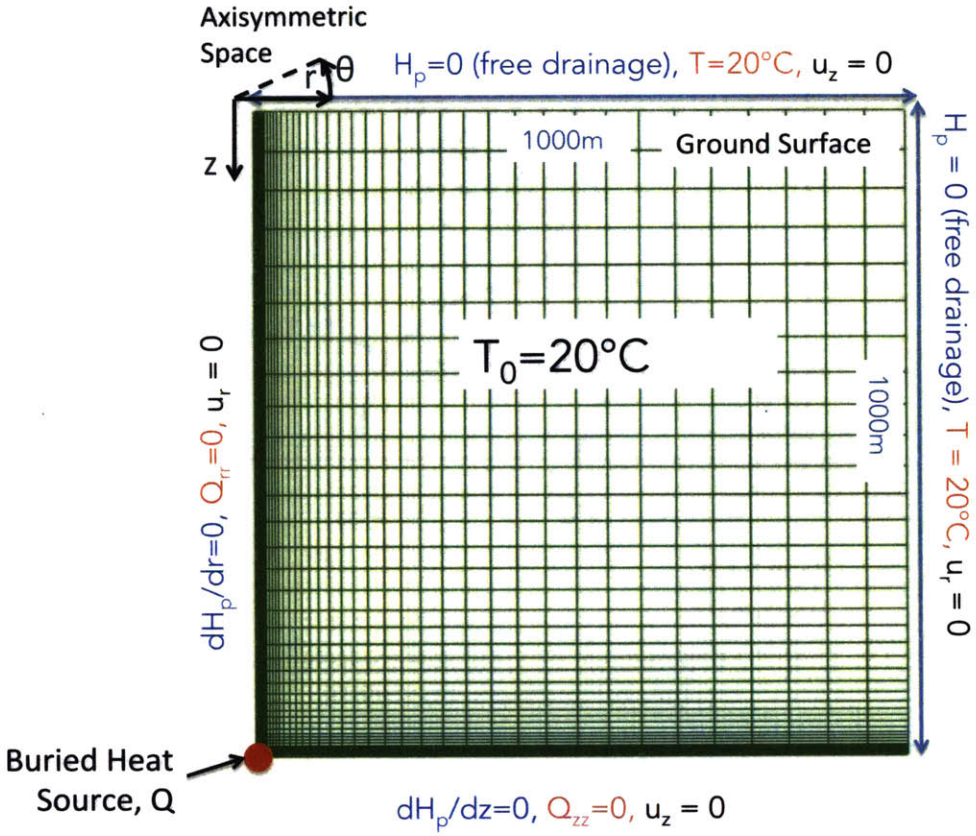

Figure 2.20: Geometry and mesh of Code_Bright model to study the analytic solutions proposed by Booker and Savvidou (1985) for a point heat source in a saturated clay

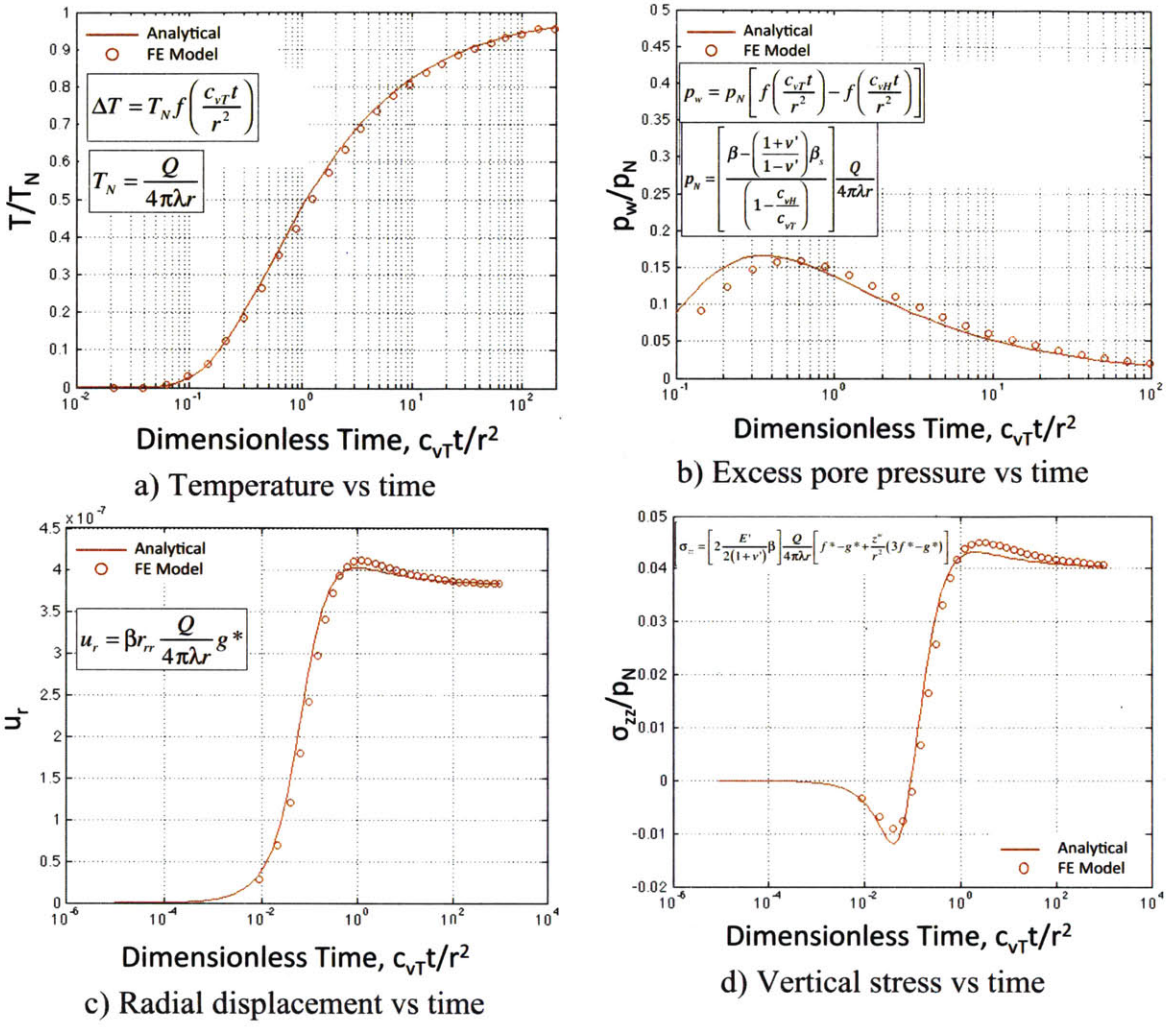

Figure 2.21: Comparison of analytical solutions (Booker and Savvidou, 1985) and Code_Bright results for point heat source in an infinite saturated clay

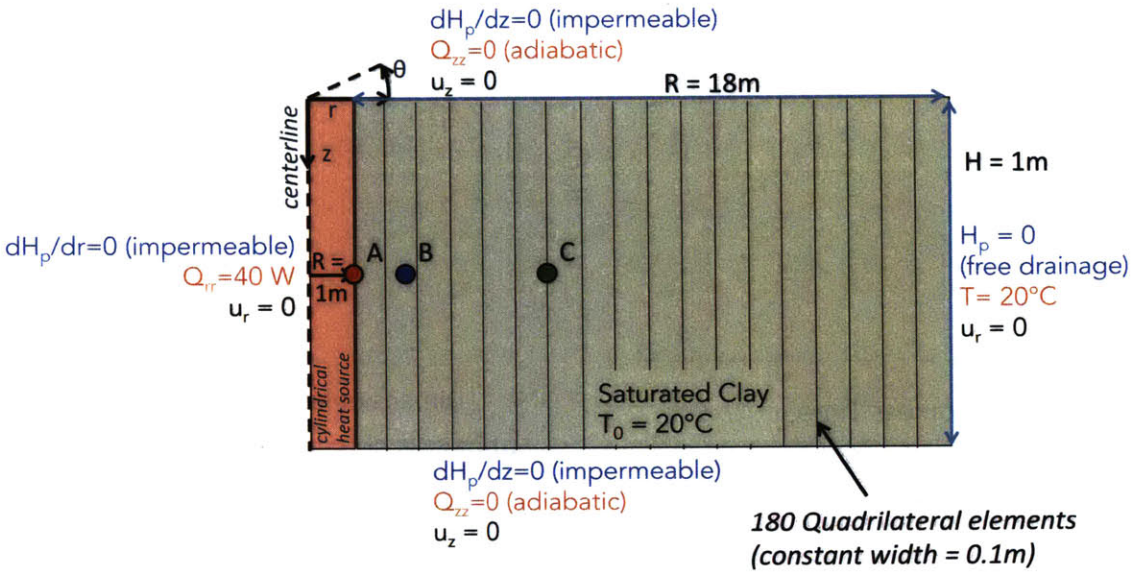

Figure 2.22: Mesh and geometry of Code_Bright 1-D model to study the problem of a radial heat source in a saturated clay

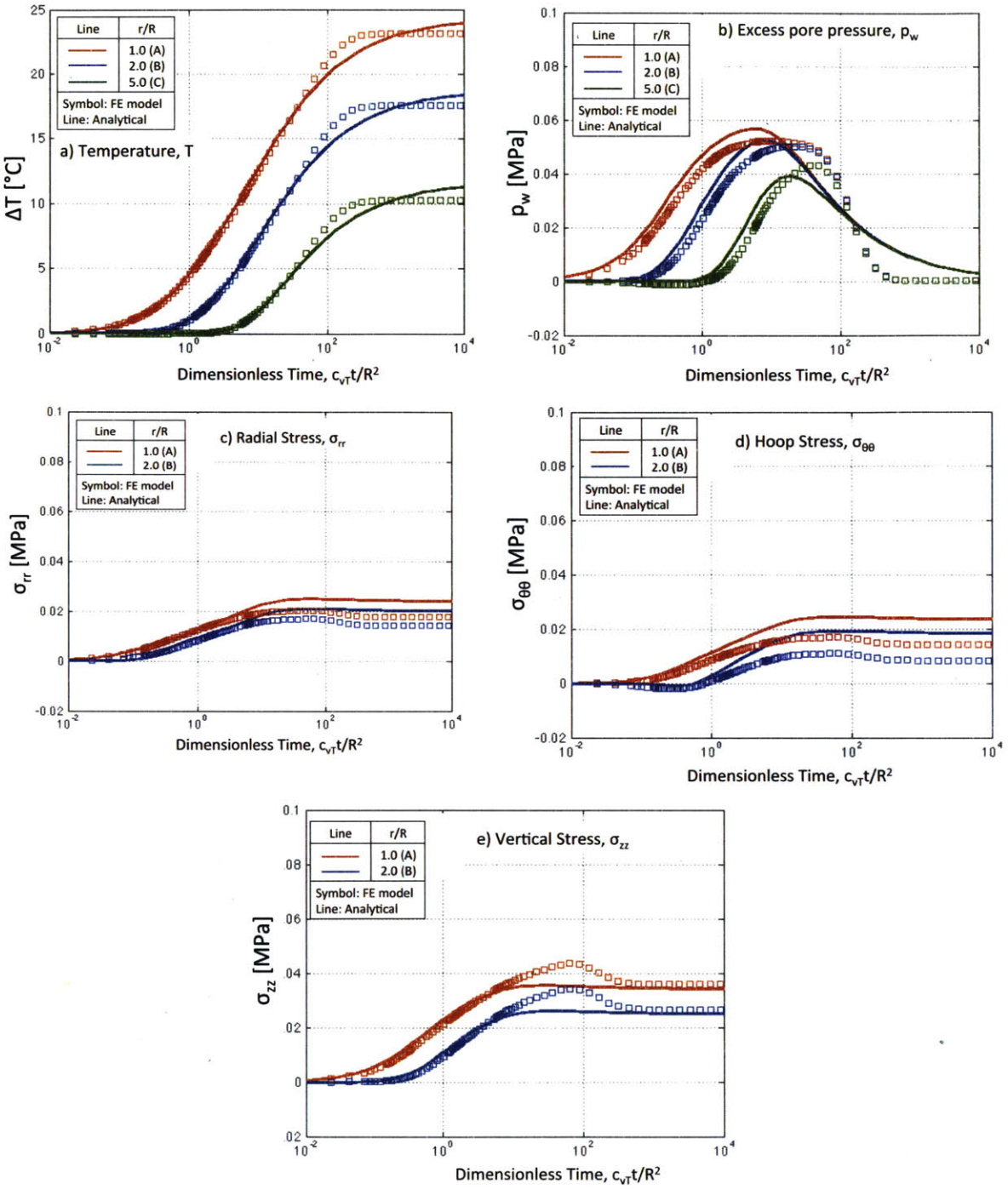

Figure 2.23: Comparison of Code_Bright results and analytic solutions (Booker and Savvidou, 1985) for the cylindrical heat source problem

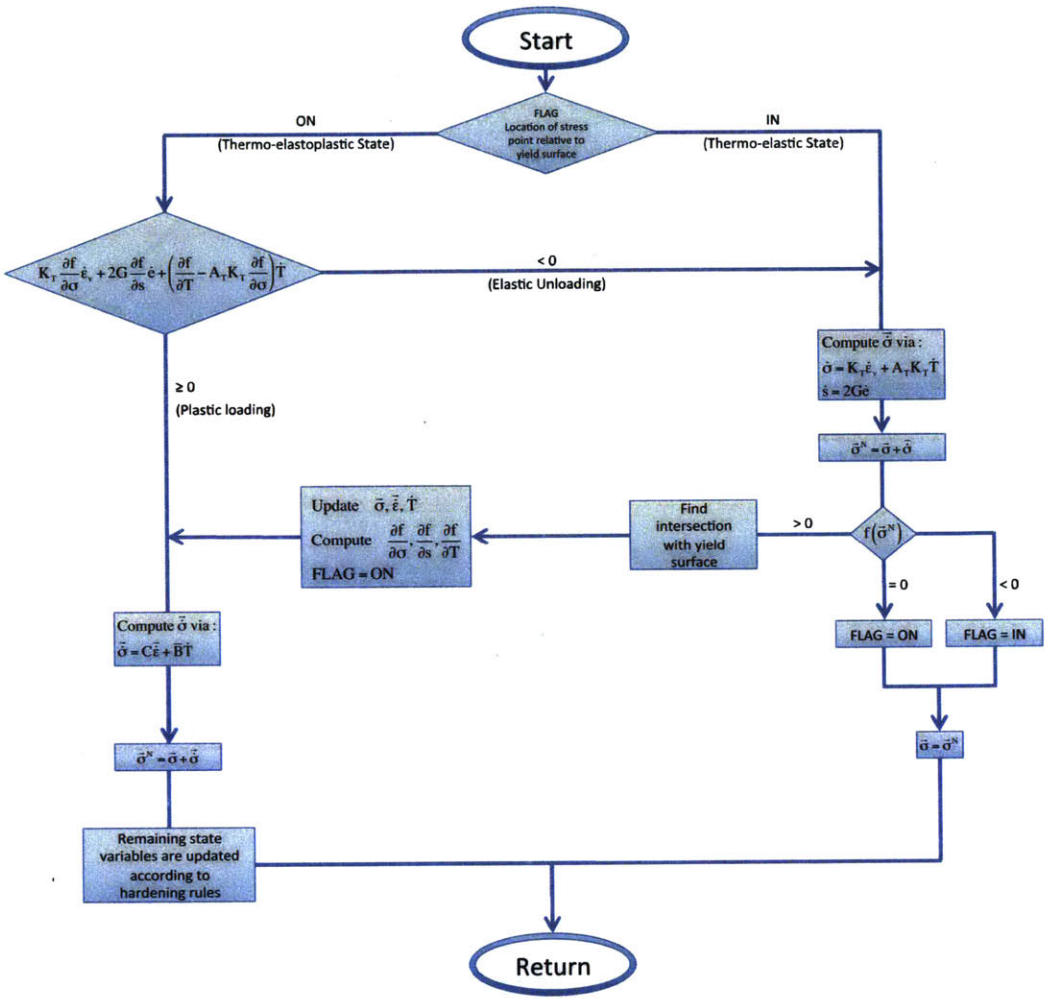

Figure 2.24: Flow chart explaining the HB90 implementation in Modlab

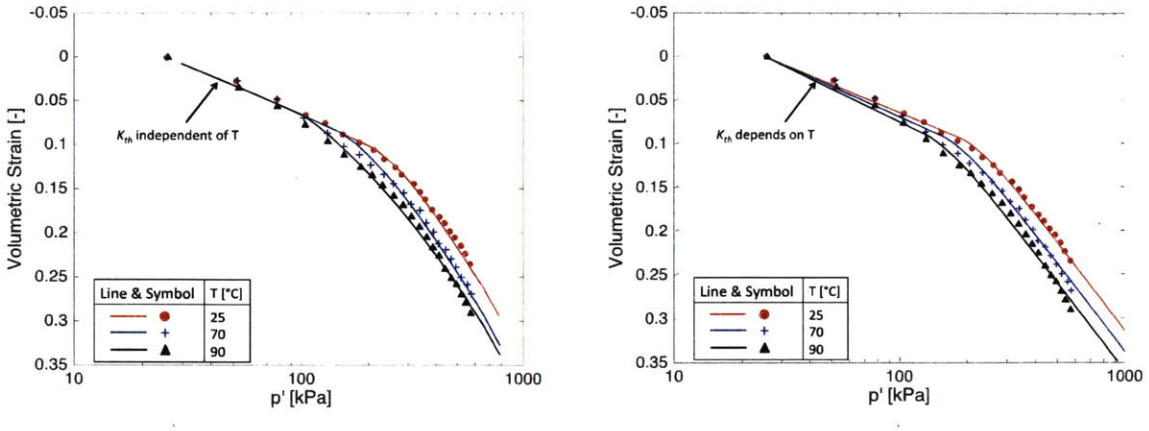

a) Code_Bright implementation b) Modlab implementation

Figure 2.25: Comparisons of HB90 predictions of hydrostatic consolidation of Bangkok Clay at different temperatures (after Abuel-Naga et al, 2006)

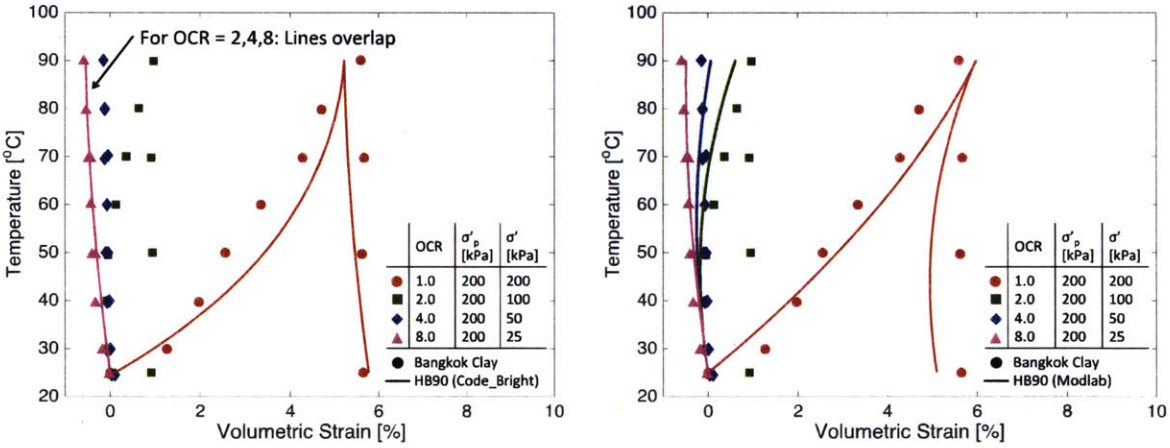

a) Code_Bright implementation b) Modlab implementation

Figure 2.26: Comparisons of HB90 predictions of thermal induced volumetric strain of Bangkok Clay (I_p = 60%, w = 90-95%) (after Abuel-Naga et al, 2006)

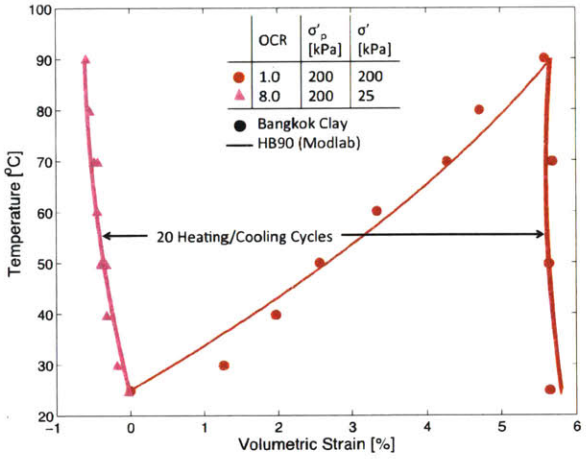

Figure 2.27: HB90 predictions of thermal induced volumetric strain of Bangkok Clay for 20 heating/cooling cycles

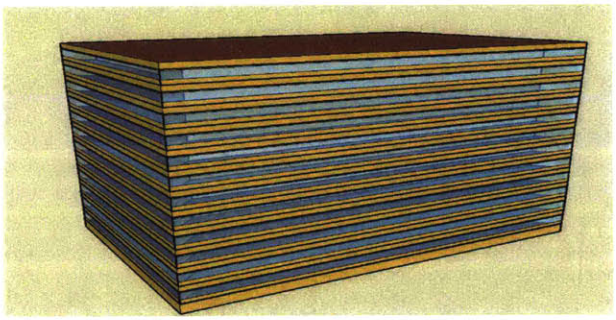

a) Large commercial office building simulated by EnergyPlus for climate zone 5A

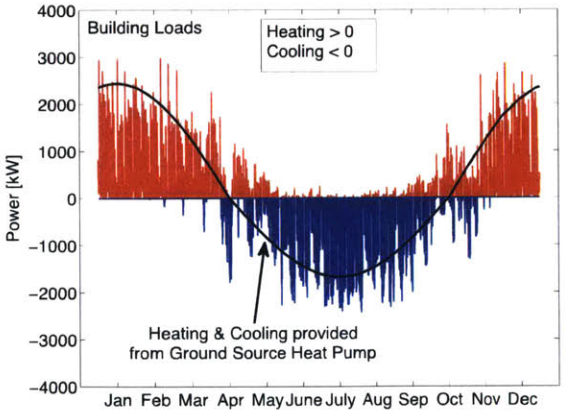

b) Building heating and cooling loads

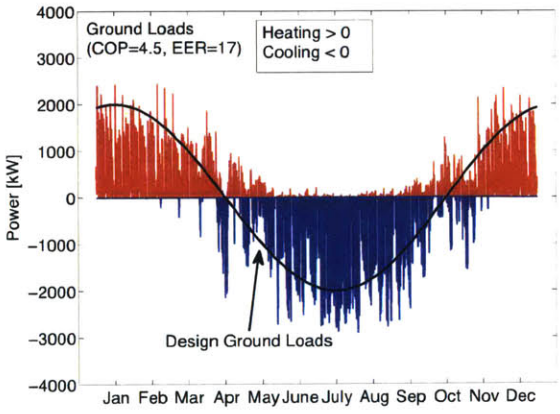

c) Ground heating and cooling loads

Figure 2.28: Heating and cooling loads for large office building in Chicago (Zymnis and Whittle, 2014)

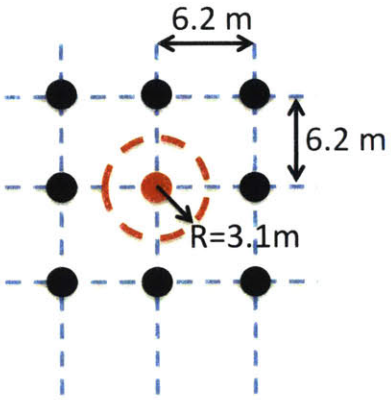

a) Plan view of grid of wells

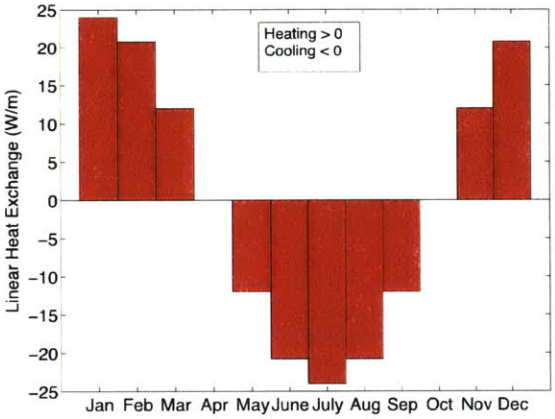

b) Monthly linear heat exchange as assumed in numerical model (heat is the same across all soil layers)

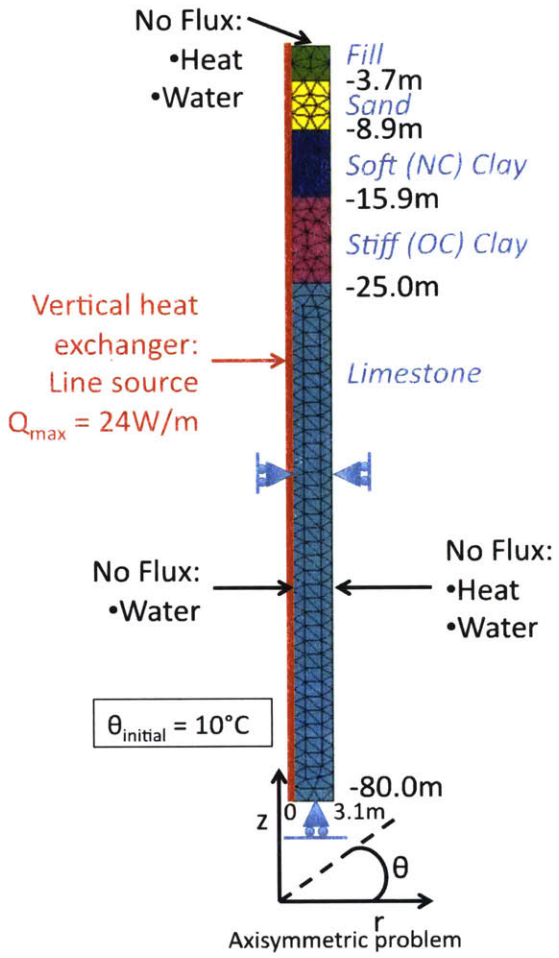

c) Boundary conditions of numerical model

Figure 2.29: Details of numerical model (solved using Code_Bright) (Zymnis and Whittle, 2014)

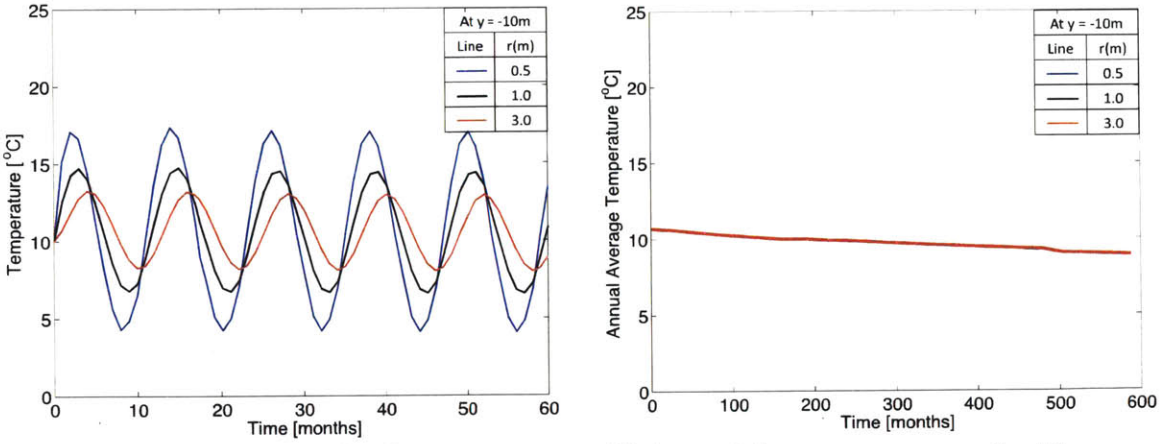

a) Actual response for 5 years b) Annual Average response for 50 years

Figure 2.30: Temperature prediction at different distances from the heat source (Zymnis and Whittle, 2014)

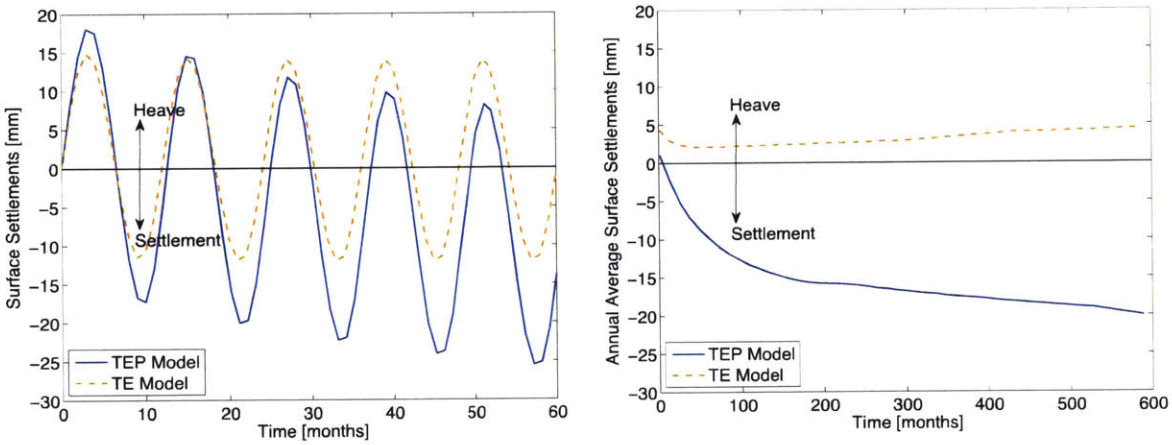

a) Actual response for 5 years b) Annual Average response for 50 years

Figure 2.31: Comparison of surface settlement predictions by the TEP and TE Models (Zymnis and Whittle, 2014)

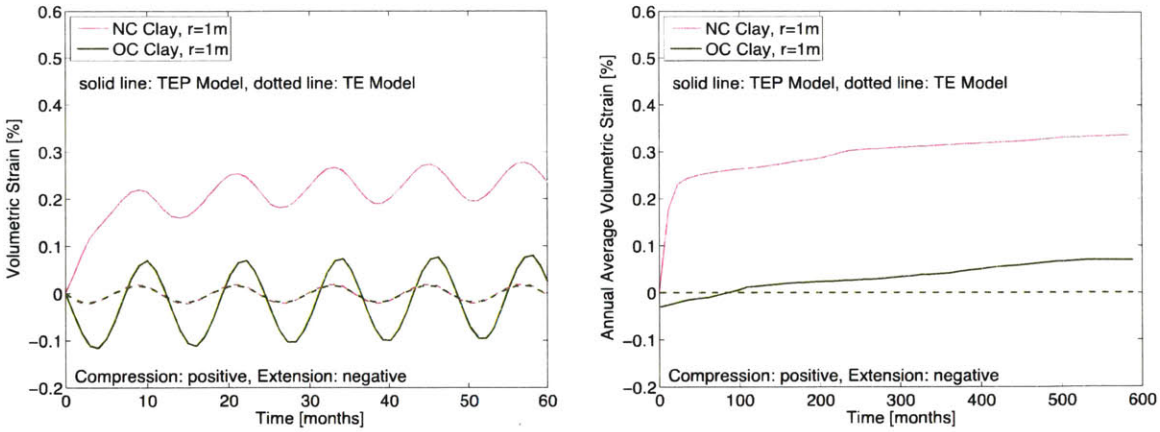

a) Actual response for 5 years b) Annual Average response for 50 years

Figure 2.32: Comparison of volumetric strain predictions by the TEP and TE Models (Zymnis and Whittle, 2014)

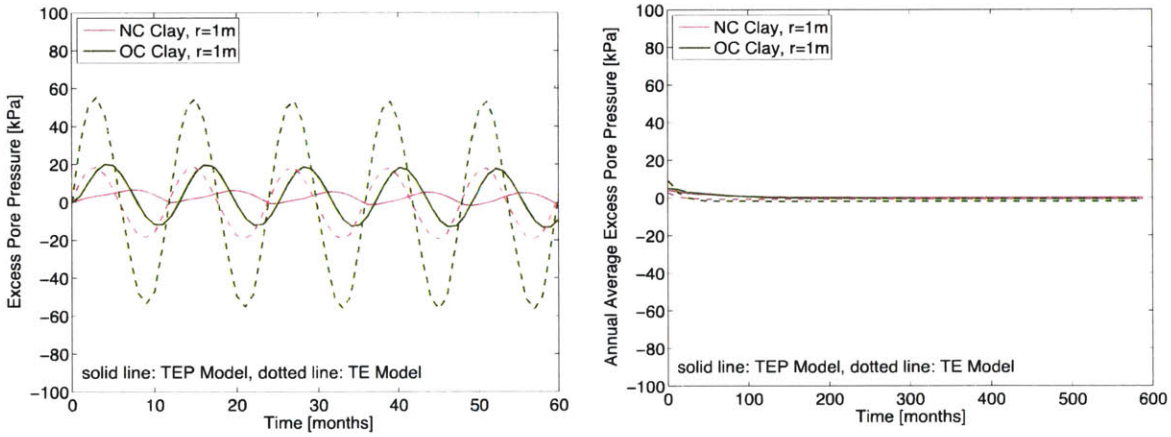

a) Actual response for 5 years b) Annual Average response for 50 years

Figure 2.33: Comparison of excess pore pressure predictions by the TEP and TE Models (Zymnis and Whittle, 2014)

Chapter 3

Tsinghua Thermosoil (TTS) Model and Calibration

3.1 Introduction

The previous chapter has highlighted some key limitations of existing constitutive models for predicting the thermo-mechanical response of clays through long-term (seasonal) cycles of heating and cooling. The current research has implemented the Tsinghua Thermosoil model (TTS; Zhang and Cheng, 2013) to address these limitations. Section 3.2 begins with a review of the key concepts and details of the TTS model formulation. One key aspect of the TTS model relates to the thermal effects on the conversion of 'bound water' (i.e., water adsorbed onto the surface of clay particles, e.g., Lambe, 1960; Paaswell, 1967; Morin and Silva, 1984; Delage et al., 2000) to free water. Section 3.3 describes a series of experiments that examine this process through measurements of temperature dependence in the specific gravity of the solid particles. Section 3.4 then presents detailed calibration techniques for TTS parameters that were developed as part of this thesis and are illustrated using recent lab data for Geneva Clay (Di Donna and Laloui, 2015). The chapter concludes with an in-depth evaluation of the TTS model, with an emphasis on the simulation of clay response to long-term cyclic heating and cooling.

3.2 Tsinghua Thermosoil (TTS) Model Formulation

The Tsinghua Thermosoil (TTS) model is based on non-equilibrium thermodynamic theory (Groot and Mazur, 1962) in order to provide a more fundamental physical basis for the thermo-mechanical response of saturated clay and sand. In contrast to prior formulations that were based on classical elasto-thermoplasticity (e.g., Hueckel and Borsetto, 1990; Cui et al., 2000; Laloui and Francois, 2009) TTS is based on Granular Solid Hydrodynamics (GSH; Jiang and Liu, 2007), a recent theoretical

framework aiming to provide a more fundamental basis for understanding different aspects of behavior for granular media (including transient and steady deformation). The TTS model does not use a yield function, flow rules or other constraints of classical plasticity, but is able to describe many key empirical observations of clay behavior, including virgin consolidation of normally consolidated clay and hysteretic stress-strain response in unloading and reloading etc. The current implementation of the TTS model makes the following assumptions:

1. Soil is fully saturated (for isothermal conditions, deformation and shear strength are controlled by effective stresses) and is composed of a mixture of solid and liquid phases (Figure 3.1). The liquid phase is divided into free water, which fully fills the macroscopic pores, whose migration is described by Darcy's Law; and bound water, which is fully adsorbed by the soil particles and fills the microscopic pore space (for sands, the specific surface area is small, SSA ~ 0.03 m^2/g while for clay particles SSA can range from 10-200 m^2/g, with the highest values for smectites).
2. All three phases are continuous in space and have the same temperature
3. There is no phase change in water for the temperature range considered (i.e., no solidification or vaporization).

3.2.1 Double Entropy Theory

Entropy is a thermodynamic quantity representing the conversion of thermal energy into mechanical work. It is often interpreted as a measure of disorder of the system. The TTS model accounts for interactions between micro-level (i.e., particle or granular level) and macro-level behavior through a double-entropy formulation. The total entropy is used to describe macroscopic phenomena (irrecoverable deformations), while the granular entropy represents microscopic phenomena associated with sliding, rolling and collision of particles (Figure 3.2), which is qualitatively similar to molecular motion and hence, can be described by granular entropy and its conjugate variable the granular temperature, $\tilde{T}_g$ [-]. It is assumed that once external loading is applied, there is a simultaneous increase in both total and granular entropies. Granular entropy is

subsequently converted to total entropy with a conversion rate $\dot{I}_g$ [J/m^{3}s] (Figure 3.2). Once external loading is removed, the particle movement and corresponding dissipation do not immediately disappear but a fully static state is achieved only after all of the granular entropy has been fully converted to total entropy (i.e., there is a time lag associated with conversion of granular entropy).

Total Entropy

According to the second law of thermodynamics, any irreversible process must cause an increase in entropy of the system. The TTS formulation (Zhang and Cheng, 2013) describes changes in the total entropy, $\dot{s}$, as the sum of entropy for each of the soil phases as follows:

$$\dot{s} = \rho_s (1-\phi)\dot{s}_s + \rho_{fw}\phi_{fw}\dot{s}_{fw} + \rho_{bw}\phi_{bw}\dot{s}_{bw} \tag{3.1a}$$

where $\phi = \phi_{fw} + \phi_{bw}$ is the total porosity, subscripts fw and bw refer to the free and bound water respectively, ρ is mass density, s_s, s_{fw} and s_{bw} are the specific entropies of the solid, free water and bound water phases[7]. The total entropy change, $\dot{s}$, is then equal to the rate of entropy production $\dot{R}/T$, plus the entropy increase due to thermal conduction minus the entropy due to water seepage:

$$\dot{s} = \frac{\dot{R}}{T} + \frac{\partial}{\partial x_i}\left(\frac{\kappa}{T}\frac{\partial T}{\partial x_i}\right) - \left(v_i^{fw} - v_i^{s}\right)\rho_{fw}\phi_{fw}\frac{\partial s_{fw}}{\partial x_i} \tag{3.1b}$$

where κ [m^2] is the intrinsic permeability of the soil and $\left(v_i^{fw} - v_i^{s}\right)$ is the relative velocity of free water and the solid skeleton.

According to non-equilibrium thermodynamics the energy dissipation rate, $\dot{R}$, [J/m^{3}s = Pa/s] is expressed as the sum of the product of dissipative forces with the corresponding dissipative flow. Dissipative forces are the driving forces that deviate the system from an equilibrium thermodynamic state. The two main dissipation mechanisms

---

[7] $s_s = c_s \ln\left(T/T_0\right) + s_{s0}$ and $s_{fw} = s_{bw} = c_w \ln\left(T/T_0\right) + s_{w0}$, where c_s and c_w are the specific heat capacities of solid and water respectively and s_{s0} and s_{w0} are the specific entropies of solid and water at reference temperature T_0.

in saturated soils are: 1) the 'transient elasticity' which is the development of non-elastic (i.e., irreversible) strains due to the deviation from the pure elastic state; and 2) the conversion of granular entropy to total entropy. The dissipative forces are the effective stress, σ'_{ij} and the granular temperature, $\tilde{T}_g$ and the corresponding flows are the irreversible strain rate due to change in elastic strain, $\dot{\varepsilon}_{ij}^{D}$, and the conversion rate of granular entropy to total entropy, $\dot{I}_g$.

$$\dot{R} = \dot{\varepsilon}_{ij}^{D}\sigma'_{ij} + \dot{I}_g\tilde{T}_g \tag{3.2}$$

The TTS model assumes that the irreversible strain rate is linked to the deviatoric and octahedral elastic strains by:

$$\dot{\varepsilon}_{ij}^{D} = \dot{\lambda}_s\tilde{T}_g^{a}e_{ij}^{e} + \dot{\lambda}_v\tilde{T}_g^{a}\varepsilon_{kk}^{e}\delta_{ij} \tag{3.3}$$

where a is a model input constant that controls rate effects, $\dot{\lambda}_s$ [1/s] and $\dot{\lambda}_v$[1/s] are material constants and e_{ij}^{e} and ε_{kk}^{e} are deviatoric and volumetric components of the elastic strain tensor. The model assumes that the deviation from equilibrium thermodynamic position is small and hence, $\dot{I}_g$ can be expressed as a linear function of $\tilde{T}_g$:

$$\dot{I}_g = \gamma\tilde{T}_g \tag{3.4}$$

where γ [Pa/s] is a material constant.

Granular Entropy

The application of external loading on granular materials causes sliding, rolling and collision of particles, which results to a change in their kinetic energy and elastic potential energy. This energy generation at the microscopic scale is referred to as 'granular fluctuation' (Zhang and Cheng, 2013) and is the source of plastic deformation for granular solids. The granular fluctuation is attenuated by heat generation at the macro-level until the fluctuation disappears. Jiang and Liu (2009) proposed that the granular fluctuation was similar to the molecular motion. Thus the granular entropy density, s_g, and its conjugate variable, granular temperature, $\tilde{T}_g$, are introduced to quantify the

granular fluctuation, although it should be pointed out that while $\tilde{T}_g$ is not the actual temperature. As opposed to total entropy of the system, which only increases, granular entropy can both increase and decrease, since only part of granular entropy is converted to total entropy. The change of granular entropy is equal to the granular entropy production rate $\dot{R}_g / \tilde{T}_g$ minus the amount of granular entropy converted to total entropy, $\dot{I}_g$, as shown in equation 3.5.

$$\rho_s(1-\phi)\dot{s}_g = \frac{\dot{R}_g}{\tilde{T}_g} - \dot{I}_g \tag{3.5a}$$

A linear relation between specific granular entropy, s_g, and granular temperature, $\tilde{T}_g$, is assumed:

$$s_g = b\tilde{T}_g \tag{3.5b}$$

where b is a material constant. Both mechanical and thermal loads can stimulate the reorganization of soil particles and hence, the granular energy production rate, $\dot{R}_g$, is given by equation 3.6a, with dissipative forces being the total strain rate, $\dot{\varepsilon}_{ij}$, and temperature rate, $\dot{T}$, with corresponding dissipative flows are σ_{ij}^g and M, respectively:

$$\dot{R}_g = \sigma_{ij}^g \dot{\varepsilon}_{ij} + M\dot{T} \tag{3.6a}$$

$$\sigma_{ij}^g = \eta_g \tilde{T}_g \dot{e}_{ij} + \zeta_g \tilde{T}_g \dot{\varepsilon}_{kk} \delta_{ij} \tag{3.6b}$$

$$M = \frac{\psi_g \tilde{T}_g \alpha_{bf} \sigma_{kk} \phi_{bw}}{3(1-\phi)} \tag{3.6c}$$

Both dissipative flows are expressed as linear functions of the dissipative forces and of granular temperature, $\tilde{T}_g$, as shown in equations 3.6b and 3.6c, with constant 'migration coefficients' η_g [Pa s], ζ_g [Pa s] and ψ_g [-]. In order to describe thermal effects, it is assumed that during heating, part of the bound water is converted to free water, causing irreversible rearrangement of the solid particles. M [Pa/s] reflects the unrecoverable particulate level movement induced by the conversion of bound to free water to simulate the irreversible volumetric deformation caused by changes in temperature and α_{bf} [1/°C],

is a key input constant for the TTS model that controls the conversion of bound water to free water during heating. It is assumed that $\psi_g = 0$ for $\dot{T} \leq 0$, since cooling does not produce irreversible thermal strain.

3.2.2 Elastic Potential Energy Function and Effective Stress Derivation

In the TTS model it is assumed that reversible energy processes result in locked-in elasticity in the system that can be expressed by the elastic potential energy function. Effective stress is expressed as the derivative of the elastic potential energy density function, ω_e:

$$\sigma'_{ij} = \frac{\partial \omega_e}{\partial \varepsilon^e_{ij}} \tag{3.7}$$

This definition is common to all 'hyperelastic' models of soil behavior (e.g., Houlsby and Puzrin, 2006). Jiang and Liu (2003) introduced a function for ω_e that can also describe the state boundary surface (i.e., limit on possible effective stress states that is linked to maximum allowable ratios of shear to normal stress):

$$\omega_e = B\left(\varepsilon^e_v\right)^{0.5}\left[\frac{2}{5}\left(\varepsilon^e_v\right)^2 + \frac{\left(\varepsilon^e_s\right)^2}{\xi}\right] \tag{3.8}$$

where ε^e_v is the elastic volumetric strain[8], $\varepsilon^e_s = \sqrt{e^e_{ij}e^e_{ij}}$ and $e^e_{ij} = \varepsilon^e_{ij} - \varepsilon^e_{kk}\delta_{ij}/3$, is the second invariant of elastic shear strain, B is an input constant, $\rho_d = G_s/(1+e)$ is the dry density of the soil, and ξ is an input parameter that controls the range of possible strains and therefore effective stress states.

Zhang and Cheng (2013) modified the above expression, to incorporate: 1) cohesion of soils; 2) critical state friction angle; and 3) thermal effects, as shown below:

$$\omega_e = \frac{2}{5}B\left(\varepsilon^e_v + c\right)^{1.5}\left(\varepsilon^e_v\right)^2 + B\xi\left(\varepsilon^e_s\right)^2\left(\varepsilon^e_v + c'\right)^{1.5} + \int 3K_e\beta_s\left(T - T_0\right)d\varepsilon^e_v \tag{3.9}$$

where $B = B_0\exp\left(B_1\rho_d\right)$ and B_0 and B_1 are input constants. It is subsequently shown that B_0 and B_1 can be related to the location and slope of the virgin consolidation line, respectively; c is linked to cohesion of soils ($c = 0$ for sands); ξ is related to the size of the

[8] $\varepsilon^e_v = \varepsilon^e_{kk}$

state boundary surface (and affects the peak internal friction), c' controls the critical state friction angle; and β_s is the linear thermal expansion coefficient for the solid skeleton.

Zhang and Cheng (2013) derive the state boundary surface, also referred to as the ultimate stress state surface (USSS) from the singularity condition of the Hessian matrix, $\det|\omega_e| = 0$. Panagiotidou et al. (2016) present an in-depth study of the shear response of the TTS model in relation to Critical State Soil Mechanics.

3.2.3 Evolution Laws of Elastic and Plastic Strain

The total strain rate $\dot{\varepsilon}_{ij}$ is the sum of elastic strain rate, $\dot{\varepsilon}^e_{ij}$, and 'irrecoverable' strain rate, $\dot{\varepsilon}^D_{ij}$, as shown below:

$$\dot{\varepsilon}^e_{ij} = \dot{\varepsilon}_{ij} - \dot{\varepsilon}^D_{ij} \tag{3.10}$$

Figure 3.3a illustrates the prediction of cyclic strain accumulation due to mechanical loading and unloading (cf., equation 3.3). In order to avoid overestimation of strain accumulation, Zhang and Cheng (2013) introduced 'hysteretic' strain, ε^h_{ij}, as an additional state variable in the TTS model formulation and its effect is illustrated in Figure 3.3b. Plastic strain rate, $\dot{\varepsilon}^D_{ij}$, is therefore expressed as a function of granular temperature $\tilde{T}_g$:

$$\dot{\varepsilon}^D_{ij} = \dot{\lambda}_s \tilde{T}^a_g \left(e^e_{ij} - e^h_{ij}\right) + \dot{\lambda}_v \tilde{T}^a_g \left(\varepsilon^e_{kk} - \varepsilon^h_{kk}\right)\delta_{ij} \tag{3.11}$$

where ε^e_{ij} and ε^h_{ij} are the elastic strain and hysteretic strain, respectively. The evolution of hysteretic strain rate is given by:

$$\dot{\varepsilon}^h_{ij} = \dot{\varepsilon}^D_{ij} - w \frac{\dot{\varepsilon}^D_{kl}\varepsilon^h_{kl}}{h\sqrt{\varepsilon^h_{mn}\varepsilon^h_{mn}}}\varepsilon^h_{ij} \tag{3.12}$$

where parameters h and w are input constants[9].

Table 3.1 presents the ten independent model state variables, which are the bound and free water porosity, φ_{bw} and φ_{fw}, the temperature T, the granular temperature $\tilde{T}_g$, the

[9] $w = 1$ for $\dot{\varepsilon}^D_{kl}\varepsilon^h_{kl} > 0$ and $w = w_0$ for $\dot{\varepsilon}^D_{kl}\varepsilon^h_{kl} \le 0$

total strain, ε, the elastic strain, ε^e, and the hysteretic strain, ε^h, (with subscripts v and s corresponding to volumetric and deviatoric invariants respectively). Finally, dry density, ρ_d, is used frequently in the model formulation but is not an independent state variable since it can be derived from total porosity ϕ:

$$\phi = \phi_{fw} + \phi_{bw} \tag{3.13}$$

$$\rho_d = G_s \rho_{fw} (1 - \phi) \tag{3.14a}$$

Similarly void ratio, e, can also be derived from total porosity:

$$e = \frac{\phi}{1 - \phi} \tag{3.14b}$$

where G_s is the specific gravity of soil and ρ_{fw} is density of free water.

3.2.4 Summary of Model Equations Expressed for Triaxial Space

The evolution of state parameters for the TTS model are summarized in equations 3.15 – 3.18, while equations 3.19 and 3.20 show the direct calculation of stresses from the state variables. Table 3.2 summarizes all input constants used in the TTS model and their calibration is described in detail in Section 3.4.

1) Change in bound water porosity φ_{bw}:

Zhang and Cheng (2013) suggest the following evolution of bound water porosity:

$$\dot{\phi}_{bw} = -\phi_{bw} \alpha_{bf} \dot{T} + \phi_{bw} \left(\dot{\varepsilon}_v + \frac{\beta_w}{1 - \beta_w \Delta T} \dot{T} \right) \tag{3.15a}$$

where β_w is the thermal expansion coefficient of water. We assume that bound water porosity is not affected by changes in total volumetric strain (i.e., deformations of the soil skeleton only change the free water porosity). The bound water porosity only changes due to conversion of bound water to free water when the clay is heated and so the expression for the evolution of bound water porosity used in this study is:

$$\dot{\phi}_{bw} = -\phi_{bw} \left(\alpha_{bf} - \frac{\beta_w}{1 - \beta_w \Delta T} \right) \dot{T} \tag{3.15b}$$

2) Evolution of granular temperature:

The granular temperature is no expressed by: $T_g = \dot{\lambda}_s^{1/a} \tilde{T}_g$ [1/s^2] and the input constants have been rearranged and are equal to: $m_2 = \dot{\lambda}_s^{1/a} \eta_g / \gamma$, $m_3 = \zeta_g / \eta_g$, $m_4 = \gamma / b$ and $m_5 = \lambda_s^{1/a} \psi_g / \dot{T} b$. By combining equations 3.4, 3.5 and 3.6 the evolution of granular temperature becomes:

$$\dot{T}_g = \frac{1}{\rho_d}\left[m_2 m_4 \left(\dot{\varepsilon}_s\right)^2 + m_2 m_3 m_4 \left(\dot{\varepsilon}_v\right)^2 + \frac{m_5 \sigma'_{kk} \alpha_{bf} \phi_{bw} \dot{T}^2}{3\left(1-\phi\right)} - m_4 T_g \right] \qquad (3.16)$$

where ρ_d is dry density, m_2, m_3, m_4, m_5 and α_{bf} are input constants for the TTS model, $\dot{\varepsilon}_s$ and $\dot{\varepsilon}_v$ are deviatoric and volumetric components of the total strain rate tensor, $\sigma'_{kk}/3$ is mean effective stress, φ is total porosity, φ_{bw} is bound water porosity and $\dot{T}$ is rate of temperature change. Equation 3.16 shows that application of external loading (strain rate, $\dot{\varepsilon}_{ij}$, or temperature rate, $\dot{T}$) causes a change in granular temperature, T_g (first two terms in right-hand side of equation 3.16), which is in turn converted to total entropy (third term in the right-hand side of equation 3.16).

3) Evolution of Elastic Strain:

By rearranging the input constant $m_1 = \dot{\lambda}_v / \dot{\lambda}_s$ and incorporating it in equations 3.10 and 3.11, the elastic volumetric and deviatoric strains become:

$$\dot{\varepsilon}_v^e = \dot{\varepsilon}_v - \dot{\varepsilon}_v^D, \quad \text{where } \dot{\varepsilon}_v^D = 3m_1 \left(T_g\right)^a \left(\varepsilon_v^e - \varepsilon_v^h\right) \qquad (3.17a)$$

$$\dot{\varepsilon}_s^e = \dot{\varepsilon}_s - \dot{\varepsilon}_s^D, \quad \text{where } \dot{\varepsilon}_s^D = \left(T_g\right)^a \left(\varepsilon_s^e - \varepsilon_s^h\right) \qquad (3.17b)$$

where $m_1 = m_{1,0}\left[1 + L_T\left(T - T_0\right)\right]$ and L_T [1/°C] is an input constant that describes the dependence of parameter m_1 on temperature.

4) Evolution of Hysteretic strain:

By expanding equation 3.12, the volumetric and deviatoric components of hysteretic strain become:

$$\dot{\varepsilon}_v^h = \dot{\varepsilon}_v^D - w\frac{\frac{1}{3}\dot{\varepsilon}_v^D\varepsilon_v^h + \dot{\varepsilon}_s^D\varepsilon_s^h}{h^{0.5}\left[\frac{1}{3}\left(\varepsilon_v^h\right)^2 + \left(\varepsilon_s^h\right)^2\right]^{0.75}}\varepsilon_v^h \tag{3.18a}$$

$$\dot{\varepsilon}_s^h = \dot{\varepsilon}_s^D - w\frac{\frac{1}{3}\dot{\varepsilon}_v^D\varepsilon_v^h + \dot{\varepsilon}_s^D\cdot\varepsilon_s^h}{h^{0.5}\left[\frac{1}{3}\left(\varepsilon_v^h\right)^2 + \left(\varepsilon_s^h\right)^2\right]^{0.75}}\varepsilon_s^h \tag{3.18b}$$

5) Stress Equations:

By combining equations 3.7 and 3.9, the effective stress is expressed by:

$$\begin{aligned} p' &= K_e\left(\varepsilon_v^e + \beta\Delta T\right) \\ q &= \sqrt{6}B\xi\varepsilon_s^e\left(\varepsilon_v^e + c'\right)^{1.5} \end{aligned} \tag{3.19}$$

where $B = B_0\exp\left(B_1\rho_d\right)$, B_0 and B_1 are input constants, β is the volumetric thermal expansion of the soil mixture, ξ is an input constant and K_e is the secant elastic bulk modulus of the solid skeleton:

$$K_e = 0.6B\left(\varepsilon_v^e + c\right)^{0.5}\varepsilon_v^e + 0.8B\left(\varepsilon_v^e + c\right)^{1.5} + 1.5B\xi\left(\varepsilon_v^e + c'\right)^{0.5}\frac{\left(\varepsilon_s^e\right)^2}{\varepsilon_v^e} \tag{3.20}$$

3.3 Conversion of Bound to Free Water

3.3.1 Structure and Properties of Adsorbed Water in Clay – Water Mixtures

In clays, water exists in one of three forms: 1) bulk; 2) double-layer; and 3) solvation water, as shown in Figure 3.4. Water in clay mineral pores is bonded to the solid mineral surfaces by electrochemical fields (Rosenquist 1959; Yariv and Cross 1979) if voids are large enough. In smaller spaces (clay platelet separations of $40\text{-}50\times10^{-10}$ m) water molecules are packed under short-range hydration forces (van Olphen 1977; Israelachvili 1985). In the former case, a diffuse double layer develops in the aqueous electrolyte, where the water molecules are bonded to the charged surface of clay mineral. Based on the theory proposed by Gouy (1910) and Chapman (1913), the thickness of a

double layer between two parallel plate surfaces can be estimated from the Debye length, L_D:

$$L_D = \left(\frac{\varepsilon_0 DkT}{2n_0 e^2 \upsilon^2} \right)^{1/2} \qquad (3.21)$$

where ε_0 is the permittivity of vacuum ($\varepsilon_0 = 8.8542\times10^{-12}$ C^2 J^{-1} m^{-1}), D is the dielectric constant, k is the Boltzmann constant ($k=1.38\times10^{-23}$ J K^{-1}), T is temperature, n_0 is the electrolyte concentration, e the unit electronic charge ($e = 1.602\times10^{-19}$ C) and υ is the cation valence.

The proposed expression reasonably describes the actual distribution of ions only for smectite particles suspended in monovalent electrolyte solutions at very low concentrations (Sposito, 1989). However, it can be useful for understanding several aspects of physicochemical forces of interaction, aggregation, flocculation, dispersion and deflocculation and the relationships of these processes to formation of soil structure and of clay compression and swelling (Mitchell and Soga, 2005).

Thermal contraction of normally consolidated clay has been linked by many authors to physicochemical clay-water interactions based on the change in thickness of the double layer with an increase in temperature (Delage et al., 2000). Plum and Esrig (1969) present two contradictory theories; i) Lambe's (1960) model, which assumes that the double layer decreases with an increase in temperature; while ii) Yong et al. (1962), assert that double layer thickness increases with temperature (due to larger repulsive forces). Morin and Silva (1984), gathered experimental evidence mostly on high porosity clays to prove that a temperature increase tends to decrease the double layer thickness and to reduce the ionic concentration, promoting a breakdown of the adsorbed water. However, Mitchell (1993) believes that the double-layer thickness should not change significantly with temperature because the direct dependence of double layer thickness on temperature is counterbalanced by a decrease of the dielectric constant as temperature increases.

Towhata et al. (1993) state that irreversible thermal contraction of normally consolidated clay cannot be explained by the double-layer theory, which is based on reversible phenomena. Paaswell (1967) suggests that heat causes thermal agitation of the water molecules bound to the clay particles, helping them move out of the bound water

layer more easily. This results in a reduction of the double-layer thickness, which brings clay particles closer and hence resulting in an irreversible volume decrease.

Campanella and Mitchell (1968) were the first to attribute the compactive thermal strains in clays to physicochemical changes in adsorbed water. The authors suggest that physico-chemical effects such as greater water adsorption and higher osmotic pressures exist at lower temperatures, which could account for swelling of clays during cooling and compression during heating. Habibagahi (1977) proposes that during a permeability test the flow of free water occurs through channels limited by the clay particles and the adsorbed water and that when a clay is heated, the thickness of the bound water layer decreases, resulting in larger channels and a higher permeability.

For very low porosity clays, with clay platelet separations of about 40-50 Å ($1Å=10^{-10}$ m) diffuse double layer theories fail to predict the interaction forces in the clay-water system (Baldi et al., 1988). At such small separations, the discrete molecular structure of the water cannot be accurately described by the diffuse double layer theory, which assumes a continuum phase. In order to describe the properties of the adsorbed water layer in very low porosity clays, Baldi et al. (1988) propose an effective thermal expansion coefficient for bound water, which is considerably lower than for free water.

The density of adsorbed water may vary from ρ_w = 1 g/cm^3 for free water to 1.4 g/cm^3 or more for the first layers of water molecules at the solid surface as shown in Figure 3.5 (De Wit and Arens 1950; Mooney et al. 1952; Anderson and Low 1958; Martin 1960; Mitchell 1976; Yong and Warkentin 1975). Anderson and Low (1958) inferred density values below 1g/cm^3 from standard measurements of partial specific volume at water contents from 0.8 to 4.0 g H_2O/g clay (Figure 3.5). De Wit and Arens (1950) determined the density of clays as a function of water content using a pycnometer technique with a petrol fraction as the suspension method. The authors report bound water density up to 1.4 g/cm^3 at water contents below 0.3 g H_2O/g clay and bound water density which is slightly higher than free water density at water contents around 2.5 g H_2O/g clay (Figure 3.5). Nitzsch (1940) reported density values from 0.25 to 0.96 g/cm^3 for water contents from 0.005 to 0.08 g H_2O/g clay. These data are at such low water contents that they do not conflict with any of the data shown in Figure 3.5.

Ebrahimi et al. (2012) calculate the density of interlayer structural water based on molecular dynamics simulations of Wyoming Na-montmorillonite (Figures 3.6a and b). For the adsorbed water density calculations, the mass of water is known and the available volume for water (unit area multiplied by thickness of water layer, d_{water}) is calculated by subtracting the thickness of the clay layer d_{clay} from the total basal layer spacing given by the simulations. Assuming a clay layer thickness d_{clay} = 6.56Å, the authors report bound water densities from 0.05 to 0.8 g/cm^3 for water contents from 0.006 to 0.28 g H_2O/g clay as shown in Figure 3.6c.

Suter et al (2007) point out that for realistic calculations, the thickness of the clay layer should also include the van der Waals radius of the oxygen surface atoms which is equal to 1.34Å and hence the thickness of the clay layer that Suter et al (2007) used in their calculations is 9.37Å. Figure 3.6c shows the adsorbed water density calculated using the work by Ebrahimi et al. (2012), but using different clay layer thicknesses. It is clearly shown that the calculated density is very sensitive to the assumed volume available for water, which depends on the thickness of the clay layer. The adsorbed water density calculated by Ebrahimi et al (2012) using a clay layer thickness d_{clay} = 9.37Å ranges from 0.315 to 1.4 g/cm^3 for water contents from 0.006 to 0.28 g H_2O/g clay and is close to 1 g/cm^3 for higher water contents. These results agree with the values reported by DeWit and Arens (1950), Mackenzie (1958) and Mooney et el (1952) as shown in Figure 3.5.

In fine-grained soils, the distinction between bound water and free water is somewhat schematic, due to the progressive decrease in tightness of the clay-water link with increased clay water distance (Delage et al., 2000). Moreover, the assumption of perfectly parallel plate structure of the solid matrix represents an idealization of the actual phenomena in clay. The proportion of adsorbed water is essentially controlled by the specific surface of the clay minerals. The adsorbed water layer adjacent to clay minerals has a thickness of about 1 nm (i.e., three water molecules) (Fripiat et al., 1984; Sposito, 1984, 1989; Mitchell, 1993), is structurally different from the free water (Sposito & Prost, 1982; Sposito, 1984), and it also has different thermodynamic properties (Low, 1979; Hueckel, 1992).

Navarro and Alonso (2001) associated secondary compression to processes of local water transfer between bound and free water (in larger voids). The water transfer

process is due to the difference between the chemical potentials of bound and free water. In fact the bound water potential depends on temperature, on bound water porosity and on the current stress. The idea of transfer of bound water to free water is also included in other theoretical formulations (Mitchell, 1993; de Jong, 1968; Berry & Poskitt, 1972; Sills, 1995) and forms the basis of the thermal component of the TTS model, as discussed in the following section.

3.3.2 Conversion of Bound Water to Free Water Assumed in TTS Model

Thermal irreversible strains are described in the TTS model based on the assumption that irreversible reorganization of clay particles takes place due to the conversion of part of the bound water to free water at elevated temperatures. As illustrated in Figure 3.7 in terms of phase diagrams, heating a clay causes a change in the volume of the solid and liquid phases due to their thermal expansion and also a reduction of the volume of the bound water phase (and corresponding increase of the volume of the free water phase) due to conversion of bound water to free water. In the TTS model it is assumed that bound water content, $w_{bw} = M_{bw} / M_s$, is given by:

$$w_{bw} = w_{bw,20} \exp\left[-\alpha_{bf}(T-20)\right], \quad \mathrm{T}\left[^{o}C\right] \tag{3.22a}$$

where M_{bw} is mass of bound water and M_s is mass of solid particles. Therefore the change in bound water content dw_{bw} due to change in temperature dT is given by:

$$\frac{\partial w_{bw}}{\partial T} = -\alpha_{bf} w_{bw}$$
$$\rightarrow \alpha_{bf} = -\frac{1}{w_{bw}} \frac{\partial w_{bw}}{\partial T} \tag{3.22b}$$

where α_{bf} [1/°C] is a key input constant for the TTS model.

Zhang and Cheng (2013) based their calibration of parameter α_{bf} on laboratory experiments undertaken by Shao (2011), Figure 3.8, who attempted to quantify the conversion of bound to free water from standard specific gravity tests at different temperatures. Shao (2011) did not ensure full saturation in the clay samples and therefore the results shown in Figure 3.8 are questionable, since they are likely affected by the diffusion of air in water, a process that depends on temperature. Moreover, Figure 3.8 shows that the bound water content at 20°C ranges from 14 – 38% (very high). Finally, it

is suspected that Figure 3.8 is mislabeled since expansive soils have larger specific surface area (SSA) and hence, are expected to have a larger bound water content than silty soils.

Given the importance of the α_{bf} parameter for the correct calibration of the TTS model, specific gravity tests were repeated as part of our study, using an improved experimental method suggested by Germaine and Germaine (2009), based on the ASTM D854 water submersion method. The goal of these experiments was to measure the amount of bound water converted to free water as a function of temperature, by undertaking multiple specific gravity tests at different temperatures. Three clay types were tested: 1) Kaolinite[10]; 2) illite-rich, Resedimented Boston Blue Clay (RBBC); and 3) smectite-rich, Eugene Island (EI) clay sourced from the Gulf of Mexico.

3.3.3 Test Materials

Casey (2014) provides detailed descriptions of RBBC and EI clays. Table 3.3 summarizes the origin, liquid limit, plasticity index and clay fraction, CF[11]. Figure 3.9 shows the USCS classification of the test materials on the Casagrande chart, Table 3.3 cites the previous investigations by other researchers on these materials and Table 3.4 summarizes the mineralogical compositions of BBC and EI clays[12]. The samples primarily contain quartz, plagioclase, K-feldspar and clay minerals in varying proportions, as well as several other minerals in minor proportions. Table 3.4 shows the percentages of clay minerals determined for the bulk (whole) samples, as well as the relative proportions within the clay size fraction (CF).

Kaolinite

Kaolinite is an inorganic clay of medium plasticity (classified ML according to USCS) with a specific surface area, SSA = 14 m^2/g. It is a layered silicate mineral, with one tetrahedral sheet of silica linked through oxygen atoms to one octahedral sheet of

---

[10] The tested Kaolin is sourced from Cornwall, UK and is produced and sold by English China Clays (ECC plc) under the name Speswhite Quality China Clay.

[11] CF is defined as the percentage of particles with an equivalent diameter of $d < 2$ μm as determined by sedimentation (ASTM, D422).

[12] The mineralogy analyses were carried out by Macaulay Scientific Consulting Ltd. of Aberdeen, U.K.

alumina. Most kaolinite is formed from feldspars and micas by acid leaching of acidic granitic rocks. Kaolinite forms in areas where precipitation is relatively high and there is good drainage to ensure leaching of cations and ions (Mitchell and Soga, 2005).

Boston Blue Clay

Natural Boston Blue Clay is a low plasticity (CL) glacio-marine clay of low sensitivity with SSA = 49 m^2/g. It was formed as glacial outwash and deposited in a marine environment about 12,000 to 14,000 years ago in the period immediately following deglaciation of the Boston basin (Kenney 1964). The clay is present throughout the Boston area varying in thickness from 20 to 40 m. A stiff overconsolidated crust (OCR of 2 - 5) forms the upper 12 to 20 m of the deposit while underneath the clay is close to normally consolidated (Santagata, 1998). Although the depositional and general characteristics of BBC are fairly similar throughout most of the Boston area, some variability can be expected in clay retrieved from different locations. The material (Series IV, 1992) used in this research was obtained during excavations for Building 68 at the MIT campus. The salt content of BBC Series IV powder used for resedimentation was measured using the conductivity method and calibrated against a KCL standard. The salt content was found to be 2.68±0.05 g per kg of dry powder. At an in-situ water content of 40 %, this would correspond to 6.70±0.12 g per litre of pore fluid. Cauble (1996) determined the organic content of Series IV powder to be 4.4% by the loss on ignition method (ASTM D2974), though Horan (2012) later measured a much lower value of just 1.4 %.

Eugene Island Clay

This high plasticity clay comes from the Eugene Island region located off the coast of Louisiana in the Gulf of Mexico. Resedimented Gulf of Mexico Eugene Island Clay (RGoM EI) is derived from two 10.2cm cores drilled in the 1990's. In this area, the basin consists of over 4 km of Pliocene and Pleistocene sedimentary fill deposited over a salt-weld. A large quantity of core material was collected from each borehole at depths ranging from approximately 2200m to 2500m. The in-situ salinity of the clay at this depth is approximately 80g/l (Betts, 2014). RGoM El has a high plasticity (w_L = 85.8 %),

SSA = 267 m^2/g and CF = 63% as determined by sedimentation. The mineralogical cf was found to be 53.9%, the dominant clay mineral being smectite. A detailed description of the geologic origin, processing and consolidation behavior of RGOM-EI is given in Betts (2014).

3.3.4 Link Between Specific Gravity Tests and Conversion of Bound to Free Water

Specific gravity, G_s, is defined as the ratio of the mass of a given volume of soil particles, M_s, to the mass of an equal volume of distilled water, M_w, at room temperature (T = 20°C), as shown below:

$$G_s = \frac{M_s}{M_w} \tag{3.23}$$

In order to perform the submersion technique on a soil, the following measurements are required:

1) mass of flask, M_B, at temperature T
2) volume of flask, V_B, at temperature T
3) total mass of flask, water and soil M_{B+W+S_T} at temperature, T
4) temperature, T at each measurement
5) mass of dry soil, M_S

The specific gravity G_{S_T} at temperature T is then calculated using equation 3.24, which is shown graphically in Figure 3.10.

$$G_{S_T} = \frac{M_s}{\left(M_B + V_{B_{TC}}\rho_{W_T} + M_S\right) - M_{B+W+S_T}} \tag{3.24}$$

By performing specific gravity tests the mass of flask, water and solids, M_{B+W+S}, is measured as a function of temperature T, and hence since the mass and volume of flask and mass of solids are known, the change in mass of water, M_W, versus temperature can be deduced. In order to account for the change in free water density, the measured specific gravity G_{S_T} must be corrected to 20°C, using equation 3.25b. Assuming that the

density of solid particles ρ_s remains constant with temperature and that the volume occupied by solids, V_S, is approximately equal to the volume occupied by water, V_W :

$$G_{S_T} = \frac{M_S}{M_{W,T}} = \frac{\rho_S V_S}{\rho_{W,T} V_{W,T}} \approx \frac{\rho_S}{\rho_{W,T}} = \frac{\rho_S}{\rho_{W,20}} \frac{\rho_{W,20}}{\rho_{W,T}} = G_S \frac{\rho_{W,20}}{\rho_{W,T}} \tag{3.25a}$$

$$\rightarrow G_S = G_{S_T} \frac{\rho_{W,T}}{\rho_{W,20}} \tag{3.25b}$$

Next we assume that the water in the soil mixture can be divided into free water and adsorbed/bound water, the mass of water M_w that is measured from a specific gravity test is equal to the mass of free water M_{fw} corresponding to volume (V_s+V_{bw}) minus the mass of bound water M_{bw}, as illustrated in Figure 3.10.

Therefore the change in mass of water ΔM_w measured in the lab for different temperatures can be expressed by:

$$\frac{\partial M_W}{\partial T} = \rho_{FW} \frac{\partial V_{FW}}{\partial T} - \frac{\partial M_{BW}}{\partial T} = \rho_{FW} \left(\frac{\partial V_S}{\partial T} + \frac{\partial V_{BW}}{\partial T} \right) - \frac{\partial M_{BW}}{\partial T} \tag{3.26a}$$

Assuming that $\frac{\partial V_S}{\partial T} \approx 0$ and using $\frac{\partial V_{BW}}{\partial T} = \frac{1}{\rho_{BW}} \frac{\partial M_{BW}}{\partial T}$:

$$\frac{\partial M_W}{\partial T} = \frac{\rho_{FW}}{\rho_{BW}} \frac{\partial M_{BW}}{\partial T} - \frac{\partial M_{BW}}{\partial T} = \left(\frac{\rho_{FW}}{\rho_{BW}} - 1 \right) \frac{\partial M_{BW}}{\partial T} \tag{3.26b}$$

From equation 3.22b, α_{bf} depends on the change of bound water content with temperature $\frac{\partial w_{BW}}{\partial T}$, which can be calculated using:

$$\alpha_{bf} w_{bw} = -\frac{\partial w_{BW}}{\partial T} = -\frac{1}{M_S} \frac{\partial M_{BW}}{\partial T} = -\frac{1}{M_S \left(\frac{\rho_{FW}}{\rho_{BW}} - 1 \right)} \frac{\partial M_W}{\partial T} \tag{3.26c}$$

The initial bound water content, w_{bw}, can be estimated as follows:

$$G_S = \frac{M_S}{\rho_{FW} (V_S + V_{BW}) - M_{BW}} = \frac{M_S}{\rho_{FW} \left(\frac{M_S}{\rho_S} + \frac{M_{BW}}{\rho_{BW}} \right) - M_{BW}} \tag{3.27a}$$

and hence, bound water content w_{bw} is given by:

$$w_{bw} = \frac{M_{BW}}{M_S} = \frac{\left(1 - G_S \frac{\rho_{FW}}{\rho_S}\right)}{G_S\left(\frac{\rho_{FW}}{\rho_{BW}} - 1\right)} \tag{3.27b}$$

Combining equations 3.26c and 3.27b the final expression for α_{bf} becomes:

$$\alpha_{bf} = -\frac{1}{w_{bw}}\frac{dw_{bw}}{dT} = -\frac{G_S\left(\frac{\rho_{FW}}{\rho_{BW}} - 1\right)}{\left(1 - G_S \frac{\rho_{FW}}{\rho_S}\right)} \frac{1}{M_S\left(\frac{\rho_{FW}}{\rho_{BW}} - 1\right)} \frac{\partial M_W}{\partial T} \tag{3.28a}$$

$$\therefore \alpha_{bf} = -\frac{G_S}{\left(1 - G_S \frac{\rho_{FW}}{\rho_S}\right)} \frac{1}{M_S} \frac{\partial M_W}{\partial T} \tag{3.28b}$$

From equation 3.28b it is deduced that α_{bf} depends on: i) the specific gravity G_S at room temperature ($T = 20°C$), determined from the specific gravity tests; ii) density of free water, ρ_{fw}, which has already been defined in equation 2.19; iii) density of solids, ρ_s, which will be determined from independent gas pycnometer measurements; iv) mass of solids, M_s; and v) change of mass of water with temperature, $\partial M_W / \partial T$, which are both measured in the specific gravity tests.

It is interesting to note the link between the change in mass of water with temperature with the change in modified specific gravity as shown below:

$$G_S = \frac{M_S}{M_W} \rightarrow \frac{1}{G_S} = \frac{M_W}{M_S}$$
$$\rightarrow \frac{\partial}{\partial T}\left(\frac{1}{G_S}\right) = \frac{1}{M_S}\frac{\partial M_W}{\partial T} \tag{3.29}$$

Based on the theory just presented, G_S is expected to decrease as temperature increases, since:

1. bound water is converted to free water as temperature increases and hence the bound water content decreases with temperature: $\partial w_{BW} / \partial T < 0$
2. the density of bound water for the first three layers of adsorbed water is reported to be higher than the density of free water: $\rho_{FW} \leq \rho_{BW} \rightarrow (\rho_{FW} / \rho_{BW} - 1) \leq 0$. From equations 3.26c and 3.29:

$$\frac{\partial}{\partial T}\left(\frac{1}{G_S}\right)=\frac{1}{M_S}\frac{\partial M_W}{\partial T}=\left(\frac{\rho_{FW}}{\rho_{BW}}-1\right)\frac{\partial w_{BW}}{\partial T}\geq 0\rightarrow\frac{\partial G_S}{\partial T}\leq 0$$

3.3.5 Laboratory Procedure

Figure 3.11 summarizes the laboratory procedure. The first step involved the calibration of the flask to obtain its volume and mass. In order to account for the variations associated with temperature, the mass of the flask filled with water M_{B+W} was measured for different temperatures. Equation 3.30a gives the theoretical equation of the mass of the flask filled with free water M_{B+W} as a function of temperature T and equation 3.30b gives the volume of the flask V_B at temperature T:

$$M_{B+W}=M_B+V_B\rho_{FW} \tag{3.30a}$$

$$V_B=V_{B_{TC}}\left\{1+(T-T_C)\beta_g\right\} \tag{3.30b}$$

where $V_{B_{TC}}$ is the volume of the flask at temperature T_c, β_g is the volumetric thermal expansion coefficient of glass (β_g = 0.100 x 10^{-4}/°C) and ρ_{FW} is the mass density of water at temperature T (equation 2.19). Calibration of the flask was done very carefully, since both mass M_B and volume V_B are incorporated into all calculations. The calibration results can be found in Appendix B.

In order to prepare the soil mixture, 30 – 40 g of oven-dried clay were mixed with 80 g of distilled water in a hand shaker and the resulting slurry was transferred into a flask. The mass of the dry clay was selected to be 30 – 40 g in order to achieve acceptable measurement resolution, as recommended by Germaine and Germaine (2009). The slurry was then de-aired using a vacuum (Figure 3.12a), in order to remove air trapped between particles and in crevices on the surface of particles and thus ensure full saturation. The flask was slowly filled with distilled water, keeping clear water at the top of the flask as shown in Figure 3.12b. The flask with its plug in resting position were placed in a cooler, which was set at the desired temperature and were left overnight for temperature equilibration. Elevated temperatures were controlled by a heater placed inside the cooler and a temperature sensor (Figure 3.13).

The next step involved measuring the mass of the flask, water and soil M_{B+W+S} at temperature T. This was done by transferring the flask to an insulated surface (e.g., the cooler lid shown in Figure 3.14a), inserting the plug in the flask while at the same time extracting the excess free water using a suction bottle, drying the rim of the flask with paper towel strips and finally placing the flask on a scale in order to measure mass M_{B+W+S} to an accuracy of ±0.01g (Figure 3.14b). Cleanliness of the neck of the flask and the glass are crucial in order to ensure accurate measurements of the mass. This step was done very quickly, the flask was handled with gloves and an insulating towel was placed between the flask and the metal surface of the scale to avoid temperature changes. The plug was then removed and the temperature in the flask was measured to 0.1°C by a digital thermometer (Figure 3.14c). Full temperature equilibration of the flask is crucial in order to ensure accurate measurements (otherwise temperature measurements would be based on the location of the thermometer).

Once the mass M_{B+W+S} and temperature T were determined, water was added to the flask to above the calibration level (Figure 3.14d), the plug was returned to resting position and the flask was placed back in the cooler. The thermometer was also stored in a small container of water in the cooler to maintain it at about the same temperature as the flask. For additional thermal insulation, two coolers were used (one inside the other as shown in Figure 3.15a) and also a black cloth covered the coolers to minimize thermal radiation losses from the heater lamp (Figure 3.15b). The procedure for measuring mass M_{B+W+S} against temperature T was repeated five times for each temperature, allowing at least two hours between measurements, to ensure temperature equilibration. The test was then repeated for different temperatures, in order to study the effect of temperature on mass M_{B+W+S}.

Once the measurements were completed, the slurry was poured into an evaporating disk, making sure that all soil particles were removed from the flask. The last step of the test involved oven-drying at 110°C the evaporating disk containing the slurry in order to determine the mass of dry soil, M_S, to 0.01g.

Oven-dried clay densities ρ_s were also obtained from independent gas pycnometer tests, using the AccuPyc1330 gas pycnometer apparatus shown in Figure 3.16 (AccuPic 1330, Operator's Manual V3.03, Micrometrics Instrument Corporation).

3.3.6 Experimental Results

Four iodine flasks were used in our experiments and a minimum of five measurements were taken at each temperature. Moreover, our aim was to keep the standard deviation of all measurements below 0.002, as recommended by Germaine and Germaine (2009), although this was not possible, as shown in the error bars in Figure 3.17 and the tabulated measurements in Appendix B.

Figure 3.17 shows modified specific gravity G_S measurements against temperature for all tested materials (Appendix B gives full results). Glass beads were tested first in order to identify procedural and technique errors (glass beads have very low SSA and minimal bound water). Figure 3.17a shows that the specific gravity of glass beads remains practically constant with temperature and all results are within the standard deviation (±0.002) from the mean. Figure 3.17b presents specific gravity measurements for Kaolinite minerals, where it is observed that the change with temperature is slightly larger than for glass beads, but remains low as would be expected due to its low specific surface area and hence, low amount of bound water. The measurement at temperature T = 37°C has a considerably larger standard deviation (±0.0074) versus the standard deviation at the rest of the measurements (±0.0026) and hence has been ignored from further calculations. The change of specific gravity of Boston Blue clay with temperature is more pronounced, as shown in Figure 3.17c. The largest decrease of specific gravity with temperature was measured for the Eugene Island clay, as shown in Figure 3.17d. However, the scatter in measurements is also considerably larger, due to the expansive nature of the clay.

Table 3.5 summarizes the modified specific gravity $G_{S,20}$ measured at 20°C as well as $\frac{1}{M}\frac{\partial M_w}{\partial T}$ deduced from linear data fits shown in Figure 3.17. It should be pointed out that parameter α_{bf} is assumed constant in the TTS model and therefore linear data fits

were selected in order to obtain constant $\frac{1}{M}\frac{\partial M_W}{\partial T}$ values, although the lab measurements show that this assumption is at best a first order approximation (cf., EI data in Fig. 3.17d). From Table 3.5 it is observed that solid density ρ_s is lower than the modified specific gravity $G_{S,20}$ obtained using the water submersion method, as is proven theoretically. From equation 3.27a and Figure 3.10, it was shown that $G_S = M_S/\left[\rho_{FW}V_S + (\rho_{FW} - \rho_{BW})V_{BW}\right]$. Assuming that the density of bound water ρ_{BW} is larger than the density of free water ρ_{FW}, the denominator of G_S is smaller than $\rho_{FW}V_S \approx V_S$ and hence:

$$G_S = \frac{M_S}{\rho_{FW}V_S + (\rho_{FW} - \rho_{BW})V_{BW}} \geq \frac{M_S}{\rho_{FW}V_S} = \rho_S \tag{3.31}$$

Values of α_{bf} calculated using equation 3.28b are shown in Table 3.5.

In order to estimate the bound water content at 20°C, $w_{bw,20}$, it is necessary to assume a value for bound water density (cf., Section 3.3.1). Our assumption is based on the conclusion reported by several authors that the bound water layer typically comprises three layers of water molecules (i.e., bound water layer thickness at room temperature $t_{bw,20} \approx 3 \times 2.75 = 8.25$ Å). Using the values of the specific surface area (SSA) shown in Table 3.5, the thickness of the bound water layer $t_{BW,20}$ at 20°C can be calculated using the expression below:

$$t_{BW,20} = \frac{V_{BW}}{Area_{BW}} = \frac{\frac{M_{BW}}{\rho_{BW}}}{SSA \cdot M_S} = \frac{w_{BW,20}}{SSA \cdot \rho_{BW}} \tag{3.32}$$

Through an iterative process (to obtain consistent values of $t_{bw,20}$ and $w_{bw,20}$) the bound water density was selected as, $\rho_{BW} = 1.07\rho_{FW}$. This value is very close to the free water density and hence, as a first estimate seems realistic. As shown in Table 3.5, the bound water content estimated for EI-GOM clay is $w_{bw,20} = 24\%$ which is considerably higher than that for RBBC ($w_{bw,20} = 5\%$) and Kaolinite ($w_{bw,20} = 1\%$). Figure 3.18a presents the

change of bound water content with temperature for all three clays, based on the exponential relation assumed in the TTS model (equation 3.22a). It is observed that for a temperature increase of 20°C, the bound water content of EI-GOM clay decreases by ~4%, and the corresponding changes for RBBC and Kaolinite are ~1.2% and ~0.3%, respectively.

Finally, Figure 3.18b presents the estimated change in the thickness of the bound water layer with temperature for all three clays tested. Our analysis predicts that a temperature increase of 20°C would result in a thickness decrease of about one water molecule for Kaolinite and RBBC and a smaller reduction for EI clay. These results are preliminary since they are taken from macroscopic specific gravity tests. Moreover, they are based on simplifying assumptions, such as the selection of the bound water density and also the selection of linear data fits. However, the results provide interesting insights regarding the effect of temperature on the conversion of bound water to free water and the reduction of the bound water content with temperature.

3.4 Cyclic Thermal Tests on Geneva Clay

Di Donna and Laloui (2015) carried out a series of drained thermal cyclic tests on samples of medium plasticity silty clay from Geneva, Switzerland (I_p = 11 - 19%, w = 22 -28%). These tests are very important for the current study, as they simulate the continuous heating and cooling of the ground that takes place due to long-term operation of vertical borehole heat exchangers, and very few similar tests have been reported in the literature.

Four soil samples (referred to as S1, S3, S4 and S4b)[13] were collected from a site near Geneva, in Switzerland, as part of a project involving the construction of a new building and the installation of a large number of borehole heat exchangers for space heating and cooling, such that thermal characterization of the ground was required for design. Table 3.6 shows the in-situ state of stress (normally consolidated clay) and the index properties of the collected samples. The four samples are saturated and the grain-size distribution is similar for the four samples, with fine fraction (d < 2μm) between 38 -

[13] Figure 3.9 shows that despite differences in liquid limit and plasticity index among the samples, all are classified as inorganic clay with medium plasticity.

45 % (Figure 3.19). The samples were conserved in a humid chamber to keep the natural conditions. For each test, the specimen was cut from the in-situ collected samples and positioned in the oedometric cell, which was then filled with demineralised water.

Two sets of experiments were undertaken: i) 1-D oedometric compression tests at constant temperatures (20°C, 40°C and 60 °C); and ii) thermal cycles under constant vertical effective stress. The details of the experimental program are provided in Table 3.7. For the oedometric tests under constant temperature, the sample was initially equilibrated at the selected temperature at a nominal vertical stress of 1kPa (weight of top cap). Once the temperature and deformation were stable incremental load sequences were performed, with loading steps up to 1000kPa (and minimum load increment ratio, LIR = 1.0) and unloading to 60kPa. Two tests were performed at 20 °C, two at 40 °C and two at 60 °C. For each of these temperatures, one test was run on S3 specimen and the other on S4 (tests 1 to 6; Table 3.7). The two specimens tested at 60 °C (tests 3 and 6; Table 3.7), after unloading to 60 kPa (OCR = 16.0) were cooled back to the ambient temperature and finally subjected to thermal cyclic loading. This provided additional information about the response of the same material to thermal cyclic loading at highly overconsolidated conditions.

For the thermal cyclic tests the specimens were initially consolidated to their in-situ vertical effective stress ($\sigma'_{v0} \sim \sigma'_p$) at ambient temperature, 20 °C, and then thermal cycles were performed in the range between 5°C and 60°C. Four of these tests were performed, one for each sample (tests 7 to 10 in Table 3.7). Vertical displacements were recorded throughout the experiments and the heating phases were applied in steps of 10°C, imposing a heating rate of 2°C per hour in order to ensure drained conditions and thus provide enough time for excess pore water pressure dissipation. The cooling phases were applied in steps of 20 °C and with a cooling rate of 5°C/h, (Table 3.7). Sample S4b was mechanically reloaded after the thermal tests were completed, in order to study the thermal-induced overconsolidation discussed in Chapter 2.

Figure 3.20 shows the four oedometric cells that were employed for the experiments which have been adapted to include temperature control. Vertical stresses were applied through calibrated dead weights and the vertical displacements were measured by four linear variable differential transformers (LVDTs). Thermal loads were

provided by a pump that circulated water from a thermo-controlled bath to a spiral tube positioned around the sample. Therefore both heating and cooling of the samples was possible. During the tests, the temperature was constantly monitored inside each cell through four thermocouples. The cells were insulated with a polystyrene box in order to minimize thermal losses. Oedometric rings made of invar (coefficient of linear thermal expansion of 5.5×10^{-7}/°C) were used in order to minimize the thermal radial deformation and guarantee 1-D oedometric conditions during temperature changes. A system for water supply was installed in order to address the water evaporation during heating and maintain constantly saturated conditions.

In addition to the standard calibrations of LVDTs and dead weights (for vertical stress) Di Donna (2014) describes the apparatus calibrated to take into account the deformation of the device induced by both mechanical and thermal loading.

3.4.1 Results of Thermal Tests on Geneva Clay

Figure 3.21 presents the oedometric test results on sample S3 at 20°C, 40°C and 60°C. It is observed that the VCLs at different temperatures are parallel, thus confirming trends reported previously in the literature (cf. Figure 2.10). Figure 3.21 shows that the effect is more pronounced for 40°C than for 60 °C temperature, which is possibly due to experimental errors. Figure 3.22 presents the combined thermal and mechanical loading on sample S4b.

Figure 3.23 presents the results of all six cyclic thermal tests undertaken: two on S3, two on S4, one on S1 and one on S4b sample. In four of these tests (tests 7 to 10), the thermal cycles were imposed on normally consolidated specimens, while two were done at OCR = 16 (tests 3 and 6). The results in Figure 3.23 show that thermal cycling of the OC specimens resulted in small dilative strains ($\varepsilon_v \approx -0.1\%$) similar to prior results (cf. Fig. 2.6 and 2.7). Assuming that the measured deformation corresponds to the thermo-elastic expansion and compression of the solid skeleton, Di Donna and Laloui (2015) computed the volumetric thermal expansion coefficient of the solid skeleton equal to 1.8×10^{-5}°C^{-1}. On the other hand, cyclic heating and cooling of NC clay specimens results in larger irreversible contractive strains (accumulated $\varepsilon_v \approx 0.5 - 0.6\%$). This phenomenon is qualitatively similar for all four specimens, but shows some quantitative differences.

These latter can be attributed to the differences in the initial void ratios (indicated in Figure 3.23), as more voids represent a higher potential for collapse (Di Donna and Laloui, 2015). In this sense, for instance, during the first heating phase the thermal contraction of the S3 sample is higher than the one of S4 sample. Moreover the experiments showed that the higher the plasticity index, the higher the thermo-plastic deformation as shown in Figure 3.24.

Di Donna and Laloui (2015) studied the effect of combined thermal and mechanical loading of Geneva Clay sample S4b. Figure 3.22 shows that the material was first consolidated to 125 kPa (from point 1 to point 2), then subjected to four thermal cycles (from point 2 to point 3) and finally loaded up to 2000 kPa (from point 3 to point 5, with an unloading phase). During this final mechanical loading phase, the material showed a first phase of elastic response (from point 3 to point 4) and then exhibits large irrecoverable deformations in re-joining the VCL. Hence, the thermal cycles induced an overconsolidation of the material, similar to prior results (cf. Figure 2.12).

3.4.2 Hydraulic Conductivity Estimates

Figures 3.25a to 3.25d summarize the engineering properties of the S3 samples of Geneva Clay from 1-D Consolidation tests at three constant temperatures. Figure 2.25a shows the tangent 1-D stiffness ($E'_{oed} = \Delta\sigma'_v/\Delta\varepsilon_v$) increases almost linearly with applied stress level. There is little effect of temperature on the stiffness properties. Figure 3.25b shows the evolution of the consolidation coefficient, c_{vH}, computed by the conventional Casagrande log time method (Casagrande, 1936). The results show that c_{vH} increases with temperature at a given level of stress. This behavior is mainly attributed to the reduction in water viscosity (Delage et al., 2000; Towhata et al., 1993). Knowing the consolidation coefficient and the oedometric modulus, it is possible to estimate the hydraulic conductivity, k, of the clay as shown in Figure 3.24c, where γ_w is the unit weight of water.

The interpreted hydraulic conductivity increases with temperature and reduces with effective stress level, as already discussed in Chapter 2. Figure 3.25d presents the evolution of the secondary consolidation coefficient C_α (or $C_{\alpha\varepsilon}$), which shows little

dependence on temperature, a result consistent with prior data published by Laloui et al. (2008), Boudali et al. (1994) and Marques et al. (2004).

3.5 TTS Model Calibration for Geneva Clay

Table 3.1 summarizes the state variables used by the TTS model. The model is driven by specified rates of strain, $\dot{\varepsilon}$, and temperature, $\dot{T}$. Initial values of the state variables can be derived by consolidating from a reference slurry state and thus assuming that most state variables apart from void ratio (and corresponding porosity and dry density) are initially zero at ambient temperature, T = 20°C. The following paragraphs illustrate TTS model calibration for intact specimens of Geneva clay[14]. Appendix C (Zymnis et al., 2015) presents another example of TTS model calibration and evaluation for high plasticity Bangkok clay.

Figure 3.26 summarizes the oedometer tests undertaken on samples S3 and S4b at 20°C. Using the Specimen Quality Designation (SQD) method recommended by De Groot and Ladd (2003) it is concluded that both samples are highly disturbed. Regarding sample S3, the vertical strain measured at σ'_{v0} = 149kPa is 6.3% which corresponds to sample quality D, while for sample S4b the vertical strain measured at σ'_{v0} = 345kPa is 8.7% which corresponds to sample quality E. These results imply that compression index C_c will be systematically underestimated. It is observed that the VCL is more clearly defined by the test on sample S4b and that the loading part of sample S3 matches the reloading curve of sample S4b. Therefore it can be deduced that sample S3 hasn't yet reached the VCL during the oedometer test but would require higher load levels (>2MPa). Therefore, calibration of the VCL was based on the sample S4b measurements.

Figure 3.27 presents the resulting TTS calibration for Geneva Clay sample S4b using the parameters shown in Table 3.8. The steps required for the calibration are:

1 – 2: 1-D Consolidation from an initially slurry condition up to σ_v' = 230kPa

2 – 3: 1-D Unloading to σ_v' = 1kPa

3 – 4: Reloading to σ_v' = 1MPa

[14] Only samples S3 and S4b were used for the calibration because the oedometer tests undertaken on samples S1 and S2 were not reported.

4 – 5: Unloading to σ_v' = 60kPa

5 – 6: Reloading to σ_v' = 3MPa

We assume a reference slurry state (σ'_{v0} = 0) with void ratio e = 2.0 (porosity φ = 0.5) based on results for clays with similar mineralogy. Figure 3.28 presents the evolution of the strain state variables $\left(\varepsilon_v^e, \varepsilon_v^h, \varepsilon_s^e, \varepsilon_s^h\right)$ of the TTS model during these steps. All internal strains start from zero in the slurry condition (point 1) and reach a constant value once the clay is consolidated along the VCL (σ_v' ~ 1kPa, Fig 3.27a). This condition occurs as the TTS model assumes there is a certain amount of locked-in elasticity at NC stress states. During unloading (step 2 - 3) the volumetric (elastic and hysteretic) strains and elastic deviatoric strains decrease (Figures 3.28a-c) and increase again during reloading, while the hysteretic deviatoric strains (ε_s^h; Figure 3.28d) have the opposite response. In these simulations a constant rate of strain is assumed $\left(\dot{\varepsilon}_\alpha = \pm 1 \times 10^{-5} / \mathrm{s}\right)$ for both loading and unloading and so the granular temperature, $T_g \approx 2.5\times10^{-8}$ s^{-2}, remains unchanged during loading, unloading and reloading (Figure 3.29)[15]. Figure 3.30 illustrates the effect that parameter m_4 (cf. eqn. 3.16) has on the evolution of T_g where it is observed that as m_4 increases the time required for T_g to reach a constant value decreases significantly (for m_4 = 1000 kg/m^{3}s, T_g reaches a steady state value almost instantaneously). The primary state variable that changes when compressing a NC clay on the VCL is void ratio (and the corresponding porosity and dry density).

3.5.1 Calibration of Mechanical Component

The main input constants that control the mechanical response of clays are B_0, B_1, m_1, m_2, h, c' and ξ (Table 3.2). For rate independence of the TTS model, parameter a=0.5 (eqns 3.16 & 3.17). The slope of the normalized virgin consolidation line (VCL) depends solely on B_1 (eqn 3.19), as shown in Figure 3.31. This figure presents results for normalized vertical stresses (σ'_v / σ'_{ref}, where σ'_{ref} is the vertical stress calculated by the TTS model at void ratio e = 0.63) As shown in Figure 3.31, the slope of the VCL increases as B_1 decreases, B_1 = 0.0162 m^3/kg provides a good fit to the measured data.

[15] In eqn. 3.16 $\dot{\varepsilon}_v$ and $\dot{\varepsilon}_s$ are not affected by the sign of strain rate during loading and unloading, since they are raised to a power of 2

Figures 3.32 and 3.33 show that the maximum value of the elastic volumetric strains (at stress states on the VCL) depends on m_1 and m_2 with larger elastic volumetric strains occurring for lower values of these parameters (eqns. 3.16 and 3.17). The reloading response (i.e., 5-6 in Fig. 3.27) also depends on parameter m_2, as shown in Figure 3.33. In our calibration we assume that parameter $m_3 = 1$ to represent the fact that volumetric and shear components contribute equally to the evolution of granular temperature (eqn. 3.16). Parameter h controls the slope of the unload curve as shown in Figure 3.34, with larger unloading slopes occurring for larger h (eqn. 3.18). Moreover, parameter h changes the magnitudes of both elastic and hysteretic volumetric strains as shown in Figure 3.34b.

Parameters c and w play a minor role for the TTS model, as shown in Figures 3.35 and 3.36. Parameter c is related to cohesion of clays (eqn. 3.19 and 3.20) and was selected $c = 0.01$ for Geneva clay. Moreover, $w = 1$ throughout our analysis (eqn. 3.18). Parameter m_4 affects transient response to changes in strain rates and is selected (m_4=6×10^4 kg m^{-3} s^{-1}) to prevent numerical oscillations of the granular temperature T_g (Figure 3.30 and eqn. 3.16).

Parameters ξ and c' affect the shear behavior of the TTS model (eqn. 3.19). Panagiotidou et al. (2016) show that the slope, M, of the critical state line simulated by the TTS model is given by:

$$M = \frac{q_f}{p'_f} = \frac{\sqrt{6}c'}{1.5\left(h + \sqrt{\frac{1.5}{m_2}}\right)} \tag{3.33}$$

For a friction angle $\varphi = 24°$, determined by triaxial tests on Geneva clay (Di Donna, 2014):

$$M = \frac{6\sin\phi}{3-\sin\phi} = 0.94 \tag{3.34}$$

from which c' can be obtained:

$$c' = \frac{1.5\left(h + \sqrt{\frac{1.5}{m_2}}\right)}{\sqrt{6}} M = \frac{1.5\left(0.05 + \sqrt{\frac{1.5}{150}}\right)}{\sqrt{6}} 0.94 = 0.0863 \tag{3.35}$$

The in-situ coefficient of earth pressure at rest $K_0\left(=\sigma'_h/\sigma'_v\right)$ depends on ξ as shown in Figure 3.37. For normally consolidated clay K_{0NC} increases with decreasing ξ (i.e., horizontal stresses are larger for smaller ξ while vertical stresses remain unchanged). Assuming K_{0NC} = 0.6 (using eqn. 3.36 suggested by Jaky, 1944) for Geneva Clay with friction angle of 24°, ξ = 0.1.

$$K_0 = 1 - \sin\phi \tag{3.36}$$

The K_0 value generally increases as the soil in unloaded and is often represented by the empirical equation proposed by Schmidt (1966):

$$K_{0OC} = K_{0NC}\left(OCR\right)^{\sin\phi'} \tag{3.37}$$

Figure 3.37 shows the K_0 values predicted by the TTS model for Geneva Clay at OCR = 8. The results show that TTS predicts K_{0OC} decreasing with OCR contrary to established soil behavior.[16] This result represents a notable limitation of the TTS model that should be addressed in future research (Panagiotidou et al., 2016) but has little effect on the thermo-mechanical response of TTS in the applications described in this thesis.

The final part of the mechanical calibration involves setting the reference void ratio for the VCL by calibrating parameter B_0 (eqn. 3.19). Figure 3.38 illustrates that the reference void ratio (i.e., e at a selected σ'_v) increases with B_0 and shows good agreement with data for Geneva Clay for $B_0 = 3.8\times10^{-4}$ Pa. It should be noted that all of the input constants (B_1, m_1, m_2, m_3, h, ξ, c' Figs. 3.32-3.37) affect the location of the VCL and hence, parameter B_0 is chosen last in the calibration process. The results show that the TTS model describes closely the 1-D compression behavior of natural Geneva Clay (samples S3 and S4b) recorded by Di Donna and Laloui (2015), as shown in Figure 3.39.

3.5.2 Thermal Components of TTS Model

The input constants that control the thermal behavior of the TTS model are α_{bf}, L_T and m_5. Parameter α_{bf} was selected based on the independent laboratory measurements of the conversion of bound water to free water described in Section 3.3. Assuming that α_{bf} is controlled primarily by mineralogy, it is assumed that properties for Geneva Clay will be

[16] For Geneva Clay we expect $K_{0OC} \approx 1.7$ at OCR = 8.0, which can only be achieved by introducing ξ = -0.038 in the TTS model. This generates an unrealistic value for NC Clay (K_{0NC} = 1.5).

similar to RBBC and Kaolinite (based on index properties in Fig. 3.9) and hence, α_{bf}=0.0237°C^{-1}. The parameter L_T affects the temperature dependence of the VCL (eqn. 3.17). Figures 3.40 a, b and c show the selection of L_T = 0.020°C^{-1}. The model predicts much smaller effects for T = 40°C vs 60°C, compared to 40°C vs 20°C, a trend not seen in the three tests reported by Di Donna and Laloui (2015). The best overall agreement is achieved for L_T = 0.020°C, which is used in all subsequent calculations.

Figure 3.41 b-d illustrate the effect of selected values of m_5 (eqn. 3.16) on predictions of thermal volumetric strains for cyclic tests at OCR = 1.0 and 16.0 (sample S3). In fact, as m_5 increases, accumulation of compressive strains for NC clay and dilative strains for OC clay both increase. For Geneva Clay, using m_5 = 0.1 s^{3}m^{-2}°C^{-1} results in slightly smaller thermal volumetric strain induced during the first heating cooling cycle for NC clay and 0.4% larger thermal strain accumulation after 4 cycles of heating-cooling compared to the lab measurements shown in Figure 3.41b. These effects are accentuated for larger m_5. For the case of the OC clay, the TTS model overestimates the accumulated dilative strains by 0.5%. Figure 3.42 compares TTS prediction to the recorded cyclic thermal volumetric strain for sample S4b, by using the input parameter m_5 = 0.1 s^{3}m^{-2}°C^{-1} used for sample S3. It is observed that the TTS model overestimates the final accumulated volumetric strain by 1.2%.

Figure 3.43 shows TTS predictions for a single cycle of heating and cooling at different initial OCRs, under constant vertical stress. The results show that the TTS model provides a reasonable estimate of thermal volumetric strains at different stress levels with a transition to dilative response for OCR = 2.0 – 4.0. Moreover, the TTS model predicts that the thermal volumetric strains are always irreversible even for OC clays, something that has been reported in some thermal tests in the literature, although prior models generally suggest elastic response for OC clays (e.g., Hueckel and Borsetto, 1990; Laloui and Francois, 2009). Figure 3.43b shows the change of porosity of bound water due to heating and cooling. As expected the conversion of bound water to free water is a reversible process that is independent of OCR (cf. eqn. 3.15b). An increase in temperature from 20°C to 60°C causes a decrease in bound water porosity $\Delta\varphi_{bw}$ = -0.6% (φ_{bw} = 1% at 20°C and φ_{bw} = 0.4% at 60°C), while at 5°C, φ_{bw} = 1.4%. Figure 3.43d presents the evolution of elastic and hysteretic volumetric strains during loading to σ_v'

=125kPa and unloading to vertical stress σ_v' corresponding to the different OCRs. It is concluded that at σ_v' = 60kPa, where $\varepsilon_v^e = \varepsilon_v^h$ the resulting thermal volumetric strains predicted by the TTS model are zero as shown by the OCR = 2 line (Figure 3.43c). This point plays a key role in the TTS model predictions, since for vertical stress larger than σ_v' = 60kPa (and hence lower OCR) the resulting thermal volumetric strains are contractive while for smaller vertical stress (and hence higher OCR) the resulting thermal volumetric strains are dilative (Figures 3.43c and d).

Zymnis and Whittle (2014) have shown cyclic thermal loading induced by shallow geothermal installations can lead to considerable thermal volumetric strains and hence, the study of cyclic thermal loading is crucial when designing shallow geothermal installations. One of the most important advantages of the TTS model is its ability to characterize the accumulation of volumetric strain during continuous cycles of heating and cooling. Figure 3.44 illustrates cyclic strain accumulation results for initial OCR's = 1.0 – 8.0 with the same temperature difference induced during the lab tests on Geneva Clay (ΔT = 55°C). Continuous heating and cooling of NC clay at vertical stress σ_v'=125kPa results in long-term accumulation of contractive strain, ε_v = 1.8%; while similar thermal cycles produce ε_v = 3.5% at σ_v' =1MPa. Continuous heating and cooling of highly overconsolidated clay (OCR = 8) results in long-term accumulation of dilative volumetric strain (ε_v = 1.27%), while clays of intermediate OCR produce smaller accumulated strain (Figure 3.44c). The TTS model predictions for NC clay provide a good fit to the laboratory measurements on Geneva Clay (Figure 3.44c). The accumulation of volumetric strain reaches a limit when $\varepsilon_v^e = \varepsilon_v^h$ as shown in Figure 3.44d. In fact all of the saturated positions form a "threshold condition" shown in Figure 3.44a that depends on the mechanical calibration of the TTS model (its location is controlled by parameters h, m_1 and m_2).

Figure 3.45 shows the predicted strain accumulation over cycles of heating and cooling with ΔT ranging from 10°C to 40°C (and T_{ave} = 20°C). The TTS model predicts that heating and cooling of normally consolidated Geneva Clay ultimately trends to same maximum volumetric strain (ε_v = 1.8%) independent of the imposed temperature range, while rates of strain accumulation are directly linked to the imposed ΔT. For example for

$\Delta T = 40°C$, the maximum strain accumulates within 40 cycles, while for $\Delta T = 10°C$, the maximum strain develops in 150 cycles. Figures 3.44 and 3.45 demonstrate the capabilities of the TTS model to describe volumetric strain accumulation due to continuous heating and cooling. As discussed in Chapter 2, there are currently no laboratory data to validate these model predictions.

3.6 Summary and Conclusions

The Tsinghua ThermoSoil model (TTS; Zhang & Cheng, 2013) presents a novel theoretical framework for simulating the coupled thermo-hydro-mechanical properties of clays. The model uses a double entropy approach (following the Granular Solid Hydrodynamics framework of Jiang & Liu, 2009) to capture effects of energy dissipation at the microscopic particulate contact level on continuum behavior. The model is able to describe strain rate and thermal dependence of clay properties. The conversion of bound to free water represents a key concept that controls irreversible thermo-mechanical strains in the TTS model. This process has been studied through laboratory measurements of specific gravity variations with temperature for three clays of different mineralogy. Calibration of the TTS model was explained in detail, using recently published cyclic thermal tests on Geneva Clay (Di Donna and Laloui, 2015). Finally the chapter illustrates the TTS model capabilities in simulating familiar aspects of thermal consolidation of clays as well as the long-term, progressive accumulation of strains associated with seasonal heating and cooling processes for shallow geothermal systems installed in clays. Further laboratory studies of thermo-mechanical properties of different types of clay are needed to evaluate the TTS model predictions.

Loading		
$\dot{\varepsilon}_v, \dot{\varepsilon}_s$	1/s	Total strain rate
$\dot{T}$	°C/s	Temperature rate
State Variables		
ϕ_{bw}, ϕ_{fw}	-	Bound and free water porosity
$\varepsilon_v^e, \varepsilon_s^e$	-	Volumetric and deviatoric elastic strains
$\varepsilon_v^h, \varepsilon_s^h$	-	Volumetric and deviatoric hysteretic strains
T_g *	$1/s^2$	Granular temperature
Deduced Variables		
ρ_d	kg/m^3	Dry density
e	-	Void ratio
* For a = 0.5		

Table 3.1: State variables used in TTS Model

Mechanical Properties	
B_0 [Pa]	Location of VCL
B_1 [m^3/kg]	Slope of VCL
c [-]	Cohesion (c=0 for sands)
h [-]	Hysteretic strains (slope of unload curve)
w [-]	Hysteretic strains (minor role)
$m_{1,0}$ [-]	Controls elastic strain evolution
m_2 [-] *	Controls elastic strain evolution and location of reload curve
m_3 [-]	Controls contribution of volumetric and deviatoric strains on granular temperature production
m_4 [kg $s^{-1}m^{-3}$] *	Rate of granular temperature production
a [-]	Controls rate effects (a=0.5 for rate independence)
c' [-]	Affects critical state response
ξ [-]	Sets coefficient of earth pressure at rest K_0
Thermal Properties	
α_{bf} [$°C^{-1}$]	Affects conversion of bound water to free water during heating
m_5 [$s^3 m^{-2} °C^{-1}$] *	Controls amount of thermal volumetric strains produced due to heating and cooling cycles
L_T [$°C^{-1}$]	Controls shift of VCL due to increase in temperature
w_T [$°C^{-1}$]	Dependence of parameter w on temperature
$\beta_{s,vol}$ [$°C^{-1}$]	Volumetric thermal Expansion of solid particles
* For a = 0.5	

Table 3.2: Input constants used in TTS model

Soil	Origin	Contributing researchers	Liquid Limit, w_L (%)	Plasticity Index, I_p (%)	Clay fraction (%)	USCS
Kaolinite	Cornwall, U.K.	Gao (2013)	48	19	65	ML
Boston Blue Clay	Boston, Massachusetts	Walbaum (1988), Ahmed (1990), Seah (1990), Sheahan (1991), Santagata (1994), Santagata (1998), Abdulhadi (2009), Moniz (2009), Horan (2012), Casey (2014)	46.5	22.7	56	CL
Eugene Island Clay	Eugene Island, Gulf of Mexico	Betts (2014), Fahy (2014)	85.8	62.9	63	CH

Table 3.3: Origin, index properties and USCS classification of tested clays (after Casey, 2014)

Soil		Chlorite (%)	Kaolinite (%)	Illite (%)	Illite – Smectite (%)	Expanda-bles (%)	Total Clay (%)
Boston Blue Clay	Whole sample	6.2	2.9		7.3*	N/A	16.4
	< 2μm fraction	5.0	2.0	65	28	5-10	
Eugene Island Clay	Whole sample	0.4	9.1		44.4*	N/A	53.9
	< 2μm fraction	1.0	4.0	8.0	87.0	70-80	
* Includes both illite and mixed layer illite-smectite							

Table 3.4: Mineralogy of natural clays tested (after Casey, 2014)

	Kaolinite	RBBC	EI-GOM
G_{s20} [-] [1]	2.632	2.803	2.858
$\frac{1}{M_s}\frac{\partial M_w}{\partial T}$ [10^{-5} / °C] [1]	1.77	6.23	19.06
ρ_s [g / cm^3] [2]	2.621	2.772	2.727
α_{bf} [1 / °C]	0.0204	0.019	0.0118
$w_{bw,20}$ [%] [3]	1.33	5.09	23.99
SSA [m^2 / g] [4]	14	49	267
t_{bw} [Å] [3]	8.897	9.72	8.639

[1] Measured from water submersion method
[2] Average values from gas pycnometer tests
[3] Assuming $\rho_{bw} = 1.07\rho_{fw}$
[4] From clay suppliers

Table 3.5: Results of laboratory tests

	S1	S3	S4	S4b
Depth, z [m]	13.6 – 13.8	14.3 – 14.6	31.4 – 31.7	15.1 – 15.4
In-situ pore water pressure, p_w [kPa] [1]	137.2	144.9	315.5	152.5
In-situ total vertical stress, σ_v [kPa]	279.9	294.1	661.0	305.0
In-situ effective vertical stress, σ'_v [kPa]	142.7	149.2	345.5	152.2
OCR [-]	1.0	1.0	1.0	1.0
Water content, w [%]	23.8	23.2 – 26.3	22.3 – 22.7	27.9
Soil Mass Density, ρ [kg/m^3]	2040	1980 – 2080	2090 - 2100	1930
Solid particle mass density, ρ_s [kg/m^3]	2710	2780	2780	2710
Dry density, ρ_d [kg/m^3]	1650	1590 – 1690	1701 – 1710	1510
Degree of saturation, S_r [%]	100	94.6 – 100	100	94.9
Liquid limit, w_L [%]	37.0	34.0	31.4	42.6
Plasticity Index, I_p [%]	16.9	12.8	11.1	18.4

[1] Water table at the surface level

Table 3.6: In-situ state of stress and identification properties of the tested soil samples (after Di Donna and Laloui, 2015)

Test Number	Test Name	Material	Type*	Tempera-ture, T [°C]	Vertical eff. stress, σ'_v [kPa]	OCR before thermal cycles
1	S3_E7_20	S3	SO	20	1 – 1000 – 60	-
2	S3_E6_40	S3	TO	40	1 – 1000 – 60	-
3	S3_E5_60	S3	TO +(TC)	60 (5 – 60)	1 – 1000 – 60	(16.0)
4	S4_E8_20	S4	SO	20	1 – 1000 – 60	-
5	S4_E5_40	S4**	TO	40	1 – 1000 – 60	-
6	S4_E6_60	S4**	TO +(TC)	60 (5 – 60)	1 – 1000 – 60	- (16.0)
7	S3_E5_cy	S3	TC	5 - 60	125	1.0
8	S4_E6_cy	S4	TC	5 - 60	250	1.0
9	S1_E3_cy	S1	TC	5 - 60	125	1.0
10	S4_E4_cy	S4b	TC +(SO)	5 - 60	125 (1000 – 60)	1.0 (-)

* SO = Standard Oedometer, TO = Thermal Oedometer, TC = Thermal Cycles
** Highly disturbed samples, results are not presented

Table 3.7: Experimental program undertaken by Di Donna and Laloui (2015)

Mechanical Properties*	
B_0 [Pa]	3.8×10^{-4}
B_1 [m^3/kg]	0.0162
c [-]	0.01
h [-]	0.05
w [-]	1.0
$m_{1,0}$ [-]	1.0
m_2 [-]	150
m_3 [-]	1.0
m_4 [kg m^{-3} s^{-1}]	6.0×10^{4}
a [-]	0.5
c' [-]	0.0863
ξ [-]	0.1
Thermal Properties**	
α_{bf} [$°C^{-1}$]***	0.0237
m_5 [s^3 m^{-2} $°C^{-1}$]	0.1
L_T [$°C^{-1}$]	0.02
w_T [$°C^{-1}$]	0.0
$\beta_{s,vol}$ [$°C^{-1}$]	1.8×10^{-5}

* From sample S4b (Figs. 3.31 – 3.38)
** From sample S3 (Figs. 3.40 and 3.41)
*** From specific gravity measurements (Fig.3.17)

Table 3.8: Input constants used for Geneva Clay calibration of TTS model

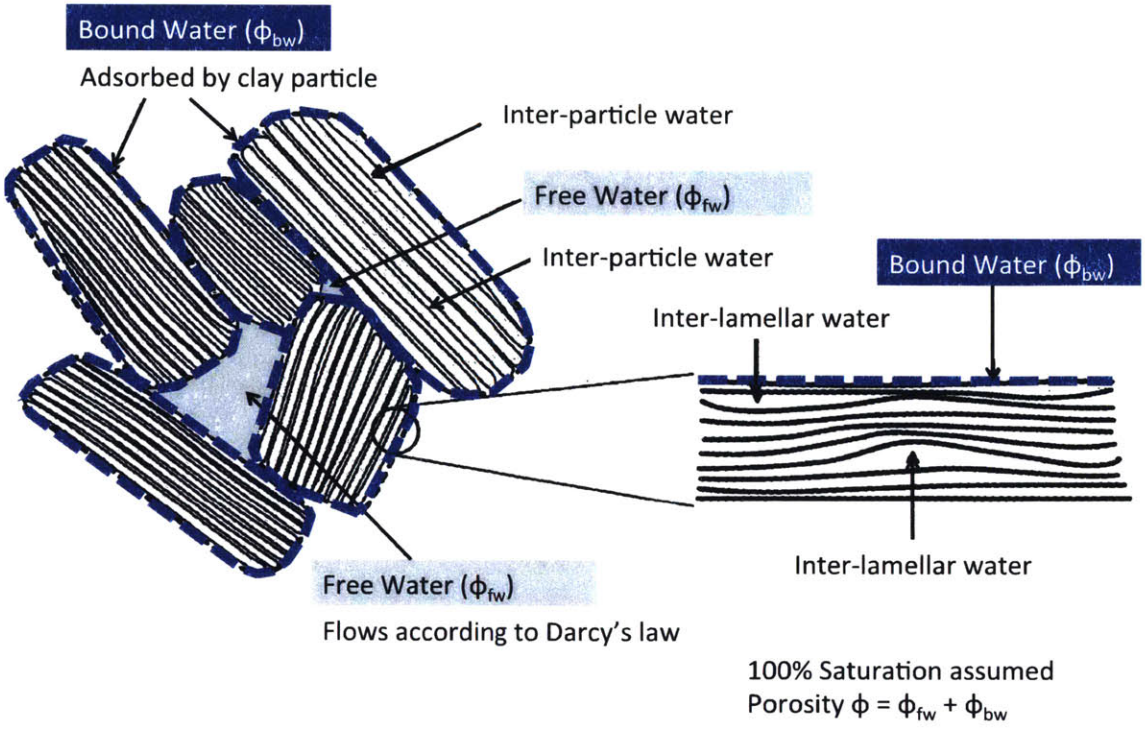

Figure 3.1: Solid, free water and bound water phases assumed in TTS model (after Cekerevac, 2003)

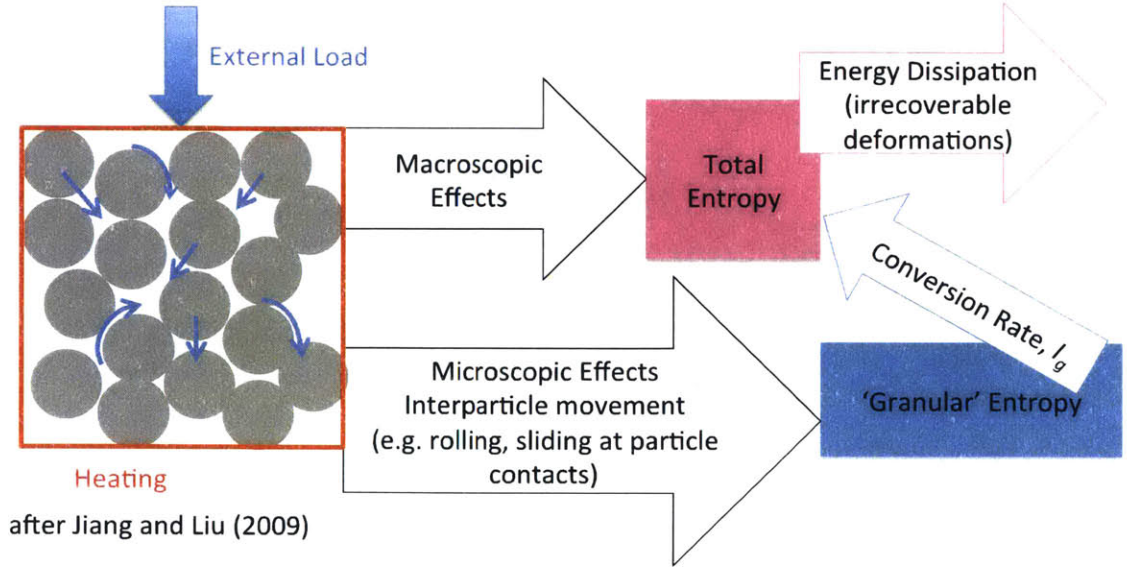

Figure 3.2: Double entropy concept assumed in TTS model

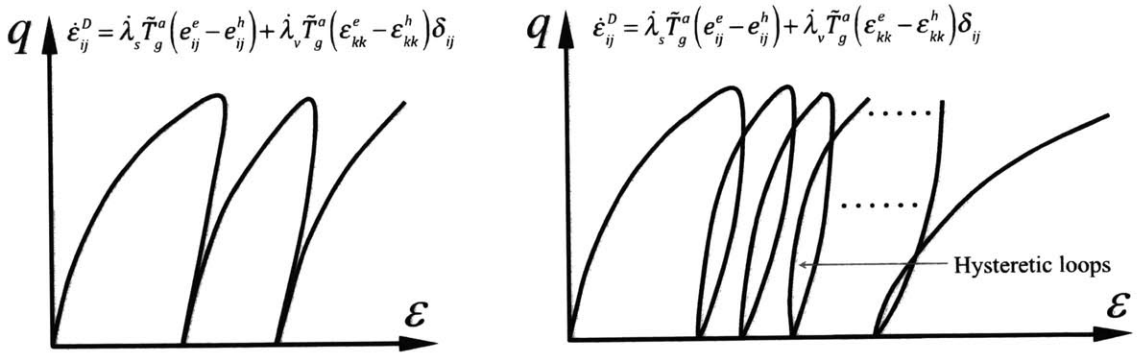

a) Hysteretic strain $\varepsilon_{ij}^h = 0$ b) Hysteretic strain $\varepsilon_{ij}^h \neq 0$

Figure 3.3: Effect of hysteretic strain on strain accumulation due to cyclic loading and unloading (after Zhang and Cheng, 2013)

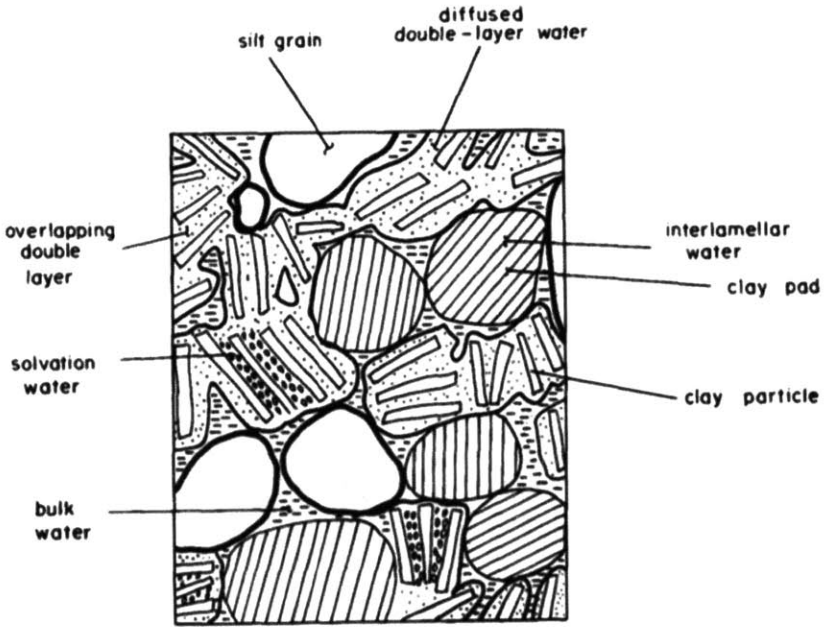

Figure 3.4: Forms of water in saturated low-porosity clay (after Baldi et al., 1988)

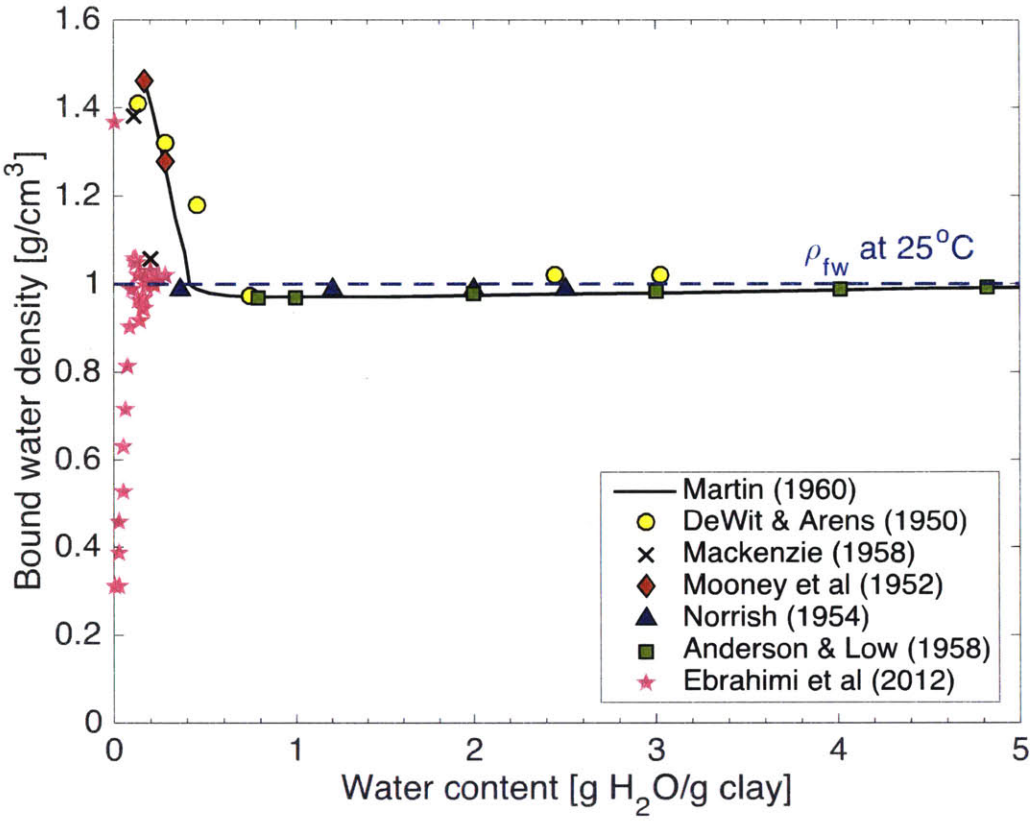

Figure 3.5: Adsorbed water density on Na-montmorillonite (after Martin, 1960)

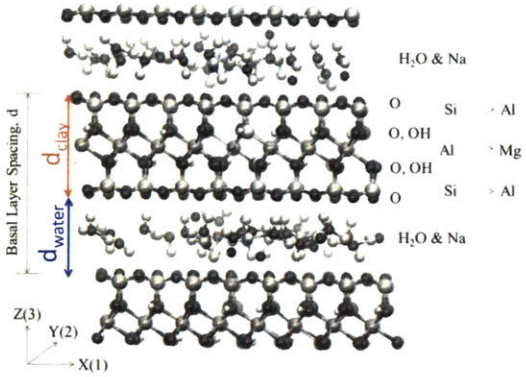

a) Typical unit cell in periodic crystal of the simulated clay mineral showing basal layer spacing d, clay layer thickness d_{clay} and water layer thickness d_{water}

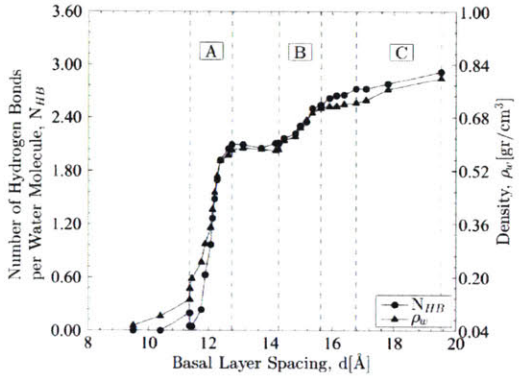

b) Change in average number of hydrogen bonds per water molecule and density of interlayer water during swelling of Wyoming Na-montmorillonite

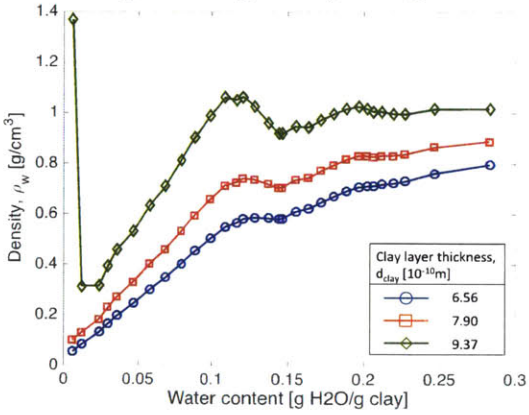

c) Adsorbed water density versus water content using different clay layer thicknesses

Figure 3.6: Molecular dynamics simulations of Wyoming Na-montmorillonite (Ebrahimi et al., 2012)

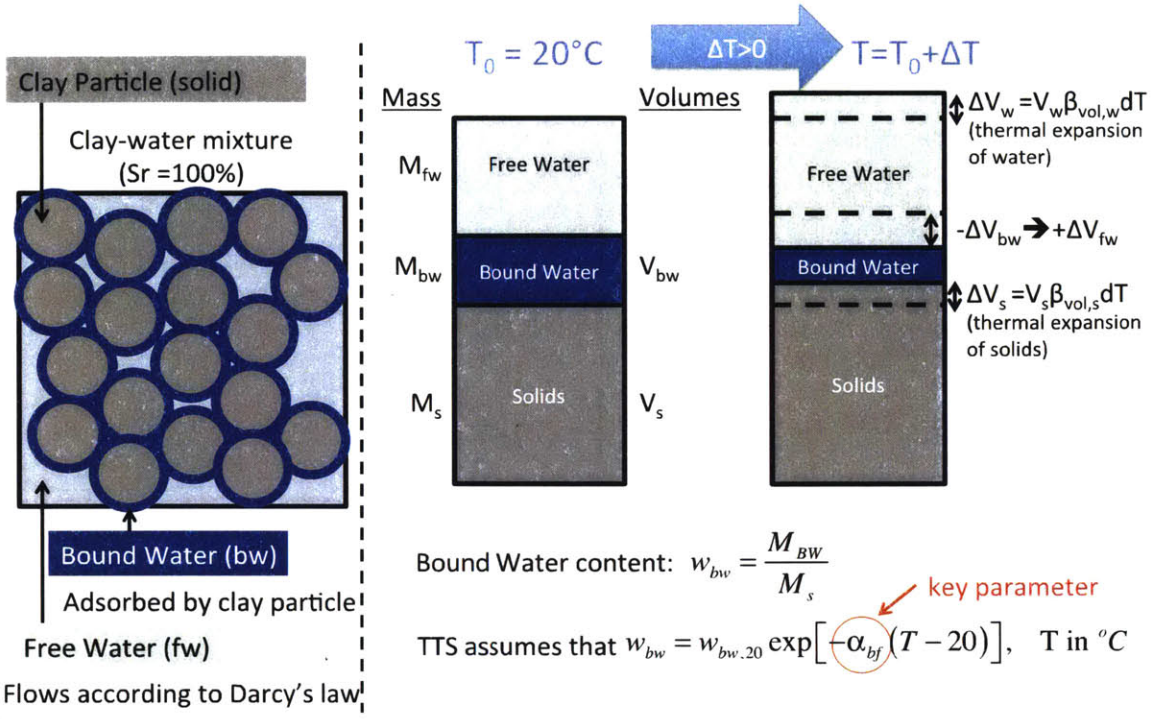

Figure 3.7: Clay response to heating, as assumed in the TTS model

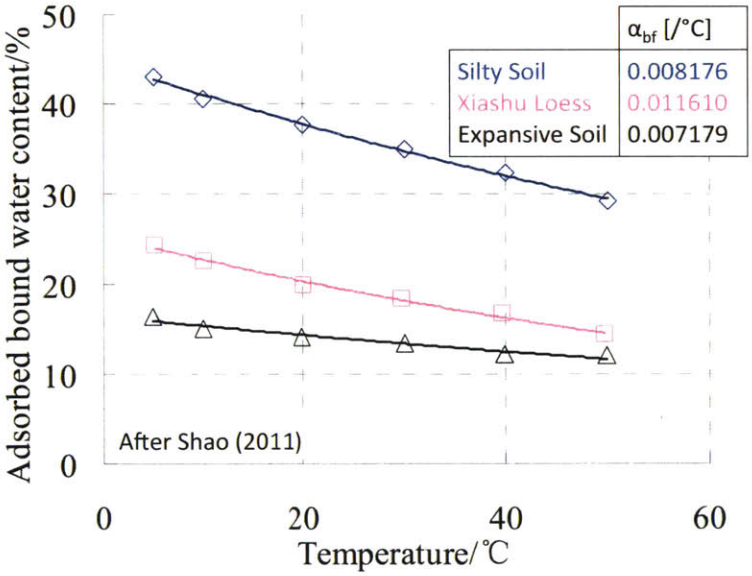

Figure 3.8: Change of bound water content with temperature as measured by Shao (2011) for three different clays

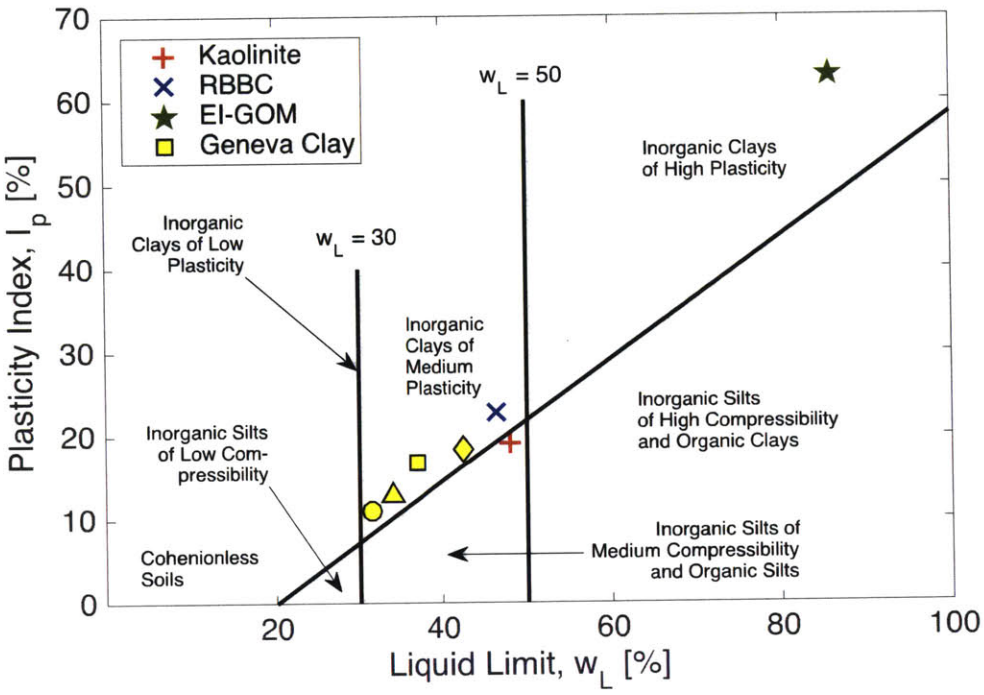

Figure 3.9: Position of the tested soils on the Casagrande chart

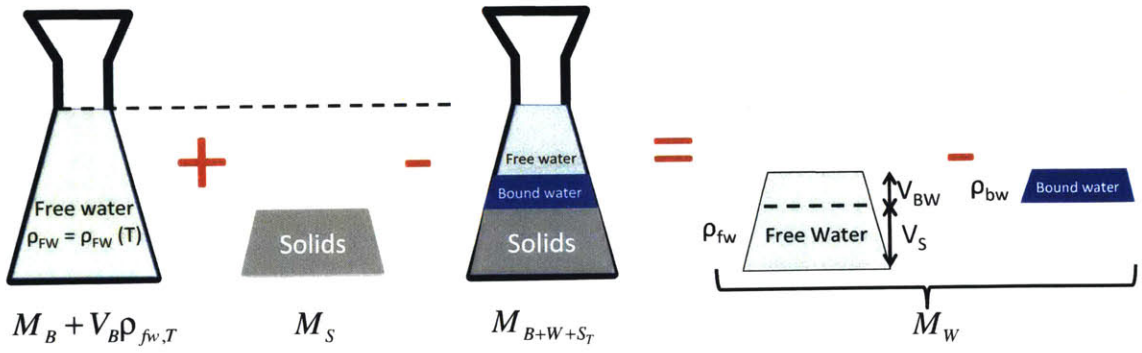

Figure 3.10: Concept of specific gravity tests and interpretation assuming conversion of bound to free water

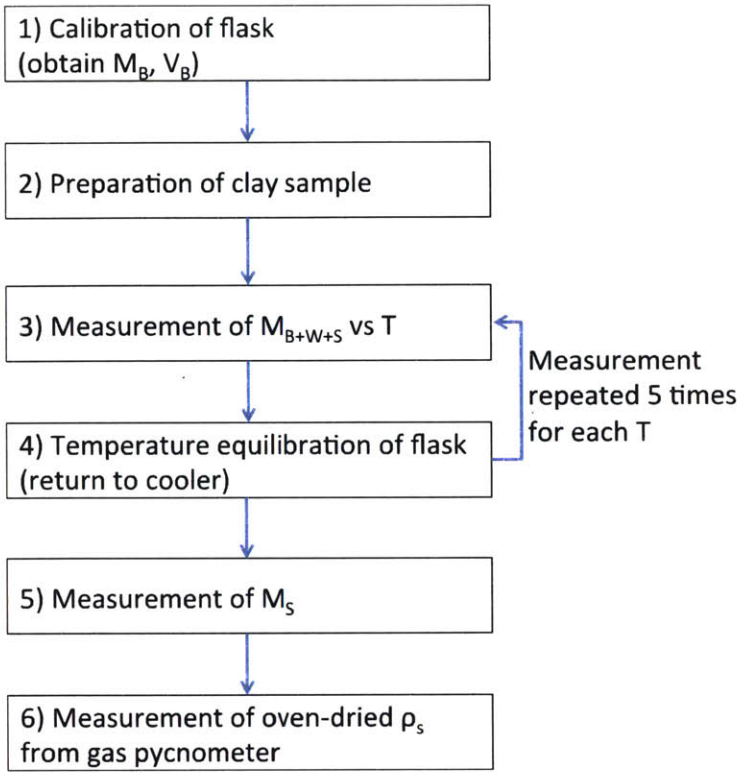

Figure 3.11: Summary of laboratory procedure for specific gravity measurements at different temperatures

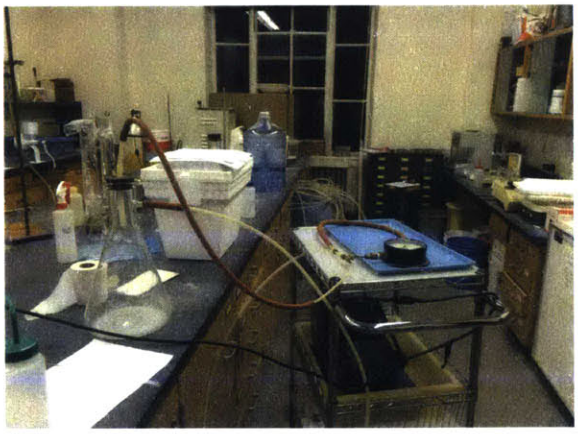

a) Vacuum used for de-airing of the slurry

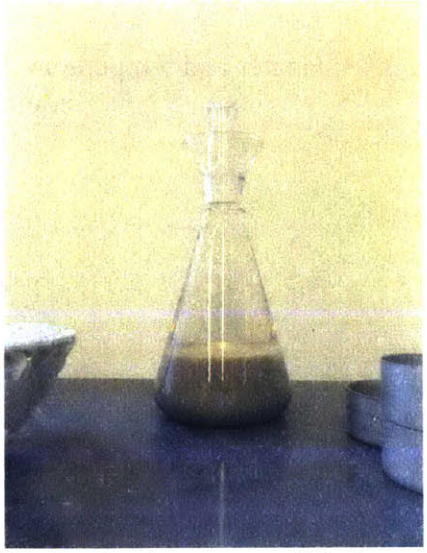

b) Distinction between solid phase and clear "free" water at top of volumetric

Figure 3.12: Preparation of soil specimens for lab tests

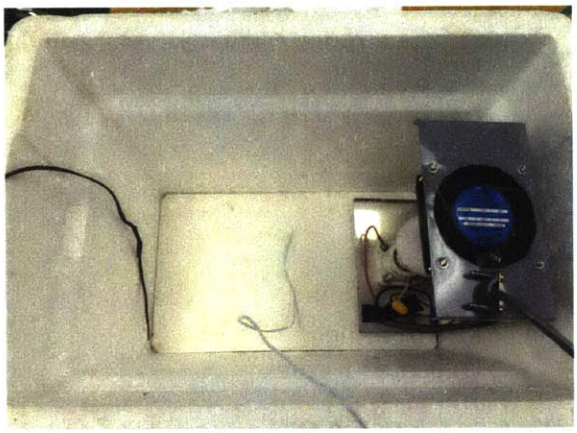

a) Heater used inside the cooler for setting required temperature

b) Heater and flasks inside the cooler

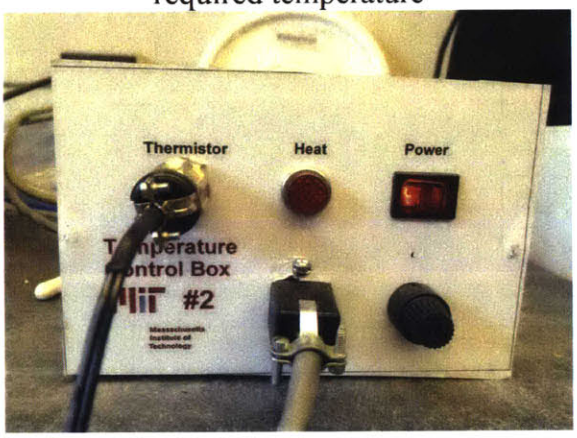

c) Temperature control box

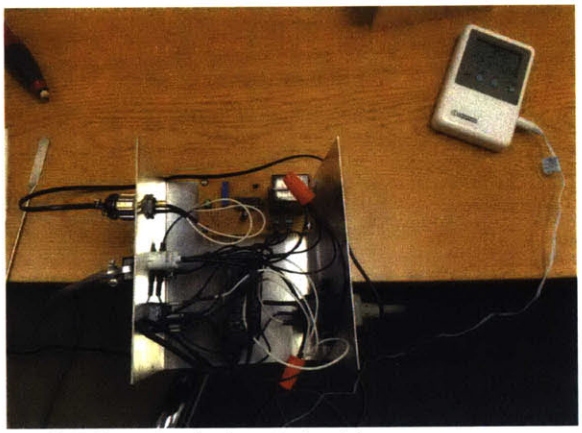

d) Electrical circuit inside temperature control box built by Dr. Germaine

Figure 3.13: Heater and temperature control box used in experiments for setting the required temperature

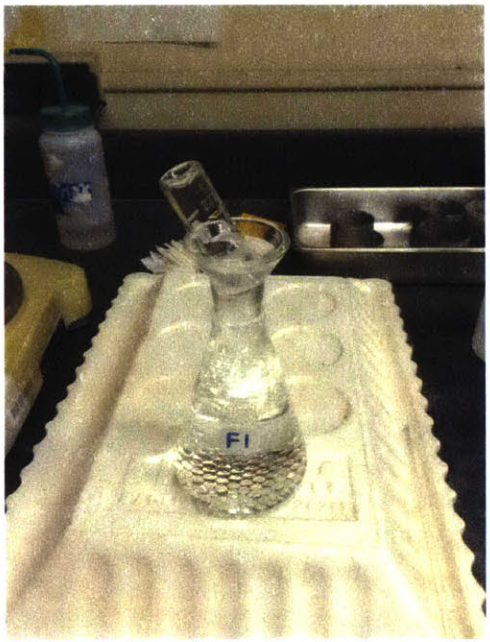

a) Cooler lid used as an insulated surface

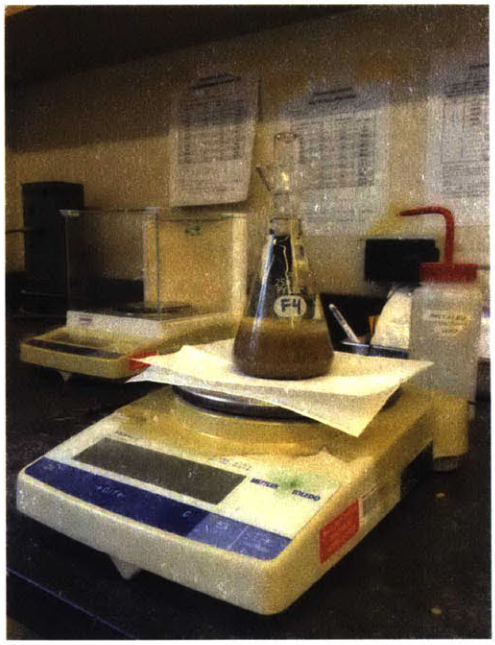

b) Mass measurement: tissue paper used as an insulator between flask and metal scale

c) Temperature measurement

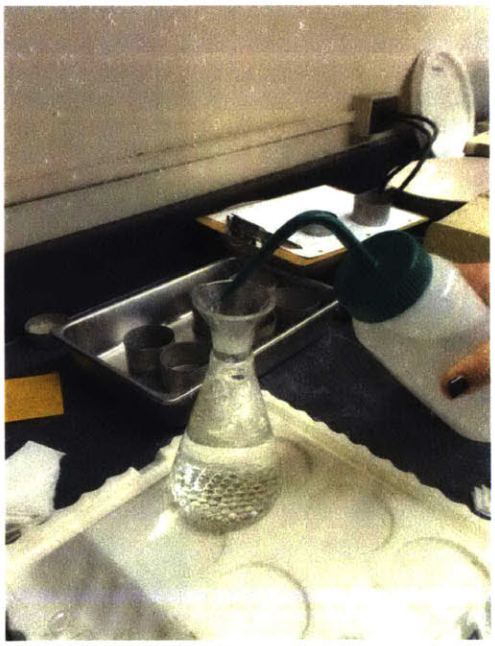

d) Refill of water after measurements have been taken

Figure 3.14: Steps followed during specific gravity tests

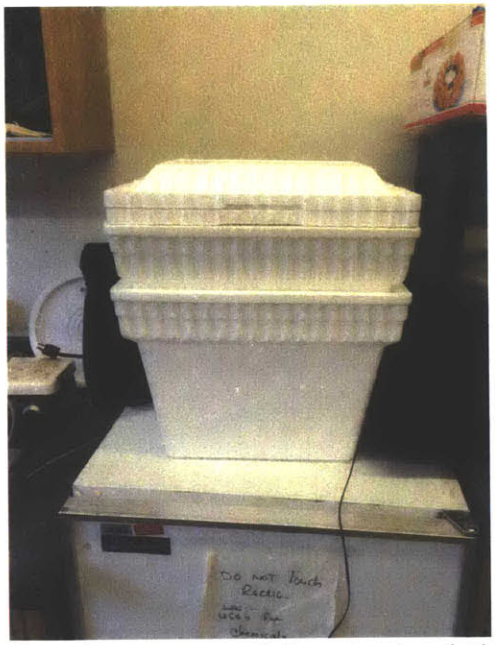

a) 2 coolers were used for extra insulation

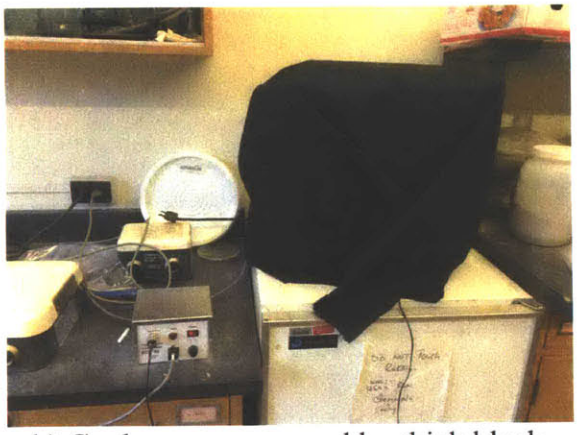

b) Coolers were covered by thick black cloth to minimize radiation heat losses from heater

Figure 3.15: Measures taken for additional thermal insulation

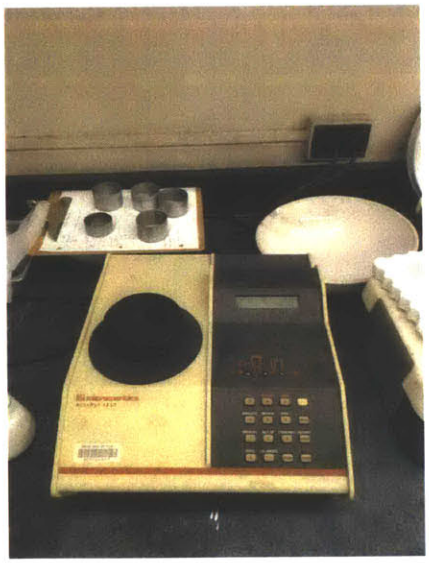

Figure 3.16: AccuPyc1330 gas pycnometer used for oven-dried solid density measurements

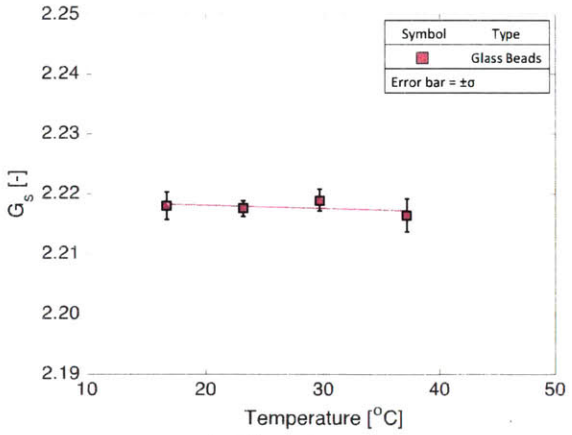

a) Glass Beads

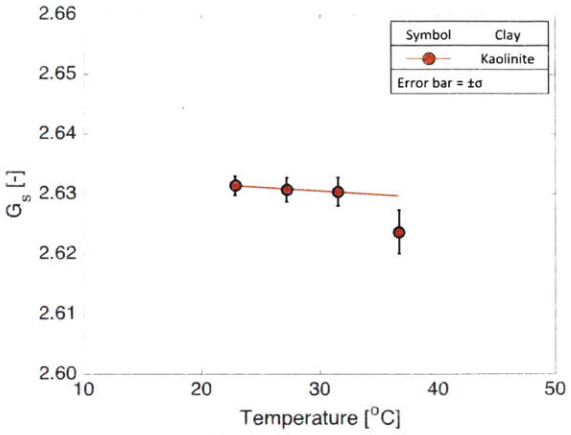

b) Kaolinite

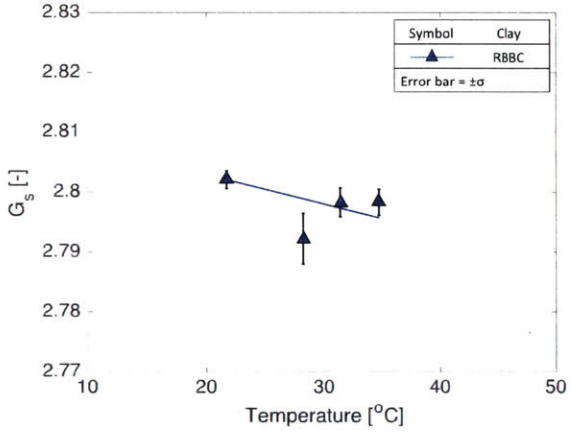

c) Boston Blue Clay

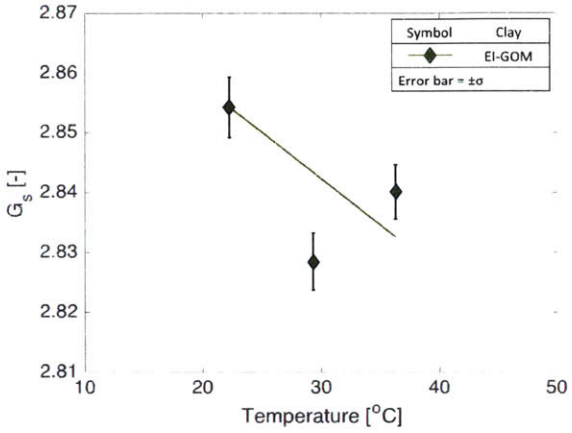

d) Eugene Island Clay

Figure 3.17: Experimental measurements and linear fits of specific gravity G_s versus temperature for: a) Glass beads, b) Kaolinite, c) RBBC and d) EI-GOM clay

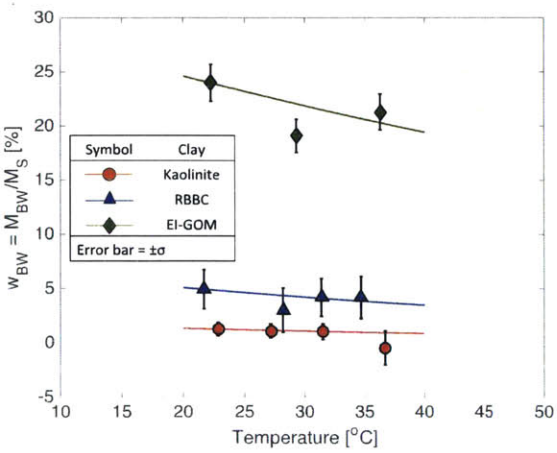

$$w_{bw} = w_{bw.20}\exp\left[-\alpha_{bf}(T-20)\right], \quad \text{T in } ^oC$$

a) Bound water content versus temperature

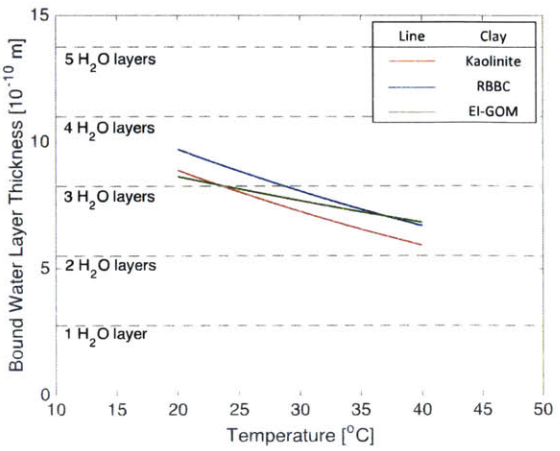

$$t_{bw} = t_{bw.20}\exp\left[-\alpha_{bf}(T-20)\right], \quad \text{T in } ^oC$$

b) Bound water layer thickness versus temperature

Figure 3.18: Effect of temperature on bound water content and thickness of bound water layer as predicted from lab measurements

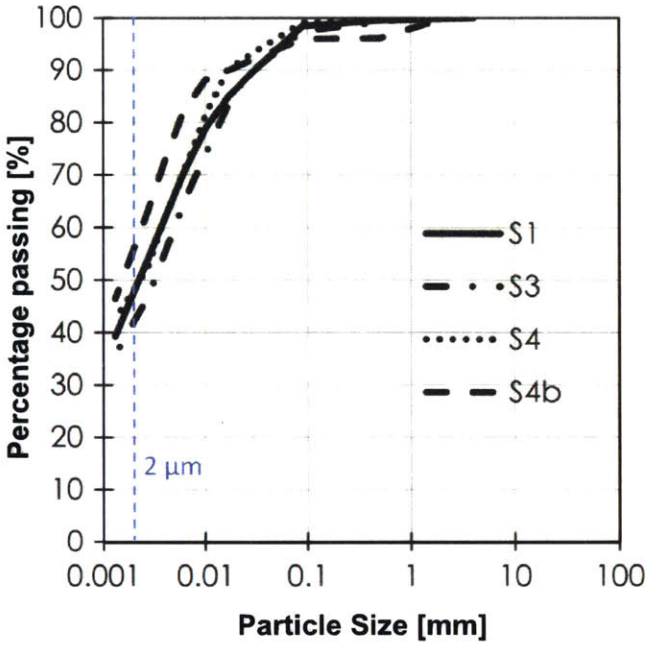

Figure 3.19: Particle size distribution of the four samples (Di Donna and Laloui, 2015)

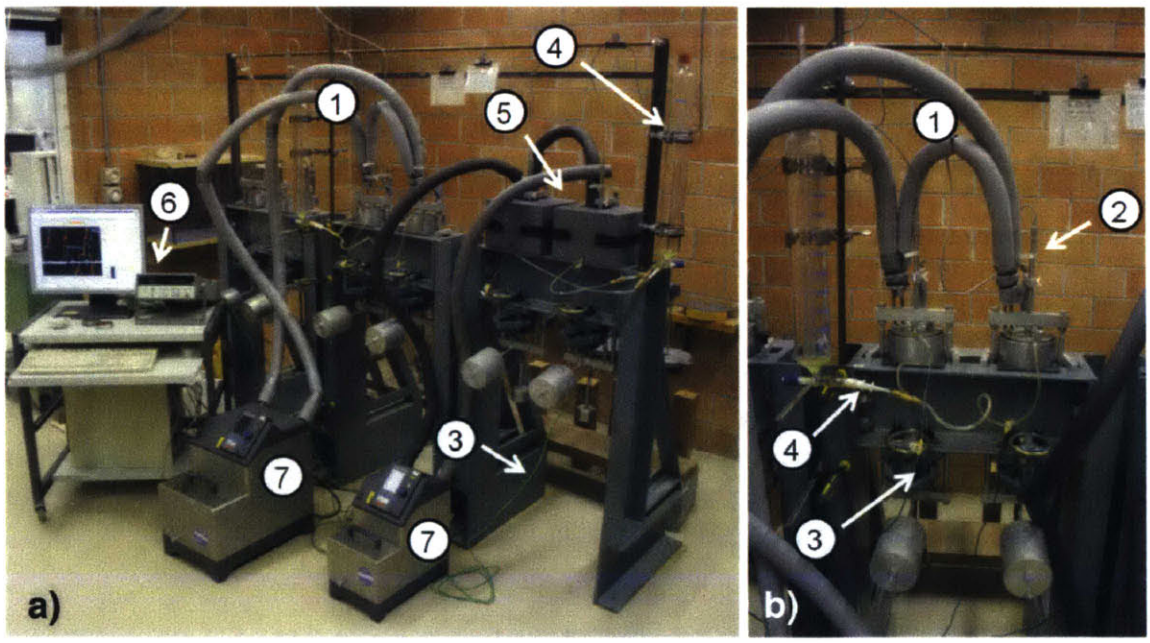

Figure 3.20: Experimental setup: (a) global view and (b) detail (1: tubes with circulating water at the desired temperature, 2: LVDTs, 3: thermocouples, 4: water supplier, 5: insulation, 6: acquisition system, 7: heaters)
(Di Donna and Laloui, 2015)

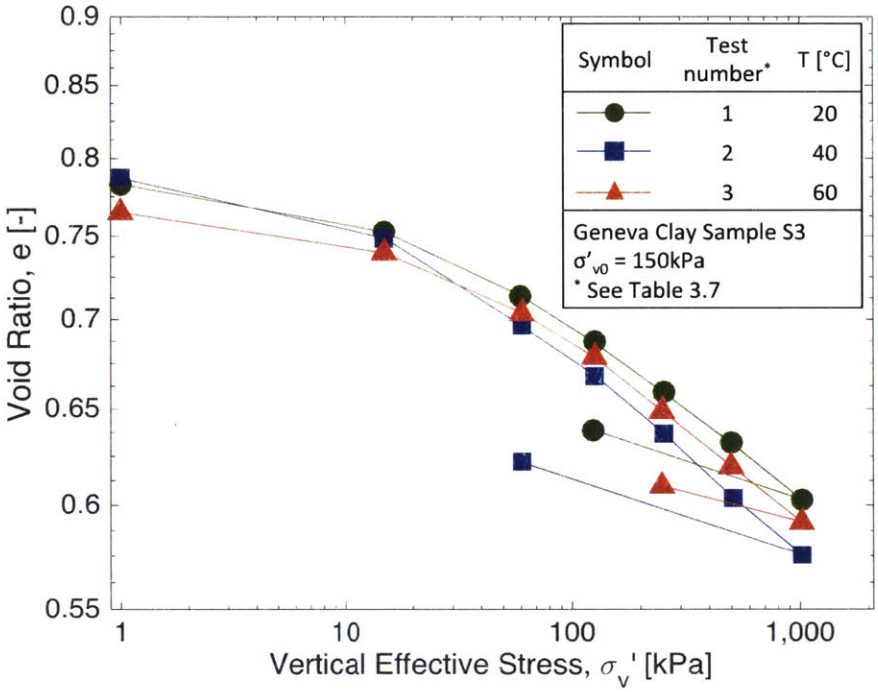

Figure 3.21: Comparison between oedometric tests at 20 °C, 40 °C and 60 °C on S3 samples (after Di Donna and Laloui, 2015)

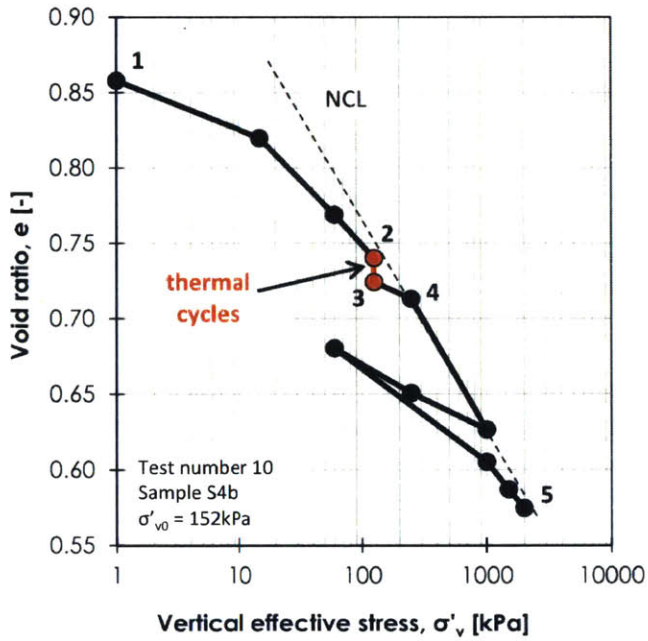

Figure 3.22: Combined mechanical and thermal cyclic loading on sample S4b (Di Donna and Laloui, 2015)

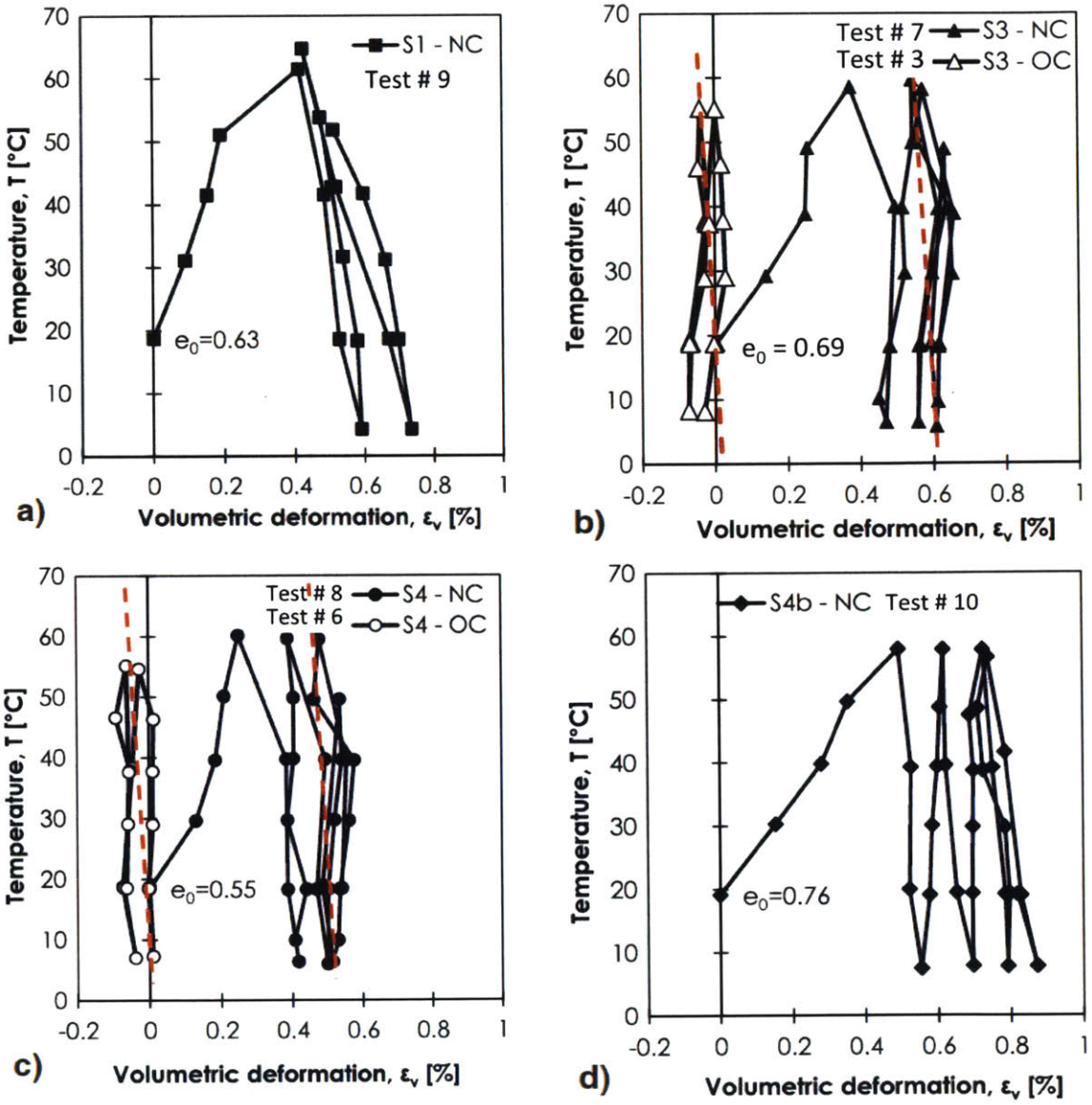

Figure 3.23: Geneva clay response to thermal cycles: (a) S1, (b) S3, (c) S4 and (d) S4b specimens (Di Donna and Laloui, 2015)

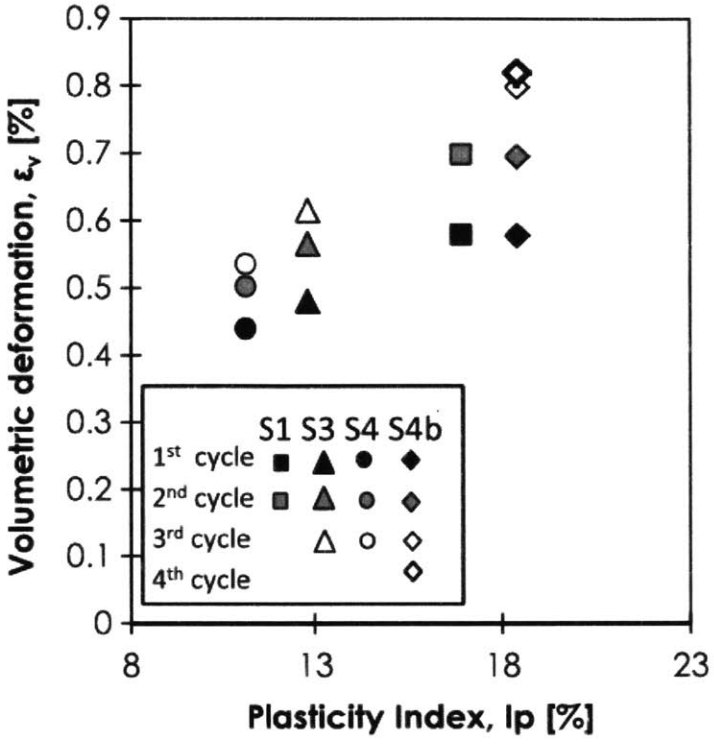

Figure 3.24: Effect of plasticity index on the accumulation of irrecoverable volumetric deformation during thermal cycles on NC samples (Di Donna and Laloui, 2015)

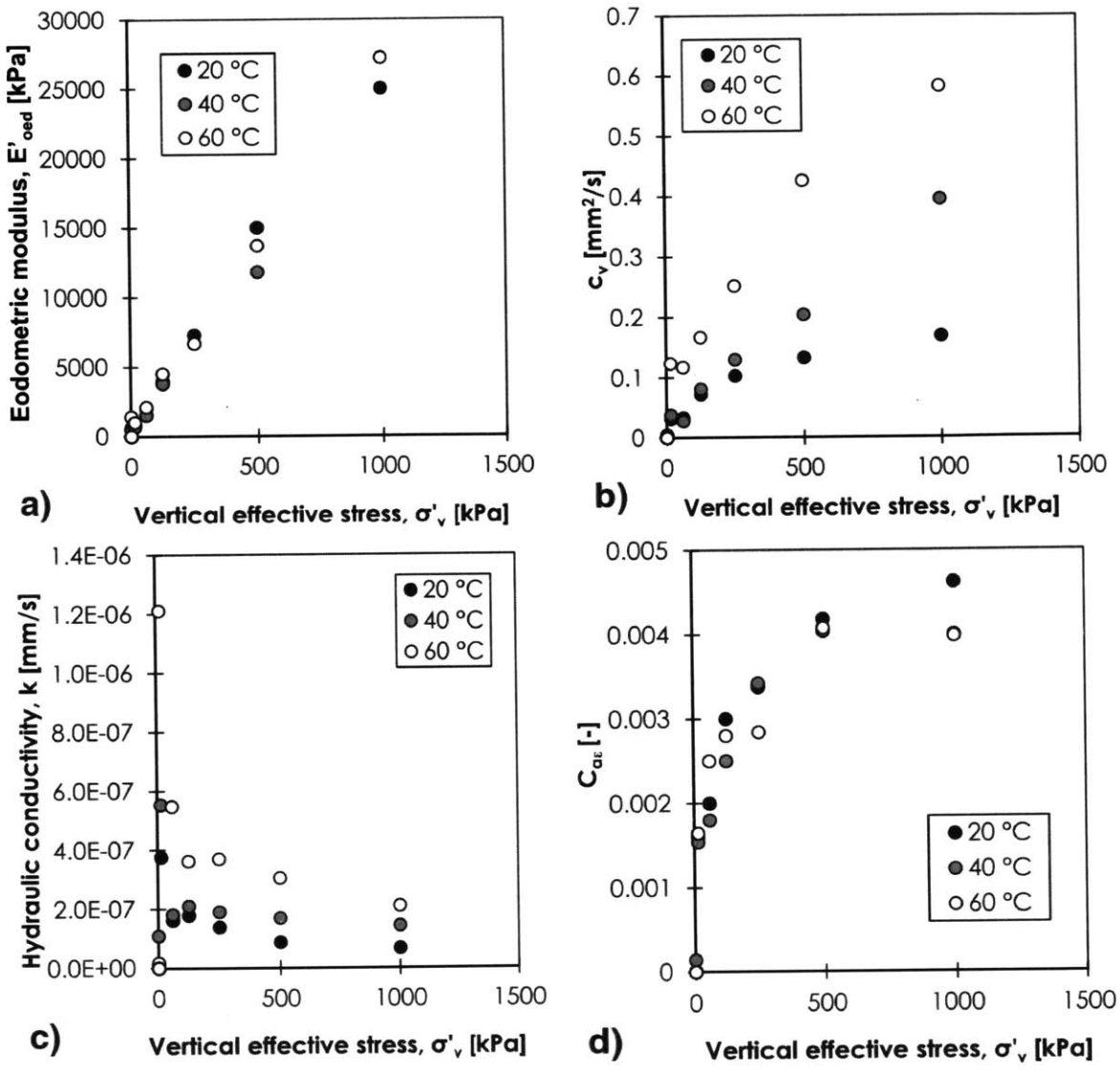

Figure 3.25: Effect of temperature on S3 samples on (a) oedometric modulus, (b) primary consolidation coefficient, (c) hydraulic permeability and (d) secondary consolidation coefficient (Di Donna and Laloui, 2015)

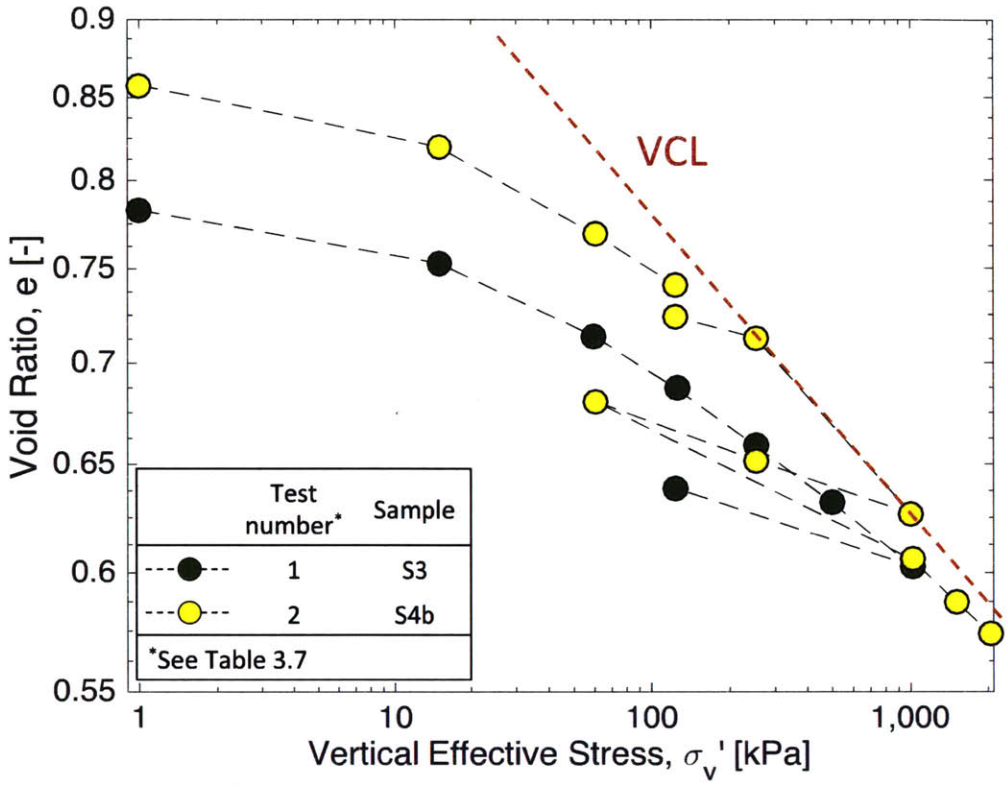

Figure 3.26: Results from oedometer tests performed on Geneva Clay samples S3 and S4b (after Di Donna and Laloui, 2015) and inferred VCL from lab data

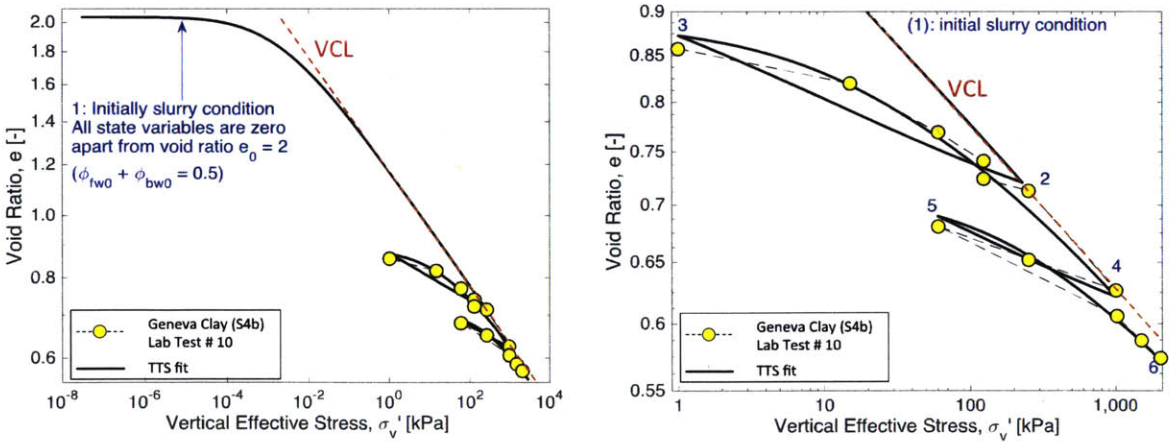

a) Slurry condition at start of calibration

b) Zoomed-in figure showing sequence of loading-unloading-reloading steps

Figure 3.27: Resulting TTS fit to Geneva Clay sample S4b and steps followed for mechanical calibration

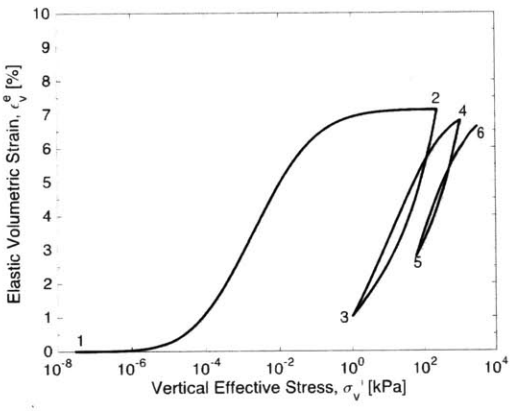

a) Elastic Volumetric Strain, ε_v^e

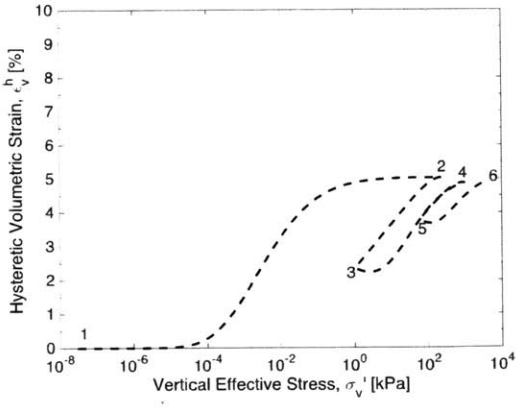

b) Hysteretic Volumetric Strain, ε_v^h

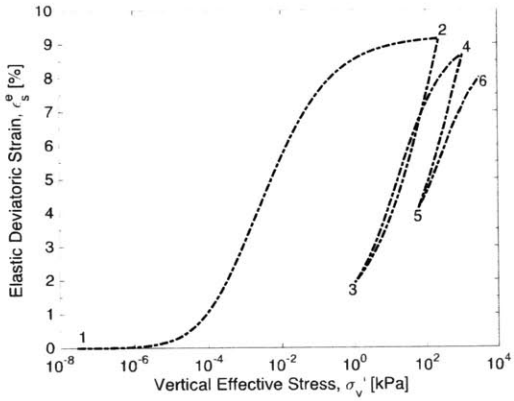

c) Elastic Deviatoric Strain, ε_s^e

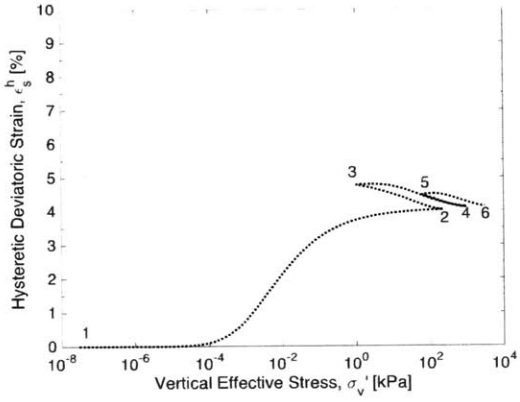

d) Hysteretic Deviatoric Strain, ε_s^h

Figure 3.28: Evolution of strain state variables during loading, unloading and reloading (numbers correspond to loading stages shown in Figure 3.26)

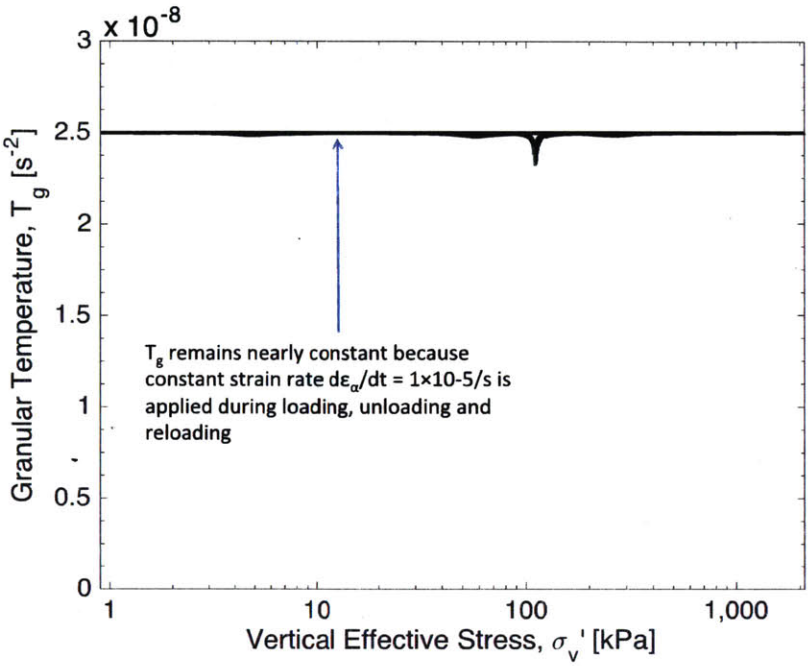

Figure 3.29: Evolution of granular temperature T_g during loading, unloading and reloading

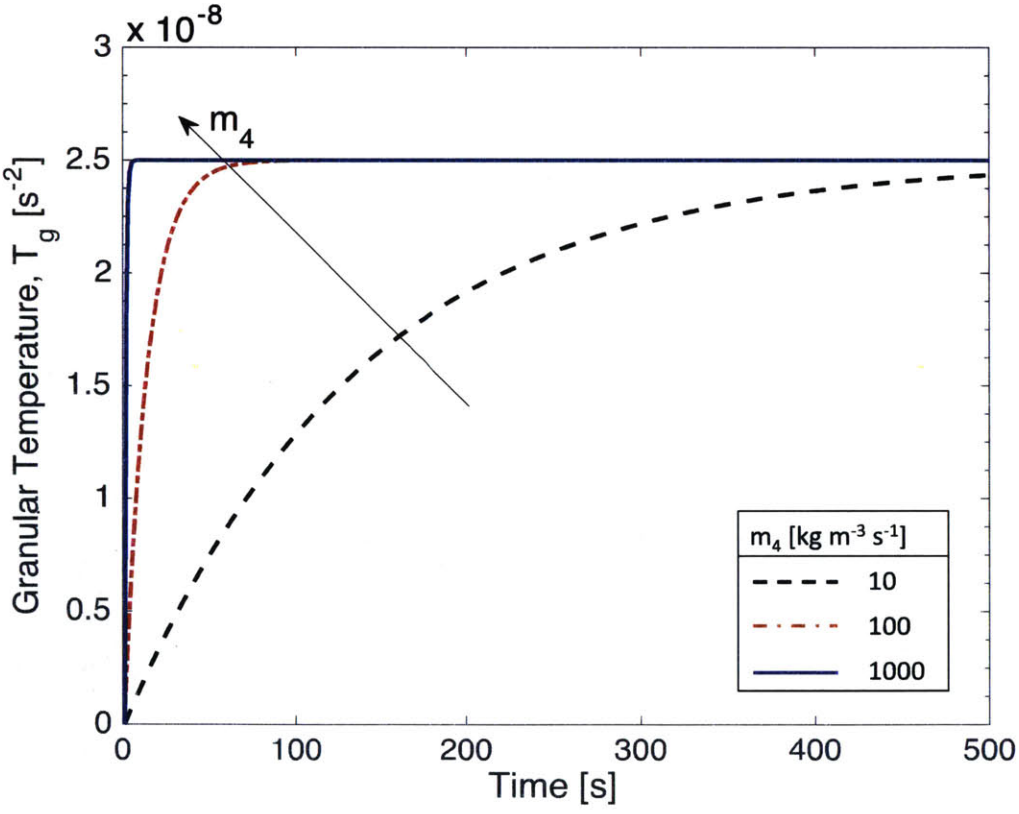

Figure 3.30: Effect of parameter m_4 on evolution of granular temperature T_g

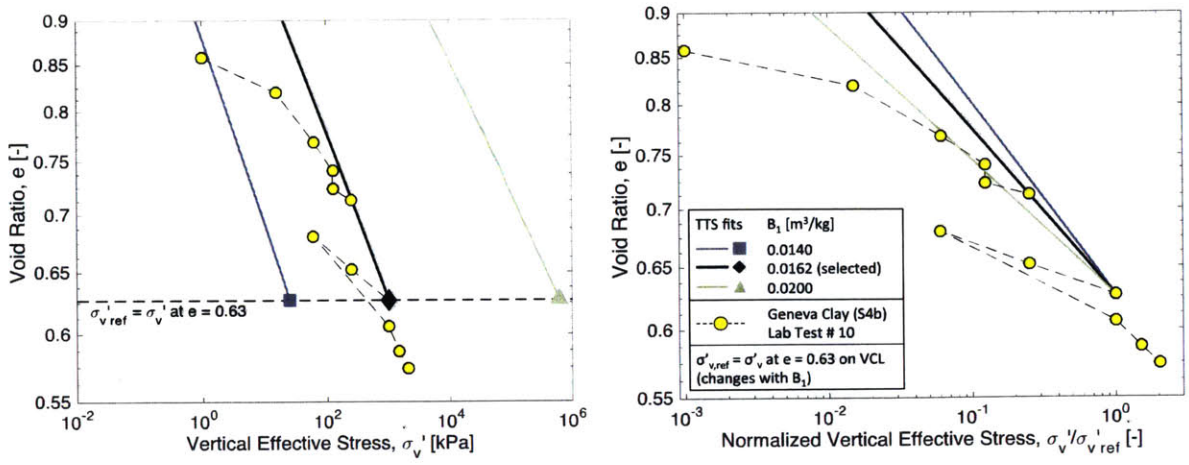

a) Selection of Reference Vertical Effective Stress, $\sigma_v'_{ref}$

b) Effect of B_1 on normalized VCL

Figure 3.31: Effect of B_1 on slope of virgin consolidation line (VCL)

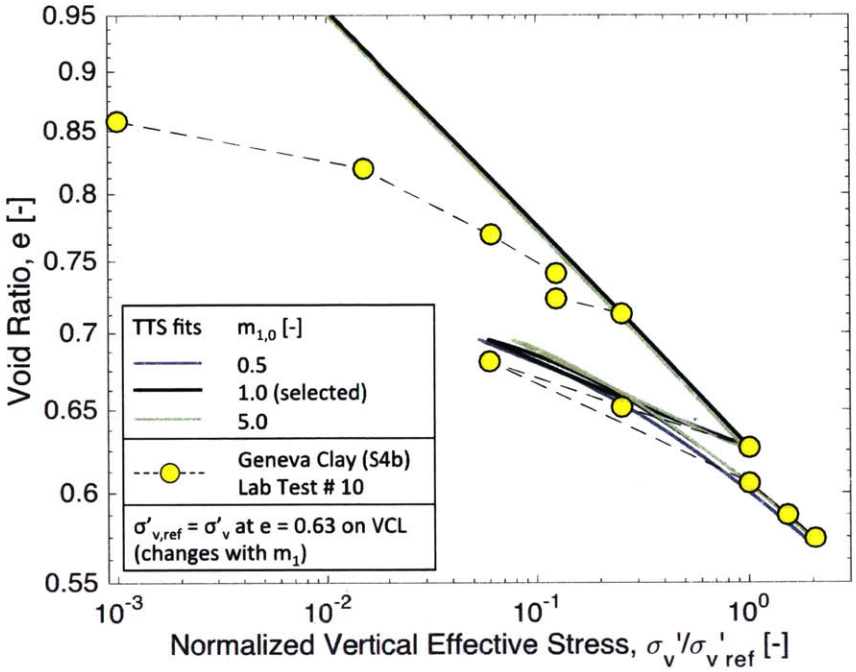

a) Effect on VCL

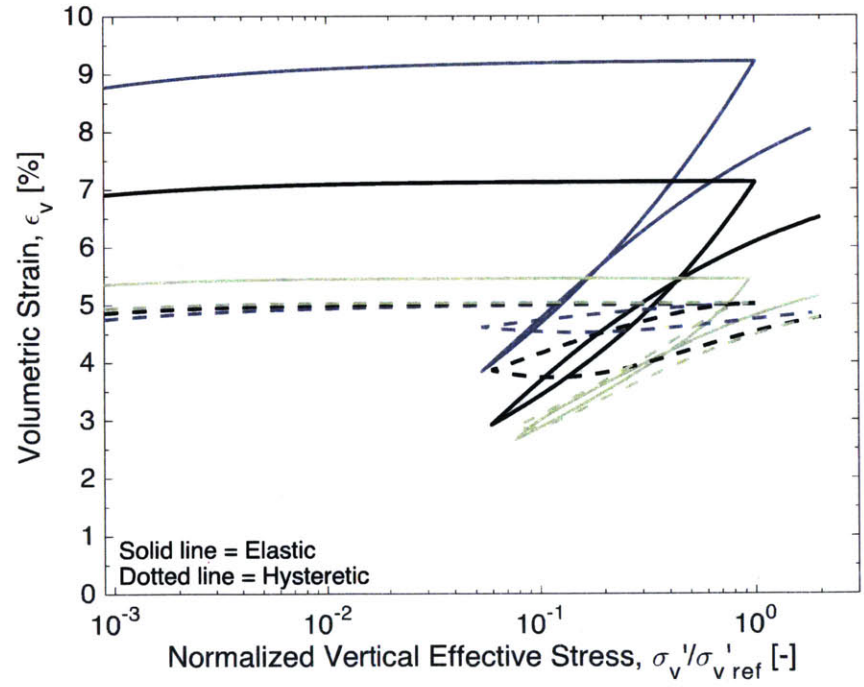

b) Effect on elastic and hysteretic volumetric strains

Figure 3.32: Effect of m_1 on TTS predictions

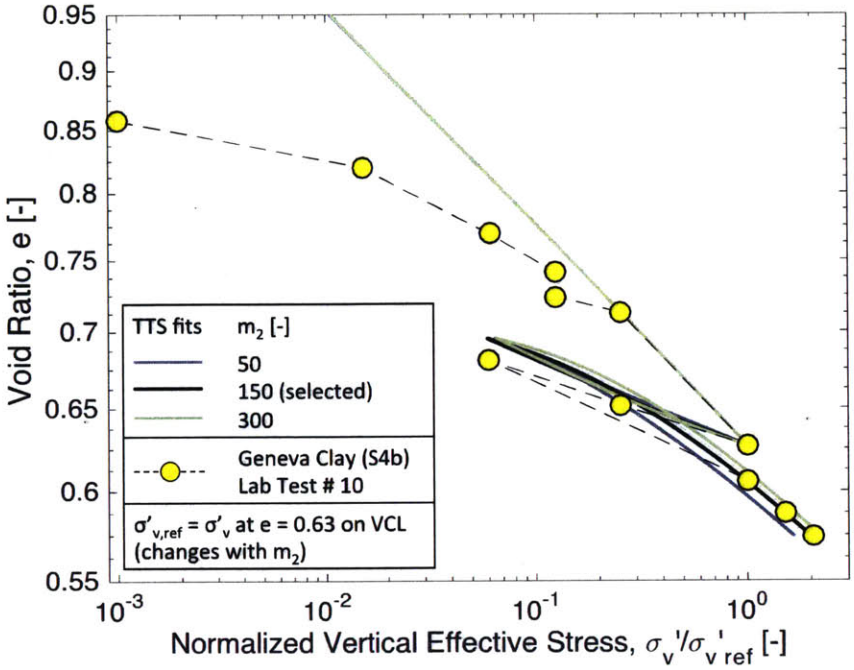

a) Effect on VCL

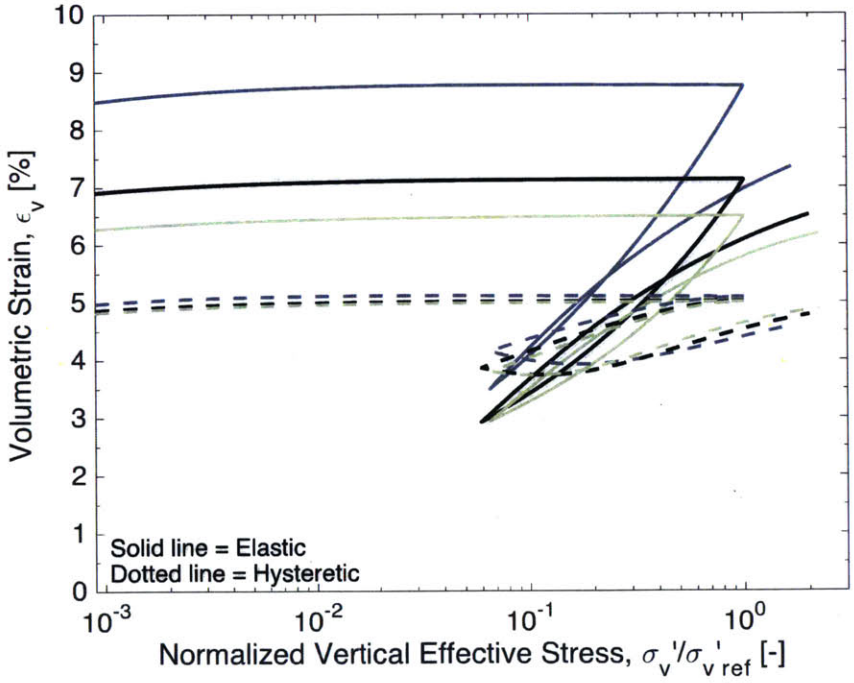

b) Effect on elastic and hysteretic volumetric strains

Figure 3.33: Effect of m_2 on TTS predictions

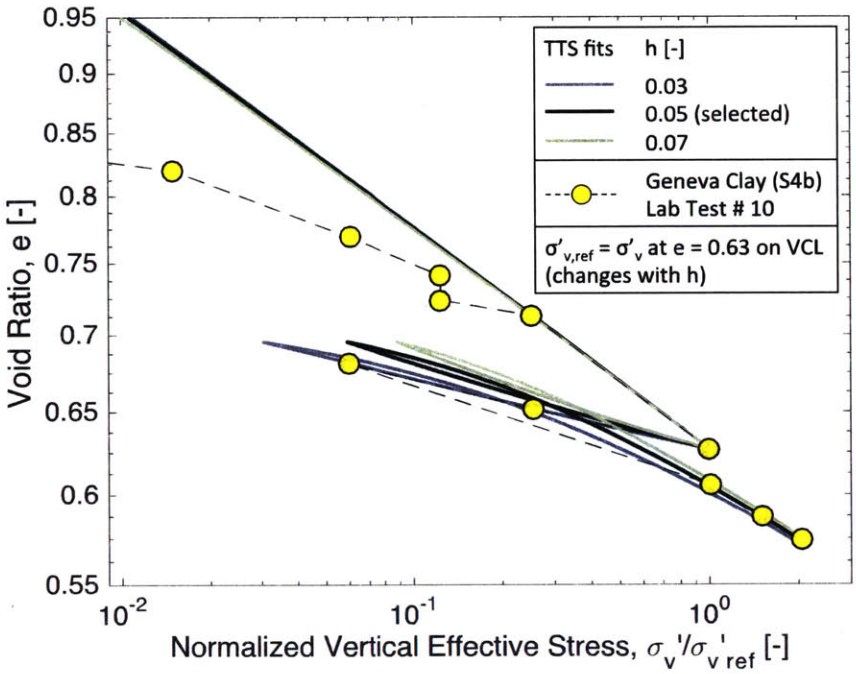

a) Effect on VCL

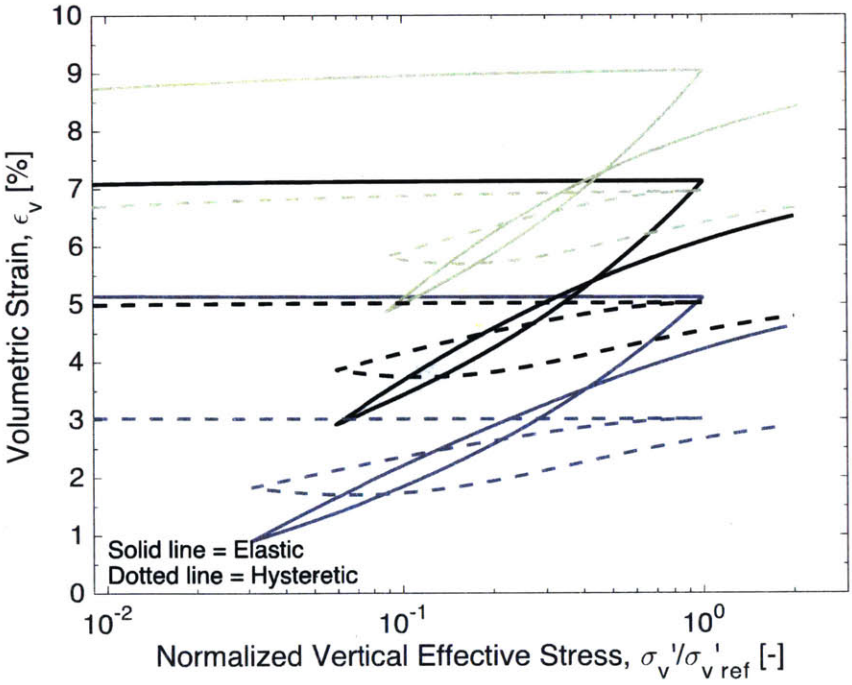

b) Effect on elastic and hysteretic volumetric strains

Figure 3.34: Effect of *h* on TTS predictions

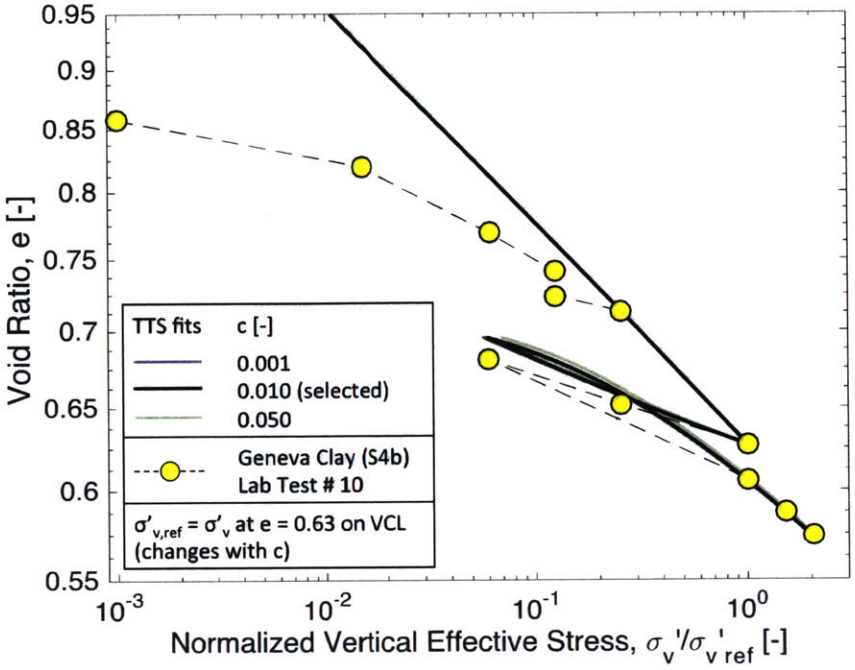

a) Effect on VCL

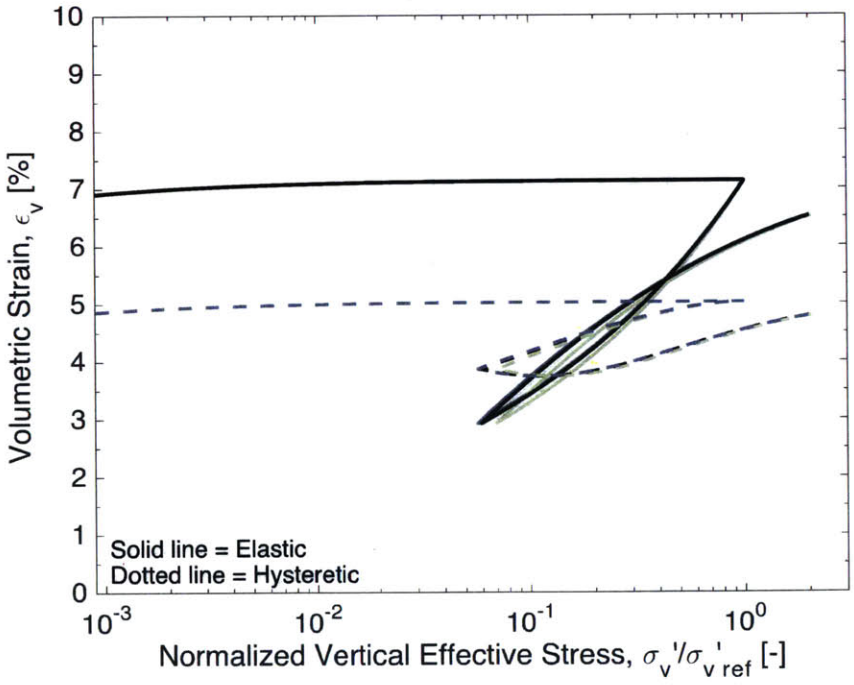

b) Effect on elastic and hysteretic volumetric strains

Figure 3.35: Effect of *c* on TTS predictions

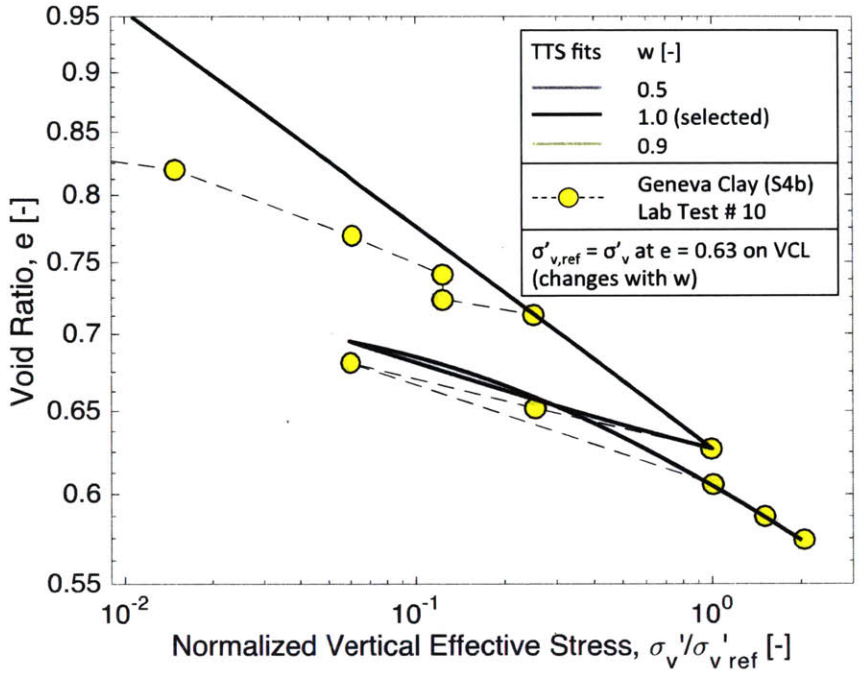

a) Effect on VCL

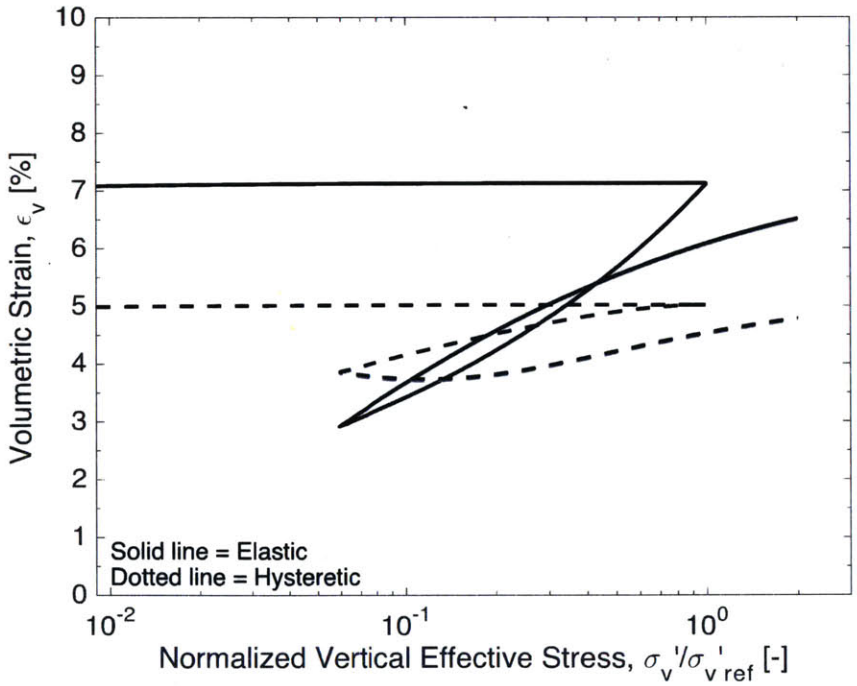

b) Effect on elastic and hysteretic volumetric strains

Figure 3.36: Effect of w on TTS predictions

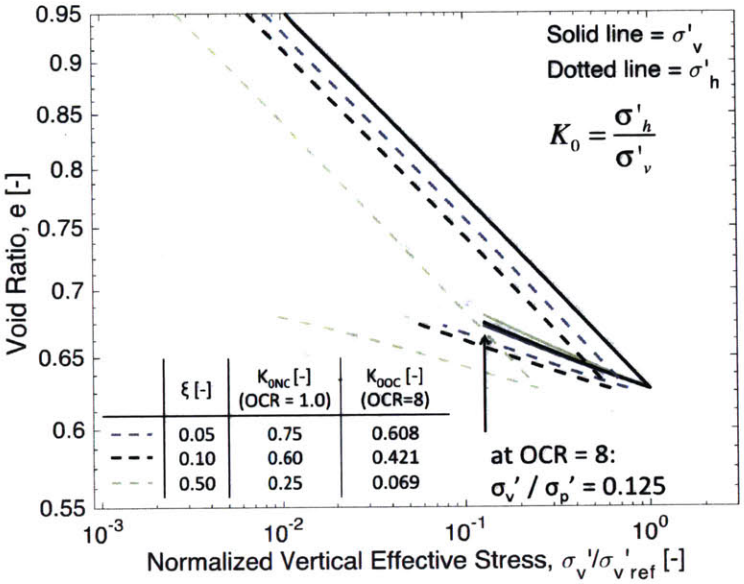

Figure 3.37: Effect of ξ on predicted coefficient of earth pressure at rest K_0 for NC and highly OC Geneva Clay

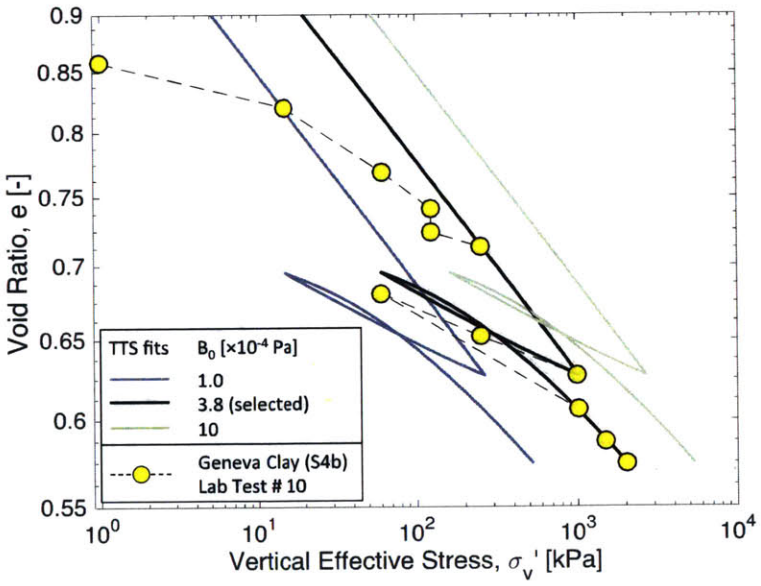

Figure 3.38: Effect of B_0 on the location of the VCL

TTS Model Parameters for Geneva Clay

B_0 [Pa]	3.8×10^{-4}	m_3 [-]	1.0
B_1 [m^3/kg]	0.0162	m_4 [kg $m^{-3}s^{-1}$]	6.0×10^{4}
c [-]	0.01	a [-]	0.5
h [-]	0.05	c' [-]	0.0863
w [-]	1.0	ξ [-]	0.1
$m_{1,0}$ [-]	1.0	ζ [-]	0.0
m_2 [-]	150		

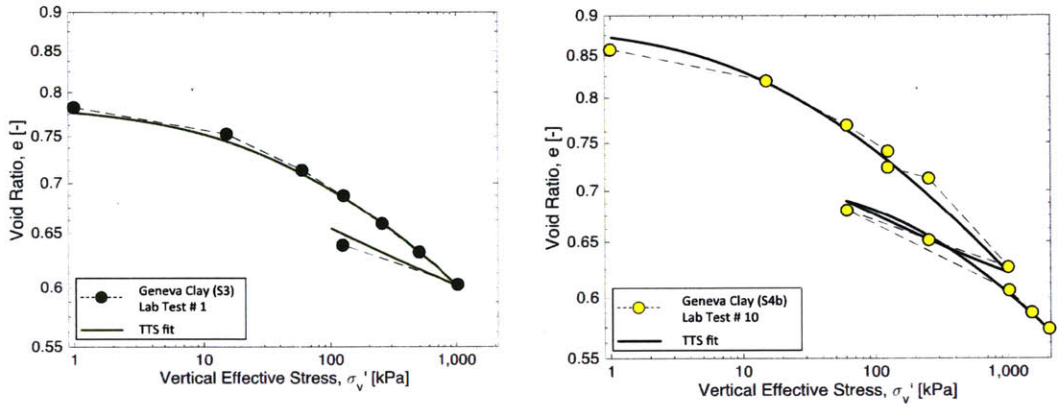

a) Sample S3

b) Sample S4b

Figure 3.39: Comparison of computed and measured 1-D Compression data for Geneva Clay based on TTS model with calibrated parameters

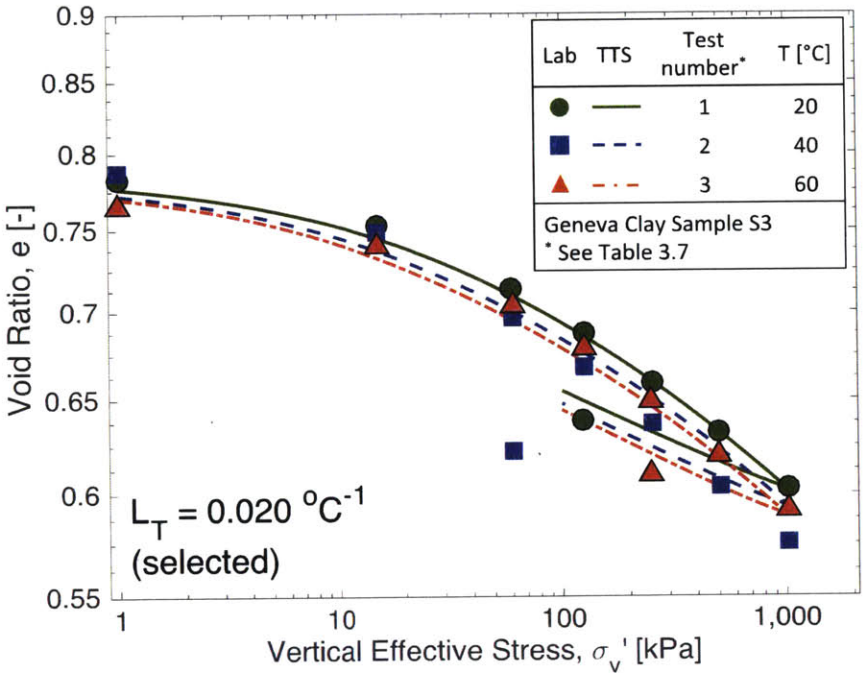

a) $L_T = 0.020\ °C^{-1}$

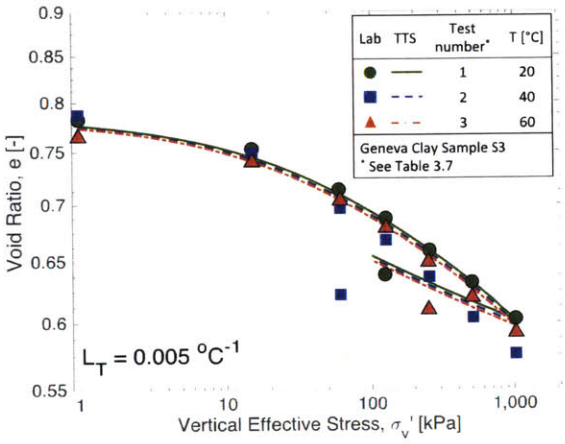

b) $L_T = 0.005\ °C^{-1}$

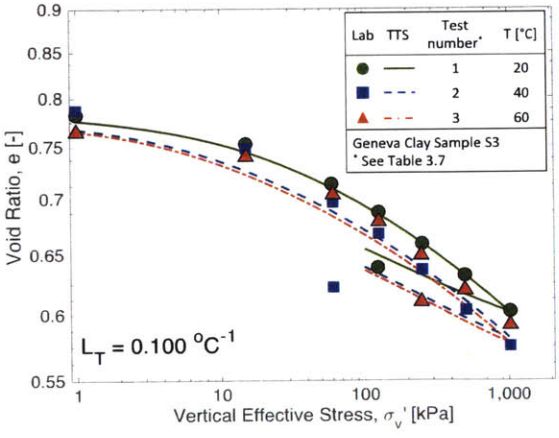

c) $L_T = 0.100\ °C^{-1}$

Figure 3.40: Effect of parameter L_T on TTS prediction of the shift of the VCL with temperature and comparison to Geneva Clay lab measurements

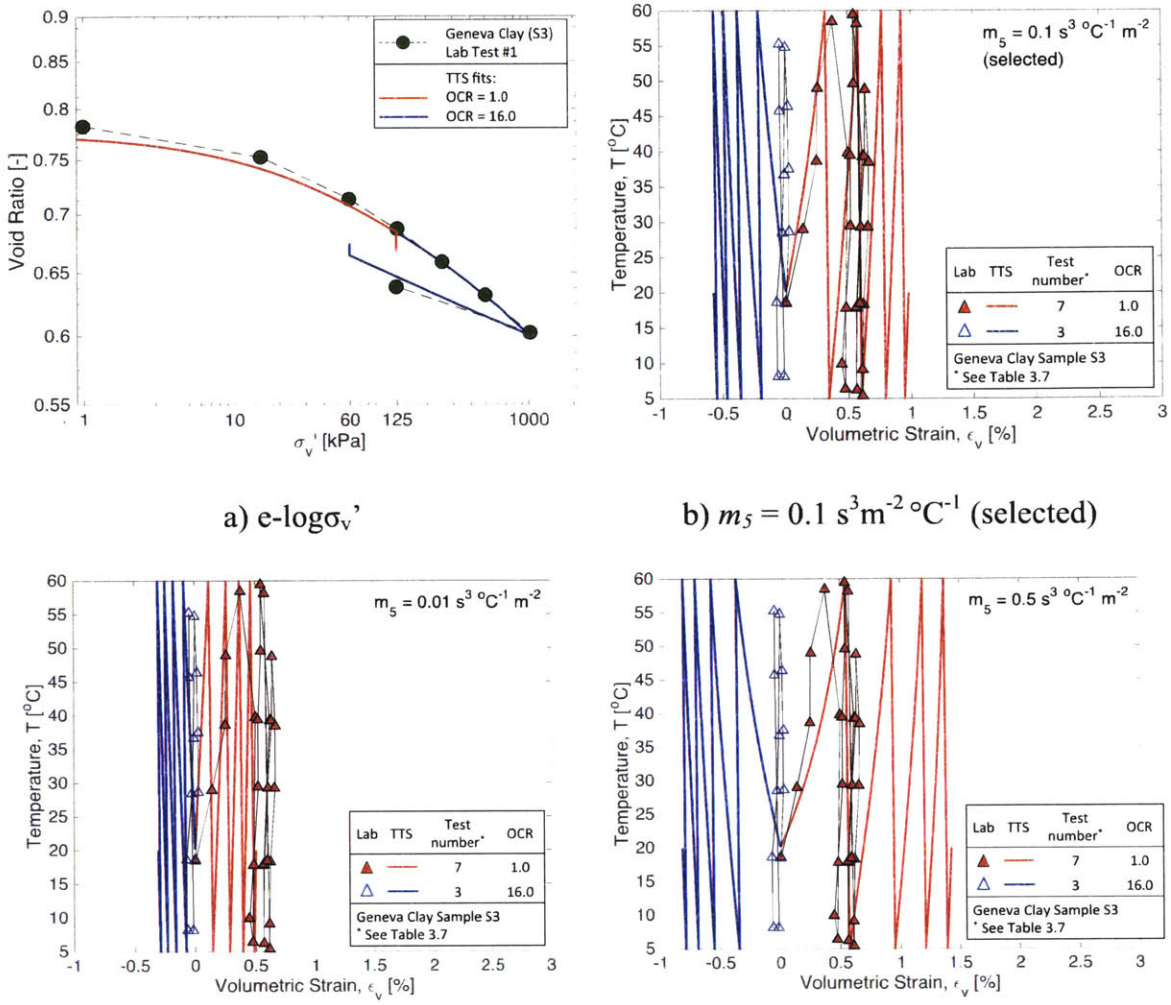

a) e-logσ_v'

b) $m_5 = 0.1\ s^3m^{-2}\,°C^{-1}$ (selected)

c) $m_5 = 0.01\ s^3m^{-2}\,°C^{-1}$

d) $m_5 = 0.5\ s^3m^{-2}\,°C^{-1}$

Figure 3.41: Effect of m_5 on TTS prediction of thermal volumetric strain with temperature and comparison to Geneva Clay S3 sample

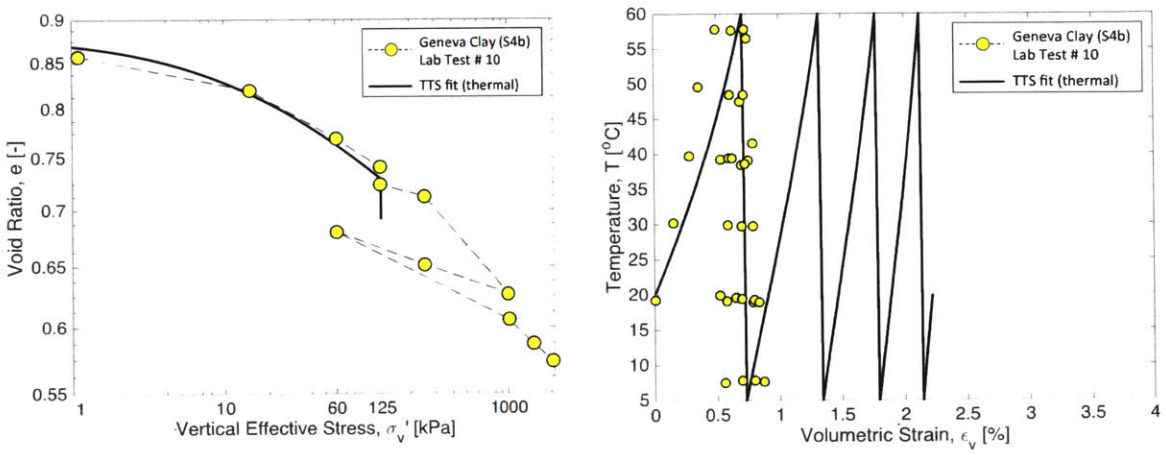

a) e-logσ_v'

b) Temperature vs thermal ε_{vol}

Figure 3.42: TTS model prediction of thermal volumetric strains recorded for Geneva Clay S4b samples using S3 sample calibration (for $m_5 = 0.1$ s^3m^{-2} °C^{-1})

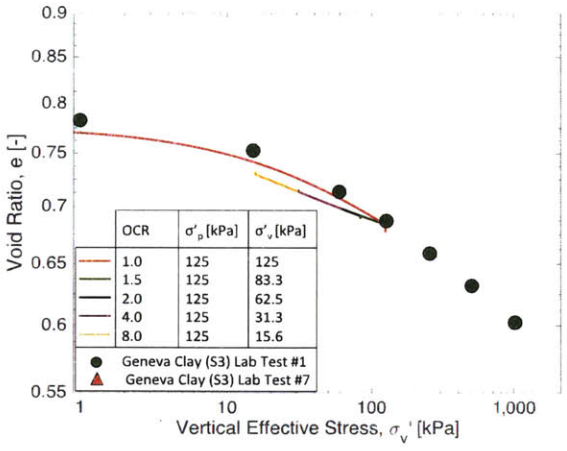

a) e-logσ_v'

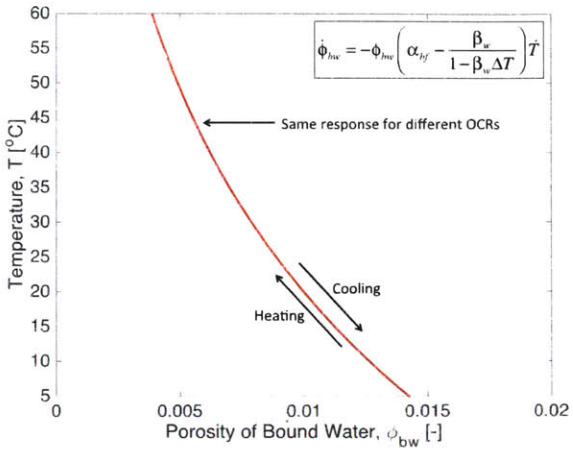

b) Change of Bound Water Porosity, φ_{bw} with temperature

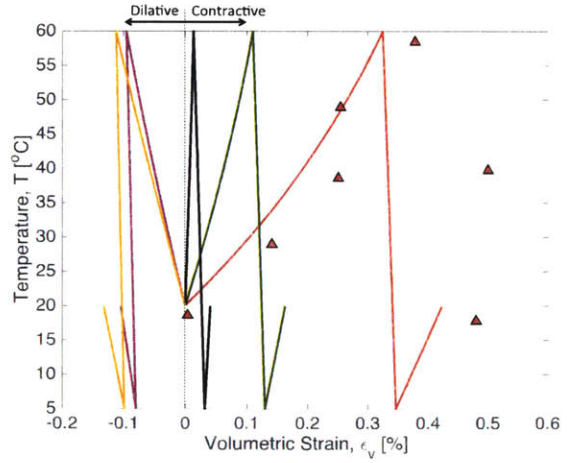

c) Temperature vs thermal ε_{vol}

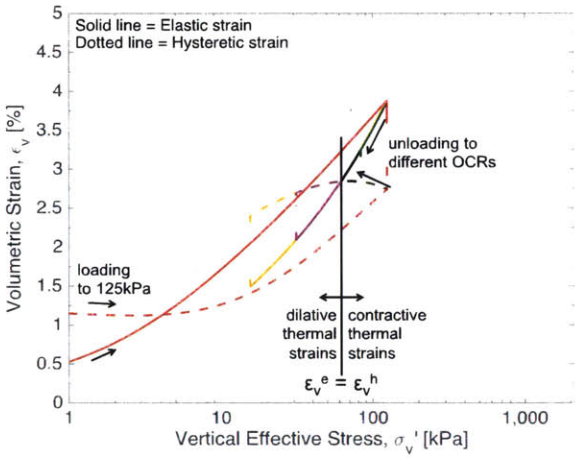

d) Illustration of TTS response based on volumetric strains

Figure 3.43: TTS model prediction of thermal volumetric strains produced due to one heating-cooling cycle for Geneva clay of different OCR using S3 sample calibration

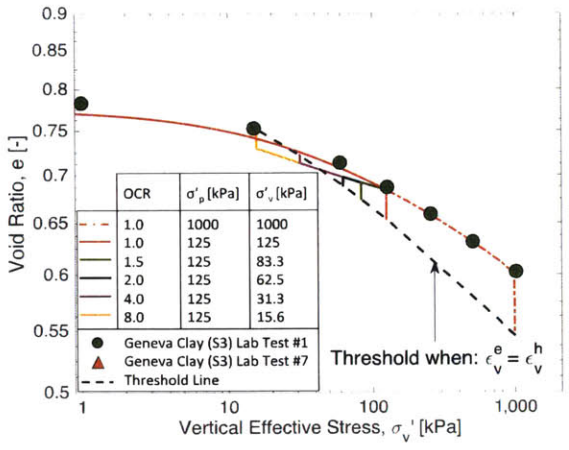

a) e-logσ_v'

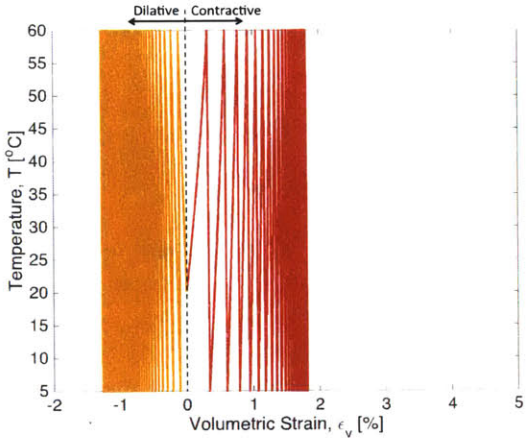

b) Temperature vs thermal ε_{vol}

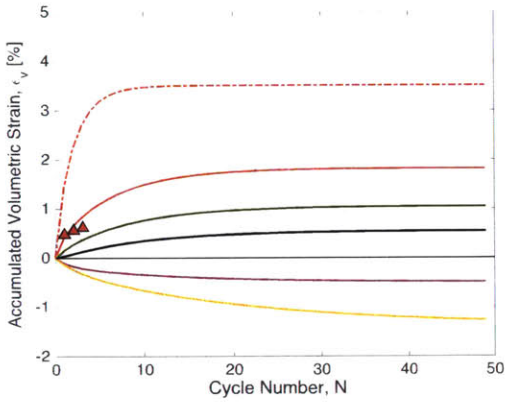

c) Accumulation versus cycle number

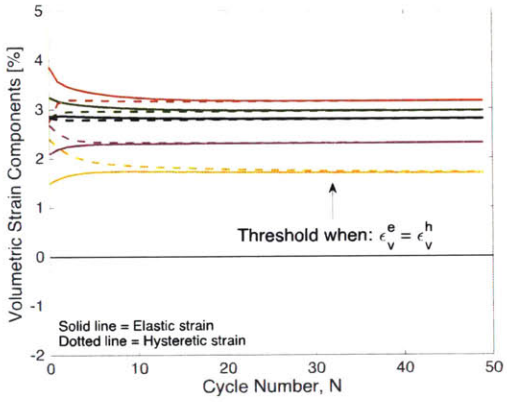

d) Explanation of TTS response based on volumetric strains

Figure 3.44: TTS model prediction of accummulated thermal volumetric strains produced due to longterm cyclic heating and cooling of Geneva clay of different OCR using S3 sample calibration

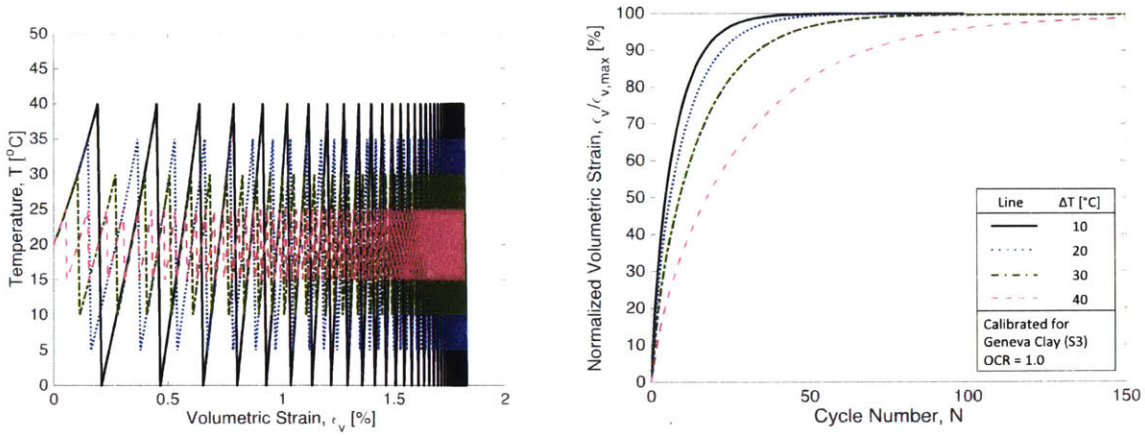

a) T vs ε_v b) $\varepsilon_v / \varepsilon_{v,max}$ vs Cycle Number

Figure 3.45: TTS model prediction of thermal volumetric strains produced due to long-term cyclic heating and cooling of NC Geneva clay with different ΔT using S3 sample calibration

Chapter 4

Numerical Simulation of Thermo-Hydro-Mechanical Response of Borehole Heat Exchangers in Clay

4.1 Introduction

This chapter describes the development of numerical analyses, based on finite difference (FD) methods, to solve coupled thermo-hydro-mechanical problems for one-dimensional (1-D) and axisymmetric problems based on a reduced set of relevant field equations described in Section 2.3[17]. The FD simulators are derived from fundamental principles and validated against results from a finite element (FE) program Code_Bright (Olivella et al., 1996 a and b). The 1-D simulator was based on a prior hydro-mechanical formulation implemented by Yuan (2016), which has been extended to incorporate thermal effects and is able to account for generalized profiles of state variables (stress history etc.) with depth. The advanced TTS model (Zhang and Cheng, 2013) was implemented to represent thermo-mechanical properties of the clay and has been compared with predictions for thermo-elastic soil in order to evaluate the importance of constitutive soil properties on predictions of engineering performance including the accumulation of ground displacements for long-term seasonal operation of borehole heat exchangers. The FD method provides a simple and efficient way for modeling long-term, THM processes for problems with simplified geometry.

4.2 Theory of Thermo-Hydro-Mechanical Coupled Consolidation

The theory of consolidation (Terzaghi, 1921; Terzaghi & Fröhlich, 1936) has traditionally been used for the prediction of long-term settlement of loaded clay layers. It is based upon the hypothesis that compression of clay is governed by the dissipation of excess pore water pressure generated by an external loading. The formulation of the coupled thermo-hydro-mechanical problem is based on the following assumptions:

1) The soil is 100% saturated with water.

[17] e.g., the current analysis do not consider convective heat transfer for seasonal heating and cooling in low permeability clays.

2) The soil particles and the pore water are incompressible.
3) The free water flows according to Darcy's law.
4) The effective stresses are controlled by the strains in the soil skeleton via the constitutive relation.
5) The strains, velocities and stress increments are small and the theory is quasistatic.
6) The soil skeleton is non-homogeneous; i.e., a spatially dependent stress-strain and velocity-pressure gradient relationship governs the soil mass.

Section 2.3 presented the derivation of the field equations governing coupled thermo-hydro-mechanical problems, assuming thermo-elastic soil properties. Equations 4.1–4.10 present the field equations governing the non-isothermal consolidation of a saturated soil using the TTS constitutive clay model presented in Chapter 3. The three primary field variables are temperature, T, pore water pressure, p_w and displacement, $\underset{\sim}{u}$. Based on Fourier's law (cf. equation 2.1) and assuming no heat source/sink (i.e., $f^Q = 0$, cf., equation 2.15a), heat conduction in saturated clay is given by:

$$c_{VT}\nabla^2 T = \frac{\partial T}{\partial t} \tag{4.1a}$$

where c_{VT} [L^2T^{-1}] is the thermal diffusivity of the soil medium:

$$c_{VT} = \frac{\lambda}{\phi\rho_w c_w + (1-\phi)\rho_s c_s} \tag{4.1b}$$

and $\nabla^2 T$ is the Laplacian of temperature, T [°C], λ is the thermal conductivity of the soil medium [W/mK], c is the specific heat capacity [J/kg °C] and ρ is mass density [kg/m^3] and subscripts s and w correspond to the solid particles and water, respectively.

The equation that links change in pore water pressure with change in temperature and volumetric strain (cf., equation 2.11) is:

$$\frac{k}{\gamma_w}\nabla^2 p_w = -\frac{\partial \varepsilon_v}{\partial t} - \beta\frac{\partial T}{\partial t} \tag{4.2}$$

where k [L/T] is the hydraulic conductivity of the soil medium, γ_w is the unit weight of water, $\nabla^2 p_w$ is the Laplacian of the pore pressure vector, ε_v is the volumetric strain ($\varepsilon_v = \underset{\sim}{\nabla}\cdot\underset{\sim}{u}$; cf., eqn. 2.8b, assuming infinitesimal strain), t is time, β is the volumetric

thermal expansion of the soil medium ($\beta = 3\beta_s(1-\phi)+\beta_w\phi$), β_s is the linear thermal expansion of the solid particles, β_w is the volumetric thermal expansion of water and φ is the porosity.

The momentum balance for the soil medium (compression positive) is (cf., equation 2.16):

$$\underset{\sim}{\nabla}\cdot\underset{\sim}{\sigma}+\underset{\sim}{f}=0 \tag{4.3}$$

where $\underset{\sim}{\sigma}$ are the total stresses and $\underset{\sim}{f}$ the body forces.

For saturated soils and assuming that the solid particles and water are incompressible the standard definition of (Terzaghi, 1921) effective stress is (cf., equation 2.17):

$$\underset{\sim}{\sigma}' = \underset{\sim}{\sigma} - p_w\underset{\sim}{I} \tag{4.4}$$

where $\underset{\sim}{\sigma}'$ is the effective stress vector, $\underset{\sim}{\sigma}$ is total stress, p_w is pore pressure and $\underset{\sim}{I}$ is the unit vector.

The current derivation assumes that the thermo-mechanical constitutive law is controlled by the TTS model (Zhang and Cheng, 2013). The evolution of the state variables of the TTS model depends on the rate of change of total volumetric and deviatoric strains ($\dot{\varepsilon}_v$ and $\dot{\varepsilon}_s$) and on the rate of change of temperature $\dot{T}$.

1) Evolution of bound water porosity, φ_{bw} (cf. equation 3.15b):

$$\dot{\phi}_{bw} = -\phi_{bw}\left(\alpha_{bf} - \frac{\beta_w}{1-\beta_w\Delta T}\right)\dot{T} \tag{4.5}$$

where α_{bf} [1/°C] is an input constant controlling the conversion of bound to free water (Section 3.3) and β_w [1/°C] is the volumetric thermal expansion coefficient of water.

2) Evolution of dry density, ρ_d:

$$\dot{\rho}_d = \rho_d\dot{\varepsilon}_v \tag{4.6}$$

3) Evolution of granular temperature, T_g (cf. equation 3.16):

$$\dot{T}_g = \frac{1}{\rho_d}\left[m_2m_4\left(\dot{\varepsilon}_s\right)^2 + m_2m_3m_4\left(\dot{\varepsilon}_v\right)^2 + \frac{m_5\sigma'_{kk}\alpha_{bf}\phi_{bw}\dot{T}^2}{3(1-\phi)} - m_4T_g\right] \tag{4.7}$$

where φ is total porosity, φ_{bw} is bound water porosity and m_2, m_3, m_4 and m_5 are input constants of the TTS model.

4) Evolution of Elastic Strain, ε^e (cf. equation 3.17):

$$\dot{\varepsilon}_v^e = \dot{\varepsilon}_v - \dot{\varepsilon}_v^D, \quad \text{where } \dot{\varepsilon}_v^D = 3m_1\left(T_g\right)^a\left(\varepsilon_v^e - \varepsilon_v^h\right) \tag{4.8a}$$

$$\dot{\varepsilon}_s^e = \dot{\varepsilon}_s - \dot{\varepsilon}_s^D, \quad \text{where } \dot{\varepsilon}_s^D = \left(T_g\right)^a\left(\varepsilon_s^e - \varepsilon_s^h\right) \tag{4.8b}$$

where ε^h is hysteretic strain and subscripts v and s correspond to volumetric and deviatoric respectively, $m_1 = m_{1,0}\left[1 + L_T\left(T - T_0\right)\right]$ and $m_{1,0}$ and L_T and a are input constants of the TTS model.

5) Evolution of Hysteretic strain, ε^h (cf. equation 3.18):

$$\dot{\varepsilon}_v^h = \dot{\varepsilon}_v^D - w\frac{\frac{1}{3}\dot{\varepsilon}_v^D\varepsilon_v^h + \dot{\varepsilon}_s^D \cdot \varepsilon_s^h}{h^{0.5}\left[\frac{1}{3}\left(\varepsilon_v^h\right)^2 + \left(\varepsilon_s^h\right)^2\right]^{0.75}}\varepsilon_v^h \tag{4.9a}$$

$$\dot{\varepsilon}_s^h = \dot{\varepsilon}_s^D - w\frac{\frac{1}{3}\dot{\varepsilon}_v^D\varepsilon_v^h + \dot{\varepsilon}_s^D \cdot \varepsilon_s^h}{h^{0.5}\left[\frac{1}{3}\left(\varepsilon_v^h\right)^2 + \left(\varepsilon_s^h\right)^2\right]^{0.75}}\varepsilon_s^h \tag{4.9b}$$

where w and h are input constants of the TTS model.

6) From equations 3.19 and 3.20 the evolution of mean effective stress and deviatoric stress can be obtained:

$$\dot{p}' = \frac{\partial p'}{\partial \varepsilon_v^e}\dot{\varepsilon}_v^e + \frac{\partial p'}{\partial \varepsilon_s^e}\dot{\varepsilon}_s^e + \frac{\partial p'}{\partial \rho_d}\dot{\rho}_d + \frac{\partial p'}{\partial T}\dot{T} \tag{4.10a}$$

$$\dot{q} = \frac{\partial q}{\partial \varepsilon_v^e}\dot{\varepsilon}_v^e + \frac{\partial q}{\partial \varepsilon_s^e}\dot{\varepsilon}_s^e + \frac{\partial q}{\partial \rho_d}\dot{\rho}_d \tag{4.10b}$$

where the partial derivatives of effective stress are summarized in Table 4.1. The input constants of the TTS model related to effective stress are B_0, B_1, c, c' and ξ.

Field equations 4.1 to 4.10 constitute complete mathematical statements of the theory of thermo-hydro-mechanical consolidation in the 1-D and axisymmetric space respectively, using the TTS thermo-mechanical constitutive model. Boundary conditions must be specified at all points around the boundary of the domain. For the 1-D simulation, boundary conditions are required at the top and bottom boundaries while

axisymmetric cases require further conditions for the radial boundaries (Figures 4.1 and 4.2). Initial conditions must be specified at all integration points of the finite difference grid at the start of the analysis (i.e., t = 0) and they involve the stress state and state variables of the TTS model, temperature, void ratio and excess pore pressure.

4.3 Finite Difference Methods

Numerical methods solve the governing partial differential equations for pore pressure, p_w, temperature, T, and displacement, $\underset{\sim}{u}$, as a function of space and time. Finite difference equations are solved at discretized points in space and time and hence, their accuracy depends on the number of points selected (Smith, 1985). The governing spatial differential equations are represented by a set of central difference equations, which are solved algebraically based on Taylor series expansions.

4.3.1 FD Formulation

Figure 4.1 presents the 1-D soil profile, which is sub-divided into N_H layers (Δz=H/ N_H) with N_H+1 integration points. The space coordinate z is a global coordinate and has its origin at the ground surface $z = 0$. Each sub-layer, Δz_j, is characterized by different field variables (T, p_w and u_z), the TTS model state variables (Table 3.1), intrinsic permeability κ [L^2] and thermal input constants (β, λ and c). The current formulation assumes that the clay type is the same across the depth of the model and so the mechanical input constants of the TTS model (Table 3.2) are the same for all points in the grid. The explicit finite difference equations that solve the consolidation equation at points interior to a layer for time $k+1$ are:

Evolution of temperature, T (cf. eqn. 4.1):

$$\frac{\Delta T\big|_{z_j,t_{k+1}}}{\Delta t_k} = c_{vT}\big|_{z_j,t_k} \frac{T\big|_{z_{j-1},t_k} - 2T\big|_{z_j,t_k} + T\big|_{z_{j+1},t_k}}{\Delta z^2} \tag{4.11}$$

Evolution of volumetric strain, ε_v (cf. eqn. 4.2):

$$\frac{\Delta \varepsilon_v\big|_{z_j,t_{k+1}}}{\Delta t_k} = -\frac{\kappa\big|_{z_j}}{\gamma_w}\left\{\frac{p_w\big|_{z_{j-1},t_k} - 2p_w\big|_{z_j,t_k} + p_w\big|_{z_{j+1},t_k}}{\Delta z^2}\right\} - \beta\big|_{z_j,t_k}\frac{\Delta T\big|_{z_j,t_{k+1}}}{\Delta t_k} \tag{4.12}$$

Momentum balance for the soil medium (cf. eqn. 4.3):

$$\frac{\sigma_{zz}\big|_{z_{j-1},t_k} - 2\sigma_{zz}\big|_{z_j,t_k} + \sigma_{zz}\big|_{z_{j+1},t_k}}{\Delta z^2} + f = 0 \tag{4.13}$$

Effective stress principle (cf. eqn. 4.4)

$$\frac{\Delta\sigma_{zz}\big|_{z_j,t_{k+1}}}{\Delta t_k} = \frac{\Delta\sigma'_{zz}\big|_{z_j,t_{k+1}}}{\Delta t_k} + \frac{\Delta p_w\big|_{z_j,t_{k+1}}}{\Delta t_k} \tag{4.14}$$

Evolution of bound water porosity, φ_{bw} (cf. eqn. 4.5):

$$\frac{\Delta\phi_{bw}\big|_{z_j,t_{k+1}}}{\Delta t_k} = -\phi_{bw}\big|_{z_j,t_k}\left(\alpha_{bf} - \frac{\beta_w}{1-\beta_w\left(T\big|_{z_j,t_k} - T_0\right)}\right)\frac{\Delta T\big|_{z_j,t_{k+1}}}{\Delta t_k} \tag{4.15}$$

Evolution of dry density, ρ_d (cf. eqn. 4.6):

$$\frac{\Delta\rho_d\big|_{z_j,t_{k+1}}}{\Delta t_k} = \rho_d\big|_{z_j,t_k}\frac{\Delta\varepsilon_v\big|_{z_j,t_{k+1}}}{\Delta t_k} \tag{4.16}$$

Evolution of granular temperature, T_g (cf. eqn. 4.7):

$$\begin{aligned}\frac{\Delta T_g\big|_{z_j,t_{k+1}}}{\Delta t_k} = \frac{1}{\rho_d\big|_{z_j,t_k}}\Bigg[& m_2 m_4\left(\frac{\Delta\varepsilon_s\big|_{z_j,t_{k+1}}}{\Delta t_k}\right)^2 + m_2 m_3 m_4\left(\frac{\Delta\varepsilon_v\big|_{z_j,t_{k+1}}}{\Delta t_k}\right)^2 + \ldots \\ & \ldots + \frac{m_5\sigma'_{kk}\big|_{z_j,t_k}\alpha_{bf}\phi_{bw}\big|_{z_j,t_k}}{3\left(1-\phi\big|_{z_j,t_k}\right)}\left(\frac{\Delta T\big|_{z_j,t_{k+1}}}{\Delta t_k}\right)^2 - m_4 T_g\big|_{z_j,t_k}\Bigg]\end{aligned} \tag{4.17}$$

Evolution of plastic strain, ε^D (cf. eqn. 4.8):

$$\frac{\Delta\varepsilon_v^D\big|_{z_j,t_{k+1}}}{\Delta t_k} = 3m_1\big|_{z_j}\left(T_g\big|_{z_j,t_k}\right)^a\left(\varepsilon_v^e\big|_{z_j,t_k} - \varepsilon_v^h\big|_{z_j,t_k}\right) \tag{4.18a}$$

$$\frac{\Delta\varepsilon_s^D\big|_{z_j,t_{k+1}}}{\Delta t_k} = m_1\big|_{z_j}\left(T_g\big|_{z_j,t_k}\right)^a\left(\varepsilon_s^e\big|_{z_j,t_k} - \varepsilon_s^h\big|_{z_j,t_k}\right) \tag{4.18b}$$

Evolution of elastic strain, ε^e (cf. eqn. 4.8):

$$\frac{\Delta\varepsilon_v^e\big|_{z_j,t_{k+1}}}{\Delta t_k}=\frac{\Delta\varepsilon_v\big|_{z_j,t_{k+1}}}{\Delta t_k}-\frac{\Delta\varepsilon_v^D\big|_{z_j,t_{k+1}}}{\Delta t_k} \tag{4.19a}$$

$$\frac{\Delta\varepsilon_s^e\big|_{z_j,t_{k+1}}}{\Delta t_k}=\frac{\Delta\varepsilon_s\big|_{z_j,t_{k+1}}}{\Delta t_k}-\frac{\Delta\varepsilon_s^D\big|_{z_j,t_{k+1}}}{\Delta t_k} \tag{4.19b}$$

Evolution of hysteretic strain, ε^h (cf. eqn. 4.9):

$$\frac{\Delta\varepsilon_v^h\big|_{z_j,t_{k+1}}}{\Delta t_k}=\frac{\Delta\varepsilon_v^D\big|_{z_j,t_{k+1}}}{\Delta t_k}-w\frac{\dfrac{\Delta\varepsilon_v^D\big|_{z_j,t_{k+1}}}{\Delta t_k}\cdot\dfrac{\varepsilon_v^h\big|_{z_j,t_k}}{3}+\dfrac{\Delta\varepsilon_s^D\big|_{z_j,t_{k+1}}}{\Delta t_k}\cdot\varepsilon_s^h\big|_{z_j,t_k}}{h^{0.5}\left[\dfrac{\left(\varepsilon_v^h\big|_{z_j,t_k}\right)^2}{3}+\left(\varepsilon_s^h\big|_{z_j,t_k}\right)^2\right]^{0.75}}\varepsilon_v^h\big|_{z_j,t_k} \tag{4.20a}$$

$$\frac{\Delta\varepsilon_s^h\big|_{z_j,t_{k+1}}}{\Delta t_k}=\frac{\Delta\varepsilon_s^D\big|_{z_j,t_{k+1}}}{\Delta t_k}-w\frac{\dfrac{\Delta\varepsilon_v^D\big|_{z_j,t_{k+1}}}{\Delta t_k}\cdot\dfrac{\varepsilon_v^h\big|_{z_j,t_k}}{3}+\dfrac{\Delta\varepsilon_s^D\big|_{z_j,t_{k+1}}}{\Delta t_k}\cdot\varepsilon_s^h\big|_{z_j,t_k}}{h^{0.5}\left[\dfrac{\left(\varepsilon_v^h\big|_{z_j,t_k}\right)^2}{3}+\left(\varepsilon_s^h\big|_{z_j,t_k}\right)^2\right]^{0.75}}\varepsilon_s^h\big|_{z_j,t_k} \tag{4.20b}$$

Evolution of effective stress in triaxial space (cf. eqn. 4.10):

$$\frac{\Delta p'\big|_{z_j t_{k+1}}}{\Delta t_k} = \frac{\Delta \varepsilon_v^e\big|_{z_j t_{k+1}}}{\Delta t_k}\Bigg\{0.6B\big|_{z_j t_k}\left(\varepsilon_v^e\big|_{z_j t_k}+c\right)^{0.5}\varepsilon_v^e\big|_{z_j t_k}+0.8B\big|_{z_j t_k}\left(\varepsilon_v^e\big|_{z_j t_k}+c\right)^{1.5}\ldots$$

$$\ldots+\Bigg[0.3B\big|_{z_j t_k}\left(\varepsilon_v^e\big|_{z_j t_k}+c\right)^{-0.5}\varepsilon_v^e\big|_{z_j t_k}+1.8B\big|_{z_j t_k}\left(\varepsilon_v^e\big|_{z_j t_k}+c\right)^{0.5}\Bigg]\Bigg[\varepsilon_v^e\big|_{z_j t_k}+\ldots$$

$$\ldots+\beta\big|_{z_j t_k}\left(T\big|_{z_j t_k}-T_0\right)\Bigg]+0.75B\big|_{z_j t_k}\xi\left(\varepsilon_s^e\big|_{z_j t_k}\right)^2\Bigg\}+\ldots$$

$$\ldots+\frac{\Delta \varepsilon_s^e\big|_{z_j t_{k+1}}}{\Delta t_k}\Bigg\{3B\big|_{z_j t_k}\xi\varepsilon_s^e\big|_{z_j t_k}\left(\varepsilon_v^e\big|_{z_j t_k}+c'\right)^{0.5}\Bigg\}+\frac{\Delta \rho_d\big|_{z_j t_{k+1}}}{\Delta t_k}B\big|_{z_j t_k}p'\big|_{z_j t_k}+\ldots \qquad (4.21a)$$

$$\ldots+\frac{\Delta T\big|_{z_j t_{k+1}}}{\Delta t_k}\Bigg\{\beta\big|_{z_j t_k}\Bigg[0.6B\big|_{z_j t_k}\left(\varepsilon_v^e\big|_{z_j t_k}+c\right)^{0.5}\varepsilon_v^e\big|_{z_j t_k}+0.8B\big|_{z_j t_k}\left(\varepsilon_v^e\big|_{z_j t_k}+c\right)^{1.5}\ldots$$

$$\ldots+1.5B\big|_{z_j t_k}\xi\left(\varepsilon_v^e\big|_{z_j t_k}+c'\right)^{0.5}\frac{\left(\varepsilon_s^e\big|_{z_j t_k}\right)^2}{\varepsilon_v^e\big|_{z_j t_k}}\Bigg\}$$

$$\frac{\Delta q\big|_{z_j t_{k+1}}}{\Delta t_k} = \frac{\Delta \varepsilon_v^e\big|_{z_j t_{k+1}}}{\Delta t_k}\Bigg[1.5\sqrt{6}\,B\big|_{z_j t_k}\xi\varepsilon_s^e\big|_{z_j t_k}\left(\varepsilon_v^e\big|_{z_j t_k}+c'\right)^{0.5}\Bigg]+\ldots \qquad (4.21b)$$

$$\ldots+\frac{\Delta \varepsilon_s^e\big|_{z_j t_{k+1}}}{\Delta t_k}\Bigg[\sqrt{6}\,B\big|_{z_j t_k}\xi\left(\varepsilon_v^e\big|_{z_j t_k}+c'\right)^{1.5}\Bigg]+\frac{\Delta \rho_d\big|_{z_j t_{k+1}}}{\Delta t_k}B\big|_{z_j t_k}q\big|_{z_j t_k}$$

The 1-D analysis assumes K_0 conditions with zero lateral strain ($\varepsilon_h = \varepsilon_{xx} = \varepsilon_{yy} = 0$) and hence, the volumetric strain (cf. eqns. 4.12) is equal to vertical strain (i.e., $\varepsilon_v=\varepsilon_{xx}+\varepsilon_{yy}+\varepsilon_{zz}=\varepsilon_{zz}$). Boundary conditions must be selected for the mechanical, hydraulic and thermal components based on the physical problem that is being simulated. For 1-D analyses, mechanical conditions assume a rigid base $u_z\big|_{z_{NH+1}}=0$ (i.e., a Dirichlet boundary condition, Smith, 1985). Vertical settlements u_z at point j are given by:

$$u_z\Big|_{z_j,t_{k+1}} = \varepsilon_{zz}\Big|_{z_{j+1},t_{k+1}} \times \Delta z + u_z\Big|_{z_{j+1},t_{k+1}}$$
$$u_z\Big|_{z_{NH+1}} = 0 \qquad (4.22)$$

Hydraulic boundary conditions assume a free draining top surface $\left(p_w\Big|_{z_1} = 0\right)$ and an impermeable base $\left.\frac{\partial p_w}{\partial z}\right|_{z_{NH+1}} = 0$ (i.e., a Neumann boundary condition, Smith, 1985).

In order to control fluid flux at the base, a ghost node is introduced (j = NH+2, Fig. 4.1):

$$\left.\frac{\partial p_w}{\partial z}\right|_{z_{NH+1}} = \frac{\kappa\Big|_{z_j}}{\gamma_w}\left[\frac{p_w\Big|_{z_{NH+2}} - p_w\Big|_{z_{NH}}}{2\Delta z}\right] = 0 \qquad (4.23a)$$

$$p_w\Big|_{z_{NH+2}} = p_w\Big|_{z_{NH}} \qquad (4.23b)$$

Thermal boundary conditions at z = 0 and z = H (eqns. 4.1 and 4.11) comprise either 1) a prescribed temperature $\left(T\Big|_{z_1}$ and $T\Big|_{z_{NH+1}}\right)$ or 2) a prescribed heat flux (Q_1 and Q_{NH+1}) which can change with time. Heat flux is also controlled through ghost nodes at the top:

$$Q_1 = \lambda\Big|_{z_1}\left.\frac{\partial T}{\partial z}\right|_{z_1} = \lambda\Big|_{z_1}\frac{T\Big|_{z_{-1}} - T\Big|_{z_2}}{2\Delta z} \qquad (4.24a)$$

$$T\Big|_{z_{-1}} = T\Big|_{z_2} + 2\Delta z\frac{Q_1}{\lambda\Big|_{z_1}} \qquad (4.24b)$$

and at the base:

$$Q_{NH+1} = \lambda\Big|_{z_{NH+1}}\left.\frac{\partial T}{\partial z}\right|_{z_{NH+1}} = \lambda\Big|_{z_{NH+1}}\frac{T\Big|_{z_{NH}} - T\Big|_{z_{NH+2}}}{2\Delta z} \qquad (4.24c)$$

$$T\Big|_{z_{NH+2}} = T\Big|_{z_{NH}} - 2\Delta z\frac{Q_{NH+1}}{\lambda\Big|_{z_{NH+1}}} \qquad (4.24d)$$

By combining equations 4.11 and 4.24 the temperature evolution at the boundaries $\left(T\big|_{z_1}$ and $T\big|_{z_{NH+1}}\right)$ can be calculated:

$$\frac{\Delta T\big|_{z_1 t_{k+1}}}{\Delta t_k} = c_{vT}\big|_{z_1 t_k} \frac{T\big|_{z_{-1} t_k} - 2T\big|_{z_1 t_k} + T\big|_{z_2 t_k}}{\Delta z^2} = c_{vT}\big|_{z_1 t_k} \frac{2\Delta z \dfrac{Q_1}{\lambda\big|_{z_1}} - 2T\big|_{z_1 t_k} + 2T\big|_{z_2 t_k}}{\Delta z^2} \quad (4.25a)$$

$$\frac{\Delta T\big|_{z_{NH+1} t_{k+1}}}{\Delta t_k} = c_{vT}\big|_{z_{NH+1} t_k} \frac{T\big|_{z_{NH} t_k} - 2T\big|_{z_{NH+1} t_k} + T\big|_{z_{NH+2} t_k}}{\Delta z^2} = c_{vT}\big|_{z_{NH+1} t_k} \frac{2T\big|_{z_{NH} t_k} - 2T\big|_{z_{NH+1} t_k} - 2\Delta z \dfrac{Q_{NH+1}}{\lambda\big|_{z_{NH+1}}}}{\Delta z^2}$$

(4.25b)

Similar conditions apply for axisymmetric simulations, intended to represent conditions for a borehole heat exchanger embedded within a clay layer underlain by a rigid, impermeable and adiabatic base. It is assumed that the soil profile of depth H consists of NH layers ($NH + 1$ points) of constant thickness $\Delta z = H / NH$, as shown in Figure 4.2. The soil has a radius R and a total of $NR+1$ integration points in the radial direction (Figure 4.2). In the radial direction, nodes at radius r_i are located at variable distance Δr_i, which increases geometrically:

$$\mathrm{R} = \sum_{i=2}^{N_R+1} \Delta r_i = \sum_{i=2}^{N_R+1} \alpha_r \Delta r_{i-1} \quad (4.26)$$

where Δr_1 is the spacing of the first node and is selected small relative to the radius r_1 at the left boundary for accuracy (e.g., in the current simulator $\Delta r_1 / r_1 = 6\%$) and c which is calibrated for given soil radius R and Δr_1, using equation 4.26. The space coordinates (r, z) are global coordinates and have their origin at the ground surface ($z = 0$) and centerline ($r = 0$) respectively, as shown in Figure 4.2. The soil properties are calculated for each point, based on porosity $\phi\big|_{r_i, z_j}$ and temperature $T\big|_{r_i, z_j}$. The finite difference representation of equations 4.1 and 4.2 with variable radial spacing is written[18]:

[18] Appendix D presents the derivation for variable spacing.

$$\frac{\Delta T\big|_{r_i,z_j,t_{k+1}}}{\Delta t_k} = c_{vT}\big|_{r_i,z_j,t_k}\left(\frac{T\big|_{r_i,z_{j-1},t_k} - 2T\big|_{r_i,z_j,t_k} + T\big|_{r_i,z_{j+1},t_k}}{\Delta z^2} + \ldots\right.$$
$$\left. + \frac{2\left[\alpha_r T\big|_{r_{i-1},z_j,t_k} - (1+\alpha_r)T\big|_{r_i,z_j,t_k} + T\big|_{r_{i+1},z_j,t_k}\right]}{\alpha_r(1+\alpha_r)\Delta r_i^2} + \frac{1}{r_i}\frac{T\big|_{r_{i+1},z_j,t_k} - T\big|_{r_{i-1},z_j,t_k}}{(1+\alpha_r)\Delta r_i}\right) \quad (4.27)$$

$$\frac{\Delta \varepsilon_v\big|_{r_i,z_j,t_{k+1}}}{\Delta t_k} = -\frac{\kappa\big|_{z_j}}{\gamma_w}\left\{\frac{p_w\big|_{r_i,z_{j-1},t_k} - 2p_w\big|_{r_i,z_j,t_k} + p_w\big|_{r_i,z_{j+1},t_k}}{\Delta z^2} + \ldots\right.$$
$$\ldots + \frac{2\left[\alpha_r p_w\big|_{r_{i-1},z_j,t_k} - (1+\alpha_r)p_w\big|_{r_i,z_j,t_k} + p_w\big|_{r_{i+1},z_j,t_k}\right]}{\alpha_r(1+\alpha_r)\Delta r_i^2} + \ldots \quad (4.28)$$
$$\left. \ldots + \frac{1}{r_i}\frac{p_w\big|_{r_{i+1},z_j,t_k} - p_w\big|_{r_{i-1},z_j,t_k}}{(1+\alpha_r)\Delta r_i}\right\} - \beta\big|_{r_i,z_j,t_k}\frac{\Delta T\big|_{r_i,z_j,t_{k+1}}}{\Delta t_k}$$

The model assumes a constant total vertical stress across the top boundary $\left(\sigma_{zz}\big|_{r_i,z_1} = \text{const.}\right)$ and a rigid base $\left(u_z\big|_{r_i,z_{NH+1}} = 0\right)$. It is then assumed that there is no radial displacement in the system either at the surface of the heat exchanger $\left(u_r\big|_{r_1,z_j} = 0\right)$ or at the right boundary $\left(u_r\big|_{R,z_j} = 0\right)$, which represents a plane of symmetry between the heat exchangers in the array. This condition assumes that neighboring heat exchangers produce similar thermal flux and hence, generate equal and opposite horizontal displacements (Figure 4.3). The horizontal strains are effectively zero everywhere $\left(\varepsilon_{rr} = \varepsilon_{\theta\theta} = 0\right)$ and hence vertical strains are again equated with the volumetric strains. This model is an approximation of conditions within a large array of heat exchangers.

The hydraulic boundary conditions adopted are a free draining top $\left(p_w\big|_{r_i,z_1} = 0\right)$ and an impermeable base $\left(p_w\big|_{r_i,z_{NH+2}} = p_w\big|_{r_i,z_{NH}}\right)$, similar to the 1-D case (equation 4.23b). It

is assumed that the surface of the heat exchanger ($r = R_{HE}$) is impermeable and it is modeled with the aid of a ghost node at the left boundary ($i = -1$):

$$\left.\frac{\partial p_w}{\partial z}\right|_{R_{HE},z_j} = \frac{\kappa|_{z_j}}{\gamma_w}\left[\frac{p_w|_{r_{-1},z_j} - p_w|_{r_2,z_j}}{2\Delta r_1}\right] = 0 \qquad (4.29a)$$

$$p_w|_{r_{-1},z_j} = p_w|_{r_2,z_j} \qquad (4.29b)$$

Similarly, due to symmetry of the heat exchanger array, it is assumed that there is zero fluid flux at the right boundary. This is also simulated using a ghost node r_{NR+2} such that the excess pore pressure $p_w|_{r_{NR+2},z_j} = p_w|_{r_{NR},z_j}$.

The simulations assume an adiabatic top surface and base and using ghost nodes, the temperatures at the top and bottom are equal to $T|_{r_i,z_{-1}} = T|_{r_i,z_2}$ and $T|_{r_i,z_{NH+2}} = T|_{r_i,z_{NH}}$, respectively. The thermal conditions at the right boundary are also adiabatic due to symmetry of the heat exchanger array and with the aid of ghost nodes $T|_{r_{NR+2},z_j} = T|_{r_{NR},z_j}$.

The left boundary represents the heat exchanger surface. The heat exchanger is modeled as a cylindrical heat source of radius r = R_{HE} and a linear heat flux Q_{lin} along the centerline. In order to calculate the heat flux Q_{cyl} across the heat exchanger surface (i.e., at r = R_{HE}) the following expression is used:

$$Q_{cyl} = \frac{Q_{lin}}{2\pi R_{HE}} \qquad (4.30)$$

Assuming that the only heat transfer process taking place in the heat exchanger borehole is due to the thermal conductivity of the grout surrounding the U-tube (Figure 4.4), the change of temperature in the radial direction at r = R_{HE} is given by:

$$\frac{\partial T}{\partial r} = -\frac{1}{\lambda_g}\frac{Q_{lin}}{2\pi R_{HE}} \qquad (4.31)$$

where λ_g, is the thermal conductivity of the grout. Therefore in this simplified case, it is concluded that the effective borehole thermal resistance, R_b, is given by:

$$R_b = \frac{1}{2\pi\lambda_g} \tag{4.32}$$

Appendix A provides details about the borehole geometry and methods for estimating the borehole thermal resistance, R_b. In order to simulate the heat exchanger boundary, ghost nodes are assumed at the left boundary, and their temperature $T\big|_{r_{-1},z_j}$ is given by:

$$\frac{T\big|_{r_{-1},z_j} - T\big|_{r_2,z_j}}{2\Delta r_1} = \frac{Q_{HE,lin}}{R_{HE}}\rho_{HE} \tag{4.33a}$$

$$T\big|_{r_{-1},z_j} = T\big|_{r_2,z_j} + 2\Delta r_1 \frac{Q_{HE,lin}}{R_{HE}}\rho_{HE} \tag{4.33b}$$

4.3.2 Modified Euler Integration Scheme with Error Control (Sloan, 1987)

The time discretization method used in the current finite difference simulators is a modified Euler integration scheme with error control proposed by Sloan (1987). Since the explicit method is accurate only for very small time steps, it is usual to subdivide Δt into smaller substeps and compute the field response over each substep. Traditionally, the number of substeps is determined from an empirical rule and each substep is assumed to be of the same size.

The integration scheme proposed by Sloan (1987) is based on a modified Euler scheme, where the error in the integration process is controlled by selecting the size of each substep automatically as the integration proceeds over each time interval. This integration scheme has been applied for both the calculation of pore water pressures and the calculation of effective stress given by the constitutive relation as a result of strain increment (shown in Figure 4.5). For the first-order Euler algorithm, pore water pressure p_w^{k+1} at the end of a time step Δt^k is given by:

$$p_w^{k+1} = p_w^k + \Delta p_w^{k+1} \tag{4.34}$$

In the modified Euler algorithm, temperature $\hat{p}_w^{k+1}$ at the end of a time step Δt^k is given by:

$$\hat{p}_w^{k+1} = p_w^k + \frac{1}{2}\left(\Delta p_w^{k+1} + \Delta p_w^{k+2}\right) \tag{4.35}$$

By subtracting equation 4.34 from 4.35, an estimate of the local error in p_w^{k+1} is obtained:

$$E^{k+1} \approx \frac{1}{2}\left(-\Delta p_w^{k+1} + \Delta p_w^{k+2}\right) \tag{4.36}$$

The relative error R^{k+1} for each substep is given by:

$$R^{k+1} = \frac{\left\|E^{k+1}\right\|}{\left\|p_w^{k+1}\right\|} \tag{4.37}$$

Sloan (1987) controls the relative error to a specified tolerance value (TOL):

$$R^{k+1} \leq TOL \tag{4.38}$$

where TOL is a small positive number and is dimensionless[19]. By controlling the local relative error for each sub-step, the global relative error in the overall solution is controlled.

To begin the integration procedure, a value for Δt^k is assumed and values for p_w^{k+1}, $\hat{p}_w^{k+1}$, E^{k+1} and R^{k+1} are calculated using equations 4.34 to 4.37. If equation 4.38 is satisfied, then the pore pressure p_w^{k+1} is updated based on equation 4.35 and the integration for this time step is complete. If equation 4.38 is not satisfied, then it is necessary to reduce the size of Δt^k and repeat the calculation. During the integration procedure the size of each sub-step is determined by a local extrapolation technique. Step sizes may increase or decrease, depending on the estimated value of R^{k+1}. Assuming that the current sub-step size is Δt^k, the next sub-step size is given by:

$$\Delta t^{k+1} = q\Delta t^k \tag{4.39}$$

where q is given by:

$$0.1 \leq q = 0.8\left(\frac{TOL}{R^{k+1}}\right)^{1/2} \leq 2.0 \tag{4.40}$$

[19] TOL controls the relative error R^{k+1}, which is dimensionless, since it is equal to the local error E^{k+1} normalized by the total value T^{k+1}.

The tolerance used for the calculation of excess pore water pressures is TOL = 1×10^{-6} and for the calculation of effective stress is TOL = 1×10^{-8}, both smaller than the range recommended by Sloan (1987) (TOL = 10^{-2} to 10^{-5}).

4.3.3 Details of the Computer Program

The flow chart in Figure 4.5 illustrates the algorithm used in the proposed finite difference formulation. The first step specifies the geometry, boundary conditions, initial ground temperature, T_0 and input constants for the soil profile. Table 3.1 summarizes the mechanical input constants for the TTS model and Table 4.3 summarizes the thermal and input parameters which include the linear thermal expansion coefficient $\beta_{s,lin}$, the thermal conductivity λ_s, specific heat capacity c_{ps} of the solid particles and the hydraulic input constants which include the intrinsic permeability κ_0 [m^2] at a reference void ratio e_0 and the change of intrinsic permeability with void ratio, C_k[20]. The thermal properties of the clay mixture are calculated based on the rules of mixtures presented in Section 2.4, assuming full saturation and using built-in properties of water (Table 4.2).

The initial state variables are assumed to vary with depth (based on stress history) but are assumed constant with radius. The initial effective stress distribution and the state variables of the TTS model are based on the field geometry and on the stress history (OCR). The distribution of intrinsic permeability, κ [L^2] depends on the void ratio assumed at different depths. After the initial conditions are calculated, they are stored and a new time step is applied. Time steps are not constant but are selected based on the automatic time stepping technique recommended by Sloan (1987). Once a new time step is defined the change of temperature, $\dot{T}$ and strain $\dot{\varepsilon}_v$ and $\dot{\varepsilon}_s$ are calculated across the boundaries and all intermediate points. The calculation of effective stress is controlled by the constitutive model. Convergence is checked assuming a strict tolerance [TOL = 10^{-8}] and if the results are satisfactory, calculation of excess pore pressures takes place from the effective stress principle (equations 4.14). A convergence check takes place again to ensure that excess pore pressures are within the specified tolerance [TOL = 10^{-6}]. If the

[20] $(e-e_0)=C_k\log_{10}(\kappa/\kappa_0)$

convergence is not OK, automatic sub-stepping results in smaller time steps that meet the convergence criteria. If the convergence criteria are met, then the updated state variables are stored and the calculation is repeated with the next time step until the analysis is complete.

4.4 Validation of FD Simulators

4.4.1 Validation of 1-D Simulator

The 1-D FD simulator was validated against the finite element program (FE) Code_Bright (Olivella et al., 1996 a and b) that solves coupled thermo-hydro-mechanical (THM) processes in geological media for both saturated and unsaturated soils. The FE program is based on a full two-dimensional (2-D) formulation for the thermo-hydro-mechanical problem and models both heat conduction and heat convection. The FE model that was built for the validation of the FD simulators assumes thermo-elastic properties for the clay.

The reference problem involves uniform clay with layer thickness H = 10m (Figure 4.6). The boundary conditions assumed at the top are: 1) free drainage, 2) a constant total vertical stress σ_v = 10kPa and 3) a sinusoidal heat flux with period equal to 1 year (365 days) and maximum value Q_{max} = 5W/m^2:

$$Q\left[\mathrm{W/m^2}\right]=5\sin\left(\frac{2\pi t}{365}\right) \tag{4.41}$$

where t is time in days. The base of the model is assumed: 1) impermeable, 2) rigid, and 3) adiabatic.

The mesh used in the Code_Bright model is composed of 100 quadrilateral elements and 202 nodes. The FD simulator uses 31 grid points (N_H+1 = 31) equally spaced at Δz = 0.333m. Table 4.4 summarizes the input constants assumed in the FD simulator and the FE model. The dynamic viscosity of water assumed in the FD simulator was changed to match the expression used in Code_Bright:

$$\mu(T)=2.1\times10^{-6}\exp\left(\frac{1808.5}{273.15+T}\right)\ \mathrm{Pa\cdot s} \tag{4.42}$$

where temperature T is defined in [°C]. Figures 4.7, 4.8 and 4.9 summarize the evolution of temperature, excess pore water pressure and vertical strain for points at the top, middle and base of the clay layer, while Figure 4.10 presents the evolution of surface settlements. Results for the FD simulator match closely the FE model results: the temperature predictions in Figure 4.7 show the largest fluctuations close to the top boundary where heat flux is imposed (T = 6.5°C - 16°C), while points further away from the heat source have small temperature fluctuations in the 1-year period (Figure 4.7). The initial excess pore water pressures, correspond to the imposed total vertical stress applied ($\Delta\sigma_v$ = 10kPa, Figure 4.8). Subsequent changes in p_w reflect the generation of pore pressures through temperature changes and dissipation towards the free surface. The dissipation process dominates the response at the top (for t ≤ 10 days) but subsequent dissipation is delayed by temperature change, only reaching p_w = 0 at t = 300 days. From Figure 4.9 it can be deduced that the vertical strains developed near the top are larger than those deeper in the soil over the one-year period of the simulation. Finally Figure 4.10 shows the accumulation of surface settlements after one year, $u_z|_{z_1} = 5mm$. Figures 4.11, 4.12 and 4.13 show the spatial distributions of temperature, excess pore pressures and vertical strains with depth at three-month intervals. There is minimal change in temperature at the base of the model (~1°C) while the most pronounced changes occur in the top 5m (Fig. 4.11). More than 70% of the initial excess pore pressures remains at the base of the model ($\Delta p_w/p_{w0}$ = 0.7) after 1 year (Fig. 4.12), while volumetric strains increase from $\varepsilon_v \approx 0.02\%$ to 0.05% from the base to the top of the model at t = 1 year (Fig. 4.13).

Figures 4.14 to 4.18 compare the coupled THM response predicted by the 1-D simulator (cf. Figures 4.7 to 4.13) to the uncoupled hydro-mechanical (HM) consolidation of the same clay due to application of the vertical stress at the top (σ_v = 10kPa) but assuming isothermal conditions (i.e., temperature remains constant). Figure 4.14 shows that the excess pore pressures developed near the top are very similar for the THM and HM problems due to the close proximity to the free draining surface. For points deeper in the clay layer the the generation of pore pressures due to thermal changes is more pronounced and this is evident from the fact that the excess pore

pressures dissipate faster for the HM problem compared to the THM problem. Figure 4.15 compares vertical strain predictions for the THM and HM problems at different points of the clay layer. Vertical strains are larger at the top due to the fastest dissipation of excess pore pressures arising from the mechanical load and also vertical strains at the top are very similar between the two models. The vertical strain predictions diverge for points deeper in the clay layer, as the result of the generation of excess pore pressures due to the thermal problem. Figure 4.16 compares predictions of surface settlements between the THM and HM models. The HM model predicts larger settlements than the THM model (e.g., at t = 200days $u_{z,HM}$ = 4mm and $u_{z,THM}$ = 2mm) but the settlements converge at the end of the 1-year operation. Figure 4.17 compares excess pore pressure versus depth for the two models at three-month intervals. The excess pore pressures predicted by the THM model are larger than the HM model for the first six months but after that the excess pore pressures of the THM problem are smaller near the top and larger near the base (e.g., after 1 year of operation, $p_{w,THM} > p_{w,HM}$ for $z < 5$m). Similar conclusions are drawn for the distribution of vertical strain with time (Figure 4.18).

4.4.2 Validation of Axisymmetric Simulator

The FD axisymmetric simulator was also validated against Code_Bright assuming thermo-elastic clay properties. The reference model has depth H = 10m and radius R = 3m (Fig. 4.19). The boundary conditions assumed at the top are:

1. free drainage
2. constant total vertical stress σ_v = 10kPa
3. adiabatic

At the base, the boundary conditions are:

1. impermeable
2. rigid
3. adiabatic

The conditions on the surface of the heat exchanger (R_{HE} = 0.075m) are:

1. impermeable
2. zero radial displacement ($u_r = 0$)
3. the BHE produces a sinusoidal heat flux of maximum value Q_{max} = 10W/m:

$$Q = 10\sin\left(\frac{2\pi t}{365}\right) \tag{4.43}$$

where Q [W/m] is the vertical heat flux along the BHE centerline and t is time in days. Finally, the conditions assumed at the right boundary are:

1. impermeable
2. zero radial displacement ($u_r = 0$)
3. adiabatic

The mesh used in the Code_Bright model is composed of 3300 quadrilateral elements and 3434 nodes. In the FD simulator, 31 grid points are used in the vertical direction (NH+1 = 31, Δz = 0.333m) and 21 in the radial direction (NR+1 = 21, Δr_1=0.005m and α_r = 1.2939, see eqn. 4.26) and are located at variable distance from the centerline, as described earlier. The input constants assumed in Code_Bright and the FD model are the same as those for the 1-D validation (Table 4.4).

Figures 4.20 through 4.24 compare the predictions of temperature, excess pore water pressure and vertical strain corresponding to different points of the axisymmetric geometry from the proposed FD simulator and FE model (Code_Bright). The agreement between independent numerical calculations confirms the accuracy of the FD simulator. As expected, points closest to the heat exchanger experience the largest temperature fluctuation (Fig. 4.20a). The spatial distribution of temperature (shown at quarterly intervals in Figs. 4.21a and 4.21b) show that temperature fluctuations are only significant over a radial distance $r \leq 1.5$m and there is no vertical variation in temperatures.

At the start of the simulations all points have excess pore pressure equal to the total stress applied at the top (p_{w0} = 10kPa), which dissipate with the passage of time and concurrently develop with changes in temperature (through thermo-hydro-mechanical response of the clay). Figures 4.22a and 4.23a show temporal and spatial changes in pore pressure at the mid-plane of the model. There is minimal radial variation in excess pore pressure and 3.3kPa ($\Delta p_w/p_{w0} \approx 33\%$) of initial excess pore pressures remain after one year. The pore pressure response varies with depth and is dominated by one-way drainage to the top surface of the model. Figure 4.23b shows the distribution of pore pressures with depth at three-month intervals. These results confirm that the largest excess pore pressures are developed at the base, due to the largest distance from the drainage surface

with 11kPa of maximum excess pore pressure at t = 125 days and 5kPa remaining after one year of operation. Figure 4.24a shows that the vertical strain developed at three points located at the mid-depth (z/H = 0.5) but at different radial distances is very similar, while from Figure 4.24b it can be deduced that the largest vertical strains occur near the top of the clay due to one-way dissipation of excess pore pressures.

Figure 4.25 shows FE model predictions of strain in the vertical, ε_{zz}, radial, ε_{rr}, and hoop directions, $\varepsilon_{\theta\theta}$, as well as the corresponding volumetric strain, ε_v. The radial and hoop strains are much smaller than the vertical strain ($\varepsilon_{rr} \leq 0.002\%$ and $\varepsilon_{\theta\theta} \leq 0.0007\%$) and hence, the $\varepsilon_{zz} \approx \varepsilon_v$ as assumed in the FD simulator.

Figure 4.26 compares the surface settlement predictions for a point located on the heat exchanger surface ($r = R_{HE}$) and for a point located at r = R. The FD model predicts that the surface settlement evolution of the two points is slightly different, corresponding to the fact that the point on the heat exchanger experiences a larger temperature fluctuation than the point further away, resulting in different vertical settlements. In comparison, the FE model assumes that the surface settlements are constant with radial distance and hence, doesn't predict any differential settlement (Figure 4.27). The difference in the two model predictions can be attributed to the arching effect that takes place in the FE code, due to the existence of stiffened soil surrounding the heat exchanger. This results in the FE code assuming differential vertical stress distribution across the top. In the FD simulator, the total vertical stress is assumed constant across the top (σ_v = 10kPa) while in the FE model, the total vertical stress is larger at points closer to the heat exchanger (at r < 0.4m), as shown in Figure 4.28. This point is also illustrated in Figure 4.29, where the total vertical stress at r = 3m is constant with time and equal to 10kPa while the total vertical stress on the heat exchanger is larger and follows a harmonic function resulting from the assumed operation of the heat exchanger. It can therefore be concluded that the FD model simulations provide an upper bound on differential surface settlements, due to the fact that the FD simulator assumes constant total vertical stress at the top (with zero radial and hoop strain) compared to the FE model that allows for differential vertical stress and general states of strain within the clay mass.

4.5 Comparison between Thermo-Elastic and TTS Predictions

This section compares thermo-elastic and TTS model predictions within the FD simulator in order to assess the importance of using more accurate constitutive models when simulating the thermo-hydro-mechanical response of clays to cyclic heating and cooling. The thermal and thermo-elastic properties of the clay are presented in Table 4.5 while the TTS model properties were selected based on Geneva clay calibrations (Table 4.6 and Section 3.4). Figure 4.30a shows the initial stress profile within the 10m clay layer, with a vertical effective stress σ'_{v0} = 215kPa at z = 0. The horizontal effective stress was based on K_{0NC} = 0.6. There is a small change in void ratio (Figure 4.30b). Hydraulic properties were based on Geneva Clay measurements shown in Figure 3.23c undertaken by Di Donna and Laloui (2015) and the same intrinsic permeability distributions were assumed in the two models (Figure 4.31). The initial strain state variables $\left(\varepsilon_v^e, \varepsilon_v^h, \varepsilon_s^e, \varepsilon_s^h\right)$ of the TTS model are shown in Figure 4.32 and the initial temperature of the ground, T_0 = 10°C. The same initial conditions were assumed in both the 1-D and axisymmetric space simulations.

4.5.1 Comparison Between 1-D Response for Thermo-Elastic and TTS Models

Figure 4.33 shows the boundary conditions assumed at the top of the 1-D model: 1) free drainage (hydraulic head H_p = 0), 2) surface traction $\sigma_v = \sigma'_v$ = 215kPa (excess pore pressures have already dissipated at the start of the test) and 3) a sinusoidal heat flux with period, t_p = 365 days and maximum value, Q_{max} = 10W/m^2 (cf. eqn. 4.41). Boundary conditions are the same as those assumed in Section 4.4.1 and the same mesh is used (Fig. 4.33). The numerical simulations consider behavior over a 10-year period.

Figure 4.34 shows that the heat transfer process is independent of the constitutive model assumed for the clay (same temperature predictions for both soil models) with no net heating or cooling of the ground. The heat transfer process depends on the thermal properties of the solid particles and water (cf. eqn. 4.11), which are the same for the two models. Since the thermal properties of the soil are derived based on rules of mixture, the only effect of the soil models is via the porosity, φ (and corresponding void ratio, e). As shown in Figure 4.34 the temperature at the top fluctuates between T = 6°C - 16°C. There

is a small net accumulation of temperature at the base of the clay (T increases to 11.5°C), for these simulations.

The thermo-elastic model predicts small, reversible excess pore pressures (Figure 4.35) while the TTS model captures the accumulation of excess pore pressure. Excess pore pressures developed at points close to the free draining surface are very small (0.5 – 6.5 kPa) while those near the base rise to p_w = 33kPa, after 10 years of operation. This is also evident from Figure 4.35b, which shows predictions of excess pore pressure versus depth at selected times. It can be noted that the thermo-elastic model predicts excess pore pressures that oscillate between a given range (for example at z = 1.7m, p_w = -6kPa to 6kPa) while the TTS model predicts the accumulation of excess pore pressures due to long-term cyclic heating and cooling.

The vertical strains predicted by the thermo-elastic model are small and reversible, while the TTS model predicts an irrecoverable accumulation of vertical strains with time due to regular seasonal heating and cooling (Figure 4.36). The point close to the top develops the largest volumetric strains ($\Delta\varepsilon_v \approx 0.08\%$/year) as a result of the larger temperature fluctuation while strains at the base of the clay are small and slightly dilative ($\varepsilon_v \approx -0.05\%$). After 10 years of operation, the vertical strains predicted by the TTS model for depths larger than 7m are nearly zero while the vertical strain near the top is 1.25%. The surface settlements predicted by the thermo-elastic model are small ($u_{z,max}$ = 2.5mm) while those predicted by the TTS model are significant and irreversible (after 10 years u_z = 34mm), as shown in Figure 4.37.

4.5.2 Comparison Between Axisymmetric Response for Thermo-Elastic and TTS Models

Comparison between the thermo-elastic and TTS model predictions were also undertaken for the axisymmetric space, assuming H = 10m (NH+1 = 31 points), R = 3m (NR+1 = 21 points) and the same initial stresses, state variables and soil properties as in the 1-D model (Figure 4.38). The boundary conditions assumed at the top are: 1) free drainage, 2) constant vertical stress $\sigma_v = \sigma'_v$ = 215kPa (p_{w0} = 0) and 3) adiabatic. The boundary conditions assumed at the base are: 1) impermeable, 2) rigid ($u_z = 0$) and 3) adiabatic. The boundary conditions assumed on the heat exchanger surface are: 1)

impermeable, 2) zero radial displacement $u_r = 0$ and 3) a sinusoidal heat flux with period, t_p = 365 days and maximum value, Q_{max} = 10W/m^2 (cf. eqn. 4.46). Finally, the boundary conditions assumed at the right are: 1) impermeable 2) radial displacement $u_r = 0$ and 3) adiabatic. The models simulated the clay response for a 10-year period.

Figures 4.39 through 4.46 present predictions of temperature, excess pore water pressure, vertical strain and surface settlements corresponding to different points in the axisymmetric model of a vertical heat exchanger. Figures 4.39 and 4.40 show that the heat transfer process is independent of the mechanical model, since the thermo-elastic and TTS model predictions of temperature are identical. As expected the point on the heat exchanger experiences the largest temperature fluctuation (T = 7.5 – 13.5°C, Fig. 4.39a). Figures 4.39b and 4.40b show that points located at different depths but at the same distance from the heat exchanger, have the same temperature evolution. Figure 4.40 shows that the temperature of the ground is equilibrated at the end of each year and therefore the distributions of temperature at time t = 1, 2 and 10 years is the same.

From Figures 4.41 and 4.42 it is evident that the thermo-elastic model predicts small and reversible excess pore pressure, while the TTS model predicts the accumulation of excess pore pressure due to long-term cyclic heating and cooling. From Figure 4.41a it is observed that points at depth z = H/2 but at different radial distances have the same magnitude of excess pore pressure but with a phase lag. Figure 4.42a shows that at time t = 10years the points closer to the heat exchanger have accumulated larger excess pore pressures than points further away (at r = 0.075m, excess pore pressure p_w = 29kPa, while at r = 3m, excess pore pressure p_w = 27kPa) due to the larger temperature swing experienced. Points located at the same radial distance r = R/2 but at different depths have very different responses, with the point at the base having the largest excess pore pressures since it is further away from the drainage surface. This is also confirmed in Figure 4.42b, which shows the distribution of excess pore pressures versus depth for selected times.

The vertical strains predicted by the thermo-elastic model are small and reversible, while those predicted by the TTS model (for mechanical properties of NC Geneva clay) are larger and accumulate after each cycle (Figures 4.43 and 4.44). From

Figure 4.43a it is observed that the vertical strain predicted by the thermo-elastic model at three points located at the same depth z/H = 0.5 but different radial distances is nearly zero, while the TTS model predicts considerably larger vertical strains near the heat exchanger than further away (after 10 years, at r = 0.075m ε_{zz} = 0.9% while at r = 3m ε_{zz} = 0.13%) due to the larger temperature swing experienced near the heat exchanger. From Figure 4.43b it can be deduced that the vertical strains predicted by the TTS model near the free drainage top are larger than those deeper in the soil, since the excess pore pressures at the top dissipate almost immediately as opposed to deeper points, where the excess pore pressures haven't dissipated yet and hence, the corresponding volumetric strains haven't taken place. These conclusions are confirmed by Figure 4.44, which shows distributions of vertical strain versus radial distance and depth for different moments in time. Figure 4.45 shows that the surface settlements predicted by the thermo-elastic model are negligible compared to those predicted by the TTS model. The TTS model predicts constant strains for r = 2-3m (Figure 4.44) but large differential strains closer to the surface of the heat exchanger. After 10 years, the maximum surface settlement is u_z = 100mm (Fig. 4.46) while the differential settlement $\Delta u_z \approx$ 85mm (from r = 0.075m to 3m, Figure 4.46b).

4.6 Summary and Conclusions

Finite difference (FD) simulators that solve fully coupled thermo-hydro-mechanical problems in the one-dimensional (1-D) and axisymmetric space have been developed and validated in this chapter. The FD simulators were derived based on fundamental principles and simplified engineering approximations and were validated against results from the finite element (FE) program Code_Bright (for thermo-elastic soil behavior). The advanced TTS model (Zhang and Cheng, 2013) was implemented within the simulator and comparison between thermo-elastic and TTS model predictions clearly stress the importance of using advanced constitutive models, capable of describing the accumulation of ground displacements, when studying the response of clay to the long-term operation of a vertical heat exchanger. It is concluded that finite differences provide a simple and efficient way for modeling the long-term thermo-hydro-mechanical response of clay to seasonal heating and cooling.

$\frac{\partial p'}{\partial \varepsilon_v^e}$	$0.6B\left(\varepsilon_v^e+c\right)^{0.5}\varepsilon_v^e+0.8B\left(\varepsilon_v^e+c\right)^{1.5}\ldots$ $+\left[0.3B\left(\varepsilon_v^e+c\right)^{-0.5}\varepsilon_v^e+1.8B\left(\varepsilon_v^e+c\right)^{0.5}\right]\left(\varepsilon_v^e+\beta\Delta T\right)+0.75B\xi\left(\varepsilon_s^e\right)^2$
$\frac{\partial p'}{\partial \varepsilon_s^e}$	$3B\xi\varepsilon_s^e\left(\varepsilon_v^e+c'\right)^{0.5}$
$\frac{\partial p'}{\partial \rho_d}$	Bp'
$\frac{\partial p'}{\partial T}$	$\beta\left[0.6B\left(\varepsilon_v^e+c\right)^{0.5}\varepsilon_v^e+0.8B\left(\varepsilon_v^e+c\right)^{1.5}+1.5B\xi\left(\varepsilon_v^e+c'\right)^{0.5}\frac{\left(\varepsilon_s^e\right)^2}{\varepsilon_v^e}\right]$
$\frac{\partial q'}{\partial \varepsilon_v^e}$	$1.5\sqrt{6}B\xi\varepsilon_s^e\left(\varepsilon_v^e+c'\right)^{0.5}$
$\frac{\partial q'}{\partial \varepsilon_s^e}$	$\sqrt{6}B\xi\left(\varepsilon_v^e+c'\right)^{1.5}$
$\frac{\partial q}{\partial \rho_d}$	Bq
$p'=\frac{\sigma_1+2\sigma_3}{3}$ Mean Effective Stress $q=\sigma_1-\sigma_3$ Deviatoric Stress $B=B_0\exp\left(B_1\rho_d\right)$ B_0, B_1, c, c', ξ are input constants of the TTS model β is the volumetric thermal expansion of the soil mixture	

Table 4.1: Partial derivatives of effective stress assumed in TTS model

Constant	Meaning	Value
β_w [10^{-4}/°C]	Vol. thermal expansion	3.4
λ_w [W/mK]	Thermal conductivity	0.6
c_w [J/kg K]	Specific heat capacity	4186
$\mu_w(T)$ [Pa s]	Viscosity of water	$\mu_w(T) = -0.00046575\ln(T) + 0.00239138$ *
$\rho_w(T)$ [kg/m^3]	Density of water	$\rho_w(T) = 1000.34038 - 7.77\times10^{-3}T - 4.95\times10^{-3}T^2$ **

* Hillel (1980)

** ASTM

Table 4.2: Properties of water assumed in numerical simulator

Constant	Meaning	Typical Range
$\beta_{s,lin}$ [10^{-6} /°C]	Linear thermal expansion of solid particles	4.0 – 18
λ_s [W/mK]	Thermal conductivity of solid particles	2.0 – 3.0
c_s [J/kg K]	Specific heat capacity of solid particles	700 - 950
k [m/s]	Hydraulic Conductivity of soil mixture	$10^{-10} - 10^{-8}$
C_k [-]	Change of k vs e	$(0.33 - 0.5)e_0$

Table 4.3: Thermal and hydraulic input constants for numerical simulator

Constant	Meaning	Selected value
$\beta_{s,lin}$ [10^{-6} /°C]	Linear thermal expansion of solid particles	6.0
λ [W/mK]	Thermal conductivity of soil mixture	2.0
c_s [J/kg K]	Specific heat capacity of solid particles	930
k [m/s]	Hydraulic conductivity	10^{-9} *
C_k [-]	Change of k vs e	10^{10} *
E' [MPa]	Young's Modulus	10
v [-]	Poisson's ratio	0.3
G_s [-]	Specific gravity	2.745

* Hydraulic conductivity is assumed constant with void ratio ($C_k = 10^{10}$)

Table 4.4: Input parameters assumed in validation of FD simulators and FE Code_Bright model

Constant	Meaning	Selected value
$\beta_{s,lin}$ [10^{-6} /°C]	Linear thermal expansion of solid particles	6.0
λ_s [W/mK]	Thermal conductivity of solid particles	2.4
c_s [J/kg K]	Specific heat capacity of solid particles	930
k [m/s]	Hydraulic Conductivity	10^{-10}
C_k [-]	Change of k vs e	0.0817
G_s [-]	Specific gravity	2.745

Table 4.5: Thermal and hydraulic input parameters assumed in TE and TTS models using FD simulators

Constant	Meaning/Effect	Geneva Clay
B_0 [Pa]	Location of VCL	3.8×10^{-4}
B_1 [m^3/kg]	Slope of VCL	0.0162
h [-]	Hysteretic strains (slope of unload curve)	0.05
$m_{1,0}$ [-]	Max. elastic strain	1.0
m_2 [-]	Max. elastic strain and reload curve	150
c' [-]	Critical state friction angle	0.0863
ξ [-]	Coefficient of earth pressure at rest K_{0NC}	0.1
α_{bf} [1/°C]	Bound to free water conversion	0.0237
m_5 [s^3/m^2°C]	Thermal volumetric strain	0.1
L_T [1/°C]	Shift of VCL vs T	0.02
a [-]	Rate effects (a = 0.5 for rate independence)	0.5
m_4 [kg/m^3s]	Rate of Granular Temperature production	6×10^{4}
m_3 [-]	Relative contribution of volumetric and deviatoric strains	1.0
c [-]	Cohesion (c = 0 for sands)	0.01
w [-]	Hysteretic strains	1.0

Table 4.6: TTS model input parameters calibrated for Geneva clay

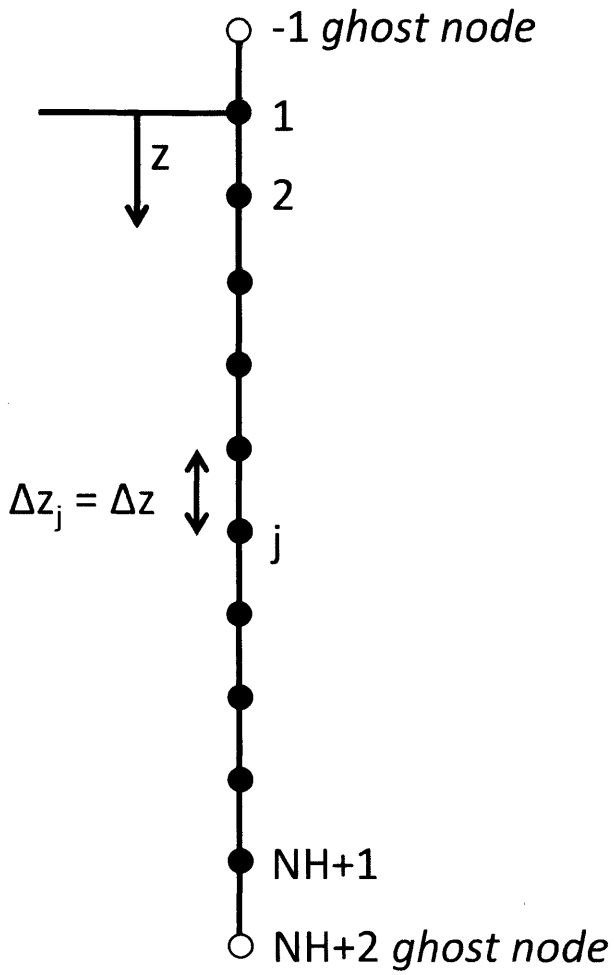

Figure 4.1: Grid of integration points and ghost nodes used in 1-D FD simulator

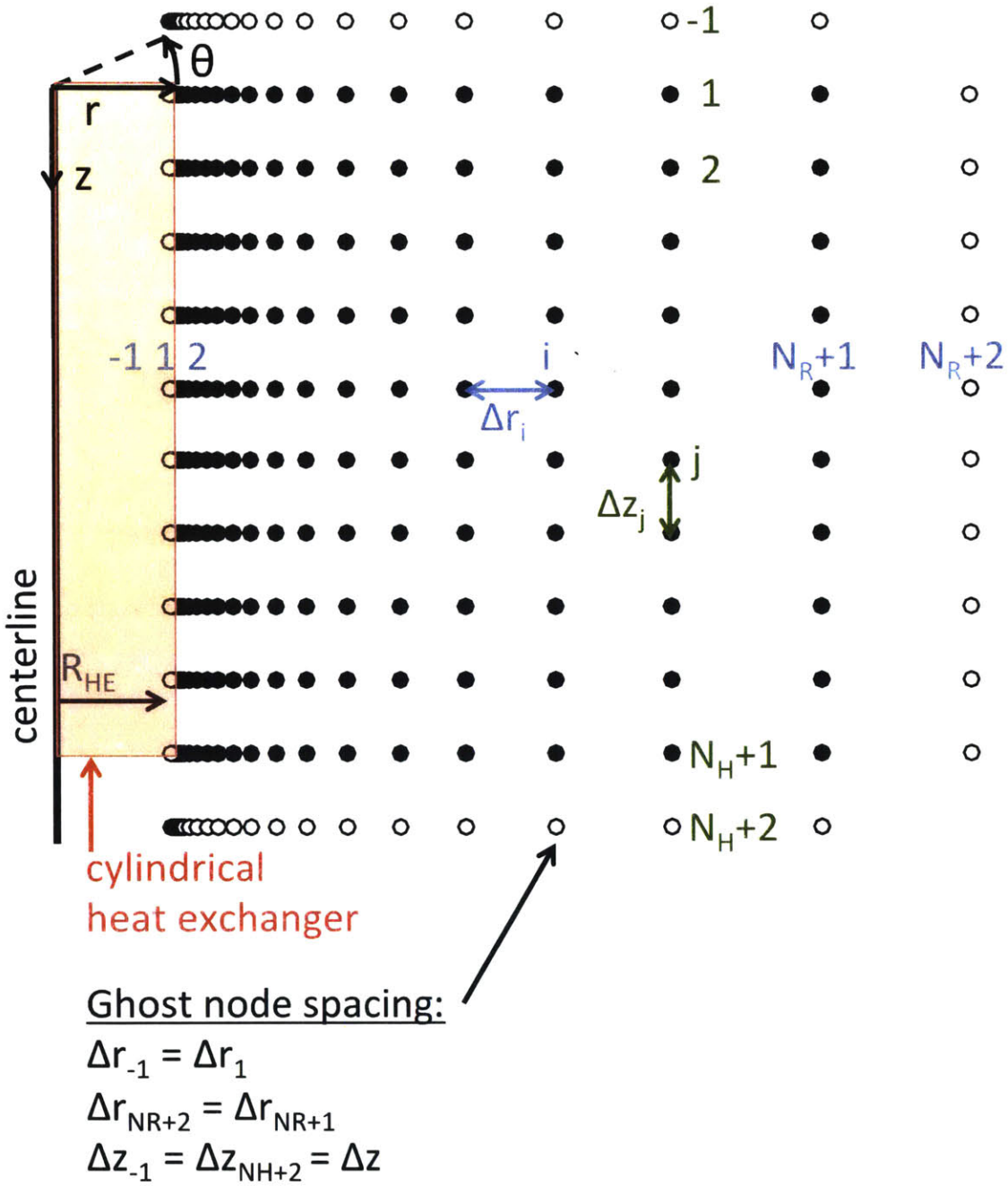

Figure 4.2: Grid of integration points and ghost nodes used in axisymmetric FD simulator

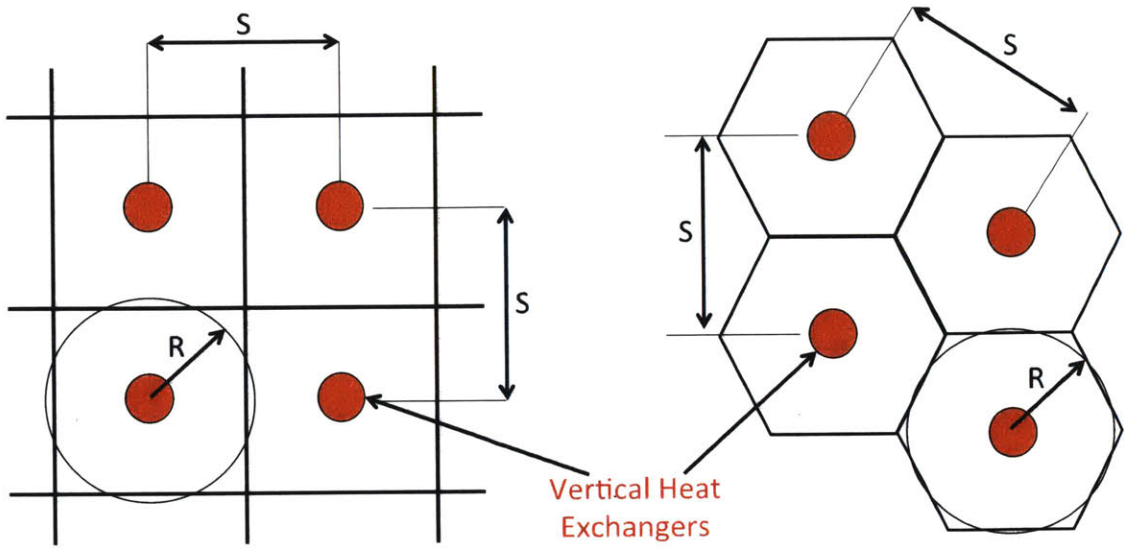

a) Square Pattern
R = 0.546 S

b) Triangular Pattern
R = 0.525 S

Figure 4.3: Plan view of main heat exchanger array arrangement options and zone of influence of each vertical heat exchanger

Heat flux at r = R_{HE}: $Q_{cyl} = \frac{Q_{lin}}{2\pi R_{HE}}$

Change of temperature in r-dir.: $\frac{\partial T}{\partial r} = -\frac{1}{\lambda_g} Q_{cyl} = -\frac{1}{\lambda_g} \frac{Q_{lin}}{2\pi R_{HE}}$

where λ_g is the coef. of heat conduction of grout

Effective Borehole Resistance: $R_b = -\frac{\partial T}{\partial r} \frac{R_{HE}}{Q_{lin}} = \frac{1}{2\pi\lambda_g}$

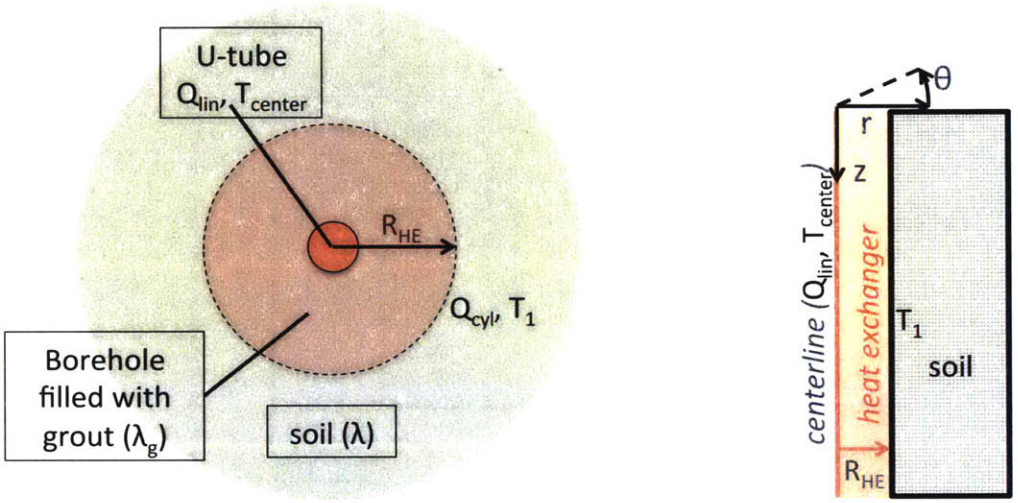

a) Plan view of heat exchanger borehole

b) Cross-section of heat exchanger borehole in axi-symmetric space

Figure 4.4: Schematic of heat exchanger borehole and calculation of effective borehole resistance, R_b.

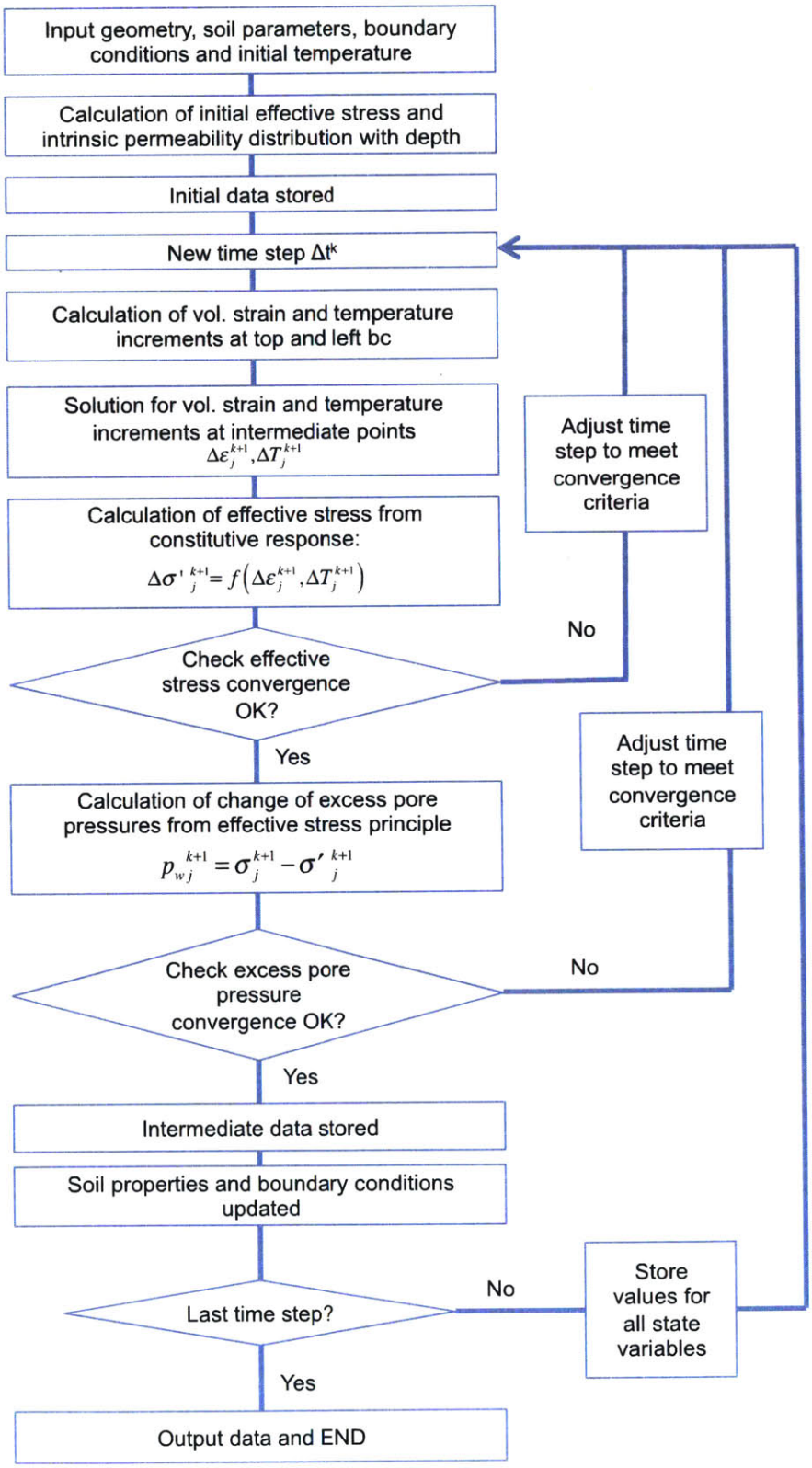

Figure 4.5: Algorithm flow chart for FD simulators

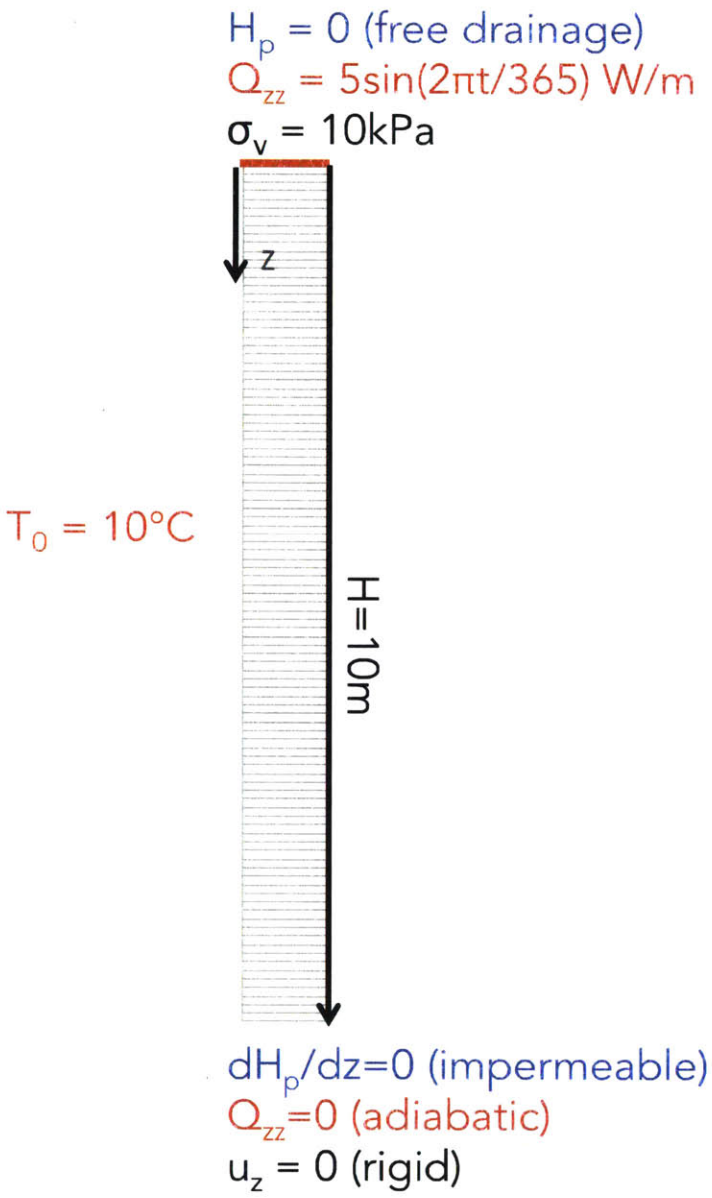

Figure 4.6: Mesh and boundary conditions assumed for 1-D reference problem using Code_Bright

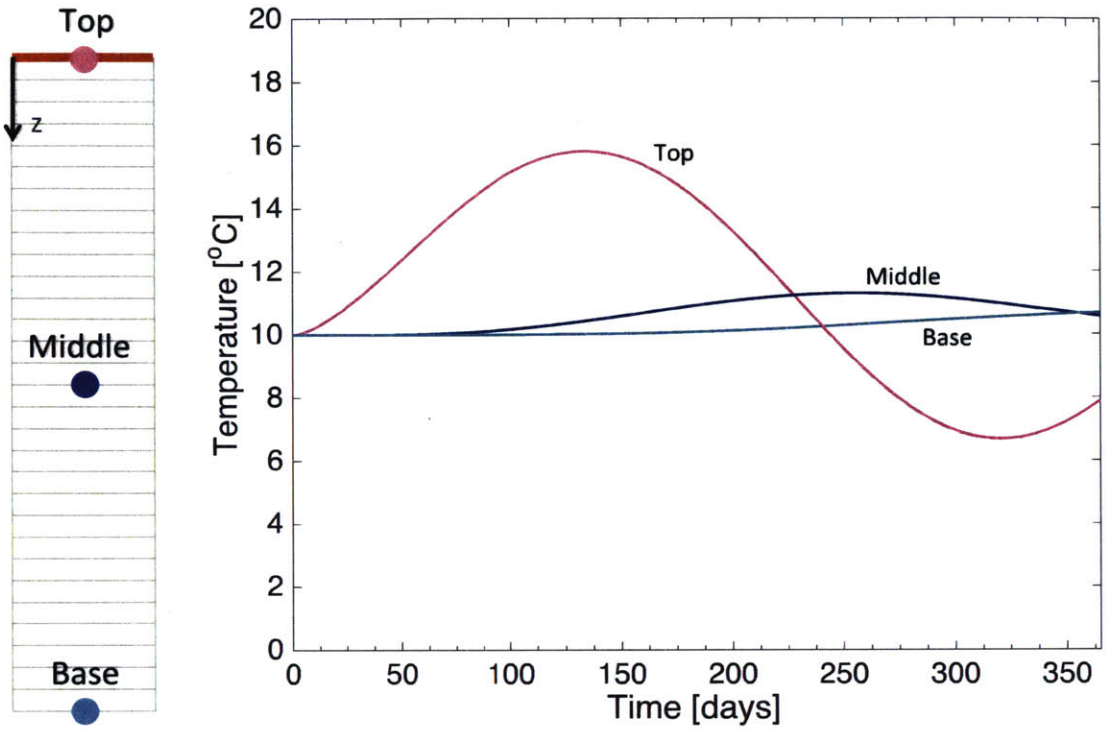

Figure 4.7: Comparison of FD (solid line) and FE (dashed line) predictions of temperature evolution at three different points of the 1-D geometry

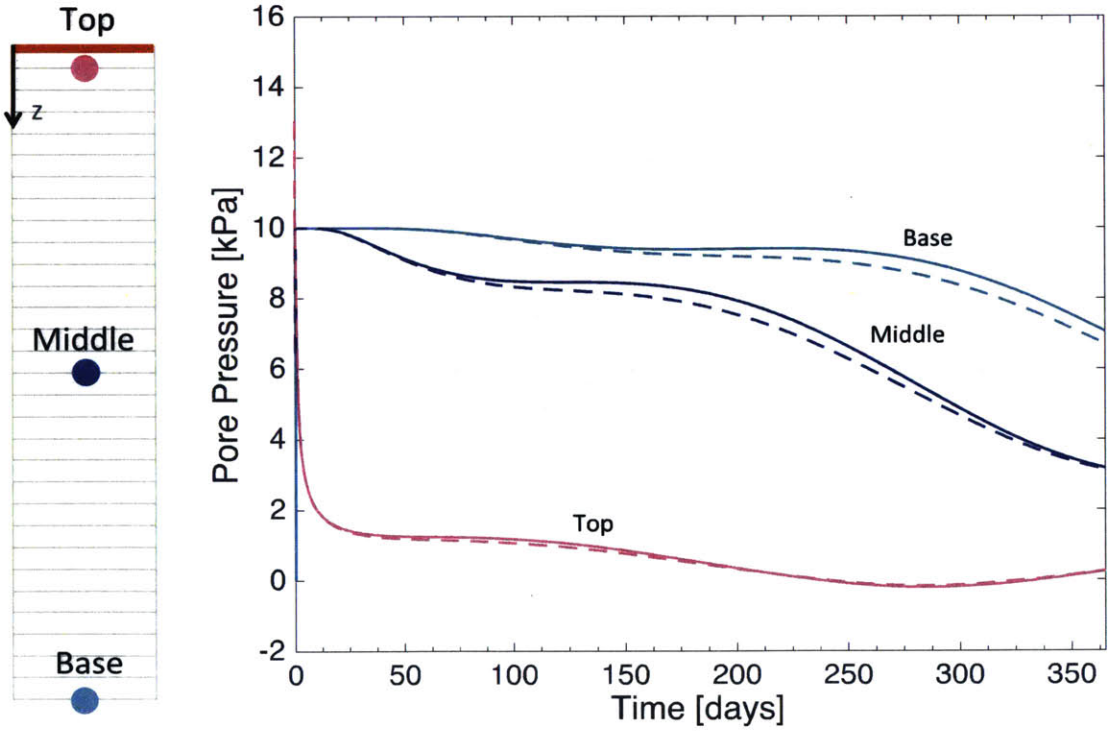

Figure 4.8: Comparison of FD (solid line) and FE (dashed line) predictions of excess pore water pressure evolution at three different points of the 1-D geometry

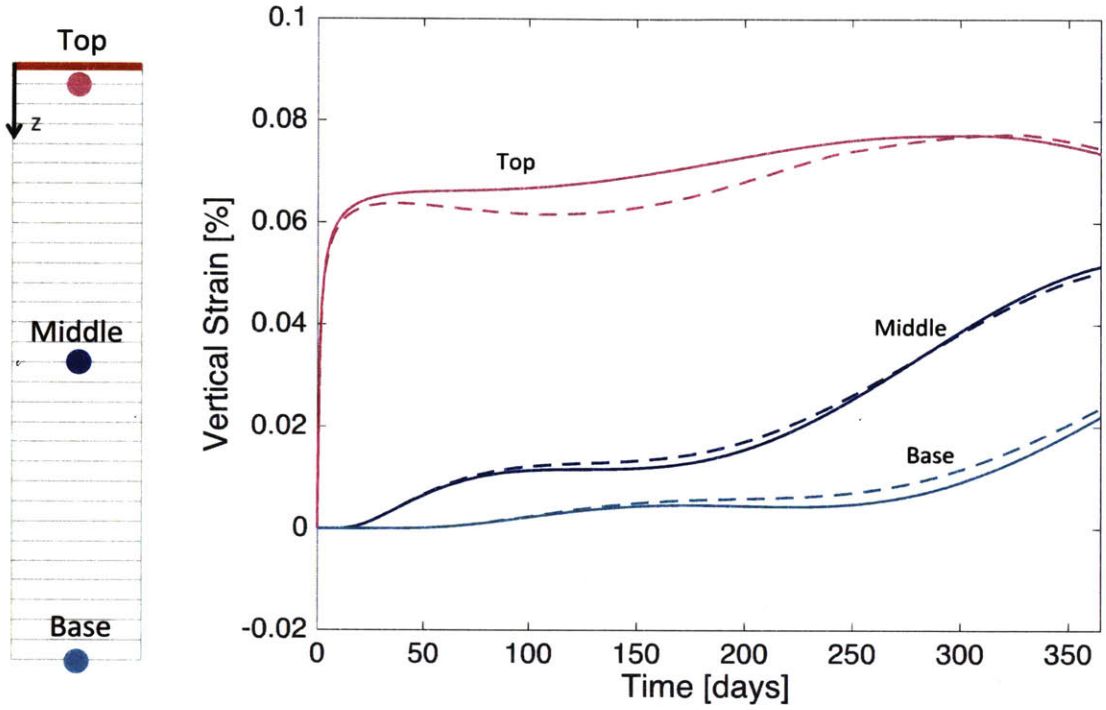

Figure 4.9: Comparison of FD (solid line) and FE (dashed line) predictions of vertical strain evolution at three different points of the 1-D geometry

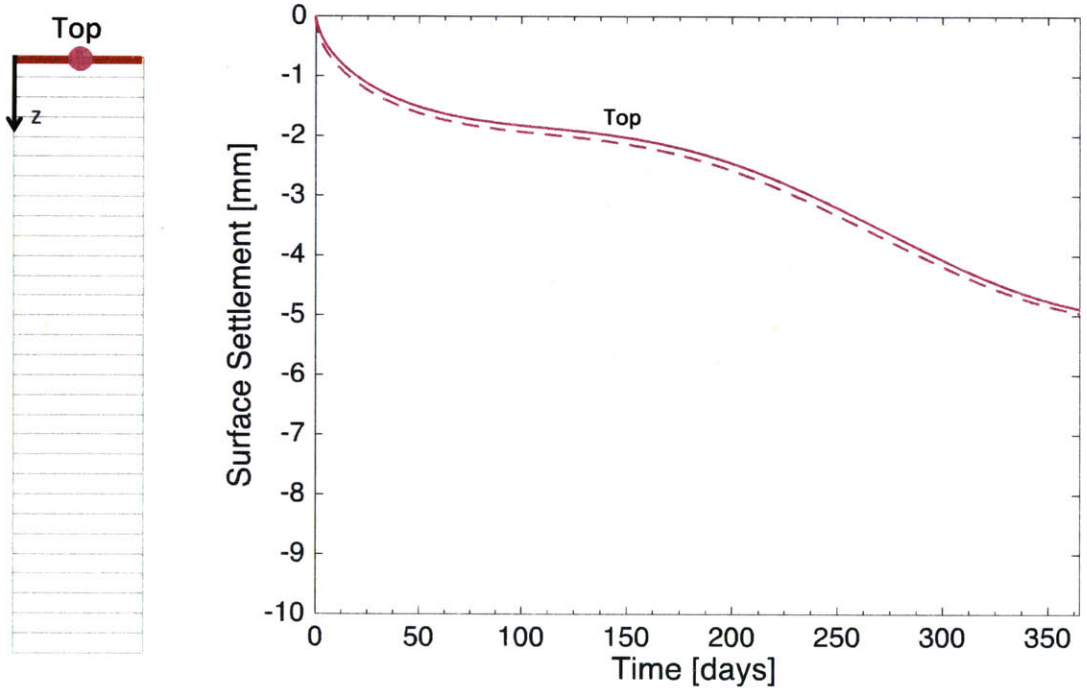

Figure 4.10: Comparison of FD (solid line) and FE (dashed line) predictions of surface settlement evolution for the 1-D geometry

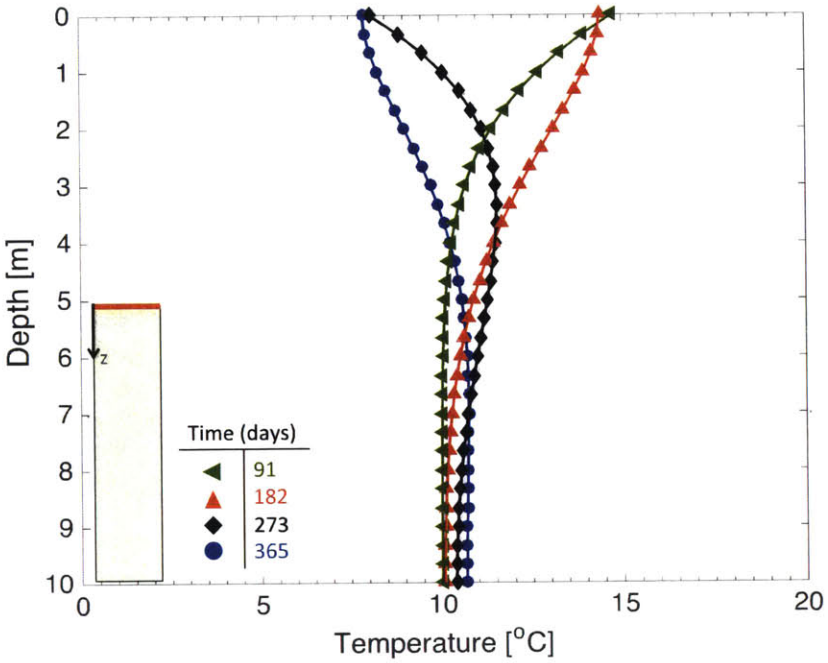

Figure 4.11: Comparison of FD (solid line with symbols) and FE (dashed line) predictions of temperature versus depth of the 1-D geometry, for different snapshots in time

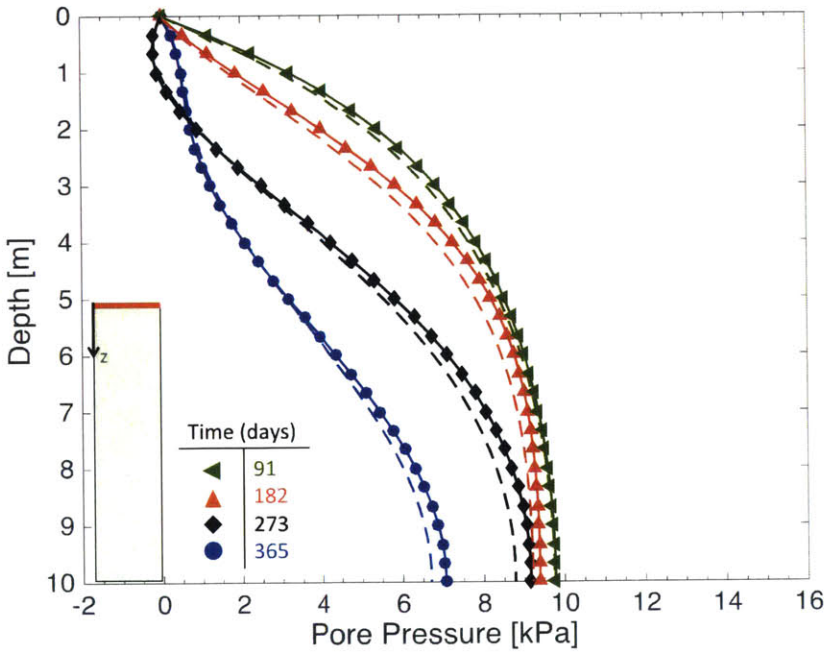

Figure 4.12: Comparison of FD (solid line with symbols) and FE (dashed line) predictions of excess pore water pressure versus depth of the 1-D geometry, for different snapshots in time

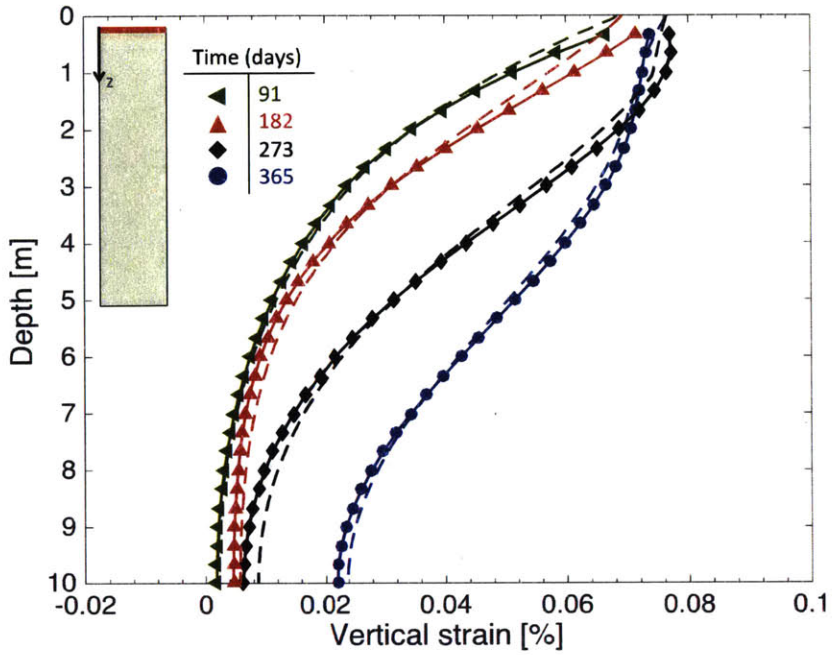

Figure 4.13: Comparison of FD (solid line with symbols) and FE (dashed line) predictions of vertical strain versus depth of the 1-D geometry, for different snapshots in time

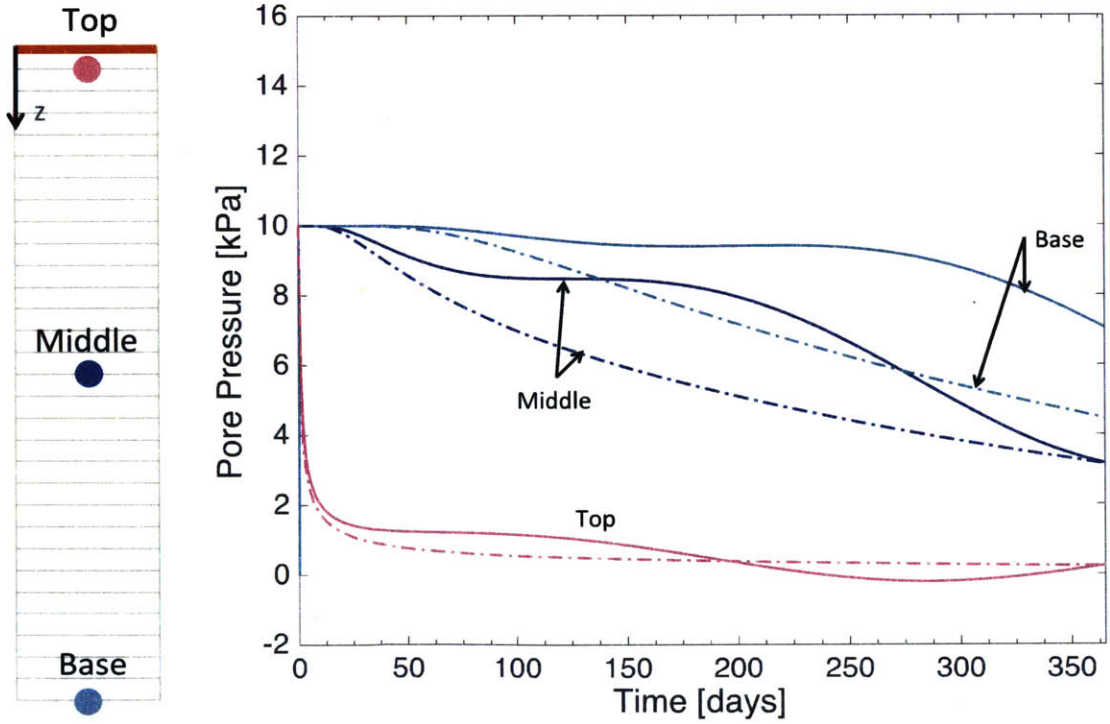

Figure 4.14: Comparison of coupled THM (solid line) and uncoupled HM (dashed line) predictions of excess pore water pressure evolution at three different points of the 1-D geometry

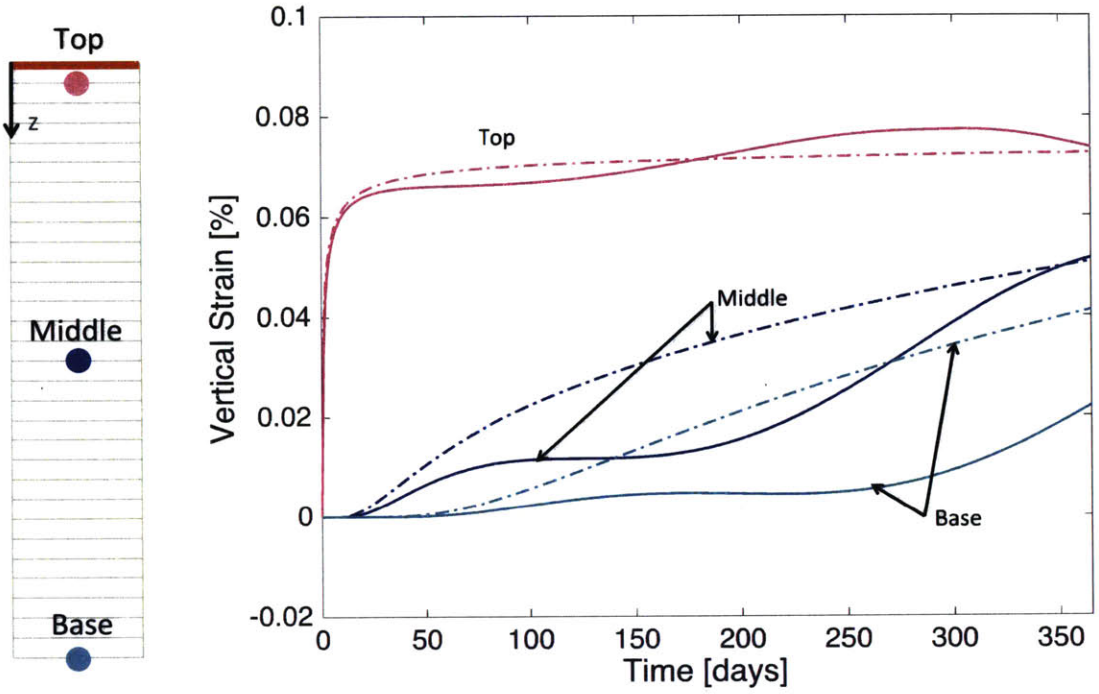

Figure 4.15: Comparison of coupled THM (solid line) and uncoupled HM (dashed line) predictions of vertical strain evolution at three different points of the 1-D geometry

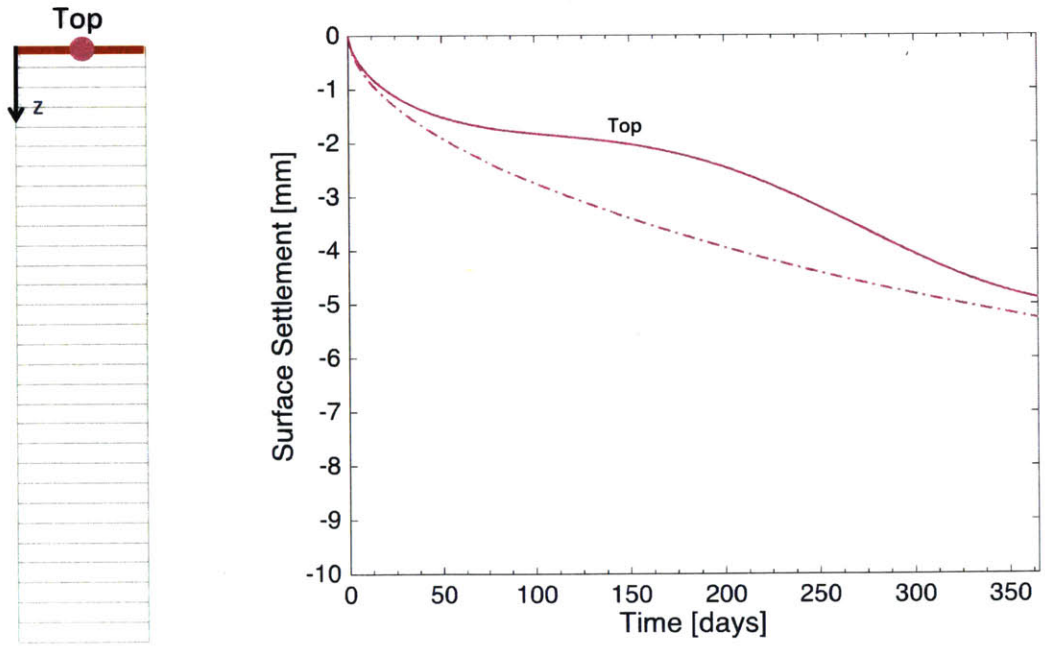

Figure 4.16: Comparison of coupled THM (solid line) and uncoupled HM (dashed line) predictions of surface settlement evolution for the 1-D geometry

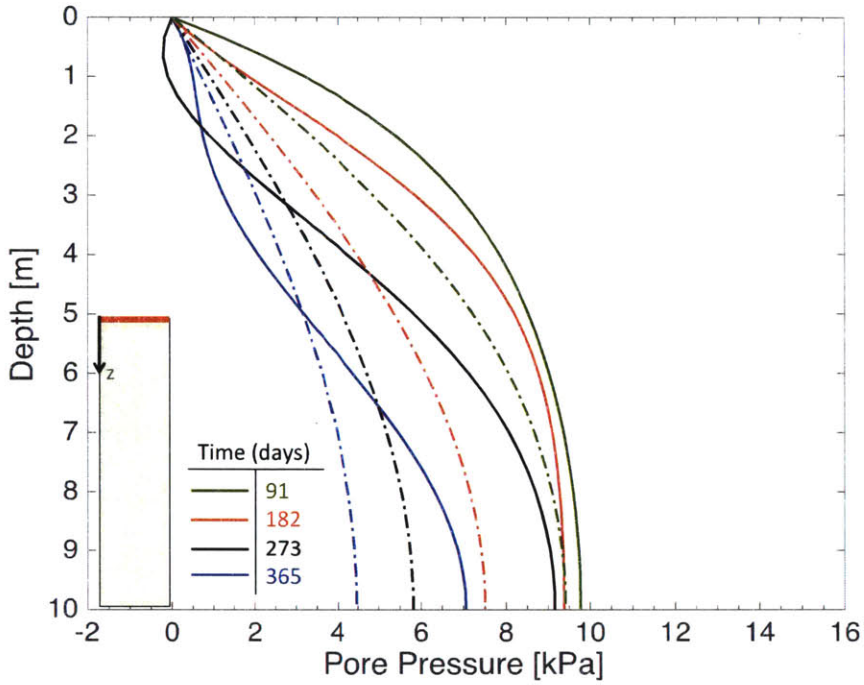

Figure 4.17: Comparison of coupled THM (solid line) and uncoupled HM (dashed line) predictions of excess pore water pressure versus depth of the 1-D geometry, for different snapshots in time

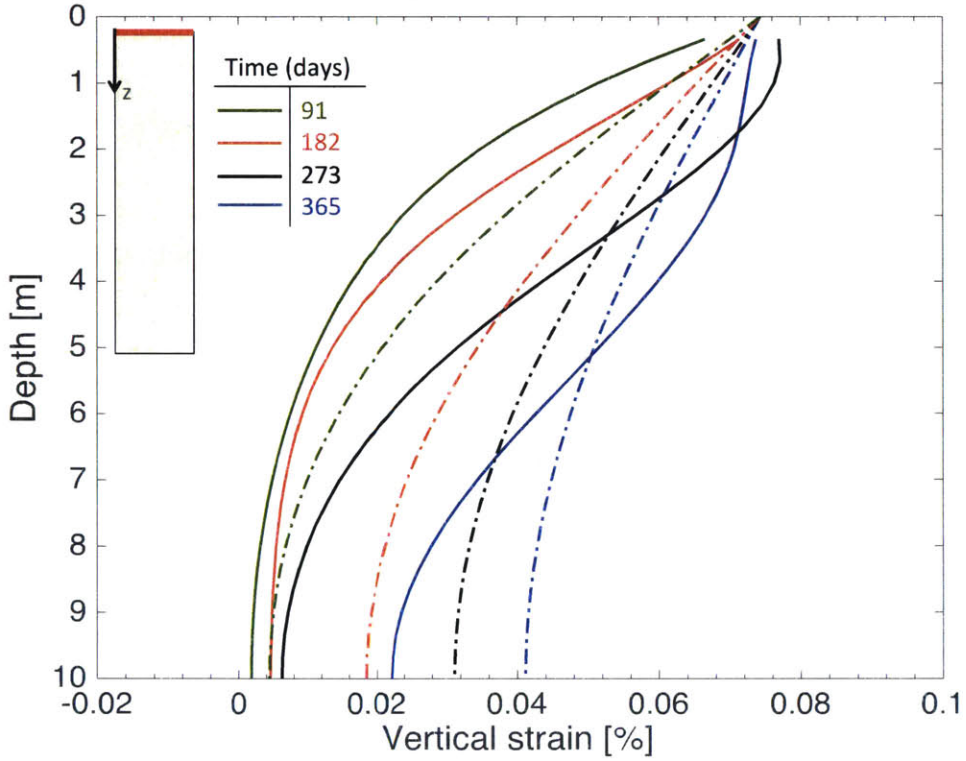

Figure 4.18: Comparison of coupled THM (solid line) and uncoupled HM (dashed line) predictions of vertical strain versus depth of the 1-D geometry, for different snapshots in time

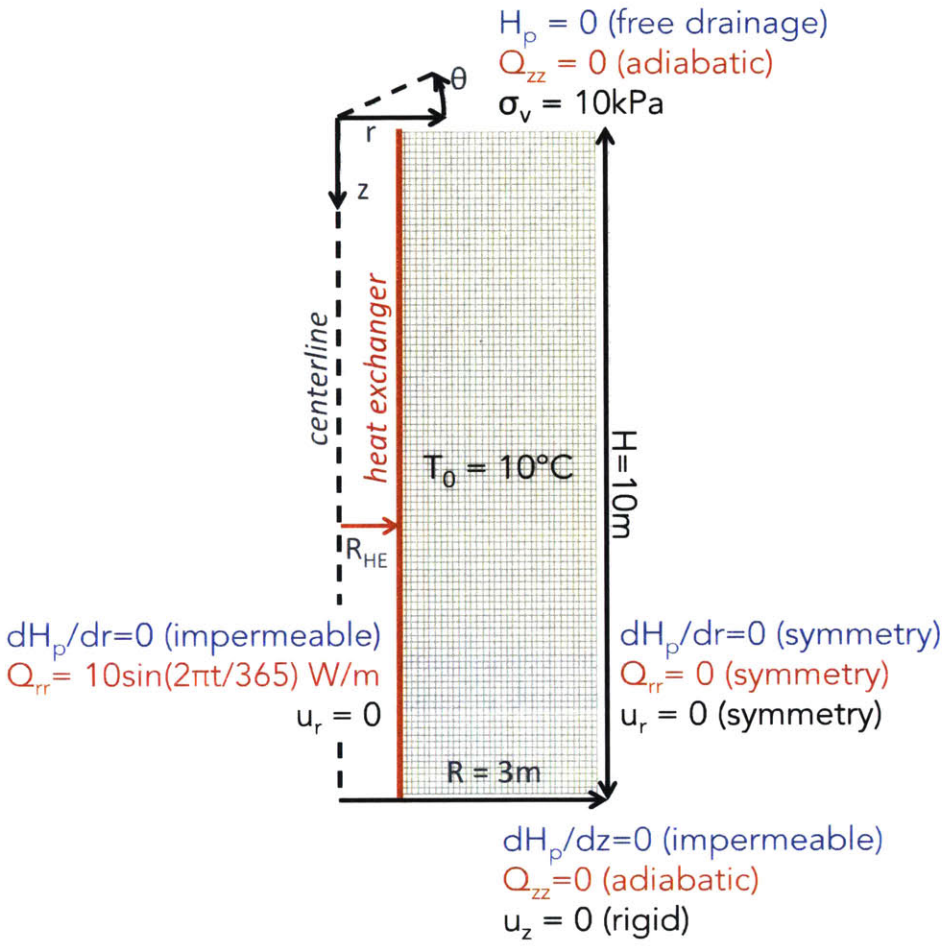

Figure 4.19: Mesh and boundary conditions assumed in the Code_Bright axisymmetric model

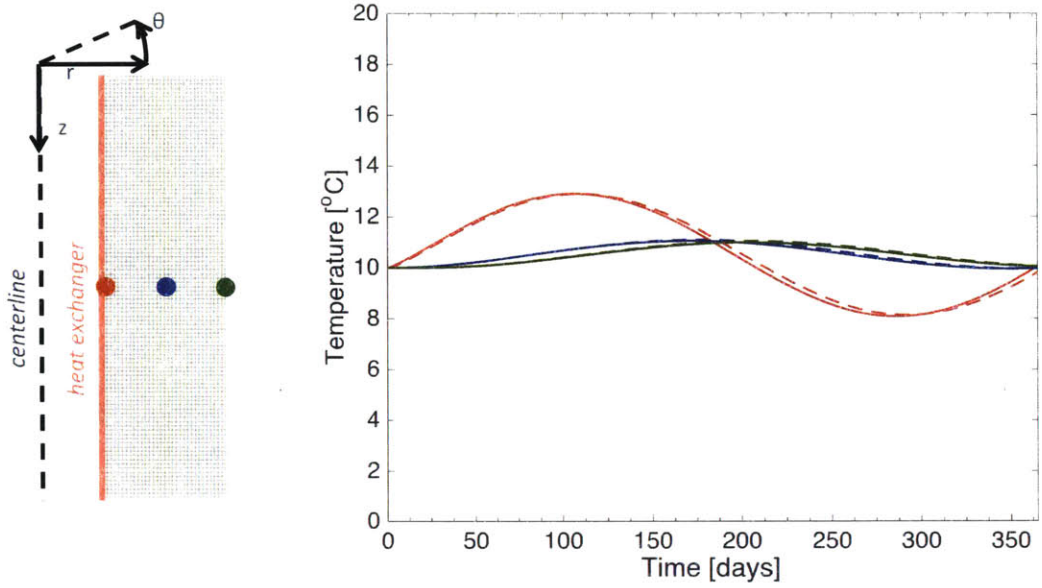

a) Points across depth z = H/2

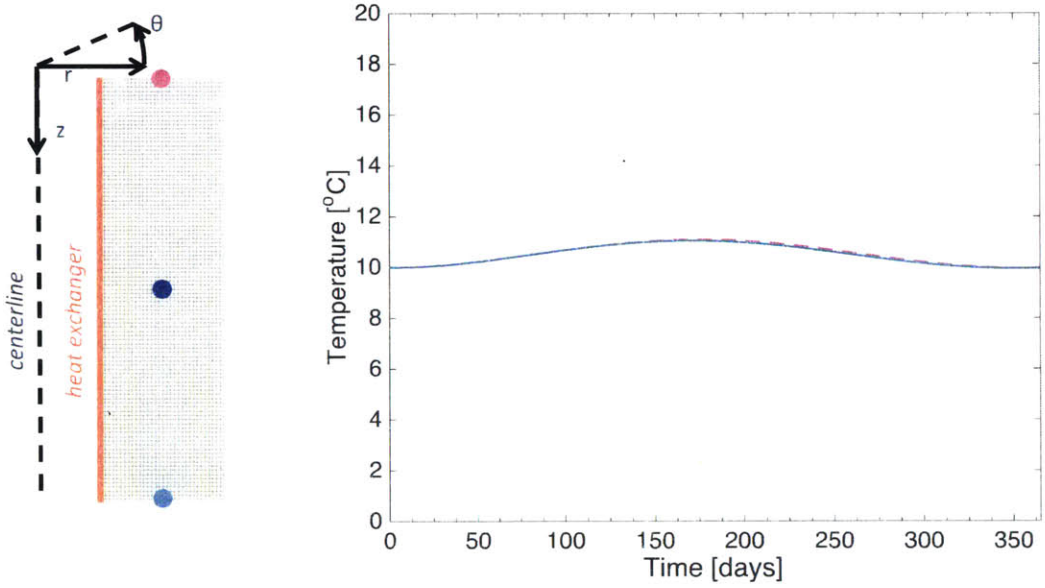

b) Points across radial distance r = R/2

Figure 4.20: Comparison of FD (solid line) and FE (dashed line) predictions of temperature evolution at different points of the axisymmetric geometry

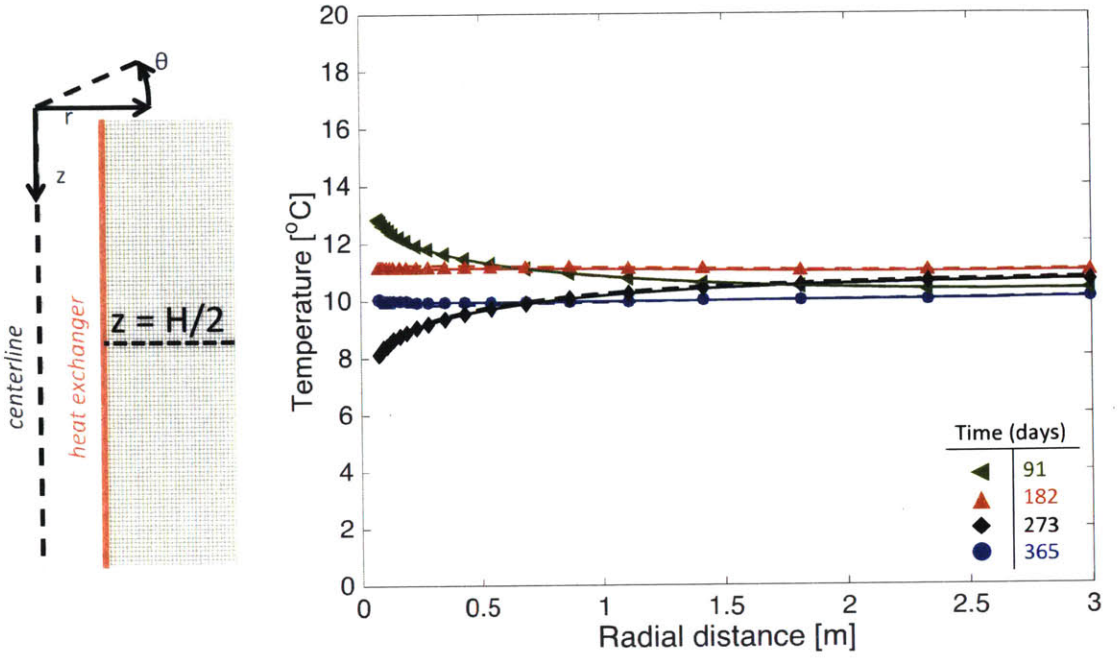

a) Temperature versus radial distance

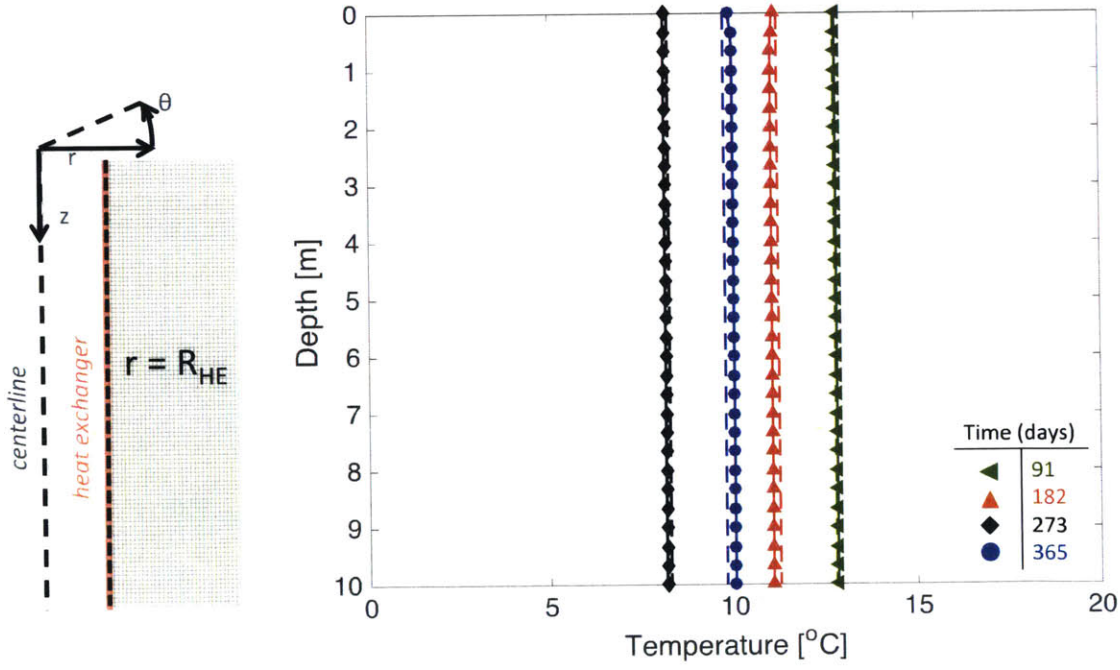

b) Temperature versus depth

Figure 4.21: Comparison of FD (solid line with symbols) and FE (dashed line) predictions of temperature at different snapshots in time

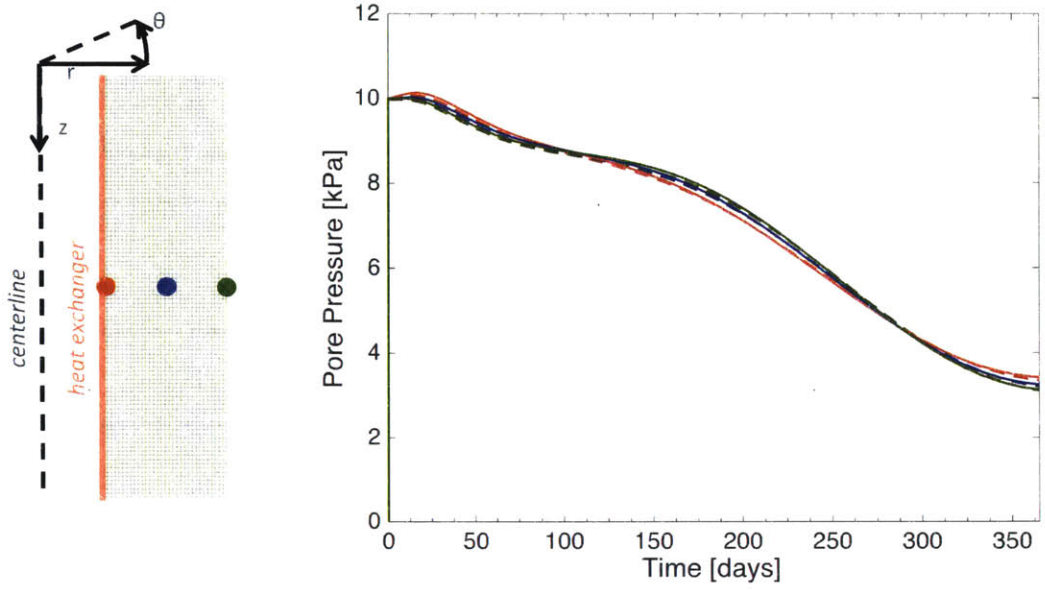

a) Points across depth z = H/2

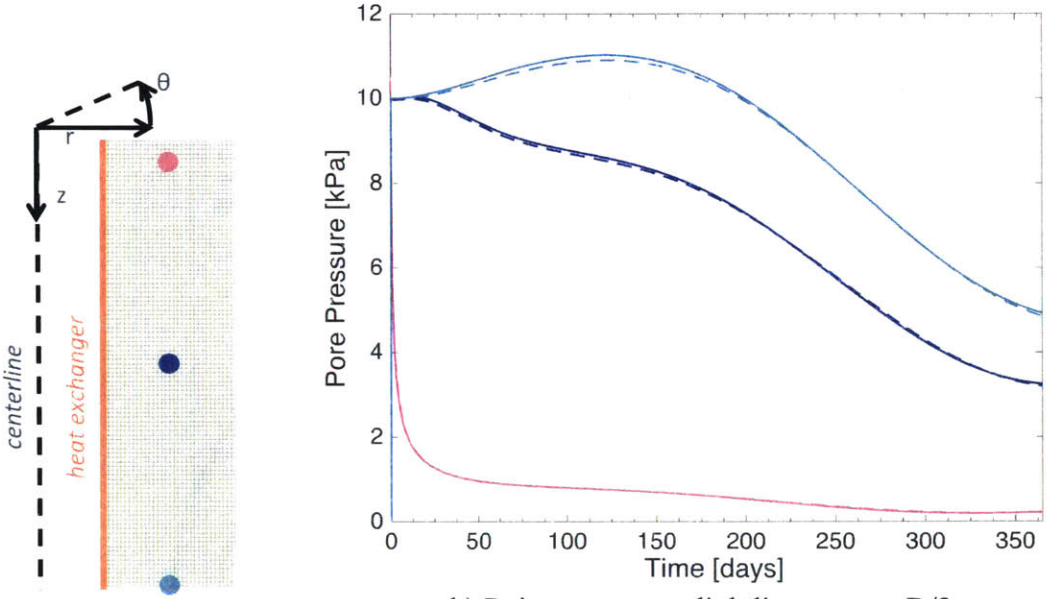

b) Points across radial distance r = R/2

Figure 4.22: Comparison of FD (solid line) and FE (dashed line) predictions of excess pore pressure evolution at different points of the axisymmetric geometry

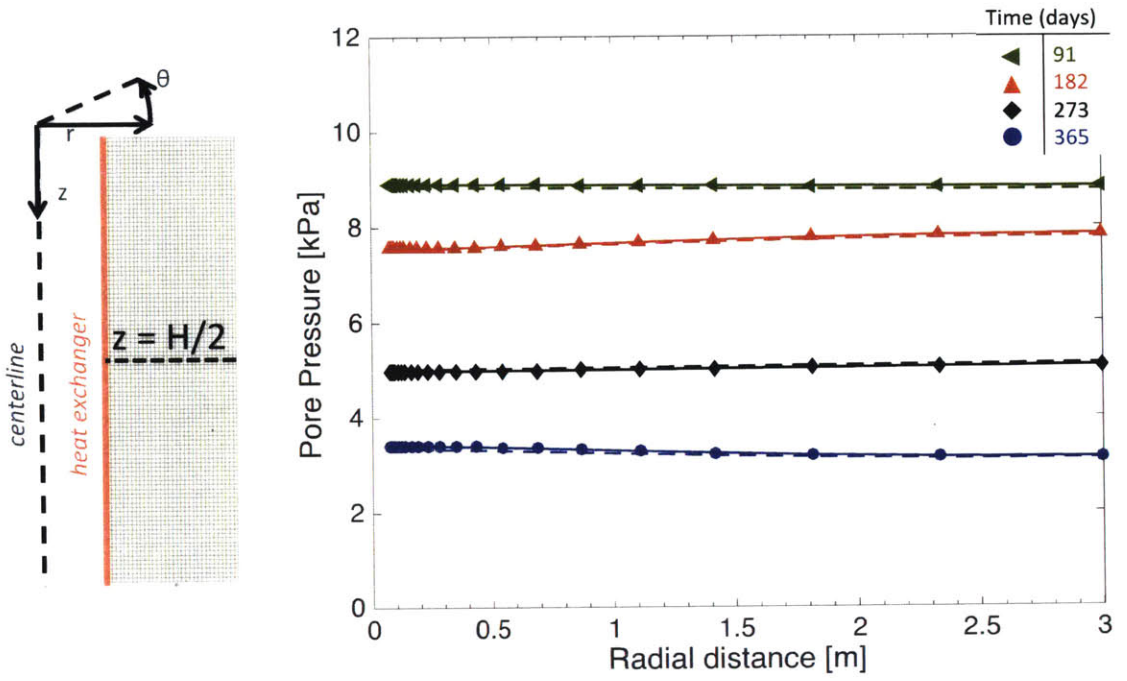

a) Excess pore pressure versus radial distance

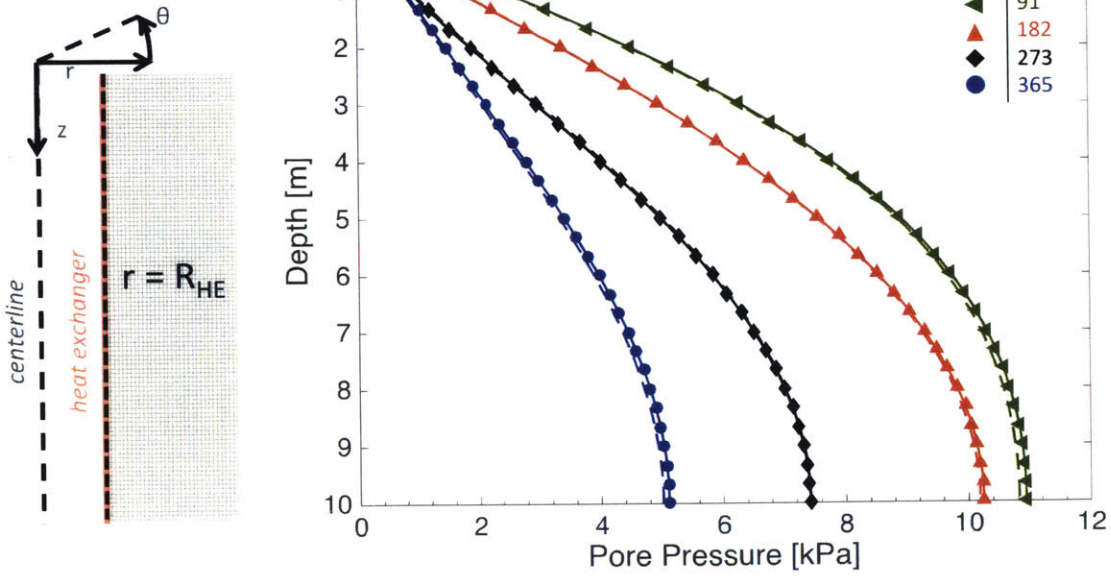

b) Excess pore pressure versus depth

Figure 4.23: Comparison of FD (solid line with symbols) and FE (dashed line) predictions of excess pore pressure at different snapshots in time

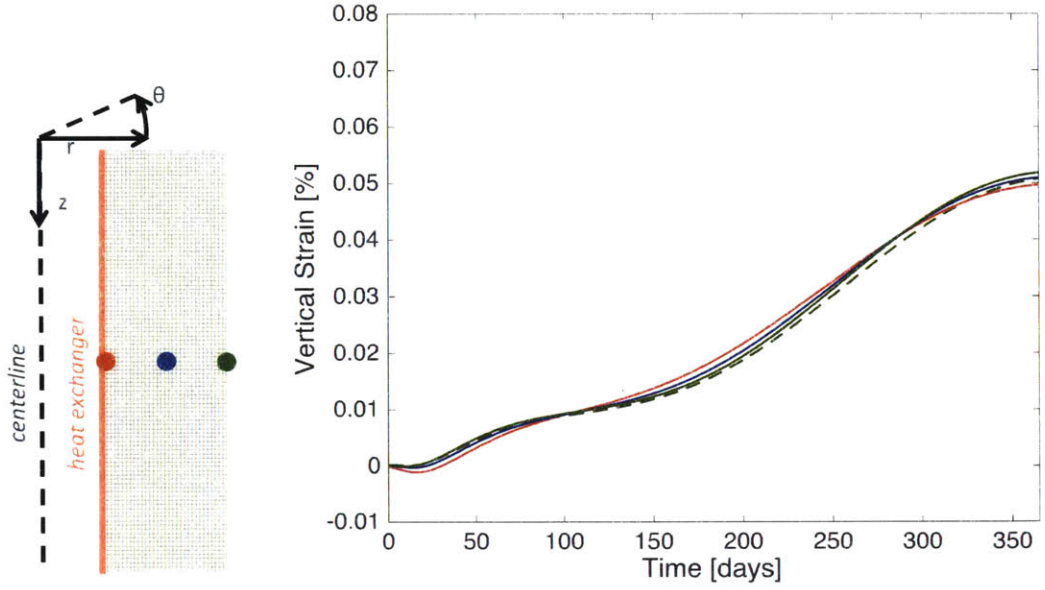

a) Points across depth z = H/2

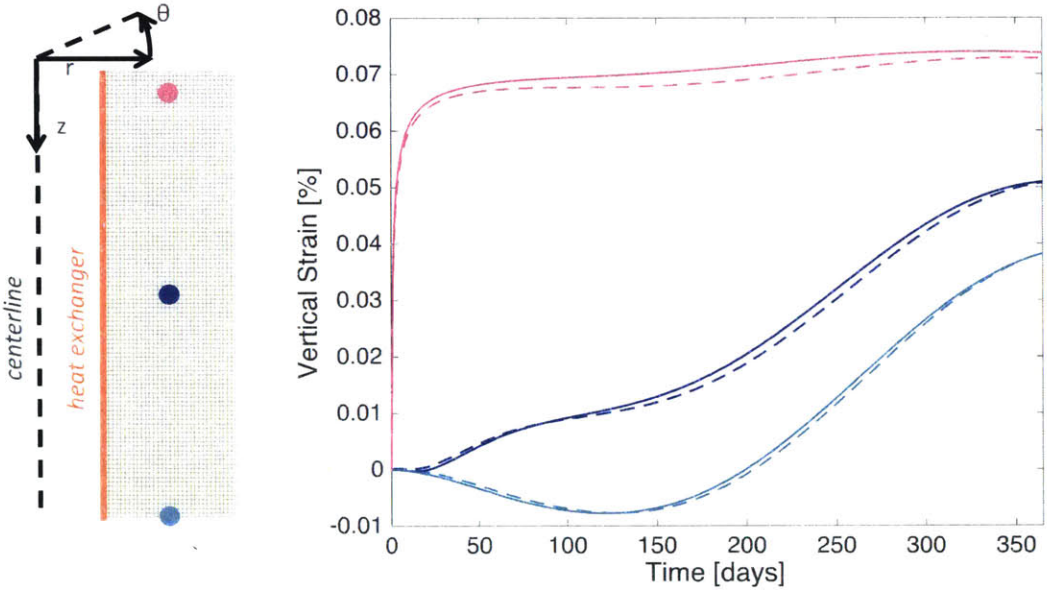

b) Points across radial distance r = R/2

Figure 4.24: Comparison of FD (solid line) and FE (dashed line) predictions of vertical strain evolution at different points of the axisymmetric geometry

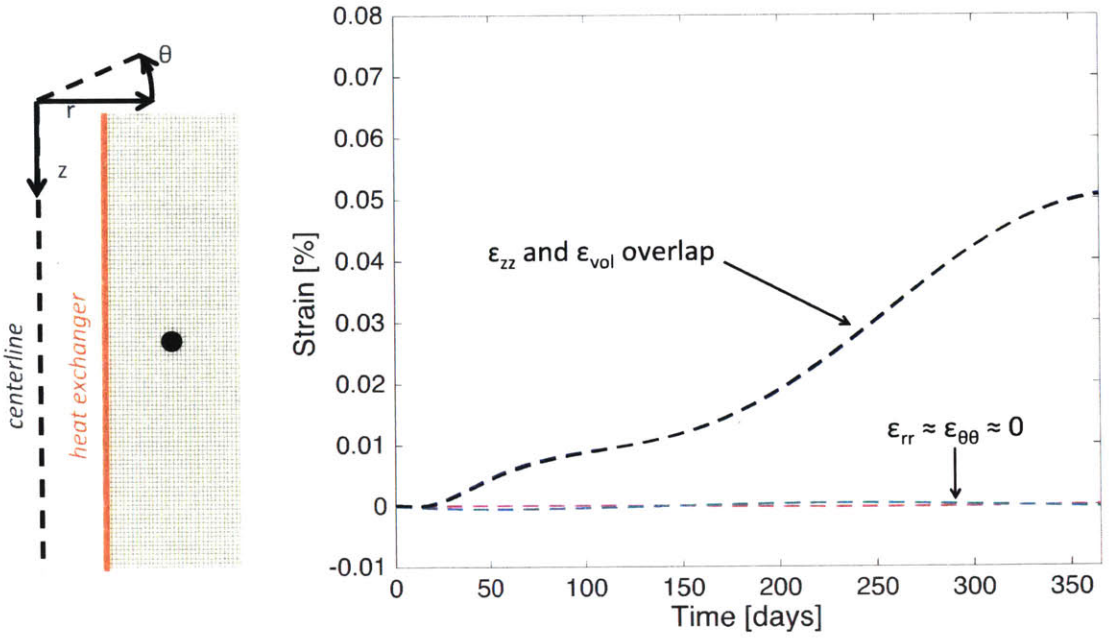

a) At depth z = H/2 and radial distance r = R/2

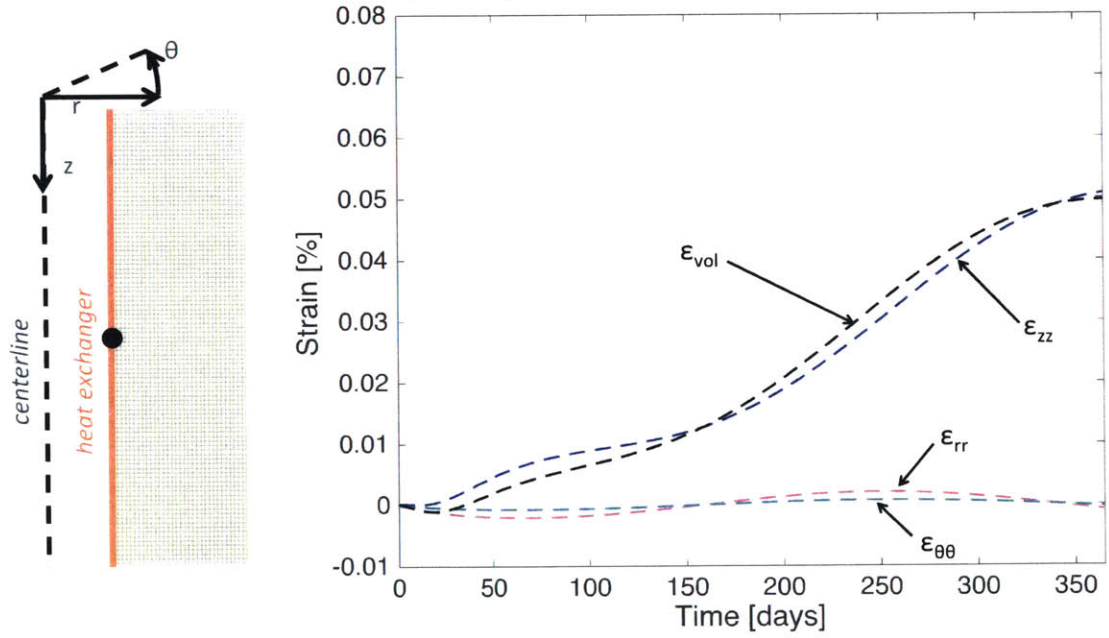

b) At depth z = H/2 and radial distance r = R_{HE}

Figure 4.25: FE model predictions of strain evolution in all directions of the axisymmetric space at: a) the middle of the axisymmetric geometry and b) on the heat exchanger

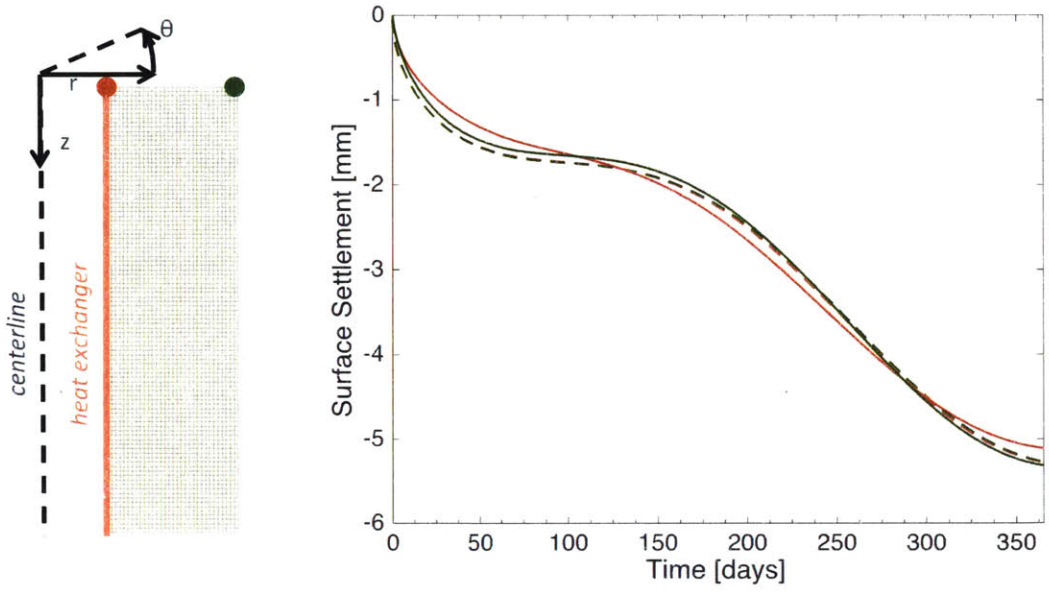

Figure 4.26: Comparison of FD (solid line) and FE (dashed line) predictions of surface settlement evolution at different points of the axisymmetric geometry

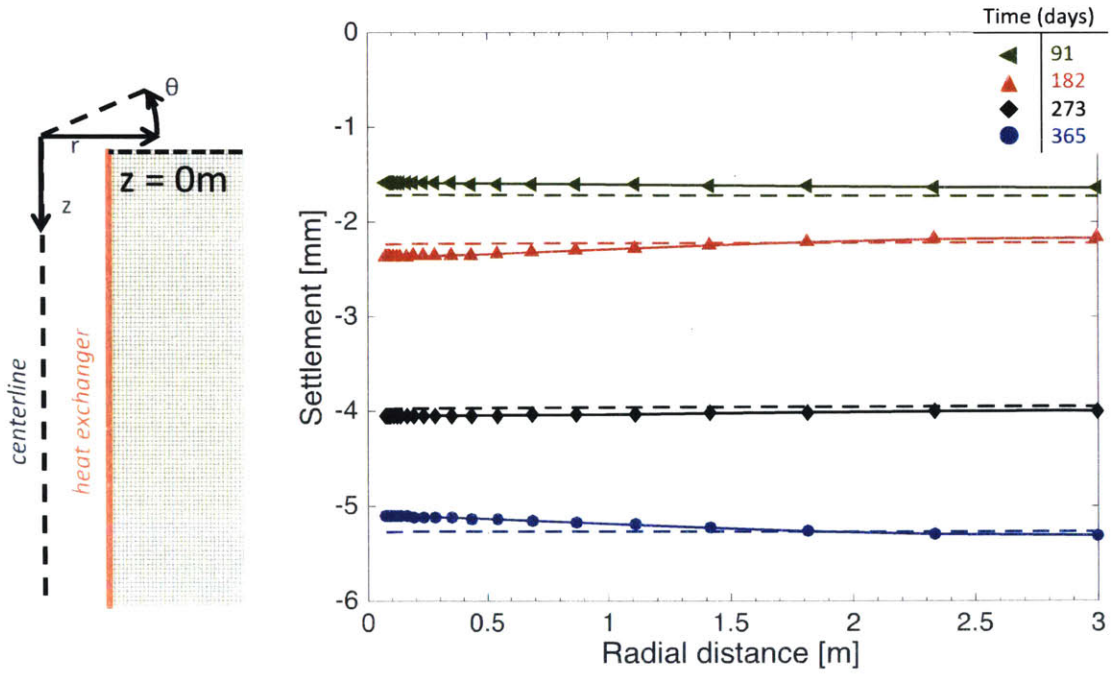

Figure 4.27: Comparison of FD (solid line with symbols) and FE (dashed line) predictions of surface settlement versus radial distance at different snapshots in time

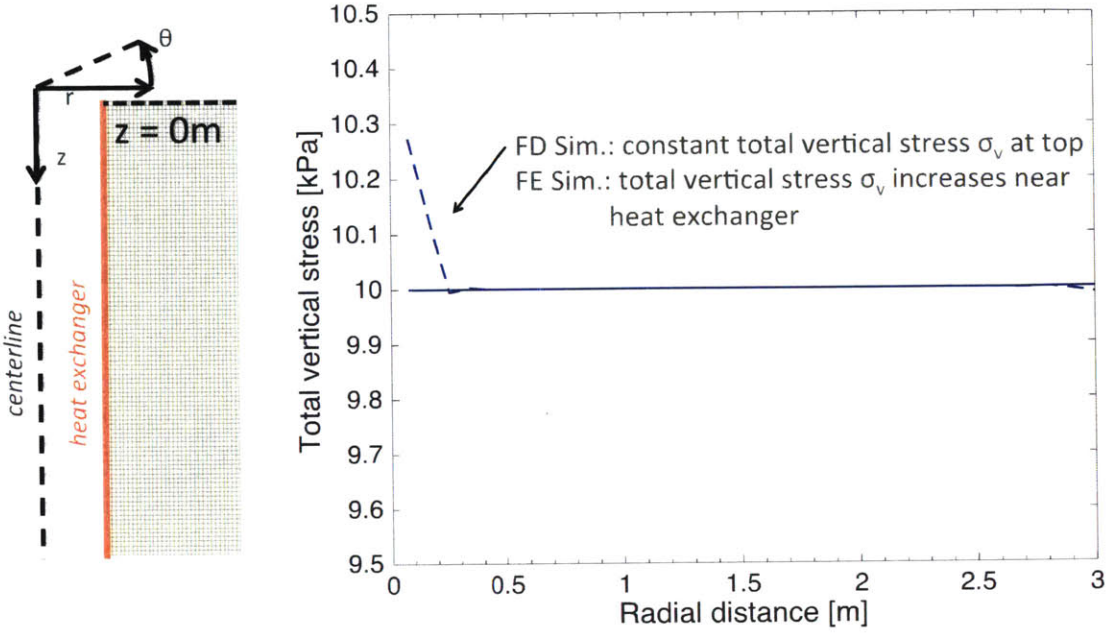

Figure 4.28: Comparison of FD (solid line) and FE (dashed line) assumption of total vertical stress at top versus radial distance

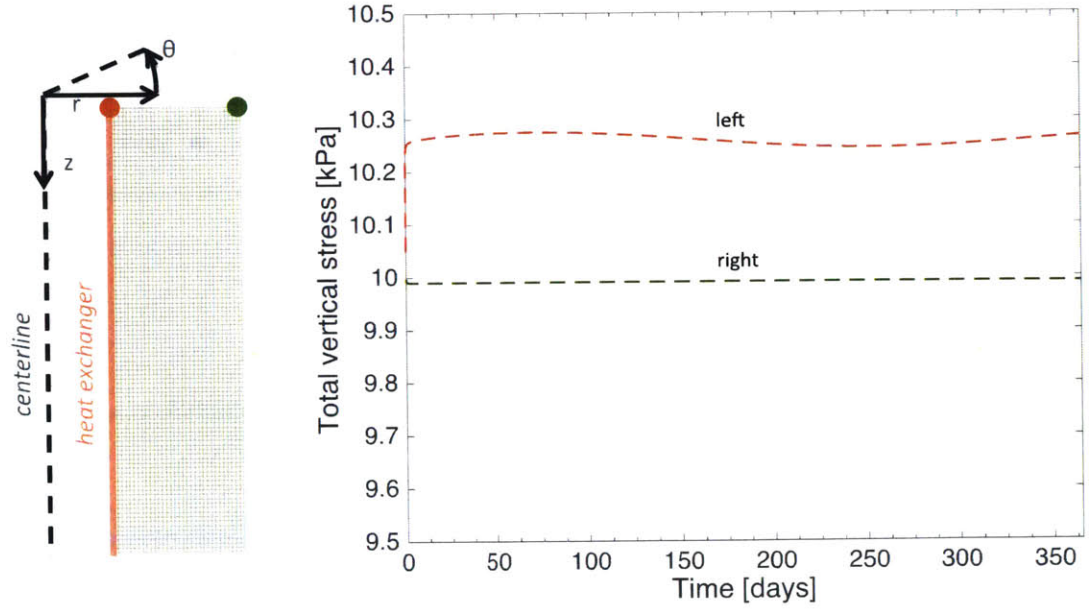

Figure 4.29: FE model assumption of total vertical stress at two different points of the top boundary versus time

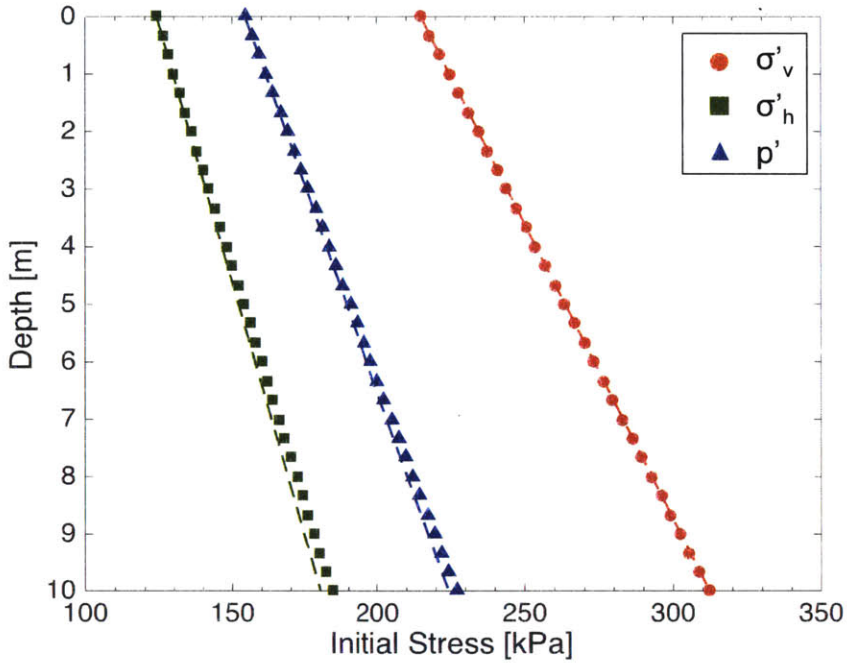

a) Stress versus depth

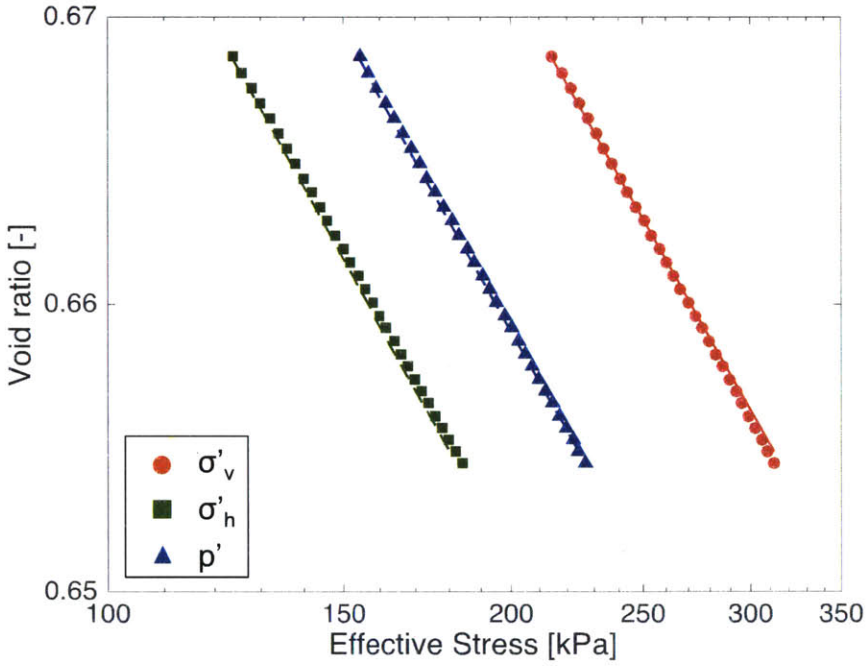

b) Stress versus void ratio

Figure 4.30: Initial stress distribution assumed in thermo-elastic and TTS models

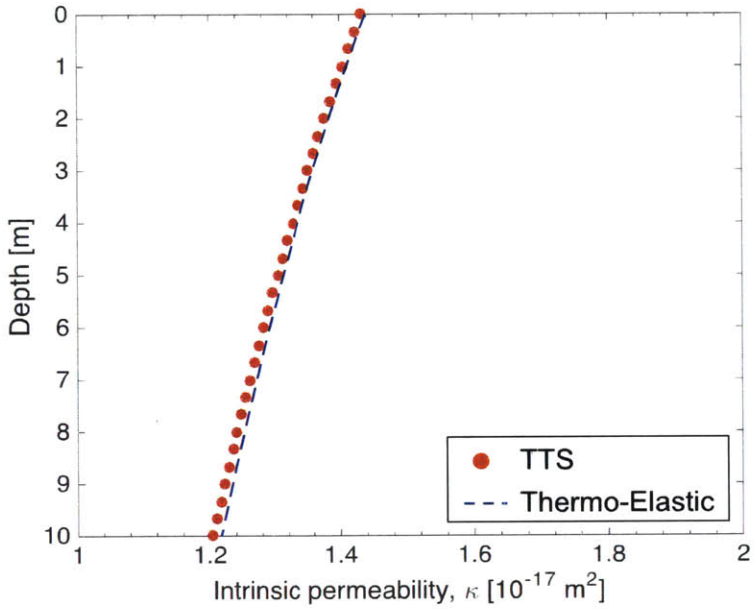

Figure 4.31: Intrinsic permeability distribution assumed in thermo-elastic and TTS models

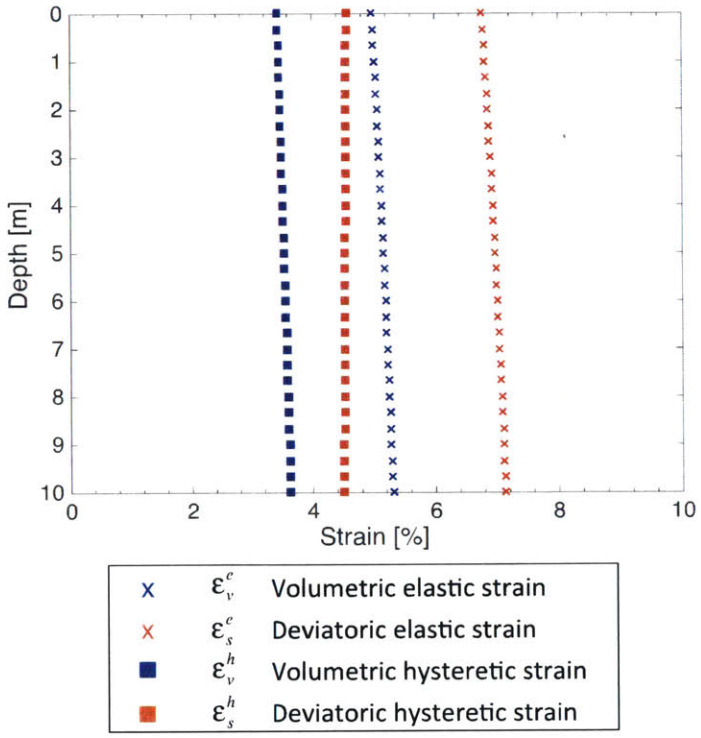

Figure 4.32: Distribution of initial TTS strain variables assumed in reference simulation

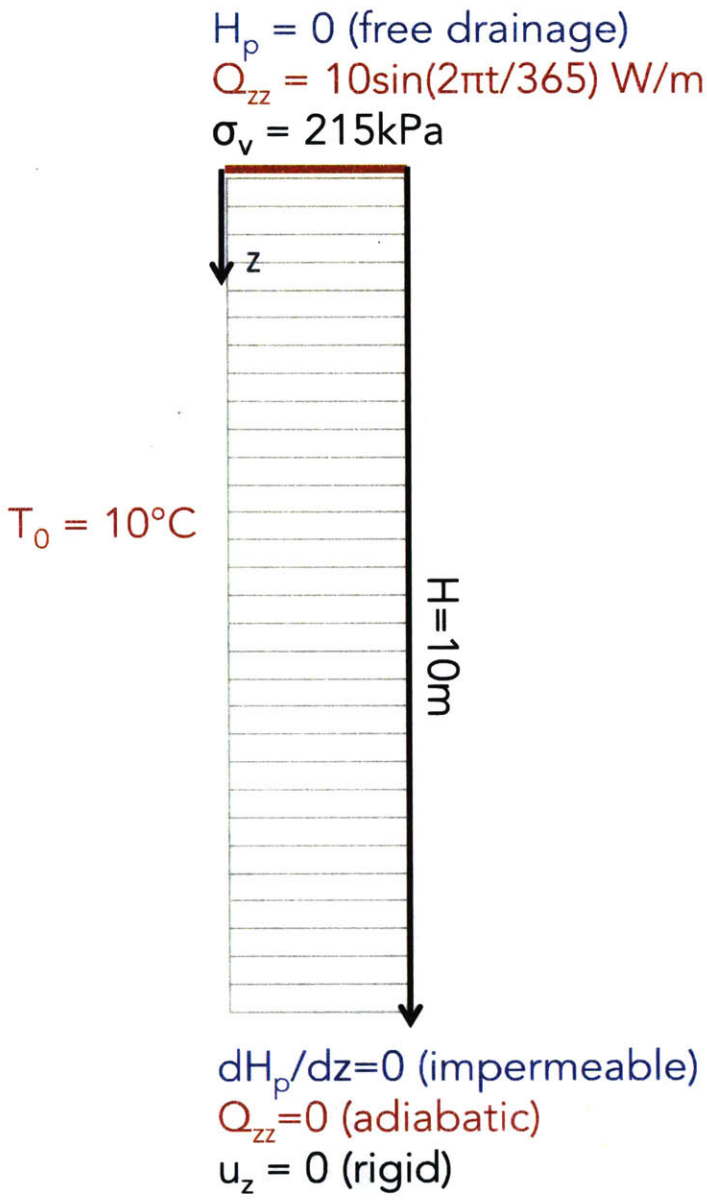

Figure 4.33: Boundary conditions assumed in 1-D simulations

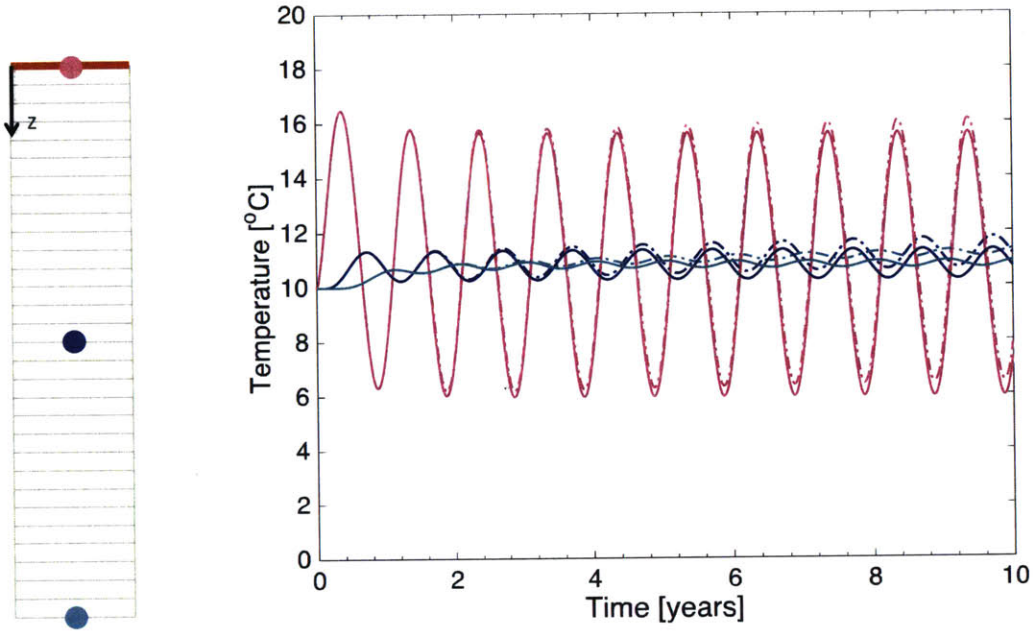

a) Temperature versus time

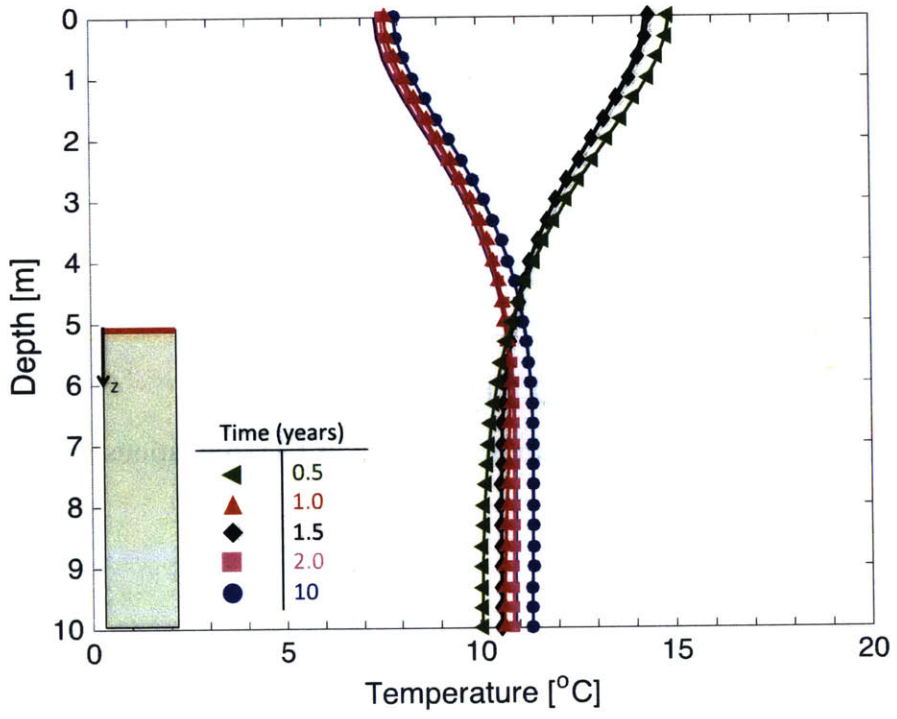

b) Temperature versus depth

Figure 4.34: Comparison of thermo-elastic (solid line) and TTS (dashed line or line with symbols) model predictions of temperature at different locations of the 1-D geometry

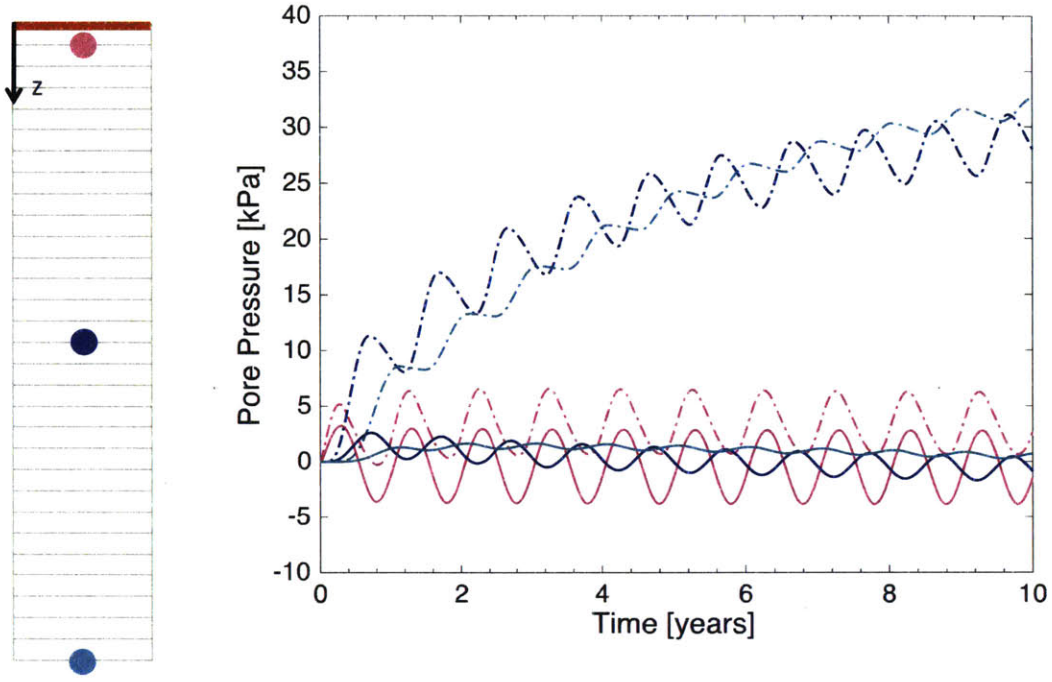

a) Excess pore pressure versus time

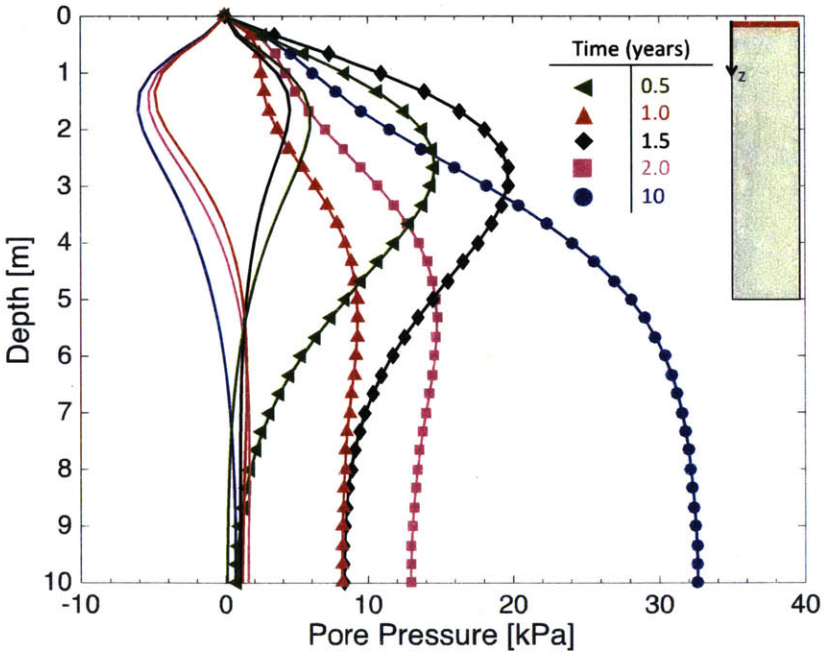

b) Excess pore pressure versus depth

Figure 4.35: Comparison of thermo-elastic (solid line) and TTS (dashed line or line with symbols) model predictions of excess pore pressure at different locations of the 1-D geometry

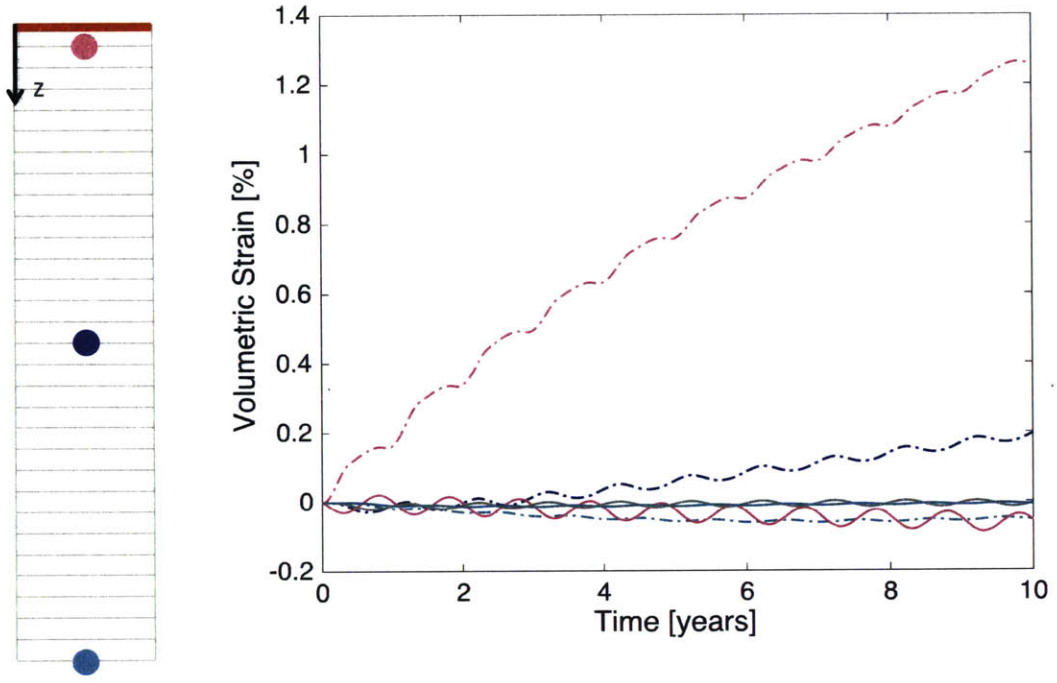

a) Vertical strain versus time

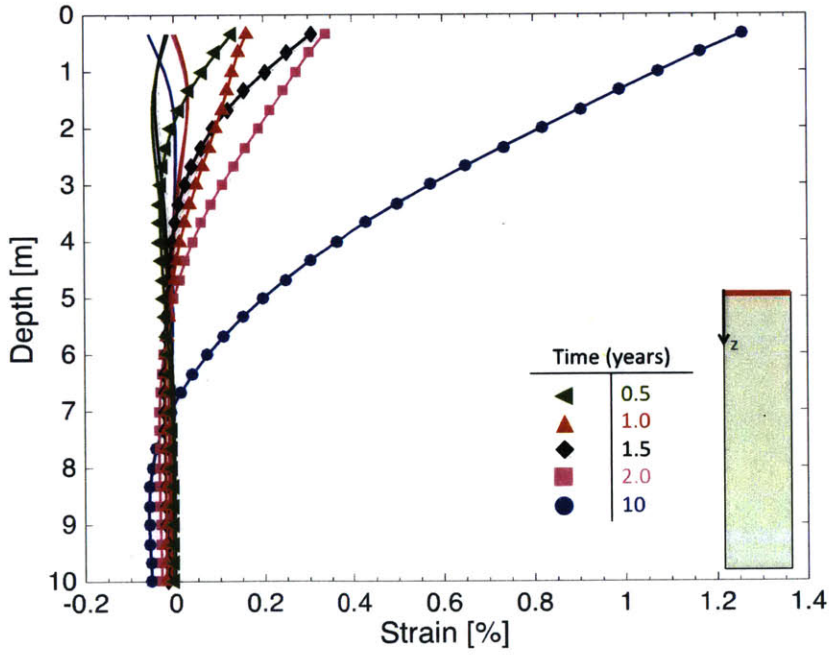

b) Vertical strain versus depth

Figure 4.36: Comparison of thermo-elastic (solid line) and TTS (dashed line or line with symbols) model predictions of vertical strain at different locations of the 1-D geometry

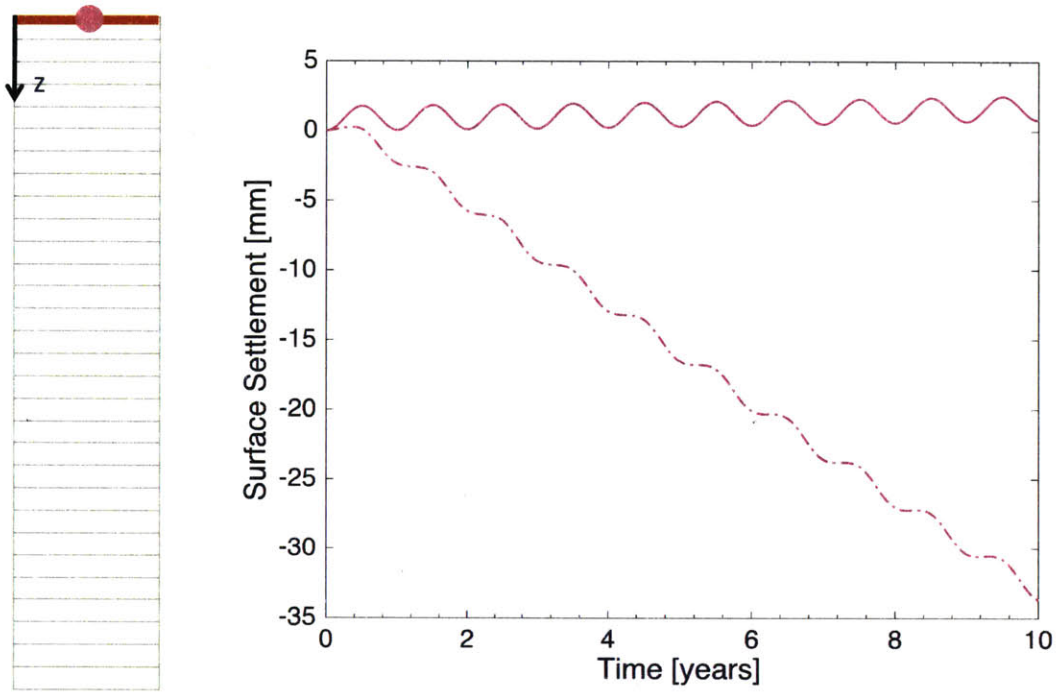

Figure 4.37: Comparison of thermo-elastic (solid line) and TTS (dashed line) model predictions of surface settlement evolution for the 1-D geometry

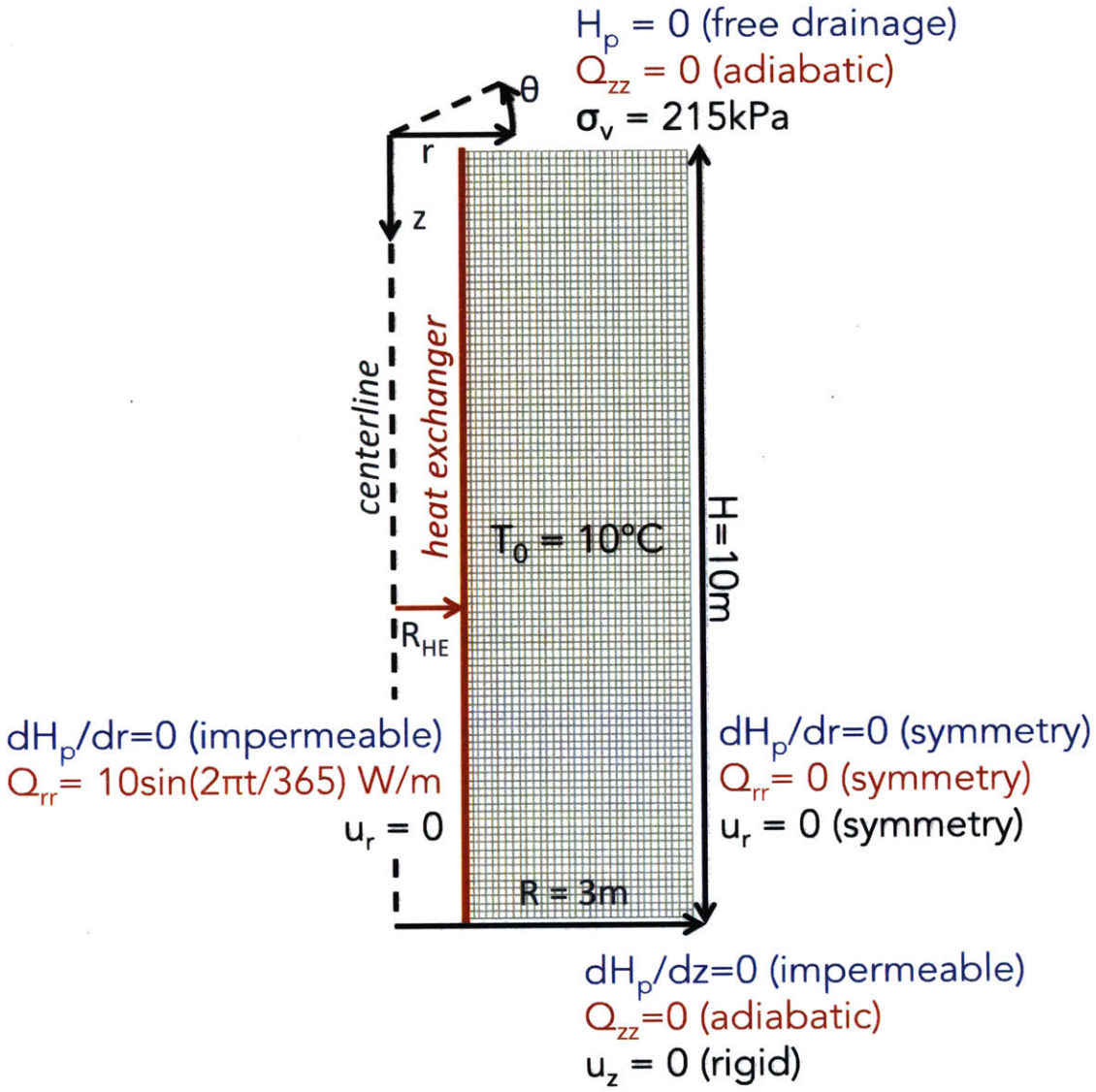

Figure 4.38: Boundary conditions assumed in axisymmetric simulations

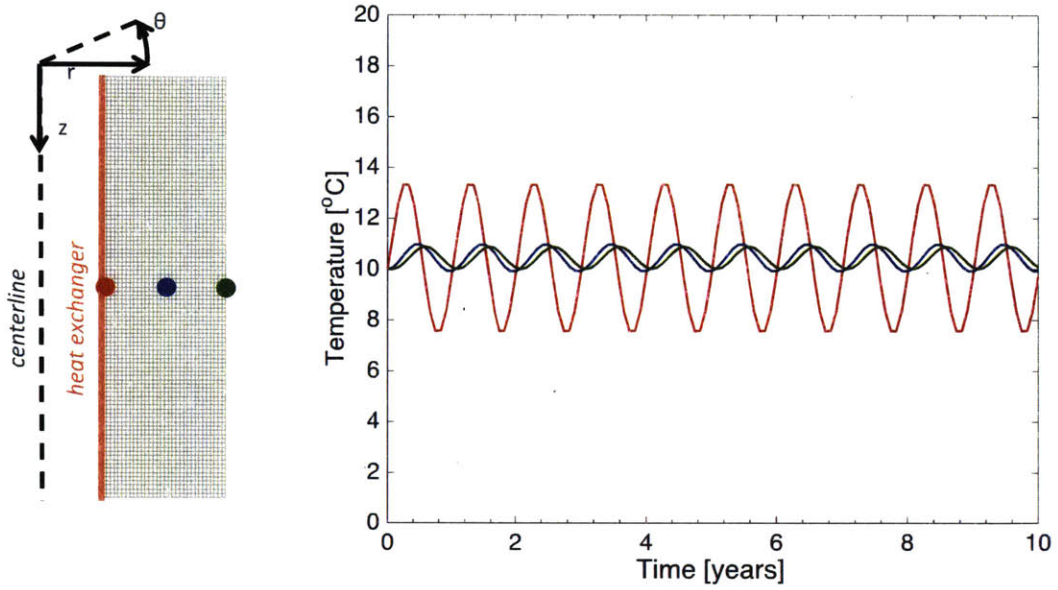

a) Points across depth z = H/2

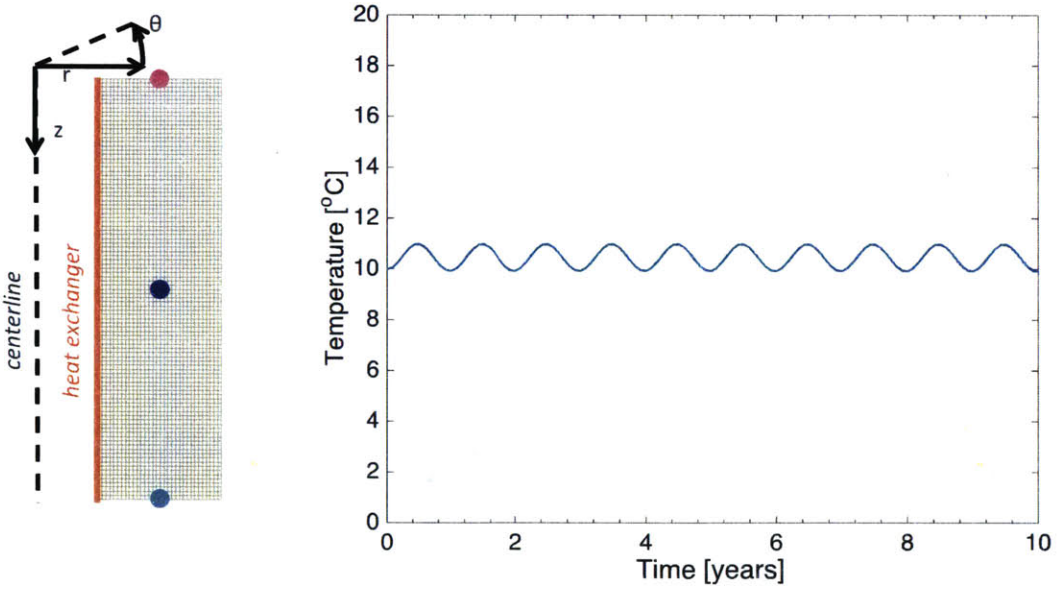

b) Points across radial distance r = R/2

Figure 4.39: Comparison of thermo-elastic (solid line) and TTS (dashed line) model predictions of temperature evolution at different points of the axisymmetric geometry

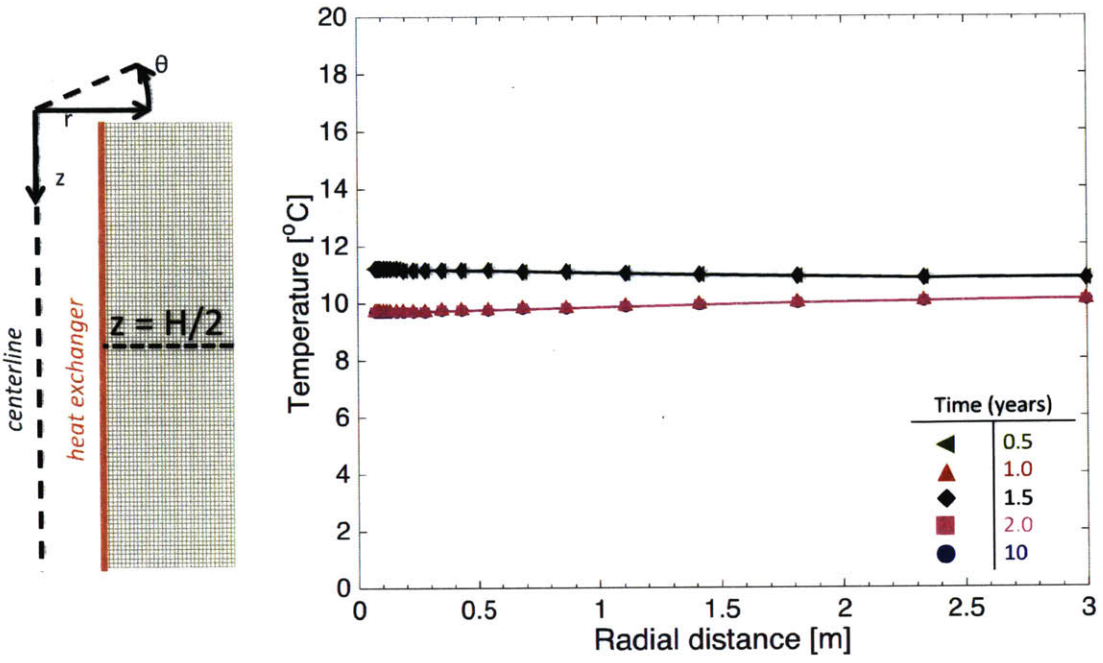

a) Temperature versus radial distance

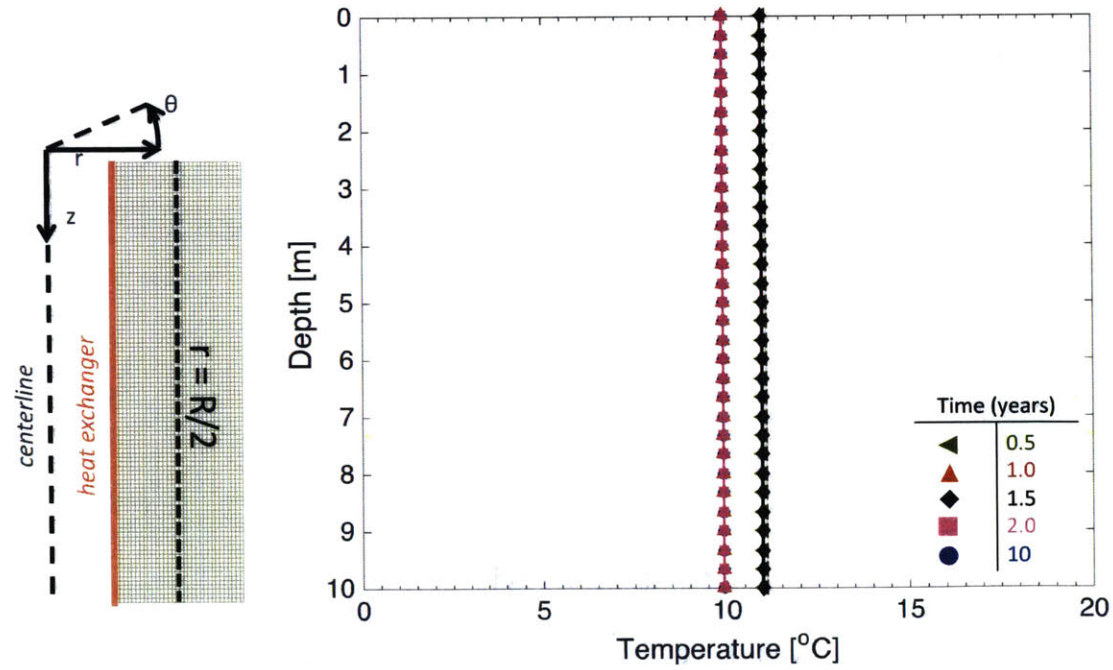

b) Temperature versus depth

Figure 4.40: Comparison of thermo-elastic (solid line) and TTS (solid line with symbols) model predictions of temperature at different snapshots in time

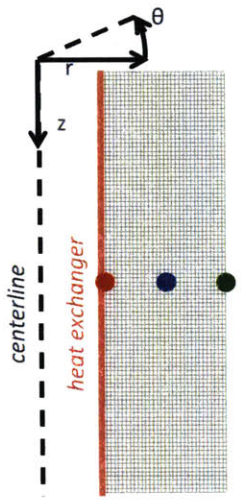

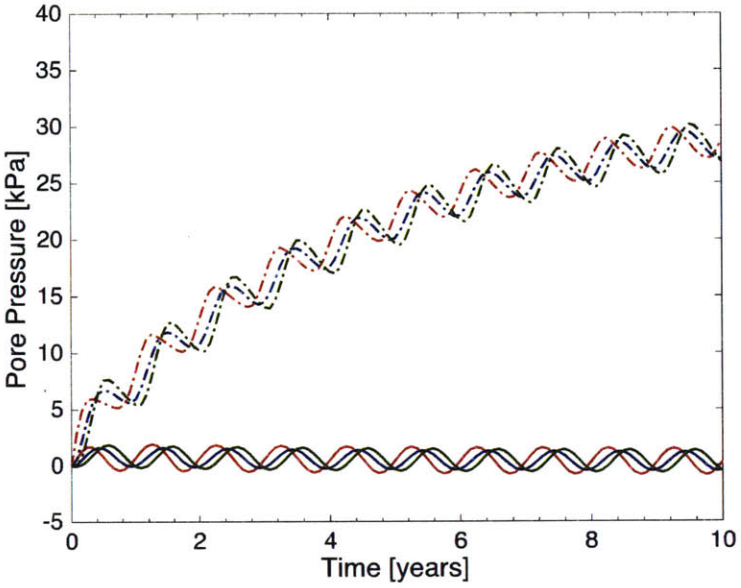

a) Points across depth z = H/2

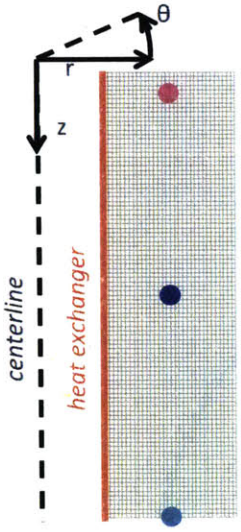

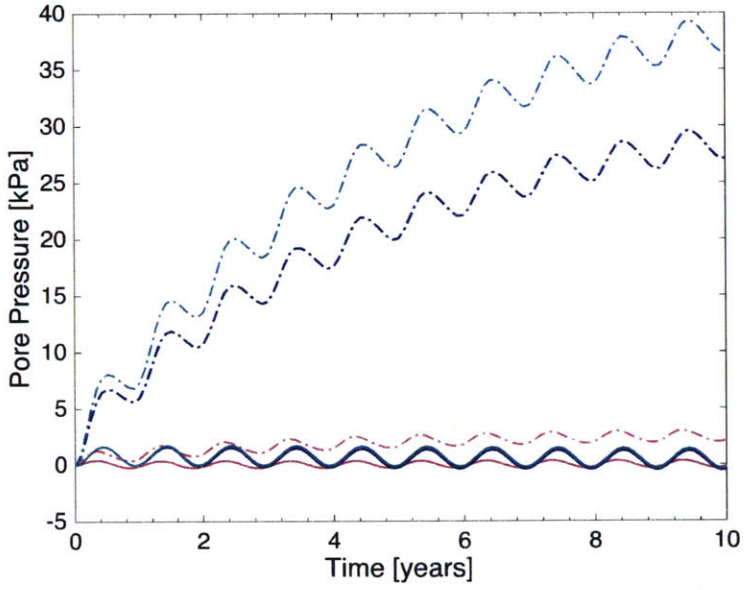

b) Points across radial distance r = R/2

Figure 4.41: Comparison of thermo-elastic (solid line) and TTS (dashed line) model predictions of excess pore pressure evolution at different points of the axisymmetric geometry

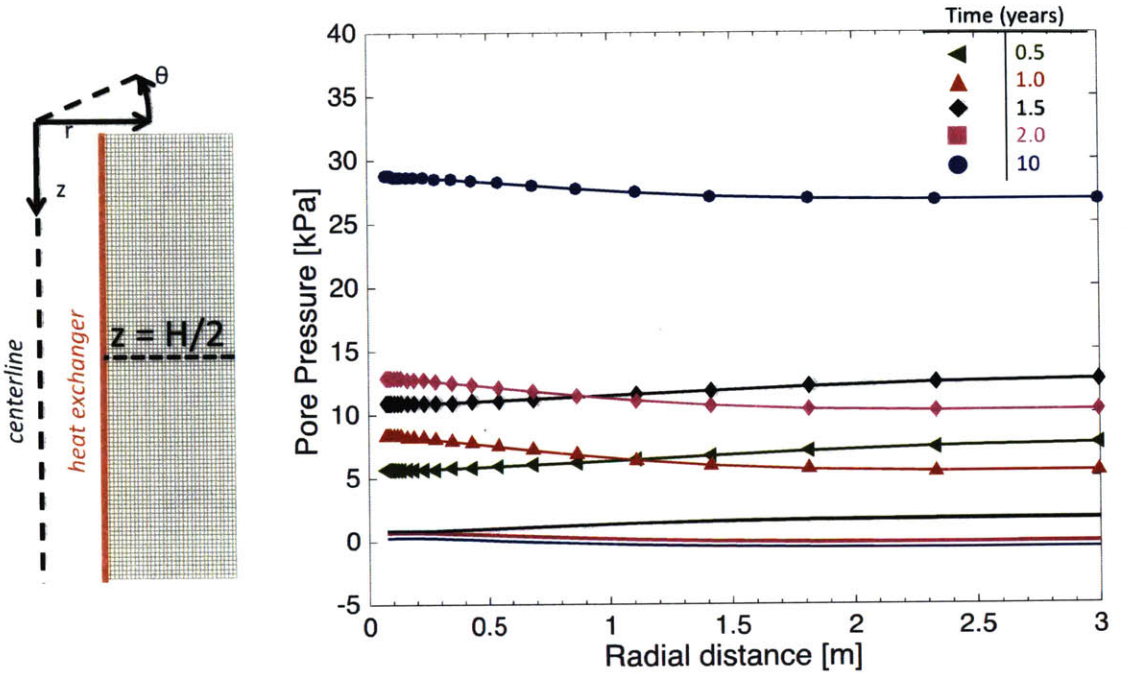

a) Excess pore pressure versus radial distance

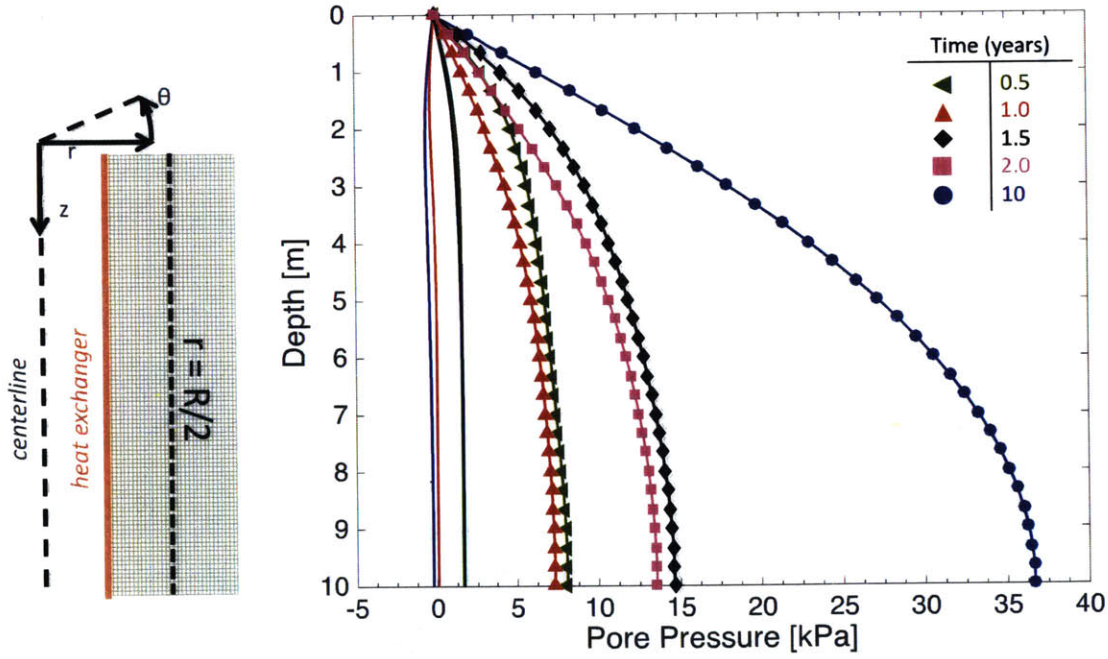

b) Excess pore pressure versus depth

Figure 4.42: Comparison of thermo-elastic (solid line) and TTS (solid line with symbols) model predictions of excess pore pressure at different snapshots in time

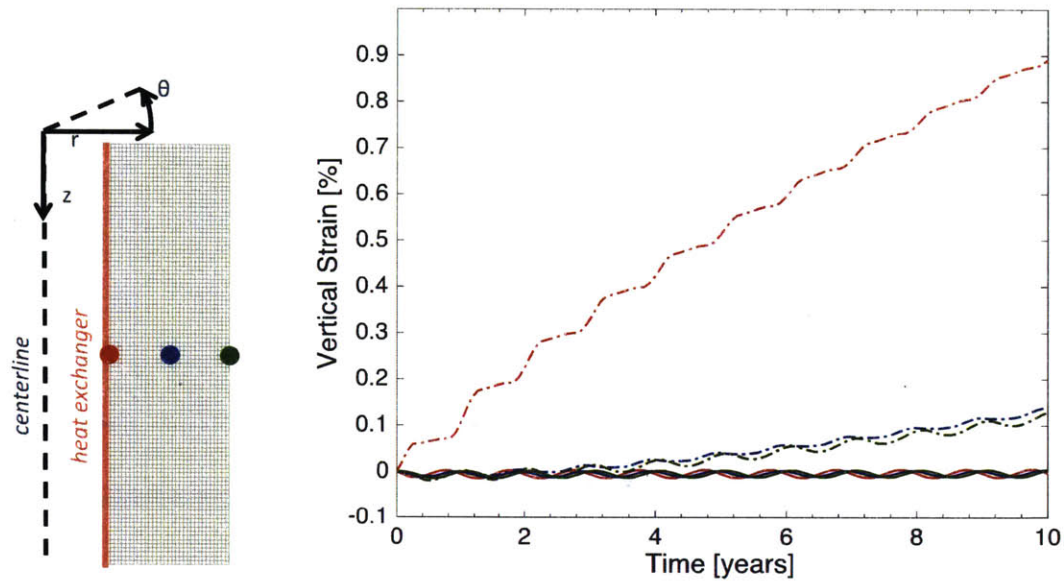

a) Points across depth z = H/2

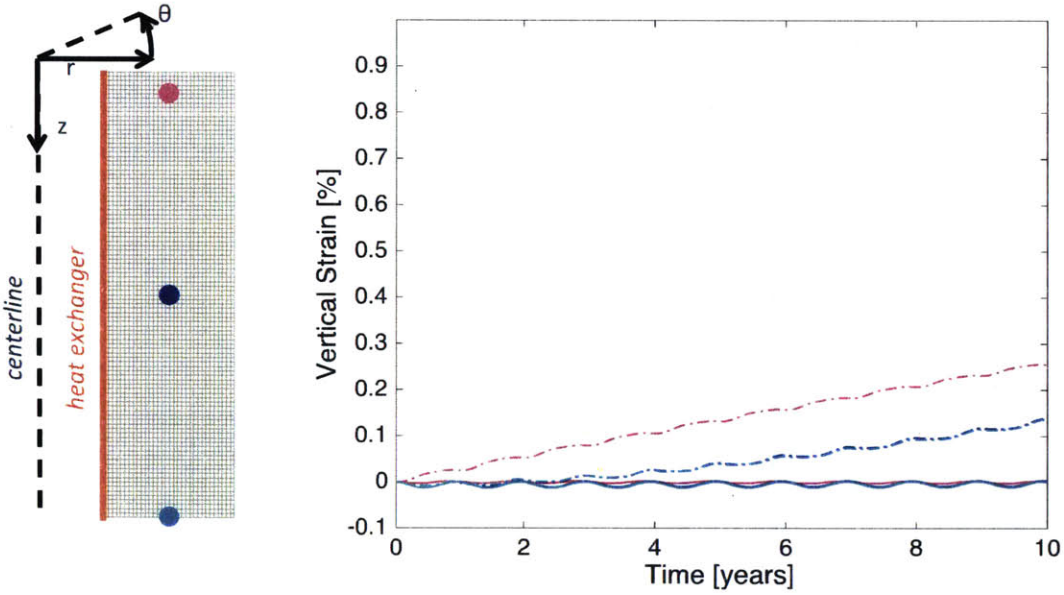

b) Points across radial distance r = R/2

Figure 4.43: Comparison of thermo-elastic (solid line) and TTS (dashed line) model predictions of vertical strain evolution at different points of the axisymmetric geometry

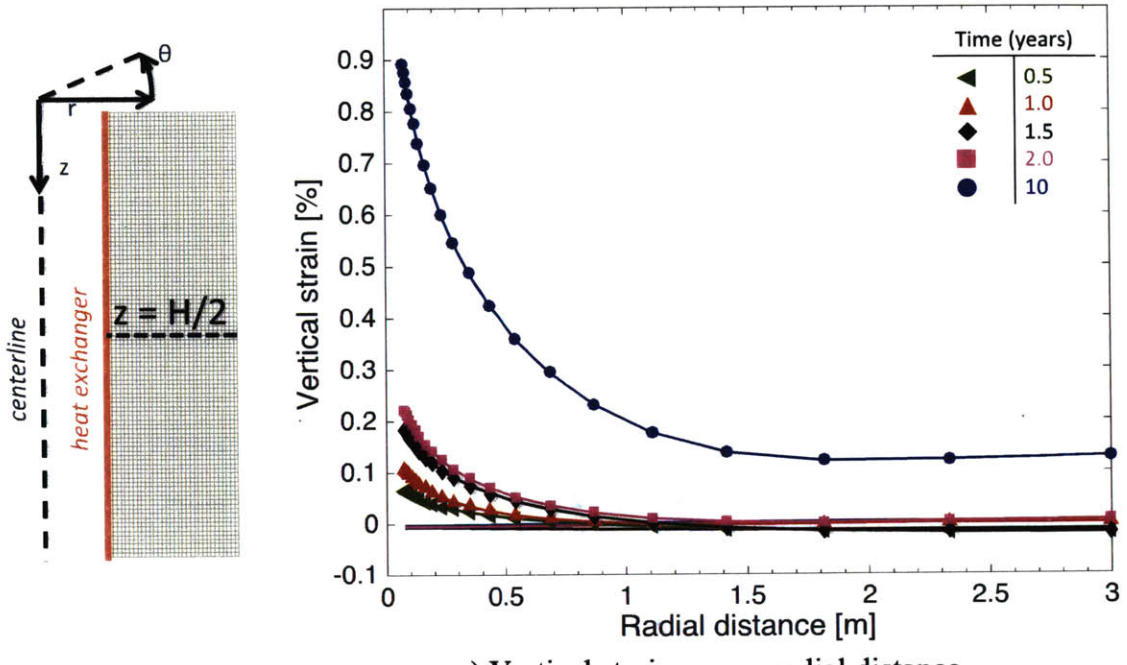

a) Vertical strain versus radial distance

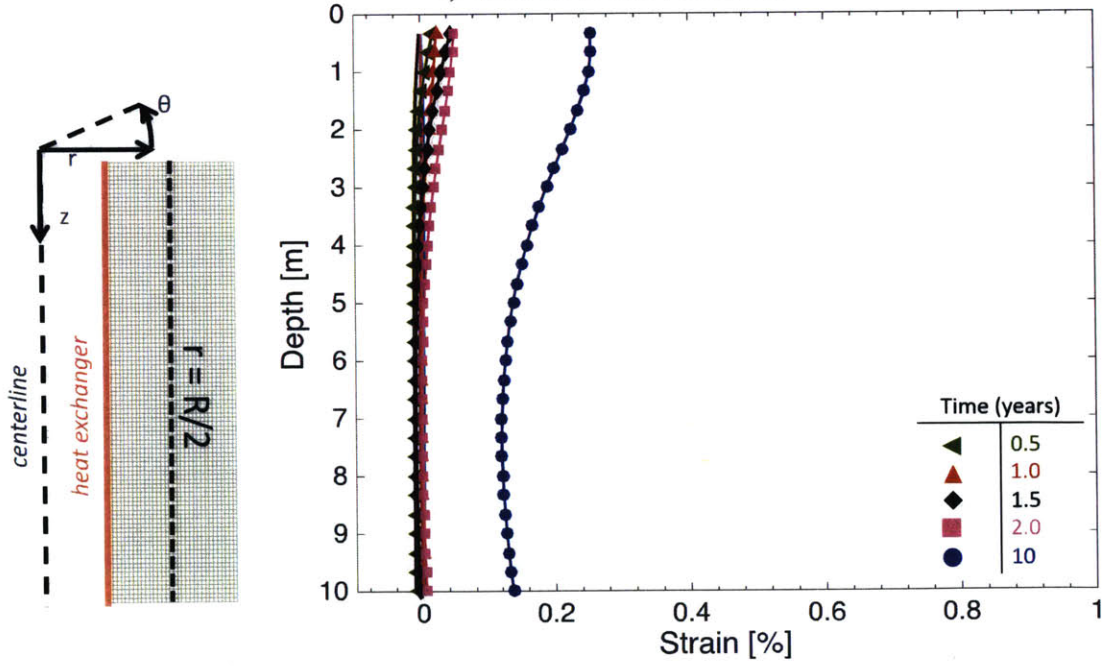

b) Vertical strain versus depth

Figure 4.44: Comparison of thermo-elastic (solid line) and TTS (solid line with symbols) model predictions of vertical strain at different snapshots in time

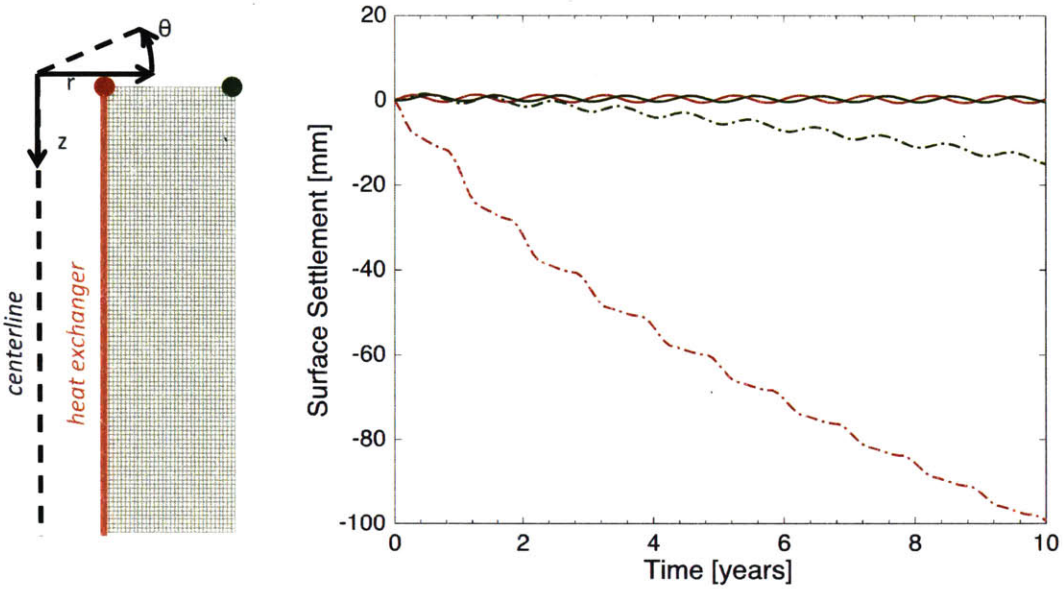

Figure 4.45: Comparison of thermo-elastic (solid line) and TTS (dashed line) model predictions of surface settlement evolution at different points of the axisymmetric geometry

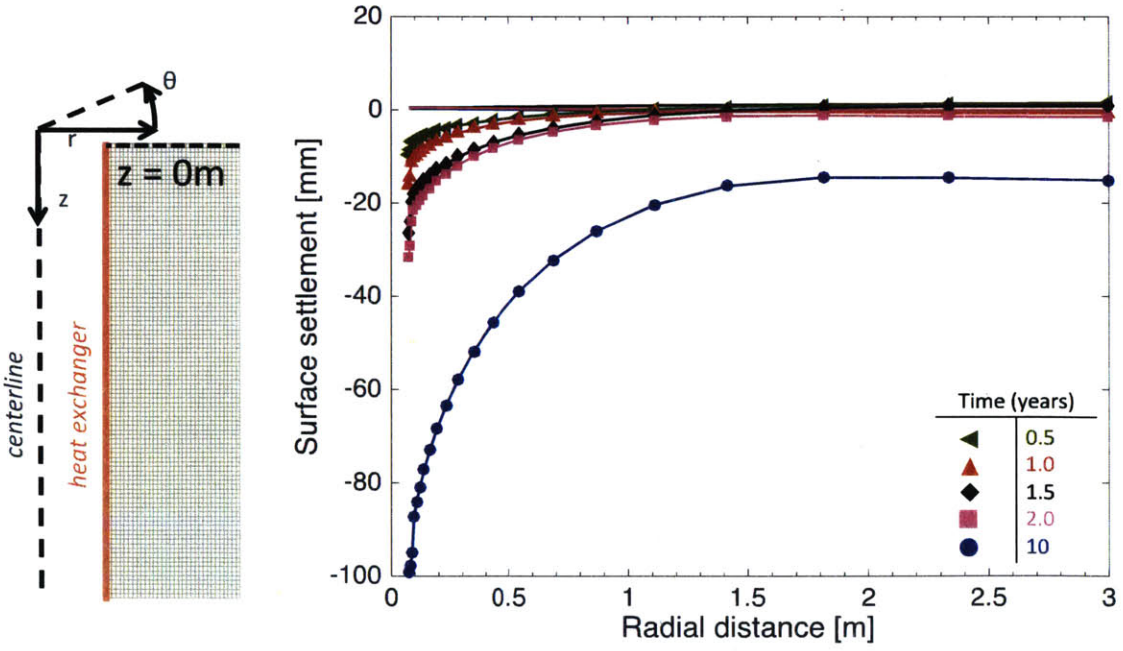

Figure 4.46: Comparison of thermo-elastic (solid line) and TTS (solid line with symbols) model predictions of surface settlement versus radial distance at different snapshots in time

Chapter 5

Parametric Study for Design of Borehole Heat Exchangers

5.1 Introduction

This chapter illustrates the role of geotechnical considerations in the design of borehole heat exchanger arrays through a hypothetical example. Following from Chapter 3, which described the calibration of the TTS model using laboratory test data for Geneva clay (Di Donna and Laloui, 2015), we now consider the design of a BHE array for a typical soil profile at the same location. We assume that a GSHP system will provide baseload, seasonal heating and cooling for a new building (i.e., heating and cooling will be designed as a hybrid system). The chapter presents a detailed parametric study to evaluate how the heat exchange rate and borehole spacing affect the predicted long-term ground response and hence, illustrate how foundation design can be linked to the design of the heat exchanger system.

5.2 Borehole Heat Exchanger (BHE) Design

The cross-section of a typical single U-tube Borehole Heat Exchanger (BHE) in the ground is shown in Figure 5.1a. The borehole is typically filled with grout to improve heat transfer and to prevent transport of contaminants within the ground. Appendix A presents conventional design recommendations from ASHRAE (Kavanaugh and Rafferty, 1997), for calculating the total required length of borehole vertical heat exchanger, L_h, needed to meet pre-specified heating and cooling loads for specified soil thermal properties. BHEs are interconnected and so the total heat exchanger length, L_h, is equal to the product of the number of BHEs, N_{BHE}, multiplied by the length of each borehole, L_{hi}:

$$L_h = N_{BHE} \times L_{hi} \tag{5.1}$$

The number of BHEs, N_{BHE}, is based on the available space for the BHE installation and thus affects the BHE array spacing, $2R$ (Figure 5.4). Since in most cases the available space is limited, BHEs are often installed as close as possible, while at the same time

trying to minimize thermal interference between adjacent heat exchangers. The maximum linear heat exchange rate is estimated by dividing the maximum estimated ground heat exchange, $Q_{max,ground}$, with the total length L_h (i.e., $Q_{max}/H = Q_{max,ground}/ L_h$).

In order to ensure that the thermal efficiency of the system does not deteriorate over time, the BHE design should ensure that the average temperature of the ground remains nearly constant from year to year. This can be done by ensuring that equal amounts of heating and cooling are exchanged with the ground in any given year with a controlled rate of heat exchange (e.g., sinusoidal seasonal pattern or other options). For example, Zymnis and Whittle (2014) illustrated the design of a hybrid shallow geothermal energy system to accommodate the heating and (most of the) cooling needs of a large office building (the balance of the cooling needs would be supplied by a traditional air conditioning system). Figure 2.29 shows the hourly heating/cooling loads for a typical large office building in Chicago, based on recommendations for DOE Commercial Benchmark Buildings (DOE, 2008). Heat exchange with the ground was modeled by a sinusoidal time function with period t = 1 year and maximum heat exchange rate Q_{max} = 24W/m (Figure 2.30). Assuming that there is zero net annual heat exchange with the ground then the average ground temperature and also efficiency of the geothermal system are expected to remain constant over the long-term.

For the purposes of the current study it is sufficient to assume a constant heat exchange versus depth. This is confirmed by a test undertaken by Acuna et al. (2009) who measured nearly constant heat exchange along the length of a 257m borehole polyethylene U-tube heat exchanger in rock. Figure 5.2a presents vertical temperature profiles obtained from a Distributed Thermal Response Test (DTRT) within the vertical borehole located in Stockholm, Sweden. The temperatures of the circulating fluid in the inlet and outlet sections of the U-tube were recorded by a distributed temperature sensing system installed inside the borehole. The average temperature of the undisturbed ground is shown in the same figure. Equation 5.2 determines the heat exchange due to the forced convection of the circulating fluid, $\dot{q}_{f,HE}$ (cf., equation 2.2):

$$\dot{q}_{f,HE} = c_f \rho_f \dot{u}_f A_U \left(\Delta T_{in} + \Delta T_{out} \right) \qquad (5.2)$$

where c_f is the specific heat capacity of the fluid, ρ_f [kg m^{-3}] is the mass density and $\dot{u}_f$

is the velocity of the circulating fluid, A_U [m^2] is the cross-section area of the U-tube ($\dot{u}_f A_U$ is the volumetric flow rate), and ΔT is the temperature difference across a length segment of the inlet and outlet sections of the U-tube in the vertical direction, as shown in Figure 5.2a.

Heat exchanger per unit length of the borehole can then be expressed from the gradients of temperatures:

$$\frac{\dot{q}_{f,HEi}}{\Delta z} = c_f \rho_f \dot{u}_f A_U \frac{\left[\left(T_{in,i} - T_{in,i+1}\right) + \left(T_{out,i+1} - T_{out,i}\right)\right]}{\Delta z} \tag{5.3}$$

where it is assumed that the convective heat flux $\dot{q}_{f,HEi}$ across a vertical distance Δz equals the change of temperature ΔT over the same vertical distance multiplied by the volumetric flow rate $\dot{u}_f A_U$, the specific heat capacity ,c_f, and the mass density, ρ_f, of the fluid. It should be noted that in the test both the heat rate from the heat source and the flow rate are maintained constant and hence steady flux conditions are reached.

For this particular test, $\dot{u}_f A_U$ = 0.50 l/s = 5 × 10^{-4} m^3/s, $c_f \rho_f$ = 4260kJ/Km^3 (with the inlet and outlet temperatures shown in Figure 5.2 measured versus depth). The calculated heat exchange with the ground, $\dot{q}_{f,HEi} / \Delta z$, for this particular heat exchanger is shown in Figure 5.2b, and is nearly constant with depth with an average value of 38.6±7.8W/m. Beier et al. (2012) suggest that the variation of heat exchange with depth is related to the change of the U-tube position within the borehole. Therefore for the purposes of the current study it is sufficient to assume a constant heat exchange with the ground along the borehole length.

5.3 Concept of Parametric Study

The parametric study is based on a project that is currently being constructed near Geneva, Switzerland, that involves the installation of a series of borehole heat exchangers that will provide heating and cooling for an overlying building. Figure 5.3a presents the characteristic local stratigraphy, which comprises 7m of rubble and alluvial deposits above a 30m thick deposit of silty Geneva clay, and compact moraine. The clay layer is further sub-divided into three 10m thick units based on measurements of stress history

(Meynet, 2015) i) normally consolidated (NC), ii) lightly overconsolidated (OC) and iii) highly OC. The groundwater table is located at the top of the clay layer (z = 7.2m). Di Donna and Laloui (2015) have undertaken high quality, drained cyclic thermal tests on natural clay samples obtained from this site and the TTS model has been calibrated for these tests, as already discussed in detail in Chapter 3.

The goal of the parametric study is to suggest optimum heat exchanger design parameters based on the thermo-hydro-mechanical response[21] of clay to long-term heating and cooling. The axisymmetric FD simulator presented in the previous chapter is used to analyze the behavior of a single heat exchanger (within a regular array) for combinations of the spacing R and maximum heat exchange Q_{max}/H (R=1 - 5m, Q_{max}/H =10 - 60 W/m), as illustrated in Figure 5.4 and Table 5.1. Each analysis considers a 50-year design life (consistent with the building itself). The heat exchanger is modeled as a cylindrical sinusoidal heat source of constant heat exchange with depth.

5.4 Simplified Geometry and Boundary Conditions

Figure 5.3b presents the simplified soil profile for the parametric study. The three Geneva clay sub-layers each have a thickness of 10m and are represented by the TTS model with input parameters previously calibrated for Geneva Clay and in-situ OCR=1.0, 2.0 and 8.0, respectively. Figure 5.3b summarizes the boundary conditions assumed in the simulations. The top layer (rubble and alluvial deposits) is modeled as a drainage surface (pressure head $H_p = p_w/\gamma_w = 0$) with a constant surface traction, V_n, equal to the weight of the building and the self-weight of the alluvium layer:

$$V_n = V_{building} + V_{alluvium} = 75 + 140 = 215\text{kPa} \qquad (5.4)$$

The weight of the building was calculated for a typical DOE commercial benchmark building, comprising 12 floors and a basement with a total floor area of 46,320m^2. Assuming that the volume occupied by the building is approximately 60m×60m×30m = 108000 m^3 and using a density $\rho_{building}$ = 250kg/m^3 for a typical steel frame building, the approximate mass is 27×10^6 kg ≈ 270MN. Therefore the resulting vertical stress from the

[21] The analyses assume that there is no convective heat transfer in the low permeability clay, an approximation validated in Chapter 4.

building is $V_{building} \approx 270\text{MN}/(60\text{m}\times 60\text{m}) \approx 75\text{kPa}$. In order to calculate the vertical stress from the alluvial deposit we have assumed a unit weight $\gamma_{alluvial} = 20\text{kN/m}^3$ and for a 7m deep layer this corresponds to $V_{alluvial} = 140\text{kPa}$. The bedrock is a compact moraine and is modeled as a rigid and impermeable boundary[22]. Regarding the thermal boundary conditions (Figure 5.3b) it has been assumed that the vertical heat exchangers extend from the ground surface and into the bedrock. Considering similar thermal properties for all layers, the top and bottom boundaries are modeled as adiabatic $\left(\partial T/\partial z = 0\right)$, since the thermal conduction is dominant in the radial direction and the heat transfer in the vertical direction is negligible (as shown in the previous chapter).

Boundary conditions assumed at the heat exchanger-soil interface are: 1) impermeable $\left(\partial H_p/\partial r = 0\right)$; 2) with radial displacement, $u_r = 0$; and 3) an imposed sinusoidal heat flux of period equal to 365 days and maximum value Q_{max}/H. The change of temperature in the radial direction (cf., equation 4.31) across the heat exchanger surface is equal to:

$$\frac{\partial T}{\partial r} = -\frac{R_b}{R_{HE}}\frac{Q_{\max}}{H}\sin\left(\frac{2\pi t}{365}\right) \qquad (5.5)$$

where t [days] is time, R_{HE} is the borehole radius, R_b [mK/W] is the effective borehole thermal resistance between the borehole wall and the fluid in the U-tube pipes. Conditions at the outer boundary represent a plane of symmetry within the BHE array and are defined by: 1) no fluid flux $\left(\partial H_p/\partial r = 0\right)$; 2) zero radial displacement $\left(u_r = 0\right)$; and 3) adiabatic conditions $\left(\partial T/\partial r = 0\right)$ (i.e., no temperature gradient) as shown in Figure 5.5.

5.5 Input Parameters and Initial Conditions

The numerical model uses a grid (NH+1 = 31, NR+1 = 21), with points equally spaced in the vertical direction ($\Delta z = 0.33\text{m}$) and variably spaced in the radial direction

[22] Due to limited information on the properties of the top and bottom layers, the boundary conditions are assumptions corresponding to a hypothetical case.

(cf., equation 4.26). The TTS model properties were selected based on the prior calibration for Geneva clay (Table 4.5). The thermal and hydraulic properties were based on samples collected from the same geographic area (Laloui et al, 2003; Laloui et al, 2006; Moreni et al, 1999) and are summarized in Table 4.4.

The properties of the heat exchanger assumed in the study are summarized in Table 5.2 and correspond to borehole with radius R_{HE} = 0.075m with a high-density polyethylene U-tube heat exchanger (λ_{pipe}=0.47W/mK) of outer diameter, 0.032m, and inner diameter 0.028m. The borehole is filled with grout of thermal conductivity equal to that for saturated Geneva clay (λ_g = 1.61W/mK) and has an equivalent thermal borehole resistance R_b = 0.1mK/W.

The initial vertical effective stress at depth z, is equal to the geostatic effective stress, $\sigma'_{v0}(z)$ calculated by:

$$\sigma'_{v0}(z) = \gamma' z + V_n \tag{5.6}$$

where G_s is the specific gravity, e_0 is the initial void ratio, γ' is the buoyant unit weight[23] and V_n = 215kPa is the surface traction assumed at the top of the clay due to the weight of the building and alluvial deposits.

In order to simulate the stress history (i.e., OCR) and obtain appropriate initial values for the state variables of the TTS model, the clay is 1-D loaded from an initial slurry condition $(\sigma'_v = 1\text{kPa})$ to $\sigma'_p = \text{OCR} \cdot \sigma'_{v0}$ and then swelled back to the current stress state, $\sigma'_v = \sigma'_{v0}$. The resulting distributions of initial vertical, horizontal and mean effective stress are shown in Figure 5.6. As suggested by Schmidt (1966) the coefficient of earth pressure at rest for OC clay, K_{0OC} can be estimated by equation 3.37. It is observed that the TTS model accurately predicts the coefficient of earth pressure at rest

[23] $\gamma' = \left(\frac{G_s + e_0}{1 + e_0} - 1 \right) \gamma_w$ for saturated soil.

for NC clay (for Geneva Clay K_{0NC} = 0.6), but underestimates K_{0OC}[24]. This is clearly a feature of the model the needs improvement.

Figure 5.7 presents the distribution of the TTS strain variables versus depth assumed at the start of the analyses (the elastic volumetric strain ε_v^e decreases as the clay is unloaded). Figure 5.8 presents the profile of intrinsic permeability, which was derived from hydraulic conductivity data reported by Di Donna and Laloui (2015) and shown in Figure 3.24c. As discussed in Chapter 4, the dependence of hydraulic conductivity k [m/s] on void ratio[25] is defined by the parameter, C_k = 0.0817. Finally, the initial ground temperature, T_0 = 10°C, is equal to the average annual air temperature in Geneva and there is zero excess pore pressure is dissipated at the start of the simulations (i.e., at t = 0, p_w = 0kPa).

5.6 Characteristic Results

This section illustrates characteristic results of thermo-hydro-mechanical behavior of Geneva clay for the case where borehole heat exchangers are positioned with radius R = 3m and maximum heat flux Q_{max}/H = 30W/m (i.e., Sim_3.0_30 in Table 5.1). Figures 5.9, 5.10 and 5.11 present predictions of temperature corresponding to different points of the axisymmetric geometry. As expected the point closest to the heat exchanger (Fig.5.9a) has the largest temperature fluctuation (T = 3 – 20°C), while points further away from the heat source exhibit a much smaller range (at r = R/2, T = 10 – 13°C; Figure 5.9b). Figures 5.9a, 5.9b, 5.9c and 5.10b show that points located at different depths, but at the same distance from the heat exchanger, have the same temperature evolution and therefore it can be deduced that the heat transfer is primarily in the radial direction. Figure 5.10 confirms that the temperature of the ground is equilibrated at the end of each year, since all of the temperature distribution lines overlap.

---

[24] For example, for OCR = 8 the TTS model predicts K_{0OC} = 0.4 as opposed to $K_{0OC} \approx 1.7$. Based on an in-depth study presented in Appendix E, it is concluded that the results of the thermo-hydro-mechanical analysis are not affected significantly by this limitation in the current TTS model formulation.

[25] $e - e_0 = C_k \log\left(\frac{\kappa}{\kappa_0}\right)$

Figures 5.12 to 5.16 present predictions of excess pore pressures corresponding to different points within the axisymmetric model. It is evident that the TTS model predicts accumulation of excess pore pressure due to long-term cyclic heating and cooling. Figure 5.12 shows the accumulation of the excess pore pressure predictions at selected points within the clay, while Figure 5.13 shows the profiles of pore pressures accumulated each decade. Figures 5.14 and 5.15 show similar results for the normalized excess pore pressures, p_w/σ'_{v0}. From Figures 5.12a and 5.14a it can be seen that points located at depth, z = H/2, and at different radial distances have the same magnitude[26] of excess pore pressure since they all have the same drainage path length (to the top of the clay layer). Figures 5.12b and 5.14b show that points located at the same radial distance, r = R/2, but at different depths have very different responses. The point near the top develops the smallest excess pore pressures due to its close proximity to the drainage boundary (alluvial deposits at z = 7.2m in Fig. 5.3) surface. On the other hand Figure 5.12b shows that the point at the base develops smaller excess pore pressures than the point at the middle for $t \leq 40$ years and the pore pressures become equal at t = 50 years as also shown in Figure 5.13b. Figure 5.14b and 5.15b show that the normalized pore pressures are always smaller at the base that at the middle. These observations are also confirmed from the contour plots in Figure 5.16. All points reach a steady state at different times. The point near the top reaches steady state conditions after 4 years ($p_{wss}/\sigma'_{v0} \approx 0.05$; Figs. 5.12b and 5.14b), while the point at the middle reaches steady-state conditions after 25 years of operation ($p_{wss}/\sigma'_{v0} \approx 0.3$), as shown in Figs. 5.13b and 5.15b, where the lines corresponding to t = 30, 40 and 50 years overlap for $z \leq 15$m. Finally, the point at the base reaches steady state conditions by the end of the 50-year simulation (Figs. 5.12b and 5.14b).

Figures 5.17 - 5.19 present predictions of vertical strain corresponding to different points within the axisymmetric model. From Figure 5.17a it is observed that the point located adjacent to the heat exchanger interface at depth, z = H/2, accumulates strain and reaches a threshold level, $\varepsilon_{zz} = 1.5\%$, after 15 years of continuous operation. Points located at the same depth but further away from the heat source also experience strain

[26] Figures 5.13a and 5.15a show that points close to the heat exchanger have slightly higher excess pore pressures.

accumulation due to cyclic heating and cooling but don't reach a limiting strain condition within 50 years of operation, primarily because temperature fluctuations are smaller further from the heat exchanger (for example at r = R/2, T = 10-13°C and $\varepsilon_{zz} = 0.9\%$ after 50 years). These observations are also confirmed from Figure 5.18a that present the same vertical strain accumulation versus temperature. Clearly the point near the heat exchanger has reached the maximum volumetric strain threshold predicted by the TTS model (i.e., further heating and cooling will not induce additional irrecoverable volumetric strain; cf., Figure 3.45) while the points further away from the heat exchanger are still accumulating strain after 50 years of operation. From Figure 5.17b it can be deduced that the vertical strains predicted by the TTS model at the top NC layer are larger compared to the vertical strain at the OC layers, because of the combined effect of two processes: 1) dissipation of excess pore pressures (due to proximity to the drainage boundary) while deeper points continue to accumulate excess pore pressures, restricting the development of volumetric strains; and 2) larger irrecoverable volumetric strains are expected for NC clay compared to OC clay (cf., Figs. 3.43 and 3.44). After 50 years, the point at the top develops $\varepsilon_{zz} = 1.6\%$ of irrecoverable volumetric strain, while the point in the middle corresponding to the lightly OC clay (i.e., OCR = 2.0) develops $\varepsilon_{zz} = 0.8\%$. On the other hand, the point at the base corresponding to the highly OC clay (i.e., OCR = 8.0) develops smaller irrecoverable dilative strains that reach a saturated steady state after 30 years ($\varepsilon_{zz} = -0.2\%$). These conclusions are also confirmed by Figure 5.18b that the points located in the NC and lightly OC clay layers develop irrecoverable contractive strains and haven't reached a threshold value after 50 years of operation, while the point in the deepest, highly OC layer has mobilized its limiting strain. Figure 5.19 shows decadal distributions of vertical strain versus radial distance and depth. From Figure 5.19a it is concluded that the points closer to the heat exchanger develop larger contractive strains compared to points further away, due to the larger temperature fluctuation and also that volumetric strains accumulate every ten years. Figure 5.19b confirms that points in the NC and lightly OC layers develop irrecoverable contractive strains while points in the highly OC layer develop dilative (i.e., extensive) strains.

Figure 5.20 shows predictions of the settlement evolution at three different locations on the surface of the clay. It is observed that the point located on the heat exchanger reaches a limiting settlement ($u_z \approx 0.37$m) after 15 years of operation while points further away experience smaller settlements that continue to accumulate. Figure 5.21 shows that surface settlements decrease from a maximum value at the heat exchanger to a minimum at the outer boundary of the model (i.e., mid-point between BHEs), and highlights the accumulation of settlements over decadal timescales. It confirms the observation that the point closest to the heat exchanger reached this threshold after 15 years and remains unchanged thereafter (i.e., no further settlement for t=20, 30, 40 and 50 years) while points further away continue to accumulate surface settlements every 10 years.

Figure 5.22a presents the predicted surface settlement versus radial distance at time t = 50 years and defines the key settlement trough characteristics: 1) maximum settlement, $u_{z,max} = 0.37$m; 2) differential settlement, Δu_z, equal to the difference between maximum and minimum settlement, $\Delta u_z = u_{z,max} - u_{z,min} = 0.18$m; and 3) area average settlement, $u_{z,ave} = 0.21$m, which is calculated using:

$$u_{z,ave} = \frac{\sum_{i=2}^{NR+1} \frac{u_{z,i} + u_{z,i-1}}{2} \pi\left(r_i^2 - r_{i-1}^2\right)}{\pi\left(R^2 - R_{HE}^2\right)} \tag{5.7}$$

where $\frac{u_{z,i} + u_{z,i-1}}{2}$ is the average settlement of a ring i located at $r = r_i$ and with an area equal to $\pi\left(r_i^2 - r_{i-1}^2\right)$ as shown in Figure 5.23.

Figure 5.22b shows a plan view of the surface settlement distribution after 50 years, where it can be deduced that most of the soil settles by $u_z \approx u_{z,ave} = 0.21$m and points close the heat exchanger experience large differential settlement.

Figure 5.24 shows a contour plot of the predicted settlements after 50 years. It can be seen that most of the ground surface settlements occur in the upper NC layer that produces large contractive strains (compared to the OC layers), while the highly OC layer experiences small heave due to the dilative strains.

5.7 Guides on Limiting Routine Foundation Settlements

The FD simulator predicts ground settlements as a result of the thermo-hydro-mechanical response of clay to long-term cyclic heating and cooling. In order to ensure that the geothermal installation doesn't affect the serviceability of the overlying structure, it is important to keep the long-term settlements below specified limits. Serviceability is very subjective and case specific, since it depends on the type of the building and its function, thus making the process of selecting general settlement limits very complex. For a thorough soil-structure interaction analysis, it is critical to understand how the building will respond to deformation and what the consequences of such deformation will be to its function. Burland and Wroth (1974) proposed a consistent set of definitions based on the predicted displacements of a number of discrete points, shown in Figure 5.25 and developed a deep beam model to explain the role of soil and structural stiffness. Often the criterion used for limiting deformation is the maximum relative rotation (angular distortion) β. Skempton and MacDonald (1956) conclude that in order to avoid cracking in walls and partitions, $\beta < 1/300$ and that values in excess of 1/500 should be avoided. Design guides are largely based on this work (e.g., Eurocode 7). However, this criterion implies that damage results from shear distortion within the building, which is not always the case (Burland et al., 1977).

Burland et al (1977) proposed "routine guidelines" for limiting foundation settlements based on empirical performance data. Figure 5.26 shows measurements of maximum foundation differential settlement, Δu_z, plotted against maximum total settlements, u_z, from 51 buildings with raft foundations on clay. It is observed that no damage has been reported for differential settlements less than 125mm and total settlements less than 250mm. As pointed out by the authors, even this differential settlement limit is conservative since the building with significant damage that had Δu_z = 125mm was reported as being founded on fill. From Figure 5.26 it is also clear that many buildings on rafts have undergone significant total settlements with no reported damage.

The settlement limits deduced from Figure 5.26 refer to foundation settlements and not ground settlements. A soil/structure interaction study involves estimating the maximum relative deflections and rotations likely to be experienced by the structure by allowing for the influence of stiffness of the superstructure. It can be deduced that a

flexible raft foundation would have settlements very similar to the ground settlements. In contrast, a very rigid raft foundation would experience significantly smaller differential settlements (Burland et al., 1977).

5.8 Results of Parametric Study

Detailed thermo-hydro-mechanical analyses were carried out for 54 combinations of heat exchanger half-spacing R and maximum heat exchange Q_{max}/H (Table 5.1), with the goal to identify optimum heat exchanger design specifications. Figure 5.27a compares 50-year surface settlements for constant R = 3m and maximum heat flux Q_{max}/H = 10-60W/m. It is observed that as heat exchange increases, the average surface settlement, $u_{z,ave}$, increases but the differential settlement, Δu_z, decreases. Figure 5.27b compares 50-year surface settlements for constant heat flux, Q_{max}/H = 30W/m, and BHE spacing ranging from, R = 1 - 5m. It can be seen that as the spacing increases, the average surface settlement, $u_{z,ave}$, decreases but the differential settlement, Δu_z, increases. These observations result from complex thermo-hydro-mechanical response of the clay and could have not been predicted in advance, based on simple thermo-mechanical concepts.

Figure 5.28 presents contour plots of average and differential long-term surface settlements for all combinations of half-spacing, R, and BHE heat exchange, Q_{max}/H. It is observed that the maximum differential settlement (Δu_z = 0.45m) occurs for R = 5m and Q_{max}/H = 10W/m, while the largest average settlement ($u_{z,ave}$ = 0.45m) occurs for R = 1m and Q_{max}/H = 60W/m. Based on the routine settlement limits recommended by Burland et al (1977), the contour lines corresponding to Δu_z = 0.125m and $u_{z,ave}$ = 0.250m are clearly marked in Figures 5.28a and 5.28b, respectively. From Figure 5.29 it is observed that combining these two lines in a single plot results in a design space of R- Q_{max}/H solutions, where the ground surface settlements are below the recommended limits. It should be stressed that these analyses adopt a conservative approach by assuming a fully flexible raft foundation (i.e., one that has the same differential settlements as the ground). If we considered the bending stiffness of the foundation itself then the ground differential settlement limit would increase (i.e., a contour line to the right of the current one would have been selected) and therefore, the design space would increase significantly. Furthermore, as shown in Figure 5.30 the maximum surface settlements predicted by the

simulator, $u_{z,max} \geq 0.250$m (i.e., are higher than the recommended limit) and hence, we have applied the 'total surface settlement' to the area average computed settlements.

Figures 5.31a and 5.31b present contour plots of computed minimum and maximum temperatures, respectively for different combinations of half-spacing R and heat exchange Q_{max}/H. It is observed that the maximum temperature predicted inside the design space is 29°C, which is well below the boiling temperature of water. However, the minimum temperature predicted is -4°C for R = 3.2m and Q_{max}/H = 53W/m and hence the solutions recommended at the top right part of the design space should be avoided, in order to prevent freezing of the surrounding clay. Figure 5.32 presents contour plots of maximum and minimum normalized excess pore pressures predicted for different combinations of half-spacing R and heat exchange Q_{max}/H. It is observed that the excess pore pressures range from $\Delta p_w/\sigma'_{v0}$ = -0.04 to 0.4 inside the recommended design space.

5.9 Summary and Conclusions

The chapter describes a detailed parametric study that has been carried out to understand how the long-term ground movements are controlled by thermo-mechanical properties of the clay, and design properties of the borehole heat exchanger (array spacing, 2R, and maximum BHE heat exchange, Q_{max}/H). It is accurate to assume that the heat exchange with the ground is nearly constant with depth, as shown by the experiment undertaken by Acuna et al. (2009).

The parametric study has shown that continuous, long-term operation of BHE arrays generates significant irreversible ground settlements. Contour plots of long-term surface settlements induced by combinations of R and Q_{max}/H clearly demonstrate the long-term effects of continuous heating and cooling of Geneva clay and suggest optimum design parameters that ensure long-term serviceability of the overlying building foundations. A design space has been derived, with combinations of R and Q_{max}/H that produce surface settlements below routine design limits for raft foundations (Burland et al., 1977). Furthermore, it is concluded that controlling the net annual heat exchange with the ground to be zero (e.g., from a sinusoidal heat source) maintains the average ground temperature in the long-term and hence does not deteriorate the efficiency of the BHE array.

Qmax/H [W/m]	Radius R [m]								
	1.0	1.5	2.0	2.5	3.0	3.5	4.0	4.5	5.0
10	Sim_1_10	Sim_1.5_10	Sim_2_10	Sim_2.5_10	Sim_3_10	Sim_3.5_10	Sim_4_10	Sim_4.5_10	Sim_5_10
20	Sim_1_20	Sim_1.5_20	Sim_2_20	Sim_2.5_20	Sim_3_20	Sim_3.5_20	Sim_4_20	Sim_4.5_20	Sim_5_20
30	Sim_1_30	Sim_1.5_30	Sim_2_30	Sim_2.5_30	Sim_3_30	Sim_3.5_30	Sim_4_30	Sim_4.5_30	Sim_5_30
40	Sim_1_40	Sim_1.5_40	Sim_2_40	Sim_2.5_40	Sim_3_40	Sim_3.5_40	Sim_4_40	Sim_4.5_40	Sim_5_40
50	Sim_1_50	Sim_1.5_50	Sim_2_50	Sim_2.5_50	Sim_3_50	Sim_3.5_50	Sim_4_50	Sim_4.5_50	Sim_5_50
60	Sim_1_60	Sim_1.5_60	Sim_2_60	Sim_2.5_60	Sim_3_60	Sim_3.5_60	Sim_4_60	Sim_4.5_60	Sim_5_60

Table 5.1: Scope of parametric study for BHE arrays in Geneva clay profile

Input constant	Meaning	Selected value
$r_{p,int}$ [m]	Inner radius of HDPE U-tube pipe	0.014
$r_{p,ext}$ [m]	Outer radius of HDPE U-tube pipe	0.016
R_{HE} [m]	Borehole radius	0.075
L_u [m]	Center-to-center distance between U-tube pipes	0.055
A_U [m^2]	Cross-section area of U-tube pipe	6.16×10^{-4}
h_{conv} [$W/m^2 K$]	Fluid convection coefficient	1000
λ [W/m K]	Coefficient of thermal conductivity of saturated clay	1.61
λ_{pipe} [W/m K]	Coefficient of thermal conductivity of HDPE pipe material	0.47
λ_{grout} [W/m K]	Coefficient of thermal conductivity of grout	1.61

Table 5.2: Properties of U-tube assumed for BHE arrays in Geneva clay profile

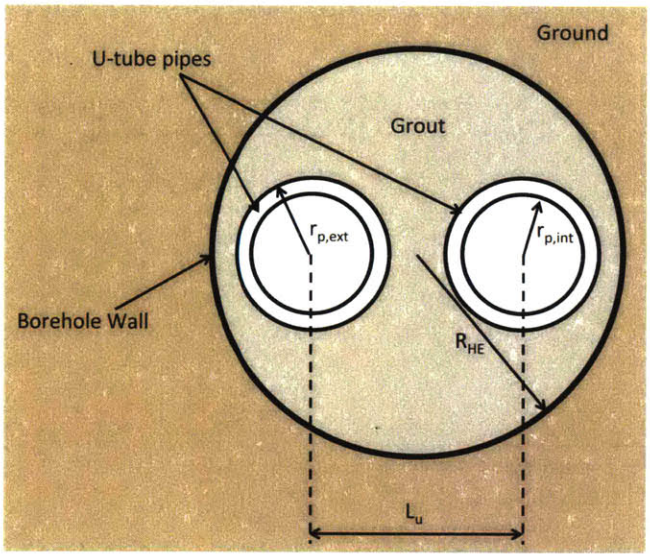

Figure 5.1: Cross-section of a typical heat exchanger borehole
(after Philippe & Bernier, 2010)

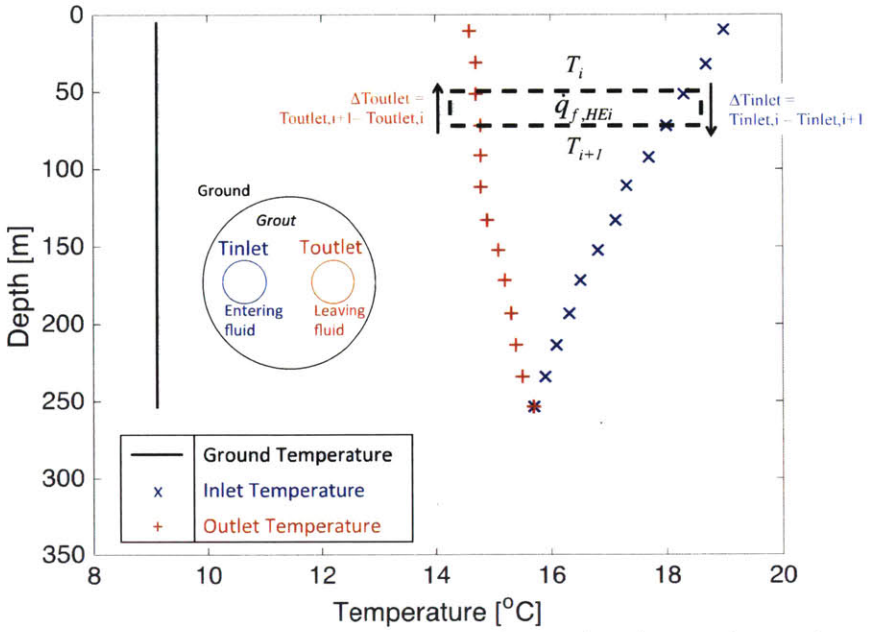

a) Measured fluid temperatures in inlet and outlet sections of u-tube

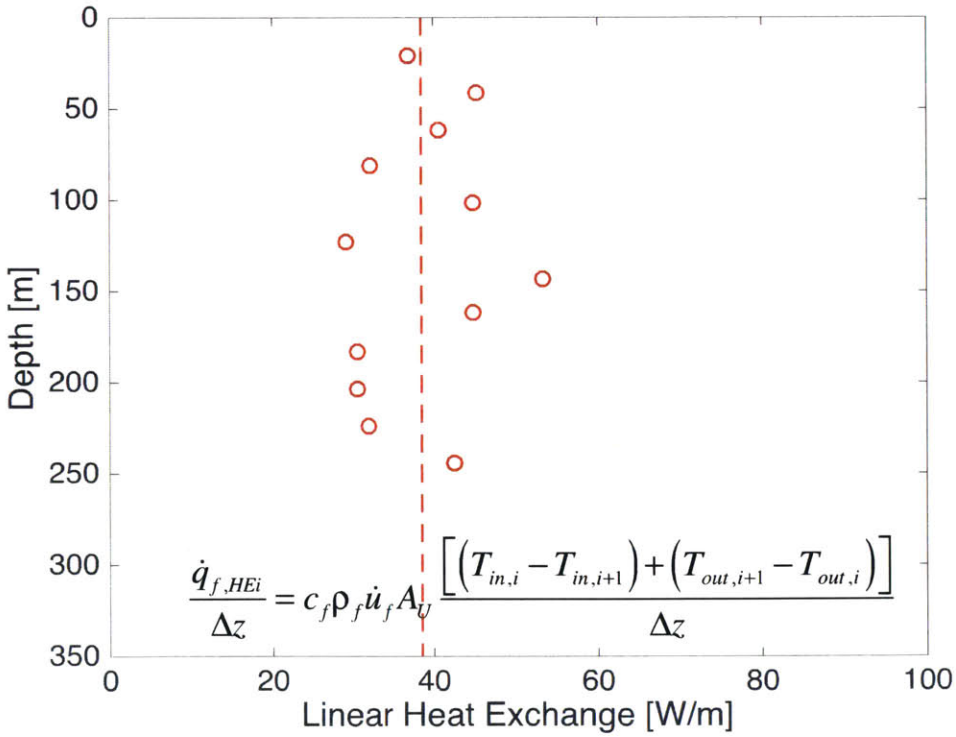

b) Calculated heat exchange from circulating fluid

Figure 5.2: Distributed Thermal Response Test (DTRT) measurements in a u-tube borehole heat exchanger (after Acuna et al, 2009)

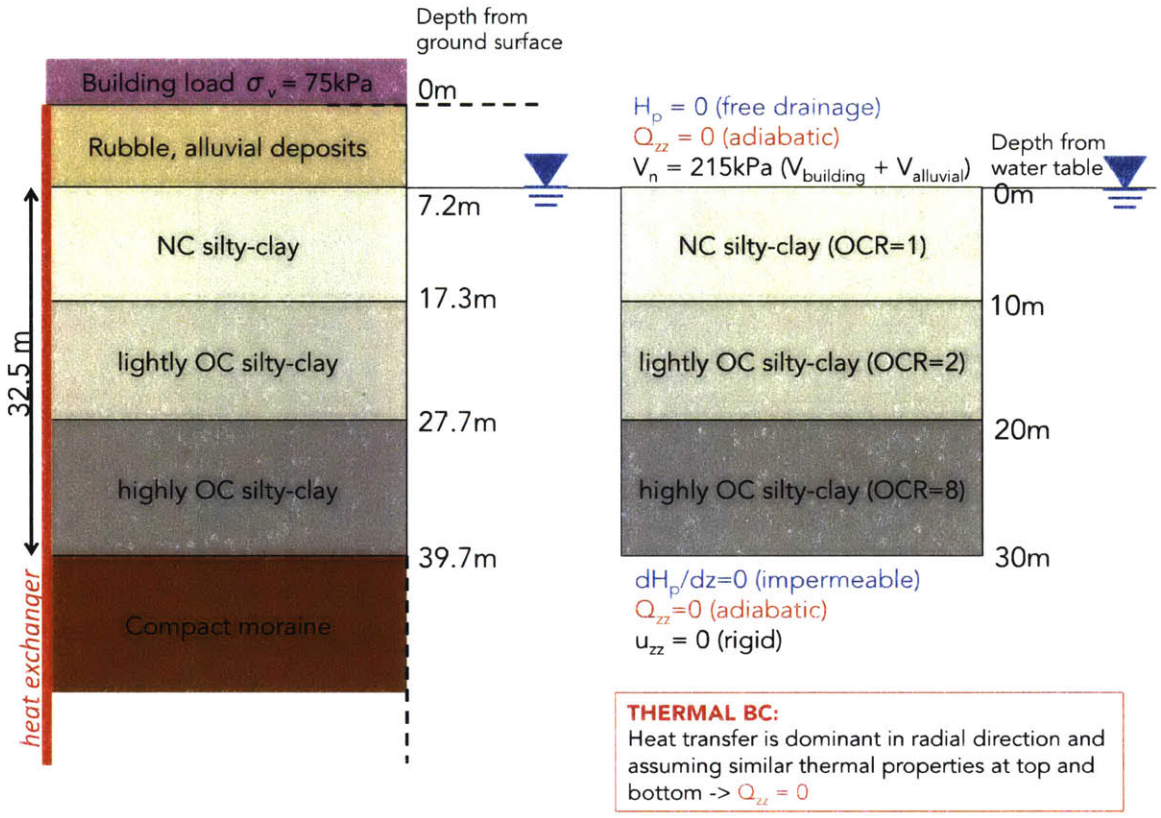

a) Actual soil stratigraphy recorded near Geneva, Switzerland

b) Simplified soil stratigraphy assumed in parametric study

Figure 5.3: Soil profile considered in parametric study

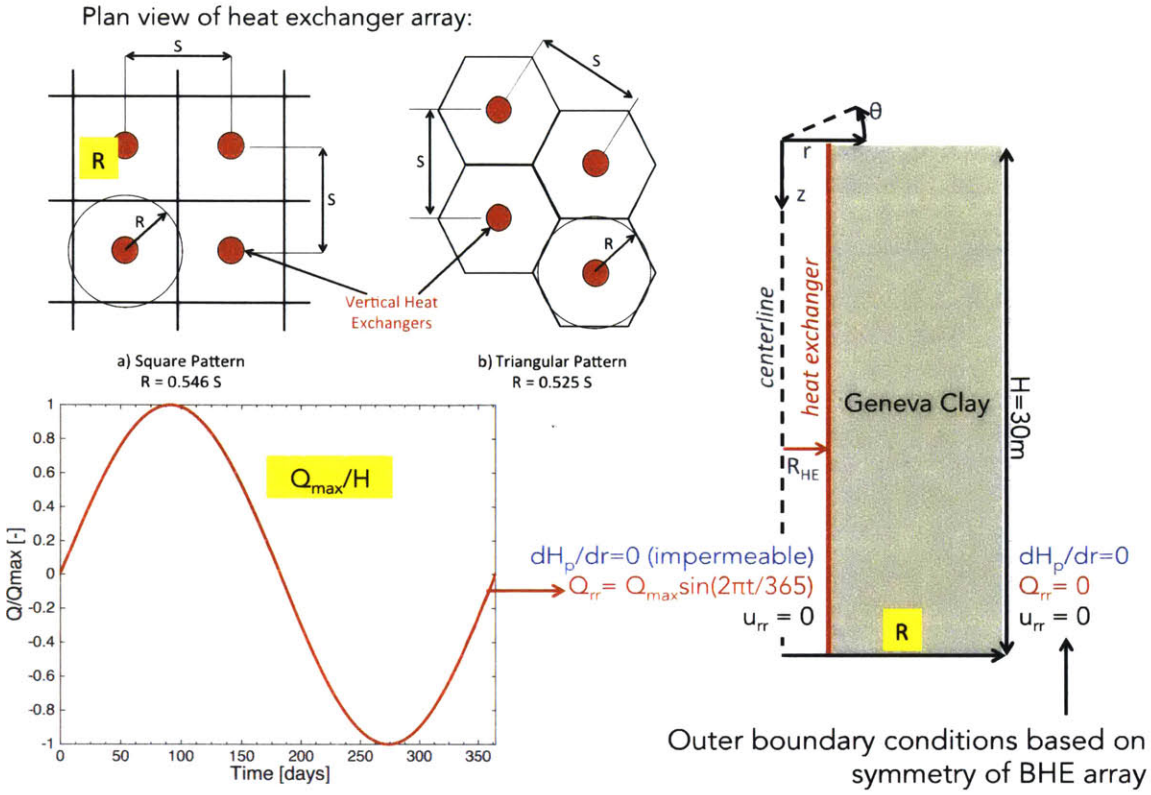

Figure 5.4: Concept of proposed parametric study

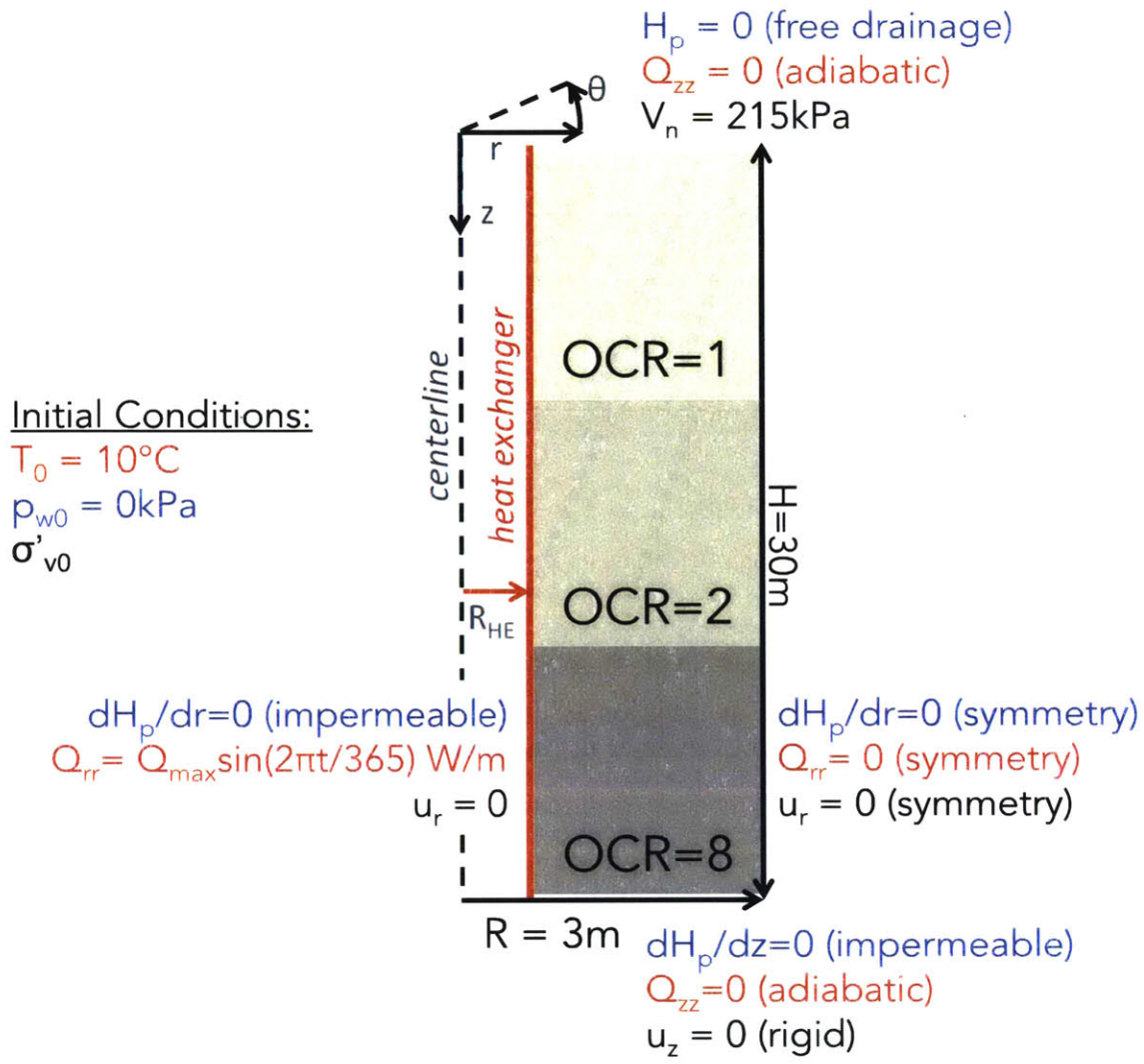

Figure 5.5: Boundary conditions assumed in parametric analyses of borehole heat exchanger in Geneva clay

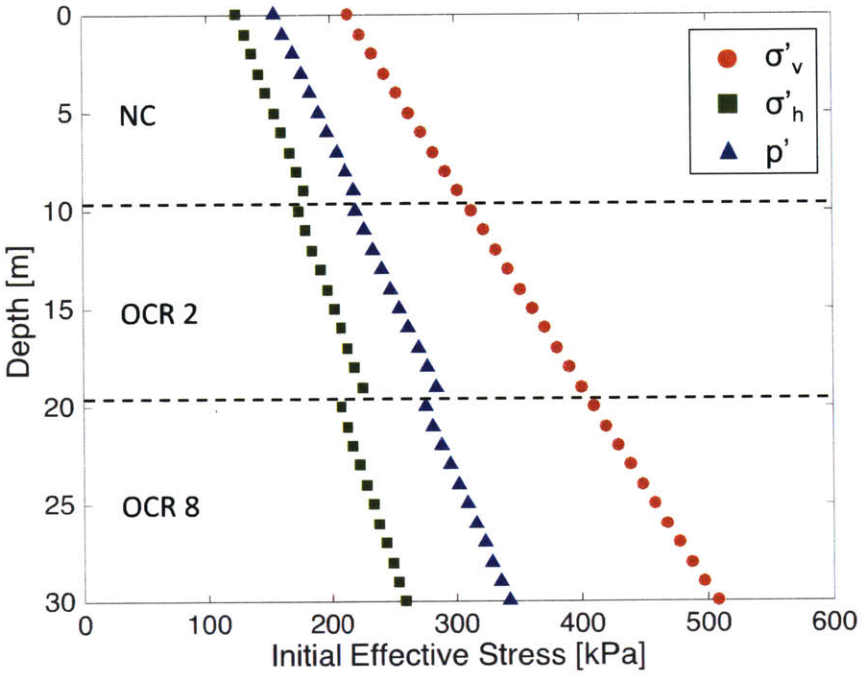

Figure 5.6: Initial effective stress distribution assumed in parametric analyses of borehole heat exchanger in Geneva clay

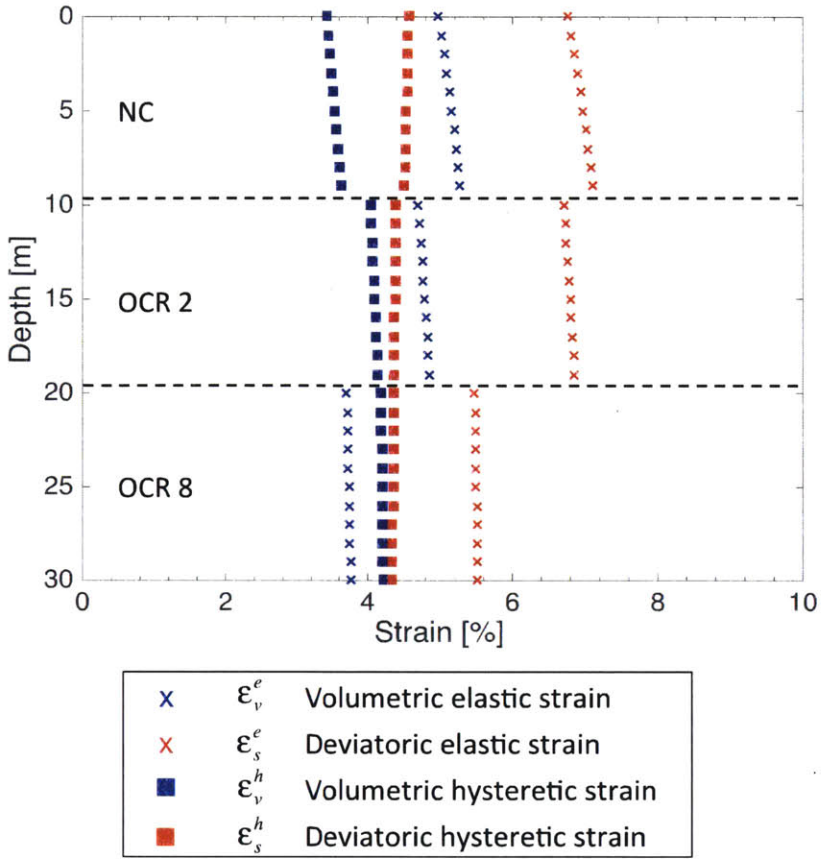

Figure 5.7: Distribution of initial TTS strain variables assumed in parametric analyses of borehole heat exchanger in Geneva clay

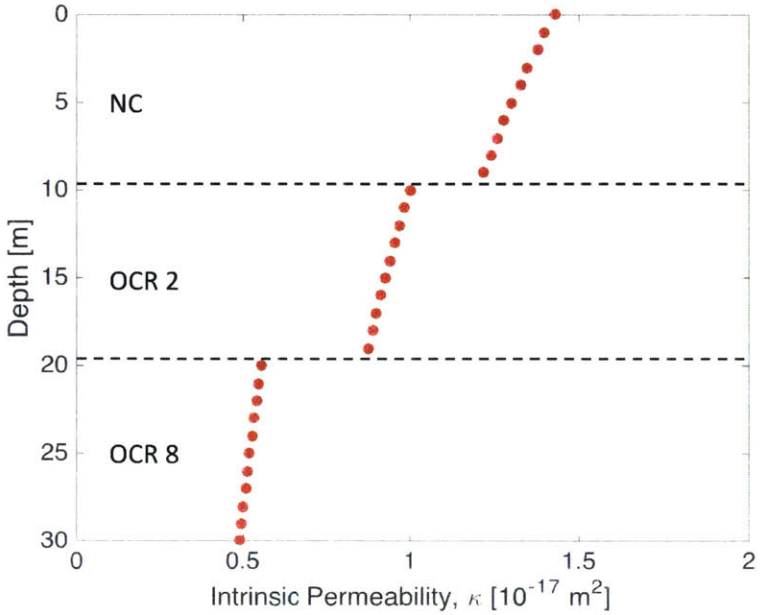

Figure 5.8: Intrinsic permeability distribution assumed in parametric analyses of borehole heat exchanger in Geneva clay

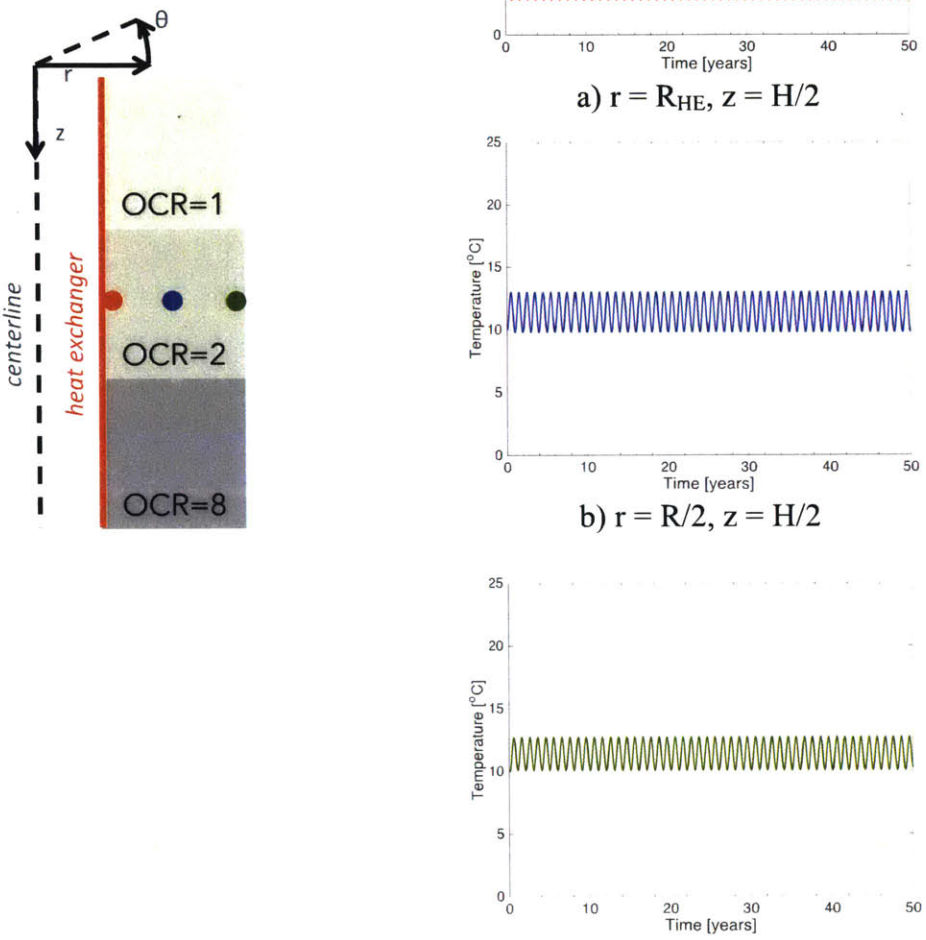

Figure 5.9: Predictions of temperature evolution at different points with the same depth (depth z = H/2) of the axisymmetric geometry for R=3m, Q_{max}/H = 30W/m

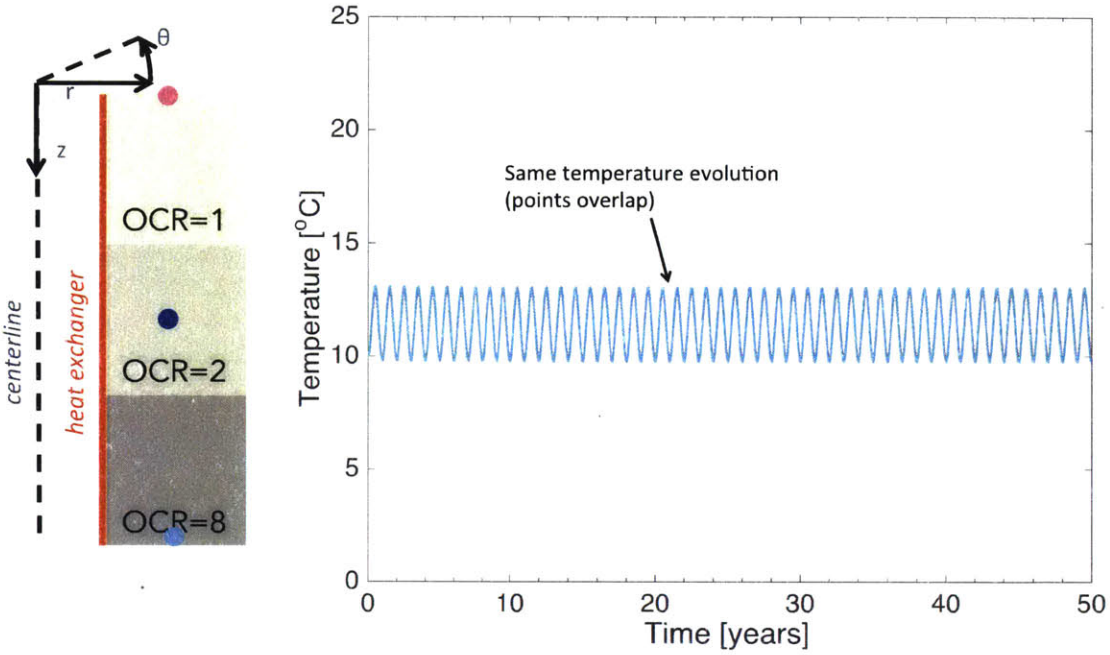

Figure 5.10: Predictions of temperature evolution at different points with the same radial distance (r = R/2) of the axisymmetric geometry for R=3m, Q_{max}/H = 30W/m

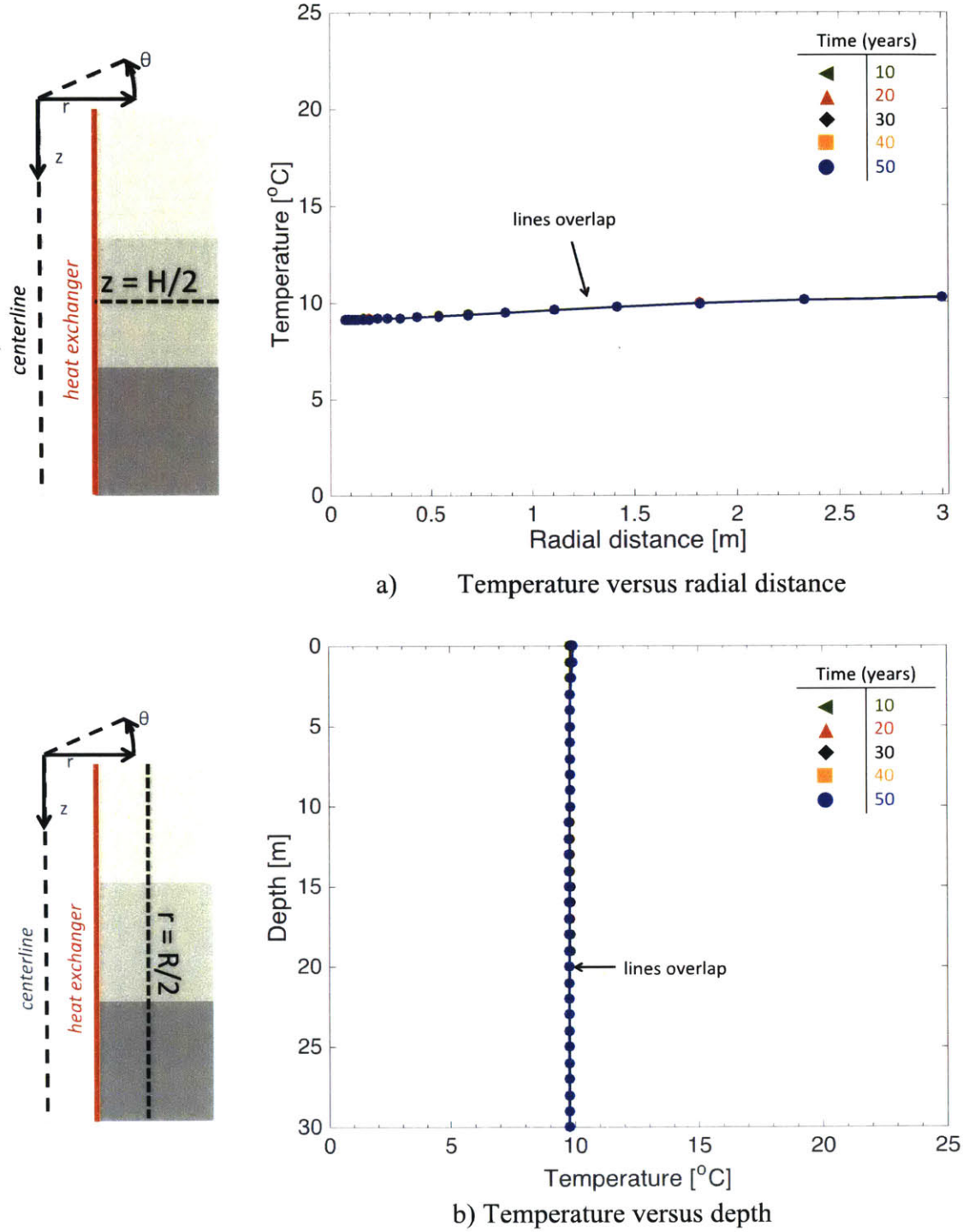

Figure 5.11: Predictions of temperature distribution at different snapshots in time for the illustrative case (R=3m, Q_{max}/H = 30W/m)

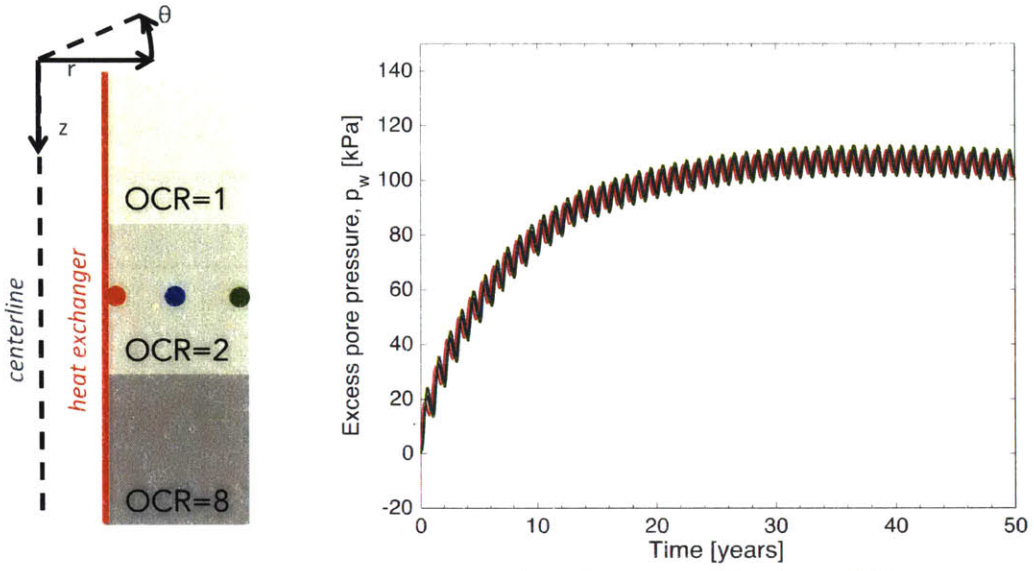

a) Points across depth z = H/2

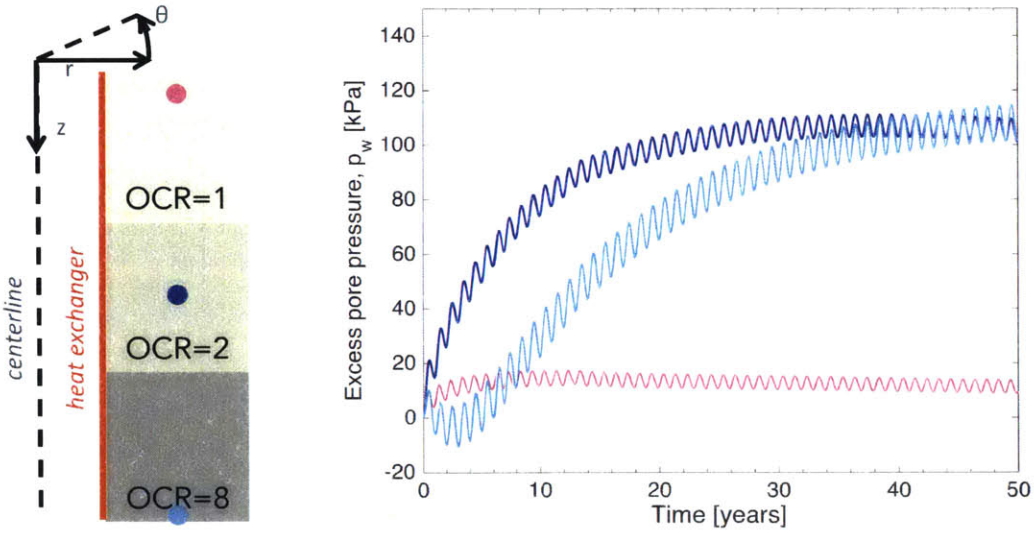

b) Points across radial distance r = R/2

Figure 5.12: Predictions of excess pore pressure evolution at different points of the axisymmetric geometry for the illustrative case (R=3m, Q_{max}/H = 30W/m)

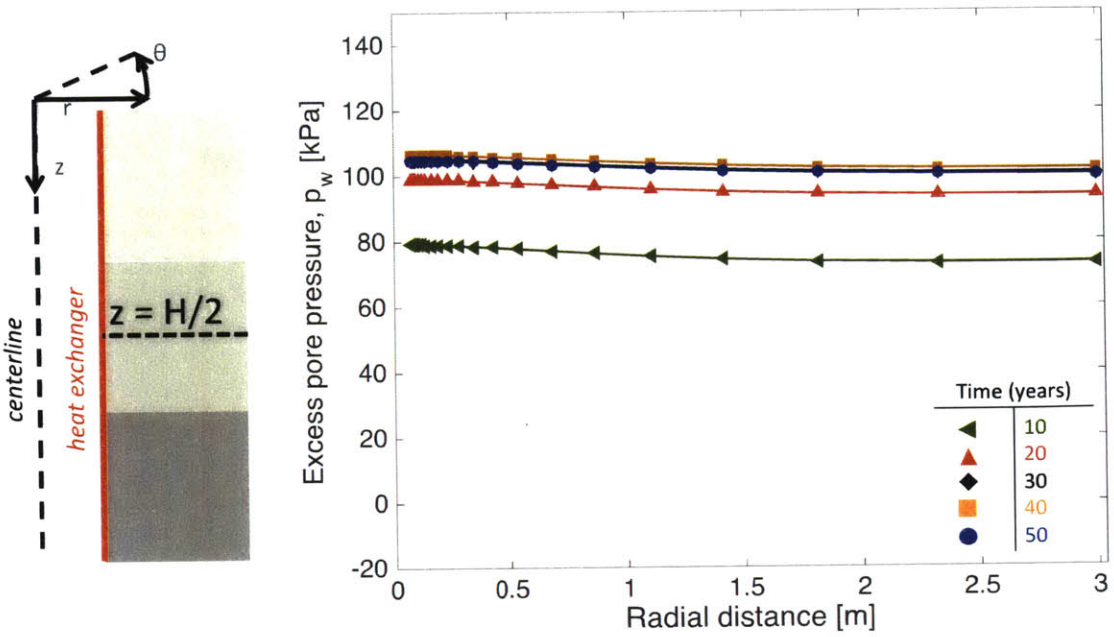

a) Excess pore pressure versus radial distance

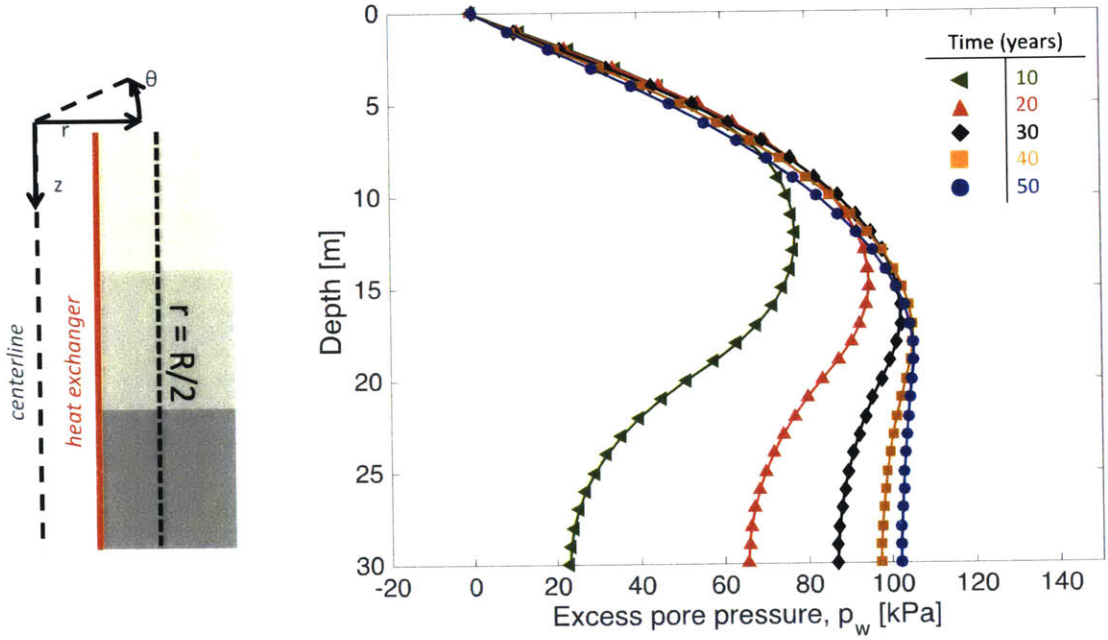

b) Excess pore pressure versus depth

Figure 5.13: Predictions of excess pore pressure distribution at different snapshots in time for the illustrative case (R=3m, Q_{max}/H = 30W/m)

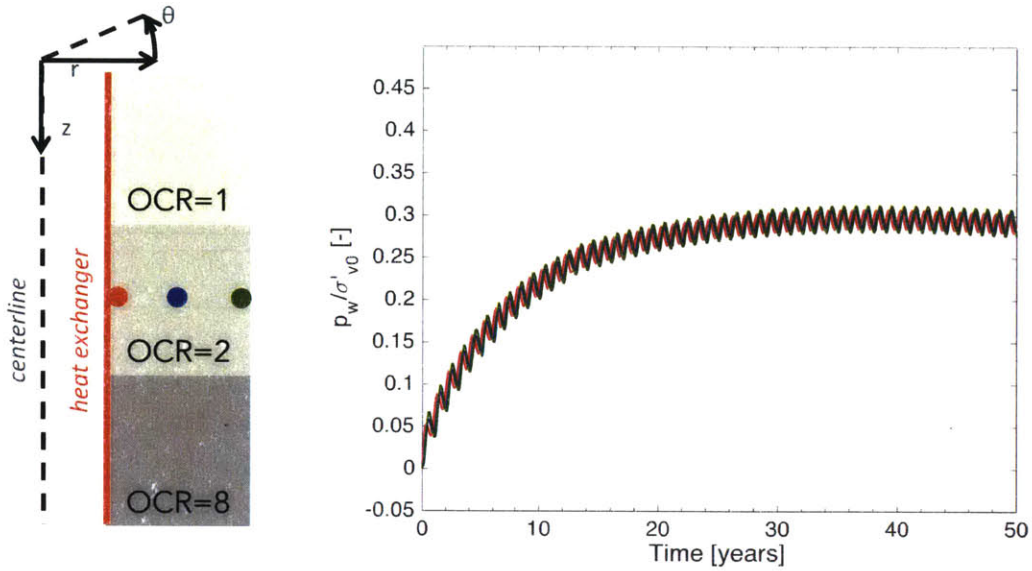

a) Points across depth z = H/2

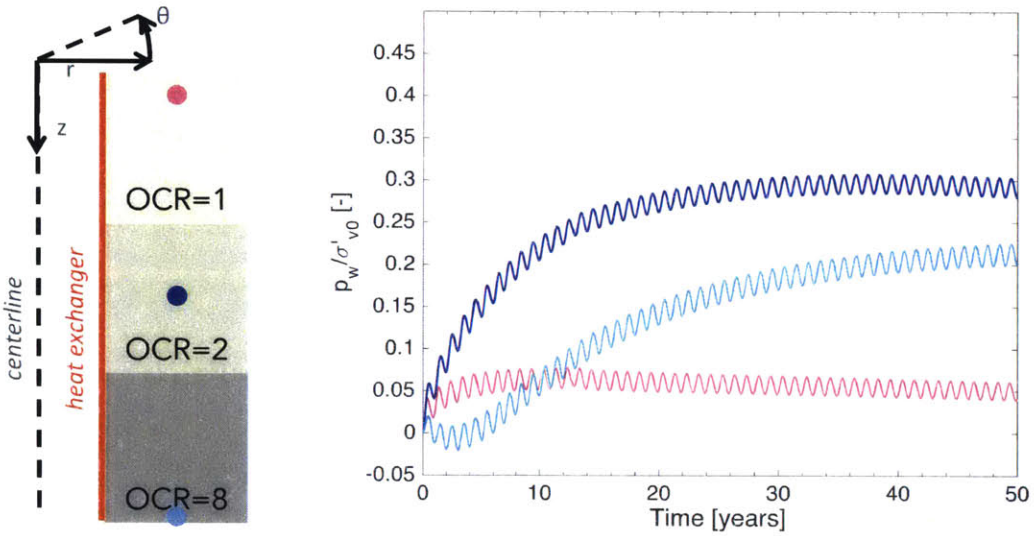

b) Points across radial distance r = R/2

Figure 5.14: Predictions of normalized excess pore pressure evolution at different points of the axisymmetric geometry for the illustrative case (R=3m, Q_{max}/H = 30W/m)

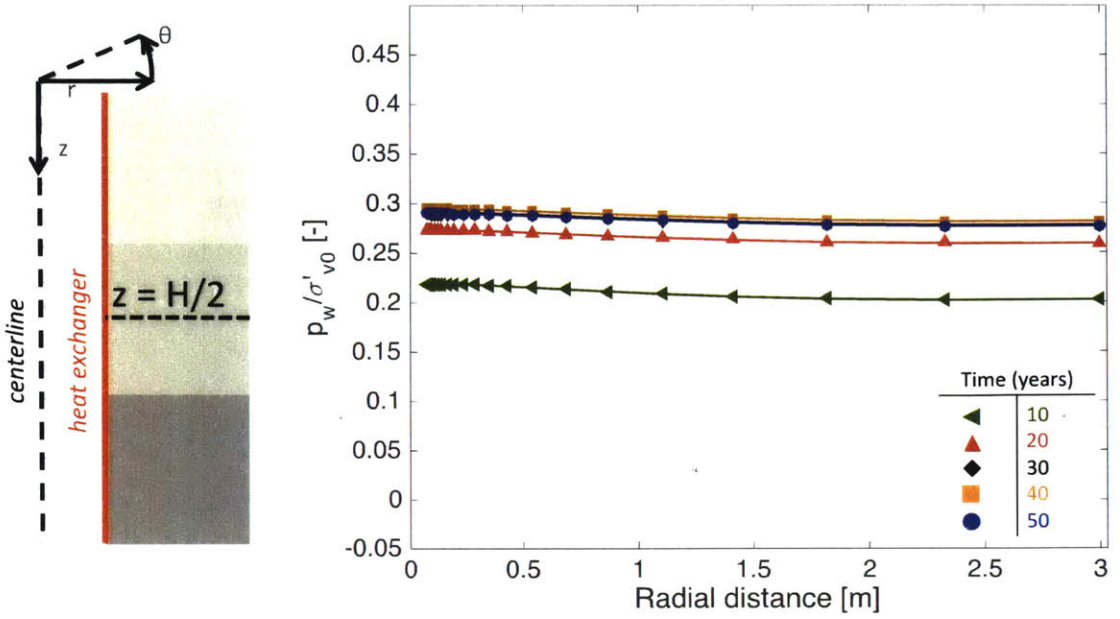

a) Excess pore pressure versus radial distance

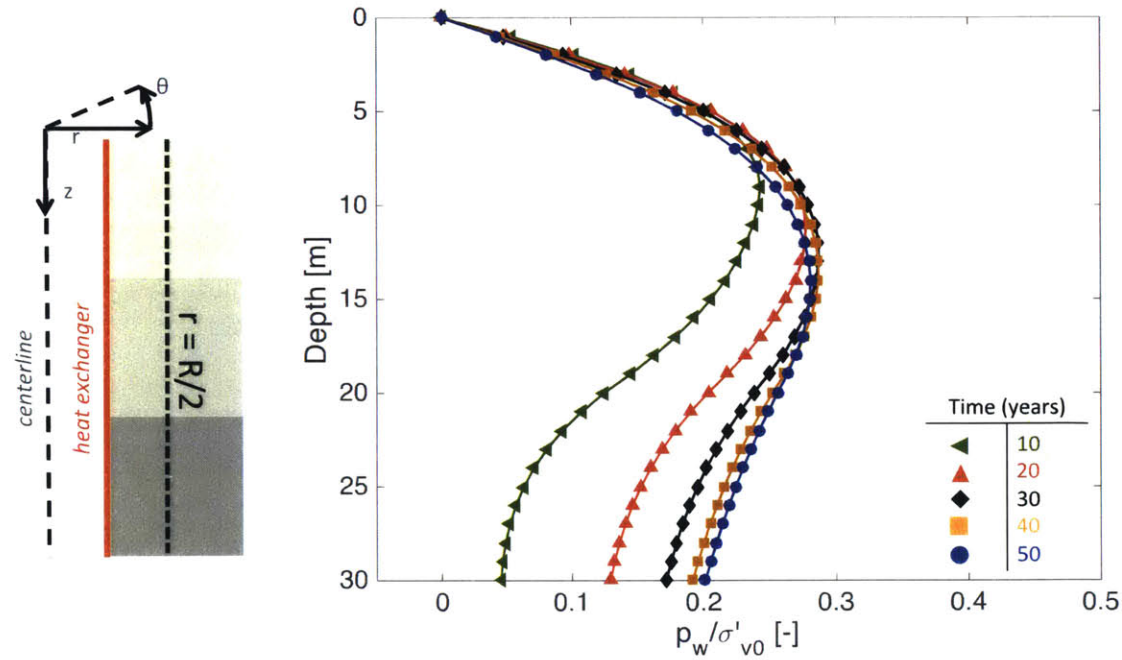

b) Excess pore pressure versus depth

Figure 5.15: Predictions of normalized excess pore pressure distribution at different snapshots in time for the illustrative case (R=3m, Q_{max}/H = 30W/m)

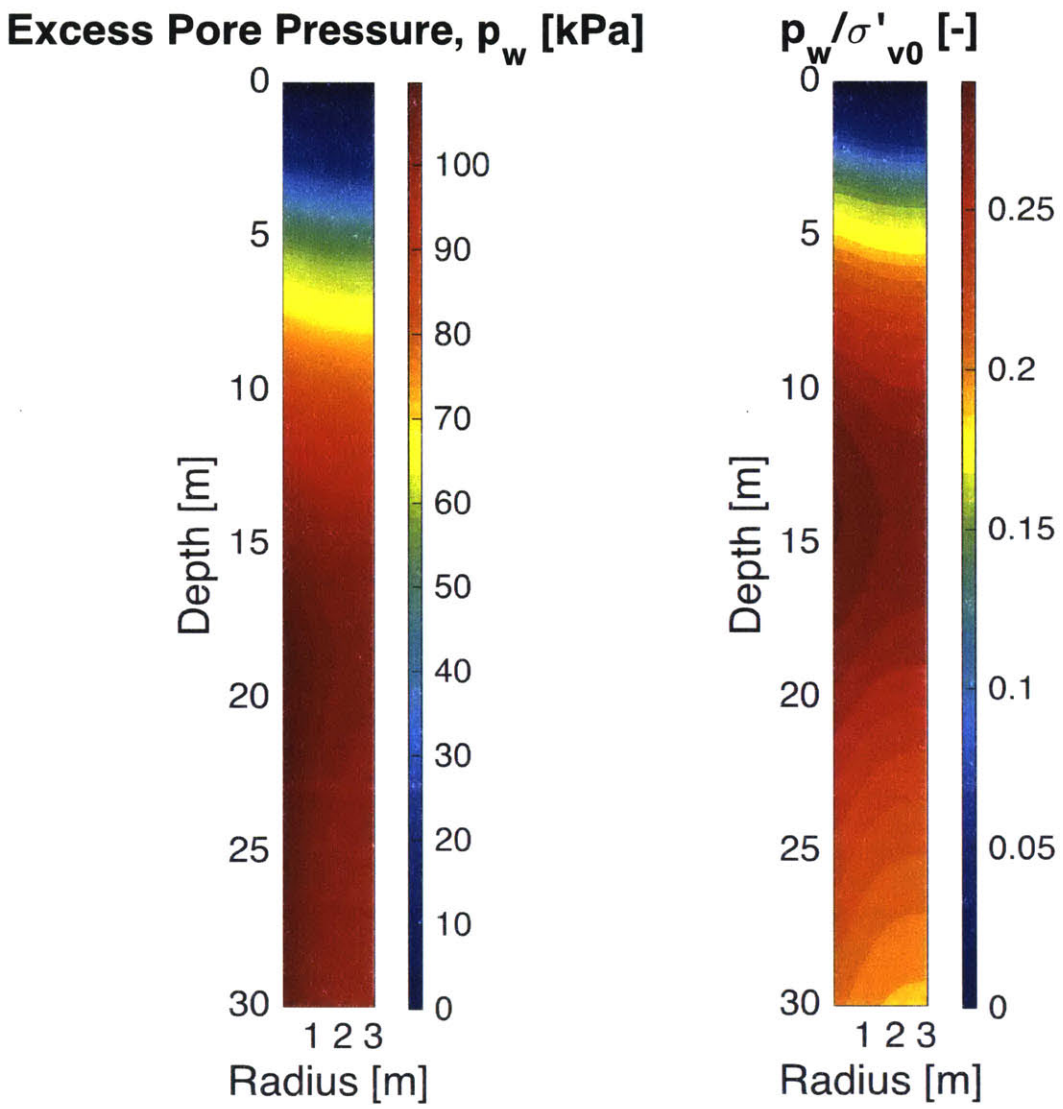

a) Excess pore pressure at t = 50 years

b) Norm, excess pore pressure at t = 50 years

Figure 5.16: Contour plots of predictions of: a) excess pore pressure and b) normalized excess pore pressures after 50 years of continuous operation for the illustrative case (R=3m, Q_{max}/H = 30W/m)

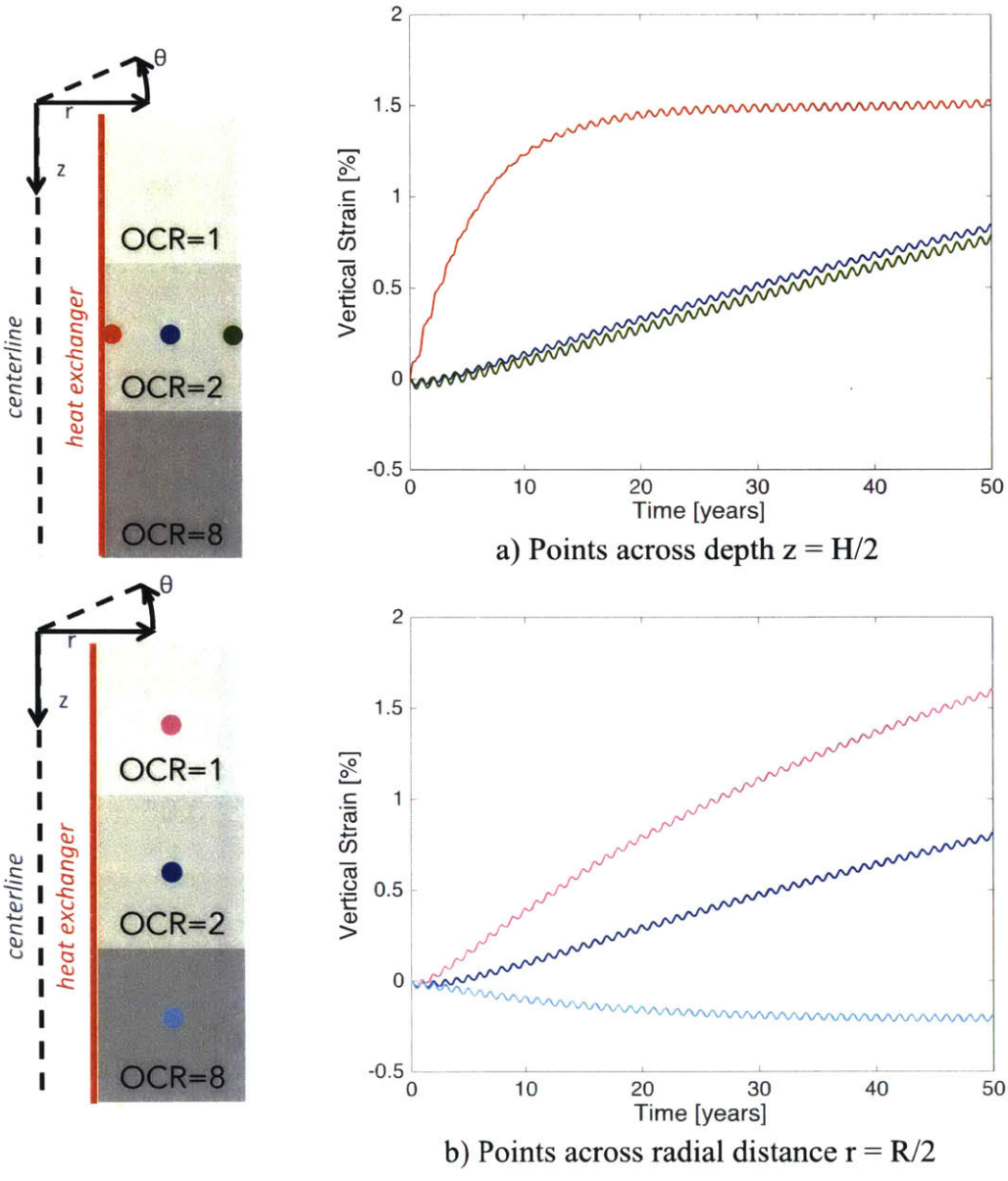

Figure 5.17: Predictions of vertical strain evolution at different points of the axisymmetric geometry for the illustrative case (R=3m, Q_{max}/H = 30W/m)

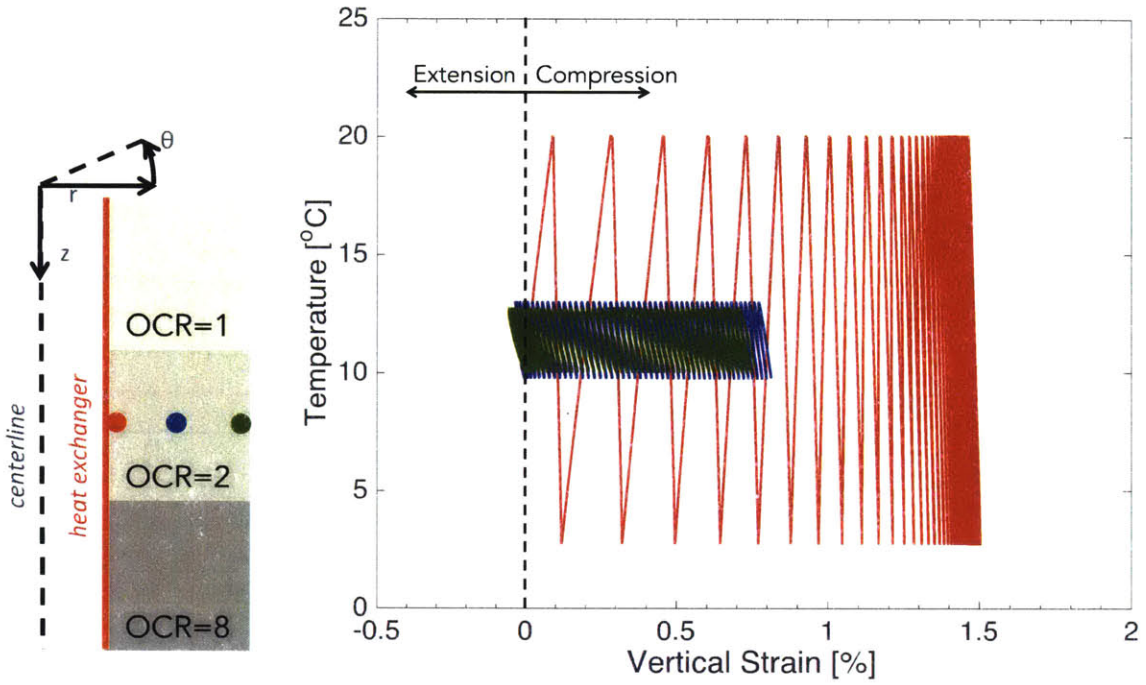

a) Points across depth z = H/2

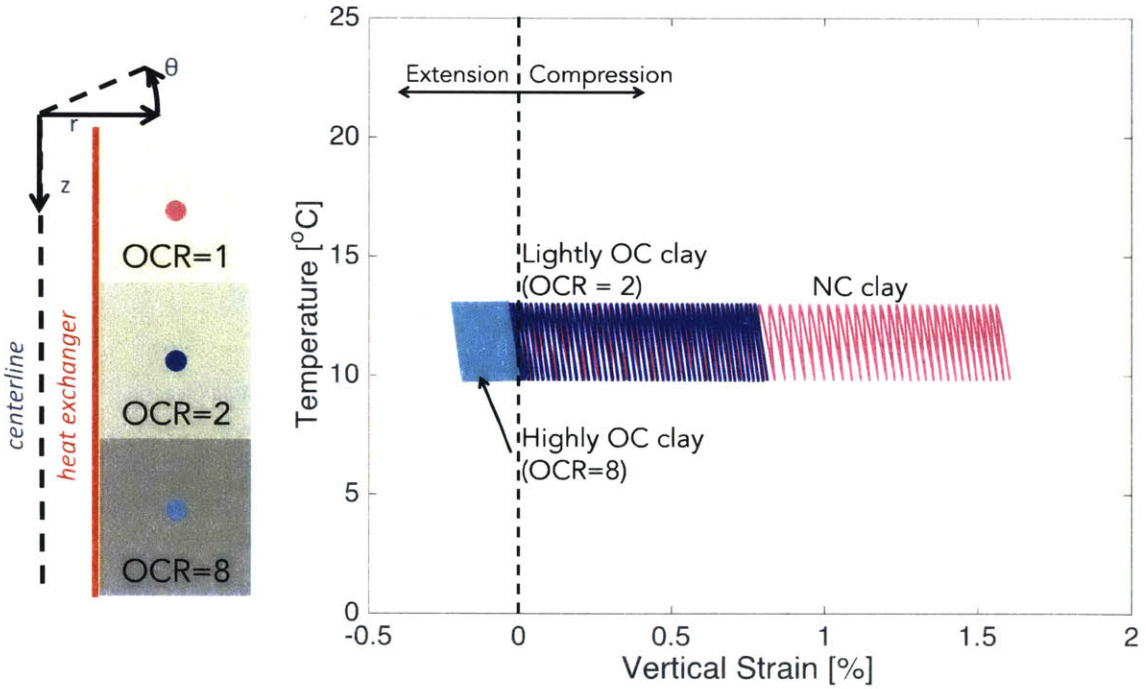

b) Points across radial distance r = R/2

Figure 5.18: Predictions of vertical strain versus temperature at different points of the axisymmetric geometry for the illustrative case (R=3m, Q_{max}/H = 30W/m)

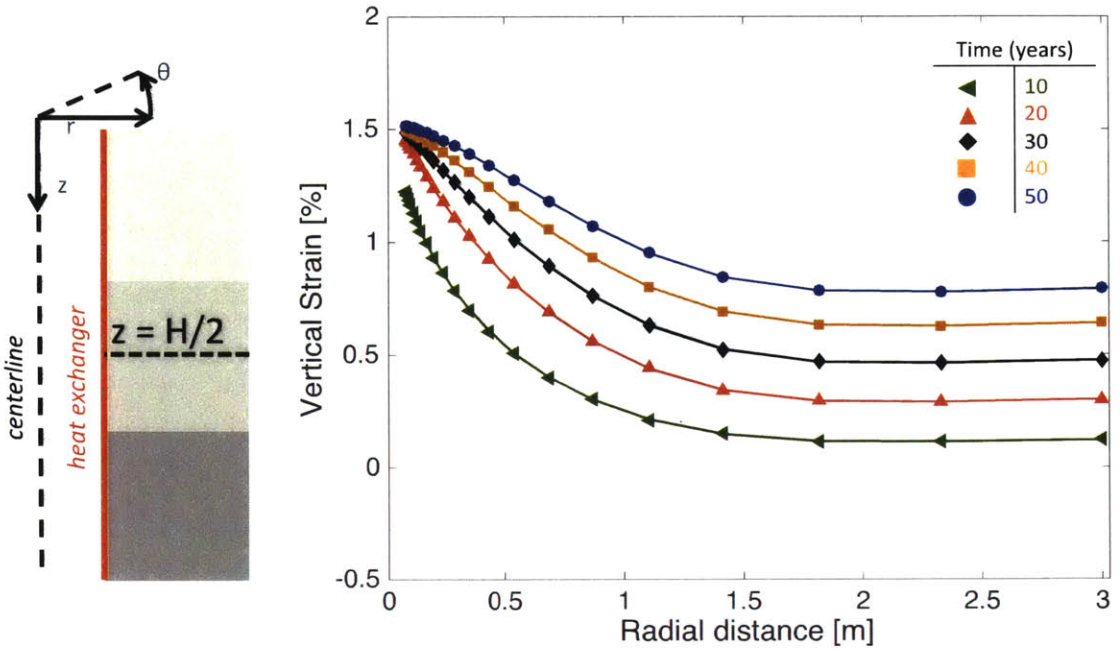

a) Vertical strain versus radial distance

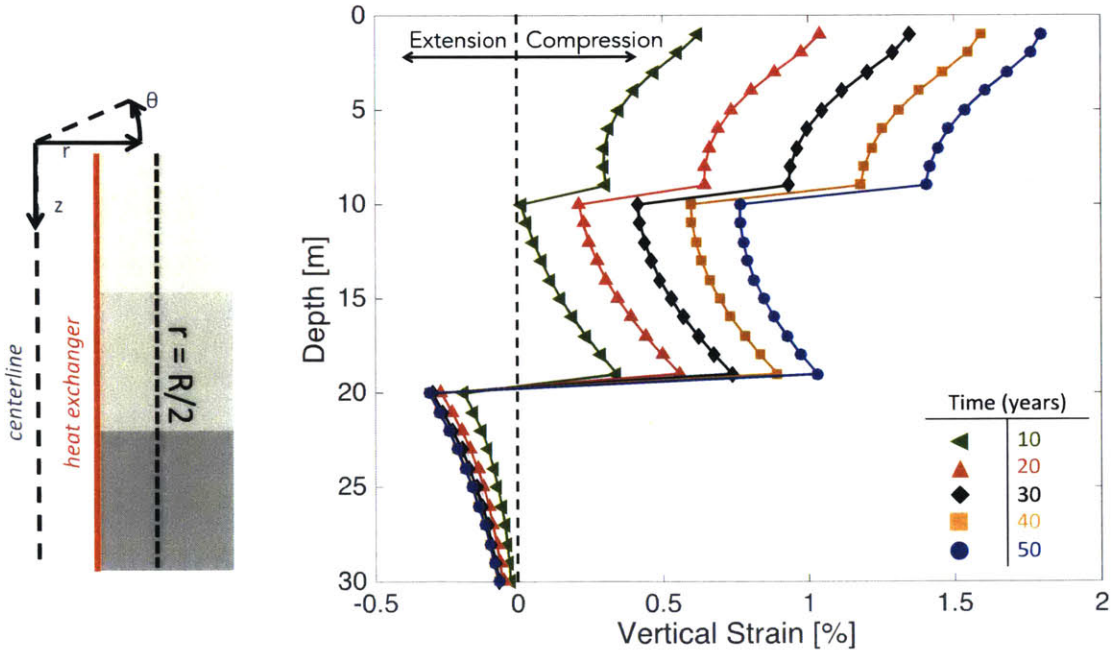

b) Vertical strain versus depth

Figure 5.19: Predictions of vertical strain distribution at different snapshots in time for the illustrative case (R=3m, Q_{max}/H = 30W/m)

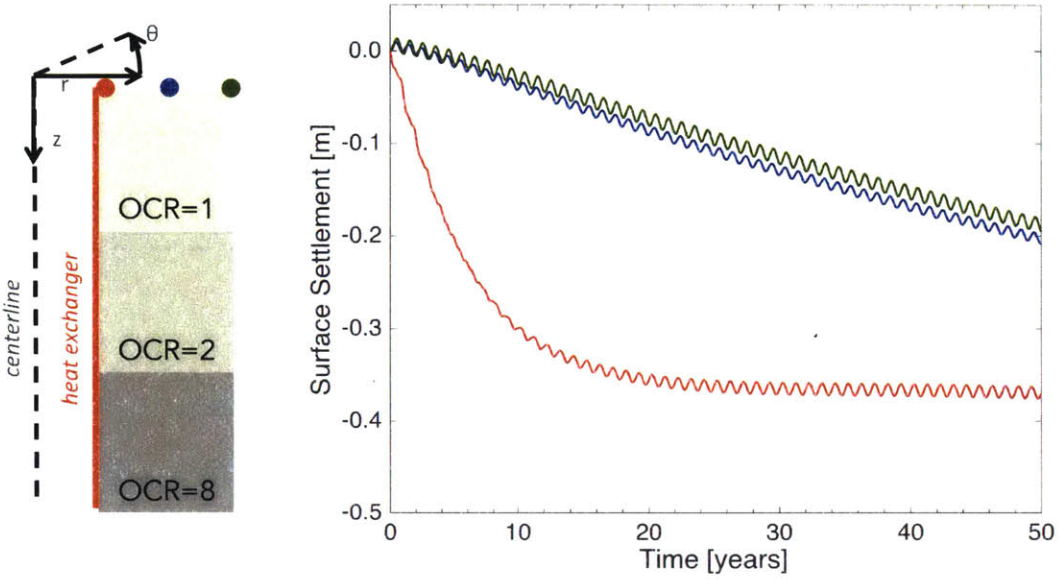

Figure 5.20: Predictions of surface settlement evolution at different points of the axisymmetric geometry for the illustrative case (R=3m, Q_{max}/H = 30W/m)

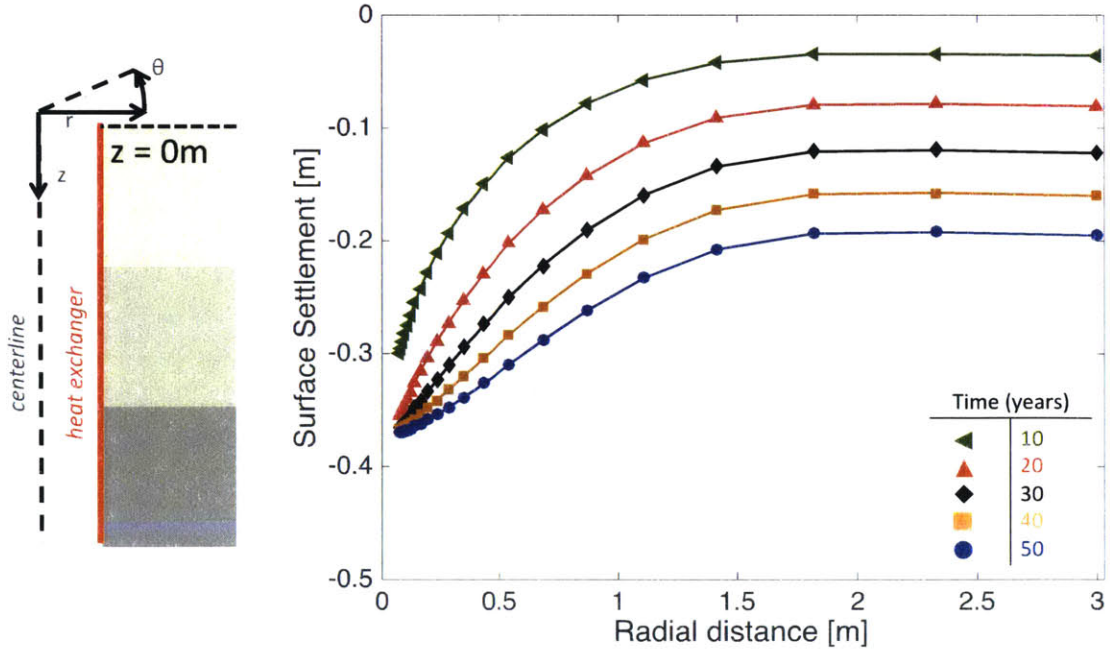

Figure 5.21: Predictions of settlement distribution at different snapshots in time for the illustrative case (R=3m, Q_{max}/H = 30W/m)

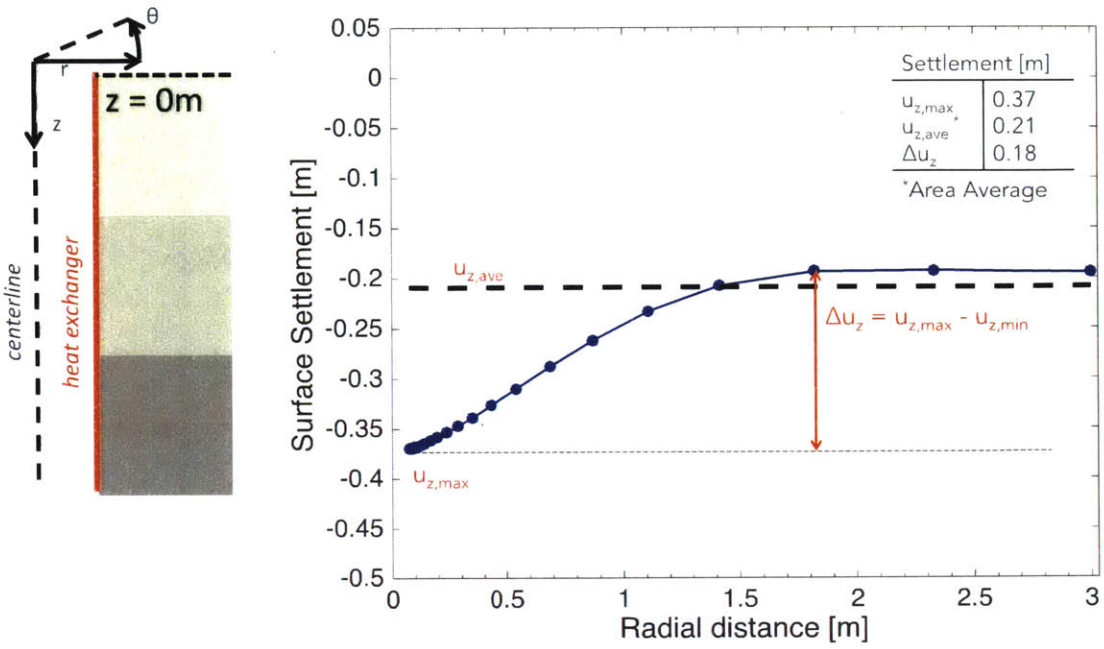

a) Settlement vs radial distance

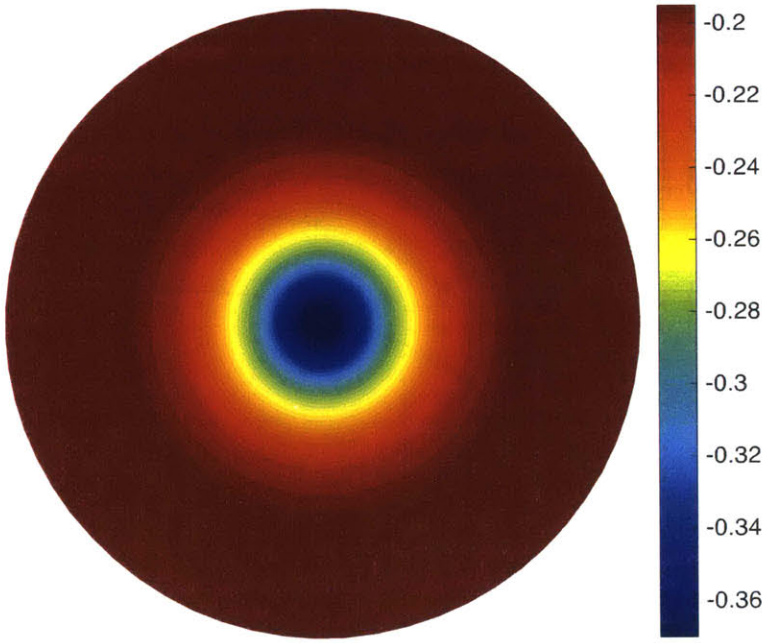

b) Plan view of 50-year surface settlements

Figure 5.22: Prediction of settlement distribution versus radial distance at t = 50 years corresponding to the illustrative case (R=3m, Q_{max}/H = 30W/m) and definition of surface settlement measurements

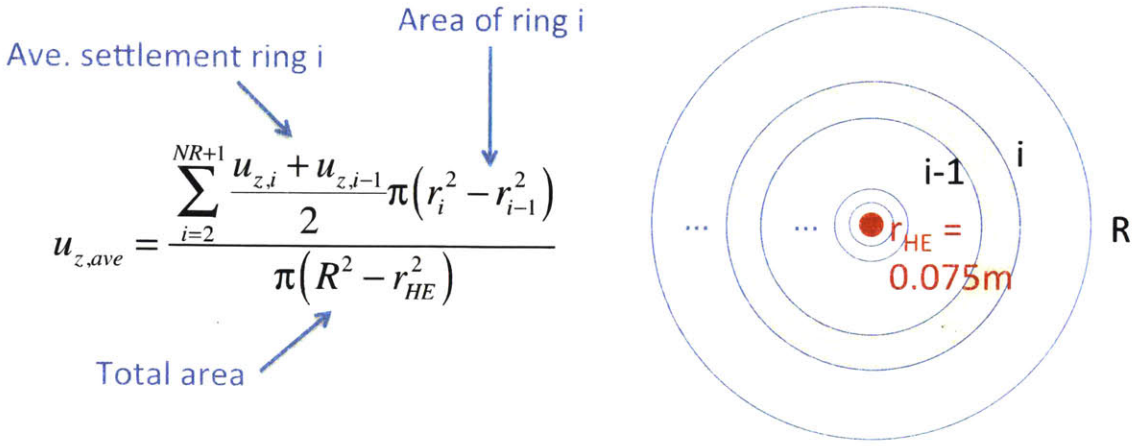

Figure 5.23: Calculation of area average surface settlement, $u_{z,ave}$

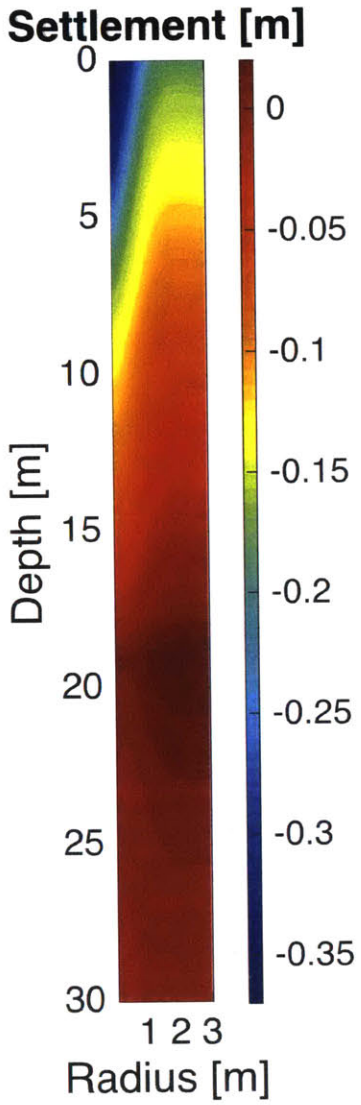

Figure 5.24: Contour plot of settlement predictions after 50 years of continuous operation for the illustrative case (R=3m, Q_{max}/H = 30W/m)

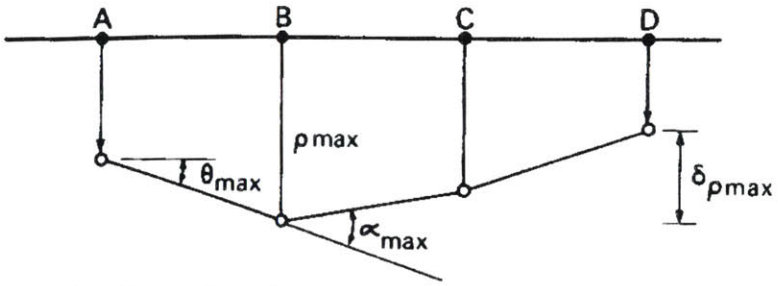

(a) Definitions of settlement ρ, relative settlement δρ, rotation θ and angular strain ∝

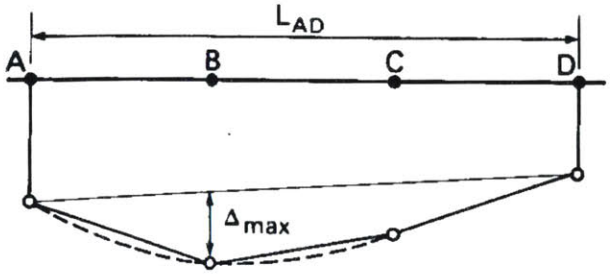

(b) Definitions of relative deflection Δ and deflection ratio Δ/L

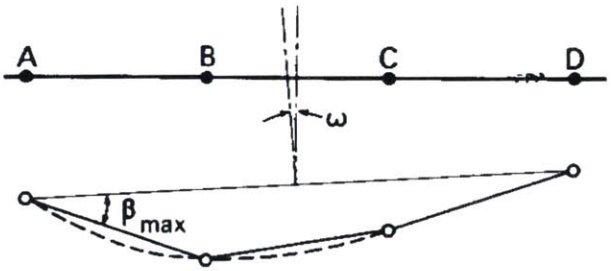

(c) Definitions of tilt ω and relative rotation (angular distortion) β

Figure 5.25: Definitions of foundation settlement (Burland and Wroth, 1974)

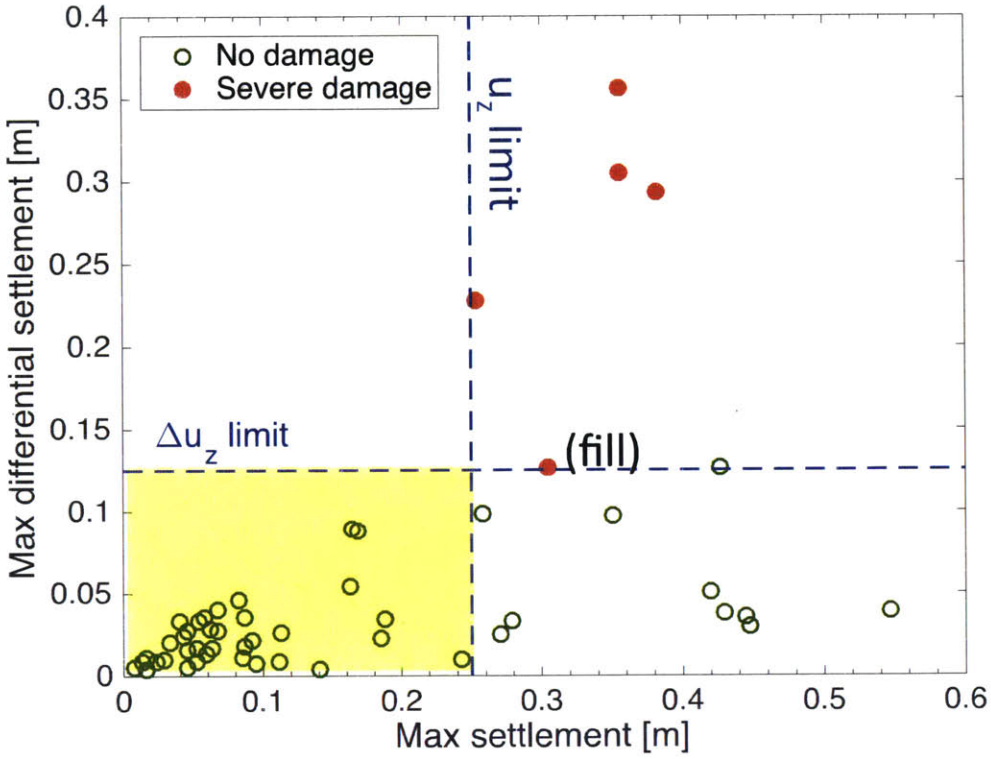

Figure 5.26: Raft foundation settlements on clay from 51 buildings
(after Burland, Broms and De Mello, 1977)

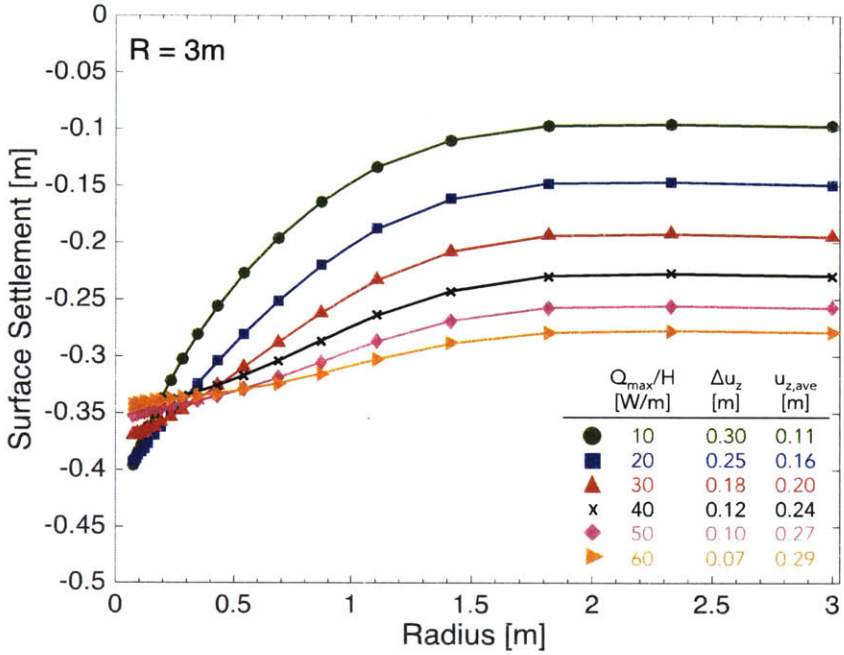

a) Constant R and variable Q_{max}/H

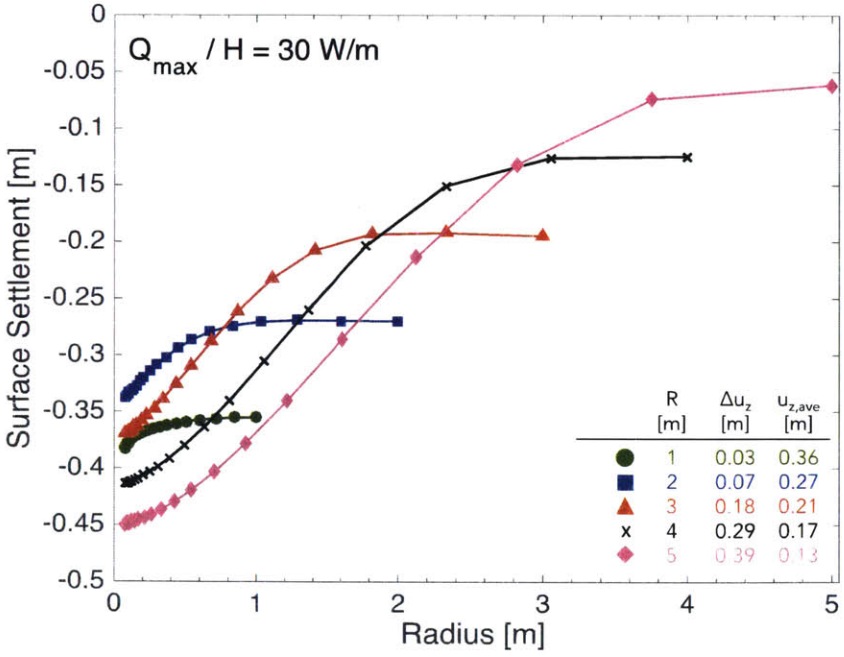

b) Constant Q_{max}/H and variable R

Figure 5.27: Predictions of surface settlements for different combinations of spacing R and maximum heat exchange Q_{max}/H

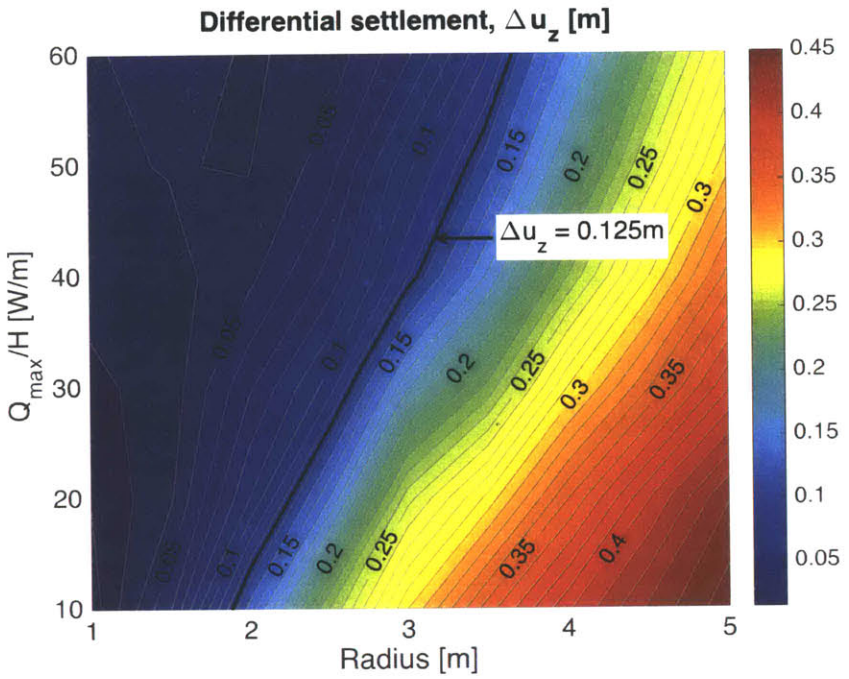

a) Differential settlements, Δu_z

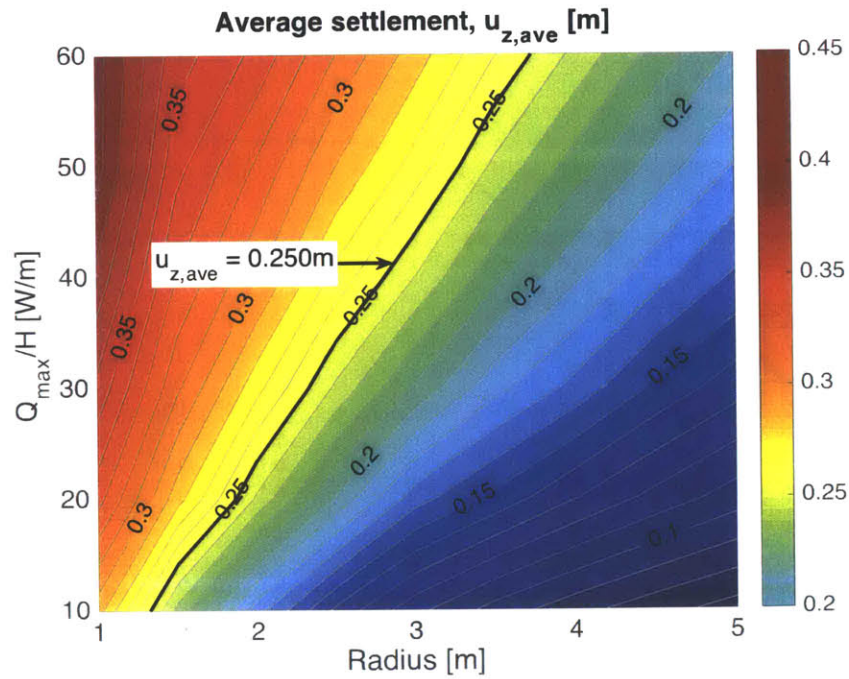

b) Average settlements, $u_{z,ave}$

Figure 5.28: Contour plots of predicted differential and average surface settlements for different combinations of spacing R and maximum heat exchange Q_{max}/H

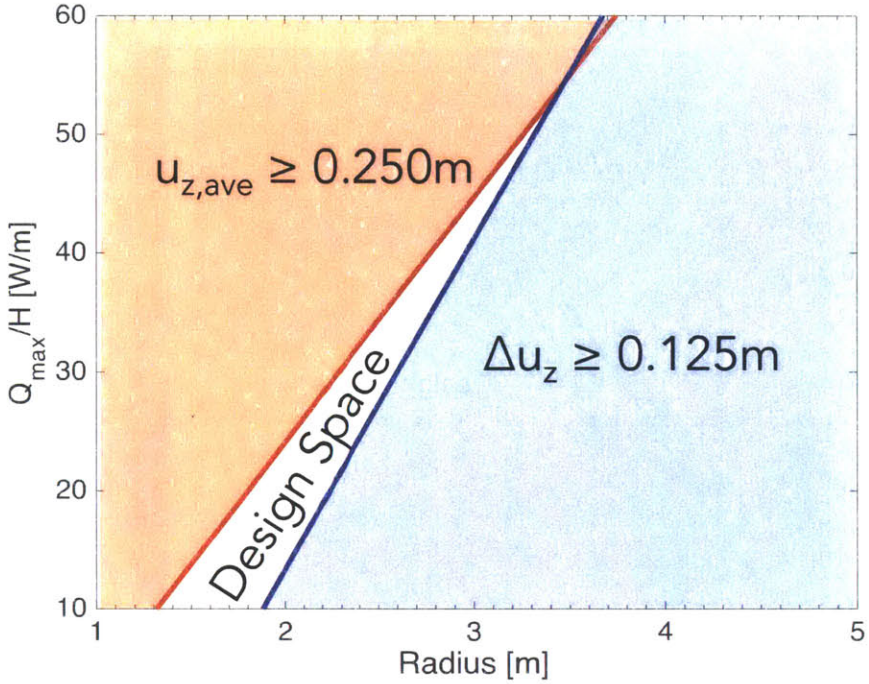

Figure 5.29: Resulting R - Q_{max}/H design space based on foundation settlement limits recommended by Burland et al. (1977)

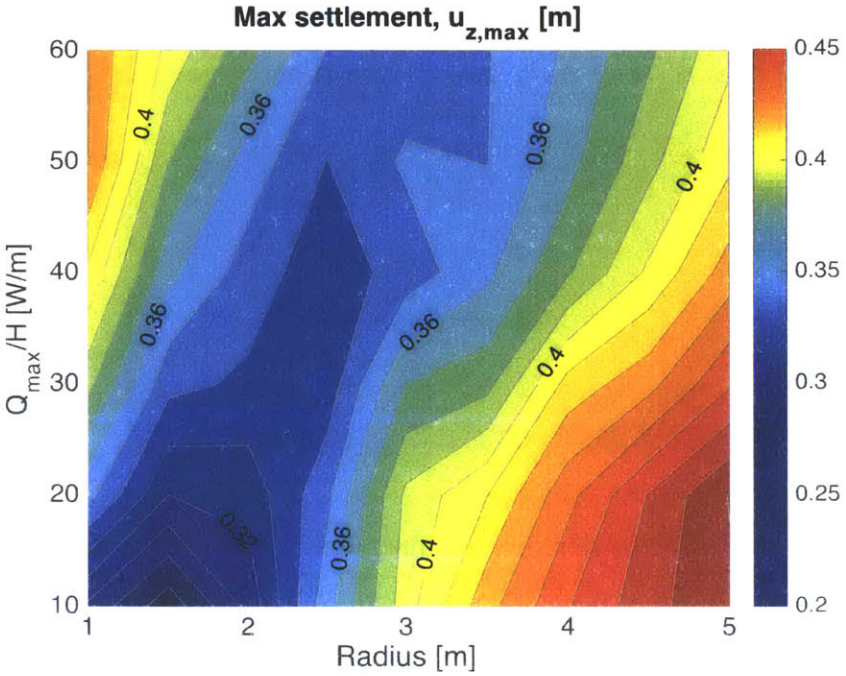

Figure 5.30: Contour plot of predicted maximum surface settlements for different combinations of spacing R and maximum heat exchange Q_{max}/H

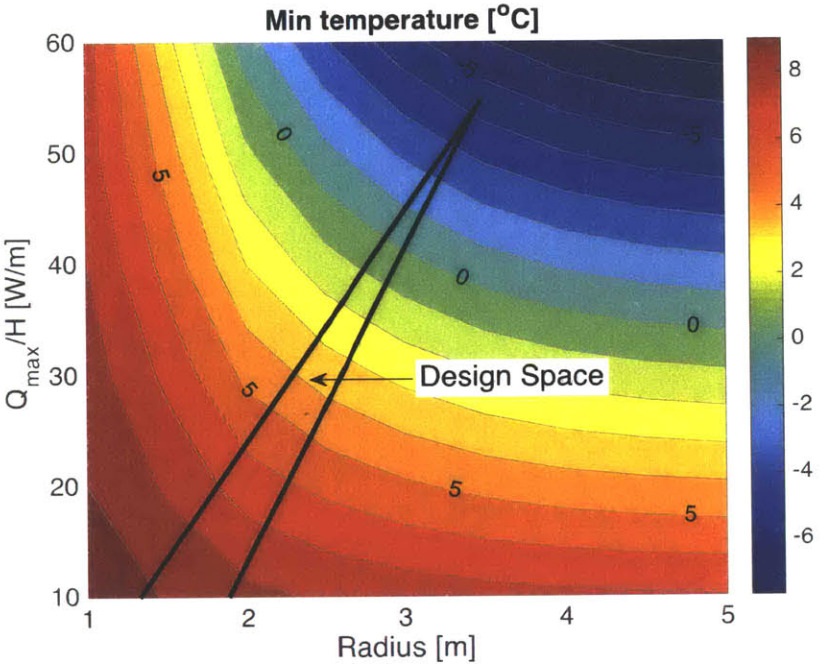

a) Minimum temperature

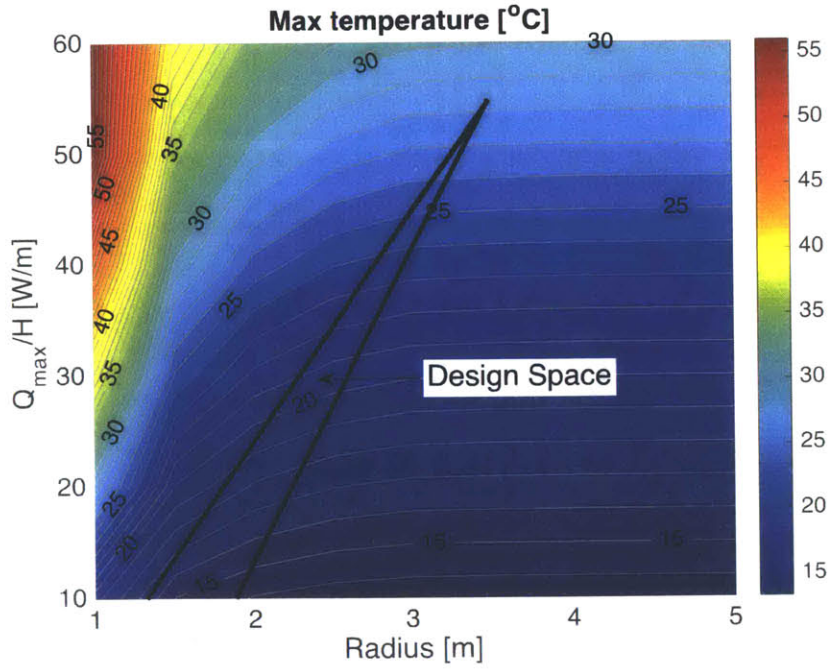

b) Maximum temperature

Figure 5.31: Contour plots of predicted minimum and maximum temperature for different combinations of spacing R and maximum heat exchange Q_{max}/H

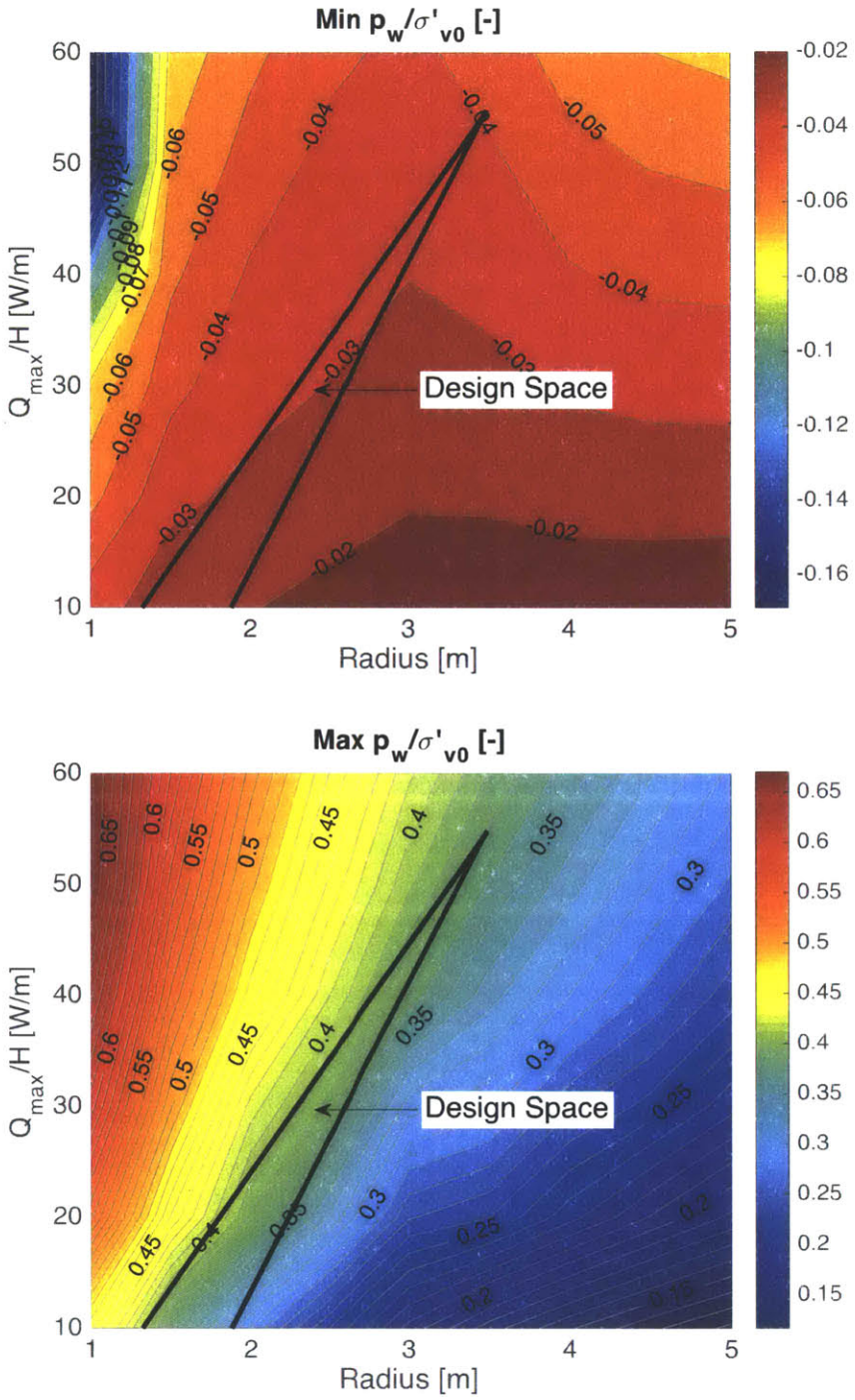

Figure 5.32: Contour plots of predicted minimum and maximum normalized excess pore pressure p_w/σ_{v0}' temperature for different combinations of spacing R and maximum heat exchange Q_{max}/H

Chapter 6

Summary, Conclusions and Recommendations for Future Work

6.1 Summary

The goal of this research was to develop reliable methods for studying the thermo-hydro-mechanical (THM) response of clay to long-term seasonal heating and cooling induced by borehole heat exchangers in clay. Ground source heat pump (GSHP) systems are among the most energy efficient technologies for space heating and cooling[27] reducing the HVAC costs and contributing to reductions in greenhouse emissions. The current analyses focus on the design of heat exchangers that seasonally transfer equal amounts of heating and cooling (building base loads), inducing fluctuations in ground temperature. Extensive laboratory experiments have shown that temperature has a significant effect on the response of clays and that cyclic heating and cooling results in accumulation of irreversible strains. Therefore in-depth analysis of the coupled thermo-hydro-mechanical response of clays to long-term seasonal heating and cooling is important to ensure reliable operation of GSHP systems using BHE arrays.

The first part of the thesis involves an in depth study of the recently developed Tsinghua ThermoSoil (TTS) model based on the framework of Granular Solid Hydrodynamics. Chapter 2 summarizes the simplified field equations for THM analyses in saturated clay with conductive heat transfer (i.e., zero convection case). Chapter 2 also presents relevant data on thermo-mechanical response of clay measured in lab tests and simulated by current thermo-elastoplastic soil models. Chapter 3 presents the Tsinghua Thermosoil (TTS) constitutive model (Zhang and Cheng, 2013), a novel theoretical framework for simulating the coupled thermo-mechanical properties of clays. The model uses a double entropy approach (after Jiang & Liu, 2009) to capture effects of energy dissipation at the microscopic particulate contact level on continuum behavior. Irreversible thermal effects are based on the assumption that bound structural water is

[27] GSHPs achieve coefficients of performance, COP = 3 – 6, compared to COP = 1.75 – 2.5 for air source heat pumps.

converted to free water when the temperature of the clay increases. A series of specific gravity tests at different temperatures were undertaken in order to study this phenomenon further and attempt to quantify this process for three different clays. We propose a procedure for calibrating input parameters for the TTS model from 1-D consolidation tests performed at different temperatures, and thermal strains due to cycles of heating and cooling. The model was calibrated for the case of low plasticity Geneva clay based on data published by Di Donna and Laloui (2015).

The second part of the thesis (Chapter 4) involved the developments of a finite difference (FD) simulator that integrates the TTS model to solve simplified THM problems for a borehole heat exchanger (with conductive heat transfer). Results from the FD simulator were validated against results from more comprehensive finite element models (assuming thermo-elastic properties).

The third part of the thesis (Chapter 5) presents a parametric study using the FD axisymmetric analyses to simulate long-term performance of a BHE array for a reference building project (in Geneva clay). The parametric study evaluates ground movements for different combinations of radial spacing of BHEs and maximum rates of heat exchange (R and Q_{max}/H). The parametric study gives useful guidelines for heat exchanger design and identifies a design space of optimum solutions that meet pre-specified settlement criteria.

6.2 Conclusions

Our study has developed a systematic framework for analyzing the thermo-hydro-mechanical response of clay to seasonal heating and cooling due to the long-term operation of BHE arrays. Three main conclusions can be drawn:

1) Ground source heat pump (GSHP) systems represent a very promising solution for space heating and cooling, especially as these systems increase in scale and are incorporated within urban environments. Current designs do not consider geotechnical characterization such as the impact of long-term seasonal heating and cooling on foundations or adjacent facilities. Preliminary studies have stressed the need to use coupled thermo-hydro-mechanical models in order to ensure reliable long-term operation and to include more realistic models of thermo-mechanical properties.

2) The TTS model successfully describes strain accumulation due to cyclic heating and cooling and represents an advance on pre-exiting thermo-mechanical formulations. The model accurately describes thermo-mechanical behavior of clay recorded in lab tests and a procedure for calibration of the input constants of the TTS model has been proposed, using recently published thermal tests on low plasticity Geneva clay (Di Donna and Laloui, 2015). Areas of improvement of the TTS model formulation have been identified (e.g., the in-situ coefficient of earth pressure at rest for OC clays, K_{0OC} and also overestimation of the dilative strain induced by highly OC clays). More cyclic thermal tests on clay are necessary in order to validate key predictions of the model regarding long-term strain accumulation.

3) Our parametric study is the first of its kind to use numerical simulations to estimate ground deformations associated with seasonal heat exchange for a BHE array. Our work has demonstrated that the long-term operation of borehole heat exchangers in clay for a realistic (but hypothetical) site in Geneva induces significant (total and differential) settlements. These are critically related to the stress history of the clay (i.e, OCR) and to the design characteristics of the BHE array (spacing R and maximum rates of heat exchange Q_{max}/H). The in-depth parametric study has identified optimum heat exchanger design solutions that maintain the long-term surface settlements below threshold limits, in order to avoid adverse effects on overlying structures. Although these predictions apply to the particular site in Geneva, our methodology is general and can be employed in other sites.

6.3 Recommendations for Future Work

An immediate next step is to extend the current framework for a real design case, where the actual heating and cooling requirements and structural loads of the building will be incorporated. In this way the numerical simulation tools developed herein will provide long-term predictions of the ground response due to an actual borehole heat exchanger array and suggest optimum design solutions.

Regarding the clay thermo-mechanical behavior, more cyclic thermal tests are needed on different clay types and for more heating and cooling cycles (ideally more than

ten). These tests will further improve the understanding of the accumulation of volumetric strains due to cyclic heating and cooling. Comparison to TTS model predictions will validate the model performance and evaluate its predictive capabilities.

Implementation of the TTS model in a general finite element code (e.g., Plaxis with the thermal extension) will allow for the study of more complex geometries and problems. Incorporating information about the stiffness of the building and its foundations will enable the study of the soil-structure interaction and provide estimates of the resulting foundation differential settlements. This will allow us for an in-depth estimation and possible expansion of the borehole heat exchanger design space.

Improvements and refinements of the TTS model formulation are necessary in order to solve problems involving the shear response of clay. These issues are currently addressed by Panagiotidou (2016).

Finally, evaluation of the actual thermo-hydro-mechanical field performance of clay due to large-scale heating and cooling is necessary in order to validate our results. A documented case study that shows long-term field measurements of temperature, excess pore pressure and ground displacements would be necessary for validation of the proposed framework.

References

Abdulhadi, N.O. (2009), "An Experimental Investigation into the Stress-Dependent Mechanical Behavior of Cohesive Soil with Application to Wellbore Instability," *Ph.D. Thesis*, Massachusetts Institute of Technology.

Abuel-Naga, H.M., Bergado, D.T., Ramana, G.V., Grino, L., Rujivipat, P. & They, Y. (2006) "Experimental evaluation of engineering behavior of Bangkok clay under elevated temperature," *ASCE Journal of Geotechnical and Geoenvironmental Engineering*, 132(7), 902-910.

AccuPic 1330 (2001), "Operator's Manual V3.03," Micrometrics Instrument Corporation.

Acuna, J., Mogensen, P. and Palm, B. (2009), "Distributed thermal response test on a U-pipe borehole heat exchanger," *Proceedings of 11th International Conference on Energy Storage EFFSTOCK*, Stockholm, Sweden, June 14–17, Paper 18

Adam, D., and Markiewicz, R. (2002), "Nutzung der geothermischen Energie mittels erdberuhrter Bauwerke," *Osterr. Ing. Archit. Z.* 147, No. 4, 5 and 6.

Agar, J. G., Morgenstern, N. R. and Scott, J. D. (1986), "Thermal expansion and pore pressure generation in oil sands," *Canadian Geotechnical Journal*, 23(3), 327-333, doi: 10.1139/t86-046.

Ahmed, I. (1990), "Investigation of Normalized Behaviour of Resedimented Boston Blue Clay using Geonor Direct Simple Shear," *S.M. Thesis*, Massachusetts Institute of Technology.

Alonso, E. E., Gens, A. & Josa, A. (1990), "A constitutive model for partially saturated soils," *Géotechnique* 40, No. 3, 405–430.

Anderson, D. M. and Low, P. F. (1958), "The density of water adsorbed by Li-, Na-, and K-bentonite," *Soil Sci. Soc. Amer. Proc.*, v. 22, pp. 99-103.

Arnold, D. (2000), "The Equitable Building – The genesis of modern air conditioned buildings," Chartered Institution of Buildings Services Engineers (CIBSE) Conference , Dublin, 2000.

ASME (1980), "The Equitable Building heat pump system," Information booklet from dedication ceremony 8/5/80, Oregon Section of the American Society of Mechanical Engineers (ASME).

ASTM C1113/C1113M-09(2013) Standard Test Method for Thermal Conductivity of Refractories by Hot Wire (Platinum Resistance Thermometer Technique)

ASTM D2487 Standard Practice for Classification of Soils for Engineering Purposes (Unified Soil Classification System), in ASTM 04.08 Soil and Rock (1), Revision 11

ASTM D2974 Standard Test Methods for Moisture, Ash, and Organic Matter of Peat and Other Organic Soils, in ASTM 04.08 Soil and Rock (1), Revision 13

ASTM D422 Standard Test Method for Particle-size Analysis of Soils, in ASTM 04.08 Soil and Rock (1), 2007

ASTM D4318 Standard Test Methods for Liquid Limit, Plastic Limit, and Plasticity Index of Soils, in ASTM 04.08 Soil and Rock (1), Revision 12

ASTM D854 Standard Test Methods for Specific Gravity of Soil Solids by Water Pycnometer, in ASTM 04.08 Soil and Rock (1), 2002

ASTM E1225 - 13 Standard Test Method for Thermal Conductivity of Solids Using the Guarded-Comparative-Longitudinal Heat Flow Technique

Bailey, W.A. (1961), "Effects of Salt on the Shear Strength of Boston Blue Clay," *SB Thesis*, Massachusetts Institute of Technology.

Baldi, G., Hueckel, T., and Pellegrini, R. (1988), "Thermal volume changes of the mineral–water system in low-porosity clay soils," *Canadian Geotechnical Journal*, Vol. 25, pp. 807–825.

Baldi, G., Hueckel, T., Peano, A. & Pellegrini, R. (1991). Developments in modeling of thermo-hydro-geomechanical behaviour of Boom clay and clay-based buffer materials, Report 13365/2 EN. Luxembourg: Publications of the European Communities.

Ball, D.A., Fischer, R.D., Talbert, S.G., Hodgett, D. and Auer, F. (1983), "State-of-the-art survey of existing knowledge for the design of ground source heat pump systems," Battelle Columbus Laboratories Report ORNL/Sub 80 - 7800/2, Columbus, Ohio, USA, 75 pp.

Banks, D. (2012), "An introduction to thermogeology: ground source heating and cooling, 2nd edition" John Wiley & Sons, Ltd, UK

Beier, R. A., Acuna, J., Mogensen, P. and Palm, B. (2012), "Vertical temperature profiles and borehole resistance in a U-tube borehole heat exchanger," *Geothermics* 44 (2012) 23– 32

Berman, D.R. (1993), "Characterization of the Engineering Properties of Boston Blue Clay at the MIT Campus", *S.M. Thesis*, Massachusetts Institute of Technology.

Bernier, M., (2006), "Closed-loop ground coupled heat pump systems," *ASHRAE Journal* 48 (6), 12–19.

Berry, P. L. & Poskitt, T. J. (1972), "The consolidation of peat," *Géotechnique* 22, No. 1, 27–52.

Betts, W.S. (2014), "Compression and Permeability Behavior of Gulf of Mexico Mudrocks, Resedimented and In-situ", *M.S. Thesis*, University of Texas at Austin

Booker, J.R. & Savvidou, C. (1985), "Consolidation around a point heat source," *International Journal for Numerical and Analytical methods in Geomechanics*, 9, 173-184.

Boudali, M., Leroueil, S., and Srinivasa Murthy, B.R. (1994), "Viscous behaviour of natural clays," *In Proceedings of the 13th International Conference on Soil Mechanics and Foundation Engineerin*g, New Delhi, Vol. 1, pp. 411–416.

Bouma, J. (2002), "Heat pumps – Better by nature," *IEA Heat Pump Centre Newsletter* 20(2): 10 – 27.

Brandl, H. (2006), "Energy foundations and other thermo-active ground structures," *Géotechnique,* 56 (2), 81-122.

Burghignoli, A., Desideri, A., and Miliziano, S. (1995), "Discussion on volume change of clays induced by heating as observed in consolidation tests (Towhata et al. 1993)," *Soils and Foundations*, 35(3): 122–124.

Burland, J. B. and Wroth, C. P. (1974), "Settlement of buildings and associated damage. State-of-the-Art Review," *Proc. Conf. Settlement of Structures*, Cambridge, Pentech Press, London, pp. 611-654.

Burland, J. B., Broms, B. B. and De Mello, V. F. B. (1977), "Behaviour of Foundations and Structures," *Proc. of the Ninth International Conference on Soil Mechanics and Foundation Engineering (ICSMFE)*, Tokyo, Vol. 2, pp. 495-546.

Campanella, R.G., and Mitchell, J.K. (1968), "Influence of temperature variations on soil behavior," *ASCE Journal of the Soil Mechanics and Foundation Engineering Division,* 94(SM3), pp. 709–734.

Canadian Geoexchange Coalition (2010), "The State of the Canadian Geothermal Heat Pump Industry 2010 – Industry Survey and Market Analysis," *Canadian Geoexchange Coalition Report*, Montreal, Quebec, November 2010.

Casagrande, A. (1936), "The determination of preconsolidation load and its practical significance," *Conference on Soil Mechanics Foundation Engineering*, Cambridge, MA, 3, 60-66.

Casey, B. (2014), "The Consolidation and Strength Behavior of Mechanically Compressed Fine-Grained Sediments", *Ph.D. Thesis*, Massachusetts Institute of Technology.

Cauble, D.F. (1996), "An Experimental Investigation of the Behavior of a Model Suction Caisson in a Cohesive Soil", *Ph.D. Thesis*, Massachusetts Institute of Technology.

CEC (2002), "Energy performance of buildings Directive," (Directive 2002/91/EC of the European Parliament and the Council). Brussels: Commission of the European Communities.

CEN. 2002. EN (1990), "Eurocode – Basis of Structural design, European Committee for Standardization," Brussels

CEN. 2004. EN (1997-1), "Eurocode 7 - Geotechnical Design – Part 1: General rules, European Committee for Standardization," Brussels

CEN. 2007. EN (1997-2), "Eurocode 7 - Geotechnical Design – Part 2: Ground investigation and testing, European Committee for Standardization," Brussels

Cekerevac, C. (2003), "Thermal effects on the mechanical behaviour of saturated clays: an experimental and constitutive study," *Ph.D. Thesis*, École Polytechnique Federale de Lausanne

Cekerevac, C. and Laloui, L. (2004), "Experimental study of thermal effects on the mechanical behaviour of a clay," *International Journal for Numerical and Analytical Methods in Geomechanics*, 28(3), 209-228, doi: 10.1002/Nag.332.

Chapman, D. L. (1913), "A contribution to the theory of electrocapillarity," *Philosophical Magazine*, Vol. 25, No. 6, pp. 475-481.

Cho, W. J., Lee, J. O. & Chun, K. S. (1999), "The temperature effects on hydraulic conductivity of compacted bentonite," *Appl. Clay Sci.* 14, No. 1–3, 47–58.

www.concord.org, http://blog.concord.org/page/3 accessed on May 10, 2016.

Crandall, A.C. (1946), "House heating with earth heat pump," *Electrical World* 126: 94 – 95 [New York edition].

Cui, Y. J., Sultan, N. & Delage, P. (2000), "A thermomechanical model for saturated clays," *Canadian Geotechnical Journal* 37, No. 3, 607–620.

Cui, Y. J., Le, T. T., Tang, A. M., Delage, P., and Li X. L. (2009), "Investigating the time-dependent behaviour of Boom clay under thermomechanical loading," *Géotechnique* 59, No. 4, 319-329.

Curtis, R.H. (2001), "Earth Energy in the UK," Geo - Heat Center (GHC) Bulletin 22/4, Klamath Falls, Oregon, USA, December 2001.

Dafalias, Y., and Herrmann, L. (1980), "A bounding surface soil plasticity model," *Proc., Int. Symp. Soils under Cyclic Transient Loading,* G. N. Pande and O. C. Zienkiewicx, eds., Balkema, Rotterdam, 335–345.

Delage, P., Sultan, N. and Cui Y. J. (2000), "On the thermal consolidation of Boom clay," *Canadian Geotechnical Journal* 37: 343–354.

De Vries D. A. (1966), "Thermal properties of soils," In Van Wijk W. R. editor, *Physics of the plant environment*, Amsterdam, North-Holland Publishing Co.

De Wit, C. T. and Arens, P. L. (1950), "Moisture content and density of some clay minerals and some remarks on the hydration pattern of clay," *Trans. 4th Int. Cong. Soil Sci.*, v. 2, pp. 59-62.

De Jong, G. J. (1968), "Consolidation models consisting of an assembly of viscous elements or a cavity channel network," *Géotechnique* 18, 195–228.

Di Donna, A. (2014), "Thermo-mechanical aspects of energy piles," *Ph.D. Thesis*, École Polytechnique Federale de Lausanne

Di Donna, A. and Laloui, L. (2015), "Response of soil subjected to thermal cyclic loading: Experimental and constitutive study," *Engineering Geology* 190, pp. 65-76

DOE (2008) "DOE Commercial Building Benchmark Models," *presented at the ACEEE Summer Study on Energy Efficiency in Buildings, Pacific Grove, California*

DTI (2006), "Our energy challenge: Power from the people, Microgeneration Strategy," March 2006. London: Department of Trade and Industry.

Ebrahimi, D., Pellenq, R. J. M., and Whittle A. J. (2012), "Nanoscale Elastic Properties of Montmorillonite upon Water Adsorption," *ACS Langmuir* 28, 16855−16863.

Eriksson, L. G. (1989), "Temperature effects on consolidation properties of sulphide clays," *12th International Conference on Soil Mechanics and Foundation Engineering*, Rio de Janeiro, 3, 2087-2090.

Fahy, B.P. (2014), "The Influence of Salinity on the Mechanical Behavior of High Plasticity Soils", *S.M. Thesis*, Massachusetts Institute of Technology

François, B. and Laloui, L. (2008), "ACMEG-TS: a constitutive model for unsaturated soils under non-isothermal conditions," *International Journal for Numerical and Analytical Methods in Geomechanics*, 32, 1955-1988

Fripiat, J. J., Letellier, M., and Levitz, P. (1984), "Interaction of water with clay surfaces," *Philosophical Transactions of the Royal Society of London*, A311, pp. 287-299.

Gao, B. (2013), "Pore Pressure within Dipping Reservoirs in Overpressure Basins", *M.S. Thesis*, The University of Texas at Austin

Gens, A. & Olivella, S. (2001b), "Numerical analysis of radioactive waste disposal," *In Environmental geomechanics* (ed. B. A. Schrefler), pp. 203–234. Wien: Springer.

Gens, A. (2003), "The role of geotechnical engineering for nuclear energy utilization," *Proc. 13th. Eur. Conf. Soil Mech. Geotech. Engng*, Prague 3, 25–67.

Gens, A. & Olivella, S. (2005), "Numerical modelling in nuclear waste storage engineering," *Proc. 11th IACMAG Int. Conf.,* Turin 4, 555–570.

Gens, A., Garitte, B., Olivella, S. and Vaunat, J. (2009a), "Applications of multiphysical geomechanics in underground nuclear waste storage," *Eur. J. Env. Civil Engng* 13, No. 7–8, 937–962.

Gens, A., Sanchez, M., Guimaraes, L. do N., Alonso, E. E., Lloret, A., Olivella, S., Villar, M. V. & Huertas, F. (2009b), "A full-scale in situ heating test for high-level nuclear waste disposal: observations, analysis and interpretation," *Géotechnique* 59, No. 4, 377–399.

Gens, A. (2010), "Soil–environment interactions in geotechnical engineering," *Géotechnique* 60, No 1, pp. 3-74.

Geoexchange BC (2007a), "Professional guidelines for geoexchange systems in British Columbia. Part 1: Assessing site suitability and ground coupling options," Burnaby, BC: Geoexchange BC.

Germaine, J.T. & Germaine, A.V. (2009), "Geotechnical Laboratory Measurements for Engineers," John Wiley and Sons

Graham, J., Tanaka, N., Crilly, T. and Alfaro, M. (2001), "Modified Cam-Clay modelling of temperature effects in clays," *Canadian Geotechnical Journal*, 38(3), 608-621.

Groot, S. R. D., and Mazur, P. (1962), "Non-equilibrium thermodynamics," Amsterdam, North-Holland Pub. Co.

Gouy, G. (1910), "Sur la constitution de la charge electrique a la surface d'un electrolyte," *Anniue Physique (Paris)*, Serie 4, Vol. 9, pp. 457-468.

Habibagahi, K. (1977), "Temperature effect and the concept of effective void ratio," *Indian Geotechnical Journal*, 1: 14–34.

Heap, R.D. (1979), "Heat Pumps," E. & F.N. Spon Ltd., London , 155 pp.

Hellström, G. (1991), "Ground heat storage; thermal analysis of duct storage systems," *Ph.D. Thesis*, University of Lund, Lund, Sweden.

Hillel, D. (1980), "Fundamentals of soil physics," Academic Press, New York.

Horan, A.J. (2012), "The Mechanical Behavior of Normally Consolidated Soils as a Function of Pore Fluid Salinity", *S.M. Thesis*, Massachusetts Institute of Technology.

Houlsby G. T., Amorosi A., and Rojas E., (2005), "Elastic moduli of soils dependent on pressure: A hyperelastic formulation," *Géotechnique* 55(5): 383-392.

Hueckel, T. & Borsetto, M. (1990) "Thermoplasticity of saturated soils and shales: Constitutive equations," *ASCE Journal of Geotechnical Engineering*, 116(2), 1765-1777.

Hueckel, T. & Baldi, G. (1990), "Thermoplasticity of saturated clays: experimental constitutive study," *J. Geotech. Engng ASCE* 116, No. 12, 1768–1796.

Hueckel, T. and Pellegrini, R. (1992), "Effective stress and water pressure in saturated clays during heating–cooling cycles," *Canadian Geotechnical Journal*, 29(6), pp. 1095-1102.

Hueckel, T., Pellegrini, R. and Del Olmo, C. (1998), "A constitutive study of thermo-elastoplasticity of deep carbonatic clays," *International Journal for Numerical and Analytical Methods in Geomechanics,* 22(7), 549-574.

Hujeux, J. C. (1979). "Calcul numérique de problèmes de consolidation lastoplastique," *PhD thesis*, Ecole Centrale, Paris.

IGSHPA (2008), "What is IGSHPA? History," International Ground Source Heat Pump Association. Available at http://www.igshpa.okstate.edu/about/about_us.htm, last accessed 2008.

Israelachvili, J. N. (1985), "Intermolecular and surface forces," Academic Press, Orlando, FA

Jâky, J. (1944), "A nyugalmi nyomâs tényezöje (The coefficient of earth pressure at rest)," *Magyar Mérnok és Epitész Egylet Közlönye (Journal for Society of Hungarian Architects and Engineers)*, October, pp. 355-358.

Jiang, Y., and Liu, M. (2007), "From elasticity to hypoplasticity: dynamics of granular solids," *Phys Rev Lett.* 99(10): 105501

Jiang, Y., and Liu, M. (2009), "Granular solid hydrodynamics," *Granular Matter*, 11(3), 139–156, 2009.

Kavanaugh, S. P, and Rafferty, K. D. (1997), "Ground-Source Heat Pumps: Design of geothermal systems for commercial and institutional buildings," *American Society of Heating, Refrigerating and Air-Conditioning Engineers (ASHRAE)*

Kelley, I. (2006), "Ground-source heat pumps deliver both high efficiency and reliability – Good news for both contractors and their customers," *Wisconsin Perspective*, September – October 2006, pp. 14 – 16.

Kenney, T.C. (1964), "Sea-Level Movements and the Geologic Histories of the Postglacial Marine Soils at Boston, Nicolet, Ottawa and Oslo," *Géotechnique* 14 (3), pp. 203-230.

Khemissa, M. (1998), "Mesure de la perméabilité des argiles sous contrainte et temperature," *Rev. Fr. Géotech.* 82, 11–22.

Kingery, W.D., Bowen, H.K., Uhlmann, D.R. (1976), "Introduction to Ceramics," 2nd edition, Wiley, New York 978-0471478607.

Laloui, L., (2001), "Thermo-mechanical behaviour of soils," *Environmental geomechanics.* EPFL Press, Lausanne, pp. 809–843.

Laloui, L. and Cekerevac, C. (2003), "Thermo-plasticity of clays: an isotropic yield mechanism," *Computers and Geotechnics*, 30(8), 649-660.

Laloui, L., Moreni, M. and Vulliet, L. (2003), "Behavior of a dual-purpose pile as foundation and heat exchanger," *Canadian Geotechnical Journal*, 40(2), 388-402, doi: 10.1139/T02-117.

Laloui, L., Nuth, M. and Vulliet, L. (2006), "Experimental and numerical investigations of the behaviour of a heat exchanger pile," *International Journal for Numerical and Analytical Methods in Geomechanics*, 30(8), 763-781, doi: 10.1002/Nag.499.

Laloui, L., Leroueil, S., and Chalindar, S., (2008), "Modelling the combined effect of strain rate and temperature on one-dimensional compression of soils," *Canadian Geotechnical Journal* 45 (12), 1765–1777.

Laloui, L. and Francois, B. (2009), "ACMEG-T: Soil thermoplasticity model," *Journal of Engineering Mechanics-ASCE*, 135(9), 932-944.

Lambe, T.W. (1960), "The structure of compacted clay," *ASCE Journal of the Soil Mechanics and Foundation Engineering Division*, 125: 682–706.

Leroueil, S. & Marques, M. E. S. (1996)," Importance of strain rate and temperature effects in Geotechnical Engineering," *ASCE Measuring and Modeling Soil Behavior (GSP 61),* 1-60.

Lima, A. (2009). Thermo-hydro-mechanical behaviour of natural Boom clay: an experimental study. PhD thesis, Universitat Politecnica de Catalunya, Spain

Low, P. F. (1979), "Nature and properties of water in montmorillonite-water systems," *Soil Science Society of America Journal*, Vol. 43, No. 5, pp. 651-658.

Lu, N., and Likos, W. J., (2006), "Suction stress characteristic curve for unsaturated soil," *Journal of Geotechnical and Geoenvironmental Engineering*, ASCE, Vol. 132, No. 2, pp. 131-142.

Lund, J.W., Bjelm, L., Bloomquist, G. and Mortensen, A.K. (2008), "Characteristics, development and utilization of geothermal resources – A Nordic perspective," *Episodes* 31(1): 140 – 147.

Makowski, M. W., and Mochlinski, K. (1956), "An evaluation of two rapid methods of assessing the thermal resistivity of soil," *Proc Instn Elect Engng*, Vol. 103, pp. 453 – 464 [Part A].

Marcotte, D. & Pasquier, P. (2008a), "On the estimation of thermal resistance in borehole thermal conductivity test," *Renewable Energy* 33, No. 11, 2407–2415.

Martin, R. T. (1960), "Adsorbed water on clay: A review," *Clays and Clay minerals*, Vol. 9, pp. 28-70.

Marques, M.E.S., Leroueil, S., and Almeida, M.d.S., (2004), "Viscous behaviour of St-Roch-del'Achigan clay, Quebec," Canadian Geotechnical Journal Vol. 41, No. 1, pp. 25–38.

Meynet (2015), Karakas & Francais SA, personal communication.

Midttømme, K., Banks, D., Ramstad, R.K., Saether, O.M. and Skarphagen, H. (2008), "Ground source heat pumps and underground thermal energy storage – Energy for the future," . Slagstad , T. (ed.), Geology for Society, Norges geologiske undersøkelse, Trondheim, Norway, Geological Survey of Norway Special Publication 11, 93 – 98 .

Mitchell, J. K. (1976), "Fundamentals of soil behaviour, 1st edn.," Wiley New York.

Mitchell, J. K. (1993), "Fundamentals of soil behaviour, 2nd edn.," Wiley New York.

Mitchell, J. K., and Soga, K., (2005), "Fundamentals of soil behaviour, 3rd edn.," Wiley New York.

Modaressi, H. and Laloui, L. (1997), "A thermo-viscoplastic constitutive model for clays," International Journal for Numerical and Analytical Methods in Geomechanics, 21(5), 313-335.

Moniz, S.R. (2009), "The Influence of Effective Consolidation Stress on the Normalized Extension Strength Properties of Resedimented Boston Blue Clay," *M.Eng. Thesis*, Massachusetts Institute of Technology

Mooney, R. W., Keenan, A. G., and Wood, L. A. (1952), "Adsorption of water vapor on montmorillonite," *Journal of the Americal Chemical Soc*iety, Vol. 74, pp. 1371-1374.

Moreni, M., Laloui, L., Steinmann, G., Vulliet, L., Fromentin, A. and Pahud, D. (1999), "Test en conditions réelles du comportement statique d'un pieu soumis à des sollicitations thermomécaniques," *Office Fédéral de l'énergie*, OFEN.

Morin, R., and Silva, A. J. (1984), "The effects of high pressure and high temperature on some physical properties of ocean sediments," *Journal of Geophysical Research*, 89(B1), pp. 511–526.

Navarro, V., and Alonso, E. E. (2001), "Secondary compression of clays as a local dehydration process," *Géotechnique* 51, No. 10, 859–869

Neal, W.E.J. (1978), "Heat pumps for domestic heating and heat conservation," *Physics in Technology* 9: 154 – 161.

Nitzsch, W. V. (1940), "Uber den Bau der Hydrathulle der anorganischen Bodenkolloide," Kolloid-Z, Vol. 93, pp. 110-115.

ODPM (2006), "Approved document, the Building Regulations 2000, Conservation of fuel and power, Part L2A. New Buildings other than dwellings," London: Office of The Deputy Prime Minister

Olivella, S., Carrera, J., Gens, A. & Alonso, E. E. (1994), "Nonisothermal multiphase flow of brine and gas through saline media," *Transp. Porous Media* 15, No. 3, 271–293.

Olivella, S., Carrera, J., Gens, A. & Alonso, E. E. (1996a), "Porosity variations in saline media caused by temperature gradients coupled to multiphase flow and dissolution/precipitation," *Transp. Porous Media* 25, No. 1, 1–25.

Olivella, S., Gens, A., Carrera, J. & Alonso, E. E. (1996b), "Numerical formulation for a simulator (CODE_BRIGHT) for the coupled analysis of saline media," *Engng Comput.* 13, No. 7, 87–112.

Paaswell, R.E. (1967), "Temperature effects on clay soil consolidation," *Journal of the Soil Mechanics and Foundation Engineering Division, ASCE,* 93(SM3): 9–22.

Panagiotidou, A. I., Cheng, X., and Whittle, A. J., (2016), personal communication.

Plum, R.L., and Esrig, M.I. (1969), "Some temperature effects on soil compressibility and pore water pressure," *In Effects of temperature and heat on engineering behavior of soils,* Highway Research Board, Special Report 103, pp. 231–242.

Preene, M. (2008), "Sustainable groundwater-source cooling for buildings," *Proc. Instn Civ. Engrs*, Engng Sustainability 161, No. 2, 123–133.

Preene, M. & Powrie, W. (2009) "Ground energy systems: from analysis to geotechnical design," *Géotechnique*, 59(3), 261-271.

Pusch, R., (1986), "Permanent crystal lattice contraction, a primary mechanism in thermally induced alteration of Na bentonite," *MRS Online Proc. Libr.* 84. http://dx.doi.org/10.1557/PROC-84-791.

Rees, S. W., Adjali, M. H., Zhou, Z., Davies, M., and Thomas, H. R. (2000), "Ground heat transfer effects on the thermal performance of earth contact structures," *Renewable and Sustainable Energy Reviews*, 4 (3), pp. 213-265.

Robinet, J.C., Rahbaoui, A., Plas, F. and Lebon, P., (1996), "A constitutive thermomechanical model for saturated clays," *Engineering Geology*, *41*(1), pp.145-169.

Romero, E., Gens, A. & Lloret, A. (2001), "Temperature effects on the hydraulic behaviour of an unsaturated clay," *Geotech. Geol. Engng* 19, 3–4, 311–332.

Roscoe, K. H. & Burland, J. B. (1968), "On the generalised stress–strain behaviour of 'wet' clay," *In Engineering plasticity* (eds J.Heyman and F. A. Leckie), pp. 535–609. Cambridge: Cambridge University Press.

Rosenquist, T. (1959), "Physico-chemical properties of soils in soil-water system," ASCE Journal of the Soil Mechanics and Foundations Division, Vol. 85(SM2), pp. 31-53.

Rybach, L. and Sanner, B. (2000), "Ground-source heat pumps. The European perspective," GHC Bulletin (Geo - Heat Center, Klamath Falls, Oregon) March 2000:16 – 26.

Sailer, E., Taborda, D. M. G., and Keirstead, J. (2015) "Assessment of Design Procedures for Vertical Borehole Heat Exchangers," In *Proceedings of the Fortieth Workshop on Geothermal Reservoir Engineering.*

Sanner, B. (2001), "Some history of shallow geothermal energy use," *Proceedings of UNESCO/IGA International Summer School on Direct Application of Geothermal Energy / International Geothermal Days* Germany 2001 (Bad Urach).

Sanner, B. (2008), "Guidelines, standards, certification and legal permits for ground source heat pumps in the European Union," *9th International IEA Heat Pump Conference* 20th – 22nd May, Zürich, Switzerland.

Santagata, M.C. (1994), "Investigation of Sample Disturbance in Soft Clays Using Triaxial Element Tests," *S.M. Thesis*, Massachusetts Institute of Technology.

Santagata, M.C. (1998), "Factors Affecting the Initial Stiffness and Stiffness Degradation of Cohesive Soils," *Ph.D. Thesis*, Massachusetts Institute of Technology

Schaefer, L.A. (2000), "Single Pressure Absorption Heat Pump Analysis," *PhD Dissertation*, Georgia Institute of Technology, USA, May 2000, 176 pp.

Schmidt, B. (1966), "Discussion of earth pressures at rest related to stress history," *Canadian Geotechnical Journal*, Vol. 3, No. 4, pp. 239-242.

Schofield, A. N. & Wroth, C. P. (1968), "Critical state soil mechanics," London: McGraw-Hill.

Seah, T.H. (1990), "Anisotropy of Resedimented Boston Blue Clay", *Sc.D. Thesis*, Massachusetts Institute of Technology.

Shao, Y. X. (2011), "Experimental study on temperature effect on engineering properties of clayey soils," *Ph. D. Thesis,* in Chinese, Nanjing University, China

Sheahan, T.C. (1991), "An Experimental Study of the Time-Dependent Undrained Shear Behaviour of Resedimented Clay Using Automated Stress-Path Triaxial Equipment," *Sc.D. Thesis*, Massachusetts Institute of Technology.

Sills, G. (1995), "Time dependent processes in soil consolidation," *In Compression and consolidation of clayey soils* (eds H. Yoshikuni and O. Kusakabe), pp. 875–889. Rotterdam: Balkema.

Skempton, A.W. and MacDonald D. H. (1956), "Allowable settlement of buildings," *Proc. Instn. Civ. Engrs.,* part 3, vol. 5, pp. 727-768.

Sloan, S. W. (1987), "Supstepping schemes for the numerical integration of elastoplastic stress-strain relations," *International Journal for Numerical Methods in Engineering*, Vol. 24, pp. 893 – 911.

Smith, D. W., and Booker, J. R. (1989), "Boundary integral analysis of transient thermoelasticity," *International Journal for Numerical and Analytical Methods in Geomechanics*, *13*(3), 283-302.

Spitler, J.D. (2005), "Ground source heat pump system research – Past, present and future," *International Journal of HVAC & R Research* 11 (2), pp. 165 – 167.

Sposito, G. (1989), "The Chemistry of Soils," Oxford University Press.

Sposito, G. (1984), "The surface chemistry of soils," Oxford University Press.

Sposito, G. & Prost, R. (1982), "Structure of water adsorbed on smectites," *Chem. Rev.* 82, No. 6, 553–573.

Sultan, N., Delage, P. & Cui, Y.-J. (2002), "Temperature effects on the volume change behaviour of Boom clay," *Engng Geol.* 64, No 2–3, 135–145.

Sumner, J.A. (1948), "The Norwich heat pump," *Proceedings of the Institution of Mechanical Engineers* 158/1: 22 – 29, with discussion pp. 39 – 51.

Sumner, J.A. (1976a), "Domestic Heat Pumps," Prism Press, Dorchester, 117 pp.

Suter, J. L., Coveney, P. V., Greenwell, H. C., and Thyveetil, M. A. (2007), "Large-Scale Molecular Dynamics Study of Montmorillonite Clay: Emergence of Undulatory Fluctuations and Determination of Material Properties," *J. Phys. Chem. C*, 111, 8248-8259.

Terzaghi, K. (1921), "Die physikalischen Grundlagen der technisch-geologischen Gutachtens," *Osterr. Ing. Archit. Verein Z.*, vol. 73, no. 36/37, pp. 237-241.

Terzaghi, K., (1923), "Die Berechnung des Durchlassigkeitszifferdes Tones aus dem Verlauf der hydrodynamischen Spannungserscheinungen," Sitz. Akad. Wissen Wien MAth-Naturwiss KI Abt. IIa 132, 125–138.

Terzaghi, K. and Fröhlich, O. K. (1936), "Theorie der Setzung von Tonschichten," *F. Deuticke, Leipzig.*

Thomas, H. R., He, Y., Ramesh, A., Zhou, Z., Villar, M. V., and Cuevas, J. (1994), "Heating unsaturated clay – an experimental and numerical investigation," *Proc. 3rd European Conference on Numerical Methods in Geotechnical Engineering* – ECONMIG 94, Manchester, UK, pp. 181-186.

Towhata, I., Kuntiwattanakul, P., Seko, I., and Ohishi, K. (1993), "Volume change of clays induced by heating as observed in consolidation tests," *Soils and Foundations*, 33(4): 170–183.

van Olphen, H. (1977), "An introduction to Clay Colloid Chemistry," 2nd edition, Wiley Interscience, New York.

Van Rooyen, M., and Winterkorn, H. F. (1957), "Theoretical and practical aspects of the thermal conductivity of soils and similar granular systems," *Highway Research Board Bulletin* Vol. 168, pp. 142 – 205.

Verein Deutscher Ingegneure: VDI 4640– Blatt 1, (2010), "Thermal use of the underground. Fundamentals, approvals, environmental aspects," Düsseldorf, Verein Deutscher Ingegneure.

Verein Deutscher Ingegneure: VDI 4640 – Blatt 2, (2001), "Thermal use of the underground. Ground source heat pump systems," Düsseldorf,Verein Deutscher Ingegneure.

Volckaert, G., Bernier, F., Alonso, E. E., Gens, A., Samper, J., Villar, M. V., Martin-Martin, P. L., Cuevas, J., Campos, R., Thomas, H., Imbert, C. and Zingarelli, V. (1996), "Thermal hydraulic-mechanical and geochemical behaviour of the clay barrier in radioactive waste repositories (model development and validation)," EUR 16744 EN. Luxembourg: Publications of the European Communities.

Walbaum, M. (1988), "Procedure for Investigation of Sample Disturbance using the Direct Simple Shear Apparatus," *S.M. Thesis*, Massachusetts Institute of Technology.

Woodside, W., and Messmer, J.H. (1961), "Thermal conductivities of porous media I: unconsolidated soils," *J. Appl Phys*, Vol. 39, No. 9, pp. 1699-1706.

Yariv, S., and Cross, H. (1979), "Geochemistry of colloid systems," Springer-Verlag, Berlin, Federal Republic of Germany.

Yong, R.T., Taylor, L., and Warkentin, B.P. (1962), "Swelling pressures of sodium montmorillonite at depressed temperature," *In Proceedings of the 11th National Conference on Clays and Clay Minerals*, pp. 268–281.

Yong, R. N., and Warkentin, B. R. (1975), "Soil properties and behavior," Elsevier, Amsterdam, The Netherlands.

Yuan, Y. (2016), "A new elasto-viscoplastic model for rate-dependent behavior of clays," *Ph.D. Thesis*, Massachusetts Institute of Technology.

Zhang Z. & Cheng X. (2013), "Simulation of nonisothermal consolidation of saturated soils based on a thermodynamic model," *Scientific World Journal*, Hindawi Publishing Co., http://dx.doi.org/10.1155/2013/192163.

Zogg, M. (2008), "History of heat pumps: Swiss contributions and international milestones," Report of the Swiss Department of Environment, Transport, Energy and Communications (DETEC) and the Swiss Federal Office of Energy (SFOE).

Zymnis, D. M. & Whittle, A. J. (2014), "Numerical Simulation of a Shallow Geothermal Heating/Cooling System," *Proc. ASCE GeoCongress GSP 234*, 2767-2776.

Zymnis, D. M., Whittle, A. J., and Cheng, X., (2015), "TTS Model for Thermo-mechanical behavior of clay," *Proc. ICE XVI ECSMGE, Geotechnical Engineering for Infrastructure and Development Conference*, pp. 4109-4114, doi:10.1680/ecsmge.60678

Appendix A

Conventional Borehole Heat Exchanger (BHE) Design

Borehole Heat Exchanger (BHE) design involves the calculation of the total length of heat exchanger required to meet the heating and cooling demands of a specific building. Design guidelines have been proposed by several industry led organizations in countries where the technology is most popular such as the US, UK, Austria, Germany and Switzerland (Sanner, 2008).

According to ASHRAE recommendations (Kavanaugh and Rafferty, 1997) the total required length of vertical heat exchanger, L_h, can be found from:

$$L_h = \frac{q_a R_{ga} + \left(C_{fh} q_{lh}\right)\left(R_b + PLF_m R_{gm} + F_{sc} R_{gd}\right)}{T_g - \frac{T_{wi} + T_{wo}}{2} - T_p} \qquad \text{(A.1)}$$

where q_a is the net annual average heat transfer to the ground, q_{lh} is the building design heating load, R_b is the equivalent borehole resistance, R_{ga}, R_{gm} and R_{gd} are 'effective thermal resistances of the ground' based on constant heating (from a cylindrical source) over periods of one year, one month and one day, respectively, C_{fh} is a correction factor to account for the heat absorbed by the heat pump during heating, PLF_m is the partial load factor during the design month, F_{sc} is the short-circuit heat loss factor, T_g is the undisturbed ground temperature, T_{wi} and T_{wo} are the liquid temperature at heat pump inlet and outlet and T_p is the temperature penalty due to the interference of adjacent bores.

A simplified equation for L_h has been suggested by Bernier (2006) and is provided below:

$$L_h = \frac{q_h R_b + q_y R_{10y} + q_m R_{1m} + q_h R_{6h}}{T_m - \left(T_g + T_p\right)} \qquad \text{(A.2)}$$

where q_h and q_m represent the peak hourly and monthly ground loads respectively, q_y is the yearly average ground heat load, R_{10y}, R_{1m} and R_{6h} are effective ground thermal resistances corresponding to 10 years, one month and six hour ground loads respectively, R_b is the effective borehole thermal resistance, T_g is the undisturbed ground temperature and T_p is a temperature penalty that represents a correction to the undisturbed ground

temperature due to thermal interference of adjacent boreholes. T_m is the average fluid temperature between the two legs of the U-tube, is assumed to be constant along the depth of the borehole and equal to the average of the fluid inlet temperature, T_{in} and outlet temperature, T_{out}, to the GSHP (i.e., $T_m = (T_{in} + T_{out})/2$).

Sailer at al. (2015) conclude that analytical methods such as the ASHRAE guidelines (Kavanaugh and Rafferty, 1997; 2014) are the most reliable for designing BHE systems since they allow for different input parameters and design specifications. Other more simplified procedures, such as the German and UK specifications, are based on a given set of input parameters that ensure a good long-term system performance but do not allow for design optimization. For example the German VDI 4640 guideline is only applicable to double U-pipes, with tabulated heat extraction rates corresponding to given operation hours and ground thermal conductivities, ignoring the borehole arrangement and characteristics (Sailer et al. 2015).

The heat that can be exchanged with the ground depends on the maximum possible heat flux density in the absorber pipe system. Heat transfer between the absorber fluid and the pipe wall occurs by forced convection of the fluid within the BHE, while heat transfer at the interface (i.e., from the pipe wall to the grout) and also from the grout to the surrounding soil takes place by conduction. As suggested by Brandl (2006) an optimized performance of the system would consider the diameter and length of pipes, the properties of the pipe material, the heat conductivity, specific heat capacity, density and viscosity of the circulating fluid and finally the flow velocity and flow conditions (laminar or turbulent) within the absorber pipes. As a reference, pile foundations with diameter D = 0.3-0.5m, typically achieve heat exchange rates 40-60W/m along each pile (Brandl, 2006).

The effective borehole thermal resistance, R_b, is the thermal resistance between the borehole wall and the fluid in the U-tube pipes. It is the sum of three effective thermal resistances (equation A.3): 1) the convective thermal resistance inside each tube, R_{conv} 2) the conductive resistance of the tube material, R_{pipe} and 3) the conductive resistance of the grout, R_{grout}, which are obtained by analytical solutions proposed by Hellstrom (1991) and are presented in equations A.3-A.6.

$$R_b = R_{grout} + \frac{R_{pipe} + R_{conv}}{2} \tag{A.3}$$

$$R_{conv} = \frac{1}{2\pi r_{p,in} h_{conv}} \tag{A.4}$$

$$R_{pipe} = \frac{\ln\left(\frac{r_{p,ext}}{r_{p,\text{int}}}\right)}{2\pi\lambda_{pipe}} \tag{A.5}$$

$$R_{grout} = \frac{1}{4\pi\lambda_{grout}}\left[\ln\left(\frac{R_{HE}}{r_{p,ext}}\right) + \ln\left(\frac{R_{HE}}{L_u}\right) + \frac{\lambda_{grout} - \lambda}{\lambda_{grout} + \lambda}\ln\left(\frac{R_{HE}^4}{R_{HE}^4 - \left(\frac{L_u}{2}\right)^4}\right)\right] \tag{A.6}$$

where h_{conv} is the fluid convection coefficient, $r_{p,int}$ and $r_{p,ext}$ are the inner and outer radii of the pipe, R_{HE} is the borehole radius L_u is the center-to-center distance between the two pipes (Figure 5.1), and λ_{pipe}, λ_g and λ are the coefficients of the thermal conductivity of the pipe material, grout and ground respectively. For turbulent flows h_{conv} is usually above 1000 W/m^2 K while for laminar flows it is generally below 100 W/m^2 K.

A parametric study was undertaken to study the effect of the coefficient of thermal conductivity of the pipe material, λ_{pipe} and of the grout λ_{grout} on the borehole thermal resistance, R_b. The input constants assumed in the study are summarized in Table A.1. A typical U-tube size was selected (1 ¼" SDR 11, $r_{p,int}$ = 0.014m and $r_{p,ext}$ = 0.016m) based on ASHRAE recommendations (Kavanaugh and Rafferty, 1997) with a borehole radius R_{HE} = 0.075m and a spacing between the inlet and outlet tubes L_u = 0.055m. Turbulent flow was assumed in the calculations (i.e., h_{conv} = 1000 W/m^2 K) and the coefficient of the thermal conductivity of the ground was selected for saturated Geneva clay λ = 1.61 W/mK. The range of values assumed for λ_{pipe} = 0.42 – 0.51 W/mK, based on typical values for high-density polyethylene (HDPE), while the range of values assumed for λ_{grout} = 0.865 – 3.461 W/mK. Figure A.1 compares the contribution of each thermal resistance (i.e., R_{conv}, R_{pipe}, R_{grout}) on the total borehole thermal resistance R_b for different λ_{pipe} and λ_{grout}. The bar at the right is calculated assuming minimum values of thermal expansion coefficients (λ_{pipe} = 0.42 W/mK and λ_g = 0.865 W/mK), the bar at the

right assuming maximum values (λ_{pipe} = 0.51 W/mK and λ_g = 3.461 W/mK) and the bar in the middle showing results corresponding to average λ_{pipe} = 0.47 W/mK and $\lambda_g = \lambda =$ 1.61 W/mK appropriate for saturated Geneva clay. It is observed that for turbulent flow, R_{conv} has minimal contribution, since most of the thermal resistance is due to the thermal conductivity of the grout. Moreover, it is observed that when assuming a low coefficient of thermal conductivity of the grout (λ_{grout} = 3.461 W/mK), R_b is significantly higher compared to when assuming a high value (λ_{grout} = 0.865 W/mK). Since the coefficient of thermal conductivity of the HDPE material has small variability, its effect on R_{pipe} is negligible as shown in Figure A.1. The results are also compared to a simplified borehole thermal resistance $R_{b,sim}$ (equation A.8) which was derived by replacing the U-tube with a linear heat source located at the center of the borehole and surrounded by grout (Figure 4.5).

$$\frac{\partial T}{\partial r} = -\frac{Q}{2\pi\lambda_{grout} R_{HE}} \tag{A.7}$$

$$R_{b,sim} = \frac{\Delta T}{Q} = \frac{\Delta T}{R_{HE}} \frac{R_{HE}}{Q} = -\frac{\partial T}{\partial r} \frac{R_{HE}}{Q} = \frac{1}{2\pi\lambda_{grout}} = 0.1 \text{W/mK} \tag{A.8}$$

The simplified value $R_{b,sim}$ = 0.1W/mK gives an average value for borehole resistance R_b and hence has been selected for the parametric study simulations. Figure A.2 presents the effect of typical U-tube sizes on R_b, assuming the same input constants as before. It is deduced that for a typical range of U-tubes, the size of the U-tube has a minimal effect on R_b.

Input constant	Meaning	Selected value
$r_{p,int}$ [m]	Inner radius of HDPE U-tube pipe	0.014
$r_{p,ext}$ [m]	Outer radius of HDPE U-tube pipe	0.016
R_{HE} [m]	Borehole radius	0.075
L_u [m]	Center-to-center distance between U-tube pipes	0.055
h_{conv} [W/m^2 K]	Fluid convection coefficient	1000
λ [W/m K]	Coefficient of thermal conductivity of saturated clay	1.61
λ_{pipe} [W/m K]	Coefficient of thermal conductivity of HDPE pipe material	0.42 – 0.51
λ_{grout} [W/m K]	Coefficient of thermal conductivity of grout	0.87 – 3.46

Table A.1: Input constants assumed in calculation of effective borehole thermal resistance, R_b for typical U-tube size 1 ¼" SDR 11

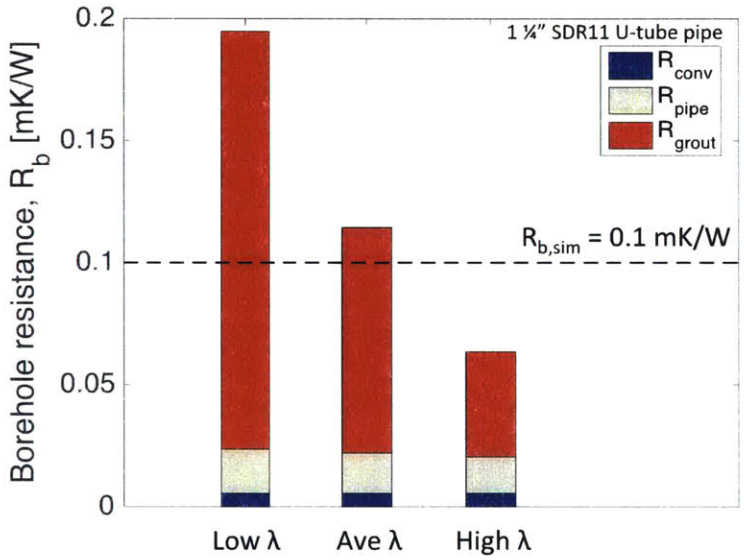

Figure A.1: Effective borehole thermal resistivity R_b for different coefficients of thermal conductivity of the grout and the pipe material and contribution of resistivity components on total resistivity

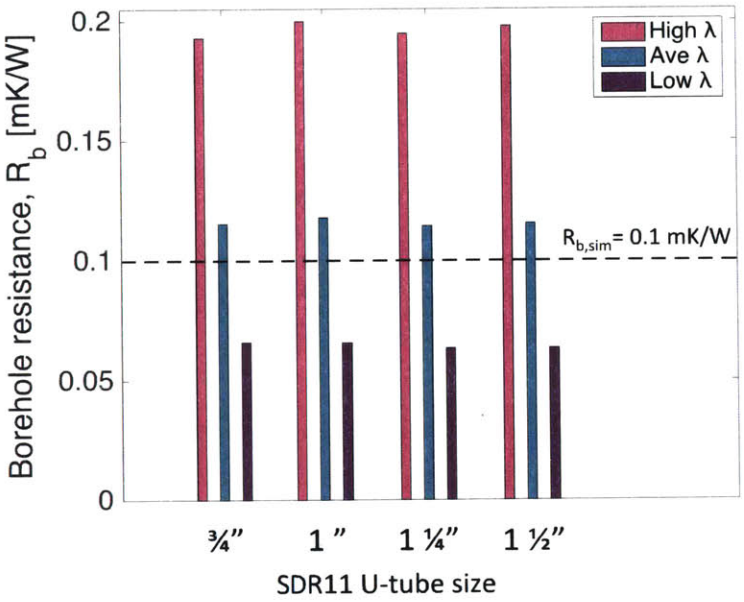

Figure A.2: Effective borehole thermal resistance, R_b, for different coefficients of thermal conductivity of the grout and the pipe material and different U-tube sizes

Appendix B
Tabulated Results from Specific Gravity Tests

B.1) Calibration of Flasks

Table B.1 summarizes the results from the calibration of four iodine flasks (F1, F4, F6 and F7) at different temperatures, while Tables B.2 to B.13 show the measurements.

	F1	F4	F6	F7
Mass (g)	147.46	142.82	146.50	142.14
Volume (cm^3)	271.60	277.12	273.23	273.71

Table B.1: Summary of results from calibration of four flasks (F1, F4, F6, F7)

Calibration of flask F1:

MIT GEOTECHNICAL LABORATORY
SPECIFIC GRAVITY FLASK CALIBRATION
DATA SHEET

Project: PhD Thesis Date:
Flask Number: F1 Flask Type: Test By: DMZ

Determination Number (5 required)	Mass Dry Bottle (gm)	Date	Time	Mass Bottle & Water (gm)	Temperature (°C)	Mass Density Pure Water (gm/cm^3)	Volume (cm^3)	Volume at 20°C (cm^3)
1	147.45	11/18/14	18:30	418.48	21.8	0.9978186	271.62	271.61
2	147.45	11/18/14	18:55	418.45	22.0	0.9977736	271.60	271.59
3	147.45	11/18/14	19:15	418.43	22.1	0.9977510	271.58	271.58
4	147.46	11/18/14	19:30	418.44	22.2	0.9977283	271.60	271.60
5	147.47	11/18/14	19:45	418.46	22.3	0.9977055	271.63	271.62
Average	147.46						271.61	271.60
Std. Dev.	0.0080						0.016507643	0.016462479

Notes: a) Make all mass measurements to 0.01 gm and check scale zero after each measurement
b) Make temperature measurement to 0.1 degree and check various locations in flask
c) Wear cloth gloves when handling flask to prevent temperature change while setting volume
d) Set volume, measure mass, measure temperature, and then add water
e) Place flask on insulated block while setting volume
f) Use all seven digits of water density
g) Compute volume to 0.01 cm^3
h) Standard deviation should be less then 0.04 cm^3

Table B.2: Calibration of flask F1 at room temperature

MIT GEOTECHNICAL LABORATORY
SPECIFIC GRAVITY FLASK CALIBRATION
DATA SHEET

Project: PhD Thesis — Date: _____
Flask Number: F1 — Flask Type: _____ — Test By: DMZ

Determination Number (5 required)	Mass Dry Bottle (gm)	Date	Time	Mass Bottle & Water (gm)	Temperature (°C)	Mass Density Pure Water (gm/cm^3)	Volume (cm^3)	Volume at 20°C (cm^3)
1	147.45	11/18/14	10:45	418.96	7.6	0.9999954	271.51	271.54
2	147.45	11/18/14	11:10	418.99	10.2	0.9997461	271.60	271.63
3	147.45	11/18/14	11:30	418.88	12.0	0.9995343	271.55	271.57
4	147.46	11/18/14	11:55	418.84	14.1	0.9992467	271.59	271.60
5	147.47	11/18/14	12:20	418.78	15.5	0.9990307	271.59	271.60
6		11/18/14	12:50	418.77	16.8	0.9988128	271.64	271.65
7		11/18/14	13:30	418.70	17.8	0.9986337	271.62	271.62
8		11/18/14	14:40	418.61	19.3	0.9983466	271.60	271.60
9		11/18/14	16:00	418.57	20.2	0.9981636	271.61	271.61
10		11/18/14	16:30	418.52	20.9	0.9980158	271.60	271.60
11		11/18/14	17:00	418.50	21.1	0.9979726	271.59	271.59
12		11/18/14	17:30	418.49	21.5	0.9978852	271.61	271.60
Average	147.46						271.60	271.61
Std. Dev.	0.0080						0.021441468	0.019369959

Table B.3: Calibration of cooled flask F1

MIT GEOTECHNICAL LABORATORY
SPECIFIC GRAVITY FLASK CALIBRATION
DATA SHEET

Project: PhD Thesis — Date: _____
Flask Number: F1 — Flask Type: _____ — Test By: DMZ

Determination Number (5 required)	Mass Dry Bottle (gm)	Date	Time	Mass Bottle & Water (gm)	Temperature (°C)	Mass Density Pure Water (gm/cm^3)	Volume (cm^3)	Volume at 20°C (cm^3)
1	147.45	11/19/14	10:20	414.48	63.6	0.9798237	272.52	272.40
2	147.45	11/19/14	10:44	415.81	50.1	0.9875266	271.74	271.66
3	147.45	11/19/14	11:10	416.60	43.2	0.9907668	271.65	271.59
4	147.46	11/19/14	11:30	417.01	39.5	0.9923102	271.64	271.59
5	147.47	11/19/14	11:45	417.41	36.5	0.9934621	271.73	271.69
6		11/19/14	12:10	417.58	33.8	0.9944227	271.64	271.60
7		11/19/14	12:35	417.79	31.8	0.9950877	271.67	271.64
8		11/19/14	13:15	417.96	29.6	0.9957734	271.65	271.63
9		11/19/14	14:20	418.14	27.3	0.9964391	271.65	271.63
10		11/19/14	15:20	418.22	26.1	0.9967656	271.64	271.63
11		11/19/14	16:20	418.26	25.2	0.9970011	271.62	271.60
12		11/19/14	17:05	418.31	24.8	0.9971032	271.64	271.63
Average	147.46						271.66	271.63
Std. Dev.	0.0080						0.03912255	0.029509881

Table B.4: Calibration of heated flask F1

Calibration of flask F4:

MIT GEOTECHNICAL LABORATORY
SPECIFIC GRAVITY FLASK CALIBRATION
DATA SHEET

Project: PhD Thesis — Date: _____
Flask Number: F4 — Flask Type: _____ — Test By: DMZ

Determination Number (5 required)	Mass Dry Bottle (gm)	Date	Time	Mass Bottle & Water (gm)	Temperature (°C)	Mass Density Pure Water (gm/cm³)	Volume (cm³)	Volume at 20°C (cm³)
1	142.81	11/18/14	18:30	419.35	21.7	0.9978409	277.13	277.12
2	142.82	11/18/14	18:55	419.33	21.9	0.9977961	277.12	277.11
3	142.82	11/18/14	19:15	419.31	22.1	0.9977510	277.11	277.11
4	142.82	11/18/14	19:30	419.31	22.2	0.9977283	277.12	277.11
5	142.84	11/18/14	19:45	419.33	22.3	0.9977055	277.14	277.14
Average	142.82						277.12	277.12
Std. Dev.	0.0098						0.012587401	0.012421662

Notes: a) Make all mass measurements to 0.01 gm and check scale zero after each measurement
b) Make temperature measurement to 0.1 degree and check various locations in flask
c) Wear cloth gloves when handling flask to prevent temperature change while setting volume
d) Set volume, measure mass, measure temperature, and then add water
e) Place flask on insulated block while setting volume
f) Use all seven digits of water density
g) Compute volume to 0.01 cm^3
h) Standard deviation should be less then 0.04 cm^3

Table B.5: Calibration of flask F4 at room temperature

MIT GEOTECHNICAL LABORATORY
SPECIFIC GRAVITY FLASK CALIBRATION
DATA SHEET

Project: PhD Thesis — Date: _____
Flask Number: F4 — Flask Type: _____ — Test By: DMZ

Determination Number (5 required)	Mass Dry Bottle (gm)	Date	Time	Mass Bottle & Water (gm)	Temperature (°C)	Mass Density Pure Water (gm/cm³)	Volume (cm³)	Volume at 20°C (cm³)
1	142.81	11/18/14	10:45	419.82	7.6	0.9999954	277.00	277.03
2	142.82	11/18/14	11:10	419.81	10.5	0.9997131	277.07	277.09
3	142.82	11/18/14	11:30	419.85	12.3	0.9994959	277.17	277.19
4	142.82	11/18/14	11:55	419.69	14.1	0.9992467	277.08	277.09
5	142.84	11/18/14	12:20	419.66	15.7	0.9989983	277.12	277.13
6		11/18/14	12:50	419.60	16.5	0.9988645	277.09	277.10
7		11/18/14	13:30	419.59	17.7	0.9986521	277.14	277.15
8		11/18/14	14:40	419.49	19.2	0.9983664	277.12	277.12
9		11/18/14	16:00	419.40	20.2	0.9981636	277.09	277.09
10		11/18/14	16:30	419.37	20.9	0.9980158	277.10	277.10
11		11/18/14	17:00	419.37	21.2	0.9979509	277.12	277.11
12		11/18/14	17:30	419.33	21.5	0.9978852	277.09	277.09
Average	142.82						277.11	277.11
Std. Dev.	0.0098						0.029264335	0.031189547

Table B.6: Calibration of cooled flask F4

MIT GEOTECHNICAL LABORATORY
SPECIFIC GRAVITY FLASK CALIBRATION
DATA SHEET

Project: PhD Thesis Date:
Flask Number: F4 Flask Type: Test By: DMZ

Determination Number (5 required)	Mass Dry Bottle (gm)	Date	Time	Mass Bottle & Water (gm)	Temperature (°C)	Mass Density Pure Water (gm/cm³)	Volume (cm³)	Volume at 20°C (cm³)
1	142.81	11/19/14	10:20	415.69	60.1	0.9819940	277.87	277.76
2	142.82	11/19/14	10:44	416.81	48.7	0.9882221	277.25	277.17
3	142.82	11/19/14	11:10	417.48	42.9	0.9908970	277.18	277.12
4	142.82	11/19/14	11:30	417.84	39.4	0.9923501	277.14	277.08
5	142.84	11/19/14	11:45	418.14	36.6	0.9934252	277.14	277.09
6		11/19/14	12:10	418.40	33.7	0.9944569	277.11	277.08
7		11/19/14	12:35	418.67	31.8	0.9950877	277.21	277.18
8		11/19/14	13:15	418.76	29.7	0.9957433	277.12	277.09
9		11/19/14	14:20	419.01	27.3	0.9964391	277.17	277.15
10		11/19/14	15:20	419.09	26.1	0.9967656	277.16	277.15
11		11/19/14	16:20	419.09	25.3	0.9969754	277.11	277.09
12		11/19/14	17:05	419.12	24.8	0.9971032	277.10	277.09
Average	142.82						277.15	277.12
Std. Dev.	0.0098						0.04772702	0.038310418

Table B.7: Calibration of heated flask F4

Calibration of flask F6:

MIT GEOTECHNICAL LABORATORY
SPECIFIC GRAVITY FLASK CALIBRATION
DATA SHEET

Project: PhD Thesis Date:
Flask Number: F6 Flask Type: Test By: DMZ

Determination Number (5 required)	Mass Dry Bottle (gm)	Date	Time	Mass Bottle & Water (gm)	Temperature (°C)	Mass Density Pure Water (gm/cm³)	Volume (cm³)	Volume at 20°C (cm³)
1	146.50	11/18/14	18:30	419.16	21.7	0.9978409	273.25	273.25
2	146.50	11/18/14	18:55	419.13	22.0	0.9977736	273.24	273.23
3	146.50	11/18/14	19:15	419.10	22.1	0.9977510	273.21	273.21
4	146.50	11/18/14	19:30	419.10	22.1	0.9977510	273.21	273.21
5	146.50	11/18/14	19:35	419.11	22.3	0.9977055	273.24	273.23
Average	146.50						273.23	273.23
Std. Dev.	0.0000						0.01578716	0.016106064

Notes: a) Make all mass measurements to 0.01 gm and check scale zero after each measurement
b) Make temperature measurement to 0.1 degree and check various locations in flask
c) Wear cloth gloves when handling flask to prevent temperature change while setting volume
d) Set volume, measure mass, measure temperature, and then add water
e) Place flask on insulated block while setting volume
f) Use all seven digits of water density
g) Compute volume to 0.01 cm^3
h) Standard deviation should be less then 0.04 cm^3

Table B.8: Calibration of flask F6 at room temperature

MIT GEOTECHNICAL LABORATORY
SPECIFIC GRAVITY FLASK CALIBRATION
DATA SHEET

Project: PhD Thesis — Date: _____
Flask Number: F6 — Flask Type: _____ — Test By: DMZ

Determination Number (5 required)	Mass Dry Bottle (gm)	Date	Time	Mass Bottle & Water (gm)	Temperature (°C)	Mass Density Pure Water (gm/cm³)	Volume (cm³)	Volume at 20°C (cm³)
1	146.50	11/18/14	10:45	419.65	7.9	0.9999701	273.16	273.20
2	146.50	11/18/14	11:10	419.58	10.6	0.9997018	273.16	273.19
3	146.50	11/18/14	11:30	419.54	12.4	0.9994829	273.18	273.20
4	146.50	11/18/14	11:55	419.45	14.4	0.9992021	273.17	273.18
5	146.50	11/18/14	12:20	419.43	15.8	0.9989819	273.21	273.22
6		11/18/14	12:50	419.39	16.8	0.9988128	273.21	273.22
7		11/18/14	13:30	419.35	17.9	0.9986153	273.23	273.23
8		11/18/14	14:40	419.31	19.3	0.9983466	273.26	273.26
9		11/18/14	16:00	419.20	20.3	0.9981428	273.21	273.21
10		11/18/14	16:30	419.18	20.7	0.9980585	273.21	273.21
11		11/18/14	17:00	419.18	21.1	0.9979726	273.23	273.23
12		11/18/14	17:30	419.15	21.4	0.9979072	273.22	273.22
Average	146.50						273.21	273.22
Std. Dev.	0.0000						0.029491714	0.022672925

Table B.9: Calibration of cooler flask F6

MIT GEOTECHNICAL LABORATORY
SPECIFIC GRAVITY FLASK CALIBRATION
DATA SHEET

Project: PhD Thesis — Date: _____
Flask Number: F6 — Flask Type: _____ — Test By: DMZ

Determination Number (5 required)	Mass Dry Bottle (gm)	Date	Time	Mass Bottle & Water (gm)	Temperature (°C)	Mass Density Pure Water (gm/cm³)	Volume (cm³)	Volume at 20°C (cm³)
1	146.50	11/19/14	10:20	415.51	59.6	0.9822941	273.86	273.73
2	146.50	11/19/14	10:44	416.68	48.3	0.9884173	273.35	273.27
3	146.50	11/19/14	11:10	417.41	42.2	0.9911973	273.32	273.26
4	146.50	11/19/14	11:30	417.75	38.7	0.9926261	273.27	273.21
5	146.50	11/19/14	11:45	418.00	36.0	0.9936455	273.24	273.19
6		11/19/14	12:10	418.26	33.2	0.9946263	273.23	273.19
7		11/19/14	12:35	418.50	31.5	0.9951840	273.32	273.28
8		11/19/14	13:15	418.60	29.4	0.9958334	273.24	273.21
9		11/19/14	14:20	418.80	27.1	0.9964945	273.26	273.24
10		11/19/14	15:20	418.85	26.0	0.9967922	273.23	273.21
11		11/19/14	16:20	418.89	25.2	0.9970011	273.21	273.20
12		11/19/14	17:05	418.96	24.8	0.9971032	273.25	273.24
Average	146.50						273.26	273.23
Std. Dev.	0.0000						0.044095029	0.031973716

Table B.10: Calibration of heated flask F6

Calibration of flask F7:

MIT GEOTECHNICAL LABORATORY
SPECIFIC GRAVITY FLASK CALIBRATION
DATA SHEET

Project: PhD Thesis — Date: _____
Flask Number: F7 — Flask Type: _____ — Test By: DMZ

Determination Number (5 required)	Mass Dry Bottle (gm)	Date	Time	Mass Bottle & Water (gm)	Temperature (°C)	Mass Density Pure Water (gm/cm³)	Volume (cm³)	Volume at 20°C (cm³)
1	142.14	11/18/14	18:30	415.26	21.7	0.9978409	273.71	273.70
2	142.14	11/18/14	18:55	415.26	21.9	0.9977961	273.72	273.71
3	142.14	11/18/14	19:15	415.25	22.0	0.9977736	273.72	273.71
4	142.15	11/18/14	19:30	415.24	22.1	0.9977510	273.71	273.70
5	142.15	11/18/14	19:45	415.25	22.2	0.9977283	273.73	273.72
Average	142.14						273.72	273.71
Std. Dev.	0.0049						0.007930073	0.007495234

Notes: a) Make all mass measurements to 0.01 gm and check scale zero after each measurement
b) Make temperature measurement to 0.1 degree and check various locations in flask
c) Wear cloth gloves when handling flask to prevent temperature change while setting volume
d) Set volume, measure mass, measure temperature, and then add water
e) Place flask on insulated block while setting volume
f) Use all seven digits of water density
g) Compute volume to 0.01 cm^3
h) Standard deviation should be less then 0.04 cm^3

Table B.11: Calibration of flask F7 at room temperature

MIT GEOTECHNICAL LABORATORY
SPECIFIC GRAVITY FLASK CALIBRATION
DATA SHEET

Project: PhD Thesis — Date: _____
Flask Number: F7 — Flask Type: _____ — Test By: DMZ

Determination Number (5 required)	Mass Dry Bottle (gm)	Date	Time	Mass Bottle & Water (gm)	Temperature (°C)	Mass Density Pure Water (gm/cm³)	Volume (cm³)	Volume at 20°C (cm³)
1	142.14	11/18/14	10:45	415.75	8.1	0.9999527	273.62	273.66
2	142.14	11/18/14	11:10	415.71	10.7	0.9996905	273.65	273.68
3	142.14	11/18/14	11:30	415.72	12.7	0.9994433	273.73	273.75
4	142.15	11/18/14	11:55	415.62	14.5	0.9991870	273.70	273.72
5	142.15	11/18/14	12:20	415.61	15.8	0.9989819	273.74	273.76
6		11/18/14	12:50	415.52	17.0	0.9987777	273.71	273.72
7		11/18/14	13:30	415.49	18.0	0.9985967	273.73	273.74
8		11/18/14	14:40	415.41	19.5	0.9983066	273.73	273.73
9		11/18/14	16:00	415.35	20.3	0.9981428	273.71	273.71
10		11/18/14	16:30	415.33	20.7	0.9980585	273.72	273.72
11		11/18/14	17:00	415.31	21.1	0.9979726	273.72	273.72
12		11/18/14	17:30	415.28	21.3	0.9979291	273.70	273.70
Average	142.14						273.71	273.72
Std. Dev.	0.0049						0.02468113	0.022230456

Table B.12: Calibration of cooled flask F7

MIT GEOTECHNICAL LABORATORY
SPECIFIC GRAVITY FLASK CALIBRATION
DATA SHEET

Project: PhD Thesis — Date:
Flask Number: F7 — Flask Type: — Test By: DMZ

Determination Number (5 required)	Mass Dry Bottle (gm)	Date	Time	Mass Bottle & Water (gm)	Temperature (°C)	Mass Density Pure Water (gm/cm³)	Volume (cm³)	Volume at 20°C (cm³)
1	142.14	11/19/14	10:20	411.70	61.2	0.9813249	274.69	274.57
2	142.14	11/19/14	10:44	412.91	48.0	0.9885626	273.90	273.82
3	142.14	11/19/14	11:10	413.56	42.0	0.9912822	273.80	273.75
4	142.15	11/19/14	11:30	413.90	38.6	0.9926652	273.76	273.72
5	142.15	11/19/14	11:45	414.15	36.2	0.9935724	273.77	273.73
6		11/19/14	12:10	414.39	33.4	0.9945588	273.74	273.71
7		11/19/14	12:35	414.54	31.6	0.9951520	273.72	273.70
8		11/19/14	13:15	414.73	29.4	0.9958334	273.73	273.71
9		11/19/14	14:20	414.93	27.1	0.9964945	273.75	273.74
10		11/19/14	15:20	415.00	25.9	0.9968186	273.73	273.72
11		11/19/14	16:20	415.08	25.1	0.9970268	273.75	273.75
12		11/19/14	17:05	415.11	24.7	0.9971285	273.75	273.75
Average	142.14						273.76	273.74
Std. Dev.	0.0049						0.050600196	0.033509789

Table B.13: Calibration of heated flask F7

B.2) Specific Gravity Measurements for Glass Beads

Table B.14 summarizes the results from the specific gravity measurements for glass beads at different temperatures using the water submersion method and four flasks (F1, F4, F6 and F7), while Tables B.15 to B.29 present the measurements.

Glass Beads		
T_{ave} [°C]	$G_{s20,ave}$ [-]	St. Dev. [-]
16.73	2.2181	0.0015
23.14	2.2176	0.0018
33.24	2.2190	0.0011
39.93	2.2156	0.0022

Table B.14: Summary of specific gravity, $G_{s20,}$ for glass beads using water submersion method at different temperatures and four flasks (F1, F4, F6 and F7)

Measurements from Flask F1

MIT GEOTECHNICAL LABORATORY
SPECIFIC GRAVITY TEST
DATA SHEET

Project	PhD Thesis	Boring No.		Date Start	11/20/14
Test No.	SG100	Sample No.	glass beads	Date End	
Specimen Location		Sample Depth		Tested By	DMZ

Flask No. F1 Calibration Date 11/18/14 Flask Volume (cm^3) 271.60 Flask Mass (gm) 147.46

Dry Mass of Soil		Before Test Going into Flask	After Test Taken out of Flask
Tare No.		M3	
Mass Tare+Wet Soil	(gm)		
Mass Tare+Dry Soil	(gm)	52.06	
Mass Tare	(gm)	19.64	
Mass Dry Soil	(gm)	32.42	
Water Content	(%)		

Determination Number (3 required)	Date	Time	Mass Bottle, Water & Soil (gm)	Temperature (°C)	Mass Density Pure Water* (gm/cm^3)	Specific Gravity of Soil at T
1	11/20/14	17:00	436.22	23.1	0.9975195	2.220
2	11/20/14	17:20	436.21	23.1	0.9975195	2.219
3	11/20/14	17:40	436.22	23.1	0.9975195	2.220
4	11/20/14	18:05	436.21	23.1	0.9975195	2.219
5	11/20/14	18:25	436.20	23.2	0.9974958	2.218
6	11/20/14	18:45	436.20	23.3	0.9974720	2.219
Average						2.219
Std. Dev.						0.000884852

Make all mass measurements to 0.01 gm and check scale zero after each measurement

Make temperature measurement to 0.1 degree and check various locations in flask

Wear cloth gloves when handling flask to prevent temperature change while setting volume

Set volume, measure mass, measure temperature, and then add water

Place flask on insulated block while setting volume
Use six digits for water density

Notes: a) Compute Specific Gravity to 0.001
b) Standard deviation should be less then 0.002
c) Water density calculated based on ASTM recommendations $\rho_w = 1.00034038 - 7.77x10^{-6}T - 4.95x10^{-6}T^2$, [T] = °C

Table B.15: Measurements of specific gravity, G_{s20}, at T_{ave} = 23°C for glass beads (flask F1)

Determination Number (3 required)	Date	Time	Mass Bottle, Water & Soil (gm)	Temperature (°C)	Mass Density Pure Water* (gm/cm^3)	Specific Gravity of Soil at 20C
1	11/21/14	13:10	436.73	11.2	0.9996324	2.220
2	11/21/14	13:30	436.68	12.7	0.9994433	2.220
3	11/21/14	13:55	436.62	14.4	0.9992021	2.219
4	11/21/14	14:25	436.55	16.1	0.9989322	2.218
5	11/21/14	16:40	436.44	18.8	0.9984448	2.220
6	11/21/14	17:10	436.40	19.7	0.9982663	2.220
7	11/21/14	17:40	436.37	20.1	0.9981844	2.219
8	11/21/14	18:40	436.36	20.8	0.9980372	2.222
Average						2.220
Std. Dev.						0.001301479

Table B.16: Measurements of specific gravity, $G_{s20,}$ at T_{ave} = 17°C for glass beads (flask F1)

Determination Number (3 required)	Date	Time	Mass Bottle, Water & Soil (gm)	Temperature (°C)	Mass Density Pure Water* (gm/cm^3)	Specific Gravity of Soil at 20C
1	11/20/14	20:25	432.64	58.9	0.9827101	2.241
2	11/20/14	20:48	433.81	50.0	0.9875769	2.232
3	11/20/14	21:11	434.43	44.3	0.9902818	2.222
4	11/20/14	21:50	434.91	39.6	0.9922703	2.220
5	11/20/14	22:15	435.20	36.6	0.9934252	2.220
6	11/20/14	22:42	435.43	34.0	0.9943540	2.220
7	11/20/14	23:20	435.62	31.7	0.9951199	2.219
8	11/20/14	23:40	435.71	30.6	0.9954676	2.220
9	11/21/14	0:00	435.78	29.6	0.9957734	2.219
10	11/21/14	0:15	435.85	28.8	0.9960109	2.221
11	11/21/14	0:30	435.91	28.1	0.9962135	2.222
12	11/21/14	0:45	435.92	27.6	0.9963552	2.218
Average						2.220
Std. Dev.						0.001310204

Table B.17: Measurements of specific gravity, $G_{s20,}$ at T_{ave} = 33°C for glass beads (flask F1)

Determination Number (3 required)	Date	Time	Mass Bottle, Water & Soil (gm)	Temperature (°C)	Mass Density Pure Water* (gm/cm³)	Specific Gravity of Soil at 20C
1	11/22/14	11:45	432.49	60.6	0.9816913	2.258
2	11/22/14	12:00	433.45	52.4	0.9863417	2.224
3	11/22/14	12:20	434.17	46.0	0.9895088	2.212
4	11/22/14	12:40	434.69	41.7	0.9914089	2.219
5	11/22/14	13:00	435.01	38.3	0.9927817	2.215
6	11/22/14	13:20	435.26	35.8	0.9937181	2.218
Average						2.216
Std. Dev.						0.002921124

Table B.18: Measurements of specific gravity, $G_{s20,}$ at T_{ave} = 40°C for glass beads (flask F1)

Measurements from Flask F4

MIT GEOTECHNICAL LABORATORY
SPECIFIC GRAVITY TEST
DATA SHEET

Project PhD Thesis | Boring No. | Date Start 11/20/14
Test No. SG101 | Sample No. glass beads | Date End
Specimen Location | Sample Depth | Tested By DMZ

Flask No. F4 | Calibration Date 11/18/14 | Flask Volume (cm³) 277.12 | Flask Mass (gm) 142.82

Dry Mass of Soil		Before Test Going into Flask	After Test Taken out of Flask
Tare No.		LL1	
Mass Tare+Wet Soil	(gm)		
Mass Tare+Dry Soil	(gm)	52.66	
Mass Tare	(gm)	24.95	
Mass Dry Soil	(gm)	27.71	
Water Content	(%)		

Determination Number (3 required)	Date	Time	Mass Bottle, Water & Soil (gm)	Temperature (°C)	Mass Density Pure Water* (gm/cm³)	Specific Gravity of Soil at 20C
1	11/20/14	17:00	434.49	23.0	0.9975431	2.218
2	11/20/14	17:20	434.48	23.1	0.9975195	2.217
3	11/20/14	17:40	434.48	23.1	0.9975195	2.217
4	11/20/14	18:05	434.46	23.1	0.9975195	2.213
5	11/20/14	18:25	434.46	23.2	0.9974958	2.214
6	11/20/14	18:45	434.45	23.3	0.9974720	2.214
Average						2.215
Std. Dev.						0.001863333

Table B.19: Measurements of specific gravity, $G_{s20,}$ at T_{ave} = 23°C for glass beads (flask F4)

Determination Number (3 required)	Date	Time	Mass Bottle, Water & Soil (gm)	Temperature (°C)	Mass Density Pure Water* (gm/cm^3)	Specific Gravity of Soil at 20C
1	11/21/14	13:10	434.99	11.2	0.9996324	2.214
2	11/21/14	13:30	434.95	12.7	0.9994433	2.215
3	11/21/14	13:55	434.88	14.7	0.9991565	2.215
4	11/21/14	14:25	434.82	16.3	0.9988986	2.216
5	11/21/14	16:40	434.72	18.8	0.9984448	2.218
6	11/21/14	17:10	434.69	19.5	0.9983066	2.219
7	11/21/14	17:40	434.66	20.0	0.9982050	2.218
8	11/21/14	18:40	434.63	20.8	0.9980372	2.220
Average						2.217
Std. Dev.						0.002235306

Table B.20: Measurements of specific gravity, $G_{s20,}$ at T_{ave} = 17°C for glass beads (flask F4)

Determination Number (3 required)	Date	Time	Mass Bottle, Water & Soil (gm)	Temperature (°C)	Mass Density Pure Water* (gm/cm^3)	Specific Gravity of Soil at 20C
1	11/20/14	20:25	430.78	59.4	0.9824135	2.253
2	11/20/14	20:48	431.95	50.5	0.9873243	2.234
3	11/20/14	21:11	432.61	44.6	0.9901475	2.221
4	11/20/14	21:50	433.11	40.1	0.9920692	2.221
5	11/20/14	22:15	433.40	36.9	0.9933137	2.216
6	11/20/14	22:42	433.63	34.5	0.9941806	2.217
7	11/20/14	23:20	433.85	32.1	0.9949904	2.219
8	11/20/14	23:40	433.93	30.9	0.9953740	2.216
9	11/21/14	0:00	434.01	30.0	0.9956523	2.218
10	11/21/14	0:15	434.08	29.1	0.9959226	2.218
11	11/21/14	0:30	434.13	28.6	0.9960693	2.220
12	11/21/14	0:45	434.18	28.0	0.9962420	2.221
Average						2.219
Std. Dev.						0.002054455

Table B.21: Measurements of specific gravity, $G_{s20,}$ at T_{ave} = 33°C for glass beads (flask F4)

Determination Number (3 required)	Date	Time	Mass Bottle, Water & Soil (gm)	Temperature (°C)	Mass Density Pure Water* (gm/cm³)	Specific Gravity of Soil at 20C
1	11/22/14	11:45	431.28	56.7	0.9839861	2.270
2	11/22/14	12:00	432.01	49.7	0.9877273	2.226
3	11/22/14	12:20	432.61	44.4	0.9902372	2.217
4	11/22/14	12:40	432.99	40.9	0.9917422	2.215
5	11/22/14	13:00	433.30	37.6	0.9930501	2.210
6	11/22/14	13:20	433.52	35.4	0.9938622	2.212
Average						2.214
Std. Dev.						0.002842791

Table B.22: Measurements of specific gravity, $G_{s20,}$ at T_{ave} = 40°C for glass beads (flask F4)

Measurements from Flask F6

MIT GEOTECHNICAL LABORATORY
SPECIFIC GRAVITY TEST
DATA SHEET

Project PhD Thesis | Boring No. | Date Start 11/20/14
Test No. SG102 | Sample No. glass beads | Date End
Specimen Location | Sample Depth | Tested By DMZ

Flask No. F6 | Calibration Date 11/18/14 | Flask Volume (cm³) 273.22 | Flask Mass (gm) 146.50

Dry Mass of Soil		Before Test Going into Flask	After Test Taken out of Flask
Tare No.		I6	
Mass Tare+Wet Soil	(gm)		
Mass Tare+Dry Soil	(gm)	53.87	
Mass Tare	(gm)	24.18	
Mass Dry Soil	(gm)	29.69	
Water Content	(%)		

Determination Number (3 required)	Date	Time	Mass Bottle, Water & Soil (gm)	Temperature (°C)	Mass Density Pure Water* (gm/cm³)	Specific Gravity of Soil at 20C
1	11/20/14	17:00	435.37	23.0	0.9975431	2.218
2	11/20/14	17:20	435.37	23.1	0.9975195	2.219
3	11/20/14	17:40	435.36	23.1	0.9975195	2.217
4	11/20/14	18:05	435.35	23.1	0.9975195	2.216
5	11/20/14	18:25	435.34	23.2	0.9974958	2.215
6	11/20/14	18:45	435.34	23.3	0.9974720	2.216
Average						2.217
Std. Dev.						0.001533905

Table B.23: Measurements of specific gravity, $G_{s20,}$ at T_{ave} = 23°C for glass beads (flask F6)

Determination Number (3 required)	Date	Time	Mass Bottle, Water & Soil (gm)	Temperature (°C)	Mass Density Pure Water* (gm/cm^3)	Specific Gravity of Soil at 20C
1	11/21/14	13:10	435.85	11.1	0.9996442	2.213
2	11/21/14	13:30	435.81	12.7	0.9994433	2.214
3	11/21/14	13:55	435.77	14.7	0.9991565	2.219
4	11/21/14	14:25	435.74	16.0	0.9989489	2.222
5	11/21/14	16:40	435.58	18.9	0.9984253	2.217
6	11/21/14	17:10	435.57	19.5	0.9983066	2.220
7	11/21/14	17:40	435.54	20.0	0.9982050	2.219
8	11/21/14	18:40	435.50	20.7	0.9980585	2.218
Average						2.218
Std. Dev.						0.003147578

Table B.24: Measurements of specific gravity, $G_{s20,}$ at T_{ave} = 17°C for glass beads (flask F6)

Determination Number (3 required)	Date	Time	Mass Bottle, Water & Soil (gm)	Temperature (°C)	Mass Density Pure Water* (gm/cm^3)	Specific Gravity of Soil at 20C
1	11/20/14	20:25	431.98	57.9	0.9832961	2.255
2	11/20/14	20:48	433.05	49.1	0.9880254	2.232
3	11/20/14	21:11	433.64	43.5	0.9906357	2.220
4	11/20/14	21:50	434.08	39.4	0.9923501	2.220
5	11/20/14	22:15	434.33	36.5	0.9934621	2.215
6	11/20/14	22:42	434.53	34.3	0.9942502	2.216
7	11/20/14	23:20	434.72	32.0	0.9950229	2.215
8	11/20/14	23:40	434.82	30.9	0.9953740	2.217
9	11/21/14	0:00	434.89	30.0	0.9956523	2.217
10	11/21/14	0:15	434.97	29.1	0.9959226	2.219
11	11/21/14	0:30	435.02	28.4	0.9961272	2.219
12	11/21/14	0:45	435.07	27.8	0.9962988	2.220
Average						2.218
Std. Dev.						0.002060319

Table B.25: Measurements of specific gravity, $G_{s20,}$ at T_{ave} = 33°C for glass beads (flask F6)

Determination Number (3 required)	Date	Time	Mass Bottle, Water & Soil (gm)	Temperature (°C)	Mass Density Pure Water* (gm/cm³)	Specific Gravity of Soil at 20C
1	11/22/14	11:45	432.32	55.6	0.9846061	2.256
2	11/22/14	12:00	433.05	48.5	0.9883199	2.219
3	11/22/14	12:20	433.64	43.4	0.9906795	2.218
4	11/22/14	12:40	433.98	40.0	0.9921096	2.214
5	11/22/14	13:00	434.26	37.1	0.9932389	2.213
6	11/22/14	13:20	434.46	34.9	0.9940401	2.213
Average						2.214
Std. Dev.						0.002297597

Table B.26: Measurements of specific gravity, G_{s20}, at T_{ave} = 39°C for glass beads (flask F6)

Measurements from Flask F7

MIT GEOTECHNICAL LABORATORY
SPECIFIC GRAVITY TEST
DATA SHEET

Project PhD Thesis | Boring No. | Date Start 11/20/14
Test No. SG103 | Sample No. glass beads | Date End
Specimen Location | Sample Depth | Tested By DMZ

Flask No. F7 | Calibration Date 11/18/14 | Flask Volume (cm³) 273.71 | Flask Mass (gm) 142.14

Dry Mass of Soil		Before Test Going into Flask	After Test Taken out of Flask
Tare No.		51	
Mass Tare+Wet Soil	(gm)		
Mass Tare+Dry Soil	(gm)	51.99	
Mass Tare	(gm)	20.90	
Mass Dry Soil	(gm)	31.09	
Water Content	(%)		

Determination Number (3 required)	Date	Time	Mass Bottle, Water & Soil (gm)	Temperature (°C)	Mass Density Pure Water* (gm/cm³)	Specific Gravity of Soil at 20C
1	11/20/14	17:00	432.27	23.0	0.9975431	2.218
2	11/20/14	17:20	432.28	23.1	0.9975195	2.221
3	11/20/14	17:40	432.26	23.1	0.9975195	2.218
4	11/20/14	18:05	432.27	23.1	0.9975195	2.219
5	11/20/14	18:25	432.26	23.2	0.9974958	2.219
6	11/20/14	18:45	432.25	23.3	0.9974720	2.218
Average						2.219
Std. Dev.						0.001151026

Table B.27: Measurements of specific gravity, G_{s20}, at T_{ave} = 23°C for glass beads (flask F7)

Determination Number (3 required)	Date	Time	Mass Bottle, Water & Soil (gm)	Temperature (°C)	Mass Density Pure Water* (gm/cm^3)	Specific Gravity of Soil at 20C
1	11/20/14	20:25	429.02	58.0	0.9832379	2.280
2	11/20/14	20:48	429.99	48.9	0.9881239	2.234
3	11/20/14	21:11	430.56	43.4	0.9906795	2.221
4	11/20/14	21:50	430.99	39.3	0.9923898	2.221
5	11/20/14	22:15	431.24	36.5	0.9934621	2.217
6	11/20/14	22:42	431.44	34.3	0.9942502	2.217
7	11/20/14	23:20	431.64	32.1	0.9949904	2.220
8	11/20/14	23:40	431.73	31.0	0.9953426	2.220
9	11/21/14	0:00	431.80	30.0	0.9956523	2.219
10	11/21/14	0:15	431.87	29.1	0.9959226	2.219
11	11/21/14	0:30	431.93	28.4	0.9961272	2.220
12	11/21/14	0:45	431.97	27.9	0.9962705	2.221
Average						2.219
Std. Dev.						0.001385734

Table B.28: Measurements of specific gravity, $G_{s20,}$ at T_{ave} = 33°C for glass beads (flask F7)

Determination Number (3 required)	Date	Time	Mass Bottle, Water & Soil (gm)	Temperature (°C)	Mass Density Pure Water* (gm/cm^3)	Specific Gravity of Soil at 20C
1	11/22/14	11:45	429.30	54.8	0.9850495	2.249
2	11/22/14	12:00	430.02	48.3	0.9884173	2.227
3	11/22/14	12:20	430.56	43.3	0.9907232	2.219
4	11/22/14	12:40	430.87	40.2	0.9920286	2.216
5	11/22/14	13:00	431.16	37.3	0.9931637	2.216
6	11/22/14	13:20	431.34	35.2	0.9939336	2.214
Average						2.219
Std. Dev.						0.004856169

Table B.29: Measurements of specific gravity, $G_{s20,}$ at T_{ave} = 41°C for glass beads (flask F7)

B.3) Specific Gravity Measurements for Kaolinite

Table B.30 summarizes the results from the specific gravity measurements for Kaolinite at different temperatures using the water submersion method and four flasks (F1, F4, F6 and F7), while Tables B.31 to B.46 present the measurements.

Kaolinite		
T_{ave} [°C]	$G_{s20,ave}$ [-]	St. Dev. [-]*
22.83	2.6314	0.0016
27.15	2.6307	0.0020
31.53	2.6304	0.0024
36.70	2.6237	0.0036
* Calculated from normalized $G_{s20}(T)/G_{s20}(20°C)$ and then multiplied by $G_{s20,ave}(T)$		

Table B.30: Summary of specific gravity, $G_{s20,}$ for Kaolinite using water submersion method at different temperatures and four flasks (F1, F4, F6 and F7)

Measurements from Flask F1

MIT GEOTECHNICAL LABORATORY
SPECIFIC GRAVITY TEST
DATA SHEET

Project	PhD Thesis	Boring No.		Date Start	1/30/15
Test No.	SG108	Sample No.	kaolinite	Date End	
Specimen Location		Sample Depth		Tested By	DMZ

Flask No. F1 Calibration Date 1/30/15 Flask Volume (cm^3) 271.46 Flask Mass (gm) 147.45

Dry Mass of Soil		Before Test Going into Flask	After Test Taken out of Flask
Tare No.		Plastic container 1	C2
Mass Tare+Wet Soil	(gm)		
Mass Tare+Dry Soil	(gm)	88.35	1021.80
Mass Tare	(gm)	51.09	984.88
Mass Dry Soil	(gm)	37.26	36.92
Water Content	(%)		

Determination Number (3 required)	Date	Time	Mass Bottle, Water & Soil (gm)	Temperature (°C)	Mass Density Pure Water* (gm/cm^3)	Specific Gravity of Soil at 20C
1	1/26/15	12:15	441.29	20.7	0.9980585	2.634
2	1/26/15	13:00	441.23	21.8	0.9978186	2.634
3	1/26/15	14:18	441.14	23.4	0.9974481	2.634
4	1/26/15	15:11	441.10	24.0	0.9973027	2.633
5	1/26/15	16:00	441.05	24.7	0.9971285	2.632
Average						2.634
Std. Dev.						0.000901758

Table B.31: Measurements of specific gravity at T_{ave} = 23°C for kaolinite (flask F1)

Determination Number (3 required)	Date	Time	Mass Bottle, Water & Soil (gm)	Temperature (°C)	Mass Density Pure Water* (gm/cm^3)	Specific Gravity of Soil at 20C
1	1/22/15	11:40	440.89	27.5	0.9963833	2.637
2	1/22/15	14:30	440.86	27.8	0.9962988	2.635
3	1/22/15	15:30	440.89	27.4	0.9964112	2.635
4	1/22/15	17:00	440.88	27.1	0.9964945	2.630
5	1/22/15	18:00	440.90	27.1	0.9964945	2.633
Average						2.634
Std. Dev.						0.002721405

Table B.32: Measurements of specific gravity at T_{ave} = 27°C for kaolinite (flask F1)

Determination Number (3 required)	Date	Time	Mass Bottle, Water & Soil (gm)	Temperature (°C)	Mass Density Pure Water* (gm/cm^3)	Specific Gravity of Soil at 20C
1	1/21/15	12:30	440.57	31.4	0.9952159	2.631
2	1/21/15	14:00	440.56	31.7	0.9951199	2.634
3	1/21/15	15:30	440.54	32.1	0.9949904	2.636
4	1/21/15	17:10	440.53	32.2	0.9949578	2.636
5	1/21/15	18:40	440.53	32.1	0.9949904	2.634
Average						2.634
Std. Dev.						0.001958249

Table B.33: Measurements of specific gravity at T_{ave} = 32°C for kaolinite (flask F1)

Determination Number (3 required)	Date	Time	Mass Bottle, Water & Soil (gm)	Temperature (°C)	Mass Density Pure Water* (gm/cm^3)	Specific Gravity of Soil at 20C
1	1/16/15	11:30	440.10	37.0	0.9932763	2.634
2	1/16/15	14:30	440.03	37.4	0.9931259	2.628
3	1/16/15	16:00	440.04	37.3	0.9931637	2.628
4	1/16/15	18:30	440.11	36.8	0.9933510	2.632
5	1/16/15	20:30	440.08	37.0	0.9932763	2.630
Average						2.630
Std. Dev.						0.002680404

Table B.34: Measurements of specific gravity at T_{ave} = 37°C for kaolinite (flask F1)

Measurements from Flask F4

MIT GEOTECHNICAL LABORATORY
SPECIFIC GRAVITY TEST
DATA SHEET

Project	PhD Thesis	Boring No.		Date Start	
Test No.		Sample No.	kaolinite	Date End	
Specimen Location		Sample Depth		Tested By	DMZ

Flask No. F4 Calibration Date 1/30/15 Flask Volume (cm^3) 276.95 Flask Mass (gm) 142.81

Dry Mass of Soil		Before Test Going into Flask	After Test Taken out of Flask
Tare No.		Plastic Container 3	C1
Mass Tare+Wet Soil	(gm)		
Mass Tare+Dry Soil	(gm)	86.47	1029.48
Mass Tare	(gm)	48.62	992.65
Mass Dry Soil	(gm)	37.85	36.83
Water Content	(%)		

Determination Number (3 required)	Date	Time	Mass Bottle, Water & Soil (gm)	Temperature (°C)	Mass Density Pure Water* (gm/cm^3)	Specific Gravity of Soil at 20C
1	1/26/15	12:15	442.06	20.6	0.9980797	2.630
2	1/26/15	13:00	442.01	21.6	0.9978631	2.631
3	1/26/15	14:18	441.91	23.1	0.9975195	2.629
4	1/26/15	15:11	441.85	23.9	0.9973272	2.626
5	1/26/15	16:00	441.81	24.5	0.9971788	2.626
Average						2.629
Std. Dev.						0.002339891

Table B.35: Measurements of specific gravity at T_{ave} = 23°C for kaolinite (flask F4)

Determination Number (3 required)	Date	Time	Mass Bottle, Water & Soil (gm)	Temperature (°C)	Mass Density Pure Water* (gm/cm^3)	Specific Gravity of Soil at 20C
1	1/22/15	11:40	441.65	27.3	0.9964391	2.631
2	1/22/15	14:30	441.60	27.6	0.9963552	2.626
3	1/22/15	15:30	441.64	27.2	0.9964668	2.628
4	1/22/15	17:00	441.65	27.0	0.9965220	2.627
5	1/22/15	18:00	441.66	27.0	0.9965220	2.629
Average						2.628
Std. Dev.						0.002035411

Table B.36: Measurements of specific gravity at T_{ave} = 27°C for kaolinite (flask F4)

Determination Number (3 required)	Date	Time	Mass Bottle, Water & Soil (gm)	Temperature (°C)	Mass Density Pure Water* (gm/cm^3)	Specific Gravity of Soil at 20C
1	1/21/15	12:30	441.35	31.3	0.9952477	2.631
2	1/21/15	14:00	441.33	31.4	0.9952159	2.629
3	1/21/15	15:30	441.28	31.7	0.9951199	2.624
4	1/21/15	17:10	441.27	31.9	0.9950553	2.626
5	1/21/15	18:40	441.28	31.7	0.9951199	2.624
Average						2.627
Std. Dev.						0.003167733

Table B.37: Measurements of specific gravity at T_{ave} = 32°C for kaolinite (flask F4)

Determination Number (3 required)	Date	Time	Mass Bottle, Water & Soil (gm)	Temperature (°C)	Mass Density Pure Water* (gm/cm^3)	Specific Gravity of Soil at 20C
1	1/16/15	11:30	440.79	37.0	0.9932763	2.621
2	1/16/15	14:30	440.74	37.4	0.9931259	2.618
3	1/16/15	16:00	440.79	37.1	0.9932389	2.622
4	1/16/15	18:30	440.81	36.7	0.9933881	2.619
5	1/16/15	20:30	440.80	37.0	0.9932763	2.622
Average						2.621
Std. Dev.						0.001870026

Table B.38: Measurements of specific gravity at T_{ave} = 37°C for kaolinite (flask F4)

Measurements from Flask F6

MIT GEOTECHNICAL LABORATORY
SPECIFIC GRAVITY TEST
DATA SHEET

Project PhD Thesis | Boring No. | Date Start
Test No. | Sample No. Kaolinite | Date End
Specimen Location | Sample Depth | Tested By DMZ

Flask No. F6 | Calibration Date 1/30/15 | Flask Volume (cm^3) 273.05 | Flask Mass (gm) 146.49

Dry Mass of Soil		Before Test Going into Flask	After Test Taken out of Flask
Tare No.		Plastic Container 4	C3
Mass Tare+Wet Soil	(gm)		
Mass Tare+Dry Soil	(gm)	82.96	999.71
Mass Tare	(gm)	47.37	964.20
Mass Dry Soil	(gm)	35.59	35.51
Water Content	(%)		

Determination Number (3 required)	Date	Time	Mass Bottle, Water & Soil (gm)	Temperature (°C)	Mass Density Pure Water* (gm/cm^3)	Specific Gravity of Soil at 20C
1	1/26/15	12:15	441.06	20.5	0.9981009	2.635
2	1/26/15	13:00	441.00	21.6	0.9978631	2.635
3	1/26/15	14:18	440.90	23.1	0.9975195	2.632
4	1/26/15	15:11	440.86	23.8	0.9973516	2.632
5	1/26/15	16:00	440.81	24.5	0.9971788	2.631
Average						2.633
Std. Dev.						0.001869398

Table B.39: Measurements of specific gravity at T_{ave} = 23°C for kaolinite (flask F6)

Determination Number (3 required)	Date	Time	Mass Bottle, Water & Soil (gm)	Temperature (°C)	Mass Density Pure Water* (gm/cm^3)	Specific Gravity of Soil at 20C
1	1/22/15	11:40	440.66	26.8	0.9965769	2.631
2	1/22/15	14:30	440.62	27.4	0.9964112	2.631
3	1/22/15	15:30	440.64	27.1	0.9964945	2.631
4	1/22/15	17:00	440.65	26.9	0.9965495	2.630
5	1/22/15	18:00	440.67	26.7	0.9966041	2.632
Average						2.631
Std. Dev.						0.000454531

Table B.40: Measurements of specific gravity at T_{ave} = 27°C for kaolinite (flask F6)

Determination Number (3 required)	Date	Time	Mass Bottle, Water & Soil (gm)	Temperature (°C)	Mass Density Pure Water* (gm/cm^3)	Specific Gravity of Soil at 20C
1	1/21/15	12:30	440.34	31.0	0.9953426	2.629
2	1/21/15	14:00	440.36	31.1	0.9953110	2.634
3	1/21/15	15:30	440.32	31.3	0.9952477	2.630
4	1/21/15	17:10	440.32	31.3	0.9952477	2.630
5	1/21/15	18:40	440.33	31.2	0.9952794	2.630
Average						2.630
Std. Dev.						0.002186591

Table B.41: Measurements of specific gravity at T_{ave} = 32°C for kaolinite (flask F6)

Determination Number (3 required)	Date	Time	Mass Bottle, Water & Soil (gm)	Temperature (°C)	Mass Density Pure Water* (gm/cm^3)	Specific Gravity of Soil at 20C
1	1/16/15	11:30	439.93	35.5	0.9938263	2.623
2	1/16/15	14:30	439.85	36.8	0.9933510	2.631
3	1/16/15	16:00	439.88	36.2	0.9935724	2.626
4	1/16/15	18:30	439.88	36.2	0.9935724	2.626
5	1/16/15	20:30	439.88	36.3	0.9935358	2.628
Average						2.627
Std. Dev.						0.002864535

Table B.42: Measurements of specific gravity at T_{ave} = 37°C for kaolinite (flask F6)

Measurements from Flask F7

MIT GEOTECHNICAL LABORATORY
SPECIFIC GRAVITY TEST
DATA SHEET

Project: PhD Thesis | Boring No.: | Date Start:
Test No.: | Sample No.: Kaolinite | Date End:
Specimen Location: | Sample Depth: | Tested By: DMZ

Flask No.: F7 | Calibration Date: 1/30/15 | Flask Volume (cm^3): 273.55 | Flask Mass (gm): 142.15

Dry Mass of Soil		Before Test Going into Flask	After Test Taken out of Flask
Tare No.		Plastic Container 5	A28 (ceramic bowl)
Mass Tare+Wet Soil	(gm)		
Mass Tare+Dry Soil	(gm)	84.95	1007.19
Mass Tare	(gm)	47.07	969.50
Mass Dry Soil	(gm)	37.88	37.69
Water Content	(%)		

Determination Number (3 required)	Date	Time	Mass Bottle, Water & Soil (gm)	Temperature (°C)	Mass Density Pure Water* (gm/cm^3)	Specific Gravity of Soil at 20C
1	1/26/15	12:15	438.54	20.8	0.9980372	2.632
2	1/26/15	13:00	438.47	22.0	0.9977736	2.632
3	1/26/15	14:18	438.38	23.3	0.9974720	2.629
4	1/26/15	15:11	438.34	24.0	0.9973027	2.629
5	1/26/15	16:00	438.31	24.6	0.9971537	2.630
Average						2.630
Std. Dev.						0.001587312

Table B.43: Measurements of specific gravity at T_{ave} = 23°C for kaolinite (flask F7)

Determination Number (3 required)	Date	Time	Mass Bottle, Water & Soil (gm)	Temperature (°C)	Mass Density Pure Water* (gm/cm^3)	Specific Gravity of Soil at 20C
1	1/22/15	11:40	438.17	26.8	0.9965769	2.631
2	1/22/15	14:30	438.12	27.4	0.9964112	2.629
3	1/22/15	15:30	438.13	27.1	0.9964945	2.627
4	1/22/15	17:00	438.17	26.9	0.9965495	2.632
5	1/22/15	18:00	438.16	26.8	0.9965769	2.629
Average						2.630
Std. Dev.						0.0018486

Table B.44: Measurements of specific gravity at T_{ave} = 27°C for kaolinite (flask F7)

Determination Number (3 required)	Date	Time	Mass Bottle, Water & Soil (gm)	Temperature (°C)	Mass Density Pure Water* (gm/cm^3)	Specific Gravity of Soil at 20C
1	1/21/15	12:30	437.84	31.3	0.9952477	2.631
2	1/21/15	14:00	437.83	31.3	0.9952477	2.630
3	1/21/15	15:30	437.82	31.4	0.9952159	2.629
4	1/21/15	17:10	437.82	31.5	0.9951840	2.631
5	1/21/15	18:40	437.81	31.6	0.9951520	2.630
Average						2.630
Std. Dev.						0.000879892

Table B.45: Measurements of specific gravity at T_{ave} = 32°C for kaolinite (flask F7)

Determination Number (3 required)	Date	Time	Mass Bottle, Water & Soil (gm)	Temperature (°C)	Mass Density Pure Water* (gm/cm^3)	Specific Gravity of Soil at 20C
1	1/16/15	11:30	437.44	35.8	0.9937181	2.628
2	1/16/15	14:30	437.37	36.9	0.9933137	2.634
3	1/16/15	16:00	437.37	36.5	0.9934621	2.627
4	1/16/15	18:30	437.38	36.5	0.9934621	2.629
5	1/16/15	20:30	437.36	36.6	0.9934252	2.627
Average						2.629
Std. Dev.						0.002893911

Table B.46: Measurements of specific gravity at T_{ave} = 37°C for kaolinite (flask F7)

B.4) Specific Gravity Measurements for Resedimented Boston Blue Clay (RBBC)

Table B.47 summarizes the results from the specific gravity measurements for RBBC at different temperatures using the water submersion method and four flasks (F1, F4, F6 and F7), while Tables B.48 to B.63 present the measurements.

RBBC		
T_{ave} [°C]	$G_{s20,ave}$ [-]	St. Dev. [-]*
21.68	2.8021	0.0015
28.17	2.7922	0.0042
31.39	2.7983	0.0024
34.69	2.7983	0.0022
* Calculated from normalized $G_{s20}(T)/G_{s20}(20°C)$ and then multiplied by $G_{s20,ave}(T)$		

Table B.47: Summary of specific gravity, $G_{s20,}$ for RBBC using water submersion method at different temperatures and four flasks (F1, F4, F6 and F7)

Measurements from Flask F1

MIT GEOTECHNICAL LABORATORY
SPECIFIC GRAVITY TEST
DATA SHEET

Project	PhD Thesis	Boring No.		Date Start	3/18/15
Test No.	SG108	Sample No.	BBC	Date End	
Specimen Location		Sample Depth		Tested By	DMZ

Flask No. F1 Calibration Date 1/30/15 Flask Volume (cm^3) 271.46 Flask Mass (gm) 147.45

Dry Mass of Soil		Before Test Going into Flask	After Test Taken out of Flask
Tare No.		Plastic container 1	T-11
Mass Tare+Wet Soil	(gm)		
Mass Tare+Dry Soil	(gm)	92.95	
Mass Tare	(gm)	55.65	
Mass Dry Soil	(gm)	37.30	36.80
Water Content	(%)		

Determination Number (3 required)	Date	Time	Mass Bottle, Water & Soil (gm)	Temperature (°C)	Mass Density Pure Water* (gm/cm^3)	Specific Gravity of Soil at 20C
1	3/18/15	10:25	441.96	21.5	0.9978852	2.791
2	3/18/15	11:35	441.95	21.5	0.9978852	2.789
3	3/18/15	13:00	441.95	21.7	0.9978409	2.791
4	3/18/15	14:00	441.94	21.8	0.9978186	2.790
5	3/18/15	15:15	441.93	21.9	0.9977961	2.790
Average						2.790
Std. Dev.						0.001019407

Table B.48: Measurements of specific gravity at T_{ave} = 22°C for RBBC (flask F1)

Determination Number (3 required)	Date	Time	Mass Bottle, Water & Soil (gm)	Temperature (°C)	Mass Density Pure Water* (gm/cm^3)	Specific Gravity of Soil at 20C
1	3/23/15	11:00	441.47	28.6	0.9960693	2.783
2	3/23/15	12:20	441.52	27.7	0.9963271	2.780
3	3/23/15	14:10	441.51	27.8	0.9962988	2.779
4	3/23/15	15:45	441.49	28.0	0.9962420	2.778
5	3/24/15	11:23	441.38	29.5	0.9958034	2.778
Average						2.779
Std. Dev.						0.002023078

Table B.49: Measurements of specific gravity at T_{ave} = 28°C for RBBC (flask F1)

Determination Number (3 required)	Date	Time	Mass Bottle, Water & Soil (gm)	Temperature (°C)	Mass Density Pure Water* (gm/cm^3)	Specific Gravity of Soil at 20C
1	3/21/15	16:15	441.25	31.6	0.9951520	2.785
2	3/21/15	17:30	441.26	31.6	0.9951520	2.787
3	3/21/15	18:30	441.27	31.3	0.9952477	2.784
4	3/21/15	20:00	441.28	31.3	0.9952477	2.786
5	3/21/15	21:30	441.27	31.4	0.9952159	2.785
Average						2.785
Std. Dev.						0.0011391

Table B.50: Measurements of specific gravity at T_{ave} = 31°C for RBBC (flask F1)

Determination Number (3 required)	Date	Time	Mass Bottle, Water & Soil (gm)	Temperature (°C)	Mass Density Pure Water* (gm/cm^3)	Specific Gravity of Soil at 20C
1	3/19/15	10:00	441.01	34.5	0.9941806	2.785
2	3/19/15	13:10	440.98	34.8	0.9940753	2.784
3	3/19/15	15:40	440.99	34.9	0.9940401	2.788
4	3/19/15	17:45	440.97	35.0	0.9940047	2.786
5	3/19/15	19:50	440.97	34.8	0.9940753	2.782
Average						2.785
Std. Dev.						0.002235872

Table B.51: Measurements of specific gravity at T_{ave} = 35°C for RBBC (flask F1)

Measurements from Flask F4

MIT GEOTECHNICAL LABORATORY
SPECIFIC GRAVITY TEST
DATA SHEET

Project PhD Thesis | Boring No. | Date Start 3/18/15
Test No. | Sample No. BBC | Date End
Specimen Location | Sample Depth | Tested By DMZ

Flask No. F4 Calibration Date 1/30/15 Flask Volume (cm^3) 276.95 Flask Mass (gm) 142.81

Dry Mass of Soil		Before Test Going into Flask	After Test Taken out of Flask
Tare No.		1	U1A
Mass Tare+Wet Soil	(gm)		
Mass Tare+Dry Soil	(gm)	92.54	
Mass Tare	(gm)	55.65	
Mass Dry Soil	(gm)	36.89	36.51
Water Content	(%)		

Determination Number (3 required)	Date	Time	Mass Bottle, Water & Soil (gm)	Temperature (°C)	Mass Density Pure Water* (gm/cm^3)	Specific Gravity of Soil at 20C
1	3/18/15	10:25	442.71	21.5	0.9978852	2.812
2	3/18/15	11:35	442.73	21.5	0.9978852	2.817
3	3/18/15	13:00	442.71	21.6	0.9978631	2.813
4	3/18/15	14:00	442.70	21.8	0.9978186	2.814
5	3/18/15	15:15	442.70	21.9	0.9977961	2.815
Average						2.814
Std. Dev.						0.00164708

Table B.52: Measurements of specific gravity at T_{ave} = 22°C for RBBC (flask F4)

Determination Number (3 required)	Date	Time	Mass Bottle, Water & Soil (gm)	Temperature (°C)	Mass Density Pure Water* (gm/cm^3)	Specific Gravity of Soil at 20C
1	3/23/15	11:00	442.23	28.2	0.9961848	2.801
2	3/23/15	12:20	442.26	27.7	0.9963271	2.800
3	3/23/15	14:!0	442.26	27.7	0.9963271	2.800
4	3/23/15	15:45	442.27	27.7	0.9963271	2.802
5	3/24/15	11:23	442.18	29.5	0.9958034	2.812
Average						2.803
Std. Dev.						0.004844389

Table B.53: Measurements of specific gravity at T_{ave} = 28°C for RBBC (flask F4)

Determination Number (3 required)	Date	Time	Mass Bottle, Water & Soil (gm)	Temperature (°C)	Mass Density Pure Water* (gm/cm^3)	Specific Gravity of Soil at 20C
1	3/21/15	16:15	441.98	31.7	0.9951199	2.806
2	3/21/15	17:30	442.03	31.3	0.9952477	2.810
3	3/21/15	18:30	442.03	31.2	0.9952794	2.808
4	3/21/15	20:00	442.03	31.2	0.9952794	2.808
5	3/21/15	21:30	442.02	31.3	0.9952477	2.808
Average						2.808
Std. Dev.						0.001339883

Table B.54: Measurements of specific gravity at T_{ave} = 31°C for RBBC (flask F4)

Determination Number (3 required)	Date	Time	Mass Bottle, Water & Soil (gm)	Temperature (°C)	Mass Density Pure Water* (gm/cm^3)	Specific Gravity of Soil at 20C
1	3/19/15	10:00	441.78	34.4	0.9942155	2.813
2	3/19/15	13:00	441.72	34.8	0.9940753	2.808
3	3/19/15	15:40	441.74	34.9	0.9940401	2.814
4	3/19/15	17:45	441.73	34.8	0.9940753	2.810
5	3/19/15	19:50	441.73	34.9	0.9940401	2.812
Average						2.811
Std. Dev.						0.002515412

Table B.55: Measurements of specific gravity at T_{ave} = 35°C for RBBC (flask F4)

Measurements from Flask F6

MIT GEOTECHNICAL LABORATORY
SPECIFIC GRAVITY TEST
DATA SHEET

Project PhD Thesis | Boring No. | Date Start 3/18/15
Test No. | Sample No. BBC | Date End
Specimen Location | Sample Depth | Tested By DMZ

Flask No. F6 | Calibration Date 1/30/15 | Flask Volume (cm^3) 273.05 | Flask Mass (gm) 146.49

Dry Mass of Soil		Before Test Going into Flask	After Test Taken out of Flask
Tare No.		Plastic Container 1	B1
Mass Tare+Wet Soil	(gm)		
Mass Tare+Dry Soil	(gm)	92.99	
Mass Tare	(gm)	55.65	
Mass Dry Soil	(gm)	37.34	37.23
Water Content	(%)		

Determination Number (3 required)	Date	Time	Mass Bottle, Water & Soil (gm)	Temperature (°C)	Mass Density Pure Water* (gm/cm^3)	Specific Gravity of Soil at 20C
1	3/18/15	10:25	442.88	21.5	0.9978852	2.795
2	3/18/15	11:35	442.88	21.5	0.9978852	2.795
3	3/18/15	13:00	442.89	21.6	0.9978631	2.798
4	3/18/15	14:00	442.87	21.8	0.9978186	2.796
5	3/18/15	15:15	442.87	21.9	0.9977961	2.797
Average						2.796
Std. Dev.						0.001467608

Table B.56: Measurements of specific gravity at T_{ave} = 22°C for RBBC (flask F6)

Determination Number (3 required)	Date	Time	Mass Bottle, Water & Soil (gm)	Temperature (°C)	Mass Density Pure Water* (gm/cm^3)	Specific Gravity of Soil at 20C
1	3/23/15	11:00	442.42	28.0	0.9962420	2.784
2	3/23/15	12:20	442.47	27.6	0.9963552	2.789
3	3/23/15	14:10	442.44	27.7	0.9963271	2.784
4	3/23/15	15:45	442.43	27.8	0.9962988	2.783
6	3/23/15	11:23	442.32	29.3	0.9958632	2.783
Average						2.785
Std. Dev.						0.002483856

Table B.57: Measurements of specific gravity at T_{ave} = 28°C for RBBC (flask F6)

Determination Number (3 required)	Date	Time	Mass Bottle, Water & Soil (gm)	Temperature (°C)	Mass Density Pure Water* (gm/cm^3)	Specific Gravity of Soil at 20C
1	3/21/15	16:15	442.22	31.4	0.9952159	2.796
2	3/21/15	17:30	442.20	31.4	0.9952159	2.792
3	3/21/15	18:30	442.21	31.5	0.9951840	2.796
4	3/21/15	20:00	442.22	31.2	0.9952794	2.793
6	3/21/15	21:30	442.21	31.5	0.9951840	2.796
Average						2.794
Std. Dev.						0.002098731

Table B.58: Measurements of specific gravity at T_{ave} = 31°C for RBBC (flask F6)

Determination Number (3 required)	Date	Time	Mass Bottle, Water & Soil (gm)	Temperature (°C)	Mass Density Pure Water* (gm/cm^3)	Specific Gravity of Soil at 20C
1	3/19/15	10:00	441.98	34.2	0.9942849	2.795
2	3/19/15	13:10	441.94	34.4	0.9942155	2.790
3	3/19/15	15:40	441.94	34.7	0.9941105	2.796
4	3/19/15	17:45	441.93	34.7	0.9941105	2.794
5	3/19/15	19:50	441.92	34.7	0.9941105	2.792
Average						2.793
Std. Dev.						0.002317743

Table B.59: Measurements of specific gravity at T_{ave} = 35°C for RBBC (flask F6)

Measurements from Flask F7

MIT GEOTECHNICAL LABORATORY
SPECIFIC GRAVITY TEST
DATA SHEET

Project PhD Thesis | Boring No. | Date Start 3/18/15
Test No. | Sample No. BBC | Date End
Specimen Location | Sample Depth | Tested By DMZ

Flask No. F7 | Calibration Date 1/30/15 | Flask Volume (cm^3) 273.55 | Flask Mass (gm) 142.15

Dry Mass of Soil		Before Test Going into Flask	After Test Taken out of Flask
Tare No.		Plastic Container 1	B2
Mass Tare+Wet Soil	(gm)		
Mass Tare+Dry Soil	(gm)	94.07	
Mass Tare	(gm)	55.65	
Mass Dry Soil	(gm)	38.42	38.19
Water Content	(%)		

Determination Number (3 required)	Date	Time	Mass Bottle, Water & Soil (gm)	Temperature (°C)	Mass Density Pure Water* (gm/cm^3)	Specific Gravity of Soil at 20C
1	3/18/15	10:25	439.73	21.5	0.9978852	2.810
2	3/18/15	11:35	439.71	21.6	0.9978631	2.807
3	3/18/15	13:00	439.71	21.7	0.9978409	2.808
4	3/18/15	14:00	439.70	21.8	0.9978186	2.807
5	3/18/15	15:15	439.68	21.9	0.9977961	2.804
Average						2.807
Std. Dev.						0.002091962

Table B.60: Measurements of specific gravity at T_{ave} = 22°C for RBBC (flask F7)

Determination Number (3 required)	Date	Time	Mass Bottle, Water & Soil (gm)	Temperature (°C)	Mass Density Pure Water* (gm/cm^3)	Specific Gravity of Soil at 20C
1	3/23/15	11:00	439.27	27.9	0.9962705	2.798
2	3/23/15	12:20	439.30	27.6	0.9963552	2.800
3	3/23/15	14:10	439.27	27.8	0.9962988	2.797
4	3/23/15	15:45	439.30	27.9	0.9962705	2.804
5	3/23/15	11:23	439.22	29.3	0.9958632	2.809
Average						2.802
Std. Dev.						0.00497968

Table B.61: Measurements of specific gravity at T_{ave} = 28°C for RBBC (flask F7)

Determination Number (3 required)	Date	Time	Mass Bottle, Water & Soil (gm)	Temperature (°C)	Mass Density Pure Water* (gm/cm^3)	Specific Gravity of Soil at 20C
1	3/21/15	16:15	439.04	31.4	0.9952159	2.805
2	3/21/15	17:30	439.04	31.4	0.9952159	2.805
3	3/21/15	18:30	439.04	31.4	0.9952159	2.805
4	3/21/15	20:00	439.06	31.3	0.9952477	2.808
5	3/21/15	21:30	439.03	31.4	0.9952159	2.803
Average						2.805
Std. Dev.						0.001612194

Table B.62: Measurements of specific gravity at T_{ave} = 31°C for RBBC (flask F7)

Determination Number (3 required)	Date	Time	Mass Bottle, Water & Soil (gm)	Temperature (°C)	Mass Density Pure Water* (gm/cm^3)	Specific Gravity of Soil at 20C
1	3/19/15	10:00	438.76	34.5	0.9941806	2.801
2	3/19/15	13:10	438.76	34.7	0.9941105	2.805
3	3/19/15	15:40	438.76	34.7	0.9941105	2.805
4	3/19/15	17:45	438.75	34.7	0.9941105	2.803
5	3/19/15	19:50	438.75	34.7	0.9941105	2.803
Average						2.803
Std. Dev.						0.001561331

Table B.63: Measurements of specific gravity at T_{ave} = 35°C for RBBC (flask F7)

B.5) Specific Gravity Measurements for Eugene Island – Gulf of Mexico (EI-GOM) Clay

Table B.64 summarizes the results from the specific gravity measurements for EI_GOM at different temperatures using the water submersion method and four flasks (F1, F4, F6 and F7), while Tables B.65 to B.76 present the measurements.

EI_GOM		
T_{ave} [°C]	$G_{s20,ave}$ [-]	St. Dev. [-]*
22.2	2.8543	0.0051
36.3	2.8401	0.0045
29.3	2.8285	0.0047
* Calculated from normalized $G_{s20}(T)/G_{s20}(20°C)$ and then multiplied by $G_{s20,ave}(T)$		

Table B.64: Summary of specific gravity, G_{s20}, for EI_GOM using water submersion method at different temperatures and four flasks (F1, F4, F6 and F7)

Measurements from Flask F1

MIT GEOTECHNICAL LABORATORY
SPECIFIC GRAVITY TEST
DATA SHEET

Project PhD Thesis | Boring No. | Date Start 3/28/15
Test No. | Sample No. GOM-EI | Date End
Specimen Location | Sample Depth | Tested By DMZ

Flask No. F1 | Calibration Date 1/30/15 | Flask Volume (cm^3) 271.46 | Flask Mass (gm) 147.45

Dry Mass of Soil		Before Test Going into Flask	After Test Taken out of Flask
Tare No.			
Mass Tare+Wet Soil	(gm)		
Mass Tare+Dry Soil	(gm)		230.78
Mass Tare	(gm)		200.02
Mass Dry Soil	(gm)		30.76
Water Content	(%)		

Determination Number (3 required)	Date	Time	Mass Bottle, Water & Soil (gm)	Temperature (°C)	Mass Density Pure Water* (gm/cm^3)	Specific Gravity of Soil at 20C
1	3/28/15	15:15	438.30	21.8	0.9978186	2.852
2	3/28/15	16:30	438.23	22.0	0.9977736	2.836
3	3/28/15	17:30	438.24	22.2	0.9977283	2.842
4	3/28/15	18:30	438.22	22.3	0.9977055	2.838
5	3/28/15	19:30	438.21	22.4	0.9976826	2.837
6	3/28/15	19:30	438.21	22.4	0.9976826	2.837
Average						2.841
Std. Dev.						0.006390675

Table B.65: Measurements of specific gravity at T_{ave} = 22°C for EI-GOM (flask F1)

Determination Number (3 required)	Date	Time	Mass Bottle, Water & Soil (gm)	Temperature (°C)	Mass Density Pure Water* (gm/cm^3)	Specific Gravity of Soil at 20C
1	4/1/15	11:00	437.68	29.2	0.9958929	2.815
2	4/1/15	12:15	437.68	29.2	0.9958929	2.815
3	4/1/15	14:45	437.66	29.6	0.9957734	2.818
4	4/2/15	9:30	437.65	29.7	0.9957433	2.817
5	4/2/15	11:00	437.64	29.6	0.9957734	2.813
Average						2.816
Std. Dev.						0.002027388

Table B.66: Measurements of specific gravity at T_{ave} = 29°C for EI-GOM (flask F1)

Determination Number (3 required)	Date	Time	Mass Bottle, Water & Soil (gm)	Temperature (°C)	Mass Density Pure Water* (gm/cm^3)	Specific Gravity of Soil at 20C
1	3/31/15	10:00	437.17	36.0	0.9936455	2.830
2	3/31/15	12:20	437.12	36.5	0.9934621	2.829
3	3/31/15	14:30	437.11	36.4	0.9934990	2.824
4	3/31/15	16:45	437.09	36.7	0.9933881	2.827
5	3/31/15	18:45	437.11	36.6	0.9934252	2.829
6	3/31/15	20:45	437.08	36.8	0.9933510	2.826
Average						2.828
Std. Dev.						0.002317593

Table B.67: Measurements of specific gravity at T_{ave} = 36°C for EI-GOM (flask F1)

Measurements from Flask F4

MIT GEOTECHNICAL LABORATORY
SPECIFIC GRAVITY TEST
DATA SHEET

Project	PhD Thesis	Boring No.		Date Start	3/28/15
Test No.		Sample No.	GOM	Date End	
Specimen Location		Sample Depth		Tested By	DMZ

Flask No. F4 Calibration Date 1/30/15 Flask Volume (cm^3) 276.95 Flask Mass (gm) 142.81

Dry Mass of Soil		Before Test Going into Flask	After Test Taken out of Flask
Tare No.		2	TO5
Mass Tare+Wet Soil	(gm)		
Mass Tare+Dry Soil	(gm)	75.68	
Mass Tare	(gm)	50.11	
Mass Dry Soil	(gm)	25.57	24.71
Water Content	(%)		

Determination Number (3 required)	Date	Time	Mass Bottle, Water & Soil (gm)	Temperature (°C)	Mass Density Pure Water* (gm/cm^3)	Specific Gravity of Soil at 20C
1	3/28/15	15:15	435.22	21.8	0.9978186	2.855
2	3/28/15	16:30	435.23	22.0	0.9977736	2.862
3	3/28/15	17:30	435.22	22.1	0.9977510	2.861
4	3/28/15	18:30	435.19	22.4	0.9976826	2.857
5	3/28/15	19:30	435.18	22.4	0.9976826	2.854
6	3/30/15	10:45	435.19	22.4	0.9976826	2.857
7	3/30/15	11:30	435.19	22.5	0.9976596	2.859
8	3/30/15	12:15	435.18	22.6	0.9976365	2.857
Average						2.858
Std. Dev.						0.002889803

Table B.68: Measurements of specific gravity at T_{ave} = 22°C for EI-GOM (flask F4)

Determination Number (3 required)	Date	Time	Mass Bottle, Water & Soil (gm)	Temperature (°C)	Mass Density Pure Water* (gm/cm^3)	Specific Gravity of Soil at 20C
1	4/1/15	11:00	434.68	29.0	0.9959521	2.836
2	4/1/15	12:15	434.68	29.0	0.9959521	2.836
3	4/1/15	14:45	434.63	29.6	0.9957734	2.835
4	4/2/15	9:30	434.62	29.6	0.9957734	2.831
5	4/2/15	11:00	434.64	29.4	0.9958334	2.833
Average						2.834
Std. Dev.						0.001962384

Table B.69: Measurements of specific gravity at T_{ave} = 29°C for EI-GOM (flask F4)

Determination Number (3 required)	Date	Time	Mass Bottle, Water & Soil (gm)	Temperature (°C)	Mass Density Pure Water* (gm/cm³)	Specific Gravity of Soil at 20C
1	3/31/15	10:00	434.09	36.1	0.9936090	2.842
2	3/31/15	12:20	434.09	36.5	0.9934621	2.855
3	3/31/15	14:30	434.05	36.4	0.9934990	2.838
4	3/31/15	16:45	434.05	36.5	0.9934621	2.842
5	3/31/15	18:45	434.04	36.4	0.9934990	2.835
6	3/31/15	20:45	434.05	36.4	0.9934990	2.838
Average						2.842
Std. Dev.						0.006861151

Table B.70: Measurements of specific gravity at T_{ave} = 36°C for EI-GOM (flask F4)

Measurements from Flask F6

MIT GEOTECHNICAL LABORATORY
SPECIFIC GRAVITY TEST
DATA SHEET

Project PhD Thesis | Boring No. | Date Start 3/18/15
Test No. | Sample No. BBC | Date End
Specimen Location | Sample Depth | Tested By DMZ

Flask No. F6 | Calibration Date 1/30/15 | Flask Volume (cm³) 273.05 | Flask Mass (gm) 146.49

Dry Mass of Soil		Before Test Going into Flask	After Test Taken out of Flask
Tare No.		3	B2
Mass Tare+Wet Soil	(gm)		
Mass Tare+Dry Soil	(gm)	76.24	
Mass Tare	(gm)	49.40	
Mass Dry Soil	(gm)	26.84	24.33
Water Content	(%)		

Determination Number (3 required)	Date	Time	Mass Bottle, Water & Soil (gm)	Temperature (°C)	Mass Density Pure Water* (gm/cm³)	Specific Gravity of Soil at 20C
1	3/28/15	15:15	434.77	21.8	0.9978186	2.858
2	3/28/15	16:30	434.76	22.0	0.9977736	2.859
3	3/28/15	17:30	434.75	22.2	0.9977283	2.859
4	3/28/15	18:30	434.74	22.3	0.9977055	2.858
5	3/28/15	19:30	434.73	22.4	0.9976826	2.856
Average						2.858
Std. Dev.						0.001088467

Table B.71: Measurements of specific gravity at T_{ave} = 22°C for EI-GOM (flask F6)

Determination Number (3 required)	Date	Time	Mass Bottle, Water & Soil (gm)	Temperature (°C)	Mass Density Pure Water* (gm/cm^3)	Specific Gravity of Soil at 20C
1	4/1/15	11:00	434.23	28.8	0.9960109	2.831
2	4/1/15	12:15	434.22	29.0	0.9959521	2.833
3	4/1/15	14:45	434.19	29.4	0.9958334	2.833
4	4/2/15	9:30	434.18	29.5	0.9958034	2.832
5	4/2/15	11:00	434.19	29.3	0.9958632	2.830
Average						2.832
Std. Dev.						0.001086116

Table B.72: Measurements of specific gravity at T_{ave} = 29°C for EI-GOM (flask F6)

Determination Number (3 required)	Date	Time	Mass Bottle, Water & Soil (gm)	Temperature (°C)	Mass Density Pure Water* (gm/cm^3)	Specific Gravity of Soil at 20C
1	3/31/15	10:00	433.70	35.4	0.9938622	2.838
2	3/31/15	12:20	433.68	36.1	0.9936090	2.853
3	3/31/15	14:30	433.63	36.4	0.9934990	2.846
4	3/31/15	16:45	433.65	36.2	0.9935724	2.846
5	3/31/15	18:45	433.64	36.3	0.9935358	2.846
6	3/31/15	20:45	433.63	36.5	0.9934621	2.849
Average						2.846
Std. Dev.						0.005334311

Table B.73: Measurements of specific gravity at T_{ave} = 36°C for EI-GOM (flask F6)

Measurements from Flask F7

MIT GEOTECHNICAL LABORATORY
SPECIFIC GRAVITY TEST
DATA SHEET

Project: PhD Thesis | Boring No.: | Date Start: 3/28/15
Test No.: | Sample No.: GOM | Date End:
Specimen Location: | Sample Depth: | Tested By: DMZ

Flask No.: F7 | Calibration Date: 1/30/15 | Flask Volume (cm^3): 273.55 | Flask Mass (gm): 142.15

Dry Mass of Soil		Before Test Going into Flask	After Test Taken out of Flask
Tare No.		4	FLO
Mass Tare+Wet Soil	(gm)		
Mass Tare+Dry Soil	(gm)	72.10	
Mass Tare	(gm)	46.85	
Mass Dry Soil	(gm)	25.25	24.17
Water Content	(%)		

Determination Number (3 required)	Date	Time	Mass Bottle, Water & Soil (gm)	Temperature (°C)	Mass Density Pure Water* (gm/cm^3)	Specific Gravity of Soil at 20C
1	3/28/15	15:15	430.83	21.8	0.9978186	2.860
2	3/28/15	16:30	430.83	22.6	0.9976365	2.876
3	3/28/15	17:30	430.80	22.2	0.9977283	2.857
4	3/28/15	18:30	430.78	22.4	0.9976826	2.855
5	3/28/15	19:30	430.80	22.4	0.9976826	2.861
6	3/30/15	10:45	430.78	22.4	0.9976826	2.855
7	3/30/15	11:30	430.78	22.6	0.9976365	2.859
8	3/30/15	12:15	430.78	22.6	0.9976365	2.859
Average						2.861
Std. Dev.						0.006256937

Table B.74: Measurements of specific gravity at T_{ave} = 22°C for EI-GOM (flask F7)

Determination Number (3 required)	Date	Time	Mass Bottle, Water & Soil (gm)	Temperature (°C)	Mass Density Pure Water* (gm/cm^3)	Specific Gravity of Soil at 20C
1	4/1/15	11:00	430.29	28.8	0.9960109	2.833
2	4/1/15	12:15	430.28	29.0	0.9959521	2.835
3	4/1/15	14:45	430.23	29.5	0.9958034	2.831
4	4/1/15	9:30	430.24	29.3	0.9958632	2.829
5	4/1/15	11:00	430.24	29.4	0.9958334	2.832
Average						2.832
Std. Dev.						0.001960569

Table B.75: Measurements of specific gravity at T_{ave} = 29°C for EI-GOM (flask F7)

Determination Number (3 required)	Date	Time	Mass Bottle, Water & Soil (gm)	Temperature (°C)	Mass Density Pure Water* (gm/cm^3)	Specific Gravity of Soil at 20C
1	3/31/15	10:00	429.75	35.7	0.9937543	2.846
2	3/31/15	12:20	429.71	36.0	0.9936455	2.842
3	3/31/15	14:30	429.71	36.1	0.9936090	2.845
4	3/31/15	16:45	429.69	36.3	0.9935358	2.845
5	3/31/15	18:45	429.67	36.4	0.9934990	2.841
Average						2.844
Std. Dev.						0.001872831

Table B.76: Measurements of specific gravity at T_{ave} = 36°C for EI-GOM (flask F7)

B.6 Gas Pycnometer Measurements

	Oven-dried Clay Density, ρ_s (g/cm^3)		
Trial Number	Kaolinite	RBBC	EI_GOM
1	2.618	2.779	2.729
2	2.628	2.771	2.726
3	2.628	2.770	2.728
4	2.618	2.765	2.725
5	2.612	2.774	2.725
Average	2.621	2.772	2.727
St. Dev.	0.007	0.005	0.002

Table B.77: AccuPyc1330 gas pycnometer measurements for oven-dried Kaolinite, RBBC and EI-GOM

Appendix C

TTS model for thermo-mechanical behavior of clay

Modèle TTS pour l'étude du comportement thermo-mécanique de l'argile

D.M. Zymnis[*1], A.J. Whittle[2] and X. Cheng[3]
[1] *Dept. of Civil & Environmental Engineering, MIT, Cambridge MA, USA*
[2] *Dept. of Civil & Environmental Engineering, MIT, Cambridge MA, USA*
[3] *Dept. of Civil Engineering, Tsinghua University, Beijing, China*
[*] *Corresponding Author*

ABSTRACT

'Shallow geothermal energy' is a term used to refer to the seasonal storage of thermal energy within the ground, typically at depths from about 10m below the ground surface (where temperatures are steady) to 100^{+}m. Heating and cooling of buildings is accomplished using high efficiency heat pumps while heat exchange can be effected through boreholes, piles and other buried infrastructures using open or closed systems. While utilization of shallow geothermal energy has become increasingly popular in sustainable building designs, urban district-scale applications of these resources are critically dependent on the response of the ground. For closed-system heat exchangers in clay, long-term ground deformations of clay can be anticipated due to coupling of thermo-mechanical properties.

Tsinghua ThermoSoil (TTS) is a recently developed constitutive model, based on fundamental thermodynamic principles, that provides a generalized framework for describing time and temperature dependence of soil behavior including the response under cyclic loading. This paper illustrates TTS model calibration and evaluation at the laboratory element level, using limited data available in the geotechnical literature, and demonstrates how predictive capabilities of the model can provide credible estimates of long-term ground response to cycles of seasonal heating and cooling.

C.1 Introduction

Seasonal storage and extraction of thermal energy within the ground can improve the efficiency of heating and cooling systems, and hence, contribute as a renewable source of energy for buildings. These shallow geothermal systems operate on the

principle that extant subsurface temperatures at depths greater than 10-15m are in the range 10-15°C (similar to average air temperatures in much of N. Europe and N. America; Brandl, 2006). In situ temperatures rise at a rate of 3°C/100m below depths of 100m, and hence the greatest potential for shallow geothermal systems lies within a small depth range. For many urban applications this involves seasonal heating and cooling of subsurface clays, with potential to induce deformations that affect foundations of adjacent structures or buried infrastructures.

Shallow geothermal energy installations can be designed as open-systems that utilize the local subsurface geohydrology or more generic closed-systems that involve two main components: 1) ground heat exchangers (typically plastic tubes that circulate the heat carrier fluid) that are embedded within boreholes or integrated in subsurface structural elements such as pile foundations ('energy piles', Brandl, 2006); and 2) Ground Source Heat Pumps (GSHP's) that connect the heat exchangers to the heating/cooling distribution system in the building. GSHP's operate on the principle that they produce 3-4kW of heat for every 1kW of electric power (i.e., a coefficient of performance, COP = 3-4, compared to direct electric heating).

While utilization of shallow geothermal energy has become increasingly popular in sustainable building designs, urban district-scale applications of these resources are critically dependent on the response of the ground. Laboratory tests have shown that clays can undergo permanent/irrecoverable strains due to thermal load cycles. For example, Abuel-Naga et al. (2006) have measured the volumetric response for specimens of high plasticity Bangkok clay consolidated at water contents close to the liquid limit (I_p = 60%, w_L = 103%, w = 90-95%) with stress histories corresponding to OCR's = 1-8 that are heated under drained conditions from ambient (22°C) to 90°C and then cooled to their original temperature, Figure C.1. The results range from large net compressive strains for the normally consolidated specimen (De_{vol} = 5.5%) to small net dilation (De_{vol} = -0.4%) at OCR = 8.

Figure C.2a presents three drained isotropic, isothermal compression tests on the Bangkok clay at T = 25°, 70°, 90°C, and Figure C.2b shows results from a fourth test where the specimen is loaded after a cycle of heating and cooling (25°-90°-25°C). These data confirm that the virgin consolidation line varies with temperature while heating and

cooling produces an apparent overconsolidation similar to drained creep (secondary compression) as observed by Leroueil and Marques (1996). The underlying causes of this behavior may ultimately be linked to the nanoscale surface force interactions in clay-water systems (i.e., balance of attractive and repulsive forces between clay particles).

Although the temperature change imposed in these examples far exceeds the range expected in shallow geothermal systems, the results serve to illustrate the importance of coupling of thermo-mechanical properties for clays. To date most analyses of thermo-mechanical problems in geotechnical engineering have assumed either thermo-elastic (e.g., Booker & Savvidou, 1985) or thermo-plastic (Hueckel & Borsetto, 1990) properties of the clays. Models of the latter type consider thermal hardening of the yield surface based on conventional elasto-plastic, critical state soil models. This assumption limits model capabilities for describing material response under fluctuating/cyclic thermal or mechanical loading conditions.

This paper introduces an alternative framework based on conservation laws and non-equilibrium thermodynamics as developed by Zhang and Cheng (2013). The formulation, referred to as the Tsinghua ThermoSoil model (TTS) provides a more general framework that can account for the accumulation of mechanical strains through cycles of heating and cooling.

C.2 Summary of TTS Model

The TTS model (Zhang & Cheng, 2013) was developed in order to provide a comprehensive framework for describing the coupled Thermo-Hydro-Mechanical (THM) response of fully saturated clays and sands. The model is based on the formulation of Granular Solid Hydrodynamics (GSH; after Jiang & Liu, 2007, 2009), which assumes that a granular system at rest can be described by its elastic energy. Quasi-static external loading produces inelastic deformations and a transient elastic response (due to relaxation of the elastic potential energy). The reversible energy processes of the model are expressed as elastic deformations occurring at the soil particle contacts (stored elastic potential energy), while irreversible processes include the energy dissipation mechanisms occurring both at the macroscopic and microscopic (rolling and sliding at particle contacts) scales. These phenomena are expressed within the continuum model by a

double entropy theory, where the kinetic energy at the microscopic level influences the macroscopic response through a conversion of granular to total entropy.

Zhang and Cheng (2013) represent clay as an isothermal mixture of continuous solid and liquid phases. The liquid phase is partitioned into i) free water, which fills the macroscopic pores and flows according to Darcy's law, and ii) bound water, which is fully absorbed by the clay particles and fills the microscopic pore space. When the clay is heated, part of the bound water is converted to free water, while during cooling the mass of bound water remains unchanged. This provides the underlying thermo-mechanical coupling in the TTS model.

The TTS model expresses the effective stresses, $\sigma_{ij}^{'}$, as the derivative of the elastic potential energy function, ω_e:

$$\sigma_{ij}^{'} = \frac{\partial \omega_e}{\partial \varepsilon_{ij}^{e}} \tag{1}$$

where ε_{ij}^{e} is the elastic strain tensor (Zhang & Cheng, 2014).

Hyperelastic stress-strain properties can then be derived from the elastic potential energy function:

$$\begin{aligned} \omega_e = {} & \frac{2}{5} B\left(\varepsilon_v^e + c\right)^{1.5} \left(\varepsilon_v^e\right)^2 \\ & + B\left(\varepsilon_v^e + c'\right)^{1.5} \left[\xi \left(\varepsilon_s^e\right)^2 + \frac{\zeta}{\sqrt{6}} \cos 3\theta \left(\varepsilon_{III}^e\right)^2 \right] \\ & + \int 3K_e \beta_T \Delta T d\varepsilon_v^e \end{aligned} \tag{2a}$$

$$\text{and } B = B_0 \exp\left(B_1 \rho_d\right) \tag{2b}$$

$$\dot{\rho}_d = \rho_d \dot{\varepsilon}_v \tag{2c}$$

$$\Delta T = T - T_0 \tag{2d}$$

where T and T_0 are the current and reference temperature, r_d is the dry density of the clay, K_e and b_T are the secant elastic bulk modulus and thermal expansion of the clay skeleton, respectively. $\left(\varepsilon_v^e, \varepsilon_s^e, \varepsilon_{iii}^e\right)$ are the three invariants of the elastic strain tensor, and q the Lode angle (in elastic strain space). Values of B_0, B_1, c, c' z, x, are material constants.

The parameters z, x, constrain possible effective stress states of the clay within a 'state boundary surface' (as proposed by Jiang & Liu, 2009), while c is related to the

cohesive component of shear strength and c' defines the critical state criterion for shearing to large strains. Equations 2b and 2c describe the density evolution during drained compression and represent the virgin consolidation behavior typically observed for clays.

The model assumes that the total strain rate is decomposed into the sum of elastic and irrecoverable/dissipative components:

$$\dot{\varepsilon}_{ij}^{e} = \dot{\varepsilon}_{ij} - \dot{\varepsilon}_{ij}^{D} \tag{3}$$

Energy dissipation is related to the concept of granular entropy that considers the rolling and sliding at particle contacts and the conversion of bound to free water. The principal drivers for granular entropy production are the applied/total strain ($\dot{\varepsilon}_v, \dot{\varepsilon}_s$) and temperature rates ($\dot{T}$). The entropy conjugate 'granular temperature', T_g, is a state variable that reflects these processes. The evolution of granular temperature is related to strain and temperature rates through a series of migration coefficients, ($m_2 - m_5$) as follows:

$$\dot{T}_g = \frac{m_2 m_4 (\dot{\varepsilon}_s)^2 + m_2 m_3 m_4 (\dot{\varepsilon}_v)^2}{\rho_d} + \frac{m_5 p' \alpha_{bf} \phi_{bw} (\dot{T})^2}{3(1-\phi)\rho_d} - m_4 \frac{T_g}{\rho_d} \tag{4}$$

where φ and φ_{bw} are the total porosity and porosity of the bound water, a_{bf} is a constant that defines the rate of conversion of bound to free water and p' is the mean effective stress.

The rates of dissipative strain are then related to the current state of granular temperature and elastic strain:

$$\begin{aligned} \dot{\varepsilon}_v^D &= 3m_1 (T_g)^a (\varepsilon_v^e - \varepsilon_v^h) \\ \dot{\varepsilon}_s^D &= (T_g)^a (\varepsilon_s^e - \varepsilon_s^h) \end{aligned} \tag{5}$$

where the coefficient $m_1 = m_{10}(1+L_T DT)$, a is a constant that controls the strain rate dependency of the clay (a = 0.5 corresponds to rate independence), and ($\varepsilon_v^h, \varepsilon_s^h$) are components of the hysteretic strain that describe hysteresis during cyclic loading.

Zhang and Cheng (2013) propose the following evolution equations for hysteretic strain rates:

$$\dot{\varepsilon}_v^h = \dot{\varepsilon}_v^D - w\frac{\dot{\varepsilon}_v^D \cdot \varepsilon_v^h + \dot{\varepsilon}_s^D \cdot \varepsilon_s^h}{h^{0.5}\left[\frac{(\varepsilon_v^h)^2}{3} + (\varepsilon_s^h)^2\right]^{0.75}}\varepsilon_v^h$$

$$\dot{\varepsilon}_s^h = \dot{\varepsilon}_s^D - w\frac{\dot{\varepsilon}_v^D \cdot \varepsilon_v^h + \dot{\varepsilon}_s^D \cdot \varepsilon_s^h}{h^{0.5}\left[\frac{(\varepsilon_v^h)^2}{3} + (\varepsilon_s^h)^2\right]^{0.75}}\varepsilon_s^h \qquad (6)$$

where h is a constant, $w = w_0(1 + w_T \Delta T)$ and:

$$\begin{cases} w_0 = 1; & \dot{\varepsilon}_{ij}^D \varepsilon_{ij}^h > 0 \\ 0 < w_0 = w_{given} < 1; & \dot{\varepsilon}_{ij}^D \varepsilon_{ij}^h \le 0 \end{cases} \qquad (7)$$

It is important to note that the model does not require a separate definition of the loading reversal condition typically used in elasto-plastic formulations.

C.3. Model Calibration

Table C.1 summarizes the state variables used by the TTS model. The model is driven by specified rates of strain and temperature. Initial values of the other state variables can be derived by consolidating from a reference slurry state.

The following paragraphs illustrate TTS model calibration for the high plasticity Bangkok clay. The input constants that affect the hydrostatic compression of clays are B_0, B_1, c, m_1, m_2 and m_3. As a first step, the slope of the normalized virgin consolidation line (VCL) depends solely on B_1, as shown in Figure C.3, while the normalized unload-reload curve depends on parameters c, h and the product $m_1(m_2m_3)^{0.5}$ (eqns. 4,5). As an example, the effect of parameter h is illustrated in Figure C.4. Specific values of m_2 and m_3 can be calibrated from shear tests. The final part of the mechanical calibration involves setting the correct location of the VCL line by calibrating parameter B_0 (see Figure C.5).

The input constants that control the thermal component of the TTS model are α_{bf}, L_T, w_T, m_4 and m_5. The TTS model successfully captures the shift of the VCL for different temperature levels. As shown in Figure C.6, the temperature dependence of the VCL is controlled by L_T (eqn. 5).

The TTS model successfully simulates the thermal volumetric strains induced by heating and cooling Bangkok Clay samples of different initial stress. Figure C.7 illustrates the effects of parameter m_5 on the induced thermal volumetric strains from which it can be concluded that the TTS model is able to capture a wide range of thermal behaviors. It should be pointed out that thermal strains are also affected by input constants α_{bf} and m_4.

C.4. Evaluation of TTS Model

As already presented in Figures C.3-C.7, the TTS model represents a very powerful tool for simulating important soil behavior features such as hydrostatic consolidation and thermal response of clays observed at the laboratory element level. Zymnis and Whittle (2014) have shown cyclic thermal loading induced by shallow geothermal installations can lead to considerable thermal volumetric strains and hence, the study of cyclic thermal loading is crucial when designing shallow geothermal installations. One of the most important advantages of the TTS model is its ability to characterize the accumulation of volumetric strain during continuous cycles of heating and cooling.

Figure C.8 illustrates the predicted strain accumulation over seasonal cycles of heating and cooling with DT = 5 – 65°C. The TTS model predicts that heating and cooling of normally consolidated Bangkok Clay ultimately trends to same maximum volumetric strain (ε_{vol} = 25%) independent of the imposed temperature range, while rates of strain accumulation are directly linked to the imposed DT. Figure C.9 shows further cyclic strain accumulation results for initial OCR's = 1.0 – 8.0 with DT = 65°C. Continuous heating and cooling of highly overconsolidated clay (OCR = 8) results in longterm accumulation of large dilative volumetric strain (ε_{vol} = 15%), while clays of intermediate OCR produce smaller accumulated strain. Accumulation of volumetric strain stops once the "saturation line" is reached. As shown in the right of Figure C.9, the "saturation line" is represented by a line parallel to the VCL, the location of which depends on parameters h, w and $m_1(m_2m_3)^{0.5}$.

The results presented herein are preliminary but demonstrate the capabilities of the TTS model to describe volumetric strain accumulation due to continuous heating and

cooling. We are not aware of any existing laboratory data to validate the model predictions.

C.5. Conclusions

The Tsinghua ThermoSoil model (TTS; Zhang & Cheng, 2013) presents a novel theoretical framework for simulating the coupled thermo-hydro-mechanical properties of clays. The model uses a double entropy approach (after Jiang & Liu, 2009) to capture effects of energy dissipation at the microscopic particulate contact level on continuum behavior. The model is then able to describe strain rate and thermal dependence of clay properties.

This paper provides a brief illustration to show that the TTS model is able to simulate familiar aspects of thermal consolidation of clays as well as the long-term, progressive accumulation of strains associated with seasonal heating and cooling processes for shallow geothermal systems installed in clays. Further laboratory studies of thermo-mechanical properties are now needed to validate the model predictions.

Acknowledgements

The Authors are grateful for seed funding provided by the Tsinghua-Cambridge-MIT low carbon energy university alliance (TCM-LCEUA). The first Author (DMZ) also received a Robert A Brown, Onassis Foundation, Exponent and Martin Foundation Fellowships for her Ph.D. studies.

References

Abuel-Naga, H.M., Bergado, D.T., Ramana, G.V., Grino, L., Rujivipat, P. & They, Y. (2006) "Experimental evaluation of engineering behavior of Bangkok clay under elevated temperature," *ASCE Journal of Geotechnical and Geoenvironmental Engineering*, 132(7), 902-910.

Booker, J.R. & Savvidou, C. (1985), "Consolidation around a point heat source," *International Journal for Numerical and Analytical methods in Geomechanics*, 9, 173-184.

Brandl, H. (2006), "Energy foundations and other thermo-active ground structures," *Geotechnique,* 56 (2), 81-122.

Hueckel, T. & Borsetto, M. (1990) "Thermoplasticity of saturated soils and shales: Constitutive equations," *ASCE Journal of Geotechnical Engineering*, 116(2), 1765-1777.

Jiang, Y. & Liu, M. (2007) "From elasticity to hypoplasticity: dynamics of granular solids," Phys Rev Lett. 99(10): 105501

Jiang, Y. & Liu, M. (2009) "Granular solid hydrodynamics," *Granular Matter*, 11(3), 139–156, 2009.

Leroueil, S. & Marques, M. E. S. (1996)," Importance of strain rate and temperature effects in Geotechnical Engineering," *ASCE Measuring and Modeling Soil Behavior (GSP 61),* 1-60.

Zhang Z. & Cheng X. (2013), "Simulation of nonisothermal consolidation of saturated soils based on a thermodynamic model," *Scientific World Journal*, Hindawi Publishing Co., http://dx.doi.org/10.1155/2013/192163.

Zhang Z. & Cheng X. (2014), "Effective stress in saturated soil: a granular hydrodynamics approach," *Granular Matter*, DOI 10.1007/s10035-014-0524-2.

Zymnis, D. M. & Whittle, A. J. (2014), "Numerical Simulation of a Shallow Geothermal Heating/Cooling System," *Proc. ASCE GeoCongress GSP 234*, 2767-2776.

Loading	
$\dot{\varepsilon}_v, \dot{\varepsilon}_s$	Total strain rate
$\dot{T}$	Temperature rate
State Variables	
f_{bw}, f_{fw}	Bound and free water porosity
$\varepsilon_v^e, \varepsilon_s^e$	Elastic strains
$\varepsilon_v^h, \varepsilon_s^h$	Hysteretic strains
T_g	Granular temperature
ρ_d	Dry density

Table C.1. State variables used by TTS Model

Mech. Properties		m_3	1.0
B_0 [MPa]	0.2	m_4 [kg/°Cm^3]	60000
B_1 [m^3/kg]	0.0043	a [-]	0.5
c [-]	0.14	**Thermal Properties**	
h [-]	0.03	α_{bf} [1/°C]	0.05
w [-]	0.96	m_5[1/m^2s^3°C]	0.001
m_1	1.0	L_T [1/°C]	0.0075
m_2	50.0	w_T [1/°C]	0.001

Table C.2. Input constants used in TTS calibration for Bangkok Clay

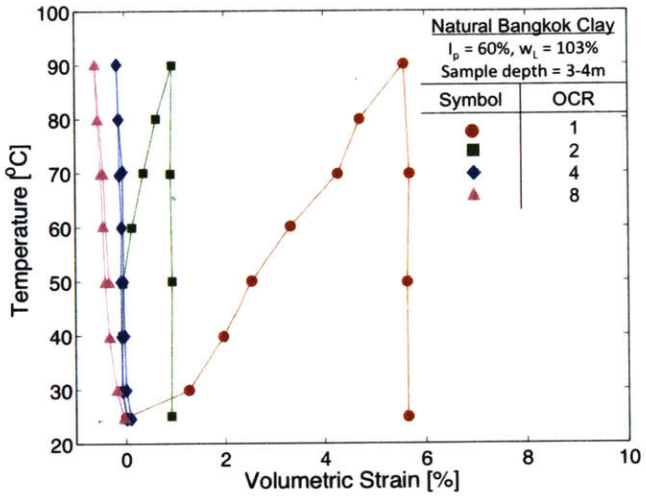

Figure C.1: Effect of OCR on volumetric strain for drained heating/cooling cycle of Bangkok Clay (after Abuel-Naga et al., 2006)

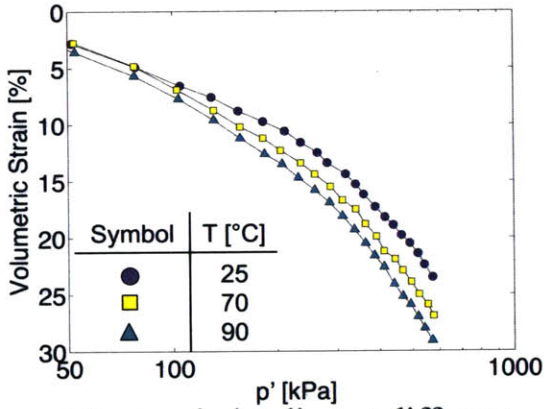

a) Isotropic loading at different temperatures

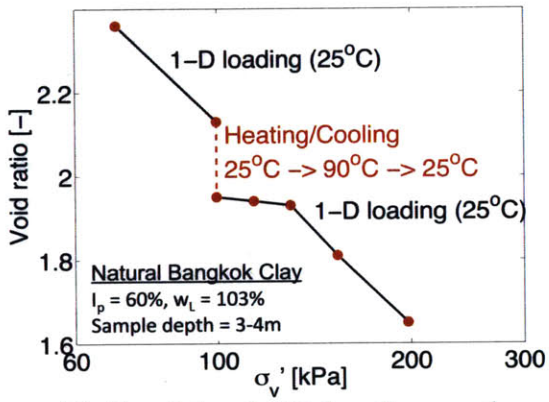

b) Combined 1D loading and heating/cooling

Figure C.2: Dependence of location of virgin consolidation line on temperature of Bangkok Clay (after Abuel-Naga et al., 2006)

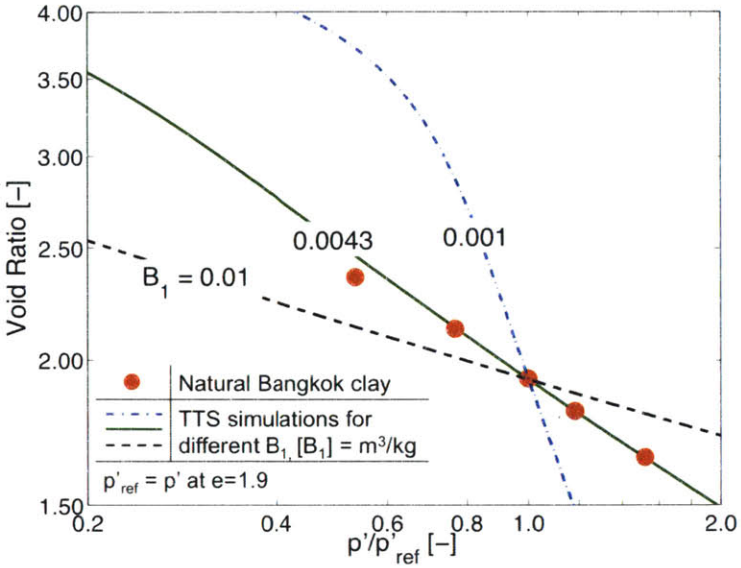

Figure C.3: Effect of B_1 on slope of VCL as predicted by the TTS model for soft Bangkok clay (Abuel-Naga et al., 2006)

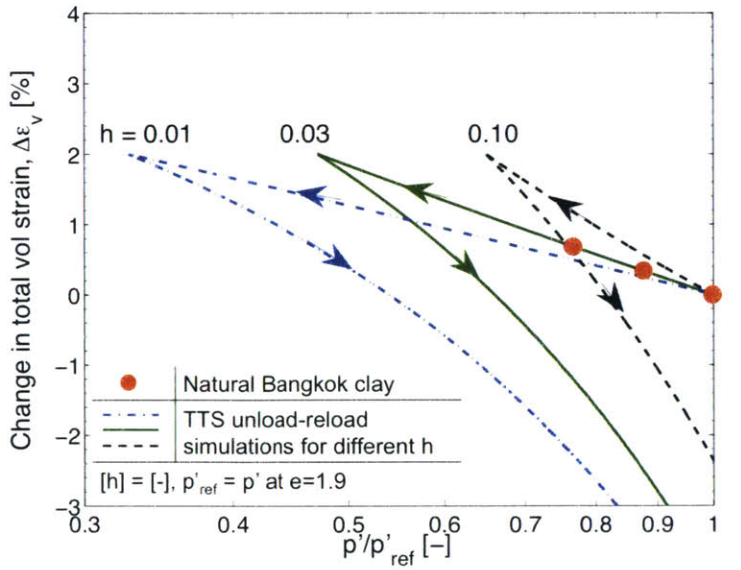

Figure C.4: Effect of h on unload-reload curve as predicted by the TTS model for soft Bangkok clay (Abuel-Naga et al., 2006)

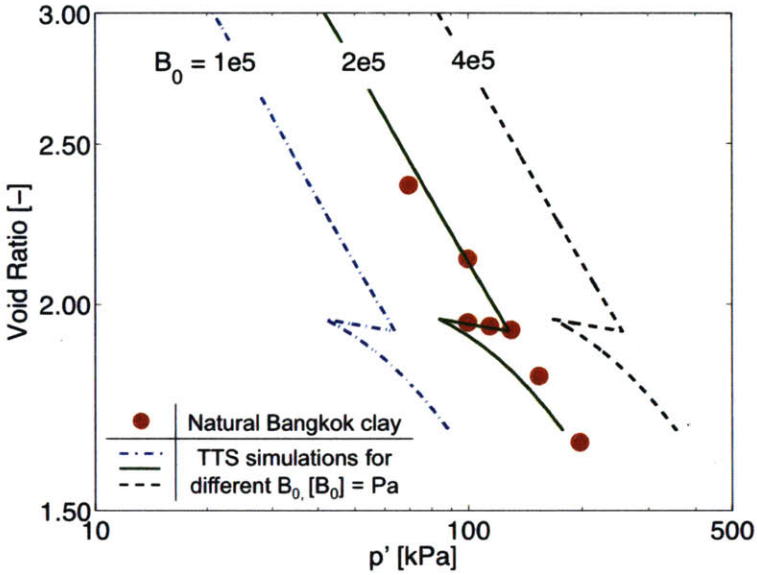

Figure C.5: Effect of B_0 on location of VCL as predicted by the TTS model for soft Bangkok clay (Abuel-Naga et al., 2006)

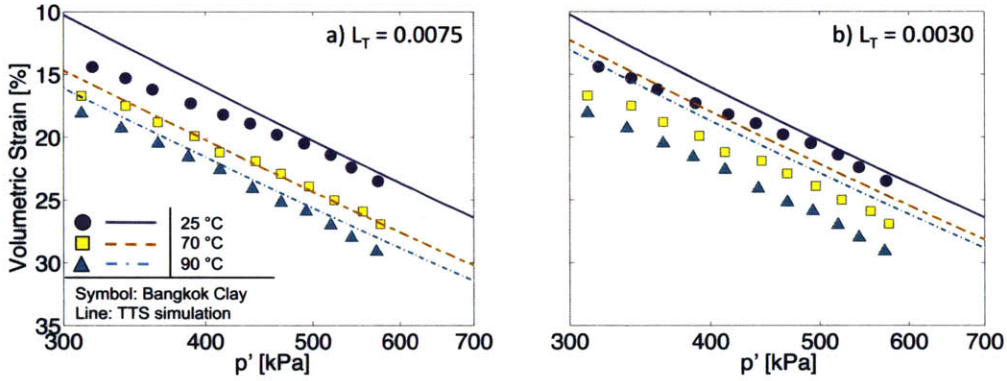

Figure C.6: Effect of L_T on dependence of location of VCL on temperature for soft Bangkok clay (Abuel-Naga et al., 2006)

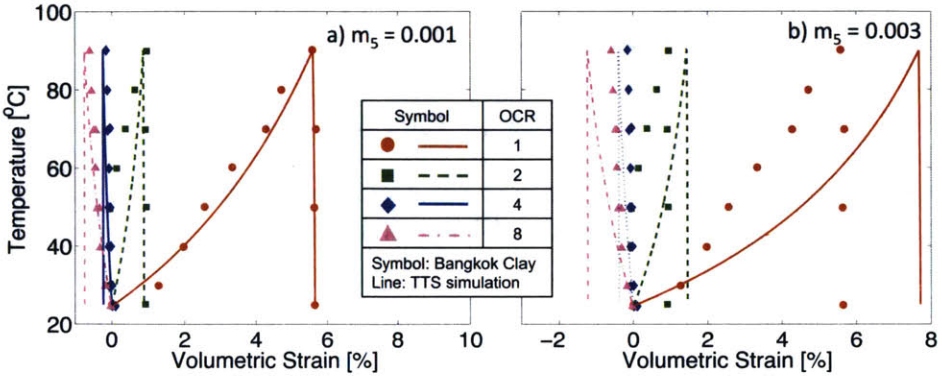

Figure C.7: Thermal volumetric strains corresponding to Bangkok Clay samples of different OCRs

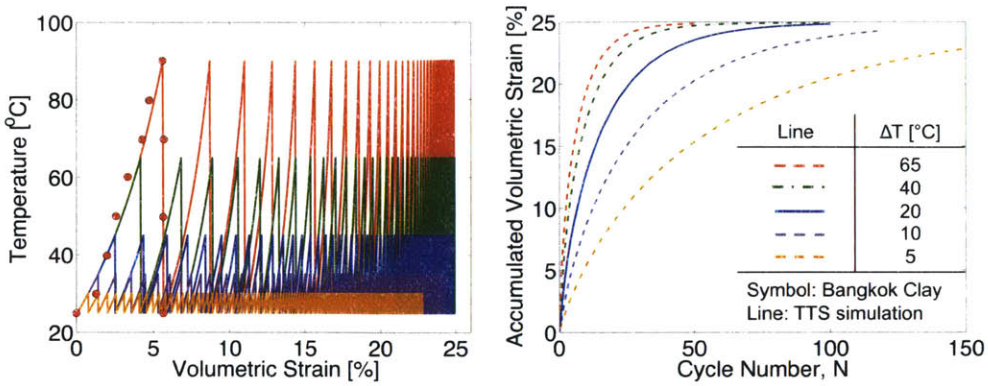

Figure C.8: Cyclic thermal tests on NC clay for different heating and cooling temperatures as predicted by the TTS model

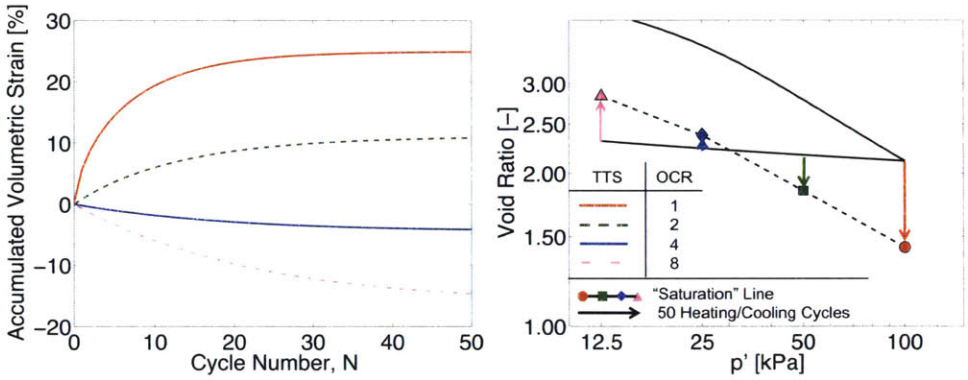

Figure C.9: Effect of stress history on accumulation of volumetric strains due to cyclic heating-cooling Bangkok Clay as predicted by TTS

Appendix D

Derivation of Finite Difference Equations in Axisymmetric Space of Variable Radial Spacing

As shown schematically in Figure D.1, the radial spacing at point $i+1$, $\Delta r_{i+1} = \alpha_r \Delta r_i$. The change in temperature at the radial direction is thus given by:

$$\frac{\partial T_{i,j}^{k+1}}{\partial r} = \left(\frac{T_{i,j+1}^{k} - T_{i,j-1}^{k}}{\Delta r_i + \Delta r_{i+1}} \right) = \frac{T_{i,j+1}^{k} - T_{i,j-1}^{k}}{\Delta r_i \left(1+\alpha_r\right)} \tag{D.1}$$

The second derivative of temperature in the radial direction can be viewed as the first derivative of temperature flux (equation D.1) as shown below:

$$\begin{aligned}
\frac{\partial^2 T_{i,j}^{k+1}}{\partial r^2} &= \frac{\partial}{\partial r}\left(\frac{\partial T_{i,j}^{k+1}}{\partial r} \right) = \frac{1}{\frac{\Delta r_i + \Delta r_{i+1}}{2}} \left(\frac{T_{i,j+1}^{k} - T_{i,j}^{k}}{\Delta r_{i+1}} - \frac{T_{i,j}^{k} - T_{i,j-1}^{k}}{\Delta r_i} \right) \\
&= \frac{2}{\Delta r_i \left(1+\alpha_r\right)} \left(\frac{T_{i,j+1}^{k} - T_{i,j}^{k}}{\alpha_r \Delta r_i} - \frac{T_{i,j}^{k} - T_{i,j-1}^{k}}{\Delta r_i} \right) \\
&= \frac{2}{\Delta r_i \left(1+\alpha_r\right)} \left(\frac{T_{i,j+1}^{k} - T_{i,j}^{k}}{\alpha_r \Delta r_i} - \frac{\alpha_r T_{i,j}^{k} - \alpha_r T_{i,j-1}^{k}}{\alpha_r \Delta r_i} \right) \\
&= \frac{2}{\alpha_r \left(1+\alpha_r\right) \Delta r_i^2} \left[\alpha_r T_{i,j-1}^{k} - \left(1+\alpha_r\right) T_{i,j}^{k} + T_{i,j+1}^{k} \right]
\end{aligned} \tag{D.2}$$

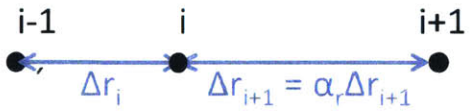

Figure D.1: Radial spacing Δr_i at point i, relative to radial spacing Δr_{i+1} at point $i+1$

Appendix E

TTS Model Prediction of K_0 with Stress History and Effect on BHE Simulation

Using the formula suggested by Jaky (1944) K_{0NC} = 0.6 for Geneva clay with friction angle of 24°.

$$K_{0NC} = 1 - \sin\phi \tag{E.1}$$

The value of the coefficient of earth pressure at rest for overconsolidated clays K_{0OC} is greater than that for normally consolidated clay and varies with OCR (after Schmidt, 1966):

$$K_{0OC} = K_{0NC}\left(OCR\right)^{\sin\phi'} \tag{E.2}$$

For example, for overconsolidated Geneva clay with OCR = 8, using equation E.2 results in K_{0OC} = 1.7.

As discussed in Chapter 3, the TTS input constant, ξ, is calibrated based on K_{0NC} (for Geneva clay, ξ = 0.1). Figure E.1 presents vertical and horizontal effective stress calibrated for Geneva clay. It is observed that for NC clay, K_{0NC} = 0.6 but for OCR = 8, K_{0OC} = 0.42, which is significantly lower than the expected value K_{0OC} = 1.7. If parameter ξ is calibrated for K_{0OC} = 1.7, ξ = -0.038 which results in K_{0NC} = 1.5 (Figure E.2) which is also unrealistic. Failing to predict a correct K_0 is a limitation of the TTS model that should be addressed in the future. The effects of this limitation on the thermo-hydro-mechanical response of the TTS model are discussed herein.

Table E.1 presents TTS model calibrations based on K_{0NC} and K_{0OC} (referred to as Models 1 and 2, respectively). Furthermore, the thermal and hydraulic constants were selected based on Geneva clay calibrations and are the same as those used in the parametric study (Table 4.4). The FD simulator was run using these two sets of parameters for OCR = 8. The Geneva clay layer is assumed to have a thickness of 10m and the radial dimension is R = 3m. The boundary conditions assumed in both models are summarized in Figure E.3. Figure E.4 presents the initial effective stress distribution assumed in each model. Both models have the same vertical effective stress distribution

but different horizontal stress distribution corresponding K_{0OC} = 0.42 for Model 1 and K_{0OC} = 1.7 for Model 2.

The simulations are run for 10 years and comparisons of the resulting thermo-hydro-mechanical response are presented. From Figure E.5 it can be seen that the two models produce the same temperature evolution (thermal response is uncoupled from mechanical response as described previously). From Figure E.6 it is observed that Model 1 predicts excess pore pressures that are slightly smaller than Model 2 (both cases generate negative excess pore pressures and the difference is less than 15kPa at all times). The difference between the two models decreases after four years of operation (Figure E.6b). Finally from Figure E.7 it can be deduced that the two models predict similar surface vertical displacements, with Model 2 predicting slightly higher heave than Model 1 (maximum difference being ~ 4mm).

It can therefore be concluded that although the TTS model does not accurately represent K_{0OC}, the resulting THM response is not significantly affected. It was therefore decided that all three Geneva clay layers assumed in the parametric study would have the same TTS model input constants, even though these result in initial horizontal stresses that are inconsistent with established correlations. This discrepancy has negligible impact on the results of the parametric study presented in Chapter 5.

TTS input constant	Model 1	Model 2
B_0 [Pa]	3.8×10^{-4}	8.5×10^{-4}
B_1 [m^3/kg]	0.0162	0.0162
h [-]	0.05	0.05
$m_{1,0}$ [-]	1.0	1.0
m_2 [-]	150	150
c' [-]	0.0863	0.0863
ξ [-]	0.1	-0.038
α_{bf} [1/°C]	0.0237	0.0237
m_5 [s^3/m^2°C]	0.1	0.1
L_T [1/°C]	0.02	0.02
a [-]	0.5	0.5
m_4 [kg/m^3 s]	$6x10^4$	$6x10^4$
m_3 [-]	1.0	1.0
c [-]	0.01	0.01
w [-]	1.0	1.0

Table E.1: TTS model input parameters assumed in Model 1 and Model 2 Geneva clay calibrations

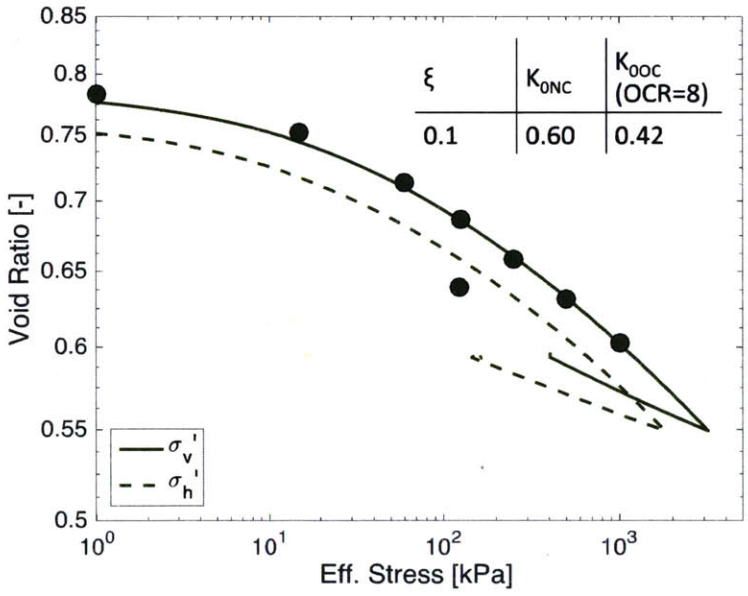

Figure E.1: Vertical (solid line) and horizontal (dashed line) effective stress assumed with Geneva clay calibration Model 1

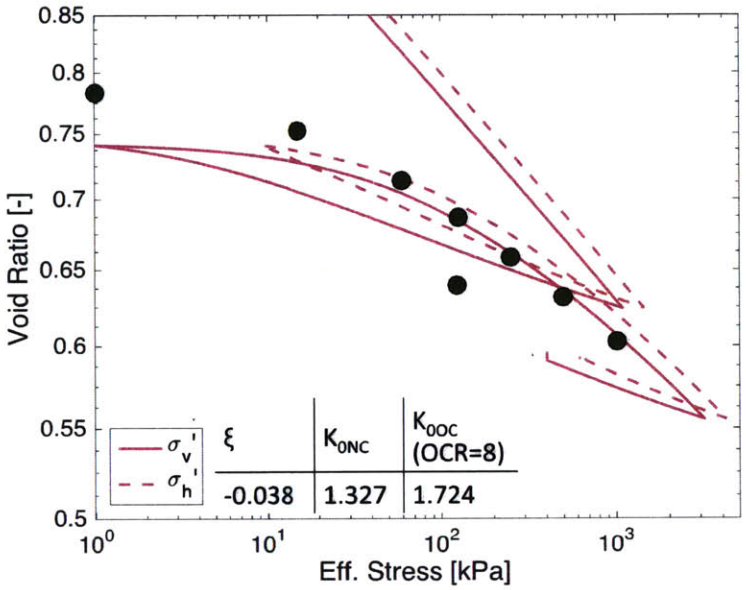

Figure E.2: Vertical (solid line) and horizontal (dashed line) effective stress assumed with Geneva clay calibration Model 2

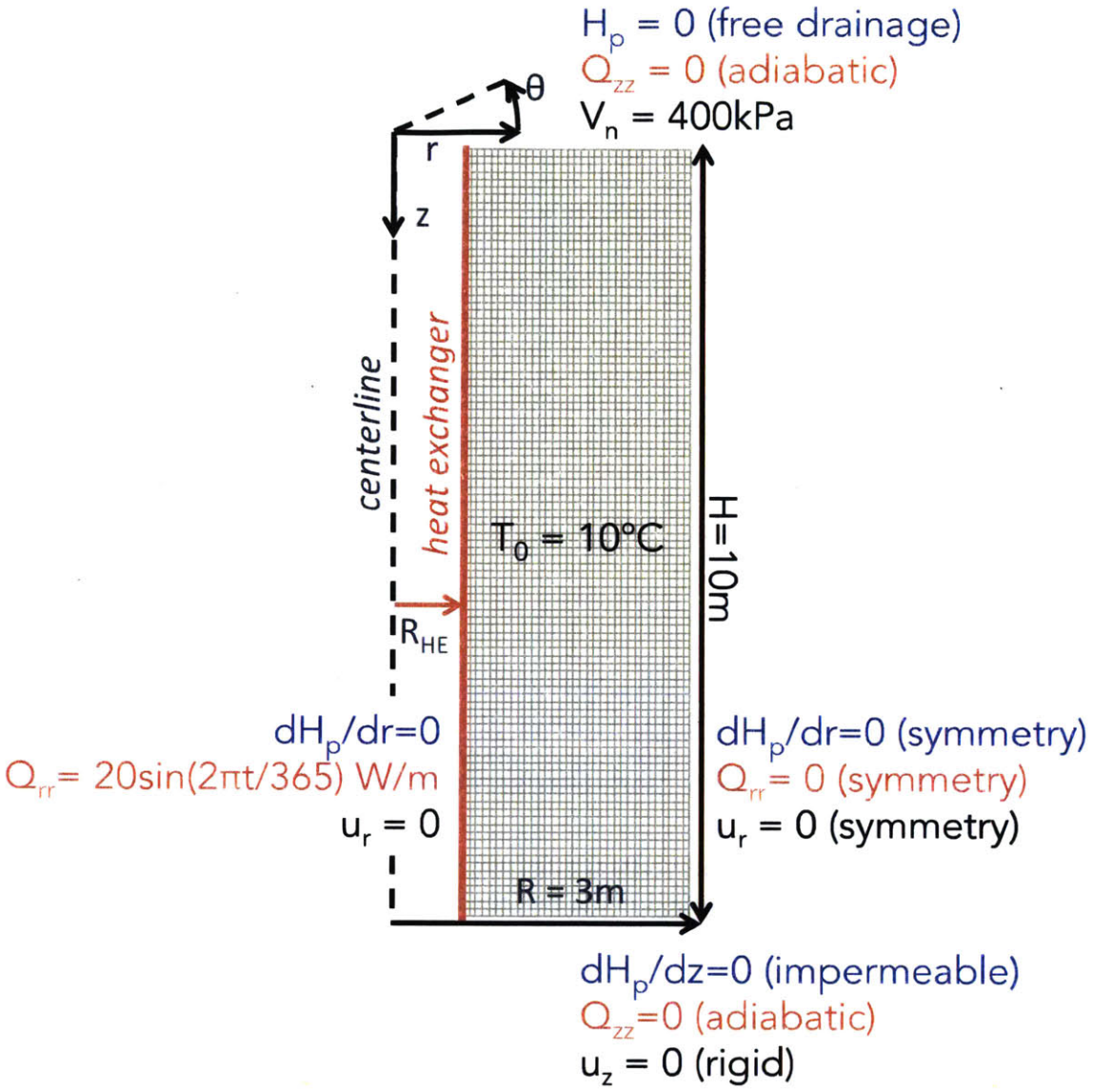

Figure E.3: Boundary conditions assumed in THM simulations

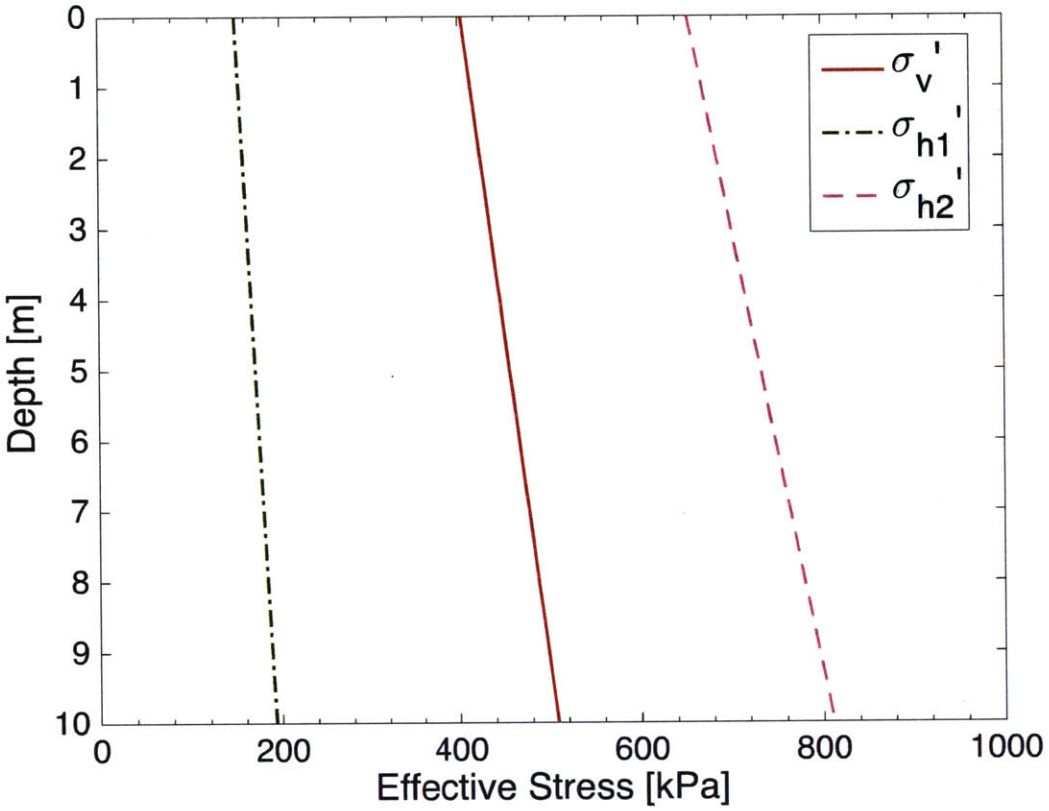

Figure E.4: Initial horizontal and vertical effective stress distribution versus depth assumed in the two models

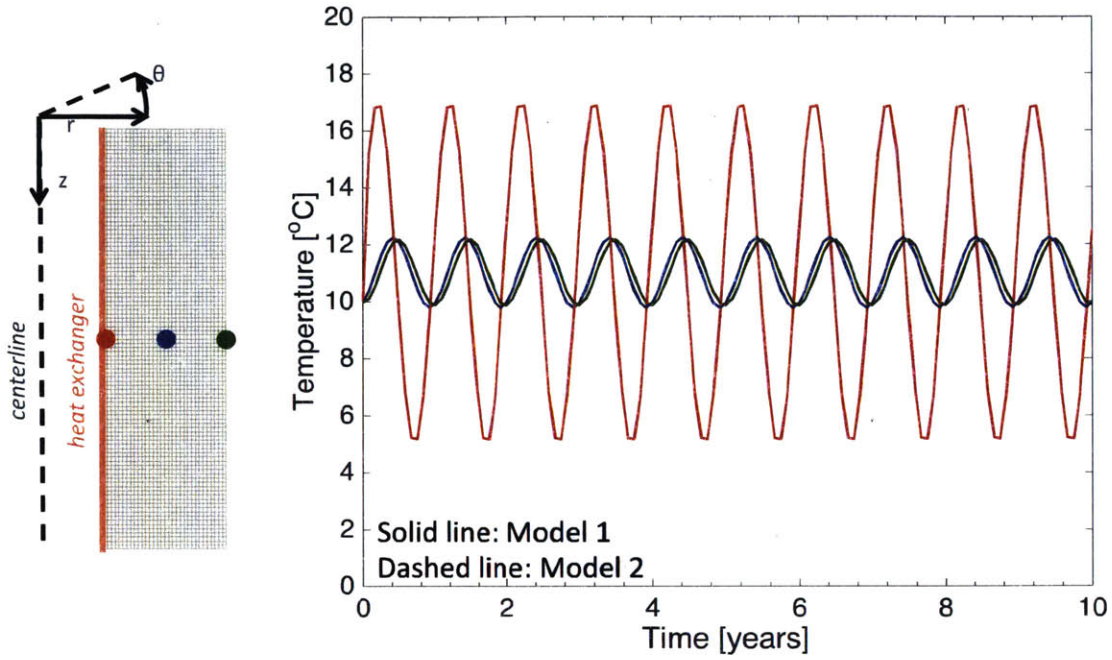

Figure E.5: Comparison of predictions of temperature evolution at different points of the axisymmetric geometry for model 1 (solid line) and model 2 (dashed line)

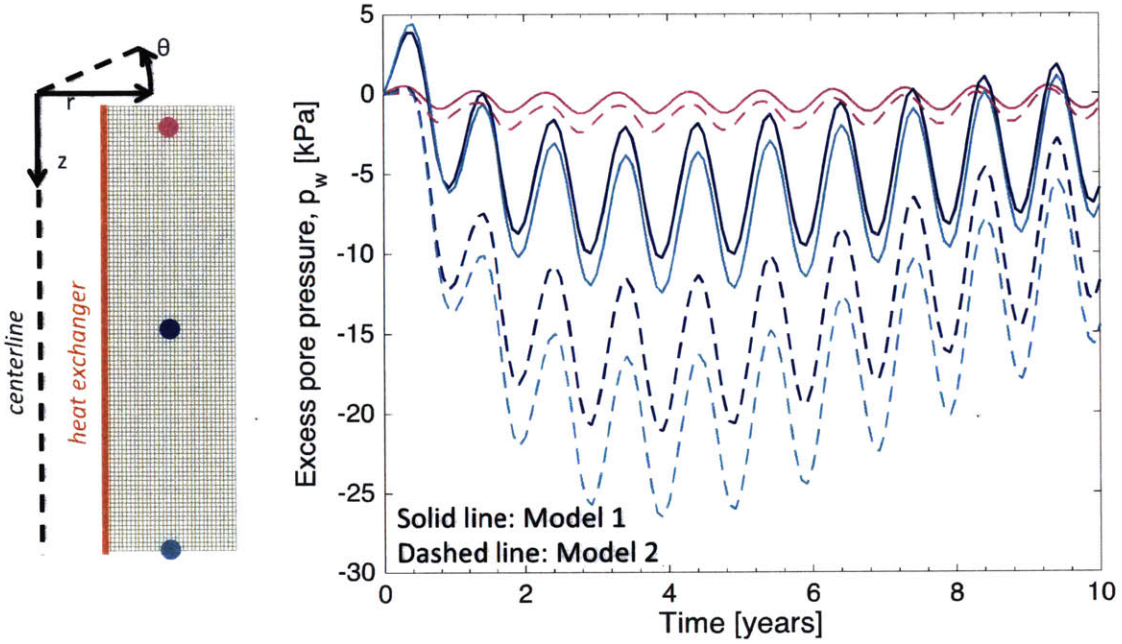

a) Excess pore pressure versus time

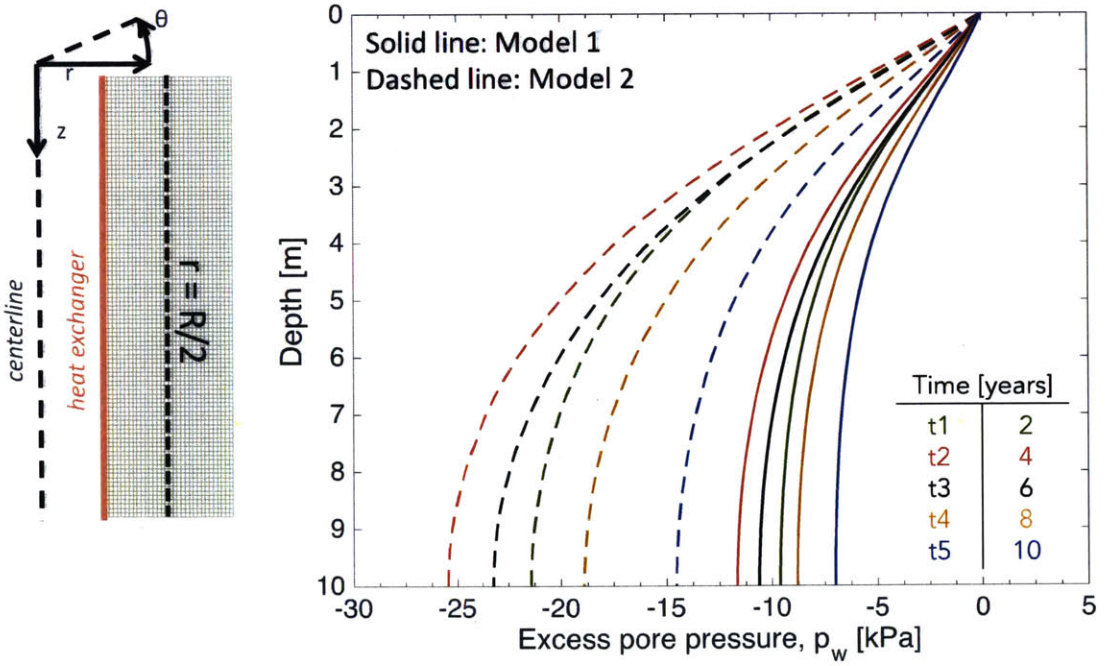

b) Excess pore pressure versus depth

Figure E.6: Comparison of predictions of excess pore pressure at different points of the axisymmetric geometry for model 1 (solid line) and model 2 (dashed line)

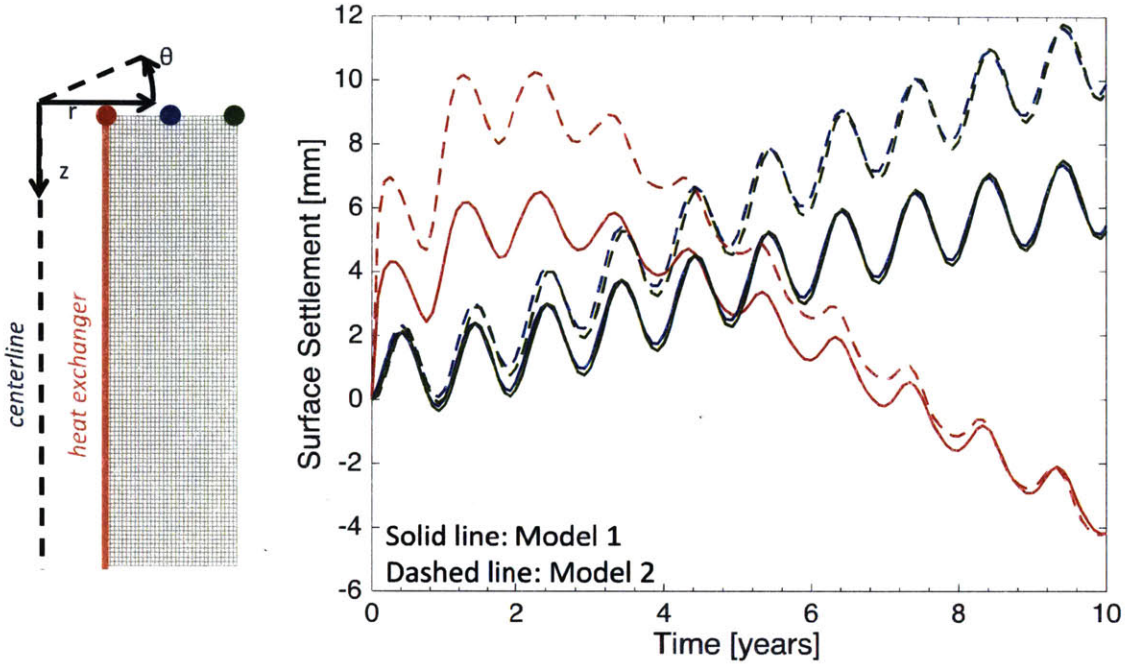

Figure E.7: Comparison of predictions of surface settlement evolution at different points of the axisymmetric geometry for model 1 (solid line) and model 2 (dashed line)